

به نام خدا



# مرکز دانلود رایگان مهندسی متالورژی و مواد

[www.Iran-mavad.com](http://www.Iran-mavad.com)



# THERMOTROPIC LIQUID CRYSTAL POLYMERS

*Thin-film Polymerization,  
Characterization, Blends,  
and Applications*

EDITED BY

**Tai-Shung Chung, Ph.D.**

*Department of Chemical and Environmental Engineering  
National University of Singapore*

*Institute of Materials Research and Engineering  
Singapore*



[www.iran-mavad.com](http://www.iran-mavad.com)

مرجع دانشجویان و مهندسين مواد

# **Thermotropic Liquid Crystal Polymers: Thin-film Polymerization, Characterization, Blends, and Applications**

a **TECHNOMIC**® publication

Technomic Publishing Company, Inc.  
851 New Holland Avenue, Box 3535  
Lancaster, Pennsylvania 17604 U.S.A.

Copyright © 2001 by Technomic Publishing Company, Inc.  
All rights reserved

No part of this publication may be reproduced, stored in a retrieval system, or transmitted, in any form or by any means, electronic, mechanical, photocopying, recording, or otherwise, without the prior written permission of the publisher.

Printed in the United States of America  
10 9 8 7 6 5 4 3 2 1

Main entry under title:

Thermotropic Liquid Crystal Polymers: Thin-film Polymerization,  
Characterization, Blends, and Applications

A Technomic Publishing Company book

Bibliography: p.

Includes index p. 351

Library of Congress Catalog Card No. 00-111664  
ISBN No. 1-56676-943-4

[www.iran-mavad.com](http://www.iran-mavad.com)

مرجع دانشجویان و مهندسين مواد

# Contents

*Preface*

*Acknowledgements*

*List of Contributors*

## **1. INTRODUCTION OF LIQUID CRYSTALLINE MATERIALS**

TAI-SHUNG CHUNG, SI-XUE CHENG and MICHAEL JAFFE

1. History of Development of Liquid Crystalline Materials
2. Classification and Structure of Liquid Crystalline Materials
3. Liquid Crystal Textures
4. Theories of Liquid Crystal State
5. Main-Chain Liquid Crystalline Polymers
6. References

## **2. INVESTIGATION AND SYNTHESIS OF LIQUID CRYSTALLINE POLYMERS BY THIN FILM POLYMERIZATION**

SI-XUE CHENG and TAI-SHUNG CHUNG

1. Introduction
2. Experimental Detail of Thin Film Polymerization
3. Morphological Changes during Thin Film Polymerization of Liquid Crystalline Polymers
4. Investigation of the Effects of Reaction Conditions on the Synthesis of Liquid Crystalline Polymers

[www.iran-mavad.com](http://www.iran-mavad.com)

مرجع دانشجویان و مهندسين مواد

5. Investigation of the Formation of Liquid Crystallinity
6. Investigation of the Electric Response of Liquid Crystalline Polymer during Polymerization
7. References

### **3. CRYSTALLIZATION OF MAIN CHAIN LIQUID CRYSTALLINE POLYMERS**

SONG-LIN LIU, K. P. PRAMODA and TAI-SHUNG CHUNG

1. Introduction
2. Polymer Crystallization: Theory
3. Main Chain LCP Crystallization
4. References

### **4. THE THERMAL STABILITY AND DEGRADATION BEHAVIOR OF THERMOTROPIC LIQUID CRYSTALLINE POLYMERS (TLCPs)**

XING JIN, K. P. PRAMODA and TAI-SHUNG CHUNG

1. Introduction
2. Thermal Stability and Degradation Mechanisms of TLCPs
3. Thermal Degradation Kinetics
4. References

### **5. X-RAY SCATTERING FROM LIQUID CRYSTALLINE POLYMERS**

CHAOBIN HE

1. Introduction
2. Numerical Simulation of X-ray Diffraction Patterns of Nematic Systems
3. Numerical Simulation of X-ray Diffraction Patterns of Smectic Systems
4. Monodomain and Polydomain Structures
5. X-ray Scattering from Unoriented Liquid Crystalline Polymers, Powder Diffraction Method
6. X-ray Scattering from Oriented Liquid Crystalline Polymers—Fiber Scattering
7. Summary
8. Appendix 1

9. Appendix 2

10. References

## **6. SURFACE TENSION INVESTIGATIONS OF THERMOTROPIC LIQUID CRYSTALLINE POLYMERS**

KUI-XIANG MA and TAI-SHUNG CHUNG

1. Introduction
2. Estimation of Surface Tension of a Solid
3. Surface Tension of Commercial Thermotropic Liquid Crystalline Polymers
4. Surface Tension Evolution during Thin-Film Polymerization
5. References

## **7. LCP BLENDS**

JIASONG HE and JUN ZHANG

1. Introduction
2. In situ Composites
3. In situ Hybrid Composites
4. Nomenclature
5. References

## **8. RHEOLOGY AND PROCESSING OF THERMOTROPIC LIQUID CRYSTALLINE POLYMERS**

K. S. SEO

1. Introduction
2. Molecular Dimension of Thermotropic Liquid Crystalline Polymers
3. Dynamics of Liquid Crystalline Polymers
4. Rheology of Thermotropic Liquid Crystalline Polymers
5. Processing of Thermotropic Liquid Crystalline Polymers
6. References

## **9. LIQUID CRYSTAL ELASTOMERS, NETWORKS, AND GELS**

PING XIE and RONGBEN ZHANG

1. Introduction
2. Liquid Crystalline Elastomers (LCEs)

[www.iran-mavad.com](http://www.iran-mavad.com)

مرجع دانشجویان و مهندسين مواد

3. Liquid Single Crystal Elastomer (LSCE), Anisotropic Network, and Gels
4. Potential Application of LCE, Anisotropic Network, and Gels
5. References

## **10. THERMOSETTING LIQUID CRYSTAL POLYMERS**

PING XIE and RONGBEN ZHANG

1. Introduction
2. Synthesis and Phase Behavior of TS-LCP
3. Reaction Kinetics of LC Networks
4. Physical Properties and Potential Application
5. References

## **11. LCP EXTRUSION AND APPLICATIONS**

RICHARD W. LUSIGNEA

1. Introduction
2. LCP Background
3. Counter-Rotating Dies for Extrusion
4. Tube Extrusion and Applications
5. Film Extrusion and Applications
6. Blow Molding LCPs and Applications
7. LCP—Thermoplastic Blends and Alloys, Processing, and Applications
8. Conclusions
9. References

## Preface

**T**HE field of thermotropic liquid crystalline polymers has grown substantially in the last two decades, with fundamental research, publications, commercial products, and patents. In the early 1980s, Dr. Ralph Miano led my colleagues and me at Hoechst Celanese in commercializing the first thermotropic liquid crystalline polymer, based on Dr. Gordon Calundann's composition patents. Today, more than seven companies have produced thermotropic liquid crystalline polymer materials, with at least 50 variants available. Hence, it is timely to compile a comprehensive review on the nature of this type of material and the ongoing progress in this field. Such information will be useful to professionals working in this area. The goals of this book are to summarize previous work, provide new insights into this class of polymers, and add to the understanding of the formation of liquid crystallinity.

This book covers a wide range of topics and addresses different disciplines in the field. The chapters are arranged as a learning scheme for the professional, from basic science to applied engineering. The first few chapters summarize the syntheses of various polyester, polyester-amide, and polyimide liquid crystalline polymers. The science and origins of liquid crystal formation are revealed. Next, we introduce the characterizations of these materials by their different chemical and physical aspects. To help the reader, the principles of material characterizations are also discussed.

Because most commercially available thermotropic liquid crystalline polymers have been used in the form of composites, we have also incorporated a chapter on polymer blends, detailing blending mechanisms and resultant

properties. Two chapters on thermosetting liquid crystalline polymers integrate them with other topics, because of their unique importance and their applications for microelectronics and packaging. The final chapter deals with the engineering and processing aspects of thermoplastic liquid crystalline polymers for a variety of applications.

## Acknowledgements

**I** am deeply grateful to the Institute of Materials Research and Engineering in Singapore for allowing me the time necessary to bring this book together. Special thanks go to my wife, Juei-Chiuan Chung and my daughters Susan and Alice, who supported me throughout, and to my students and staff, who have studied liquid crystalline polymers and added to my knowledge of the various aspects of this unique material. I am also thankful to my many Hoechst Celanese colleagues, who have been generous in sharing their knowledge of liquid crystalline polymers.

## List of Contributors

SI-XUE CHENG

Institute of Materials Research  
and Engineering  
Singapore 117602

TAI-SHUNG CHUNG

Department of Chemical Engineering  
National University of Singapore  
Singapore 119260  
Institute of Materials Research  
and Engineering  
Singapore 117602

CHAOBIN HE

Institute of Materials Research  
and Engineering  
Singapore 117602

JIASONG HE

State Key Laboratory  
of Engineering Plastics  
Center for Molecular Science  
Institute of Chemistry  
The Chinese Academy of Sciences  
Beijing 100080, China

MICHAEL JAFFE

Department of Chemical Engineering  
Chemistry, and Environmental  
Science  
New Jersey Institute of Technology  
Newark, NJ 07102

XING JIN

Department of Materials Science  
and Engineering  
The Pennsylvania State University  
University Park, PA 16802-5005

SONG-LIN LIU

Institute of Materials Research  
and Engineering  
Singapore 117602

RICHARD W. LUSIGNEA

Superex Polymer, Inc.  
350 Second Avenue  
Waltham, MA 02451

KUI-XIANG MA

Institute of Materials Research  
and Engineering  
Singapore 117602

[www.iran-mavad.com](http://www.iran-mavad.com)

مرجع دانشجویان و مهندسين مواد

K. P. PRAMODA  
Institute of Materials Research  
and Engineering  
Singapore 117602

K. S. SEO  
Eastman Chemical Company  
Kingsport, TN 37662

PING XIE  
Institute of Chemistry  
Chinese Academy of Sciences  
Beijing 100080, China

JUN ZHANG  
State Key Laboratory  
of Engineering Plastics  
Center for Molecular Science  
Institute of Chemistry  
The Chinese Academy of Sciences  
Beijing 100080, China

RONGBEN ZHANG  
Institute of Chemistry  
Chinese Academy of Sciences  
Beijing 100080, China

# Introduction of Liquid Crystalline Materials

TAI-SHUNG CHUNG  
SI-XUE CHENG  
MICHAEL JAFFE

## 1. HISTORY OF DEVELOPMENT OF LIQUID CRYSTALLINE MATERIALS

**M**ORE than 100 years ago, the liquid crystalline (LC) phenomenon was discovered by the Austrian botanist and chemist Reinitzer. These observations were later confirmed by the German physicist Lehmann [1–3]. In the liquid crystalline state, a substance shows characteristics of a liquid in terms of its mobility, while exhibiting characteristics of a crystalline material as reflected by its optical properties.

For the first three decades of this century, basic research into liquid crystals was carried out mostly in Germany and France. In the early 1900s, Vorländer started systematic synthetic work. Under his direction, many new crystalline compounds were synthesized, and he established the rule that liquid crystalline compounds should be highly linear molecules [1]. Another early outstanding contribution to the liquid crystal field was made by Friedel, who gave the first rational explanation for the patterns observed with liquid crystals in the polarizing microscope and deduced the molecular order of these liquid crystal textures [1,2]. In 1949, Onsager pointed out the dominant role of repulsive forces in liquid crystal ordering, based on a model of long stiff rods. In 1960, Maier and Saupe indicated the importance of dispersion forces in liquid crystals based on statistical considerations. In the later-developed van der Waals theories, both the Onsager and the Maier/Saupe concepts have been united [1,4].

In the mid 1960s, the first major application of liquid crystals in electro-optical display technology was identified [1]. Later, people realized that this finding was a milestone in the history of liquid crystalline materials and that

it had greatly stimulated liquid crystal research and development [1]. Liquid crystal research work increased exponentially and spread from a few centers to many institutes around the world.

After more than two decades of research on low molecular mass liquid crystals (LMLCs), Vorländer, in 1923, realized that liquid crystalline polymers (LCPs) must exist [4,5]. The first reference to a polymeric mesophase was in 1937 when Bawden and Pirie found that a solution of tobacco mosaic virus formed two phases, one of which was birefringent at certain concentrations [4,6]. The first identified liquid crystalline phase for a synthetic polymer was a lyotropic solution of poly( $\gamma$ -benzyl-L-glutamate). A few years later, Flory postulated the highly versatile lattice model approach to LC phase formation and concluded that molecular structure and geometry (anisotropy, rigidity, linearity, and planarity) were the most important factors to induce liquid crystallinity [4–6,7]. Using this model, he revealed the relationship between liquid crystallinity, molecular aspect ratio, molecular packing, anisotropy of dispersion forces, characteristic temperature, and other factors. The recognition of the liquid crystalline properties of rigid chain polymers and the development of the underlying theory led to an immediate search for new rigid chain polymers. DuPont scientists successfully synthesized a lyotropic LCP in 1965 (a rigid backbone wholly aromatic polyamide) and later commercialized it under the trade name “Kevlar” [5,6]. This became another milestone in the history of liquid crystal-based technology. Since then, many liquid crystalline polymers with excellent mechanical properties have been synthesized, and various application areas have been explored. In the 1970s, Carborundum, Eastman-Kodak, Celanese, Amoco, and DuPont successfully synthesized and commercialized a series of thermotropic LCPs [5,6]. Thermotropic main-chain LCPs have a unique integration of properties from both the liquid crystalline and the conventional thermoplastic states, such as melt processibility, high mechanical properties, low moisture uptake, and excellent thermal and chemical resistance. At Carborundum, Economy [6] and other researchers patented an aromatic copolyester based on a biphenol monomer, later commercialized as “Ekkcel I-2000.” Eastman-Kodak reported the first well-characterized thermotropic aromatic-aliphatic copolyesters (formed by the transesterification reaction of *p*-acetoxybenzoic acid [ABA] and poly(ethylene terephthalate) [PET], later commercialized under trademark “X7G” [8]. Celanese developed various tractable wholly aromatic thermotropic polyesters and poly(ester-amide)s under the trademark “Vectra” [5,6]. Today, Kevlar fiber competes with steel, fiberglass, asbestos, and graphite in a variety of applications, including radial tires, brake linings, and composites. Vectra<sup>TM</sup> has been molded for electronic parts and extruded as strength members [5,6,8]. The successful development of these LCPs and the recognition of their unique properties are the result of comprehensive research and development that has been carried out by both academia and industry over the past three decades.

## 2. CLASSIFICATION AND STRUCTURE OF LIQUID CRYSTALLINE MATERIALS

To informatively discuss the structure and properties of liquid crystalline polymers, it is necessary to briefly describe and define liquid crystallinity, building on the knowledge developed for low molecular mass liquid crystals.

### 2.1. CLASSIFICATION AND STRUCTURE OF LCs

There are several classifications of LMMLCs. LMMLCs can be distinguished as thermotropic or lyotropic LCs [1,2], depending on whether the LC state is achieved by melting or in solution.

For thermotropic LCs, the transition to the liquid crystal state is induced by a purely thermal process. Thermotropic LCs form thermally activated mesogenic phases that extend from the crystal melting temperature,  $T_m$ , up to the clearing or isotropic temperature,  $T_i$ . Thermotropic LCs have found wide application in the electro-optical displays [1,2]. For lyotropic LCs, the transition is induced by the influence of solvents. Lyotropic LCs exhibit their phase transitions through the addition or removal of solvent [1,2].

With increasing levels of mesogenic order, liquid crystals can be classified into three basic types: nematic, smectic, and cholesteric [1,2]. The nematic phase is the most commonly observed liquid crystalline phase. The term “nematic” has its origins in the Greek word for “thread,” which describes the appearance of this mesomorphic phase between crossed polars. In the nematic phase, the centers of the molecules are arranged at random; hence, no long-range order exists [1,2]. However, within a microscopic volume element, the axes of all molecules are oriented in a specific direction, as shown in Figure 1.1. In this state, the intermolecular forces are very small, so molecules can easily pass by each other.

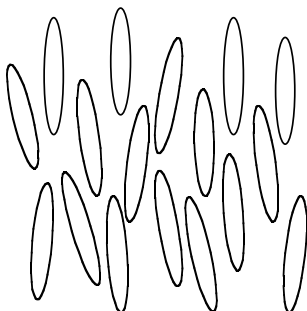
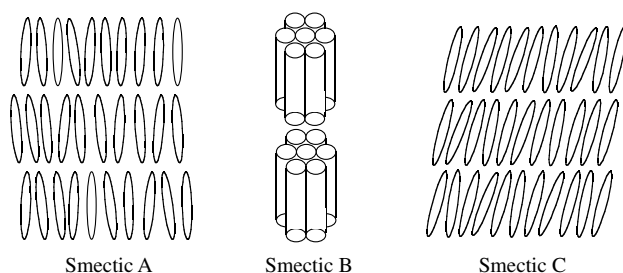


Figure 1.1 Nematic phase.

The smectic phase is more complex to describe because a number of symmetry variants exist. The term “smectic” also has a Greek origin, from the word meaning “soap.” Smectic phases are characterized by layer structures, with additional order possible in each layer. Within the layers, the centers of molecules are arranged in equidistant planes. The planes are allowed to move perpendicular to the layers, and, within the layers, different arrangements of molecules are possible. The smectic modifications are labeled according to the arrangement of the molecules within the layers. The two most common smectic phases are smectic A and smectic C. The smectic A phase is the least ordered of all the smectic phases, with the molecules with their overall long axis perpendicular to the layer plane. In smectic C phase, the orientation axis of the molecules is tilted with respect to the layer phase. In the smectic B phase, the molecules are arranged with an even higher degree of order (Figure 1.2); they have two-dimensional long-range order and positional order within the layer. Similar to smectic A, the molecules are perpendicular to the layer plane. In the case of tilted smectic phases, there are several packing possibilities depending on the direction of the tilt and the positional ordering, namely smectic I, F, G, J, and M [1,2].

The cholesteric phase is similar to that of the nematic phase on a local scale. As in the nematic phase, the molecules can be described by a director. However, the director in the cholesteric phase is twisted about an axis normal to the molecular orientation, following a helical path (Figure 1.3). The distance over which the molecular director rotates by  $2\pi$  along the helix axis is defined as the length of the cholesteric helix pitch,  $P$ . The twist is right-handed or left-handed depending on the molecular conformation. Iridescent colors are characteristic of cholesteric phases [1,2].

The origin of LC phases is rooted in molecular geometry. The most common shapes of LC molecules are rod-like, disc-like, and, in some cases, lath-like [1]. For LC molecules with different shapes, different mesophases may be formed. Rod-like molecules form nematic, smectic, and cholesteric phases. In addition, several rod-like compounds exhibit cubic mesophases. The reason for



**Figure 1.2** Smectic phase.

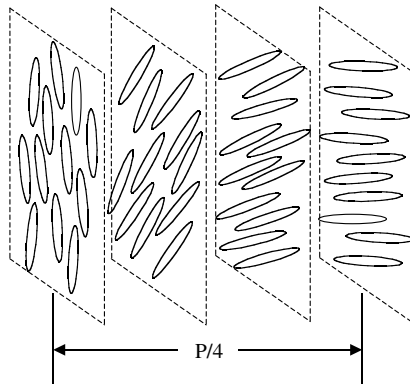


**Figure 1.3** Cholesteric phase.

the occurrence of the cubic phase is not clear. Disc-like molecules can also form a nematic phase, but, in most cases, the disc-like molecules are packed one upon another to form columns. The columns themselves are arranged in a two-dimensional network leading to columnar mesophase with hexagonal, rectangular, or oblique symmetry. As with smectic mesophases, molecular tilting is also possible. Lath-shaped molecules form a nematic phase. However, in contrast to the nematic phase of rod-like molecules, rotation around the molecular long axis is strongly hindered [1].

## 2.2. CLASSIFICATION AND STRUCTURE OF LCPs

Similar to LMMLCs, LCPs are thermotropic or lyotropic according to the conditions inducing their liquid crystallinity [3,5–8]. Classifications of LCPs into various categories have been proposed, based on molecular geometry and the nature of the mesogen attachment. LCPs are broadly divided into main-chain LCPs (Figure 1.4) and side-chain LCPs (Figure 1.5) [3, 5–8] reflecting how the mesogens are attached to the polymer backbone. Some recently developed LCPs have more complicated structures, such as the combined side-chain main-chain LCPs, LC elastomers, and LC networks [9].

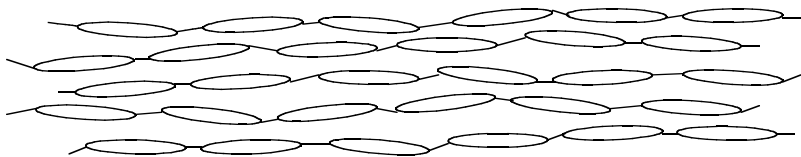


**Figure 1.4** Main-chain LCP.

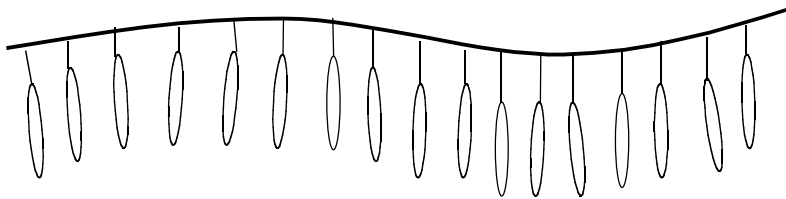


**Figure 1.5** Side-chain LCP.

### 3. LIQUID CRYSTAL TEXTURES

The term LC “texture” designates the image of a thin layer of liquid crystal observed between crossed polarizers in an optical microscope. The features of the various textures observed are caused by the existence of different kinds of characteristic defects. Often, these textures are distinctive and may be used to identify the LC type [1–3].

LCs and LCPs exhibit similar textures, although there are differences between them. Normally, the texture of an LCP is not as distinct as that of an LC because of the higher molecular weight and defect density normally associated with polymers.

While most LCPs form nematic phases, all of the textures observed with low molar mass liquid crystals have been observed in polymers. Because of the importance of nematic LCPs, the discussion of LC textures will focus on the nematic phase, with other textures being discussed in less depth.

#### 3.1. TEXTURES OF NEMATIC LCs

##### 3.1.1. Homogeneous (Monodomain) Texture

A homogeneously aligned nematic phase, also described as a monodomain, does not exhibit specific textures. The observed field is homogeneously colored under the microscope. This represents a specifically defined molecular homogeneity with the optical axis lying parallel to the surface of the sample. In order to form this texture, the glass surface, which is the LC substrate, has to be prepared by “rubbing.” For ordinary glass without a special surface treatment, other characteristic textures will be obtained [10].

##### 3.1.2. Schlieren Texture

As a result of the inherently parallel nature of the molecular long axes, nematic LCs possess intrinsic optical anisotropy. For nematic LCs, the schlieren texture is the most frequently observed texture (Figure 1.6). This texture is

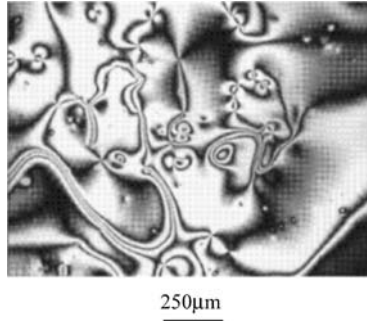


**Figure 1.6** Schlieren texture observed by polarizing microscope.

characterized by the occurrence of dark points (nuclei) from which several black brushes originate [1–3,10,11]. These dark points are the projections of vertically oriented defect lines, called disclinations. If in a complete circuit around a nucleus, the direction of the optic axis changes by  $2\pi$ , the disclination is defined as integral. If the direction of the optical axis changes by  $\pi$ , the disclination is defined as one half [1–3,10,11]. The molecular orientation around several typical disclinations in the plane parallel to the sample surface is illustrated in Figure 1.7. In this figure, the lines represent the orientation of molecules, and the gray areas are positions where the black brushes are observed. The positions of polarizer and analyzer are designated P and A, respectively, and are shown in the bottom of the figure. The strength  $S$  of the disclination is defined by  $|S| = \text{Number of brushes}/4$ . The sign of the  $S$  is positive when the brushes turn in the same direction as the rotated polarizers, and it is negative when they turn

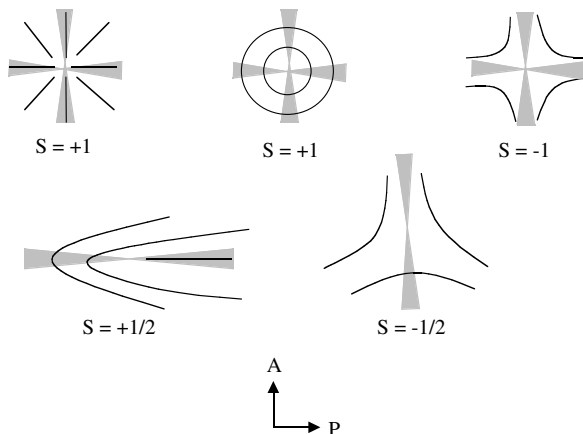


**Figure 1.7** Types of nuclei in nucleated domains.

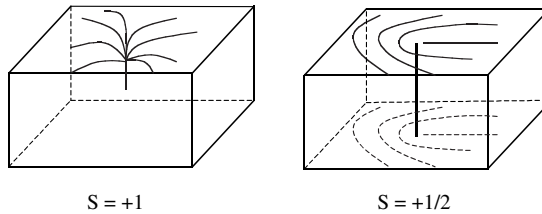


**Figure 1.8** Molecular orientation of the disclinations.

in the opposite direction [1–3,10]. When rotating the crossed polarizers, the rotation angle of the brushes is the same as the rotation angle of the polarizers for a disclination with  $S = \pm 1$  and is twice as large as the rotation angle of the polarizers for a disclination with  $S = \pm 1/2$  [11].

The three-dimensional structures of two typical nematic disclinations, with strength  $S = +1$  and  $S = +1/2$ , are shown in Figure 1.8 [1]. The disclination with the strength  $S = +1/2$  is known as the line disclination because the nucleus is a line, while the disclination with strength  $S = +1$  is known as the point disclination because the nucleus is a point (the line is not stable). In nematic phases, disclinations with both integral and half-integral strengths can form. The reason for the existence of disclinations with half-integral strength in the nematic phase is because of the absence of polarity in this phase [1].

### 3.1.3. Nematic Droplet

Nematic droplets (Figure 1.9) are unique to the nematic phase [2,10]. When cooling an isotropic melt, the nematic phase usually begins to separate at the clearing point in the form of nematic droplets. The sample forming the nematic droplets has two phases, isotropic and nematic, with the nematic droplets

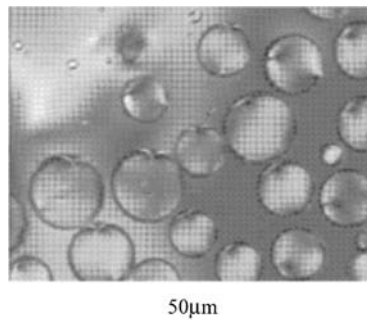


**Figure 1.9** Nematic droplets observed by polarizing microscope.

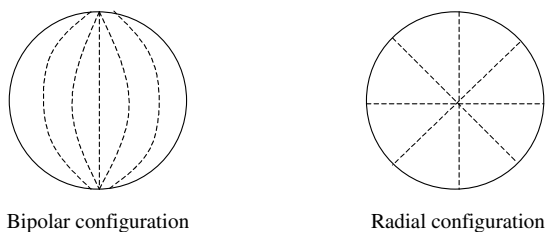


**Figure 1.10** Molecular configuration in the nematic droplets.

being surrounded by the isotropic phase. For nematic droplets, the frequently observed configurations are “bipolar configuration” and “radial configuration,” in which the molecular orientation is parallel and perpendicular to the droplet surface respectively as shown in [Figure 1.10](#) [2,10].

### 3.1.4. Inversion Wall

The inversion wall is a special schlieren texture, that is often seen when a substrate surface imposes a uniform orientation on the sample, as in the case when a glass surface is rubbed. In this texture, as shown in [Figure 1.11](#), the black brushes appear in nearly parallel pairs. The alignment of the molecules is parallel to the surface except near the wall. The total change in orientation on crossing the wall is  $\pi$ . Because the molecular orientation changes by  $\pi$  on crossing the wall, the singularities located within an inversion wall have integral values of strength. The inversion walls may form closed loops or start from disclinations with strengths of  $S = \pm 1, \pm 1/2$  [7,10].

Other textures associated with nematic LCs include the thread-like texture and the marbled texture, both of which are caused by a strong interaction of the thin nematic layer with the surrounding walls [1,3,10].

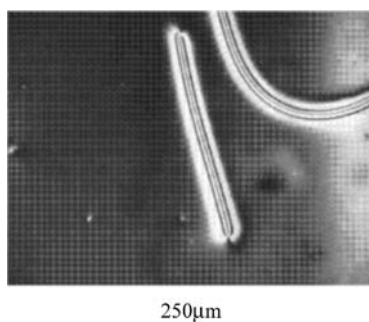


**Figure 1.11** Inversion walls observed by polarizing microscope.

### 3.2. TEXTURES OF SMECTIC LCs

Smectic A and C phases are the most common smectic phases. They exist in several texture variants. Similar to the nematic phase, smectic A phase can exhibit the homogenous texture. The corresponding texture of the smectic C is the schlieren texture, In this texture, the layers are parallel to the sample surface. The schlieren indicates strong distortions of the director field [1].

In most cases, the layers of the smectic A and the smectic C phases are not flat, but distorted. This is the origin of the typical fan-shaped or focal-conic textures commonly observed for smectic phases [1,3,10].

#### 3.2.1. Textures of Cholesteric LCs

Cholesteric phases are quite complex and are easily deformed by even small forces, causing a broad range of observable textures. Among the observed textures, the planar textures, known as “oily streaks,” are among the most commonly observed textures [1,12].

## 4. THEORIES OF LIQUID CRYSTAL STATE

### 4.1. THEORIES OF NEMATIC LCs

There are two basic theories to describe the LC state, the continuum theory mainly proposed by Oseen, Zocher, and Frank and the swarm theory supported by researchers such as Bose, Born, Ornstein, Maier, and Saupe [10,11]. The continuum theory models the liquid crystal as an anisotropic elastic medium with properties varying as a function of position. The swarm theory emphasizes molecular interactions and interprets the LC state as the result of a statistically driven thermodynamic equilibrium. In the recent work of de Gennes, Leslie and Ericksen, LC theories integrate aspects of both the continuum theory and the swarm theory [11].

Because the nematic phase is the simplest LC state, basic theoretical ideas have been focused on nematic LCs. A nematic phase is characterized by a certain type of long-range order. Within a volume element, the molecules are, on average, aligned along one common direction labeled by the unit vector  $\mathbf{n}$ . The efficiency of molecular alignment along  $\mathbf{n}$  is characterized by the order parameter  $S$  [2,13], where

$$S = \langle 3 \cos^2 \theta - 1 \rangle / 2 \quad (1)$$

and  $\theta$  is the angle between the long molecular axis and the preferred direction (optical axis).

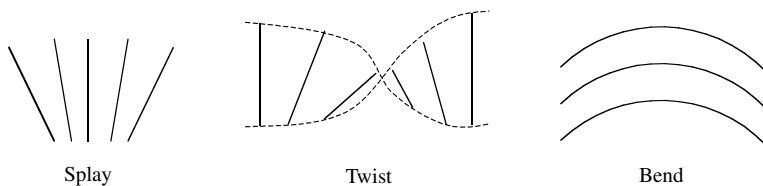


**Figure 1.12** Three kinds of deformations in nematic phase.

In most practical circumstances, however, this ideal conformation is not compatible with the constraints imposed by the walls of the container and by external forces such as electric and magnetic fields. These constraints cause some modifications of both  $\mathbf{n}$  and  $S$  at each point. The modifications of  $\mathbf{n}$  take place over macroscopic distances (typically a few microns) and are, thus, easily observed optically. From a more theoretical point of view, these macroscopic distortions can be described by a continuum theory (the analogue for liquid crystals of classical elasticity for solids). The modifications of  $S$  do not persist over long distance and cannot be detected optically [2,13].

Maier and Saupe, in their well-known molecular-statistical theory, described the intermolecular orientational forces by a mean field method. The Maier-Saupe theory successfully predicts the relationship between the molecular orientation parameter  $S$  and the nematic potential  $D$  as a function of temperature [10,14].

The elastic continuum theory is based on the assumption that  $\mathbf{n}$  varies continuously at each point within the liquid crystal. Any distortion of the original state requires a certain output of energy because the elastic torque attempts to maintain the original configuration. There are three types of distortion defined in the nematic phase: splay, twist, and bend (Figure 1.12), each associated with an elastic constant  $K_1$ ,  $K_2$ ,  $K_3$ . Assuming the forces between molecules are short range, and long-range effects are eliminated, the distortion free energy density for a nematic LC can be derived [2,13]:

$$F_d = 1/2K_1(\text{div } \mathbf{n})^2 + 1/2K_2(\mathbf{n} \cdot \text{curl } \mathbf{n})^2 + 1/2K_3(\mathbf{n} \times \text{curl } \mathbf{n})^2 \quad (2)$$

Because each constant is associated with an independent type of deformation, they all must be positive. In most cases, the bend constant  $K_3$  is the largest, while the twist constant  $K_2$  is the smallest [13,15].

In the presence of an external magnetic field  $\mathbf{H}$ , the distortion energy density  $F_d$  must be supplemented by a term  $F_m$  describing the diamagnetic response of the material. The susceptibilities  $\chi_{\parallel}$  and  $\chi_{\perp}$  measured with  $\mathbf{H}$  parallel or perpendicular to  $\mathbf{n}$  respectively differ. The difference between  $\chi_{\parallel}$  and  $\chi_{\perp}$  is  $\chi_a$  [2,13].

$$\chi_a = \chi_{\parallel} - \chi_{\perp} \quad (3)$$

In most cases, nematic LCs have positive  $\chi_a$ . This means that the nematic LCs prefer to lie parallel to a magnetic field  $\mathbf{H}$ . The corresponding free energy density is [2,13]

$$F_m = -1/2\chi_\perp H^2 - 1/2\chi_a(\mathbf{n} \cdot \mathbf{H})^2 \quad (4)$$

Similarly, for an electric field,  $\mathbf{E}$ , the contribution is

$$F_e = -\epsilon_\perp E^2/8\pi - \epsilon_a(\mathbf{n} \cdot \mathbf{E})^2/8\pi \quad (5)$$

where  $\epsilon_a = \epsilon_\parallel - \epsilon_\perp$  is the anisotropy of the dielectric constant.  $\epsilon_a$  may be of arbitrary sign, depending on the material. If  $\epsilon_a$  is negative, the optic axis tends to be normal to  $\mathbf{E}$  to minimize energy. However, alignment effects of electric fields are often complicated by certain convective instabilities associated with electric conduction. The alignment by the magnetic field is somewhat simpler [2,13].

Equations (2), (4), and (5) define the energy density in the bulk of the nematic phase. In most practical conditions, the surface forces are strong enough to impose a well-defined direction to the director  $\mathbf{n}$  on the surface. For a planar interface between a nematic and an isotropic medium such as glass, the normal to the surface is the preferred direction for  $\mathbf{n}$  [2,13]. With the assumption of strong anchoring, the total free energy density reduces to a volume integral:

$$\mathcal{F} = \int d\mathbf{r}(F_d + F_m + F_e) = \int d\mathbf{r} \mathbf{F} \quad (6)$$

where  $\mathbf{F}$  is a function of  $\mathbf{n}$  [2,13].

## 4.2. THEORIES OF LCPs

Two of the important theoretical models of LCPs were developed by Onsager and Flory, respectively [16]. In their studies, the long rigid LCP molecules are represented by hard rods of appropriate size and shape. The only interaction between the rods is an insurmountable repulsion that is incurred if one rod overlaps another. The effects of intermolecular attractions may be considered as a perturbation within the framework of the thermodynamic functions thus derived.

Onsager treated the LC state by a virial expansion method. He deduced the relationship between the volume fraction of rods, the rod length, and the rod diameter for both ordered and isotropic phases [16].

Flory originally proposed his well-known lattice model theory [17] to treat lyotropic liquid crystallinity and then extended the concept to other polymer-based systems. A limitation of the conventional lattice model is its inability to accommodate rod-like molecules in a continuously varying orientation distribution. To circumvent this difficulty, Flory proposed dividing the polymer molecule into

several submolecules, usually called segments. For simplicity, the molecules of solvent were treated as a function of the size of the rod segment [17]. Flory theory leads to several key predictions; for example, above the critical concentration of rods, a state with partial mesogenic order can form. Below the critical concentration, the orientation of the rod-like molecules is totally random; whereas above the critical concentration, the degree of order is high, implying that the transition to the LC state is discontinuous. During the phase transition, the isotropic and anisotropic phases coexist [18]. For the molecules with an axial ratio  $x$ , phase separation is predicted to occur at a volume fraction  $v_2$ .

$$v_2 \approx (8/x)(1 - 2/x) \quad (7)$$

The predicted critical axial ratio for an LC phase transition in a neat liquid is  $x = 6.4$  [17,18].

## 5. MAIN-CHAIN LIQUID CRYSTALLINE POLYMERS

### 5.1. RESEARCH FOCUS OF THERMOTROPIC MAIN-CHAIN LCPs

The thermotropic main-chain liquid crystalline polymers developed for molding applications are among the most important class of commercial LCPs. To be commercially viable, a thermotropic LCP must possess an LC transition temperature,  $T_m$ , lower than the polymer decomposition temperature,  $T_d$ . However, aromatic para linked polyester homopolymers, for example, poly (*p*-hydroxybenzoate),  $T_m$  is above 500°C while  $T_d$  is around 400°C. One of the main objectives in thermotropic LCP research has been to reduce the transition temperature to a temperature range that is suitable for conventional processing facilities, i.e., equal to or less than about 300°C. Typical approaches to lower the mesogenic transition temperature include random copolymerization, introducing kinks into the molecular backbone by using meta or ortho linkages, introducing flexible linkages into the chain, and incorporating bulky side groups onto the polymer chain [4,7,19].

Random copolymerization is an effective way to disturb the regular molecular structure of the polymer chain. The lack of periodicity along the chain inhibits crystallization and, thus, reduces the crystal size and perfection and depresses  $T_m$ . If the chosen comonomer is essentially linear, losses of chain mesogenicity can be minimized. This approach has been followed in designing thermotropic copolyesters, such as Vectra A by Celanese (now Ticona), which continues to enjoy commercial success. Vectra A is the copolyester of *p*-acetoxybenzoic acid (ABA) and 2,6-acetoxynaphthoic acid (ANA) with a mole ratio of 73/27. The melting point of this LCP is around 280°C, which is much lower than the melting points of the either poly (ABA) or poly (ANA) [6].

The introduction of kinked linkages into the polymer backbone effectively reduces the regularity of the molecule and lowers the melting temperature. However, the incorporation of kinked units has an unfavorable influence on the liquid crystallinity because the kinks disrupt the molecular linearity. Frequently used kinked monomers include isophthalic acid (with the meta linked core angle of  $120^\circ$ ), 2,5 substituted thiophene (with a core angle of  $148^\circ$ ), and so on. The induction of kinks into the molecular chain tends to lower the thermal stability of the LCPs [4,19].

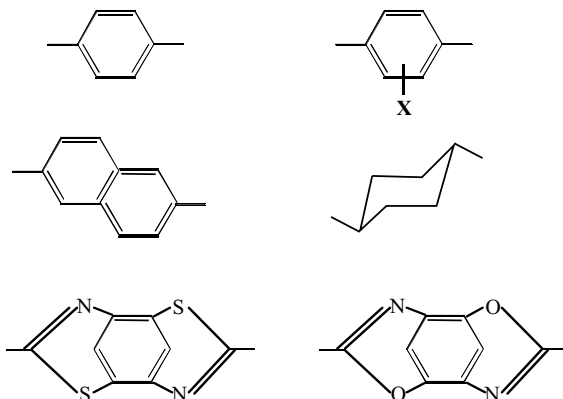
Modification of the *p*-aromatic backbone with flexible segments is another important way to improve the melt processibility. By inserting flexible segments to separate the mesogenic units along the polymer chain, the chemical periodicity of the mesogenic molecule is preserved. These polymer systems are often referred to as semi-rigid polymers. The influence of flexible linkages on the polymer melting temperature is multifold. Increased flexibility tends to lower  $T_m$  through facilitation of molecular motion, and the randomness induced by copolymerization further decreases the melting temperature. The most typical “flexible spacer” segments employed are polymethylene units  $-(CH_2)_n-$  of varying length  $n$ . Both  $T_m$  and  $T_i$  decrease in a zigzag fashion in homologous series in which the spacer length is regularly increased. This zigzag characteristic is referred as the odd-even effect;  $T_i$  tends to be higher when there is an even number of methylene groups in the spacer, but this oscillation is attenuated with increasing  $n$ . The effect is best understood by assuming the conformation of the methylene spacer to be all trans, which has the lowest energy. An even-numbered polymethylene spacer possesses a set of low energy trans conformers that force the rigid units to adopt a collinear disposition, while, in contrast, an odd-numbered spacer places the two mesogenic groups in a non-linear orientation not favorable to the formation of a nematic phase [8]. The disadvantages of the “flexible spacer” approach to increase polymer tractability is that it will disturb the liquid crystallinity and lower the thermal stability of the resultant polymer.

Introducing lateral substituent groups to *p*-oriented monomers has also been applied to lower the melting points of LCPs. Grafting bulky side groups onto the polymer main chain influences the melting temperature in several ways: it effectively increases the interchain distance and reduces the interchain forces so that the efficiency of the chain packing is reduced and the effect is much enhanced by randomly distributing the side-chain along the polymer backbone [7,20]. Introducing lateral substituents also tends to disturb the polymer liquid crystallinity.

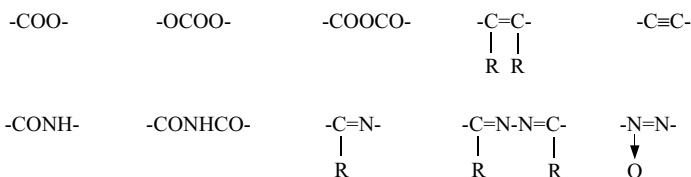
## 5.2. CHEMICAL STRUCTURES OF MAIN-CHAIN LCPs

Most commonly, the structures of main-chain LCPs include *p*-oriented cyclic, usually aromatic units, linking groups, and modifying units (include flexible spacers) [7,8,19].

The structures of frequently used cyclic units are [4,8]

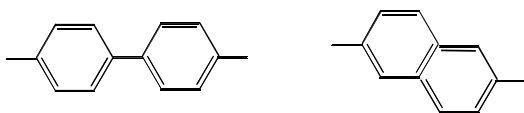


Common linking groups are [4,8]:

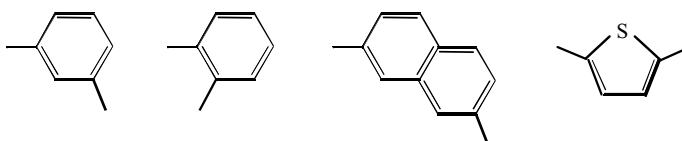


As previously mentioned, modifying the geometry and regularity of thermotropic or lyotropic LCPs can effectively control transition temperature. The structures of typical modifying units are shown below [4,6,8]:

Length and/or side step (induced by copolymerization)



Kinks



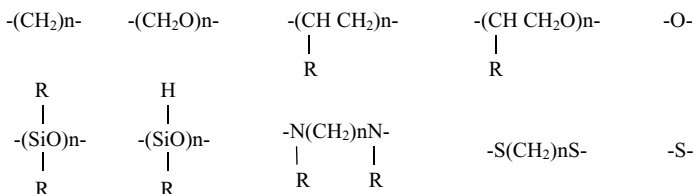
Lateral groups (as ring substitution)



[www.iran-mavad.com](http://www.iran-mavad.com)

مرجع دانشجویان و مهندسين مواد

## Flexible spacers



## 5.3. SYNTHESIS OF MAIN-CHAIN LCPs

In general, thermotropic and lyotropic LCPs are condensation polymers that are synthesized by standard polymerization methods, i.e., acidolysis, phenolysis, etc. As an example of this, some details on the polymerization of the thermotropic liquid crystalline polyester are given below. To achieve reasonable levels of polymerization reactivity, the monomers should be acetylated [8]. During polymerization, the first step is the relatively high temperature transesterification reaction of the phenyl esters of the diacids with the acetylated aryl diols. Normally, the reaction temperatures are set at 10–80°C higher than the melting point of the highest melting monomer. To reduce oxidation, the polymerization is commonly conducted in a nitrogen atmosphere. As oligomers are formed, the melt becomes turbid because of the fluctuations of orientation in the mesogenic domains. A vacuum is then applied to the stillled reaction system to further remove the by-products from the melt. The key to obtaining high molecular weight is to increase the process temperature in a multistep profile to a final temperature. The polymerization reaction can be carried out with or without a catalyst. While catalysts effectively increase reaction rates, they also affect the color and the thermal stability of the final product [8].

## 5.4. END-USE PROPERTIES AND APPLICATIONS OF MAIN-CHAIN LCPs

Most applications of main-chain LCPs utilize the high mechanical properties of these materials [5,6,20]. High modulus and high tensile strength are a result of the high molecular orientation characteristic of these polymers. In contrast, isotropic polymer molecules tend to align and to uncoil in tensile and shear field, but, on the removal of stress, the molecules can partially lose their orientation through relaxation processes, especially at temperatures near the glass or melting transition temperatures [20].

Comparing the properties of conventional polymers and LCPs, the relations of structure properties can be clearly determined. Polyethylene is the best-known example of an isotropic polymer processable to high modulus fiber.

The tensile moduli of unorientated and orientated polyethylene fiber are 1.67–4.18 and 117  $\text{GNm}^{-2}$ , respectively [20]. These values may seem quite high for thermoplastic materials, but the theoretical tensile modulus ( $334 \text{ GNm}^{-2}$ ) is much higher than these values [20]. The large difference is because the polymer chains are not fully aligned and extended. In contrast, the tensile modulus of aromatic polyester LCP fibers is 125–175  $\text{GNm}^{-2}$ . These values approach the theoretical value  $188 \text{ GNm}^{-2}$  [20].

LCP characteristics, such as high mechanical properties (strength, modulus), ease of processibility, excellent thermal resistance, low water absorption, and low gas permeability, make LCPs attractive for a wide range of applications. The applications of main-chain LCPs can be divided into several areas: extrudates (fibers, rods, sheets) used in the chemical and materials' industry, and moldings (chip carriers, connectors, switches) used in microelectronics [6].

LCP fibers are lightweight. One gram of industrial LCP fibers is the mechanical equivalent of 2 g of glass fiber or 5 g of steel wires. Fabrics of LCP fiber are used in ballistic protection garments, helmets, and military flak jackets. Helmets of LCP fibers can stop a flying bullet (from a 0.22-caliber projectile) even at very short distances. Excellent cut/tear resistance and good thermal insulation also make LCP fibers desirable for protective gloves and clothing [6].

As described by DuPont researchers, significant weight saving and low flammability are the primary driving forces behind the adoption of Kevlar by the aircraft industry. Kevlar-epoxy composites are 25–50% lighter than those from glass and aluminum and have better tensile properties. Because thermotropic LCPs offer a low viscosity for the impregnation of carbon fibers and excellent chemical resistance, LCP-carbon fiber composite has been developed as a secondary composite for the aerospace industry [6].

Sheet products made from mineral-filled LCP variants have been used for thermoforming and, after electroplating, for printing circuit boards [6].

Large-diameter melt-extruded LCP rods can be used to replace steel wire and as strength members in optical cable applications. This is because LCP rods have a balance of critical properties for these applications, including low density, flexibility, high tensile properties (which protect optical fibers from breakage), very low coefficient of thermal expansion, good chemical resistance, and almost zero water regain [6].

LCP rivets offer an attractive alternative to metal for fasteners without the high cost and high density of titanium or the corrosion problems associated with aluminum. Because Kevlar and liquid crystalline polyesters are strong, nonabrasive, dimensionally stable, and thermally stable, they also have been used to reinforce brake linings [6].

The largest volume applications of thermotropic LCPs is injection-molded parts. For injection-molding resins, the addition of fillers or fiber reinforced elements into neat LCP resins is utilized to lower cost and improve performance. Two of the major families of mesotropic LCPs on the market are Vectra from

Ticona® and Xydar from BP-Amoco. The key advantages of Vectra are its fast cycling and ease of processing. Xydar offers improved retention of mechanical properties at high temperatures. Both Vectra and Xydar are very resistant to chemical and solvent attack. In addition, LCPs are little affected by radiation [6].

The electrical properties of LCPs and polybutylene terephthalate (PBT) resins are comparable; although LCPs offer at least a few advantages over PBT in electric applications, i.e., low mold shrinkage, fast cycling time, ease of molding thin parts, low moisture regain, and excellent chemical and mechanical properties.

While LCPs have been commercial for more than 20 years, new applications are still emerging. Limitations to LCP usage include high cost and poor non-axial mechanical performance (low compressive and shear properties). It is expected that commercial LCPs are still in the growth phase, and major increases in usage will occur in the 21st century.

## 6. REFERENCES

1. D. Demus, G. Pelzl, and R. Zentel, *Topics in Physical Chemistry, vol. 3, Liquid Crystals*, Chapters 1–3, Ed. by H. Baumgärtel, E. U. Franck, W. Grünbein, and H. Stegemeyer, Steinkopff Darmstadt Springer, New York (1994).
2. G. W. Gray, P. A. Winsor, A. Saupe, H. Zocher, P. G. de Gennes, and M. Kléman, *Liquid Crystals & Plastics Crystals, vol. 1*, Chapters 1–3, Ed. by G. W. Gray and P. A. Winsor, John Wiley & Sons, New York (1974).
3. A. C. Griffin, S. R. Vaidya, M. L. Steele, and C. Noël, *Polymeric Liquid Crystals*, pp. 1–64, Ed. by A. Blumstein, Plenum Press, New York (1985).
4. M. Giordano, D. Leporini, E. Chiellini, G. Galli, and E. Chiellini, *Structure and Transport Properties in Organized Polymeric Materials*, pp. 23–94, Ed. by E. Chiellini, M. Giordano, and D. Leporini, World Scientific, Singapore (1997).
5. A. A. Collyer, *Liquid Crystal Polymers: From Structures to Applications*, Elsevier Applied Science, London (1992).
6. T. S. Chung, G. W. Calundann, and A. J. East, *Encyclopedia of Engineering Materials*, 2, 625 (1989).
7. A. M. Donald and A. H. Windle, *Liquid Crystalline Polymers*, Cambridge University Press, Cambridge (1992).
8. T. S. Chung, *Polym. Eng. Sci.*, 26, 901 (1986).
9. R. A. Weiss and C. K. Ober, *Liquid Crystalline Polymers*, Chapter 1, American Chemical Society, Washington, D.C. (1990).
10. H. Kelker and R. Hatz, *Handbook of Liquid Crystals*, Verlag Chemie, Basel (1980).
11. S. Chandrasekhar, *Liquid Crystals*, Cambridge University Press, Cambridge (1977).
12. D. Demus and L. Richter, *Textures of Liquid Crystals*, Verlag Chemie, New York (1978).
13. P. G. de Gennes and J. Prost, *The Physics of Liquid Crystals*, Clarendon Press, New York (1993).
14. G. Meier, *Advances in Liquid Crystals, vol. 4*, Ed. by G. H. Brown, Academic Press, New York (1979).
15. W. H. de Jeu, *Physical Properties of Liquid Crystal Materials*, Gordon and Breach, New York (1980).

16. A. L. Tsykalo, *Thermophysical Properties of Liquid Crystals*, pp. 121–133, Gordon and Breach, New York (1991).
17. P. J. Flory, *Proc. Royal Soc. London*, A243, 73 (1956).
18. P. J. Flory, *Recent Advances in Liquid Crystalline Polymers*, Chapter 6, Ed. by L. L. Chapoy, Elsevier Applied Science, London (1985).
19. A. H. Windle, *Liquid Crystalline and Mesomorphic Polymers*, Chapter 2, Ed. by V. P. Shibaev and L. Lam, Springer-Verlag, New York (1994).
20. A. A. Collyer, *Mater. Sci. Tech.*, 5, 309 (1989).

# Investigation and Synthesis of Liquid Crystalline Polymers by Thin Film Polymerization

SI-XUE CHENG  
TAI-SHUNG CHUNG

## 1. INTRODUCTION

**S**INCE the discovery of liquid crystalline phenomenon for low molecular weight liquid crystals (LMWLCs) more than 100 years ago, anisotropic ordering behaviors of liquid crystals (LCs) have been of considerable interest to academe [1–8]. In the 1950s, Flory postulated the lattice model for various problems in LC systems and theoretically predicted the liquid crystallinity for certain polymers [1–3]. As predicted by the Flory theory, DuPont scientists synthesized lyotropic LCPs made of rigid wholly aromatic polyamide. Later, Amoco, Eastman-Kodak, and Celanese commercialized a series of thermotropic main-chain LCPs [2]. Thermotropic LCPs have a unique combination of properties from both liquid crystalline and conventional thermoplastic states, such as melt processibility, high mechanical properties, low moisture take-up, and excellent thermal and chemical resistance. Aromatic main-chain LCPs are the most important class of thermotropic LCPs developed for structural applications [2,4–7]. Because they have wide applications in high value-added electronics and composites, both academia and industry have carried out comprehensive research and development.

To understand the relationships among the monomer structures, synthesis conditions and end used properties of LCPs are among the most important research areas. Most monomers for LCP synthesis do not have liquid crystallinity [1–7]. During the polymerization, LC phase forms, and the LC texture evolves with the progress of the polymerization, further annealing or curing reaction. Studying various defects in LC textures and the morphology of LCPs by polarizing microscope is a convenient way to investigate the

structural and physical properties of these materials. A few research groups are working in this field. Geil and his co-workers were the pioneers to employ the thin film polymerization technique to investigate the microstructure of LCPs during the syntheses of a series of aromatic polymers, including poly(*p*-oxybenzoate)(POBA) [9,10], poly(2,6-oxynaphthoate) (PONA) [11], poly(meta-oxybenzoate/2,6-oxynaphthoate) (P(mOBA/ONA)) [12], and poly(*p*-oxybenzoate/2,6-oxynaphthoate) P(OBA/ONA) [13]. In their experiments, a thin layer of monomers was sandwiched between two glass slides wrapped in aluminum foil, and the thin film polymerization was conducted on a hot stage. The morphology and crystal structure of the polymers were studied by optical microscope, TEM, and electron diffraction. There was a melting-polymerization-LC domain formation-crystallization process during the preparation of polymers [9–13]. After polymerization, the polymers with different crystal structures were obtained. POBA was composed of lamellar single crystals with 100 Å thickness. Single crystal PONA was obtained and was identified to have at least three different modes of chain packing. P(mOBA/ONA) had a similar single crystal structure to that of POBA, but with a doubling of *b* axis dimension in some crystals. Thin film polymerization of P(OBA/ONA) also developed lamellar single crystals. However, contrary to homopolymers, the lamellar texture of copolymers was not so obvious. Yee [14] and Ober [15] studied the LC texture evolution during curing of liquid crystalline epoxy. They found different curing agents led to various LC textures. Chung's group [16,17] used the thin film polymerization technique to in situ investigate the whole process of LC phase formation and evolution during the polymerization of LCPs. In the experiments, a thin layer of monomers was sandwiched between two glass slides with a ring spacer to release the acetic acid generated during the reaction. The reaction was carried out on a heating stage of a polarizing microscope. Through in situ observation of the microscope, the whole process of LC texture generation, evolution, and annihilation of different kinds of defects during the polymerization reaction were studied.

Although a fair amount of knowledge of LCPs has been obtained, many debatable issues still remain, such as

- What are the effects of reaction conditions on the formation of liquid crystallinity and the end-use properties of LCPs?
- What are the relationships between the structures of monomeric units and the properties of corresponding polymers?
- What are the critical compositions and driving mechanisms to yield the liquid crystallinity?

The thin film polymerization technique provides a powerful tool to answer these questions by experimental approach because the polymerization reactions for LCPs can be in situ investigated on the heating stage of the polarizing microscope. In addition, thin film polymerization consumes an extremely small

amount of monomers, and the reaction temperature can be accurately controlled. The success of developing this technology yielded a quick and convenient method for scientists to solve the important issues in LCP area, such as to optimize the synthesis conditions for LCPs, to investigate formation of liquid crystallinity, to synthesize new materials, to evaluate new catalysts, and so on.

## 2. EXPERIMENTAL DETAIL OF THIN FILM POLYMERIZATION

Monomer mixture with a certain mole ratio was placed on a glass slide. A drop of acetone was deposited on the glass slide to dissolve monomers. After evaporation of the solvent, a thin layer of reactant mixture was formed and attached to the glass slide and then sandwiched between two glass slides with a ring spacer. The monomers were attached on the top slide. The ring spacer was made of stainless steel with a thickness of 0.5 mm. The whole package was placed on a heating stage (Linkam THMS-600) of a microscope and was heated to a proposed temperature. The sample was held at that specific temperature during the whole reaction process. When the heating stage reached the proposed temperature, the reaction time began to be recorded. The temperature of the top slide was calibrated by testing the melting points of the pure monomers as well as by measuring with a thermocouple. The temperature difference between the heating stage set by the programmer and the top slide was  $20 \pm 2^\circ\text{C}$  in the experimental temperature range. The polymerization reaction was carried out on the top slide, and all the temperatures mentioned refer to the temperatures of the top slide. The reaction process was observed in situ by a polarizing light microscope (Olympus BX50) with crossed polarizers between which a red plate having the retardation of 530 nm was inserted or not inserted. The optical images were recorded by a software program (Image-Pro Plus 3.0) as well as a digital videocassette recorder (SONY DHR-1000NP). The data of the micrographs were analyzed by the software program (Image-Pro Plus 3.0). The sample package for thin film polymerization is shown in [Figure 2.1](#) [16,17].

## 3. MORPHOLOGICAL CHANGES DURING THIN FILM POLYMERIZATION OF LIQUID CRYSTALLINE POLYMERS

Most monomers for LCP synthesis do not have liquid crystallinity. During the polymerization, LC phase separates from the isotropic reactant melt when the degree of polymerization reaches a certain value, and the melt rapidly becomes turbid because the orientation fluctuations of the growing mesogenic domains are in the range of the wavelength of visible light. Further removal of volatiles (for example, acetic acid) from the melt is the key to increase the molecular weight. The as-synthesized LC texture and morphology not only

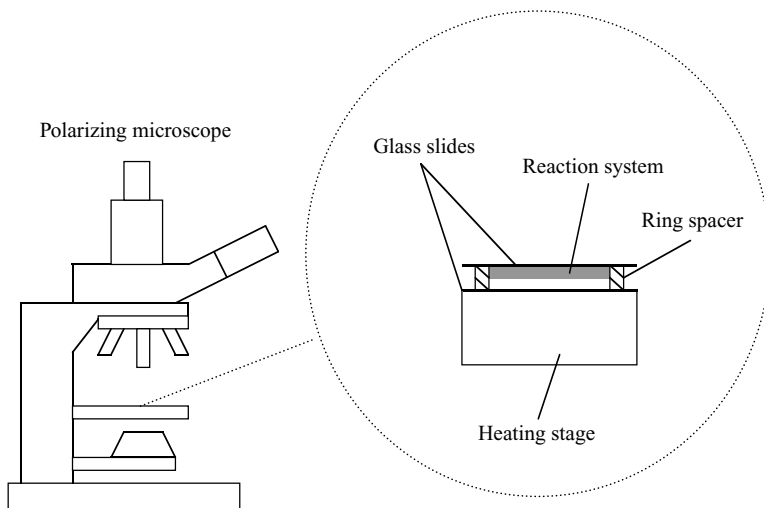


**Figure 2.1** The sample package for thin film polymerization.

determine processability for subsequent process, but also affect the properties of final products. Because melt polymerization progresses from a homogeneous phase to a heterogeneous LC phase, different optical textures associated with string-like and point-like defects can be observed. Some defects remain in the LCPs solidified from the melt polymerization, and the others disappear through annihilation during the reaction. The density and types of defects will strongly affect the rheological behavior, mechanical properties, and optical properties of polymeric materials. So, it is essential to know exactly what occurs during the polymerization of LCPs.

For different polymerization systems of LCPs with various monomer compositions and at different temperatures, there are some differences in their morphological changes. However, the appearance of the LC phase and annihilation of disclinations can be observed for all systems. The reaction system with the monomer composition of 73/27 (mole ratio) ABA/ANA at a reaction temperature of 250°C was studied in detail as a typical example. The whole polymerization reaction system starts from mixed crystals, melts to a homogeneous phase, and then changes into a heterogeneous system with the following sequence of morphological changes: generation of LC phase, annihilation of disclinations, and formation of banded texture [17].

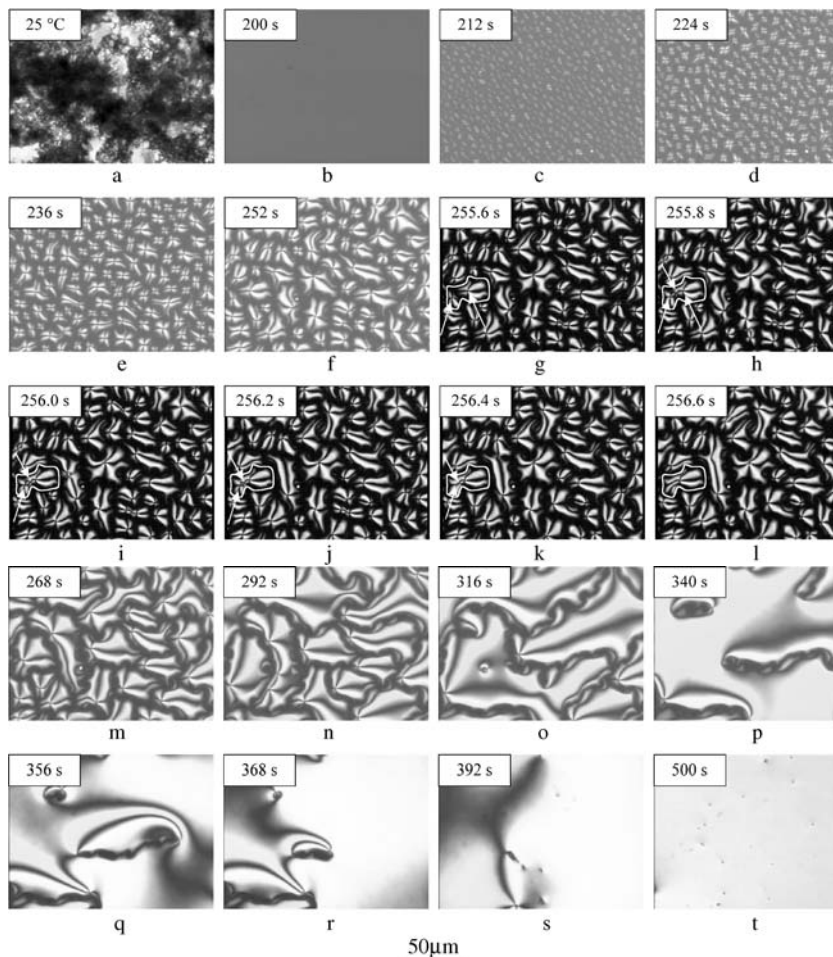
### 3.1. GENERATION OF THE LIQUID CRYSTAL PHASE

Figure 2.2 illustrates a set of micrographs showing the typical LC phase separation from a homogeneous phase and time evolution of LC texture in

[www.iran-mavad.com](http://www.iran-mavad.com)

مرجع دانشجویان و مهندسين مواد

the early stage of thin film polymerization. Figure 2.2(a) shows the crystals of the monomers. During heating, the monomers melt, and the whole view area becomes an isotropic melt phase as shown in Figure 2.2(b). In the early stage of polycondensation reaction, oligomers form in the molten monomer phase. Their molecular weight and chain length increase with reaction time. When the chain length of the oligomers reaches a certain value, they form the anisotropic phase (LC phase) and separate from the isotropic melt. Figure 2.2(c) shows the reaction-induced phase separation process during the polymerization. The dark



**Figure 2.2** Micrographs showing morphological changes in the early stage of polymerization reaction of 73/27 ABA/ANA. All the micrographs are obtained from the same area of the same sample. Reaction temperature is 250°C.

area in the micrograph is the isotropic phase, while the bright area represents the anisotropic phase. The first sign of forming the anisotropic phase is that many bright LC domains instantaneously appear in the view range. Because of the polydispersity of the chain length, oligomers are partitioned within the isotropic and the anisotropic phases according to the chain length [18]. A fraction of relatively longer chain length forms anisotropic domains, while others remain in the isotropic phase.

After the appearance of the anisotropic phase, the size of LC domains quickly increases, and, correspondingly, the number of domains decreases because of domain growth and coalescence between adjacent LC domains. Figure 2.2(g–l) illustrates a detailed coalescence process. According to the previous study, we know that black brushes originating from the points are regions where the director is either parallel or perpendicular to the plane of polarization of incident light; therefore, the incident light is extinguished by the crossed polarizers. When rotating the crossed polarizers, the position of the points remains unchanged but the brushes rotate continuously, showing that the orientation of the director changes continuously about the disclinations. If the sense of rotation is the same as that of polarizers, the disclination is a positive one. On the contrary, if the sense of rotation is opposite to that of polarizers, the disclination is a negative one [1]. The strength,  $S$ , of a disclination is determined by the number,  $N$ , of the dark brushes around the single disclination:  $|S| = N/4$ . In the thin film polymerization experiments, all the LC domains formed in the isotropic melt have the disclination strength of  $+1$ . In Figure 2.2(g), the two domains with strength  $S = +1$  are indicated by two bottom arrows. When coalescence happens, a negative disclination with strength  $S = -1$ , as indicated by the top arrow, forms at the contact point of these two domains as soon as they contact each other. The process followed is the annihilation of the two defects with opposite signs as shown in Figure 2.2(h–l). After the formation of the disclination of  $S = -1$  during coalescence, this disclination (indicated by the top arrow) and one of the adjacent disclinations of  $S = +1$  (indicated by bottom arrow) immediately move toward each other and then disappear together after 0.8 s of the coalescence. Thus, a large domain with only one disclination of  $S = +1$  is formed.

The growth of the LC phase occurs when reaction time is in the range from 202 s to 392 s for this sample. As a result, the total view area becomes an anisotropic LC phase, and the sum of the strength of all disclinations in the sample tends to be zero. The typical schlieren texture is formed at this moment [17].

### 3.2. ANNIHILATION OF DISCLINATIONS

As we know, the dynamic properties of LCP are quite different from that of LC, but the static properties of LCP are similar to that of LC [1]. In the

continuum theory of LC, the distortion energy density is given by [19]

$$F_d = 1/2K_1(\text{div } \mathbf{n})^2 + 1/2K_2(\mathbf{n} \cdot \text{curl } \mathbf{n})^2 + 1/2K_3(\mathbf{n} \times \text{curl } \mathbf{n})^2, \quad (1)$$

where  $\mathbf{n}$  is the variable director and  $K_1$ ,  $K_2$ , and  $K_3$  are elastic constants for splay, twist, and bend, respectively. According to this formula, the larger the elastic constants are, the higher the distortion energy is. Normally, the elastic constants decrease with increasing temperature and increase with increasing length of molecules. According to Odijk's deduction, the splay, twist, and bend elastic constants for the polymer chains that are not completely rigid can be expressed as follows [3]:

$$K_1 \approx 3K_2 \quad (\text{If the chain length, } L, \text{ is less than the persistence length, } q.) \quad (2)$$

$$K_1 \propto L \quad (\text{If the chain length, } L, \text{ exceeds the persistence length, } q.) \quad (3)$$

$$K_2 \approx \phi^{1/3}(q/d)^{1/3}(kT/d) \quad (4)$$

$$K_3 \approx \phi(q/d)(kT/d), \quad (5)$$

where the term  $(kT/d)$  redimensionalizes the constant to give the units of force,  $\phi = 1$  for thermotropic polymers, and  $q/d$  is the persistence ratio. Thus, the elastic constants increase with increasing persistence length. If the molecular length exceeds the persistence length, the values of  $K_2$  and  $K_3$  will tend to be constant, while  $K_1$  will increase monotonically with  $L$ .

Because the defects are caused by the deformation of molecular chains, they involve high distortion energy in the case of rigid or semi-rigid polymers. Disclinations with opposite signs tend to attract each other in order to release the energy [20–26]. This interaction leads to the annihilation and the decrease in the number of defects. In the thin film polymerization systems, the annihilation between two opposite sign disclinations and annihilation of the loops are the two methods to release the excess deformation energy.

### 3.2.1. Annihilation Between Two Opposite Disclinations

During the thin film polymerization reaction, the schlieren texture evolves to inversion walls, and, at the same time, annihilation occurs between disclinations. The micrographs in Figure 2.3 are taken from the same area of the same sample when the range of reaction time is from 450 s to 479 s. They show the annihilation process of a pair of disclinations with opposite strength,  $S = +1$  and  $-1$ . According to Figure 2.3, we can see the distance between the pair of disclinations gradually decreases. At last, two disclinations disappear together. During this process, the molecules within the area rearrange their orientation and yield a locally perfect orientation after the annihilation.

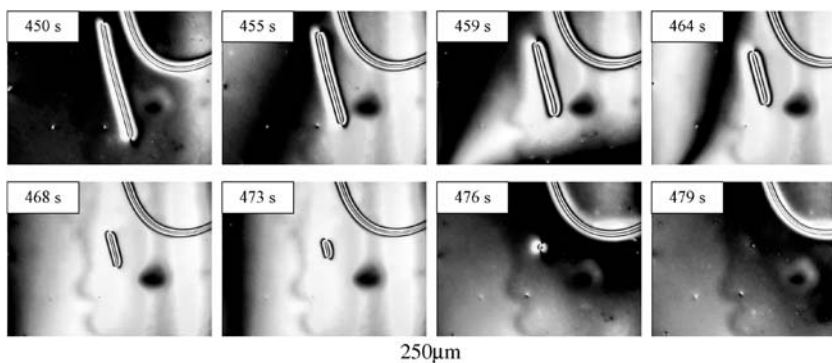


**Figure 2.3** Micrographs showing the annihilation process of a pair of disclinations with opposite signs. All the micrographs are obtained from the same area of the same sample. Monomer composition of the reaction system is 73/27 ABA/ANA. Reaction temperature is 250°C.

Figure 2.4 shows that the distance between the two disclinations decreases in an approximately linear manner with the reaction time because the slope of the straight line in logarithmic scale is 1. (Here  $t_o$  is the time that two disclinations joined and disappeared.) As frequently reported, for the non-reacting systems, the annihilation kinetics follow a power-law relationship [20–23]. Based on the experiments of thin film polymerization of aromatic thermotropic LCPs, the annihilation kinetics for reacting systems also follow the power-law relationship [17]. Although the viscosity increases with the progress of polymerization reaction because of the increase in molecular weight, its effect on annihilation

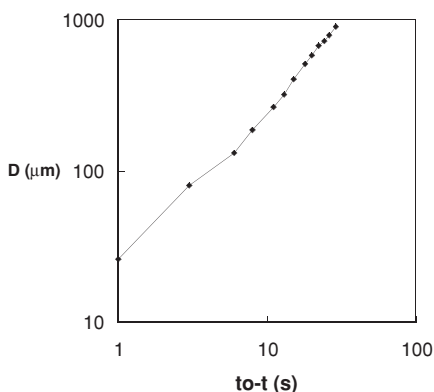


**Figure 2.4** Time dependence of the distance,  $D$ , between a pair of disclinations.  $t$  is reaction time, and  $t_o$  is the time that two disclinations joined and disappeared. Monomer composition of the reaction system is 73/27 ABA/ANA. Reaction temperature is 250°C.

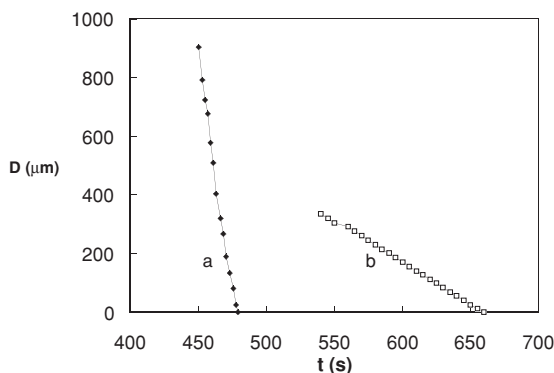


**Figure 2.5** Annihilation of two pairs of disclinations during different reaction time intervals: (a) 450 s–479 s and (b) 540 s–660 s. Monomer composition of the reaction system is 73/27 ABA/ANA. Reaction temperature is 250°C.

cannot be observed. This is due to the fact that the change in viscosity is not obvious because the annihilation happens within a relatively short time interval.

At the beginning of the polycondensation reaction, the annihilation occurs very quickly, indicating the molecular weight at this stage is relatively low, and, thus, viscosity of the system is not very high. With an increase in the reaction time, the annihilation rate slows down because the increasing viscosity restricts the motion of disclinations for further annihilation. When the energy needed for the reorganization of molecular orientation is higher than that released by the annihilation of defects, the annihilation process is completely retarded. The annihilation between two pairs of defects during different reaction time intervals in the same sample is compared in Figure 2.5. In this figure, the annihilation rate ( $v = dD/dt$ ) for the same pair of defects remains approximately the same during the whole annihilation process. For the annihilation that occurred during the time interval of 450 s to 479 s, as already shown in Figure 2.4, the annihilation rate is about 31.2  $\mu\text{m/s}$ . While for another annihilation that occurred during the time interval of 540 s to 660 s, the annihilation rate is much slower, about 2.8  $\mu\text{m/s}$ . In our reaction system at 250°C, no further movement of defects could be observed after reaction time reaches 1000 s.

However, annihilation between the defects is a complicated process and has not been fully understood yet. Although annihilation occurs between two particular disclinations, in fact, the annihilation process is affected by many factors. For example, other defects surrounding the particular pair of defects more or less affect the annihilation. In a polymerization system, a more complicated factor is added to the annihilation process due to the increase in elastic constant because of the increase in molecular weight. However, it is a universal trend that the annihilation rates for different pairs of disclinations decrease with reaction time [17].

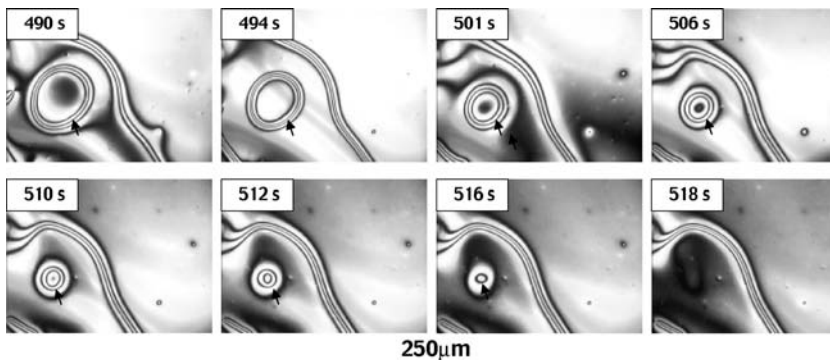


**Figure 2.6** Micrographs showing the shrinkage process of loops. All the micrographs are obtained from the same area of the same sample. Monomer composition of the reaction system is 73/27 ABA/ANA. Reaction temperature is 250°C.

### 3.2.2. Shrinkage of Loop

Figure 2.6 shows the typical annihilation of loops for the polymerization at 250°C. The images were taken at reaction time ranging from 490 s to 518 s. With an increase in the reaction time, the loops gradually shrink, change their shapes into circular ones, and finally disappear. Time dependence of the particular loop (indicated by the arrow) area,  $A$ , and perimeter,  $P$ , is shown in Figure 2.7 ( $t_0$  is the time that the loop disappeared). It can be found that the decrease in area and perimeter of the loop follows a power-law relationship within the middle stage of the shrinkage.

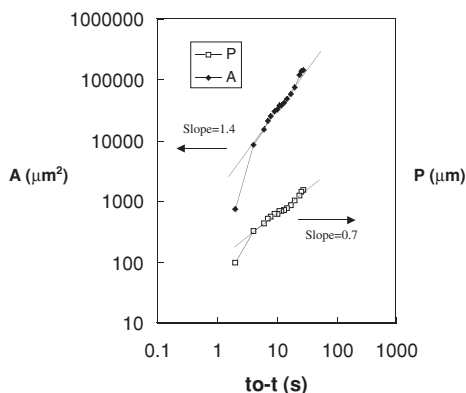


**Figure 2.7** Time dependence of area,  $A$ , and perimeter,  $P$ , of the loop.  $t$  is reaction time, and  $t_0$  is the time that the loop disappeared. Monomer composition of reaction system is 73/27 ABA/ANA. Reaction temperature is 250°C.

In the reaction systems, for the pairs of disclinations with opposite signs, in some cases, they annihilate and then completely disappear; while in other cases, the distance between two opposite disclinations decreases, but defects still exist in the system. For the loops, in some cases, they shrink, annihilate, and then disappear; while in other cases, they shrink into a small area or a spot and stay in the system. At the beginning stage of the polymerization, the density of defects in the reaction system is considerably high. After annihilation, the density dramatically decreases [17].

### 3.3. FORMATION OF BANDED TEXTURE

LCPs exhibit a variety of textures of different length scales originated from flow and deformation. A frequently observed texture called “banded texture” or “stripe texture” often emerges in the sample where relaxation or shrinkage of molecular chains occurs. The conditions inducing this texture include being subjected to shear and/or elongation flow [27], evaporating the solvent from a lyotropic LC [28], and quenching a thermotropic LC from high temperatures [29]. As a consequence of stress relaxation after shear or volume deficiency induced by solvent evaporating or quenching, banded texture appears while local order does not decrease significantly.

In the thin film polymerization system, with the increase of molecular weight, the volume deficiency causes the appearance of banded texture because adhesion to the substrate prevents uniform shrinkage in three dimensions. Figure 2.8(a) is the typical schlieren texture with two disclinations of opposite signs. The dark line connecting the defects is quite diffuse, indicating the defects are isolated. After the banded texture appears [Figure 2.8(b)], the situation changes: the defects are connected by an inversion wall (the sharp dark line). From the stripes in Figure 2.8(c), one can deduce that the strength of the left disclination is  $-1$  and the right one is  $+1$  because the macromolecular chain orientation is perpendicular to the stripes. The banded texture is fully developed within more than 10 minutes. The width of the stripes is about  $5\ \mu\text{m}$ .

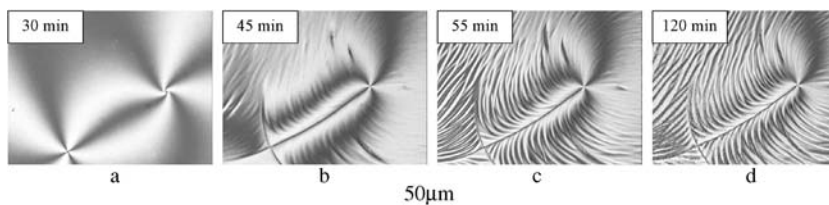


**Figure 2.8** Micrographs showing the formation of banded texture. All the micrographs are obtained from the same area of the same sample. Monomer composition of the reaction system is 73/27 ABA/ANA. Reaction temperature is  $250^{\circ}\text{C}$ .

After 120 min of reaction, the banded texture does not change much, but the morphology seems to become more coarse [17].

## 4. INVESTIGATION OF THE EFFECTS OF REACTION CONDITIONS ON THE SYNTHESIS OF LIQUID CRYSTALLINE POLYMERS

### 4.1. EFFECTS OF REACTION TEMPERATURE ON THE THIN FILM POLYMERIZATION

#### 4.1.1. Effect on the Kinetics of LC Texture Formation

At the beginning stage of polymerization reaction, LC phase is formed in the isotropic melt. The domain growth and coalescence of LC droplets lead to the formation of schlieren texture, which means the total view area becomes an LC phase. During the LC area increase process, the fraction of anisotropic phase is defined by  $X = A_{\text{anisotropic}}/A_{\text{total}}$ , where  $A_{\text{anisotropic}}$  is the area of anisotropic phase and  $A_{\text{total}}$  is the total view area. Using the software to calculate  $X$  at different reaction times, a series of curves for 73/27 ABA/ANA reaction system can be obtained and shown in Figure 2.9. It can be seen very clearly that the higher the reaction temperature is, the earlier the LC forms, and the faster LC phase increases. The time interval from appearance of LC phase to formation of schlieren texture is strongly dependent on the reaction temperature. For example, it takes 332 s to form schlieren texture after generation of LC phase at 230°C, whereas it only takes 10 s at 310°C.

#### 4.1.2. Effect on the Morphology

Table 2.1 summarizes the observation results revealing the relationship between reaction time and morphological transition at different temperatures.

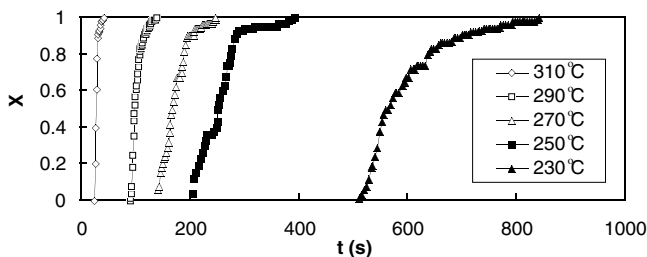


**Figure 2.9** The fraction of anisotropic phase as a function of reaction time at different reaction temperatures. Monomer composition is 73/27 ABA/ANA.

TABLE 2.1. The Effect of Reaction Temperature on the Transition Time of Morphological Changes. Monomer Composition Is 73/27 ABA/ANA.

Transition Time \ Temperature (°C)	230	250	270	290	310
Generation of LC phase (s)	510	200	140	90	20
Formation of schlieren texture (s)	842	392	247	138	30
Appearance of banded texture (min)	180	40	18	10	2.5
Full development of banded texture (min)	300	50	21	11	3.3

From Table 2.1, we can clearly see that the time for morphological change decreases with increasing reaction temperature. For example, when reaction temperatures are 230°C and 310°C, banded textures begin to form at 180 min and 2.5 min respectively.

Figure 2.10 shows the morphologies of the late stage of thin film polymerization at relatively high reaction temperatures. After banded texture fully develops, the sample surface quickly turns into a non-smooth texture. Compared to the final product obtained at a low temperature, the morphology of high temperature product is coarser and fuzzier.

#### 4.2. EFFECTS OF CATALYST ON THE THIN FILM POLYMERIZATION

For the polycondensation of wholly aromatic polyesters, several effective catalysts are known as having the capabilities of accelerating reaction as well

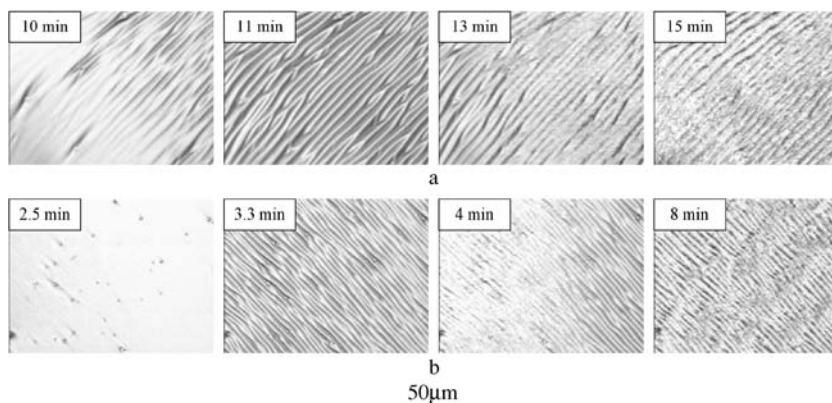


**Figure 2.10** The morphologies of the late stage of thin film polymerization at relatively high reaction temperatures: (a) 290°C and (b) 310°C. The micrographs are obtained from the same area for the same sample. Monomer composition is 73/27 ABA/ANA.

as resulting in high inherent viscosity. Representative examples of catalysts suitable for the reaction are derivatives of alkali metals, alkali-earth metals, and other metals, such as titanium, manganese, zinc, tin, and antimony for their oxides, hydrides, hydroxides, halides, alcoholates, phenolates, organic and inorganic salts, complex salts, and so forth [30–35]. Of these compounds, the above-mentioned alkali acetate compounds are particularly preferable. Generally, the typical range of the catalytic amount is from 0.001 to 1 wt% based on the total monomer reactant weight, with between 0.005 and 0.1 wt% being preferred [30–35].

Because sodium acetate ( $\text{CH}_3\text{COONa}$ ) had been extensively employed in many LCP patents and it obviously has an acceleration effect on the polymerization reaction, this catalyst was selected for extensive study. The catalyst is applied in ABA/ANA polycondensation reactions with a monomer molar ratio of 73/27.

As mentioned before, during the polycondensation reaction of an uncatalyzed system, the following morphological changes have been observed sequentially: generation of liquid crystal phase, coalescence of liquid crystal domains, formation of schlieren texture, annihilation of disclinations, and appearance of banded texture. For a catalyzed system with a low percentage of catalyst, the sequence of morphological changes is the same. Figure 2.11 is a set of micrographs taken from the same area of the same sample, illustrating the whole process of morphological changes during the catalyzed polymerization with 0.01 wt%  $\text{CH}_3\text{COONa}$  at  $250^\circ\text{C}$ . It shows that the transition times of the morphological changes for a catalyzed system are obviously earlier than that of an uncatalyzed system. The appearance of the liquid crystal phase, for example,

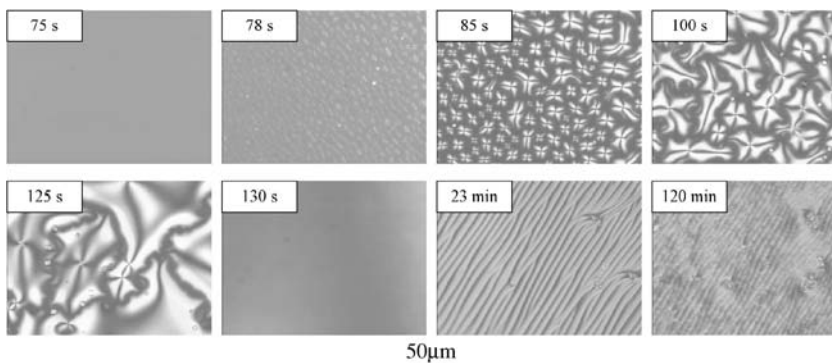


**Figure 2.11** Micrographs showing the morphologies of the reaction system at different reaction times during thin film polymerization. All the micrographs are obtained from the same area of the same sample. Monomer composition is 73/27 ABA/ANA. Catalyst content is 0.01 wt%  $\text{CH}_3\text{COONa}$ . Reaction temperature is  $250^\circ\text{C}$ .

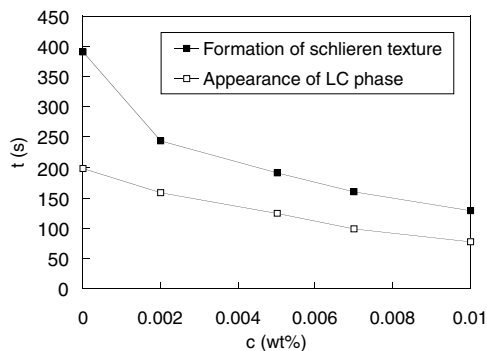


**Figure 2.12** The dependence of morphological transition time on the catalyst  $\text{CH}_3\text{COONa}$  content. Monomer composition is 73/27 ABA/ANA. Reaction temperature is  $250^\circ\text{C}$ .

needs 202 s for the uncatalyzed system, but only 78 s for the catalyzed system. Compared to the uncatalyzed system at same temperature, the banded texture for catalyzed system becomes fuzzy or unclear [36].

#### 4.2.1. Effect of Catalyst Content on the Thin Film Polymerization

The effect of catalyst content on polycondensation reactions has also been investigated by varying the  $\text{CH}_3\text{COONa}$  concentration over a range from 0 wt% to 0.01 wt%. Figure 2.12 summarizes the results from in situ observation of the catalyst effect on the 73/27 ABA/ANA polycondensation reaction systems. The sequences of morphological change for these reaction systems with different catalyst levels are similar. However, different catalyst concentrations result in different transition times. For example, it takes a much shorter time (168 s) for a catalyzed system with 0.002 wt%  $\text{CH}_3\text{COONa}$  to show the appearance of the LC phase than that for an uncatalyzed system (202 s). The transition time for each morphological change decreases with increasing catalyst content. Figure 2.12 also suggests that the transition times for LC phase appearance and schlieren texture formation decrease almost linearly with an increase in catalyst content when the catalyst content varies from 0.002 wt% to 0.01 wt%. However, further increase in catalyst content does not shorten the transition time proportionally.

The amount of a catalyst in polymerization not only determines the transition times of morphological changes but also significantly affects the morphology of final products. Figure 2.13 shows various final morphologies of LCPs synthesized from different levels of catalyst concentration. For the catalyzed systems with low catalyst concentrations of 0.002 wt% to 0.007 wt%, their morphologies are quite similar to that of an uncatalyzed system at the same reaction

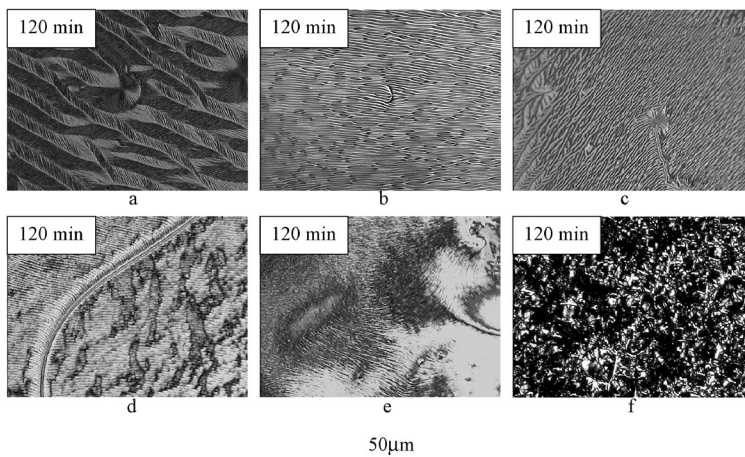


**Figure 2.13** The micrographs of final products of the reaction systems with different catalyst  $\text{CH}_3\text{COONa}$  content (a) 0.002 wt%, (b) 0.005 wt%, (c) 0.007 wt%, (d) 0.1 wt%, (e) 1 wt%, and (f) 5 wt%. Monomer composition is 73/27 ABA/ANA. Reaction temperature is  $250^\circ\text{C}$ .

temperature. The situation changes if the catalyst percentage is greater than 0.01 wt%. The LCP morphologies become coarse, and the banded textures seem to be fuzzy or unclear as discussed before. These fuzzy morphologies are quite similar to that of the uncatalyzed system reacting at a high temperature. If the system contains 5 wt% catalyst, the resultant LCP has a totally different morphology. It has an extremely high density of defects because the reaction proceeds too fast and the system viscosity increases very rapidly; thus, there is not enough time for defects to annihilate, and many defects stay in the final product. Because uncatalyzed and catalyzed systems polymerized at the same temperature produce LCPs with different morphologies, the catalyst effect on LCP processes, properties, and applications may not be ignored if the catalyst concentration is high [36].

#### 4.2.2. Kinetics Study of Catalyzed and Uncatalyzed Polycondensation Reaction

Previous works confirm that the bulk copolymerization reaction of P(OBA/ONA) is a bimolecular second-order reaction for both catalyzed and uncatalyzed systems [37]. The reaction rate equation can be expressed as follows:

$$-d[\text{COOH}]/dt = k[\text{COOH}]^2 \quad (6)$$

in which  $[\text{COOH}]$  is the concentration of acid groups and  $k$  is the reaction rate

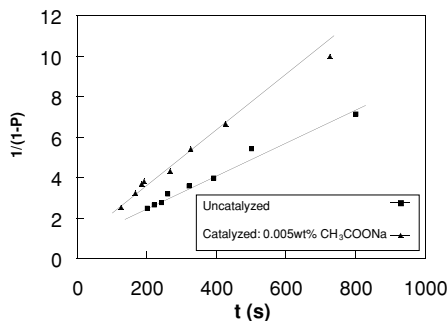


**Figure 2.14** The dependence of  $1/(1 - P)$  on the reaction time for an uncatalyzed system and a catalyzed system with 0.005 wt%  $\text{CH}_3\text{COONa}$ . Monomer composition is 73/27 ABA/ANA. Reaction temperature is  $250^\circ\text{C}$ .

constant. The extent of polymerization reaction,  $P$ , is defined as the ratio of the reacted functional groups to the total functional groups, and the number average degree of polymerization,  $DP$ , is defined as the ratio of initial acid group concentration to the current acid group concentration. So we have

$$DP = 1/(1 - P) = k[\text{COOH}]_0 t + 1 \quad (7)$$

where  $[\text{COOH}]_0$  is the initial concentration of acid groups and  $t$  is the reaction time. Figure 2.14 shows the relationship between  $1/(1 - P)$  and  $t$  for 73/27 ABA/ANA thin film polymerization reactions after appearance of the LC phase. For both uncatalyzed and catalyzed thin film polymerization systems, their reaction kinetics follow the second-order equation, which is consistent with the results obtained from the bulk polymerization [37].

LCP polymerization is unique in that there are two kinetics regions because the reaction system turns from a homogeneous to heterogeneous system due to the precipitation (phase separation) of oligomers. Thus, the reaction rate constants before and after the generation of the LC phase may be different [37–39]. For thin film polymerization, because all detectable morphological changes during polymerization under microscope observation occur after the generation of the LC phase, the study is focused on the second region.

Because of the release of acetic acid during the polycondensation reaction, the content of carbon, hydrogen, and oxygen elements in the system continuously changes with the progress of polymerization. Mathematically, one can easily develop the following relationship to express carbon element content,  $C_e$ , vs. the extent of reaction,  $P$ , as

$$C_e(\text{wt}\%) = (120.96 - 24P)/(193.5 - 60P) \quad (8)$$

TABLE 2.2. The Effect of Reaction Temperature on Carbon Content,  $C_e$ , Reaction Extent,  $P$ , and Number Average Degree of Polymerization,  $DP$ , at Certain Morphological Transitions. Monomer Composition Is 73/27 ABA/ANA.

Temperature (°C)		230	250	270	290
$C_e$ (wt%)	Generation of liquid crystal phase	66.64	67.79	68.41	68.87
	Formation of schlieren texture	68.10	69.28	69.56	70.10
$P$	Generation of liquid crystal phase	0.50	0.61	0.67	0.71
	Formation of schlieren texture	0.64	0.74	0.77	0.81
$DP$	Generation of liquid crystal phase	2.0	2.6	3.0	3.5
	Formation of schlieren texture	2.8	3.8	4.3	5.3

In order to determine the exact extent of reaction at certain morphological transitions, the reaction is stopped when the certain morphological transitions occur and then are characterized by the elemental analysis. The results are shown in Table 2.2. Figure 2.15 shows the transition times for the generation of the LC phase and the formation of schlieren textures in the catalyzed and uncatalyzed systems as a function of reaction temperature. It is very interesting to point out that the precipitation of oligomers is determined directly and much precisely from in situ observation for thin film polymerization, while it can only be calculated indirectly from the evolved acetic acid and the break in time-conversion curve for bulk polymerization. As shown in Table 2.2, the number average degree of polymerization when the LC phase appears decreases with a decrease in the reaction temperature in the experimental range of 230–290°C, and LC phase may form at the  $DP$  as low as 2 at 230°C. This low  $DP$  is because the onset of the LC phase should not be only dependent on the  $DP$ , but also on

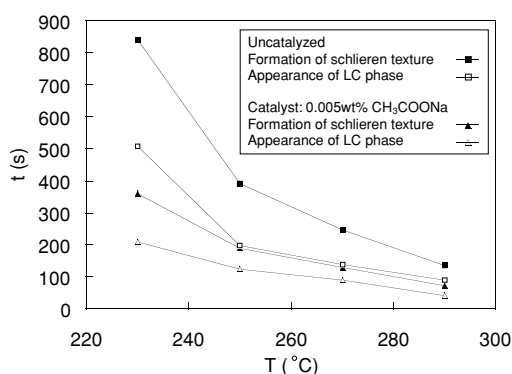


Figure 2.15 The dependence of the morphological transition time on the reaction temperature for the reaction systems with and without catalyst  $\text{CH}_3\text{COONa}$ . Monomer composition is 73/27 ABA/ANA.

TABLE 2.3. The Reaction Rate Constants for Uncatalyzed and Catalyzed Thin Film Polymerization Systems at Different Temperatures. Monomer Composition Is 73/27 ABA/ANA.

Temperature (°C)				
$k \times 10^4$ (L · mol <sup>-1</sup> · s <sup>-1</sup> ) (second region)	230	250	270	290
Uncatalyzed	2.04	7.54	14.05	29.05
Catalyst: 0.005 wt% CH <sub>3</sub> COONa	4.81	13.65	24.15	57.00

the temperature. At the constant  $DP$ , the rigidity of molecular chains increases with decreasing temperature; thus, the low  $DP$  may sufficiently yield mesogenic characteristics at a low reaction temperature.

From the data of Table 2.2 and Figure 2.15, the reaction rate constant,  $k$ , can be calculated by substituting the values of  $t$  and  $P$  into Equation (7), and the results are tabulated in Table 2.3. Interestingly, the reaction rate constant,  $k$ , for the thin film polymerization reactions is much greater than the reported value, as shown in Table 2.4, for bulk polymerization reactions [37]. For example, the  $k$  in the thin film reaction at 270°C without catalyst is  $14.05 \times 10^{-4}$  L · mol<sup>-1</sup> · s<sup>-1</sup>, while the second region  $k$  for bulk polymerization without catalyst at 275°C is  $3.2 \times 10^{-3}$  L · mol<sup>-1</sup> · min<sup>-1</sup> ( $0.53 \times 10^{-4}$  L · mol<sup>-1</sup> · s<sup>-1</sup>) [37]. The great difference is mainly due to the fact that the acetic acid in the thin film polymerization is much easier and quicker to release than that in the bulk polymerization. Using the same method,  $k$  for the catalyzed system with different catalyst levels is calculated, and the results are shown in Figure 2.16. The reaction rate constant increases with increasing catalyst content in an approximately linear manner.

To plot  $\ln k$  vs.  $1/T$ , the activation energy,  $E_a$ , can be obtained by the value from the slope. As shown in Figure 2.17, for an uncatalyzed system, the  $E_a$  is 109.9 kJ/mol, which is quite close to the value (105.8 kJ/mol) reported for bulk polymerization [37]. For a catalyzed system with 0.005 wt% CH<sub>3</sub>COONa,  $E_a$  drops slightly to about 96.9 kJ/mol [36].

TABLE 2.4. Reference Data for Reaction Rate Constants Obtained from Uncatalyzed Bulk Polymerization Reactions. Monomer Composition Is 73/27 ABA/ANA.

Temperature (°C)			
Reaction Rate Constant	250	275	300
$k_1 \times 10^3$ (L · mol <sup>-1</sup> · min <sup>-1</sup> ) (first region)	4.9	13.0	42.7
$k_2 \times 10^3$ (L · mol <sup>-1</sup> · min <sup>-1</sup> ) (second region) or $k_2 \times 10^4$ (L · mol <sup>-1</sup> · s <sup>-1</sup> ) (second region)		3.2 0.53	5.2 0.87

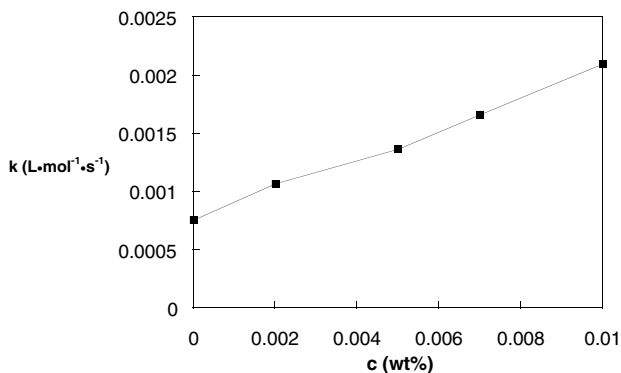


**Figure 2.16** The dependence of reaction rate constant on the catalyst  $\text{CH}_3\text{COONa}$  content. Monomer composition is 73/27 ABA/ANA. Reaction temperature is  $250^\circ\text{C}$ .

## 5. INVESTIGATION OF THE FORMATION OF LIQUID CRYSTALLINITY

Most monomers for LCP synthesis do not have liquid crystallinity. During the polymerization, LC phase forms and evolves with the progress of the polymerization, further annealing or curing reaction. Thin film polymerization technique is a very convenient way to investigate the formation of liquid crystallinity, because the LC phase can be clearly observed during the polymerization once the liquid crystallinity forms, and the reaction temperature, which is a critical parameter to form liquid crystallinity, can be accurately controlled.

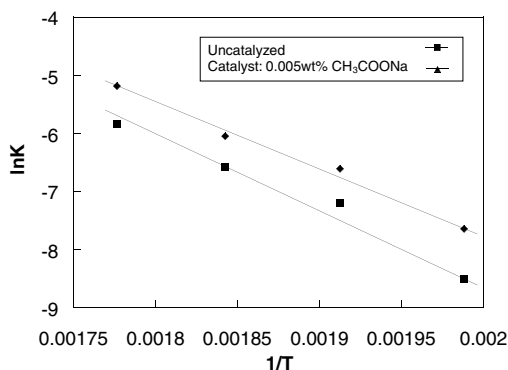


**Figure 2.17** Arrhenius plots for the thin film polymerization of P(OBA/ONA). Monomer composition is 73/27 ABA/ANA.

## 5.1. EFFECTS OF MONOMER STRUCTURES ON LIQUID CRYSTALLINITY

Polymers that exhibit liquid crystallinity, either in the melt or in their solutions, usually consist of comparatively rigid structures that confer high extension on the molecular chains. Intermolecular attractive forces also may contribute to the stabilization of the LC state. Polarizability of the molecules and their constituent groups are the molecular feature that is required to render the intermolecular force. Anisotropy of the polarizability tensors of the interacting molecules confers a corresponding anisotropy on the dispersive attractions between molecules. On this account, parallel molecular alignment may be energetically favored [1–3].

To study the effects of monomer structures and reaction conditions on liquid crystallinity and crystallization, a series of homopolymers and copolymers were synthesized. Their monomer compositions are ANA, ABA, AAA/IA, ANA/AAA/IA, and ABA/AAA/IA. The chemical structures of these monomers are shown in Figure 2.18.

ANA and ABA are among the most commonly used monomers for main-chain thermotropic LCPs. A typical example is the commercially available LCP Vectra A for which the monomer composition is 73/27 ABA/ANA [6,7]. *p*-Acetoxybenzoic acid (ABA) provides the benzene ring that potentially can form a mesogenic unit. Phenylene units in its homopolymer can rotate and, thus,

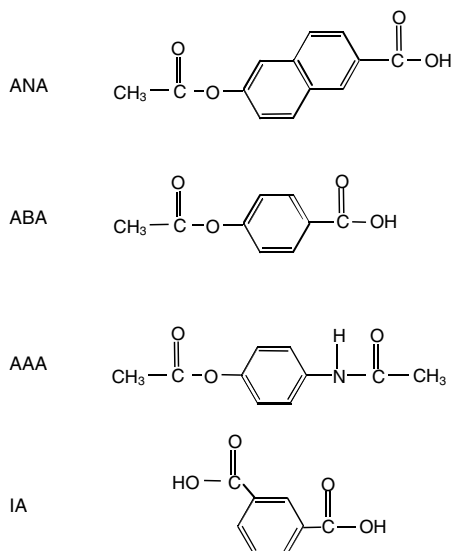


Figure 2.18 Chemical structures of the monomers.

are not collinear. In the molecular chain, additional chain motion is possible because the bridging group is an ester group. The ester group consists of angular bridging groups with parallel configuration. Each ester linkage gives a sideways displacement, but keeps the 1,4-axes of the benzene rings lying parallel, so that the ester linkage provides little opportunity for a chain to kink and keeps the chain straight. Although the straightness satisfies the requirement of forming the liquid crystallinity, the regularity and periodicity of the chain make the homopolymer become a highly crystalline material and have a quite high  $T_m$  if the molecular weight is high enough [6,7]. 2,6-Acetoxyphenylacetic acid (ANA) has a naphthoic ring to potentially form a mesogenic unit. It is usually used as a modifying unit for LCPs because of the side-step (crankshaft) effect associated with the naphthoic ring. Its homopolymer has a relative low  $T_m$  of 440°C due to the side-step effect. The homopolymer is also a crystalline material [11]. Acetoxy acetanilide (AAA) is also a frequently utilized monomer for synthesis of main-chain thermotropic LCPs, such as in Vectra B [6,7], which has the monomer composition of 60/20/20 ANA/AAA/TA (terephthalic acid). AAA provides a benzene ring potentially acting as a mesogenic unit, an amide group, and an ester group as bridging groups. Isophthalic acid (IA) is another monomer extensively employed to modify LCPs because its meta linkage can induce kink into the molecular chain. The resultant polymer may have a lower  $T_m$ . However, the meta linkage also has a detrimental effect to the stability of the LC phase, and it will disturb the liquid crystalline character if its percentage is too high [1–3]. Because of the structural character of the above monomers, the effects of monomer structures (length of mesogenic unit, kink) on the liquid crystallinity can be easily determined.

### 5.1.1. Morphological Changes during Homopolymerization Reactions with Monomer Compositions of ANA, ABA, and AAA/IA

As known to all, at certain temperatures, polymers can be morphologically divided into amorphous, crystalline, and liquid crystalline states [40,41]. In this study, the homopolymers of ANA and ABA form liquid crystalline phases in the early stage of the polymerization reactions, while the polymer of AAA/IA forms crystals.

#### 5.1.1.1. Formation of Liquid Crystallinity during Polycondensation Reactions of ANA and ABA

As shown in Figure 2.19, the homopolymerization system for pure ANA starts from a homogeneous phase and then changes into a heterogeneous system. When the sample is heated to the proposed reaction temperature, ANA crystals melt, and the whole view area becomes an isotropic melt phase. During the polycondensation reaction, oligomers form in the molten monomer phase. As

[www.iran-mavad.com](http://www.iran-mavad.com)

مرجع دانشجویان و مهندسين مواد

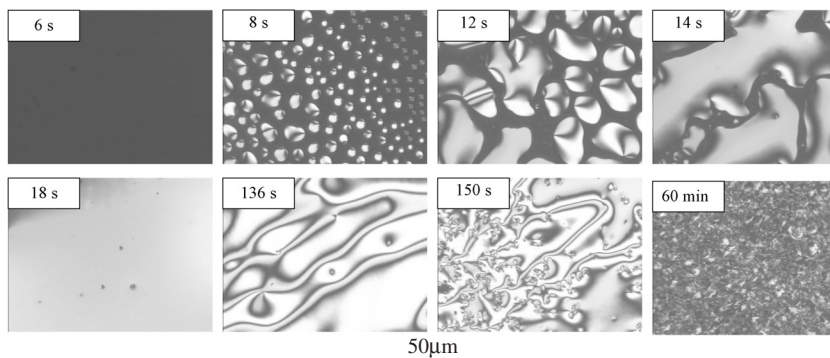


**Figure 2.19** Micrographs showing morphologies of pure ANA polymerization reaction system at different reaction times. All the micrographs are obtained from the same area of the same sample. Reaction temperature is 320°C.

shown in [Figure 2.19](#), the dark area in the micrographs is the isotropic phase of melt, while the bright area represents the LC phase. After the formation of LC domains, their sizes increase, and coalescence of adjacent LC domains occurs. During the coalescence process, annihilation between disclinations occurs to reduce free energy. The LC phase increases quickly within a very short period. When the reaction time is 18 s, the total view area becomes the LC phase. After 136 s reaction, crystallization begins to occur. After 216 s, no obvious morphological change can be observed, and the morphology is the same as the final morphology after reacting for 60 min.

For polymerization of ABA, [Figure 2.20](#) shows similar morphological changes to that of ANA. However, the major difference between them is that

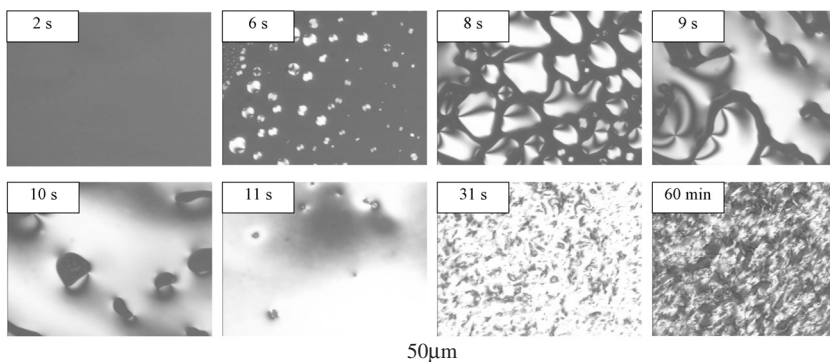


**Figure 2.20** Micrographs showing morphologies of pure ABA polymerization reaction system at different reaction times. All the micrographs are obtained from the same area of the same sample. Reaction temperature is 320°C.

polymerization of pure ABA has faster morphological transitions than that of pure ANA. This may be mainly due to the fact that the former has a lower melting point than the latter. Homopolymer of ABA is known to be a highly crystalline material and has a very high melting point. In the reaction system consisting of pure ABA, crystallization occurs much faster than that of pure ANA [41].

#### 5.1.1.2. Crystallization during Polycondensation Reaction of AAA/IA

Crystals of linear macromolecules can be grown not only from the melt or solution, but also directly from the polymerization because of the increasing molecular weight. Normally, melting point of the crystals increases with an increase in molecular weight. At a certain reaction temperature, because of the continuous increase in molecular weight, crystals will appear once the melting point of the crystals becomes higher than the reaction temperature. For the polymeric crystals grown directly during polymerization, there are two important types of homogeneous nucleation: oligomer nuclei and folded chain nuclei. Oligomer nucleation is the intermolecular path on crystallization during polymerization. It is the analogs to the fringed micelle nucleus of nucleation of an already polymerized molecule. Because the monomer is normally much shorter than the critical nucleus dimension, nucleation occurs only when sufficient reaction extent is reached. The folded chain nucleation means the molecules can still polymerize while undergoing nucleation and crystal growth. Further growth of the nucleus may occur through simultaneous or successive polymerization and crystallization [42].

Figure 2.21 shows the crystallization during the polycondensation reaction of 50/50 (mole ratio) AAA/IA. After nucleation, the radius of the spherulite increases with time almost linearly before the spherulite contacts other spherulites.

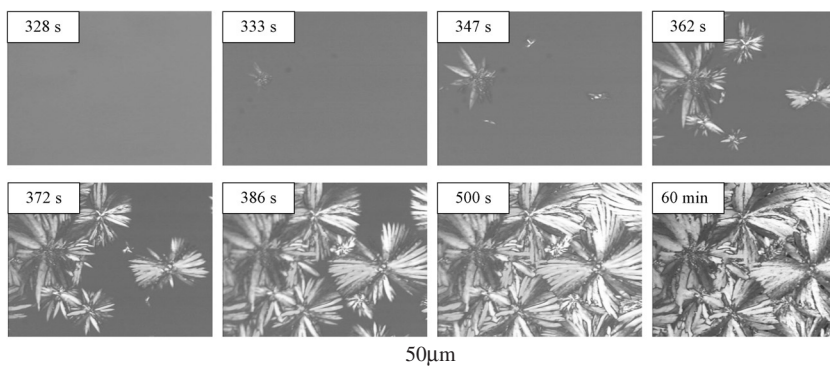


**Figure 2.21** Micrographs showing morphologies of 50/50 AAA/IA polymerization reaction system at different reaction times. All the micrographs are obtained from the same area of the same sample. Reaction temperature is 320°C.

The crystal growth rate, which is defined as the radius increase in unit time, is almost constant, about  $1.7 \mu\text{m/s}$  [41].

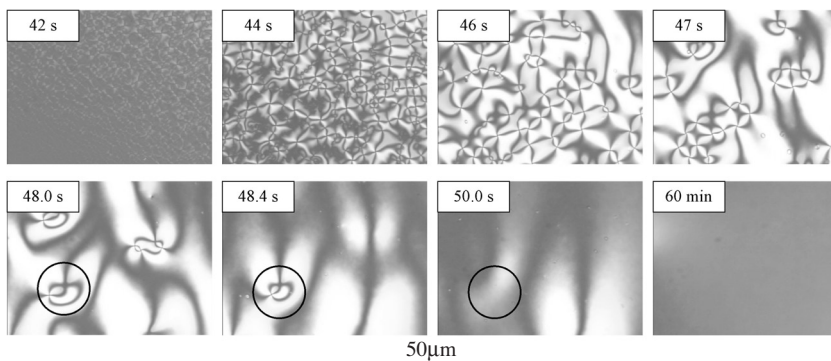
### 5.1.2. Morphological Changes during Copolymerization Reactions with Monomer Compositions of ANA/AAA/IA and ABA/AAA/IA

#### 5.1.2.1. Thin Film Polymerization Reactions of ANA/AAA/IA

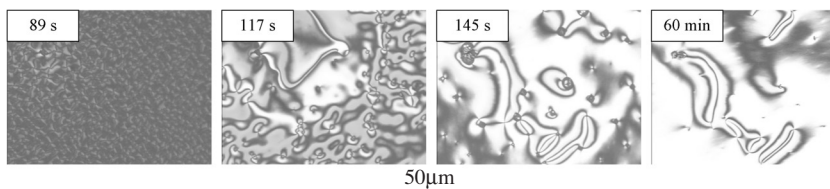
IA is a kind of modifying monomer for LCPs that introduces the kink into molecular chain to reduce the melting points of LCPs. However, the drawback of meta linkage is that it will disturb the liquid crystallinity if its content is too high. There is a critical ANA content for the reaction system ANA/AAA/IA to form liquid crystallinity or to crystallize. For example, when reaction temperature is  $320^\circ\text{C}$ , the critical ANA content is  $20 \pm 2\%$ . If the ANA content is higher than this value, the LC phase is formed; if the ANA content is lower than this value, crystallization occurs.

Figure 2.22 exhibits the generation of LC phase and time evolution of LC texture for 60/20/20 (mole ratio) ANA/AAA/IA at the reaction temperature of  $320^\circ\text{C}$ . For this system, the LC phase appears simultaneously with a high density of defects. And then, the annihilation between defects occurs rapidly to release the excess free energy. The circles in Figure 2.22 illustrate a typical example of the annihilation process when reaction time is between 48.0 s and 50.0 s, for which the annihilation rate is about  $23 \mu\text{m/s}$ . In the 60/20/20 ANA/AAA/IA reaction system, it only takes a few seconds to accomplish the annihilation process.

If ANA content is decreased to 40%, the defect density is increased in the final product, and, correspondingly, the annihilation rate decreases as shown in Figure 2.23.



**Figure 2.22** Micrographs showing morphologies of 60/20/20 ANA/AAA/IA polymerization reaction system at different reaction times. All the micrographs are obtained from the same area of the same sample. Reaction temperature is  $320^\circ\text{C}$ .



**Figure 2.23** Micrographs showing morphologies of 40/30/30 ANA/AAA/IA polymerization reaction system at different reaction times. All the micrographs are obtained from the same area of the same sample. Reaction temperature is 320°C.

As we know, rigid rod-like molecular structures, such as ANA and ABA, can import the liquid crystalline character to the materials. Defect density and annihilation process in the LC phase depend not only on monomer structure but also on monomer percentage. The higher the ANA content, the earlier the LC phase appears, and the lower the defect density after full annihilation. This interesting phenomenon is caused by the higher elastic constant values for the system having a higher concentration of ANA. In other words, the persistence length increases with an increase in corresponding ANA content.

Further decreasing ANA content, crystallization can be observed during the reaction if the ANA content is lower than the critical content to form liquid crystallinity. Figure 2.24 shows the crystallization during the polycondensation reaction of 10/45/45 ANA/AAA/IA. After nucleation, the radius of the spherulite increases with time almost linearly. The crystal growth rate is lower than the value for the 50/50 AAA/IA system.

There are many factors affecting the ability of a polymer to crystallize. The most important factor may be the regularity of the molecular structure. With

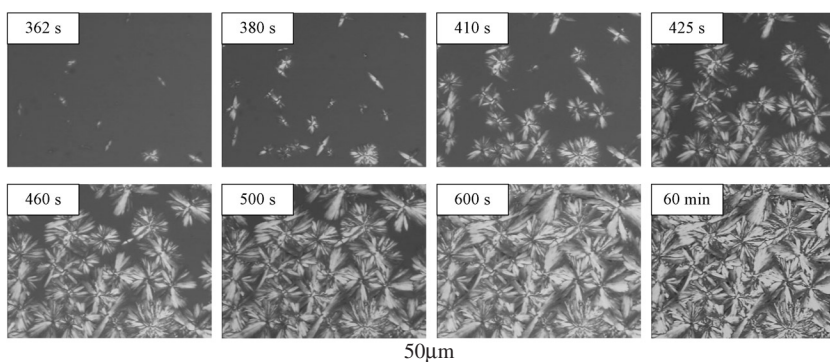


**Figure 2.24** Micrographs showing morphologies of 10/45/45 ANA/AAA/IA polymerization reaction system at different reaction times. All the micrographs are obtained from the same area of the same sample. Reaction temperature is 320°C.

high regularity, molecular chains can approach sufficiently close so that the interchain forces can maintain an ordered structure. The mobility of chains or chain segments is the other determining factor. Polymers with short repeating units and high symmetry can crystallize more readily than those with long repeating units and low symmetry. Obviously, adding the ANA units disturbs the regularity of the molecular structure, reduces the degree of periodicity along the chain, and frustrates crystal perfection. As a consequence, the crystal growth rate is lower for the system containing ANA [41].

#### 5.1.2.2. Thin Film Polymerization of ABA/AAA/IA

Similar to the ANA/AAA/IA system, LC phase appears in the ABA/AAA/IA polymerization system if the ABA content is higher than the critical content, and crystals form during the reaction if ABA content is lower than the critical content.

The generation of LC phase and time evolution of LC texture for 60/20/20 ABA/AAA/IA at the reaction temperature of 320°C is shown in Figure 2.25. Compared to the reaction of 60/20/20 ANA/AAA/IA, the annihilation for 60/20/20 ABA/AAA/IA is very slow. After the LC texture fully develops, the density of the defects is still very high.

As mentioned before, the elastic constants increase with increasing persistence length. If the molecular length,  $L$ , exceeds the persistence length, the values of  $K_2$  and  $K_3$  will tend to be constant, while  $K_1$  will increase monotonically with  $L$ . The lengths of the ANA and ABA units in the polymer chains are 8.37 Å and 6.35 Å, respectively [43]. Compared to the ANA/AAA/IA system, the main reason to cause a high defect density and a low annihilation rate in the ABA/AAA/IA system is due to molecular structure difference between ANA and ABA. ANA has a relatively longer cyclic unit to form a longer mesogenic unit. Because the molar percentages of ABA and ANA in these two reaction systems are exactly the same, the longer mesogenic unit of ANA may result in a greater persistence length. Because the elastic constants increase with increasing persistence length, the ANA/AAA/IA system has greater values of

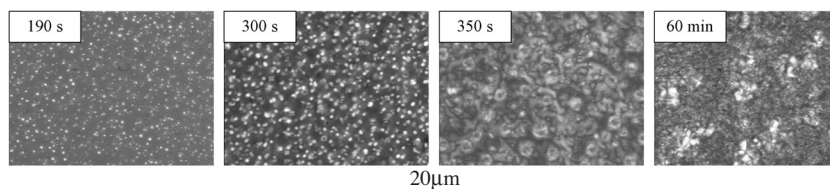


**Figure 2.25** Micrographs showing morphologies of 60/20/20 ABA/AAA/IA polymerization reaction system at different reaction times. All the micrographs are obtained from the same area of the same sample. Reaction temperature is 320°C.

the elastic constants and a higher tendency than the ABA/AAA/IA system to release energy and exhibit almost the same orientation. Thus, annihilation in the former is faster, easier, and more complete than in the latter [41].

## 5.2. EFFECTS OF REACTION TEMPERATURE ON THE LIQUID CRYSTALLINITY

As predicted by Flory, the critical aspect ratio of rod molecules for thermotropic liquid crystallinity is 6.4 [2,3]. However, in this prediction, the influence of temperature was not considered. The temperature effect was included in the form of an orientationally dependent energy function in more recent development of the Flory lattice model [3]. For LMWLCs, the aspect ratio is defined as  $L/d$ , in which  $L$  is the length and  $d$  is the diameter of the molecule. For LCPs, the aspect ratio is replaced by persistence ratio through replacing molecule length  $L$  by persistence length  $q$  [3].

In ANA/AAA/IA and ABA/AAA/IA systems, the meta linkage in IA has an angular conformation ( $120^\circ$ ). The kink created by the IA monomeric unit results in entanglement and shortens the persistence length of the polymer chain. Thus, the system containing higher content of IA (in other words, lower content of ANA or ABA) should be less likely to form liquid crystallinity because the persistence ratio increases with increasing ANA or ABA content. When the content of ANA or ABA reaches a critical value, the LC phase can be formed.

Figure 2.26 shows the critical ANA and ABA content for the reaction systems of ANA/AAA/IA and ABA/AAA/IA to form liquid crystallinity as a function of reaction temperature. For example, when reaction temperature is  $280^\circ\text{C}$ , the critical ANA content is  $22 \pm 2\%$ . If the ANA content is higher than this value, the LC phase is formed; if the ANA content is lower than this value, crystallization occurs. This figure also suggests that, for both systems, the critical content of ANA or ABA decreases with increasing reaction temperature. This interesting relationship may be due to the following possibility: reactions at

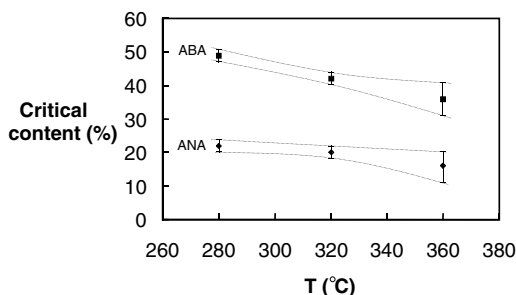


**Figure 2.26** The dependence of the critical ANA and ABA content on the reaction temperature.

different temperatures may yield different sequences of monomeric units in the chains. The other reason is due to the fact that the oligomers may form crystals at a low temperature, but exhibit the LC state at a high temperature.

An interesting phenomenon occurs when the reaction temperature is 360°C: there is an amorphous region between the critical content of ANA or ABA to form the LC state and the crystalline state. For example, if ANA content is in the range of 12% to 21%, nothing can be optically discerned until the end of the polymerization, which suggests the products should be in the amorphous state. This surprising phenomenon might be due to the reduction of persistence length at high temperatures. At low temperatures, chain rigidity is high, and the conformation of molecules tends to be straight and thus yields the LC state. However, at high temperatures, chain rigidity reduces, and the chains have the ability to form entanglements. As a result, persistence length reduces, and the amorphous state is formed. However, by further increasing ANA or ABA percentage, the LC state can still appear because the resultant polymer has a long persistence length [40,41].

## **6. INVESTIGATION OF THE ELECTRIC RESPONSE OF LIQUID CRYSTALLINE POLYMER DURING POLYMERIZATION**

### **6.1. INTRODUCTION OF THE ELECTRIC FIELD EFFECTS ON LIQUID CRYSTALLINE MATERIALS**

Since the electro-optical effect of LCs was discovered and its extensive applications were recognized, the effects of electric field on the liquid crystal materials have been of considerable interest to both academy and industry. The direct influences of the electric field on LC include shift of the phase transition temperature, variation in order parameter, and change in symmetry [44,45].

Because of the dielectric anisotropy property of LCs, the LC molecules can align either parallel or perpendicular to the electric field, theoretically, according to their values of dielectric anisotropy [44]. However, under certain conditions, the uniform director reorientation in an a-c electric field is unfavorable; the domain structure corresponding to a minimum free energy is formed. The domain patterns can be classified into two main types: orientational domains with pure director rotation without fluid motion and the electrohydrodynamic domains caused by the combined effects of the periodic director reorientation and regular vortices of material moving [44]. This kind of movement of LC materials is called “hydrodynamic flow,” mainly resulting from the effects of conductivity anisotropy of LC molecules and ionic electric current.

The movement of LC materials in an electric field is known as “electrohydrodynamic instability” [44,45]. Theoretically, it occurs when the dielectric anisotropy and conductivity anisotropy have different signs, most commonly

with negative dielectric anisotropy and positive conductivity anisotropy. The domain formation also greatly depends on the parameters of external field. In a low-frequency region, the most frequently observed one is called “Williams domains” or “Kapustin-Williams domains,” caused by a periodic distortion accompanying a certain amount of cellular flow. The spatial period is slightly shorter than the sample thickness. This frequency region is known as “conduction regime.” In many cases, the Williams domain pattern is a simple one-dimensional pattern, and the pattern stays the same when the electric field reverses. However, the pattern may be interrupted, and a two-dimensional periodicity can be found. This kind of two-dimensional pattern is identified as “fluctuating Williams domains” [45]. In a high-frequency region, a narrow band mode called the “Chevron pattern” can be observed. This frequency region is called the “dielectric regime.” In this regime, the charge oscillations cause the oscillations of LC materials, so the vortices are not stationary but in the form of “to and fro” motion [44].

To form the domain structure, there usually exists a threshold voltage. The threshold value is a function of the physical properties of an LC, such as dielectric and conductivity anisotropies, viscoelastic properties, and the experiment conditions, such as amplitude and frequency of the external field, cell thickness, and initial orientation. Previous work [19,44] suggests that the threshold voltage to form the Williams domains is not strongly dependent on the frequency, while the threshold voltage for the Chevron pattern increases with increasing frequency. With further increase in the voltage, the flow velocity increases. Finally, above a certain voltage, a new regime is reached: the domain becomes disordered and mobile, and the flow becomes turbulent. The latter phenomenon results in strong light scattering, known as “dynamic scattering” [19,44].

Although there is a fair amount of knowledge about LCPs, the study of electrical response of thermotropic main-chain liquid crystalline polymers (MCLCPs) under electrical fields is very limited. Most of the research has concentrated on low molecular weight liquid crystals (LMWLCs) [46–52]. Only a few papers reported the effects of electrical field on thermotropic MCLCPs [53,54]. In studies by Krigbaum et al. [53,54], the Kapustin-Williams domains and light dynamic scattering were observed for the polymeric nematics. The electrohydrodynamic instability of LCPs is similar to that of LMWLCs. The principal differences between them are the slow dynamics of the domain formation and the difficulty of obtaining a well-aligned pattern [45,53,54]. The critical frequency to induce instability in the conduction regime was found to be strongly dependent on the molecular weight [53]. The domains and light scattering textures can be frozen by cooling the samples in the electric fields [44].

Most monomers for LCP synthesis do not possess liquid crystallinity. During polymerization, LC phase forms, and the LC texture evolves with the progress of the reaction. The electric response of the polymerization system of LCP also

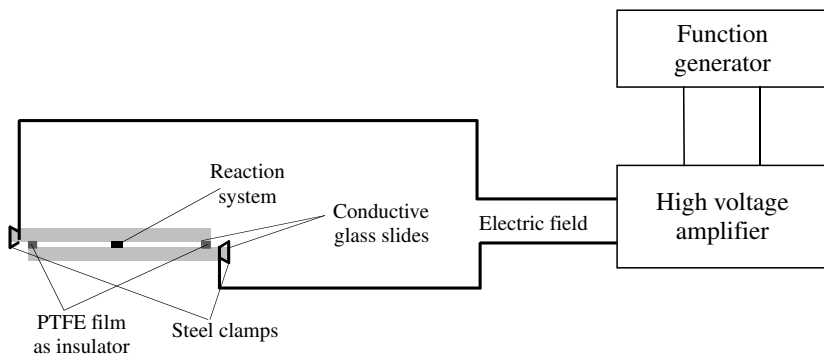


**Figure 2.27** The thin film polymerization under a-c electric field.

evolves with reaction process. Through investigation of the electric response of the reaction system, lots of important information about the properties of LCP can be obtained.

## 6.2. POLYMERIZATION OF LIQUID CRYSTALLINE POLYMER UNDER ELECTRIC FIELD

The thin film polymerization method is the same as the one without electric field. The sample package and connection of electric devices are shown in [Figure 2.27](#). Monomer mixture 73/27 ABA/ANA was sandwiched between two conductive glass slides coated with indium tin oxide (ITO). A poly(tetrafluoroethylene) (PTFE) film was used as a spacer as well as an insulator. The thickness of the sample was 80  $\mu\text{m}$ . The conductive glass slides were connected with the outputs of a high-voltage amplifier through the wires clamped by the steel clamps. Electric field was generated by a function generator (HP 33120A) and was amplified by the high-voltage amplifier (Trek P0623A). The electric fields (square wave) with different frequencies were applied to the reaction system after the generation of LC phase [55].

## 6.3. ELECTRIC RESPONSE OF THE POLYMERIZATION SYSTEM OF LIQUID CRYSTAL POLYMER

### 6.3.1. Morphology of the LCP Polymerization System Between Conductive Glass Slides

In our experiment, we applied electric field on the polymerization system after the whole view area became an LC phase. [Figure 2.28](#) shows the appearance of

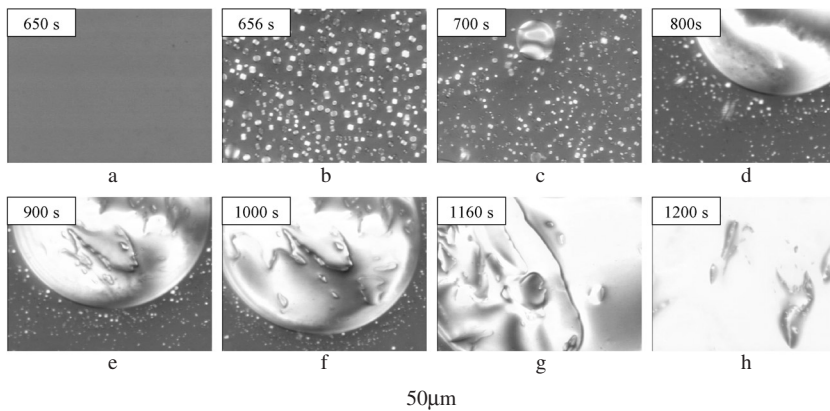


**Figure 2.28** Appearance of LC phase between two conductive glasses (without electric field). Monomer composition: 73/27 ABA/ANA. Reaction temperature: 230°C.

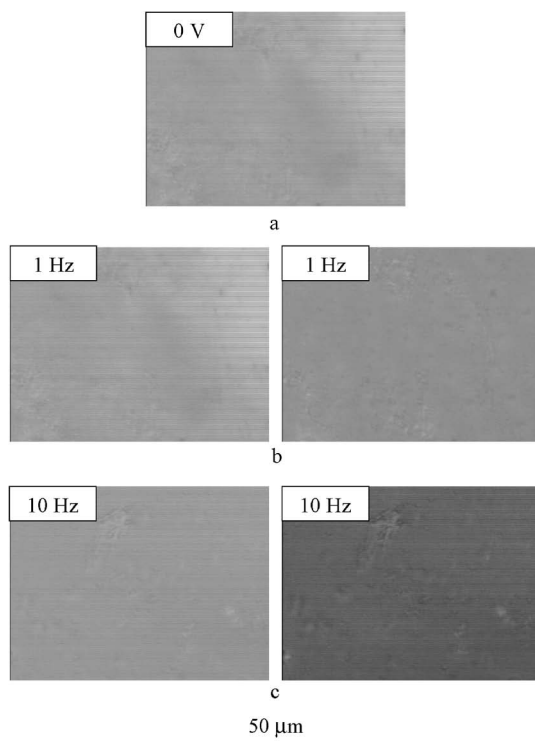


**Figure 2.29** The morphologies of LC phase without electric field and under a-c electric fields in low-frequency range: (a) Without electric field, (b) 1 Hz, and (c) 10 Hz. Voltage of the a-c electric field: 25 V. Range of reaction time: 20–30 min. Monomer composition: 73/27 ABA/ANA. Reaction temperature: 230°C.

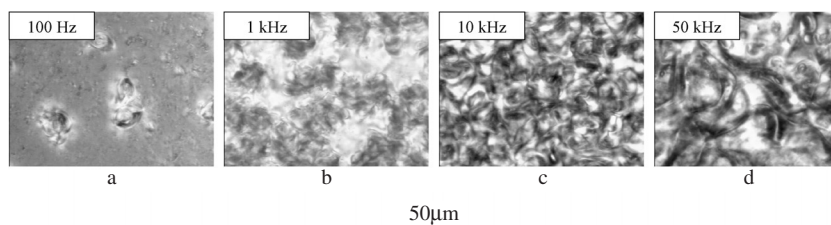
the LC phase before applying the electric field. Unlike the reaction on a normal glass slide, the LC phase generated on the conductive coating layer tends to form large, separated droplets instead of a uniform LC thin layer because of the surface properties of the conductive coating layer. Figure 2.28(c–g), shows that the bigger LC domains seem to attract the smaller LC domains to increase their areas. And, finally, a large LC domain forms and occupies the whole view area as shown in Figure 2.28(h).

### 6.3.2. Response of the LC Phase under Electric Fields with Different Frequencies

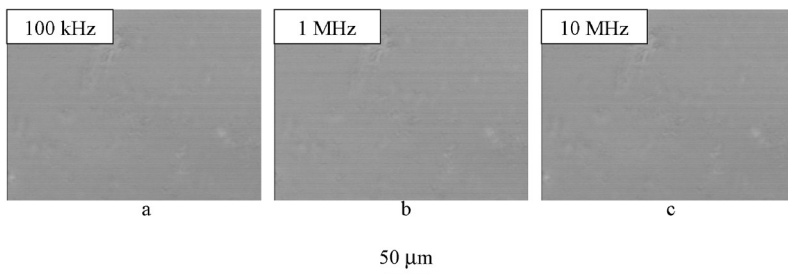
After the whole view area becomes an LC phase, we apply a-c electric fields with different frequencies and a certain voltage to observe the effects of electric fields on the LC phase. The reaction time ranges from 20 min to 30 min.

Figure 2.29 shows the morphologies of the LC phase in low-frequency range. Under these low-frequency a-c fields, orientation of LC materials can be found. Figure 2.29(a) is the morphology of the LC phase without electric field. Figure 2.29(b) shows the morphologies of the LC phase after applying the external field of 25 V (rms) and 1 Hz. The time interval to snap these two pictures is 0.5 s. Under the electric field, the LC phase becomes more transparent and twinkles when the electric field changes its direction. Figure 2.29(c) shows the morphologies of reaction system under a 10-Hz electric field. Similar orientation phenomena can be seen. The major difference between the responses under 1-Hz and 10-Hz fields is that the LC phase does not flicker obviously under a relatively high-frequency field.

With an increase in frequency, electrohydrodynamic instability can be found in a relatively wide voltage range, while the external field effect on orientation becomes less visible. When voltage is 25 V, the electrohydrodynamic flow begins to form once the frequency reaches 100 Hz. This kind of flow occurs in a wide frequency range, from 100 Hz to 60 kHz, as shown in Figure 2.30. The flow



**Figure 2.30** The morphologies of LC phase under a-c electric fields in middle-frequency range: (a) 100 Hz, (b) 1 kHz, (c) 10 kHz, and (d) 50 kHz. Voltage of the a-c electric field: 25 V. Range of reaction time: 20–30 min. Monomer composition: 73/27 ABA/ANA. Reaction temperature: 230°C.



**Figure 2.31** The morphologies of LC phase under a-c electric fields in high-frequency range: (a) 100 kHz, (b) 1 MHz, and (c) 10 MHz. Voltage of the a-c electric field: 25 V. Range of reaction time: 20–30 min. Monomer composition: 73/27 ABA/ANA. Reaction temperature: 230°C.

is faster in the middle frequency region (400 Hz to 8 kHz) and becomes slower if the frequency is outside this range. The flow becomes faster if the voltage of electric field increases. As shown in Figures 2.30(c,d) the flow patterns in a relatively high-frequency range (10 kHz to 50 kHz) are quite similar to the fluctuating Williams domains that have been reported for other polymeric nematic LCs [53,54]. However, our experiments indicate that there is no distinct morphological change from the fluctuating Williams domains to the dynamic scattering mode for the polymerized LCP system. The difference between them is the flow rate, which is faster for the dynamic scattering mode.

By further increasing the frequency, the effect of electric fields on the LC phase becomes undetectable because the director of LC cannot follow the field and exhibits an almost stationary distribution. When voltage is 25 V, the movements of LC material seem to become stationary when frequency reaches 60 kHz. Figure 2.31 gives some examples of LC morphologies under high-frequency fields with the voltage of 25 V. Comparing these pictures with the one without electric field (Figure 2.29(a)), no distinct difference can be found [55].

## 7. REFERENCES

1. A. M. Donald and A. H. Windle, *Liquid Crystalline Polymers*, Cambridge University Press, Cambridge (1992).
2. A. A. Collyer, *Liquid Crystal Polymers: From Structures to Applications*, Elsevier Science, London (1992).
3. A. H. Windle, *Liquid Crystalline and Mesomorphic Polymers*, Chapter 2, Ed. by V. P. Shibaev and L. Lam, Springer-Verlag, New York (1994).
4. H. Han and P. K. Bhowmik, *Prog. Polym. Sci.* 22, 1431 (1997).
5. R. A. Weiss and C. K. Ober, *Liquid Crystalline Polymers*, Chapter 1, American Chemical Society, Washington, D.C. (1990).

6. T. S. Chung, *Polym. Eng. Sci.*, 26, 901 (1986).
7. T. S. Chung, G. W. Calundann, and A. J. East, *Encyclopedia of Engineering Materials*, 2, 625 (1989).
8. J. Economy, *Mol. Cryst. Liq. Cryst.*, 169, 1 (1989).
9. F. Rybníkar, B. L. Yuan, and P. H. Geil, *Polymer*, 35, 1863 (1994).
10. F. Rybníkar, J. Liu, and P. H. Geil, *Macromol. Chem. Phys.*, 195, 81 (1994).
11. J. Liu, F. Rybníkar, and P. H. Geil, *J. Polym. Sci. Phys.*, B30, 1469 (1992).
12. F. Rybníkar, B. L. Yuan, and P. H. Geil, *Polymer*, 35, 1831 (1994).
13. J. Liu, F. Rybníkar, and P. H. Geil, *J. Macromol. Sci.-Phys.*, B35, 375 (1996).
14. Q. Lin, A. F. Yee, H. J. Sue, J. D. Earls, and R. E. Hefner, *J. Polym. Sci. Phys.*, B35, 2363 (1997).
15. A. Shiota and C. K. Ober, *Macromolecules*, 30, 4278 (1997).
16. S. X. Cheng, T. S. Chung, and S. Mullick, *Chem. Eng. Sci.*, 54, 663 (1999).
17. S. X. Cheng and T. S. Chung, *J. Phys. Chem.*, B103, 4923 (1999).
18. A. Nakai, W. Wang, T. Hashimoto, A. Blumstein, and Y. Maeda, *Macromolecules*, 27, 6963 (1994).
19. P. G. de Gennes and J. Prost, *The Physics of Liquid Crystal*, Clarendon Press, New York (1993).
20. W. Wang, *Liq. Cryst.*, 19, 251 (1995).
21. J. Gunther, E. L. Thomas, S. Clingman, and C. K. Ober, *Polymer*, 39, 4497 (1998).
22. S. D. Hudson, J. W. Fleming, E. Gholz, and E. L. Thomas, *Macromolecules*, 26, 1270 (1993).
23. C. Liu and M. Muthukumar, *J. Chem. Phys.*, 106, 7822 (1997).
24. H. M. Shehadeh and J. P. McClymer, *Phys. Rev. Lett.*, 79, 4206 (1997).
25. T. Shiwaku, A. Nakai, H. Hasegawa, and T. Hashimoto, *Polymer Communications*, 28, 174 (1987).
26. W. H. de Jeu, *Physical Properties of Liquid Crystal Materials*, Gordon and Breach, New York (1980).
27. C. Viney and W. S. Putnam, *Polymer*, 36, 1731 (1995).
28. W. Wang, G. Lieser, and G. Wegner, *Liq. Cryst.*, 15, 1 (1993).
29. S. Chen, W. Song, Y. Jin, and R. Qian, *Liq. Cryst.*, 15, 247 (1993).
30. U. Pedretti, B. Bresci, C. Bonfanti, P. L. Magagnini, F. P. La Mantia, and A. Roggero, U. S. Patent 5,086, 160 (1992).
31. A. J. East, L. F. Charbonneau, and G. W. Calundann, U. S. Patent 4,330,457 (1982).
32. L. F. Charbonneau, U. S. Patent 4,429,105 (1984).
33. H. Pielartzik, H. Brinkmeyer, R. V. Meyer, and B. Willenberg, U. S. Patent 5,084,547 (1992).
34. L. F. Charbonneau and G. W. Calundann, U. S. Patent 5,171,823 (1992).
35. G. W. Calundann, U. S. Patent 4,161,470 (1979).
36. T. S. Chung and S. X. Cheng, *J. Polym. Sci. Chem.*, A38, 1257 (2000).
37. P. A. Williams, X. Han, A. B. Padias, and H. K. Hall, *Macromolecules*, 29, 1874 (1996).
38. X. Han, P. A. Williams, A. B. Padias, and H. K. Hall, *Macromolecules*, 29, 8313 (1996).
39. J. Mathew, R. V. Bahulekar, R. S. Ghadage, C. R. Rajan, S. Ponrathnam, and S. D. Prasad, *Macromolecules*, 25, 7338 (1992).
40. S. X. Cheng and T. S. Chung, *J. Polym. Sci. Phys.*, B38, 2221 (2000).
41. S. X. Cheng, T. S. Chung, and S. Mullick, *J. Polym. Sci. Phys.*, B37, 3084 (1999).
42. B. Wunderlich, *Macromolecular Physics*, Academic Press, New York (1973).
43. R. A. Chivers, J. Blackwell, and G. A. Gutierrez, *Polymer*, 25, 435 (1984).
44. L. M. Blinov and V. G. Chigrinov, *Electrooptic Effects in Liquid Crystal Materials*, pp. 235–297, Springer-Verlag, New York (1994).
45. W. R. Krigbaum, *Polymer Liquid Crystals*, Chapter 10, Academic Press, New York (1982).
46. Y. Hidaka, J. H. Huh, K. Hayashi, S. Kai, and M. I. Tribelsky, *Phys. Rev. E*, 56, R6256 (1997).
47. P. Toth, A. Buka, J. Peinke, and L. Kramer, *Phys. Rev. E*, 58, 1983 (1998).
48. T. John, R. Stannarius, and U. Behn, *Phys. Rev. Lett.*, 83, 749 (1999).

49. R. K. Medya, R. N. P. Choudhary, and P. K. Mahapatra, *Liq. Cryst.*, 26, 795 (1999).
50. D. E. Lucchetta, N. Scaramuzza, G. Strangi, and C. Versace, *Phys. Rev. E*, 60, 610 (1999).
51. H. M. Shehadeh and J. P. McClymer, *Phys. Rev. Lett.*, 79, 4206 (1997).
52. G. Strangi, C. Versace, N. Scaramuzza, D. E. Lucchetta, V. Carbone, and R. Bartolino, *Phys. Rev. E*, 59, 5523 (1999).
53. W. R. Krigbaum, C. E. Grantham, and H. Toriumi, *Macromolecules*, 15, 592 (1982).
54. W. R. Krigbaum, H. J. Lader, and A. Ciferri, *Macromolecules*, 13, 554 (1980).
55. S. X. Cheng and T. S. Chung, *J. Phys. Chem.*, B104, 10506 (2000).

# Crystallization of Main Chain Liquid Crystalline Polymers

SONG-LIN LIU  
K. P. PRAMODA  
TAI-SHUNG CHUNG

## 1. INTRODUCTION

**T**HERMOTROPIC liquid crystalline polymers can crystallize to form three-dimensionally ordered crystals following the liquid crystallization phase transition. The crystallization process can take place if the crystalline phase is more thermodynamically stable than the liquid crystalline phase in that specific temperature range and the molecular chains are regular enough for crystallization [1]. The crystallization behavior of rigid rod-like thermotropic liquid crystalline polymers is expected to be different from that of flexible chain polymers. The crystallization of flexible chain polymers such as polyethylene, polypropylene is very fast because the polymer chains can be easily incorporated into crystal growing sites and the crystallinity can be very high [2]. In thermotropic liquid crystalline polymers, it is difficult for the rigid, rod-like molecules to diffuse into the crystalline region as a result of positional and orientational restrictions. Thus, it might be expected that the crystallization of rigid chain thermotropic liquid crystalline polymers is slow. On the other hand, the liquid crystallization process is an ordering process that results in alignment of molecular chains and favors the followed crystallization process starting from the liquid crystalline state. Therefore, thermotropic liquid crystalline polymers should crystallize fast from the mesophase.

For enantiotropic thermotropic liquid crystals, the crystallization may occur only from the liquid crystalline phase, provided that the temperature is sufficiently decreased to a range where the crystalline phase is the most stable one. In monotropic systems, the liquid crystalline phase is metastable, and crystallization may occur either from the isotropic melt or from the liquid crystalline

phase [3–5]. The liquid crystalline phase can only be observed if the crystal phase is supercooled. The determination of the crystal structure includes individual chain conformation and chain packing. Chain conformation is the intrinsic property of the chain molecules that tend to adopt a conformation with minimum rotational potential energy with respect to intramolecular and intermolecular interactions.

In the crystallization state, the polymer chains or portions of polymer chains are constrained to align parallel to one another. Compared to other materials, such as metals and small molecules, polymer crystals have their own uniqueness: (1) the repeating unit does not involve the molecule as a whole but merely its repeating constituents, and, therefore, one molecule may be involved in many unit cells; (2) usually, the *c*-axis corresponds to the repeating unit along the chain; the other two cell dimensions (*a*, *b*) correspond to lateral repeating distance between different chains in equivalent positions [6]. Therefore, the lattice periodicity is defined by covalent forces. In the lateral directions, intermolecular forces (van der Waals forces and/or hydrogen bonding) affect the chain packing.

In 1950s, experiments on the observation of polymer single crystals grown from very dilute solutions have confirmed the chain folding theory in flexible polymers [7]. However, the way by which the polymer chains leave and re-enter the crystals remained unsolved. The core question is how the polymer chains re-enter the crystals. The widely accepted concept about the re-entry is the so-called switchboard model [2,8]. This model involves a crystal that grows by incorporating the materials situated close to the crystal growth front. In this way, parts of a macromolecule can be separated along its backbone and crystallized into different lamellae. This anchoring of polymer chain would prevent further relations and inherently creates an uncrystallized portion.

Extended chain crystals represent the most thermodynamically stable state. However, kinetically, it is very difficult. Extended chain crystals can be grown only under extreme conditions in flexible chain polymers, such as high pressure and high temperature [9]. Nevertheless, the polymer chains of most thermotropic liquid crystalline polymers are rigid. It is unlikely for rigid, rod-like molecules to form chain-folded crystallization. Macromolecules in rigid chain polymers may take extended chain crystallization [10].

Spherulites, which are the aggregation of lamellae and represent the highest level in the morphological hierarchy, are the most commonly observed morphology in crystalline polymers [11]. They can be visualized as a radiating array of crystals. As the lamellae are generally radiating along the radius, the molecular chains are perpendicular to the radius. Homogeneous nucleation developed from a small lamellar crystal leads to the formation of Popoff-type spherulites [Figure 3.1(a)]. The distinct character is the two cavities near the center at the early development of spherulites. Heterogeneous nucleation gives

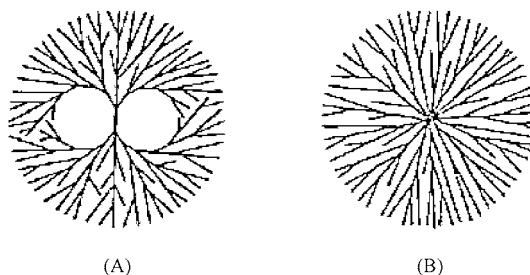


**Figure 3.1** Schematic of two types of polymer spherulites. (a) Popoff-type; (b) hedgehog type.

to the hedgehog type of spherulites [Figure 3.1(b)]. The earliest observation of spherulites from synthesized polymer was made by Bunn and Alcock [12]. In an ideal case, the spherulites should be seen as circular birefringent areas in the field of view possessing a dark Maltese cross with two arms parallel and perpendicular to the direction of polarization of the incident light when viewed between two crossed polaroids. This appearance can be accounted for by a spherically symmetrical arrangement of uniaxial index ellipsoids.

The origin of the black cross is due to the extinction arising from the coincidence of the transmission direction with the direction of the polarizer or analyzer. A plane equatorial section of a spherulite is shown in Figure 3.2. If the larger refractive index is radial, the spherulite is optically positive; if it is tangential, it is optically negative [13].

The large body of thermotropic liquid crystalline polymers is polyesters [14], some of which have been successfully commercialized. And very recently, quite a lot of thermotropic liquid crystalline polyimides have been reported [15]. In this chapter, the crystallization behavior and phase transition kinetics of thermotropic polyesters and polyimides will be discussed.

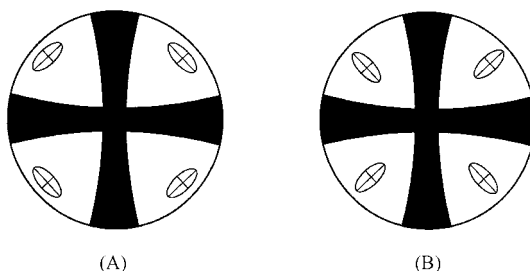


**Figure 3.2** Maltese extinction cross in spherulites and the optical properties of spherulites. (A) Direction of slow vibration is radial; (B) direction of fast vibration is radial.

## 2. POLYMER CRYSTALLIZATION: THEORY

The kinetics analysis of crystallization is not only important for the fundamental understanding of the formation of the crystalline phase but also for technical control of crystal sizes in many practical applications [16]. The base for crystallization kinetics analysis is the quantitative determination of the degree of crystallinity with crystallization time. In general, any crystallinity-sensitive properties of polymers can be used for crystallinity determination. Such properties fall generally within three classes: thermodynamic, diffraction-based, and spectroscopic. The commonly used methods for crystallinity determination include specific volume, heat of fusion, X-ray diffraction, depolarized light intensity, and infrared spectroscopy, etc. The measurements obtained by these methods lead to a sigmoidal curve with slope representing the crystallization rate as shown in Figure 3.3. The overall crystallization rate is a function of crystallization temperature ( $T_c$ ). Theoretically, a crystallizable polymer can crystallize at a temperature between the melting temperature ( $T_m$ ) and the glass transition temperature ( $T_g$ ). However, the crystallization rate may be very slow when  $T_c$  closes to  $T_m$  or  $T_g$ . When  $T_c$  approaches  $T_m$ , the overall crystallization rate decreases because of the increase in nucleation barrier that is required to be overcome to form a stable nucleus of a critical size. On the other hand, when  $T_c$  closes to  $T_g$ , the rate decreases because the chain molecules lose mobility. In between  $T_m$  and  $T_g$ , there is a maximum value for the overall crystallization rate at a certain temperature,  $T_{max}$ . The overall crystallization rate forms a bell-shaped curve as shown in Figure 3.4.

The crystallization process can be studied isothermally or non-isothermally. The isothermal study can be used to elucidate the crystallizability of polymers, the nucleation, and the crystal growth mechanism. However, most polymers are processed under non-isothermal conditions. It would be more informative to study the crystallization behavior under both isothermal and non-isothermal conditions.

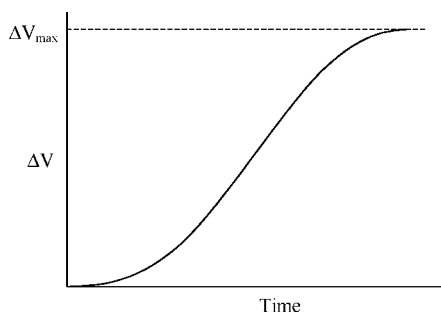
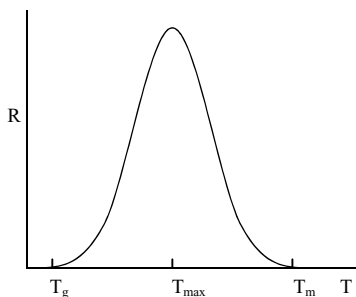


Figure 3.3 A schematic crystallization isotherm.



**Figure 3.4** The change of crystallization rate as a function of crystallization temperature,  $T_c$ .

## 2.1. ISOTHERMAL CRYSTALLIZATION

The overall crystallization that includes two steps, primary nucleation followed by crystal growth, can be well described by Avrami treatment [17,18]. This treatment involves several considerations:

- (1) The crystallization process is under isothermal condition.
- (2) The volume remains invariable during the process.
- (3) Crystals grow at a constant rate.
- (4) The number of nuclei is assumed to be either constant (athermal nucleation) or varying with time (thermal nucleation).

The overall crystallization process can be described by Equation (1):

$$1 - \theta = \exp[-Kt^n] \quad (1)$$

where  $\theta$  is the relative crystallinity at time  $t$ ,  $n$  is the dimensionality of crystal growth, and  $K$  is a temperature-dependent constant that depends on the growth geometry, the number of nuclei present, and the linear growth rate of polymer crystals. A straight line is obtained when  $\log [-\ln(1 - \theta)]$  is plotted versus  $\log(t)$ , from which  $n$  can be obtained as the slope and  $\log(K)$  as the intercept. The nature of the nucleation and the growth and nucleation rates can be assessed.

As polymer crystallization is thermally activated, the crystallization rate,  $K$ , can be described by Arrhenius equation [Equation (2)] [19]:

$$K^{1/n} = K_0 \exp(-\Delta E/RT_c) \quad (2)$$

where  $R$  is gas constant and  $K_0$  is a temperature-independent preexponential factor. The crystallization activation energy can be determined from the plot of  $(1/n) \ln K$  versus  $1/T_c$ .

Measurement of relative crystallinity  $\theta$  as a function of time,  $t$ , can be very simple, and the results are informative. However, some limitation for applying the Avrami equation must be taken into account. The volume is not constant during crystallization, the crystal growth rate may not be constant, the nucleation may vary with time, and the crystal lamellae branching and perfection process may occur over the course of crystallization.

It should be mentioned that crystallization from a liquid crystalline phase may present its own peculiarities. The orientational order associated with mesophase may act as a precursor for further crystal growth, especially in monotropic liquid crystalline polymers where the metastability of mesophase generally leads to the formation of a more stable crystal phase.

## 2.2. NON-ISOTHERMAL CRYSTALLIZATION

For non-isothermal crystallization, the process can be described by the modified Avrami equation in which the crystallization temperature is converted to time through heating or cooling rate,  $\Phi$ , by dividing crystallization temperature into infinity small [Equation (3)].

$$t = \frac{T - T_0}{\Phi} \quad (3)$$

where  $\Phi$  is the cooling rate.

The degree of crystallinity  $\theta$ , which is a function of temperature, can be defined as Equation (4):

$$\theta = \frac{\int_{T_0}^T \left( \frac{dH_c}{dT} \right) dT}{\int_{T_0}^{T_\infty} \left( \frac{dH_c}{dT} \right) dT} \quad (4)$$

where  $T_0$  and  $T_\infty$  are the initial and ending crystallization temperatures, respectively.

Non-isothermal crystallization during cooling is a cooling rate-dependent process. Ozawa extended the isothermal crystallization analysis to the non-isothermal case of controlled cooling rate [20,21]. This method accounts for the effect of cooling rate,  $\Phi$ , on crystallization from the melt by replacing  $t$  in equation (A) with  $T/\Phi$  as Equation (5):

$$1 - \theta = \exp\left(-\frac{Z(T)}{\Phi^m}\right) \quad (5)$$

where  $Z(T)$  is cooling function of the process, and  $m$  is the Ozawa exponent. The value of  $m$  is dependent on the dimension of crystal growth.

The non-isothermal crystallization activation energy can be derived by the combination of cooling rate and exothermic peak temperature ( $T_p$ ), shown as the Kissinger method [22] in Equation (6).

$$\frac{d(\ln(\Phi/T_p^2))}{d(1/T_p)} = -\frac{\Delta E}{R} \quad (6)$$

where  $R$  is the gas constant. From the slope of  $\log(\Phi/T_p^2)$  versus  $1/T_p$  plot, the non-isothermal crystallization activation energy can be calculated from the slope of the plot of  $\ln(\Phi/T_p^2)$  versus  $1/T_p$ .

## 2.3. CRYSTALLINITY DETERMINATION

The degree of crystallinity can be determined by several techniques, such as density, specific volume, ratio of the intensity of absorption bands corresponding to crystalline and amorphous fractions in infrared spectroscopy, heat of fusion or crystallization in differential scanning calorimetry and the areas under diffraction peaks in wide-angle X-ray diffraction, and the de-polarized light intensity changes during the course of crystallization. However, some techniques, such as specific volume, IR, WAXD, and NMR, require the data on the properties of the 100% crystalline and completely amorphous polymers. For highly crystalline polymers, the data on purely amorphous polymer sometimes may be difficult to obtain, which gives rise to inaccuracy. The widely used and convenient methods for the determination of the degree of crystallinity are differential scanning calorimetry method and depolarized light intensity method.

### 2.3.1. Differential Scanning Calorimetry

The degree of crystallinity after crystallization time,  $t$ , can be expressed as Equation (7):

$$\theta = \frac{\Delta H_t}{\Delta H_\infty} = \frac{\int_0^t E_t dt}{\int_0^\infty E_t dt} \quad (7)$$

where  $\Delta H_t$  is the enthalpy change at time  $t$ ,  $\Delta H_\infty$  is the total enthalpy change of the system, and  $E_t$  is the rate of energy evolution at time  $t$ .

### 2.3.2. Depolarized Light Intensity

The depolarized light intensity will increase with crystallinity (or mesophase formation) due to the light scattering of polymer crystals (or liquid crystals). This method may be more suitable for the kinetics study of liquid crystallization,

because the transition from isotropic to mesophase is very fast. The degree of crystallinity can be determined by Equation (8):

$$\theta = \frac{I_{\infty} - I_t}{I_{\infty} - I_0} \quad (8)$$

where  $I_{\infty}$ ,  $I_0$ , and  $I_t$  represent the transmitted light intensity at a long time, at initial time, and at an intermediate time, respectively.

### 3. MAIN CHAIN LCP CRYSTALLIZATION

#### 3.1. LIQUID CRYSTALLINE POLYIMIDES

Polyimide is a very important engineering plastic because of its good mechanical properties, good chemical resistance, low dielectric constant, and high thermal stability. It has been widely used in electronic devices, wafer coatings, insulation and structural composites in the form of fiber, and film [23–25]. Traditionally, aromatic polyimides are synthesized via a two-step polycondensation reaction as shown in Figure 3.5, namely, forming of poly(amic acid) and then imidization. This is due to the good organo-solubility of poly(amic acid)s [26–28] for easy processing.

In the past decade, a number of liquid crystalline polyimides have been synthesized because of the combination of good mechanical properties and processability [29–49] of polyimides. The synthesis of liquid crystalline polyimide can be traced back to 1987 when Kricheldorf [29] published his paper on liquid crystalline polyimide, although his early attempt to synthesize liquid crystalline polyimides was not successful [50]. From then, many poly(ester imide)s based on asymmetric trimellitimide and flexible spacers ( $-\text{CH}_2-$ ) were reported. The

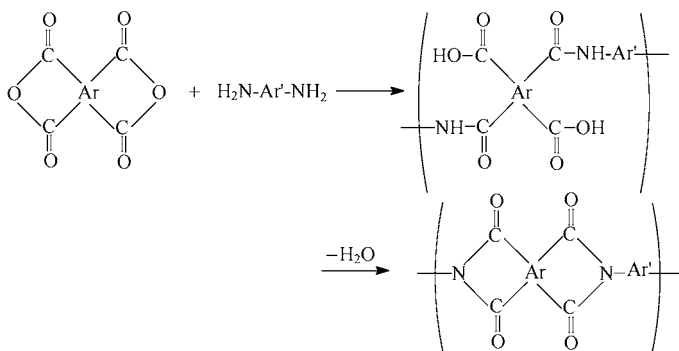


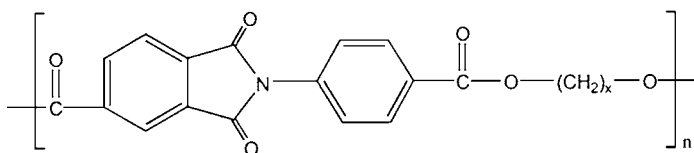
**Figure 3.5** Schematic of two-step polymerization of polyimide.

structure and liquid crystalline phase transitions were evaluated. Similar to thermotropic copolyesters, LC-polyimides containing methylene flexible spacers also exhibited an even-odd effect in melting points and clearing temperatures [30]. However, the  $T_g$  transition monotonically decreased with flexible spacer length. Most of these LC-polyimide exhibit smectic phases that can be examined by WAXD experiments. Table 3.1 summarizes some of the typical liquid crystalline polyimides reported in recent years. It is noted from this table that most liquid crystalline polyimides are derived from non-symmetric trimellitimide.

### 3.1.1. LC-PEIMs from Structure 1

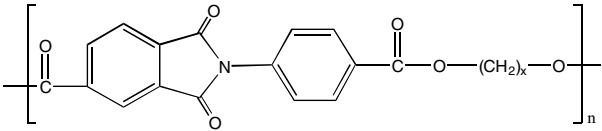
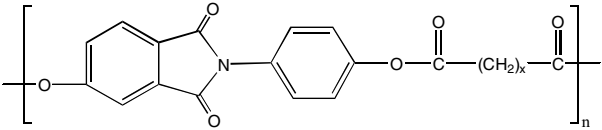
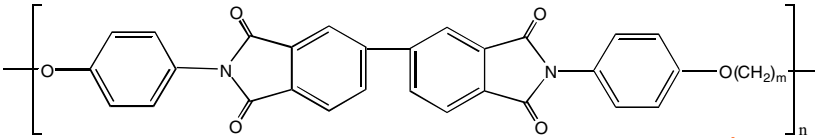
Pardey et al. [3–5] systematically studied the liquid crystal behavior and phase transition kinetics of a series of liquid crystalline poly(ester imide)s (PEIM) derived from *N*-[4-(chloroformyl) phenyl]-4-(chloroformyl) phthalimide and their respective diols with methylene units ( $n$ ) varying from four to 12. The enthalpy and entropy contributions to the mesophase transition from mesogenic group and methylene units in these PEIM are determined. The mesogenic groups have the same contributions to be 0.58 kJ/mol no matter whether  $n$  is odd or even. However, the methylene unit has a contribution of 0.8 kJ/mol when  $n$  is even, twice the contribution when  $n$  is odd (0.4 kJ/mol). The methylene length calculated in the mesophase is smaller than that of the C–C bond in the *trans* conformation, indicating that, in the layers, the methylene unit may involve a certain degree of kinks. The intermolecular d-spacing exhibits a measurable change during the transition from isotropic melt to mesophase formation, although no three-dimensional order is formed during this transition.

This series of LC-polyimides can form mesophase only during cooling. They are monotropic LC. Therefore, this series of PEIMs can crystallize from their corresponding isotropic melt and mesophase. The crystallization morphology varies when they crystallize from different states. PEIMs ( $n$  = even, except  $n$  = 4) show a grainy texture that develops in a few seconds when crystallized at temperatures below liquid crystallization transition. Further annealing doesn't result in any significant changes in this grainy texture. This morphology represents the formation of liquid crystalline phase followed by crystallization from the precursor mesophase. When PEIMs ( $n$  = even) are crystallized directly from the isotropic melt, crystallization can result in spherulitic structures.



**Structure 1** Liquid crystalline poly(ester imide)s. Monotropic, smectic A,  $x = 4-12$ .

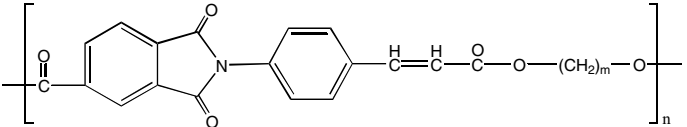
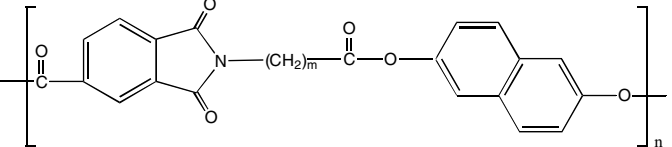
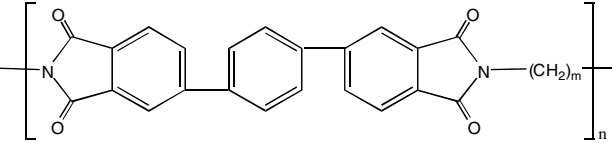
TABLE 3.1. Some Liquid Crystalline Polyimides.

Polyimide	Spacer	Phase	Ref.
	$x = 4 \sim 12$	Smectic	[3-5]
	$x = 4 \sim 12$	Nematic	[51]
	$m = 7 \sim 12$	Smectic	[38,43]

www.iran-mavad.com

مرجع دانشجویان و مهندسين مواد

TABLE 3.1. (continued)

Polyimide	Spacer	Phase	Ref.
	$m = 5 \sim 22$	Smectic	[45]
	$m = 4, 5, 10$	Nematic	[49]
	$m = 6-11$	Nematic and smectic	[54,55]

www.iran-mavad.com

مرجع دانشجویان و مهندسين مواد

TABLE 3.2. Avrami Component  $n$  Change in PEIM with Spacer Number  $x$ .

Spacer Number, $x$	$n_1$	$n_2$
4	1.7 ~ 1.9	2.0 ~ 2.8
6	2.0	1.9 ~ 2.3
7	2.0 ~ 2.1	3.0
8	2.0 ~ 2.1	2.2 ~ 2.5
9	1.9 ~ 2.1	2.1 ~ 3.0
10	2.1	1.9 ~ 2.2
11	2.0 ~ 2.5	2.1 ~ 3.0
12	1.9 ~ 2.1	2.0 ~ 3.0

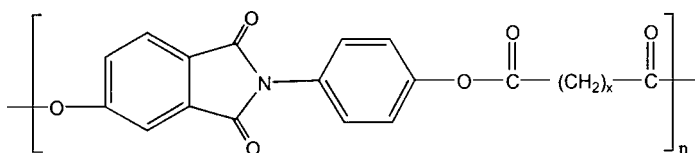
For PEIMs ( $n = \text{odds}$ ), crystallization at temperatures above the liquid crystalline transition may result in spherulitic morphology development. Kinetics analysis of these PEIMs indicates that the phase transition is mainly determined by the number of methyl units in the spacers. The liquid crystallization formation can be either transport-controlled or nucleation-controlled, depending on how far apart the liquid crystalline transition is from the glass transition temperature of the polymer. As all of these PEIMs form a monoclinic system, the lifetime of mesophase may be very short (in seconds). Therefore, kinetics analysis may involve two stages: mesophase formation followed by true crystallization (Table 3.2).

### 3.1.2. LC-PEIMs from Structure 2

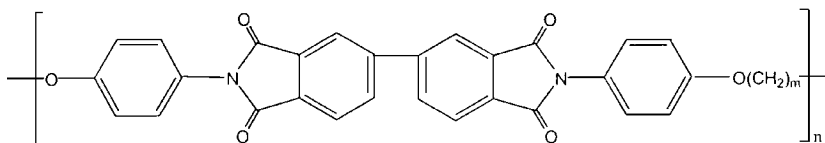
The liquid crystal behavior of the isomers of the above liquid crystalline polyimides is quite different lying in the ester group linkage [51]. It is generally accepted that stronger lateral interchain attraction favors the formation of smectic phases. This means that the linking order of the mesogen-carbonyl group favors the formation of a smectic phase while the reverse connection order favors the formation of a nematic phase. This phenomena has been observed in many thermotropic liquid crystalline polyesters [52].

### 3.1.3. LC-Polyimide from Biphenyl-3,3',4,4'-tetracarboxylic Imide

Polyimides from biphenyl-3,3',4,4'-tetracarboxylimide (BTCl) and aliphatic or aromatic diamines don't exhibit liquid crystallinity. This means that BTCl



**Structure 2** Liquid crystalline poly(ester imide)s. Enantiotropic, nematic,  $x = 4-12$ .



**Structure 3** Liquid crystalline polyimides derived from modified BTCl.

is a poor mesogen for liquid crystalline polymer synthesis. The reason for the low mesogeneity is the capability of the BTCl unit to adopt a “folded” conformation [38,43]. When BTCl is *N*-substituted with *p*-hydroxyl phenyl group, a good mesogen is obtained. All the polyimides from the modified BTCl with flexible spacer  $-(CH_2)_n-$  ( $n = 7$  to 12) exhibit thermotropic LC behavior (Structure 3). Further X-ray experiments reveal that the spacers adopt gauche conformation in the LC state.

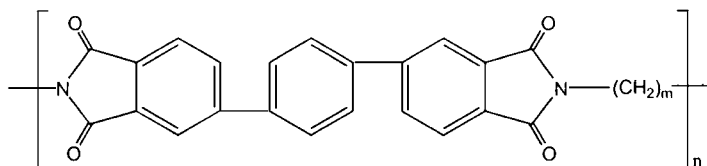
#### 3.1.4. LC-Polyimide from 4,4'-Terphenyltetracarboxylic Acid

Neither polyimides derived from 1,2,4,5-benzenetetracarboxylic dianhydride (PMDA) nor from biphenyl tetracarboxylic anhydride with aliphatic spacers have yielded a liquid crystalline phase. The need for an extra ring to obtain mesogenic properties was evident. Inoue et al. reported the existence of mesophase in a series of polyimides synthesized from the nylon-salt-type terphenyl tetracarboxylic anhydride with aliphatic diamines (Structure 4) [53–55].

All these polyimides ( $n = 8 \sim 12$ ) form a nematic phase upon heating, while polyimide ( $n = 11$ ) can form a smectic phase in a short range of temperature (Table 3.3).

#### 3.1.5. LC-Polyimide from PMDA

Evans et al. systematically studied various polyimides derived from PMDA [56]. None of those polyimides was thermotropic, despite the fact that PMDA was expected to be a mesogenic unit because of its flat, rigid, and linear structure. The authors concluded, “we are unaware of any low molecular weight liquid crystalline compounds which contain the imide functional group. This combined with the results of the studies reported here suggests that it may be



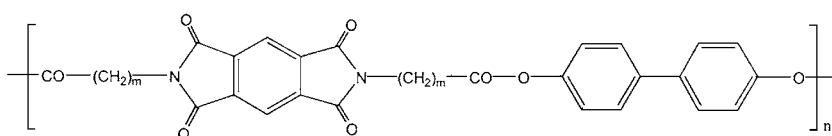
**Structure 4** Liquid crystalline polyimide derived from terphenyl imide.

TABLE 3.3. Variation of Phase Behavior with Spacer Number [53,54].

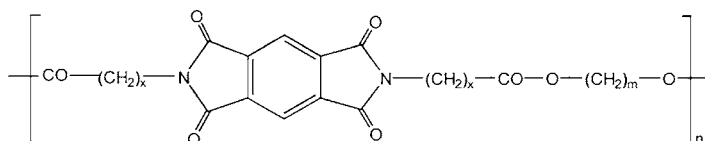
Spacer No.	$T_g(^{\circ}\text{C})$	$T_c(^{\circ}\text{C})$ ( $\Delta S$ )	$T_{ic-ic}(^{\circ}\text{C})$ ( $\Delta S$ )			$T_{ic}(^{\circ}\text{C})$ ( $\Delta S$ )
6	141	314 (15.7)				
7	135	227 (20.1)				
8	120	237 (14.7)		Nematic		289 (5.4)
9	104	194 (10.9)		Nematic		218 (1.4)
10	103	249 (10.8)		Nematic		255 (4.3)
11	89	144 (7.0)	Smectic	169 (3.1)	Nematic	210 (2.5)
12	86	217 (17.4)		Nematic		229 (4.4)

not possible to prepare thermotropic polyimides” [15, p. 84]. Other polyimides derived from PMDA and flexible diamines were also confirmed not to be thermotropic (**Structure 5**) [57]. Poly(imide-carbonate)s were reported to exhibit liquid crystallinity due to the presence of biphenyl structure [58]. However, it seems that every law has an exception. Recently, aromatic polyimides based on symmetric pyromellitimide, but having neither ester linkage nor carbonyl linkage in the backbones, have been reported to be thermotropic (**Structure 6**) [59–62]. It is also noted that no other polyimides (**Table 3.4**) from this diamine with other common dianhydrides are thermotropic, and most of those polyimides are amorphous.

Interestingly, most polyimides from 1,3-bis[4-(4'-aminophenoxy) cumyl] benzene (BACB) diamines form a layered structure in the solid state [63].



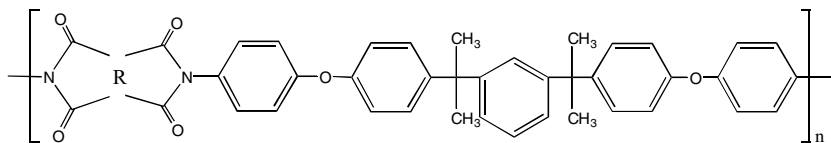
$$m = 3, 4, 5, 10, 11$$



$$x = 1, 5, 10, m = 6, 12$$

**Structure 5** Liquid crystalline polyimide derived from PMDA and flexible connectors.

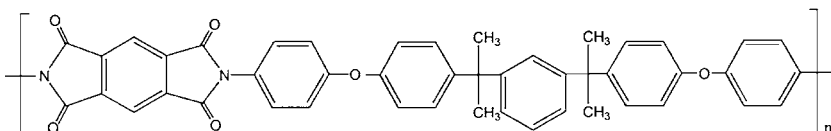
TABLE 3.4. Properties of Polyimides Derived from BACB Diamine.



<i>R</i>	$T_g(^{\circ}\text{C})$	$T_m(^{\circ}\text{C})$	Phase
	—	270 300	Liquid crystalline
	185	—	Amorphous
	185	—	Amorphous
	176	—	Amorphous
	201	—	Amorphous

Compared with aromatic thermotropic polyesters, which never form a smectic layered structure, polyimides have very strong intermolecular interactions due to the imide group. This may be attributed to the high polarity of the imide group.

The crystallization and phase transition behavior has been investigated [64–66]. Figure 3.6 shows the DSC heating and cooling curves of the liquid crystalline polyimide synthesized from PMDA and BACB. During the first heating, two strong endothermic peaks at 267 and 297°C are observed. There is a very



**Structure 6** Liquid crystalline polyimide from PMDA and aromatic diamine.

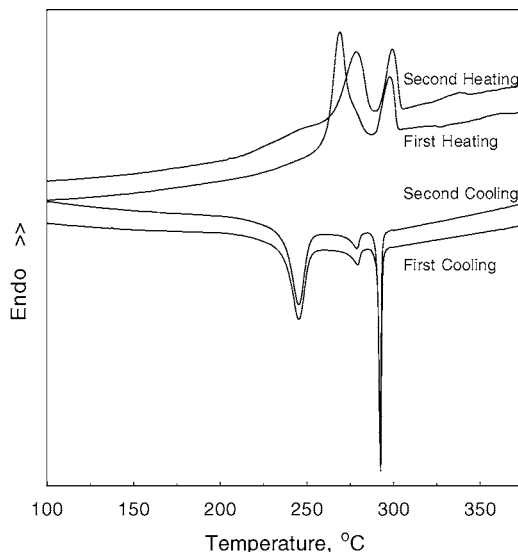


**Figure 3.6** Typical DSC heating and cooling curves for the liquid crystalline polyimide.

weak and broad transition around 340°C. In the cooling process, three exothermic peaks are observed. Two strong ones occur at 244 and 290°C, and a weak one occurs at 277°C. During subsequent heating, the first strong peak appears at 277°C, while the second strong one remains at the same position as observed in the first heating. These results show that the thermal history in sample preparation affects the phase transition behavior. To eliminate the sample preparation thermal history, all samples used in DSC experiments are the second heating or cooling. TGA experiment indicates that the stability of this polyimide in air is stable below 400°C.

Both texture observation and wide-angle X-ray diffraction have confirmed that this LC-PI forms smectic A phase. The layer spacing obtained by WAXD result is about 30.4 Å, which is in fair agreement with the computer modeled value of 28.1 Å, shown in Figure 3.7. Synchrotron radiation with heating

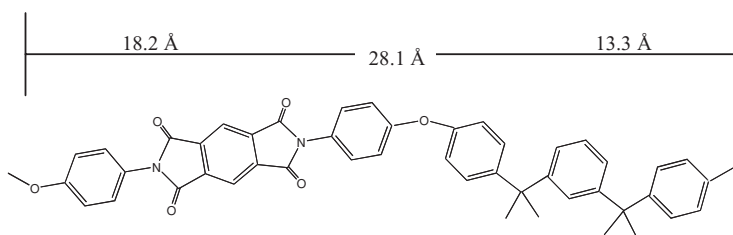


**Figure 3.7** Computer-modeled atomic distance of the repeating unit.

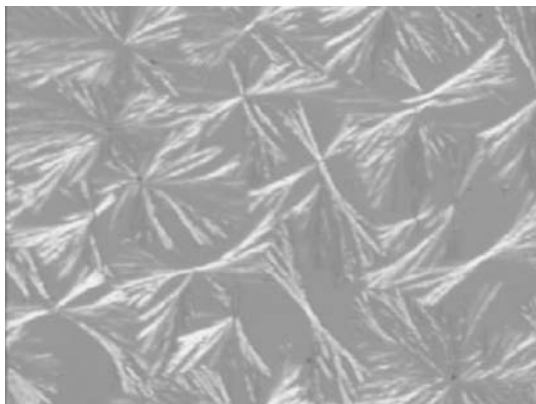


**Figure 3.8** Spherulitic morphology developed from the isotropic melt.

revealed the existence of some smectic B phase beside the smectic A glass in the powder sample in the first heating. Isothermal crystallization from the isotropic melt by optical microscope experiment disclosed the formation of spherulitic-like structure formation (Figure 3.8) beside batonnets texture, which will melt around  $344^{\circ}\text{C}$ , consistent with DSC experiment. The formation of spherulitic structure (or axialitic) was also observed in PEIMs when they were crystallized from the isotropic melt [67].

In the DSC cooling curve of the LC-PI, the first exothermic peak has been confirmed to be the transition from isotropic melt to liquid crystalline phase. A grainy texture is developed within seconds when the system is cooled to just below  $290^{\circ}\text{C}$  as shown in Figure 3.9. The transition temperature and heat of transition for the sample crystallized at  $280^{\circ}\text{C}$  are independent of crystallization time,

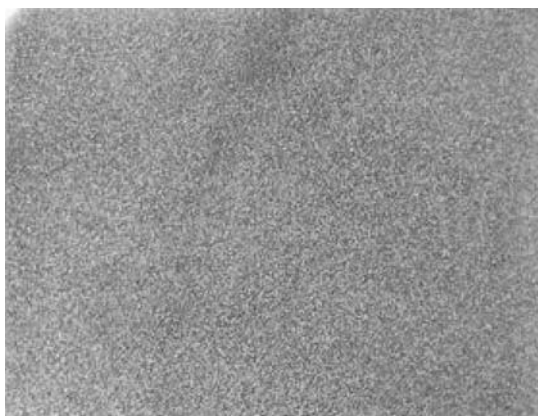


**Figure 3.9** Grainy texture formed during liquid crystallization.

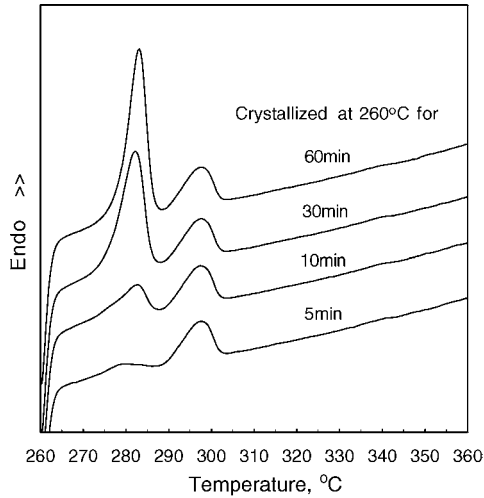


**Figure 3.10** DSC heating curves after isothermal crystallization at 260°C.

indicating that the transition from the isotropic phase to the smectic phase can be considered as a thermodynamically equilibrium phase transition. This phase transition is too fast for kinetics study by DSC method, which requires seconds for equilibrium. Magill et al. [68,69] used depolarized light intensity (DLI) to study the liquid crystalline phase transition and found the  $n$  value was around 2.

The second transition is a very weak transition from the DSC cooling curve. The crystallization process is not easily directly detected due to the weak exothermic signal in DSC. Different samples are used and are kept at 260 and 262°C for different times, and then the heat of transition during subsequent heating is calculated. From [Figure 3.10](#), it can be seen that the endothermic peak that appears at low temperature during the subsequent heating process is highly influenced by the crystallization time. Using  $(\Delta H)^{-1}$  versus  $(\log t_c)^{-1}$  curve as shown in [Figure 3.11](#),  $\Delta H_\infty$  is obtained when  $t_c$  is infinite (here  $\Delta H_\infty$  is used because crystallization time is infinite). The Avrami exponent  $n$  is obtained using  $\Delta H_\infty$  to substitute  $\Delta H_0$  by following Equations (1) and (4). The crystallization parameter  $n$  calculated from [Figure 3.12](#) is around 1. The low  $n$  value suggests that this process is a mesophase transition.

The crystallization exothermic trace is directly measurable by DSC method when the crystallization temperature chosen is between 250°C and 258°C, which is several degrees higher than the onset temperature. By following Avrami treatment, the relative crystallinity versus time is calculated. Then, the Avrami parameter  $n$  is obtained from  $\log(-\ln(1 - \theta))$  versus  $\log t_c$  curves as shown in [Figure 3.13](#). The average  $n$  value is around 2.6, which is much higher than the  $n$  value for the crystallization process observed at 260 and 262°C.

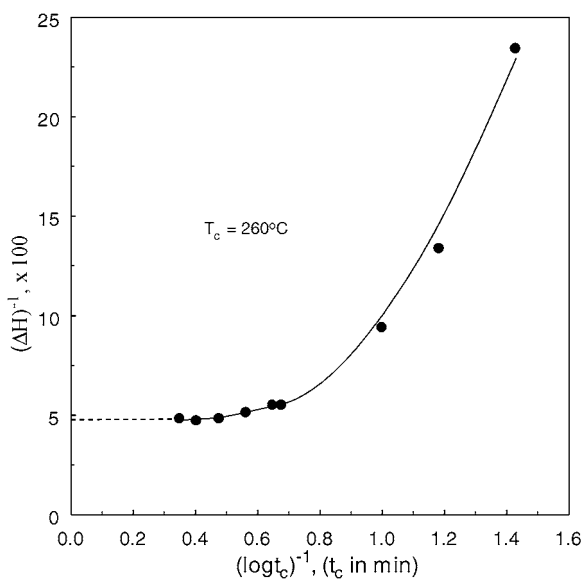


**Figure 3.11** Determination of  $\Delta H$  during isothermal crystallization.

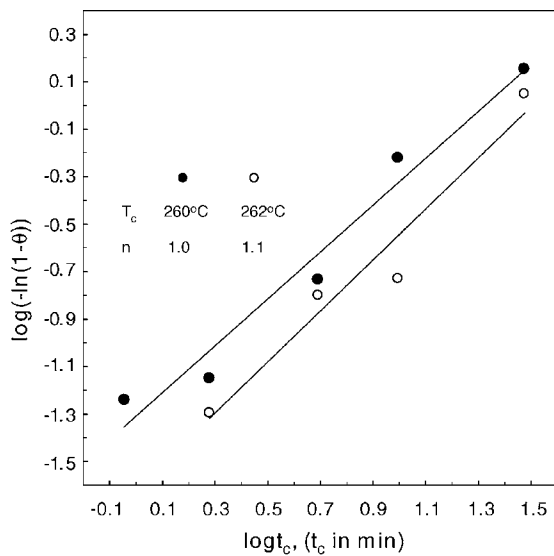


**Figure 3.12** Kinetics for crystallization at 260 and  $262^\circ\text{C}$ .

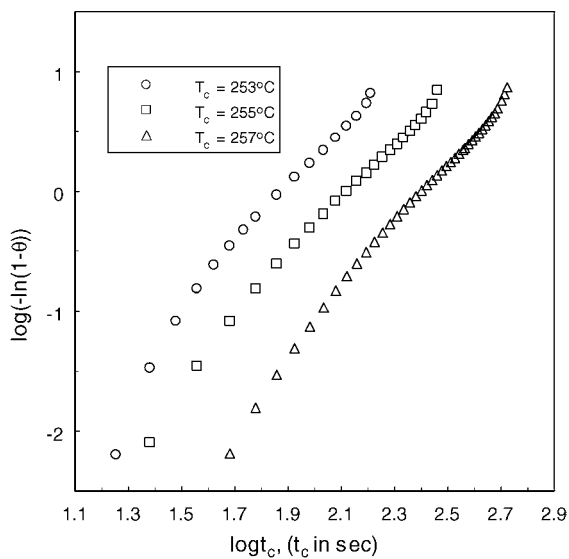


**Figure 3.13** Avrami treatment for isothermal crystallization at 253 to 257°C.

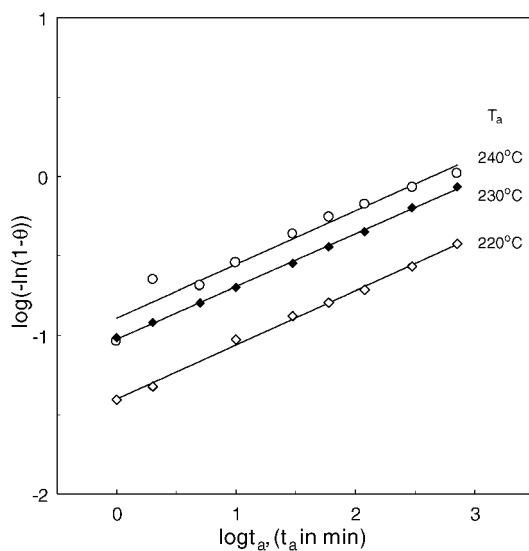


**Figure 3.14** Crystallization kinetics treatment during annealing.

TABLE 3.5. Avrami Exponents of Some Liquid Crystalline Polymers.

Transformation	Polymer	Mesophase	$n$	Ref.
Isotropic—mesophase	Polyester	Nematic	0.68–0.85	[70]
	Poly(azomethines)	Nematic	0.1–0.6	[71]
	Polyphosphazenes		2	[68,69]
	Polyester		1	[72]
	Polyesters	Smectic	2.5–3.0	[73]
	Poly(ester imide)	Smectic	~2	[3–5]
Mesophase—three-dimensional order	Copolyesters	Nematic	0.24–0.73	
	Copolyesters	Nematic	2, 0.15–0.38	
	Polyphosphazenes		2	[68,69]
	Polyphosphazenes		3, 4	[74]
	Poly(azomethines)	Nematic	2.4–3.8	[71]
	Polyesters	Nematic	2.7–4.2	[75]
	Polyesters		2	[76]
	Polyester		3–4	[77]
	Polyester (10 CH <sub>2</sub> )	Smectic	3–4	[78]
	Polyester (3 CH <sub>2</sub> )	Smectic	2	[78]
	Polyester (6 CH <sub>2</sub> )	Nematic	2	[79]
	Polyester (10 CH <sub>2</sub> )	Smectic	2.89–3.22	[79]
	Polyester		4	[72]
	PDDPT	Nematic	2 ( $T_c > 239^\circ\text{C}$ )	[80]
			3 ( $T_c < 239^\circ\text{C}$ )	[80]
	Poly(ester imide)	Smectic	2 ~ 3	[3–5]
	Polyimide	Smectic	2.6	
Isotropic—three-dimensional order	Polyphosphazene		4	[74]
	PDDPT	Nematic	2	[80]

The average values  $n$  are indicative of thermal and/or athermal nucleation followed by a three-dimensional crystal growth. Indeed, for spherulitic growth and athermal nucleation,  $n$  is expected to be 3. In the case of thermal nucleation, it is expected to be 4 [2]. However, complications in the Avrami analysis often arise because several assumptions, not completely applicable to polymer crystallization, are involved in the derivation. A comparison of some crystallization kinetics parameters is summarized in Table 3.5 [70–80].

Further study shows that this LC-PI exhibits double melting behavior, which can be induced by annealing or crystallization at lower temperatures [81]. Double melting phenomenon is also observed in some other thermotropic liquid crystalline polymers [82,83]. Literature indicated that the crystallization in solid polymers was the same as that from melt. To obtain the metastable equilibrium heat of fusion, an extrapolation of  $(\Delta H_f)^{-1}$  versus  $(\log t_a)^{-1}$  for the newly formed peak is made. The value of  $\Delta H_\infty$  is 24.8 J/g.

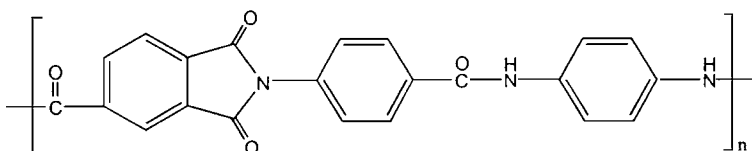
Figure 3.14 shows the crystallization kinetics during annealing for the samples annealed at different temperatures by using the Avrami treatment.

Interestingly, the Avrami exponent  $n$  is very low, around 0.3–0.4, similar to the observation for the annealing crystallization of copolyesters and copoly-esteramide [84].

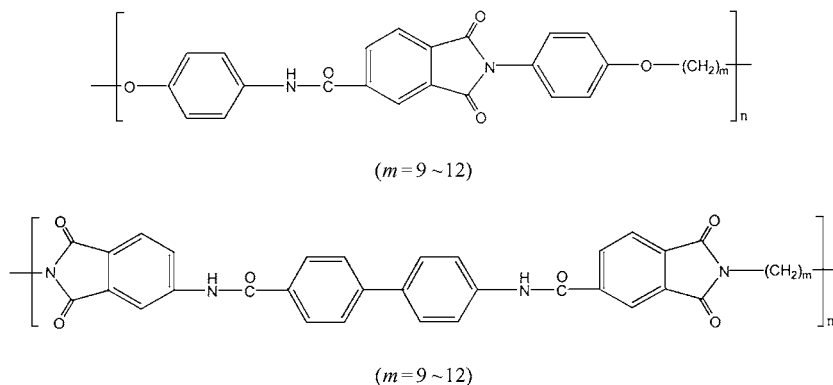
### 3.2. LC-POLY(AMIDE-IMIDE)

Aromatic polyamides exhibiting mesophases have been known, but these are, with few exceptions, lyotropic and crystalline. Poly(4-benzamide) and poly(*p*-phenylene terephthalamide) (PPTA) were the first synthetic polymers that exhibit liquid crystallinity in concentrated  $\text{H}_2\text{SO}_4$  [85,86]. Other polyaramides derived from substituted terephthalic acids or substituted *p*-phenylene diamines were also found to form lyotropic solution. In these polyaramides, all the monomers are linked in para-position to favor a linear structure in polymer chains. The linearity and high molecular weight were considered to be the basic requirements for the formation of lyotropic solutions. In lyotropic ordered polyamides, it was shown that at least three amide-linked aromatic rings are required per repeating unit to achieve a mesophase [87]. Kricheldorf et al. reported the synthesis of poly(amide imide)s exhibiting liquid crystallinity in concentrated  $\text{H}_2\text{SO}_4$  when the concentration is higher than 25% or in NMP (with 5%  $\text{CaCl}_2$ ) solutions (Structure 7) [34].

Due to the strong hydrogen bonding between polymer chains in crystalline polyamides, powerful solvents are needed to disrupt hydrogen bonding. Further screening of hydrogen bonding can be achieved by introducing a pendant group [88]. However, too many pendant groups can destroy anisotropy. There are only a few examples showing that polyamides are thermotropic. Griffin et al. [89] reported a mesophase in the temperature range 256–276°C in the copolyamide of 3,3'-dimethoxy benzidine and 4,4'-dicarboxy-1,10-diphenoxydecane. Uryu et al. [90] described two series of thermotropic polyamides based on copolymers of 4,4'-dicarboxy-1,10-diphenoxydecane in connection with  $\leq 12.5$  mol% of *p*-phenylene diamine and  $\geq 37.5$  mol% ortho-substituted benzidine, in which the ortho substituents are dimethoxy- or chloro-. Schmucki et al. [91] synthesized thermotropic polyamides derived from ortho-substituted diamines containing alkyl spacers combined with aromatic acids. Thermotropic properties have been reported in copolyesteramides containing up to 50% amide groups. Recently, Kricheldorf disclosed some thermotropic poly(amide imide)s (Structure 8) that exhibit smectic A phase in the mesophase state [44].



Structure 7 Lyotropic poly(amide imide).



**Structure 8** Structures of thermotropic liquid crystalline poly(amide imide).

### 3.3. CRYSTALLIZATION OF THERMOTROPIC LIQUID CRYSTALLINE POLYESTERS

#### 3.3.1. Vectra A

Vectra A<sup>TM</sup> is a commercially available polymer from Hoechst-Celanese. It is a random co-polyester of hydroxy benzoic acid (HBA) and hydroxy naphthoic acid (HNA), which is a well-known class of thermotropic liquid crystalline polymer (TLCP) [92–95]. Crystallization of molecules of TLCPs is considerably different from that of polymers like polyethylene or polyethylene terephthalate [1]. TLCPs have reduced flexibility compared to the latter, which implies that large translations of their molecules are required for recrystallization [96–99].

Crystallization occurs so rapidly on cooling that the process of quenching from nematic to glassy state inevitably results in some crystallization [100]. X-ray diffraction measurements on quenched samples show that the percentage of crystallinity may be as much as 30% and further increases up to 60% with annealing [101]. Annealing, especially at the melting point temperatures, also affects the chain packing. Cheng et al. [102] showed the presence of two transition processes for different molar ratios of HBA/HNA co-polyesters for the transition from nematic to solid state: (a) fast transition due to aggregation of rigid chains and (b) slow transition during the heat treatment. These two processes result in different crystal structures. The fast process leads to hexagonal packing with cylindrical symmetry along the chain direction while the slow process gives rise to orthorhombic packing [103–109]. The origin of these two transition mechanisms is not yet determined. The orthorhombic form has a higher melting temperature for 73/27 mole percent HBA/HNA and is around

320°C. Dark-field electron microscopy reveals its morphology: crystallites are lamellar in shape, around 15 nm thick (along the chain) and 100 nm long (in the lateral direction). The lamellae also have somewhat irregular boundaries. Hudson et al. [110] optimized the etchant composition to reveal clearly the periodic lamellar morphology.

Similar crystallization processes were observed for Xydar and other Hoechst Celanese LCPs by Cheng et al. [111]. Blackwell et al. [112] suggested the presence of some additional crystalline structures for some nematic LCPs, depending on preparation and heat treatment of the materials. Lin and Winter [113–115] reported that the rate of crystallization increases with supercooling, i.e., the interval between its melting point,  $T_m$ , and the desired experimental temperature,  $T$ . Moreover, they found that quenching immediately after deformation at a high temperature could lower the degree of crystallinity. Their data indicate that low cooling rates and large elongation lead to the highest crystallinity, and the crystallization rate depends on annealing temperature and mechanical and thermal history of the materials [116–119]. In addition, higher annealing temperature leads to a slower crystallization.

Chung et al. [120] re-examined the crystallization mechanism of LCPs using commercial grades, such as Vectra A-900 or A-950, which is made of 73/27 HBA/HNA, in contrast to previous works based on experimental grades. The molar mass of the average repeating units is 133.5 g/mole. Figure 3.15 shows a set of DSC heating traces for the copolymer of 73/27 HBA/HNA crystallized

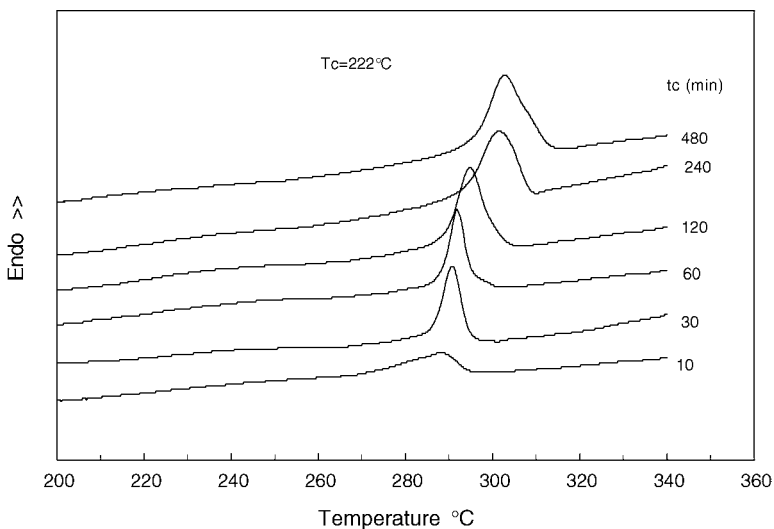


**Figure 3.15** A set of DSC traces during isothermal experiments of Vectra A-950 in the low temperature region ( $T_c = 212^\circ\text{C}$ ).

at 212°C for various periods of time,  $t_c$ . There are two transition processes that are identified as high melting peak, which is essentially invariant as a function of annealing time, and low melting peak, which has melting points dependent on the annealing time.

The heat of transitions,  $\Delta H_d(h)$  in high melting peaks, is almost independent of  $t_c$ . This implies that there is always a frozen liquid crystalline phase when quenching this polymer from 400°C to room temperature. In other words, the formation of liquid crystals from the isotropic phase can proceed very rapidly. Similar observations have been reported for a polyimide LCP quenched from 350°C in air and exhibiting a fine frozen liquid crystalline texture under polarized light microscopy [64,65].

However, in the case of the lower translational (melting) peaks, the heat of transitions,  $\Delta H_d(1)$ , increases rapidly with time. This indicates that rigid LCP chains at elevated temperatures may have a tendency to perform translational motion along the chain direction or/and rotational motion with respect to chain axis to have a better intermolecular packing and to reduce the Gibbs free energy.

Figure 3.16 and Table 3.6 show the relationships between transition temperature,  $T_d$ , and time,  $\log t_c$ , for both high and low melting peaks.  $T_d(h)$  does not change significantly with time,  $\log t_c$ . A similar phenomenon is observed for the relationship between  $\Delta H_d(h, T_c, t_c)$  and  $\log t_c$ . This clearly reveals that

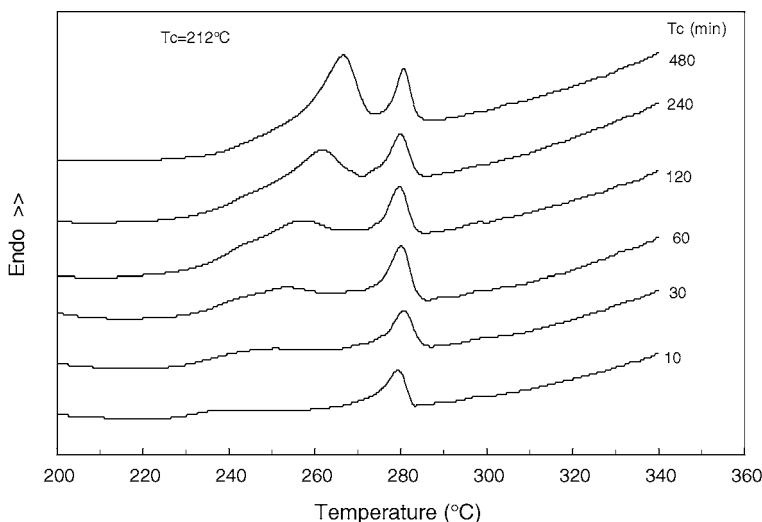


**Figure 3.16** Relationships between  $T_d$  and  $\log t_c$  of Vectra A-950 at  $T_c = 212^\circ\text{C}$  (open symbol) and  $223^\circ\text{C}$  (solid symbol) (square symbols represent the fast transition process and triangular symbols represent the slow transition process).

TABLE 3.6. Isothermal Transition Properties of Vectra™ A-950  
(Low Temperature Region).

Annealing Time (min)	$T_d(1)$ (°C)	$T_d(h)$ (°C)	$\Delta H_d(1)$ (kJ/mole)	$\Delta H_d(h)$ (kJ/mole)
$T_c = 212^\circ\text{C}$ , Heating Rate = $10^\circ\text{C}/\text{min}$				
10	237.71	279.54	0.1349	0.1149
30	243.38	281.03	0.1642	0.1138
60	252.06	280.38	0.4024	0.1254
120	255.88	280.03	0.4281	0.1263
240	260.72	280.21	0.5911	0.1268
480	266.71	280.71	0.6944	0.1274
720	267.71	280.05	0.7147	0.1287
$T_c = 222^\circ\text{C}$ , Heating Rate = $10^\circ\text{C}/\text{min}$				
10	262.19	280.53	0.2346	0.1955
30	263.69	279.52	0.4427	0.2014
60	265.55	280.04	0.5747	0.1965
120	271.56	280.85	0.6007	0.1864
240	275.28	279.18	0.6427	0.1872
480	277.85	280.85	0.7580	0.1934

liquid crystal phases quenched from the isotropic phase are difficult to further perfect with annealing at 212 and  $222^\circ\text{C}$ . However,  $T_d(1)$  in low-temperature regions increases linearly with  $\log t_c$  at different  $T_c$ , which indicates perfection processes occurring during the crystal growth for Vectra A-950.

The transition behavior changes for isothermal annealing in the temperature region above  $232^\circ\text{C}$  for the 73/27 HBA/HNA copolyester. Figure 3.17 exhibits typical DSC heating traces on isothermal experiment at  $257^\circ\text{C}$ . There is only one endothermic melting peak in each DSC run, indicating a simple transition process. The melting peak also broadens with annealing time, and the entire peak shifts to higher temperatures that are listed in Table 3.7.

The Avrami parameter,  $n$ , is computed as a function of temperature, and their values are summarized in Table 3.8. All the  $n$  values are in the low range of 0.2 to 0.5, which may be due to the fact that each crystal does not grow with a constant radial growth rate.

### 3.3.2. Vectra B

Chung et al. [121] studied both the isothermal and non-isothermal crystallization phenomena in the random copoly(ester amide) Vectra B-950 from Hoechst-Celanese, which is composed of 2,6-dihydroxynaphthoic acid (HNA), *p*-amino phenol (AP), and terephthalic acid (TA) with the molar ratio of 60/20/20. The molar mass of the average repeating units is 149.8 g/mole.

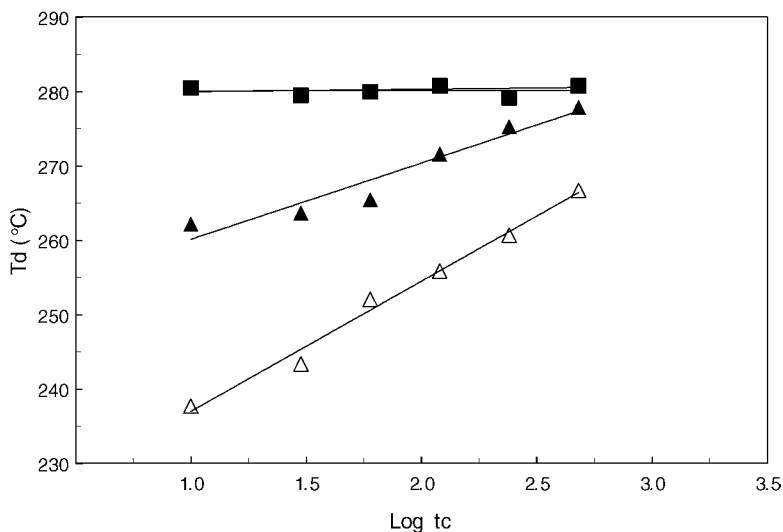


**Figure 3.17** A set of DSC heating traces on isothermal experiments at  $T_c = 257^\circ\text{C}$  for Vectra A-950.

Non-isothermal cooling curves of Vectra B950 at different cooling rates from its nematic melt are shown in Figure 3.18(a). It is clear that the faster the cooling rate, the broader the exothermic peak. The peak temperature, which represents the crystallization temperature, shifted to a higher temperature with decreasing cooling rate. It may be because a response difference between actual and reading temperatures becomes larger with increasing the heating or cooling rate.

However, one surprising phenomenon is observed in Figure 3.18(b): small endothermic peaks appear during the cooling step at cooling rates in excess of  $40^\circ\text{C}/\text{min}$ . The higher the cooling rate, the higher the number of small endothermic peaks that appear. Moreover, all these peaks are reproducible though at different temperatures. The distribution of various molecular sequences within the polymer may be responsible for this phenomenon. The distribution of molecular sequences within Vectra B950 itself may not be so even, as it is a random copolymer. This may be further aggravated by sample preparation. Although some other materials undergoing trans-esterification also exhibited similar phenomena [122,123], it is not certain that this plays an important role in this case. Moreover, studies of thermal analysis of vectran fibers and films [124] showed a similar trend and are considered as mesophase ordering.

Crystallization properties of Vectra B were studied by isothermal experiments as a function of annealing temperature and annealing time. The annealing temperatures were  $190^\circ\text{C}$ ,  $200^\circ\text{C}$ ,  $210^\circ\text{C}$ ,  $220^\circ\text{C}$ ,  $230^\circ\text{C}$ ,  $240^\circ\text{C}$ , and  $260^\circ\text{C}$ , while

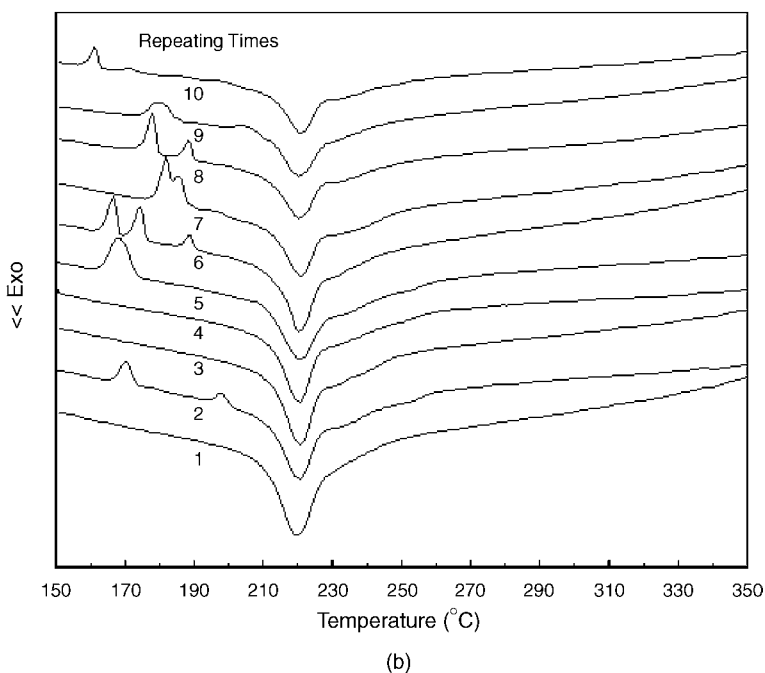
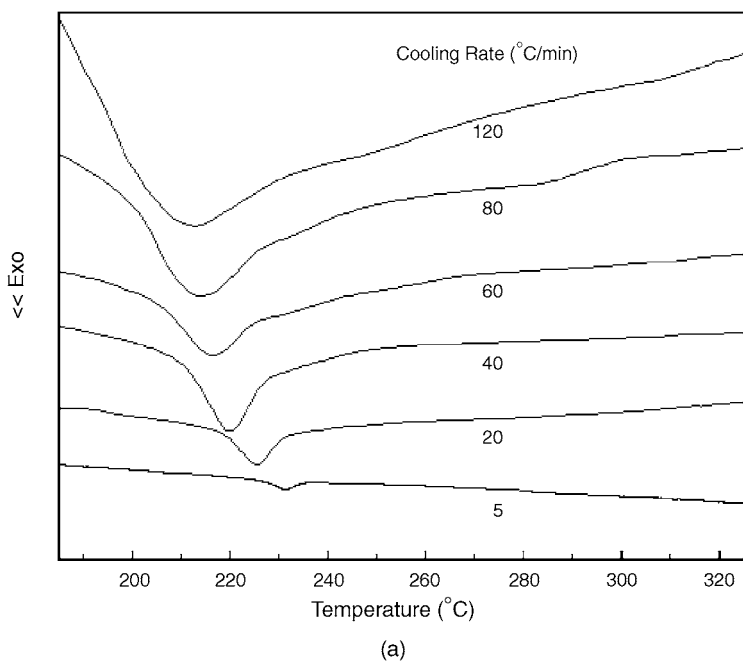


**Figure 3.18** A set of DSC cooling traces of non-isothermal experiments for Vectra B 950 cooled from nematic states (a) cooling at different cooling rates; (b) cooling at 40 °C/min.

TABLE 3.7. Isothermal Transition Properties of Vectra™ A-950 (High Temperature Region).

Annealing Time (min)	$T_d(^{\circ}\text{C})$	$\Delta H_d$ (kJ/mole)
$T_c = 232^{\circ}\text{C}$ , Heating Rate = $10^{\circ}\text{C}/\text{min}$		
5	279.54	0.3595
15	279.20	0.3774
30	279.20	0.5181
60	279.71	0.4891
120	280.38	0.6643
200	282.17	0.7021
300	284.04	0.6751
480	285.37	0.8322
720	286.04	0.9354
$T_c = 242^{\circ}\text{C}$ , Heating Rate = $10^{\circ}\text{C}/\text{min}$		
10	281.34	0.2311
30	282.51	0.2541
60	285.33	0.3786
120	287.84	0.5258
240	290.00	0.6353
480	293.16	0.7585
$T_c = 257^{\circ}\text{C}$ , Heating Rate = $10^{\circ}\text{C}/\text{min}$		
10	288.20	0.2590
30	290.63	0.3012
60	292.37	0.3256
120	295.05	0.4853
240	301.21	0.5494
480	302.85	0.7666

the annealing times were 10 min, 30 min, 60 min, 120 min, 240 min, and 480 min.

The DSC traces at  $240^{\circ}\text{C}$  are shown in Figure 3.19, which indicates the presence of two-transition processes, but the slow transition peak gradually shifts

TABLE 3.8. Avrami Parameters of the Transition Kinetics of Vectra™ A-950.

Vectra™ A-950 (73/23 HBA/HNA)		
$T_c, ^{\circ}\text{C}$	$n$	$\log K$
212	0.46	-1.71
222	0.31	-1.23
232	0.23	-1.01
242	0.37	-1.44
257	0.32	-1.34

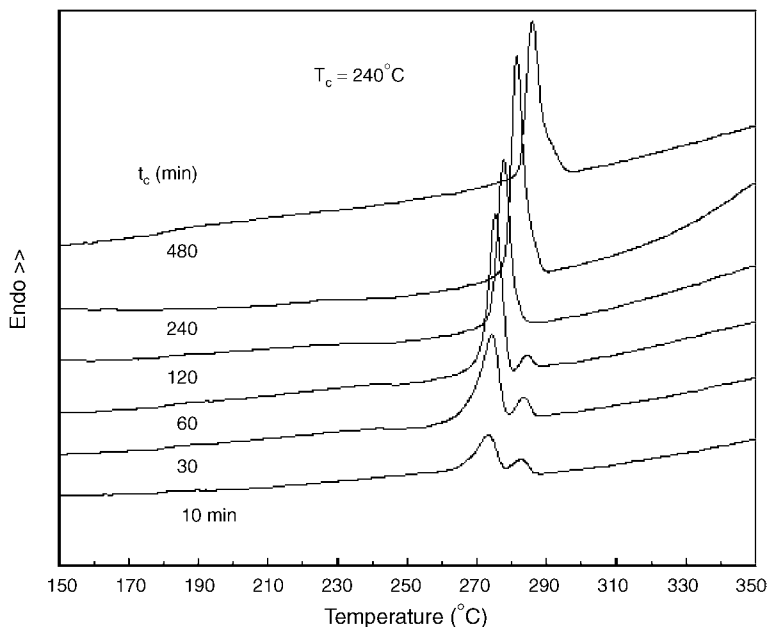


**Figure 3.19** DSC traces of Vectra B 950 annealed at  $240^\circ\text{C}$  and various annealing times.

to a higher temperature as annealing progresses with a concomitant increase of the enthalpy. On the other hand, the fast transition peak shifts only slightly with the annealing time. Eventually, the two peaks merge, so there is only one endothermic peak.

Some strange phenomena appeared when the annealing temperatures were  $200^\circ\text{C}$  and  $230^\circ\text{C}$ . Like in the previous cases, two endothermic peaks appeared at  $200^\circ\text{C}$  irrespective of how the annealing time was varied as shown in [Figure 3.20](#). As the annealing time increased, the first peak shifted to a higher temperature, and the enthalpy also increased. Some exothermic peaks appeared in the second endothermic peak and were reproducible with other samples.

Three endothermic peaks are present at  $230^\circ\text{C}$  as shown in [Figure 3.21](#) for short annealing times. The first peak shifted to a higher temperature, and its enthalpy gradually increased with annealing time and overlapped the second peak, which changed slightly with annealing time. Furthermore, the first peak continued to grow with increasing annealing time, and it eventually overlapped the third peak that changed slightly with annealing time. As the annealing time was increased to 120 or 240 minutes, the first two peaks observed at shorter annealing times completely overlapped. Thus, only two peaks were observed. When the annealing time was further increased to 480 minutes, all the peaks merged into a single endothermic peak. Regardless of how the annealing time

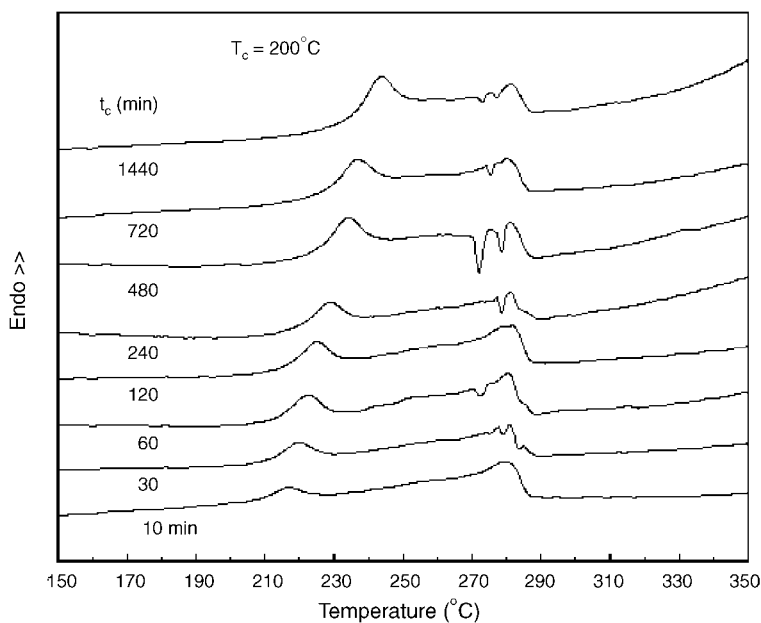


**Figure 3.20** DSC traces of Vectra B 950 annealed at  $200^\circ\text{C}$  and various annealing times.

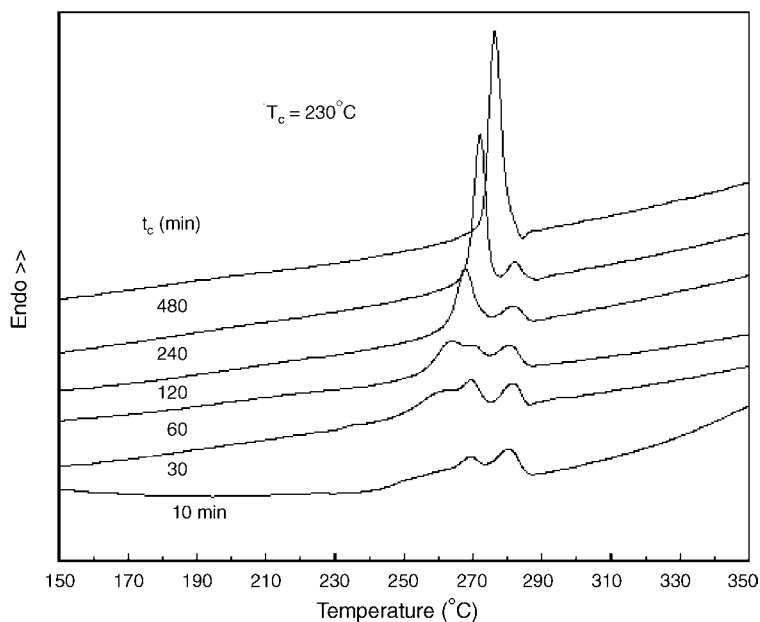


**Figure 3.21** DSC traces of Vectra B 950 annealed at  $230^\circ\text{C}$  and various annealing times.

TABLE 3.9. Isothermal Transition Properties of Vectra™ B950 (High Temperature Region).

Annealing Times (min)	$T_{cl}$ (°C)	$\Delta H_{dt}$ (J/g)
Annealing Temperature $T = 260^\circ\text{C}$		
10	280.2	1.61
30	280.2	1.62
60	284.1	1.66
120	288.9	2.56
240	292.7	3.45
480	299.1	4.03

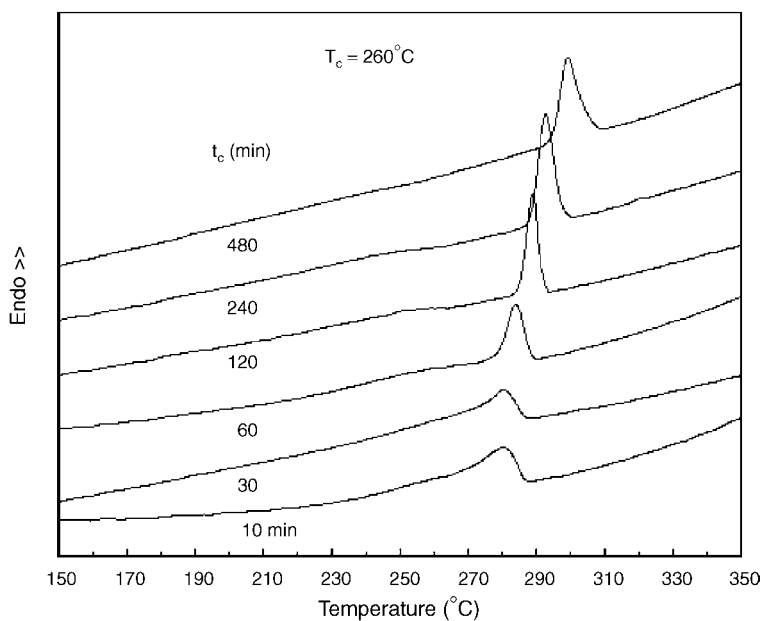
varied, only one endothermic peak appeared at a higher annealing temperature of  $260^\circ\text{C}$  as shown in Figure 3.22. The enthalpy and the temperature values are tabulated in Table 3.9.

Figure 3.23 shows the DSC traces of Vectra™ B950 annealed at 120 min and at different annealing temperatures ( $200^\circ\text{C}$ ,  $220^\circ\text{C}$ ,  $230^\circ\text{C}$ ,  $240^\circ\text{C}$ , and  $260^\circ\text{C}$ ). It can be seen that the two transitions approached each other gradually with increasing annealing temperature, and finally they merge together into one single peak when the annealing temperature is  $260^\circ\text{C}$ .

The above experimental results demonstrate a variety of thermal behaviors, which indicates that the crystallization phenomenon varies with annealing temperature and time. It was also seen conclusively that peculiar exothermic peaks appear in the second endothermic peak at an annealing temperature of  $200^\circ\text{C}$ . This phenomenon is absent at other annealing temperatures:  $190^\circ\text{C}$ ,  $210^\circ\text{C}$ ,  $220^\circ\text{C}$ , and  $240^\circ\text{C}$ , but two distinct transitions are found. One is a function of the annealing temperature and time, while the other is independent of thermal post-treatment. Three transitions are inferred at an annealing temperature of  $230^\circ\text{C}$ . The first two peaks changed in size and location when the annealing temperature and time varied, but the third was independent of thermal post-treatment. Two clear transitions can be detected at an annealing temperature of  $240^\circ\text{C}$ , and they gradually approach each other before finally overlapping into a single transition process. This single transition process also depends on annealing temperature and time. When the annealing temperature is  $260^\circ\text{C}$  or more, only one transition is present, which is also dependent on annealing temperature and time.

### 3.3.3. Blends

Morton et al. [125] studied the isothermal crystallization kinetics of polyethylene terephthalate (PET) in blends with fully aromatic liquid crystalline copolyester (Vectra A). As Vectra fractions increase in the blend, both the PET crystallization rates and the percentage of PET that is crystalline decrease.



**Figure 3.22** DSC traces of Vectra B 950 annealed at  $260^\circ\text{C}$  and various annealing times.

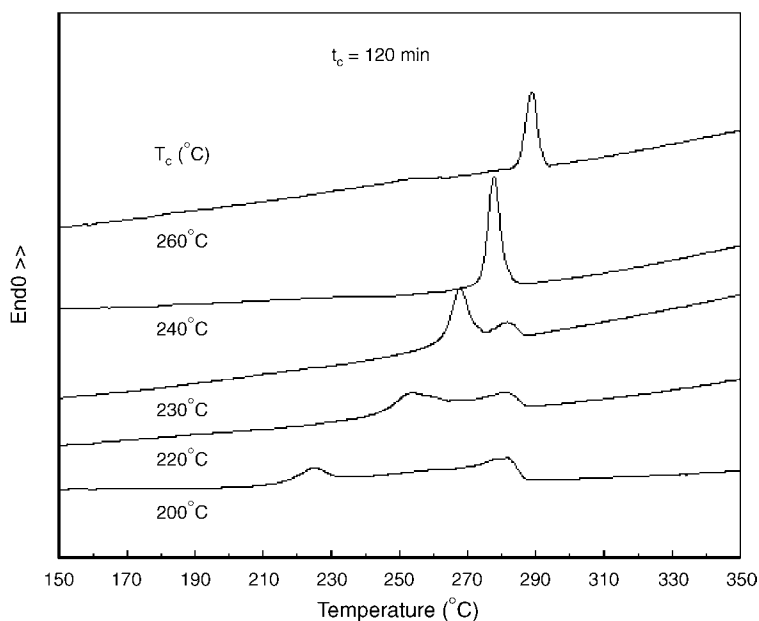


**Figure 3.23** DSC traces of Vectra B 950 annealed at 120 min and various annealing temperatures.

Differential scanning calorimetry was used to study the non-isothermal crystallization behavior of blends of poly(phenylene sulfide) (PPS) with the thermotropic liquid-crystalline copoly(ester amide) Vectra-B950 (VB) [126]. The PPS crystallization temperature and the crystallization rate coefficient increased significantly when 2–50% VB was added. The Ozawa equation was shown to be valid for neat PPS as well as for the blends. The values of the Avrami exponents matched well against those determined previously using isothermal analysis, and they are independent of the concentration of VB.

The slope of the plots of the cooling crystallization function versus  $T$  has been suggested as a criterion for the overall non-isothermal crystallization rate. The non-isothermal crystallization of PPS is hastened by the presence of the VB phase, whereas, neither the type of nucleation nor the geometry of crystal growth changes, and no reduction of the PPS degree of crystallinity could be noticed.

#### 4. REFERENCES

1. L. Mandelkern, *Crystallization of Polymers*, McGraw-Hill Book Company, New York (1964).
2. B. Wunderlich, *Macromolecular Physics, Vol. 2, Crystal Nucleation, Growth, Annealing*, Academic Press, New York (1976).
3. R. Pardey, A. Q. Zhang, P. A. Gabori, F. W. Harris, S. Z. D. Cheng, J. Adduci, J. V. Facinelli, and R. W. Lenz, *Macromolecules*, 25, 5060 (1992).
4. R. Pardey, D. X. Shen, P. A. Gabori, F. W. Harris, S. Z. D. Cheng, J. Adduci, J. V. Facinelli, and R. W. Lenz, *Macromolecules*, 26, 3687 (1993).
5. R. Pardey, S. S. Wu, J. H. Chen, F. W. Harris, S. Z. D. Cheng, A. Keller, J. Adduci, J. V. Facinelli, and R. W. Lenz, *Macromolecules*, 27, 5794 (1994).
6. A. Keller, in *Polymers, Liquid Crystals, and Low-Dimensional Solids*, ed. by Norman March and Mario Tosi, Plenum Press, New York and London (1984).
7. A. Keller, *Phil. Mag.*, 2, 1171 (1957).
8. *Crystallization of Polymers*, ed. by Marcel Dosièr, Kluwer Academic Publisher, NATO ASI series. *Series C, Mathematical and Physical Sciences*; Vol. 405 (1993).
9. B. Wunderlich and L. Melillo, *Makromol. Chem.*, 118, 250 (1968).
10. W. Wang, G. Lieser, and G. Wegner, *Liquid Crystals*, 15, 1 (1993).
11. D. C. Bassett, *Principles of Polymer Morphology*, Cambridge University Press, Cambridge and New York (1981).
12. W. Bunn and T. C. Alcock, *Trans. Faraday Soc.*, 41, pp. 317 (1945).
13. A. Keller, Morphology of crystalline polymers, in *Growth and Perfection of Crystals*, ed. by R. H. Doremus, B. W. Roberts, and D. Turnbull, J. Wiley & Sons, New York (1958).
14. H. Han and P. K. Ghosh, *Prog. Polym. Sci.*, 22, 1431 (1997).
15. H. R. Kricheldorf, Liquid-crystalline polyimides, in *Advances in Polymer Science: Progress in Polyimide Chemistry II*, Vol. 141, Springer-Verlag, Berlin (1999).
16. U. W. Gedde, *Polymer Physics*, Chapman & Hall, London (1995).
17. M. Avrami, *J. Chem. Phys.*, 7, 1103 (1939).
18. M. Avrami, *J. Chem. Phys.*, 8, 212 (1940).
19. P. Cebe and S. D. Hong, *Polymer*, 27, 1183 (1986).
20. T. Ozawa, *Polymer*, 12, 150 (1971).

21. T. Ozawa, *J. Thermal Analysis*, 9, 369 (1976).
22. H. E. Kissinger, *Analytical Chemistry*, 29, 1703 (1957).
23. P. M. Hergenrother, *Recent Development in High Temperature Organic Polymers in Polyimides and Other High-Temperature Polymers*, ed. by B. Sillion, Elsevier, New York (1991).
24. M. K. Ghosh and K. L. Mittal, *Polyimides: Fundamentals and Applications*, Marcel Dekker, New York (1996).
25. O. Wilson, H. D. Stenzenberger, and P. M. Hergenrother, *Polyimides*, Blackie & Son, Glasgow and Lon (1990).
26. E. Sroog, *Polyimides in Encyclopedia of Polymer Science and Technology*, ed. by H. F. Mark, N. G. Gaylord, and N. M. Bikales, Interscience, New York, 11, pp. 247 (1969).
27. K. L. Mittal, *Polyimides: Synthesis, Characterization, and Applications, Vol. 1*, Plenum Press, New York (1984).
28. E. Sroog, *J. Polym. Sci., Macromol. Rev.*, 11, 161 (1976).
29. H. R. Kricheldorf and R. Pakull, *Polymer*, 28, 1772 (1987).
30. H. R. Kricheldorf and R. Pakull, *Macromolecules*, 21, 551 (1988).
31. H. R. Kricheldorf, R. Pakull, and S. Buchner, *J. Polym. Sci., Part A: Polym. Chem.*, 27, 431 (1989).
32. H. R. Kricheldorf, G. Schwarz, J. de Abajo, and J. G. de la Campa, *Polymer*, 32, 942 (1991).
33. H. R. Kricheldorf, A. Domschke, and G. Schwarz, *Macromolecules*, 24, 1011 (1991).
34. H. R. Kricheldorf and S. A. Thomsen, *Makromol. Chem., Rapid Commun.*, 14, 395 (1993).
35. H. R. Kricheldorf, G. Schwarz, A. Domschke, and V. Linzer, *Macromolecules*, 26, 5161 (1993).
36. M. Sato, T. Hirata, and K. Mukaida, *Makromol. Chem.*, 193, 1729–1737 (1992).
37. H. R. Kricheldorf, V. Linzer, and C. Bruhn, *JMS—Pure Appl. Chem.*, A31, 1315 (1994).
38. H. R. Kricheldorf, V. Linzer, J. de Abajo, and J. de la Campa, *JMS—Pure Appl. Chem.*, A32, 311 (1995).
39. P. Alder, J. G. Dolden, and P. Smith, *High Perform. Polym.*, 7, 421 (1995).
40. H. R. Kricheldorf and N. Probst, *High Perform. Polym.*, 7, 471 (1995).
41. H. R. Kricheldorf and M. Gurau, *J. Polym. Sci., Part A: Polym. Chem.*, 33, 2241 (1995).
42. H. R. Kricheldorf, N. Probst, M. Gurau, and M. Berghahn, *Macromolecules*, 28, 6565 (1995).
43. H. R. Kricheldorf and V. Linzer, *Polymer*, 36, 1893 (1995).
44. H. R. Kricheldorf and M. Gurau, *JMS—Pure Appl. Chem.*, A32, 1831 (1995).
45. H. R. Kricheldorf, N. Probst, and C. Wutz, *Macromolecules*, 28, 7990 (1995).
46. H. R. Kricheldorf and V. Linzer, *Macromol. Chem. Phys.*, 197, 4183 (1996).
47. H. R. Kricheldorf and D. F. Wulff, *J. Polym. Sci., Part A: Polym. Chem.*, 34, 3511 (1996).
48. C. Fay, J. G. Smith and T. L. St. Clair, *Polymer Preprints*, 35, 541 (1994).
49. T. K. Kim, S. O. Kim, and I. J. Chung, *Polymers for Advanced Technologies*, 8, 305 (1997).
50. H. R. Kricheldorf, and R. Pakull, *J. Polym. Sci., Polym. Letters*, 23, 413 (1985).
51. J. I. Jin and C. S. Kang, *Prog. Polym. Sci.*, 22, 937 (1997).
52. J. Watanabe, M. Hayashi, Y. Nakata, T. Niori, and M. Tokita, *Prog. Polym. Sci.*, 22, 1052 (1997).
53. T. Inoue, Y. Kumagai, M. A. Kakimoto, Y. Imai, and J. Watanabe, *Macromolecules*, 30, 1921 (1997).
54. T. Inoue, M. A. Kakimoto, Y. Imai, and J. Watanabe, *Macromol. Chem. Phys.*, 198, 519 (1997).
55. T. I. Kaneko, K. Imamura, and J. Watanabe, *Macromolecules*, 30, 4244 (1997).
56. J. R. Evans, R. A. Orwoll, and S. S. Tang, *J. Polym. Sci., Part A: Polym. Chem.*, 23, 971 (1985).
57. M. Sato, T. Hirata, and K. Mukaida, *Macromol. Rapid Commun.*, 15, 203 (1994).
58. T. Hirata, M. Sato, and K. Mukaida, *Macromol. Chem. Phys.*, 195, 1611 (1994).
59. T. Asanuma, H. Oikawa, Y. Ookawa, and A. Yamaguchi, *Polymer Preprint*, 34, 827 (1993).

60. T. Asanuma, H. Oikawa, Y. Ookawa, W. Yamasita, M. Matsuo, and A. Yamaguchi, *J. Polym. Sci., Part A: Polym. Chem.*, 32, 2111 (1994).
61. S. Tamai, Y. Ookawa, and A. Yamaguchi, *40<sup>th</sup> International SAMPE Symposium and Exhibition*, 40, 1412 (1995).
62. S. Tamai, Y. Ohkawa, and A. Yamaguchi, *Polymer*, 38, 4079 (1997).
63. G. Schwarz, S. J. Sun, H. R. Kricheldorf, M. Ohta, H. Oikawa, and A. Yamaguchi, *High Perform. Polym.*, 9, 121 (1997).
64. S. L. Liu, T. S. Chung, L. Lu, Y. Torii, H. Oikawa, and A. Yamaguchi, *J. Polym. Sci. Part B: Polym. Phys.*, 36, 1679 (1998).
65. S. L. Liu, T. S. Chung, S. H. Goh, Y. Torii, A. Yamaguchi, and M. Ohta, *Polym. Eng. Sci.*, 38, 1485 (1998).
66. T. S. Chung, S. L. Liu, H. Oikawa, and A. Yamaguchi, *ANTEC'98, Society of Plastics Engineers*, Atlanta, Georgia, USA, April 26–30, pp. 1494 (1998).
67. R. Pardy, Ph.D. Thesis, The University of Akron (1993).
68. R. J. Ciora and J. H. Magill, *Macromolecules*, 23, 2350 (1990).
69. R. J. Ciora and J. H. Magill, *Macromolecules*, 23, 2359 (1990).
70. S. K. Bhattacharya, A. Misra, R. S. Stein, R. W. Lenz, and P. E. Hahn, *Polym. Bull.*, 16, 465 (1986).
71. S. Z. D. Cheng, J. J. Janimak, T. M. Lipinski, K. Sridar, X. Y. Huang, and F. W. Harris, *Polymer*, 31, 1122 (1990).
72. X. Liu, S. Hu, L. Shi, Q. Zhou, and X. Duan, *Polymer*, 30, 273 (1989).
73. H. Jonsson, E. Wallgren, A. Hult, and U. W. Gedde, *Macromolecules*, 23, 1041 (1990).
74. M. A. Gomez, C. Macro, J. G. Fatou, T. N. Bowmer, R. C. Haddon, and S. V. Chichester-Hicks, *Macromolecules*, 24, 3276 (1991).
75. M. Laus, P. Ferruti, D. Caretti, A. S. Angeloni, G. Galli, and E. Chiellini, *Thermochim. Acta*, 162, 179 (1990).
76. S. B. Warner and M. Jaff, *J. Cryst. Growth*, 48, 184 (1980).
77. J. Grebowicz and B. Wunderlich, *J. Polym. Sci., Part B: Polym. Phys.*, 21, 141 (1983).
78. M. Pracella, V. Frosini, G. Galli, and E. Chiellini, *Mol. Cryst. Liq. Cryst.*, 113, 201 (1984).
79. Y. D. Yoo and S. C. Kim, *Polym. J.*, 20, 1117 (1988).
80. Campoy, C. Macro, M. A. Gomez, and J. G. Fatou, *Macromolecules*, 25, 4392 (1992).
81. S. L. Liu, T. S. Chung, H. Oikawa, and A. Yamaguchi, *Fourteenth Annual Meeting of Polymer Processing Society*, Yokohama, Japan, June 8–12, 569 (1998).
82. L. Carpaneto, E. Marsano, B. Valenti, and G. Zanardi, *Polymer*, 33, 3865 (1992).
83. Y. C. Kim and I. J. Chung, *Polym. J.*, 25, 1257 (1993).
84. J. Watanabe, M. Hayashi, Y. Nakata, T. Niori, and M. Tokita, *Prog. Polym. Sci.*, 22, 1053 (1997).
85. S. L. Kwolek, P. W. Morgan, and W. R. Sorenson, U.S. Patent 3,063,966 (1962).
86. S. L. Kwolek, P. W. Morgan, W. R. Sorenson, J. R. Schaefgan, and L. W. Gulrich, *Macromolecules*, 10, 1390 (1977).
87. S. Aharoni, *J. Polym. Sci.*, 19, 281 (1981).
88. W. E. Krigbaum, *Macromolecules*, 21, 538 (1988).
89. C. Griffin, T. R. Brit, and G. A. Cambell, *Mol. Cryst. Liq. Cryst. (Lett.)*, 82, 145 (1982).
90. T. Uryu and J. Song, *Polym. J.*, 21, 977 (1989).
91. M. Schmucki and A. Jenkins, *Makromol. Chem.*, 190, 1303 (1989).
92. G. W. Calundann and M. Jaffe, Anisotropic polymers, their synthesis and properties, *Proceedings of the Robert A. Welch Conferences on Chemical Research, XXVI, Synthetic Polymers*, p. 247 (1982).
93. T. S. Chung, G. W. Calundann, and A. J. East, Liquid crystalline polymers and their applications, *Encyclopedia of Engineering Materials*, Vol. 2, Marcel Dekker Publisher, New York, 625 (1989).

94. M. Jaffe, G. W. Calundann, and H. N. Yoon, Fibers from naphthalene-based thermotropic liquid crystalline copolyester, *Encyclopaedia of Fibre Science and Technology*, Vol. 3, 83 (1989).
95. R. A. Weiss and C. K. Ober, *Liquid Crystalline Polymers*, American Chemical Soc., Washington D.C. (1990).
96. J. Economy and K. Goranov, *Adv. Polym. Sci.*, 117, 221 (1994).
97. M. Jaffe, J. D. Menczel, and W. E. Bessey, Fiber, in *Thermal Characterisation of Polymeric Materials*, 2nd ed. Chapter 2, 1767, Morgan Kaufmann Pub. San Francisco (1997).
98. B. Wunderlich, The basis of thermal analysis, in *Thermal Characterization of Polymeric Materials*, ed. by A. Turi, 1st edition, Chapter 2, 92; Academic Press, New York (1981).
99. T. S. Chung, *Polym. Eng. Sci.*, 26, 901 (1986).
100. G. D. Butzbach, J. H. Wendorff, and H. J. Zimmerman, *Makromol. Chem. Rapid Commun.*, 6, 821 (1985).
101. G. D. Butzbach, J. H. Wendorff, and H. J. Zimmerman, *Polymer*, 27, 1337 (1986).
102. S. Z. D. Cheng, J. J. Janimak, A. Zhang, and Z. Zhou, *Macromolecules*, 22, 4240 (1989).
103. N. D. Field, R. Baldwin, R. Layton, P. Frayer, and F. Scardiglia, *Macromolecules*, 21, 2155 (1988).
104. A. Biswas and J. Blackwell, *Macromolecules*, 21, 3146, 3152, 3158 (1988).
105. S. Z. D. Cheng, *Macromolecules*, 21, 2475 (1988).
106. S. Z. D. Cheng, A. Zhang, R. L. Johnson, Z. Wu, and H. H. Wu, *Macromolecules*, 23, 1196 (1990).
107. D. Han, S. Chang, and S. S. Kim, *Macromolecules*, 27, 7699 (1994).
108. M. H. B. Skovby, R. Lessel, and J. Kops, *J. Polym. Sci. Polym. Chem.*, 28, 75 (1990).
109. A. J. East, F. Charbonneau, and W. Calundann, U. S. Patent 4, 330, 457 (1982).
110. S. D. Hudson and A. J. Lovinger, *Polymer*, 34, 1123 (1993).
111. S. Z. D. Cheng and B. Wunderlich, *J. Polym. Sci., Polym. Phys. Ed.*, 24, 577 (1986).
112. J. Blackwell, H. M. Cheng, and A. Biswas, *Macromolecules*, 21, 39 (1988).
113. Y. G. Lin and H. H. Winter, *Liquid Crystals*, 3, 593 (1988).
114. Y. G. Lin and H. H. Winter, *Liquid Crystals*, 3, 519 (1988).
115. Y. G. Lin and H. H. Winter, *Macromolecules*, 21, 2439 (1988).
116. G. W. Calundann, U. S. Patent 4,161,470 (1979).
117. R. A. Chivers, J. Blackwell, and G. A. Gutierrez, *Polymer*, 25, 435 (1984).
118. J. Liu and P. H. Geil, *Polymer*, 34, 1366 (1993).
119. F. Rybnikar, B. L. Yuan, and P. H. Gail, *Polymer*, 35, 7699 (1994).
120. T. S. Chung, M. Cheng, S. H. Goh, M. Jaffe, and G. W. Calundann, *J. Appl. Polym. Sci.*, 72, 1139 (1999).
121. T. S. Chung, M. Cheng, P. K. Pallathadka, and S. H. Goh, *Polym. Eng. Sci.*, 39, 953 (1999).
122. L. C. Sang, H. Y. Kwan, C. K. Ho, and W. S. Tae, *Polymer*, 38, 4831 (1997).
123. A. Muhlebach, J. Economy, R. D. Johnson, T. Karis, and J. Lyerla, *Macromolecules*, 23, 1803 (1990).
124. J. D. Menczel, G. L. Collins, and S. K. Saw, *J. Thermal Anal.*, 49, 201 (1997).
125. L. I. Minkova and P. L. Magagnini, *Polymer*, 36, 2059 (1995).
126. G. P. Chang-Chien and M. M. Denn, *Polym. Adv. Tech.*, 7, 168 (1996).

# The Thermal Stability and Degradation Behavior of Thermotropic Liquid Crystalline Polymers (TLCPs)

XING JIN  
K. P. PRAMODA  
TAI-SHUNG CHUNG

## 1. INTRODUCTION

As discussed in the previous sections, thermotropic liquid crystalline polymers (TLCPs) can be divided into main-chain and side-chain TLCPs. With the easy-processing properties in the liquid crystalline phase and the high mechanical performance of the products, main-chain TLCPs have been widely used as a high-strength fiber, fiber reinforcement, in situ reinforcement additive, and injection molded article, etc. In order to obtain the products with more balanced processing properties and thermal stability and to avoid the thermally induced loss of performance in processing, the elucidation on the thermal stability and degradation behaviors of TLCPs is absolutely necessary. However, most publications on TLCPs are focused on the research of synthesis, phase transition, morphology, rheology, mechanical property, etc. [1–14], while comparatively few are on the thermal stability and degradation behaviors. In this chapter, the degradation behaviors of TLCPs are discussed from the aspects of mechanisms and kinetics, and general information about the thermal stability of TLCPs is introduced. Because main-chain TLCPs are subjected to much higher temperatures in the processing and applications than side-chain TLCPs, the focus is on main-chain TLCPs in this chapter.

## 2. THERMAL STABILITY AND DEGRADATION MECHANISMS OF TLCPs

### 2.1. COMMERCIAL TLCPs

The thermal degradation mechanisms of TLCPs, such as Ticona's Vectra, BP-Amoco's Xydar, DuPont's Zenite, and Eastman's X7G, are discussed below.

#### 2.1.1. Vectra A950

Vectra A950 has a 73/27 molar ratio of *p*-hydroxybenzoic acid (pHBA)/2,6-hydroxybenzoic acid (2,6-HNA) [15,16]. Jin and Chung [17] have studied the thermal degradation behavior of Vectra A950 by thermogravimetric analysis (TGA) and TGA-Fourier transform infra-red (FTIR). Figure 4.1 shows that there are mainly two degradation processes for Vectra A950 in air, whereas only one in N<sub>2</sub>. This result can also be observed for most other TLCPs. Figures 4.2 and 4.3 show the FTIR spectra of the volatile products from TGA in N<sub>2</sub> for Vectra A950. By observing the bands around 2350 cm<sup>-1</sup> and 670 cm<sup>-1</sup>, it can be seen that CO<sub>2</sub> is the dominant product in both N<sub>2</sub> and air, which exists all through the degradation process, and the amount of CO<sub>2</sub> is consistent with the thermal decomposition rate [17]. In Figure 4.3(a), the 1604 cm<sup>-1</sup> and 1498 cm<sup>-1</sup> bands represent the vibration of the aromatic rings. The 1604 cm<sup>-1</sup> band becomes noticeable at 460°C, and the 1498 cm<sup>-1</sup> band becomes noticeable at around 500°C, 40°C before the temperature of the maximum weight loss,

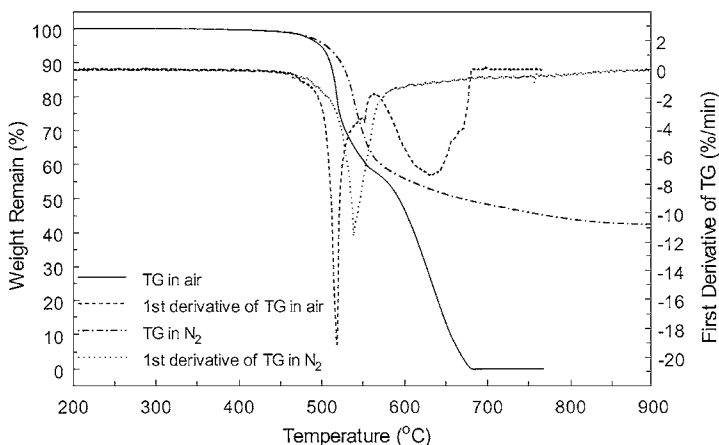
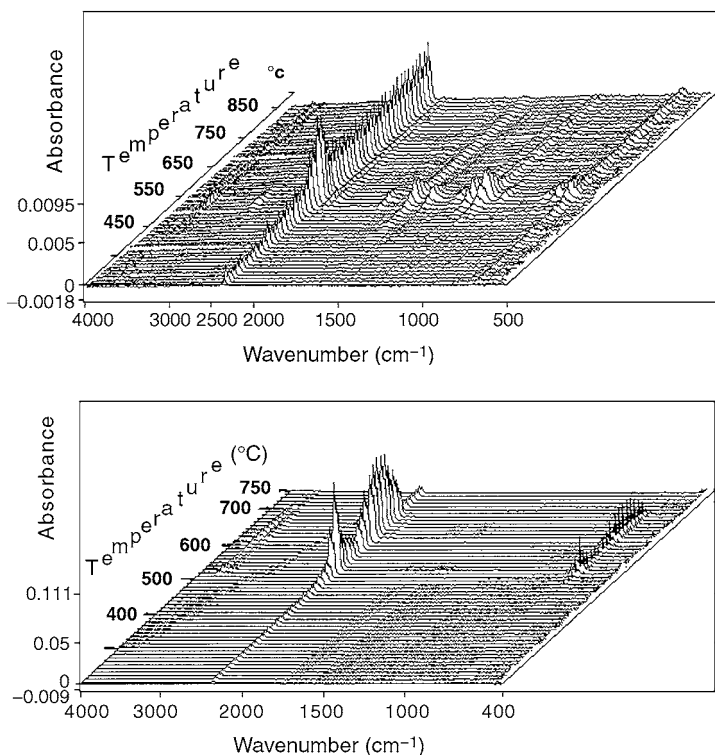
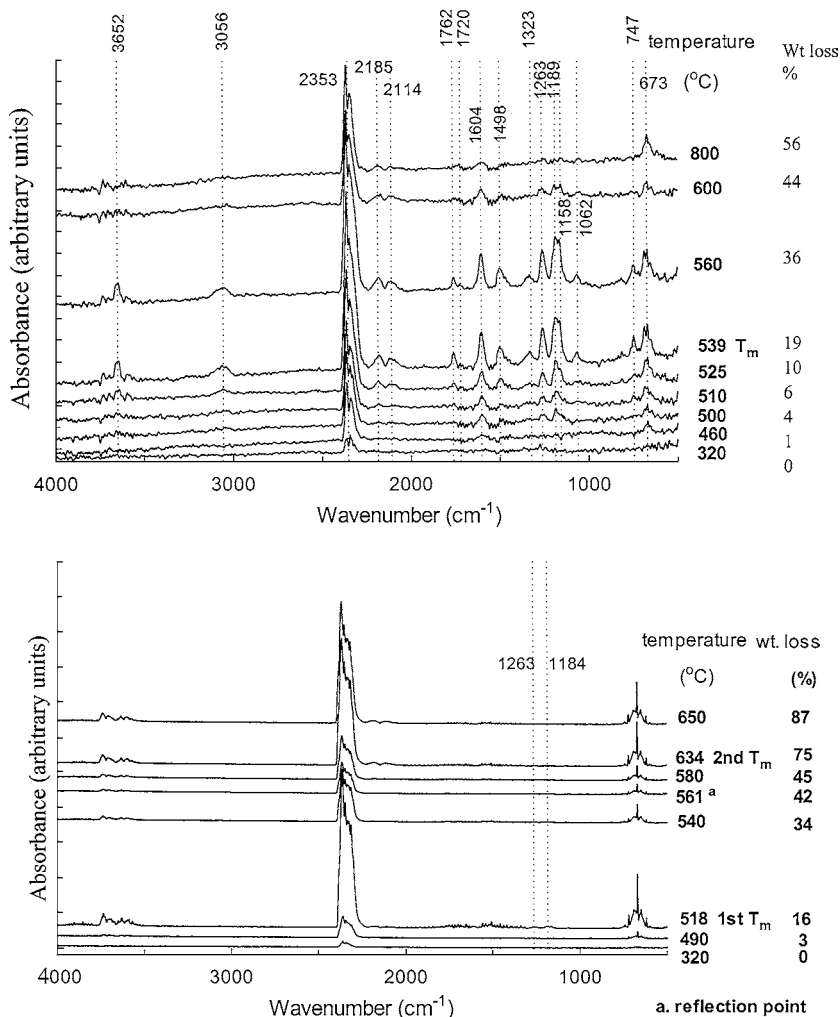


Figure 4.1 TGA data of TGA-IR for Vectra A950.



**Figure 4.2** Stacked IR spectra of the products from TGA for Vectra A950 in (a)  $N_2$  and (b) air.

$(\partial W/\partial t)_m$ . These two bands last to the end. The  $1263$  and  $1189\text{ cm}^{-1}$  bands existing from  $500$  to  $800^\circ\text{C}$  are associated with C—O stretching, and they suggest the presence of aromatic ethers. From  $510^\circ\text{C}$  onward, bands appear at  $3652$ ,  $3056$ ,  $1762$ ,  $1720$ ,  $1323$ , and  $747\text{ cm}^{-1}$  almost simultaneously. The  $3652\text{ cm}^{-1}$  band represents the O—H stretching vibration. The  $3056\text{ cm}^{-1}$  band is ascribed to the C—H stretch of the aromatic ring. The  $1762\text{ cm}^{-1}$  band results from the stretching of ester carbonyl. A band of ester C—O stretching is formed between  $1263$  and  $1189\text{ cm}^{-1}$ , at the shoulder of  $1189\text{ cm}^{-1}$  band. The  $1720\text{ cm}^{-1}$  band results from the stretching of ketone carbonyls. The  $1323\text{ cm}^{-1}$  band is caused by the in-plane deformation of the phenol O—H. The  $747\text{ cm}^{-1}$  band is assigned to the out-of-plane bending of C—H on the aromatic ring. These bands indicate the presence of phenols and aryl esters and ketones. The  $3056$  and  $747\text{ cm}^{-1}$  bands disappear around  $600^\circ\text{C}$ ,  $60^\circ\text{C}$  above the  $(\partial W/\partial t)_m$  temperature, but  $1604$  and  $1498\text{ cm}^{-1}$  bands continue to exist. This suggests the presence of aromatic rings, some H atoms on which have been substituted. The  $3652$  and  $1323\text{ cm}^{-1}$  phenol bands and the  $1762\text{ cm}^{-1}$  ester bond also disappear after  $600^\circ\text{C}$ . The



**Figure 4.3** Selected IR spectra of the products from TGA for Vectra A950 in (a) N<sub>2</sub> and (b) air.

1062 cm<sup>-1</sup> band appears after 525°C, and a shoulder at 1158 cm<sup>-1</sup> also develops gradually from 525°C onward. The 1158 and 1062 cm<sup>-1</sup> bands appear later than the 3056 and 747 cm<sup>-1</sup> bands; they represent the in-plane deformation of C—H on the substituted rings and indicate hydrogen substitution reactions on the aromatic rings.

Normally, when a charge disturbance occurs within the aromatic ring through electronic interaction between the ring and the substituents, the intensity of bands of the aromatic rings, particularly those near 1600 cm<sup>-1</sup>, will increase.

The  $1604\text{ cm}^{-1}$  band becomes noticeable before the  $1498\text{ cm}^{-1}$  band and continues to be noticeable at  $800^\circ\text{C}$ . So, the strong intensity of the  $1604\text{ cm}^{-1}$  band supports the existence of substitution on the aromatic rings with groups such as carbonyl or oxygen. Moreover, this result agrees with the fact that the  $1720\text{ cm}^{-1}$  ketone band still exists even at  $800^\circ\text{C}$  [17].

It can be seen from Figure 4.3(b) that, in contrast to the thermal decomposition in  $\text{N}_2$  as shown in Figure 4.3(a), less amount of degradation products other than  $\text{CO}_2$  and  $\text{CO}$  are formed in air atmosphere [17]. Because  $\text{CO}$  can be easily oxidized by  $\text{O}_2$ , the ratio of  $\text{CO}_2$  amount to  $\text{CO}$  amount was much greater than that degraded in  $\text{N}_2$  as shown in Figure 4.3(a). Similarly, the ratios of  $\text{CO}_2$  amount to the amounts of other decomposition products in air environment are also very high.  $\text{CO}$  does not appear until the first  $(\partial W/\partial t)_m$  stage. Its amount becomes nearly inconceivable in the period between the two maximum degradation stages and then increases again around the second stage. This suggests that the formation of  $\text{CO}$  follows two different mechanisms in the two degradation stages. Probably during the first stage,  $\text{CO}$  is mainly from the terminal  $\Phi\text{-CO}\bullet$ , while in the second stage,  $\text{CO}$  is mainly from the oxidation of the chars. Four apparent bands appeared in the range of  $3500\text{--}3800\text{ cm}^{-1}$  from the first  $(\partial W/\partial t)_m$  until the end. These bands represent the stretching of free  $\text{O-H}$  but do not represent the existence of  $\text{H}_2\text{O}$  without relatively stronger  $\text{H}_2\text{O}$  bands at around  $1300\text{--}1800\text{ cm}^{-1}$ , because, usually, the intensity of the water bands at  $1300\text{--}1800\text{ cm}^{-1}$  should not be weaker than that of the water bands at  $3500\text{--}4000\text{ cm}^{-1}$ . This suggested that some phenols are produced. The characteristic bands of  $\text{H}_2\text{O}$  at around  $3500\text{ cm}^{-1}$  and  $1630\text{ cm}^{-1}$  appear at the first  $(\partial W/\partial t)_m$ ; they decrease to become unnoticeable between the two  $(\partial W/\partial t)_m$  temperatures, and a very small amount of  $\text{H}_2\text{O}$  is formed at the second  $(\partial W/\partial t)_m$ . There are also broad bands appearing at  $1263\text{ cm}^{-1}$  and  $1184\text{ cm}^{-1}$ , which correspond to the  $\text{C-O}$  stretching vibrations, indicating the formation of products with ester or ether structures. They may also indicate the existence of phenols, because there are  $\text{C-O}$  bands in phenols also.

Sato et al. reported that Vectra A950 has a 70/30 molar ratio of pHBA/2,6-HNA [18]. TGA data show that the maximum degradation rate  $(\partial W/\partial t)_m$  occurs at  $520^\circ\text{C}$  under both helium and quasi-air at  $10^\circ\text{C min}^{-1}$  heating rate. The TGA curves under the two conditions almost superimpose each other below  $550^\circ\text{C}$ ; however, differential thermal analysis (DTA) results show much difference under two atmospheres. Under helium, a weak endothermic peak of ester bond rupture is observed at about  $550^\circ\text{C}$ , while no significant peaks exist above  $550^\circ\text{C}$ , and, finally, 40% weight remains. In quasi-air, a sharp exotherm happens at about  $550^\circ\text{C}$ , and an even larger endotherm occurs at about  $600^\circ\text{C}$ . Nearly no weight remains at the end.

With MS, both Dufour et al. [19] and Sato et al. [18] reported that the main evolved gas products for Vectra A950 are  $\text{H}_2\text{O}$ ,  $\text{CO}$ ,  $\text{CO}_2$ , and phenol.  $\text{CO}_2$  results from the decarboxylation of ester linkage, and phenol is released from

the pHBA moiety.  $\text{H}_2\text{O}$  may come from the dehydration between the hydroxy end groups formed through the hydrolysis of ester linkages. There are also minor components of benzene, benzoic acid, naphthalene, hydroxy naphthalene, and phenyl phenol or diphenyl ether. Sato et al. [18] reported that the evolution profiles of  $\text{H}_2\text{O}$ ,  $\text{CO}$ , and  $\text{CO}_2$  under quasi-air follow the pattern similar to those under helium in the range of 500–550°C; thus, the evolution of  $\text{CO}_2$  under quasi-air in this temperature range is mainly attributed to decarboxylation of the ester linkages rather than combustion. However, the larger intensities of  $\text{H}_2\text{O}$  and  $\text{CO}_2$  as well as the exothermal DTA peak under quasi-air suggest oxidation also occurs to some extent. With  $5^\circ\text{C min}^{-1}$  heating rate under helium,  $\text{CO}_2$  and  $\text{CO}$  products reach maximum amount at a temperature  $10^\circ\text{C}$  before the phenol, and the differential thermogravimetry (DTG) curve and the  $\text{CO}$  evolution profile all have a shoulder corresponding to the phenol evolution peak. Therefore, the thermal degradation of Vectra A950 proceeds stepwisely through the scission of the ester linkages releasing  $\text{CO}$  and  $\text{CO}_2$ , followed by the degradation of pHBA moiety releasing phenol and  $\text{CO}$ . The  $10^\circ\text{C}$  difference of the evolution temperature is an important reason for the good flame resistance of Vectra A950.

Dufour et al. [19] believe that inter- or intramolecular ester exchange is the main primary fragmentation process for fully aromatic polyesters. The process starts above  $500^\circ\text{C}$  and accounts for the randomization of the polymer sequence and the formation of the oligomers. Decarboxylation is the main secondary or tertiary degradation process and results ultimately in  $\text{CO}$  and  $\text{CO}_2$ . When heated at  $20^\circ\text{C min}^{-1}$  from  $30^\circ\text{C}$  to  $900^\circ\text{C}$  in inert gas, the DTG curve of Vectra A950 shows a small shoulder at  $490^\circ\text{C}$ . The sample is stable below about  $470^\circ\text{C}$ , but decomposes rapidly after that, with  $(\partial W/\partial t)_m$  at  $543^\circ\text{C}$ , and no hydroxy naphthalene is detected. During the isothermal at  $340^\circ\text{C}$  for one hour, no further weight loss occurs after an initial degradation in the first 10 minutes. Contrary to the non-isothermal measurement, phenol, naphthalene, and xanthone are not detected.

Hummel et al. [16] reported that the  $(\partial W/\partial t)_m$  of Vectra A950 is at  $522^\circ\text{C}$  with  $10^\circ\text{C min}^{-1}$  heating rate in  $\text{N}_2$ , and this conclusion is in accordance with that of the total ion current in the linear-temperature programmed pyrolysis-mass spectra (LTP-Py-MS). At  $512^\circ\text{C}$ , the strongest MS peak is phenol followed by  $\text{CO}_2$ ,  $\text{CO}$ ,  $\text{H}_2\text{O}$ , and naphthol. This suggests the fragmentation accompanied by decarboxylation, decarbonylation, and dehydration. The ester structures should be produced but are not observed; they probably remain in the residue. At  $562^\circ\text{C}$ , decarbonylation overtakes decarboxylation, most of the ester structures disappear, and phenol and naphthol are still quite strong. Among the dibenzoic fragments, dibenzofuran, diphenyl ether, and dibenzopyrone have the strongest peaks, which suggests the residue loses the aromatic ethers. There are also fragments with masses of 218 and higher containing one benzene and one naphthalene ring.

In the FTIR spectra of Vectra A950 film [16], a new carbonyl bond at  $1662\text{ cm}^{-1}$  is formed when isothermal at  $420^\circ\text{C}$ . After 18 hours, the  $1738\text{ cm}^{-1}$  ester band decreases to about a half, whereas the  $1662\text{ cm}^{-1}$  band has reached almost the intensity of the neighboring ring vibration bands. The  $1662\text{ cm}^{-1}$  band is assigned to diaryl ketone structures. When heated at  $5^\circ\text{C min}^{-1}$  i. vac., a  $3560\text{ cm}^{-1}$  band of phenolic OH begins to grow in the FTIR spectra of the residue at about  $527^\circ\text{C}$ , and a  $1227\text{ cm}^{-1}$  band of dibenzofuran develops above  $527^\circ\text{C}$  with the disappearance of  $1262, 1157\text{ cm}^{-1}$  ester bands. The above facts suggest the Fries-analogue rearrangement as in Figure 4.4, where ester groups are consumed and ketophenols are formed. This conclusion is supported by the FTIR spectra of the volatile products. The FTIR spectra of the gaseous pyrolyzate show that phenols, phenol esters,  $\text{CO}_2$ , and CO have their maximums at the maximum formation of total volatile. Diaryl ketones have a maximum about  $20^\circ\text{C}$  higher, because a rearrangement in the condensed phase is necessary for their formation.

### 2.1.2. Vectra B950

Vectra B950 has a 60/20/20 molar ratio of 2,6-HNA/*p*-hydroxy acetaniline/terephthalic acid (TA). It is the only one containing amide linkages on the polymer main chains among those commercially available TLCPs. DuPont's Kevlar also contains amide bonds, but it is lyotropic LCP instead of TLCP. There are relatively few reports about the thermal degradation of Vectra B, though there have been extensive studies on the thermal degradation of aromatic polyamide, especially Kevlar [20–29]. For Vectra B950, the temperature of 10% weight loss at  $10^\circ\text{C min}^{-1}$  was reported to be  $510^\circ\text{C}$  and  $504^\circ\text{C}$  in  $\text{N}_2$  and air, respectively [17]. The char remaining after TGA in  $\text{N}_2$  is 50% in weight. Figure 4.5 shows the FTIR spectra of volatile products from TGA in  $\text{N}_2$ . Compared with Figure 4.3(a), the rough baseline of the spectra suggests that more decomposition products are formed than that of Vectra A. This is due to the fact that amide bonds exist in Vectra B950, and, correspondingly, more bands appear in the  $3500\text{--}3800\text{ cm}^{-1}$  range, which relates to the stretching of N–H bond. The  $1628\text{ cm}^{-1}$  band represents deformation vibration of the primary amine N–H, the deformation vibration of the second amine N–H is usually very weak, and the bands around  $1341\text{ cm}^{-1}$  are assigned to the aromatic amine C–N stretching vibrations. These bands imply the existence of aromatic amine. The  $1765\text{ cm}^{-1}$  band represents the stretching vibration of ester carbonyl, and the bands around  $1715\text{ cm}^{-1}$  represent the stretching of ketone and amide carbonyl groups. The  $1490\text{ cm}^{-1}$  band and the bands around  $1600\text{ cm}^{-1}$ , which overlap with the  $1628\text{ cm}^{-1}$  one, represent the aromatic ring vibrations. The  $1265$  and  $1183\text{ cm}^{-1}$  bands of ethers continue to exist long after  $(\partial W/\partial t)_m$ . The decomposition products that exist at  $(\partial W/\partial t)_m$  appear almost simultaneously around  $480^\circ\text{C}$ . After  $560^\circ\text{C}$ ,  $50^\circ\text{C}$  above  $T_m$ , most degradation

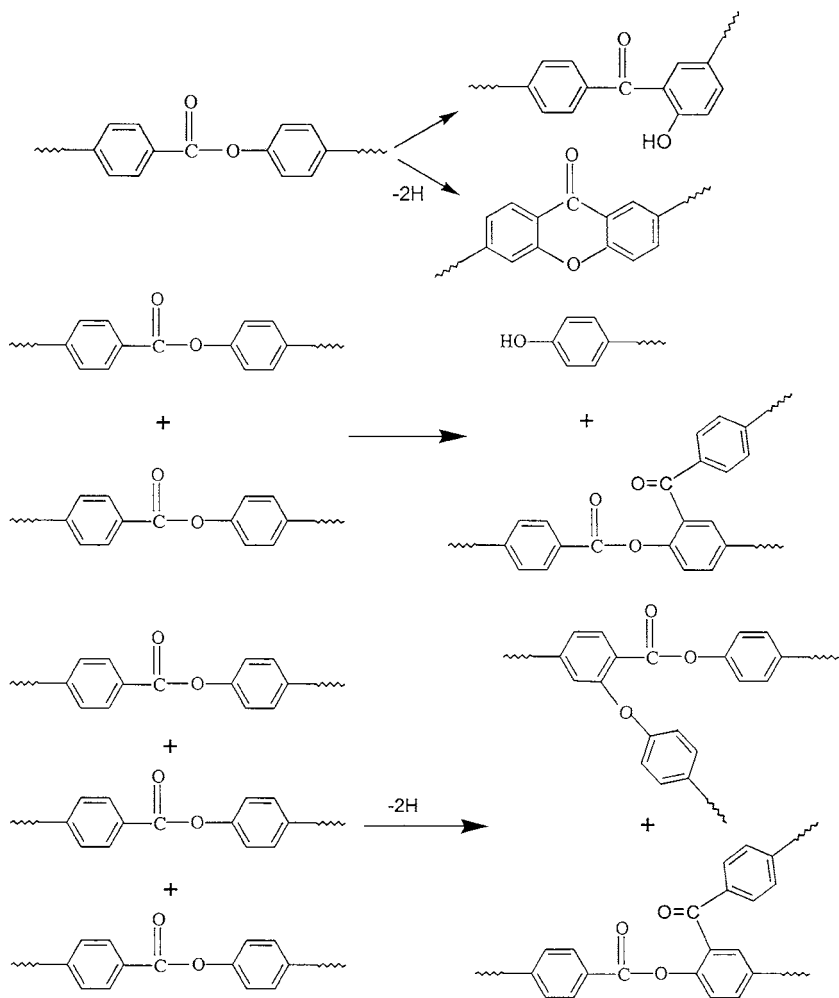


**Figure 4.4** The degradation mechanism of poly(*p*-oxybenzoyl) i. vac. suggested by Hummel et al. [16].

products continue to exist, and they decrease only gradually until the end of the decomposition. This suggests that the random chain scission takes place on the ester and amide bonds simultaneously and the various degradation processes develop at similar rates [17]. The elemental analysis of the char residues after TGA in  $N_2$  shows that there is 47% of nitrogen element left, which suggests the existence of nitrile end groups,  $R-N\equiv N-R$ , or other structures with nitrogen.

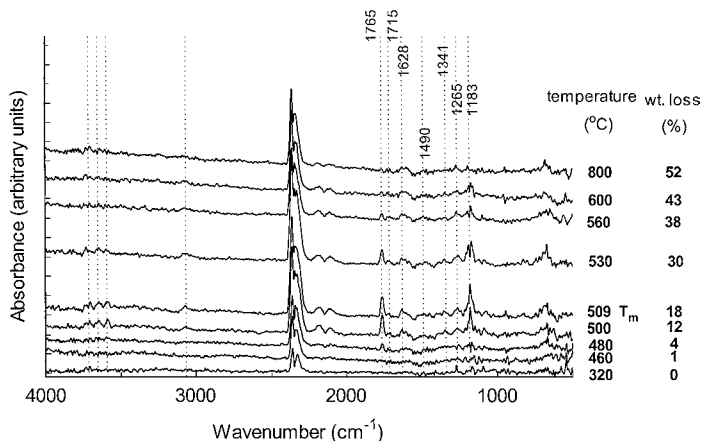


**Figure 4.5** Selected IR spectra of the products from TGA for Vectra B950 in  $N_2$ .

### 2.1.3. Xydar

Xydar SRT900 is the most representative brand of Xydar LCPs; it has 2/1/1 molar ratio of pHBA/*p,p'*-biphenol (BP)/TA. Currently there is no report on the detailed chemical structure of Xydar SRT1000, but it looks the same as Xydar SRT900 from FTIR spectra on solid sample [30]. Xydar SRT1000 is less stable than Xydar SRT900 in both  $N_2$  and air. As for the chemical structural of Xydar SRT500, it is the same as that of Xydar 900 in the paper of Sato et al. [18], but Dufour et al. [19] believe that it also contains mPA unit.

With the influence of naphthol units and amide bonds, there exists the following order of the  $E_a$  and stability at the beginning of the decomposition process: Xydar SRT900 > Vectra A950 > Vectra B950. However, the percentages of weight remaining after 560°C in  $N_2$  or after the first  $T_m$  in air follow the contrary order [17]. Dufour et al. [19] have hypothesized that the naphthol units in Vectra A950 disturb its linearity and thus make its backbone less rigid and the initial decomposition temperature lower than that of Xydar SRT500. Perhaps for the same reason, stability of Vectra A950 is lower than Xydar SRT900. Due to the fact that the average bond dissociation energy of C–N (about 73 kcal/mole) is smaller than that of C–O (about 85 kcal/mole), the introduction of amide bonds as well as the naphthol structure certainly makes Vectra B950 even less thermally stable than Vectra A950 [17].

In helium, the ester bond of Xydar SRT500 is ruptured as an endothermic reaction in the range of 470–570°C with about 48% weight loss, and  $(\partial W/\partial t)_m$  is at 540°C [18]. The main gas products are  $H_2O$ , CO,  $CO_2$ , and phenol. Phenol is evolved at a slightly higher temperature than  $CO_2$ . The char formation occurs

above 570°C and reaches about 40% in weight at 1000°C. Under quasi-air, the first  $(\partial W/\partial t)_m$  is at 540°C, and the second one occurs at 600°C with a large exothermic DTA peak corresponding to the combustion of char. Dufour et al. [19] reported that Xydar SRT500 has a  $(\partial W/\partial t)_m$  at 564°C with 20°C min<sup>-1</sup> heating rate, and char product after pyrolysis at 900°C is 37% in weight. During isotherm one hour at 440°C, no phthalic acid products are found. Crossland et al. [31] reported some TGA and Py-gas chromatography (GC)-MS data of two Ekkcel products, which are derived from pHBA, *p,p'*-BP, and TA or *m*-phthalic acid (mPA).

Sueoka et al. [32] have studied in detail the origin of the main pyrolysis products for the TLCs with 2/1/1 molar ratio of pHBA/*p,p'*-BP/TA. It was found that the major products are CO<sub>2</sub>, benzene, phenol, biphenyl, and phenyl benzoate. They used LCP containing deuterated TA units to clarify the monomer units from which the products are formed. Based on the product ratio from Py-GC/MS, they deduced that

- (1) Benzene is formed mainly from TA units in the polymer chains.
- (2) Phenol is formed mainly from pHBA units in the polymer chains.
- (3) Biphenyl is formed mostly by the recombination reaction rather than directly from BP units.
- (4) Phenyl benzoate is mostly from one TA unit and one pHBA unit by recombination reactions.
- (5) Products larger than phenyl benzoate might be formed from BP units.

With the above results, Sueoka et al. [32] concluded that the C—C bonds between an aromatic ring and carbonyl carbon are preferentially cleaved over the other types of C—C bonds, and the C—O bonds between a carbonyl carbon and a phenolic oxygen are preferentially cleaved over the C—O bonds between an aromatic ring and a phenolic oxygen. The C—C bonds between aromatic rings are not easily cleaved.

#### 2.1.4. Zenite

Zenite TLCs are the new products of DuPont, and they probably are closely related to the HX series reported before [15,33,34]. It is believed that Zenite LCPs are composed of TA, pHBA, hydroquinone, and other aromatic diols, aromatic dicarboxylic acids, and aromatic hydroxy carboxylic acids [35–37].

For both Zenite 6000 and 8000B, no residue is left after TGA experiments in air atmosphere, while about 40% weight remained after experiments in N<sub>2</sub> [30]. Figure 4.6 shows the selected FTIR spectra of the degradation products for Zenite LCPs in N<sub>2</sub>. We can see that the spectra for the two TLCs are very similar to each other. At 1% weight loss, only the bands of CO<sub>2</sub> appear.

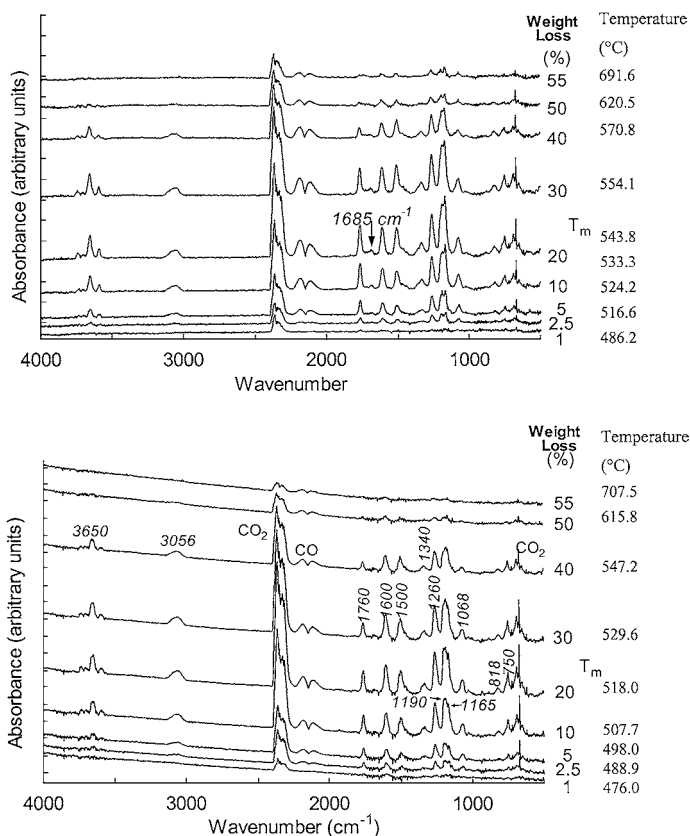


**Figure 4.6** FTIR spectra of the products from TGA in N<sub>2</sub> for (a) Zenite 6000 and (b) Zenite 8000B. (Note: T<sub>m</sub>-Temperature of the first degradation maximum).

At 2.5% weight loss, bands appear at 1760, 1600, 1500, 1260, 1190, 1165, and 1068 cm<sup>-1</sup>. The 1760 cm<sup>-1</sup> band is ascribed to the stretching of the ester carbonyl. The 1600 and 1500 cm<sup>-1</sup> bands are from the vibration of the aromatic rings. The 1260 and 1190 cm<sup>-1</sup> bands result from the C—O stretching. The 1165 and 1068 cm<sup>-1</sup> bands are associated with the C—H in-plane deformation on an aromatic ring. These bands suggest the existence of aromatic esters and ethers. These products indicate the initiation of the main chain breakdown. CO can be observed with its characteristic double bands at the right wing of the CO<sub>2</sub> 2350 cm<sup>-1</sup> band. CO amount does not become noticeable until around 5% weight loss. Almost at the same time as CO appears, bands appear around 3650 and at 3056, 1340, 818, and 750 cm<sup>-1</sup>. These bands exist from 5% to

40% weight loss and suggest the formation of phenols. Because the  $3650\text{ cm}^{-1}$  band represents the O—H stretching, the  $3056\text{ cm}^{-1}$  band is associated with the C—H stretching of aromatic rings. The  $1340\text{ cm}^{-1}$  band is caused by the in-plane deformation of the phenol O—H, and the 818, and  $750\text{ cm}^{-1}$  bands are from the out of plane bending of C—H on aromatic rings. After 40% weight loss, the  $3056$ ,  $1068$ ,  $818$  and  $750\text{ cm}^{-1}$  aromatic ring C—H bands become unnoticeable, while  $1600$  and  $1500\text{ cm}^{-1}$  bands still remain noticeable. This implies that some aromatic rings with hydrogen atoms have been substituted. There is a weak band at around  $1700\text{ cm}^{-1}$  from 10% to 30% weight loss, which results from the stretching of ketone carbonyls and suggests the formation of the aromatic ketones. It is interesting to notice that in Figure 4.6(a), the  $1185\text{ cm}^{-1}$  band has almost the same intensity as that of the  $2350\text{ cm}^{-1}$   $\text{CO}_2$  band until 40% weight loss for Zenite 6000 [30].

The above results are in accordance with Hummel's [16] hypothesis that the thermal degradation of LCPs is attributed to Fries-analogue rearrangement and main chain splitting with intra- and inter-molecular dehydrogenation mechanisms. The fact that only the bands of  $\text{CO}_2$  are noticeable at the beginning suggests that the degradation starts with the scission of the terminal carboxyl groups, forming  $\text{CO}_2$  [30]. There may also exist the evaporation of the residual monomers, solvent, and oligomers as mentioned by Hummel [16]; however, the amount of these products is too small to be observed by FTIR. The inter- or intramolecular ester exchanges as mentioned by Dufour et al. [19] may also happen at this stage, but it cannot cause the apparent weight changes of samples. The  $\text{CO}_2$  appearing at the beginning of the decomposition could be from the decarboxylation of the original terminal carboxyl group. However, the molecular weights of these four LCPs are very high, so the original amount of terminal carboxyl units should be very small. Besides, the  $\text{CO}_2$  stays higher than the amounts of other products during the whole degradation process. Therefore,  $\text{CO}_2$  should be produced from the newly formed  $\phi\text{—COO}\bullet$ , which can only result from the breakdown of the main chain [30]. Sueoka et al. [32] believed that in wholly aromatic polyesters with the structure  $\phi_1\text{—CO—O—}\phi_2$ , the C—C bonds between  $\phi_1\text{—CO}$  are preferentially cleaved over the other types of C—C bonds and the C—O bonds between  $\text{CO—O}$  are preferentially cleaved over the C—O bonds between  $\text{O—}\phi_2$ . If the  $\phi_1\text{—C}$  and  $\text{C—O}$  bonds in the  $\phi_1\text{—CO—O—}\phi_2$  structure break simultaneously, CO should be formed, and  $\text{CO}_2$  is difficult to produce with the difficulty of the break of the  $\text{O—}\phi_2$  bond. But, in fact, the  $\text{CO}_2$  amount is much higher than the CO amount throughout the degradation process. Therefore, in most of the cases, those two bonds break separately. When the C—O bond breaks first, the Fries-analogue rearrangement and recombination reactions follow next, and only a small amount of  $\phi_1\text{—CO}\bullet$  degrades further to form CO. If  $\phi_1\text{—C}$  bond is cleaved first,  $\text{CO}_2$  and  $\bullet\phi_2\text{—}$  are produced next, instead of CO and  $\bullet\text{O}\phi_2\text{—}$ , because  $\bullet\phi_2\text{—}$  radical is more stable than  $\bullet\text{O}\phi_2\text{—}$  radical [30].

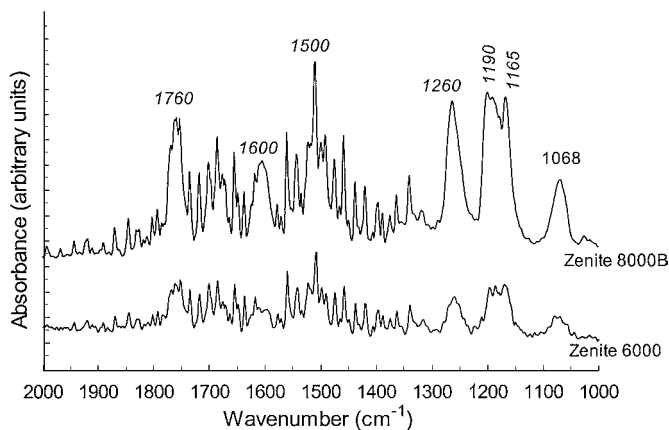


**Figure 4.7** The detailed FTIR spectra of the products at 20% weight loss in air.

Figure 4.7 displays the detailed FT-IR bands in the range of  $1000\text{--}2000\text{ cm}^{-1}$  when the weight losses of Zenite TLCPs are 20% [30]. These FT-IR bands have the same positions and shapes as those observed in  $\text{N}_2$  atmosphere as shown in Figure 4.6, though the peaks between  $1300$  and  $1800\text{ cm}^{-1}$  overlap with water bands. These bands exist only before 40% weight loss in air for the four LCPs. This clearly suggests that, though the oxidation reaction of  $\text{O}_2$  dominates all through the degradation process in air atmosphere, in the first degradation stage, there also exists the degradation mechanisms similar to that in  $\text{N}_2$ . During the second degradation stage,  $\text{O}_2$  breaks down the cross-linking formed by intermolecular reactions in the first degradation stage, and the char begins to degrade by oxidation reactions.

#### 2.1.5. X7G

X7G TLCP of Eastman is the only one with semi-flexible main chain among the commercially available brands of TLCPs at present. It contains pHBA and ethylene terephthalate (ET) units with a 60/40 molar ratio of pHBA/ET. Because polyesters such as poly(ethylene terephthalate) (PET) and poly(butylene terephthalate) (PBT) are commonly used polymers, there have been many publications [20,38–41] on the thermal degradation and stability of them, which are very helpful for the corresponding studies on X7G. The primary degradation mechanism of PET is the random scission of ester linkages through the six-membered cyclic transition state, followed by  $\beta\text{-CH}$  hydrogen transfer. The process produces a pair of carboxylic acid and vinyl end. This process should also exist to some extent during the thermal decomposition of X7G.

According to the report of Sato et al. [18], X7G has a major  $(\partial W/\partial t)_m$  at 452°C and a minor one at 514°C in helium at 10°C min<sup>-1</sup> heating rate, and the char formation at 1000°C is 24% in weight. The differential thermoanalysis (DTA) curve shows a broad exotherm in the range of 450–850°C. The degradation under quasi-air had two major  $(\partial W/\partial t)_m$  at 451 and 607°C, and a minor one at 501°C, respectively, with three corresponding DTA exothermal peaks. The main gaseous products were CO, CO<sub>2</sub>, phenol, and aliphatic compounds such as ethylene and acetaldehyde. Under both atmospheres, the stepwise evolution of acetaldehyde around 450°C suggests that the degradation mainly starts at ET blocks. The fact that a large amount of flammable organic compounds evolve prior to the main evolution of CO<sub>2</sub> is the main reason for the poorer flame resistance of X7G, compared with the wholly aromatic TLCPs. It was found that for the random copolyesters containing different ratios of pHBA and ET units, the thermal stability measured by the volatilization rate increases with increasing pHBA content, as does the final char formation [42].

## 2.2. OTHER TLCPs

### 2.2.1. Poly(*p*-oxybenzoyl) [P(pHBA)]

Actually, most commercially available TLCPs are basically based on P(pHBA) structure and modified with other mesogenic and spacer units, so P(pHBA) is discussed first in this section. P(pHBA) begins to melt at 510°C, accompanied by degradation [16]. Hummel et al. reported a three-step decomposition by TGA/ DTG/ DTA at 10°C min<sup>-1</sup> in N<sub>2</sub>. The first one at 347°C is assigned to the solid-solid transition, the second one with 2% weight loss is very weak, and the third one at 547°C with 60% weight loss indicates the main decomposition. LTP-Py-MS at 10°C min<sup>-1</sup> shows a weak peak at 402°C and a strong one with the maximum at 542°C. In the range of the main decomposition, the product amounts of phenol, dibenzopyrone + HBA, dibenzopyrone, and methane arrive at their maximums at 382, 487, 542, and 572°C, respectively. The MS of products taken at 487°C shows two series of mass numbers apart from that of oxybenzoyl unit. The hydroxybenzoyl and oxybenzoyl monomer peaks, and CO<sub>2</sub> and CO are also strong at 487°C. At 512°C, phenol shows a stronger peak than any other products, and oligomer fragments with phenoxy end groups disappear, while those with a benzoyl end group can be detected up to the dimer. The monomer peaks, CO<sub>2</sub>, CO, phenol, and the fragments derived from oxybenzoyl are still very strong at 512°C. P(pHBA) has lost most of the ester groups by elimination of carboxyl and carbonyl groups toward the end of maximum decomposition. At 572°C, the peak of diphenyl ether is the strongest, followed by dibenzopyrone and dibenzofuran. The peaks of two phenolic fragments, phenyl and diphenyl, are also remarkably strong. At 727°C, the methane is formed while other product amounts decrease to nearly unnoticeable.

Hummel et al. [16] have also observed the change of FTIR spectra of P(pHBA) film between 422 and 527°C i. vac. The ester bond at 1740  $\text{cm}^{-1}$  continually decreases, and only a small band is left at 527°C. At about 477°C, another carbonyl band is growing at 1665  $\text{cm}^{-1}$ , which is very likely caused due to the formation of a diaryl ketone structure. A third carbonyl band at 1712  $\text{cm}^{-1}$  appears at about 527°C, which can be explained by the formation of 9-fluorenone structures. A weak band at 3500  $\text{cm}^{-1}$  exists from 422°C, but disappears after about 527°C, which indicates a small amount of phenolic groups. The fact that a high absorption background gradually develops in the middle IR area suggests the carbonization of the material. The FTIR spectra of the volatile products from 507 to 527°C are governed by the  $\text{CO}_2$  band, while the CO band develops gradually [33]. A sharp band of phenol exists at 3643  $\text{cm}^{-1}$  all through the process. The bands of phenol esters and carboxylic groups disappear at 527°C, because ester groups in the residue as a source for these products are exhausted. Diaryl ketone and ether structures increase gradually, while the two bands of aromatic ring vibration around 1600  $\text{cm}^{-1}$  do not change much with increasing temperature. Figure 4.4 depicts the process of the thermal degradation i. vac. for P(pHBA) put forward by Hummel et al. [16]. The process should happen at the beginning stage of the decomposition. In the following steps, accompanying the further scission on the linkages between aromatic rings, the phenols, aromatic ketones, ethers, and esters with lower molecular weight are formed.

According to the data of Py-GC-MS, Crossland et al. [31] found that the flash pyrolysis of P(pHBA) results in the products of predominantly hydroxyl-terminated species, and they claimed that the main breakdown route is the scission of the ester groups followed by hydrogen abstraction reactions.

### 2.2.2. LC Polyimide and Polyamides

The chemical structures [43] of thermotropic polyimide and polyamide LCP's are described in Chapter 3, along with their crystallization kinetic studies. Kircheldorf et al. [44] carried out XRD and PLM characterization studies of these TLCPs and found the polyimide to be a smectic liquid crystalline. Pramoda et al. [45] studied the thermal degradation kinetics of TLC-PI (thermotropic liquid crystalline polyimide) and TLC-PA (thermotropic liquid crystalline polyamide). The apparent activation energy in the case of TLC-PI is found to be higher than the TLC-PA for degradation.

Figure 4.8 shows the FTIR spectra of gases evolved from the degradation of polyimide under inert atmosphere at various temperatures. Five FTIR spectra were selected corresponding to the following temperatures: before degradation (500°C), 550°C,  $T_{\text{max}}$ °C, after degradation (650°C), and at 700°C in the case of polyimide. The initial degradation products at 500°C from the TLC-PI are almost exclusively  $\text{CO}_2$ , which is noticeable from IR bands around 2350  $\text{cm}^{-1}$ .

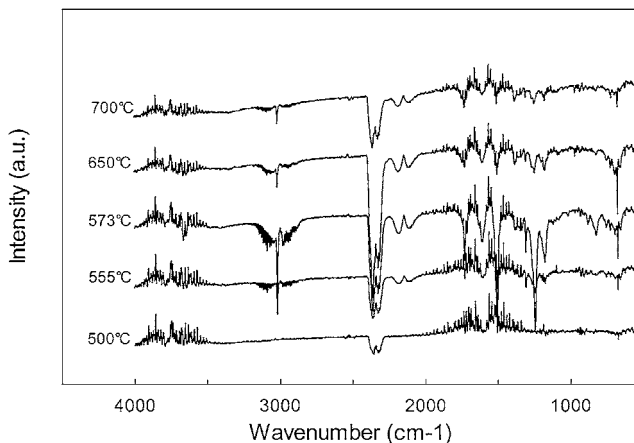


**Figure 4.8** Selected IR spectra of the products from TGA for polyimide in  $N_2$ .

The presence of CO is indicated around 555°C by its characteristic double bands. Its intensity increases as degradation continues, it is found to have a maximum at the point degradation reaches its maximum, and thereafter it decreases. However, it persists until the end of the decomposition process, indicating it is by chain scission with the formation of terminal CO. The sharp band at  $3010\text{ cm}^{-1}$  observed as the temperature reaches 555°C is assigned to C–H vibrations, and its intensity is found to be maximum at the point of maximum decomposition of the polyimide. Moreover, this band persisted until the end of degradation, though with a lowered intensity. A weak IR band around  $1300\text{--}1700\text{ cm}^{-1}$  indicates the evolution of water, unsaturated aromatic hydrocarbons, and ammonia. At 573°C, all these species were detected very clearly in the FTIR spectra of the evolved gases from TLC-PI. This confirms the maximum decomposition observed in the TGA analysis. However, the observed broad derivative peak means that the weight loss process is a heterogeneous one, i.e., the cleavage of the linkages and the evolution of the unsaturated hydrocarbons occur simultaneously. All these observations support the correlation between the TGA thermograms and the FTIR spectra.

Figure 4.9 represents the FTIR spectra of the evolved gases during the decomposition of the polyamide liquid crystalline polymers at different temperatures. Unlike for TLC-PI, the IR spectra at 500°C for TLC-PA consist of weak IR bands due to  $CO_2$  and also those corresponding to unsaturated hydrocarbons and ammonia. Such an observation suggests that the degradation had already begun, which in turn confirms that the polyamide LCPs are less thermally stable than the polyimide LCPs. Further, at 550°C, the intensities of those peaks observed at 500°C are found to increase along with some new bands. A small trace of CO is found to appear on the right side of the  $CO_2$  band at  $2350\text{ cm}^{-1}$ .

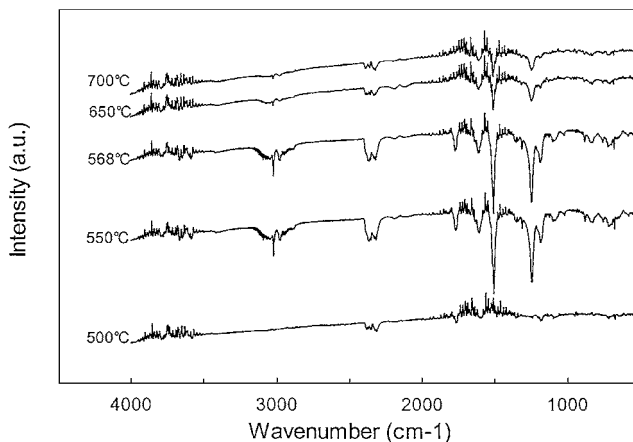


**Figure 4.9** Selected IR spectra of the products from TGA for polyamide in  $N_2$ .

In addition, sharp peaks appear at  $3010$ ,  $1500$ , and  $1240\text{ cm}^{-1}$ , which are assigned to C—H vibrations, unsaturated hydrocarbons, and N—H vibrations. The intensities of these peaks are found to increase as the decomposition continues and are highest at the maximum degradation point of the polyamide.

The IR spectra of evolved gases during the sample treatment in air show that  $CO_2$  and  $H_2O$  are the predominant gases. The gases evolved during the first stage of degradation are similar to those evolved during degradation in nitrogen. The weight loss in the second stage of degradation is primarily due to the evolution of  $CO_2$  and  $CO$ . The sharp increase in both  $CO_2$  and  $CO$  production during degradation represents the onset of homolytic bond rupture processes.

The volatile degradation products produced in air are somewhat different from those produced in nitrogen. Although the gases evolved such as  $CO$ ,  $CO_2$ , and  $H_2O$  vapor, are similar to that in  $N_2$ , the intensities of their productions are much higher in air. This phenomenon suggests that the modes of degradation are different in air and nitrogen; and, in the second stage of degradation, oxygen merely serves to further oxidize the initially formed products by thermal bond breaking processes. Moreover, the activation energy values are different for degradation in air and nitrogen. Furthermore, there are subtle differences in the types of decomposition products (other than  $CO$ ,  $CO_2$ , and  $H_2O$ ) produced in air and nitrogen environments.

### 2.2.3. TLCPs with Flexible Units on the Main Chain

Kim and Paul [46] synthesized a series of TLCPs with *p*-hydroxybenzoic acid (pHBA), terephthalic acid (TA), poly(ethylene terephthalate) (PET), and 1,4-dihydroxynaphthalene (1,4-DHN). They found that the thermal degradation

rate increases linearly with the increasing content of PET units, as the onset temperature for thermal degradation decreases. The onset temperature of TLCPs with 10/10/10/70 mol% of PET/TA/1,4-DHN/pHBA is 453.5°C with 40°C min<sup>-1</sup> heating rate; the gas atmosphere was not indicated. The thermostability of the copolymer of pHBA and PET can be increased slightly with increasing addition of vanillic acid from 0 to 5 mol% [47], and all the polymers have no significant weight loss below 416°C at 5°C min<sup>-1</sup> heating rate in N<sub>2</sub>. For the poly(ester-imide) TLCPs synthesized from 2,6-diacetoxynaphthalene and *n*-( $\omega$ -carboxyalkylene) trimellitic imides (containing 5–11 C atoms in carboxyalkylene part) [48], they are stable in N<sub>2</sub> up to at least 350°C with 10°C min<sup>-1</sup> heating rate. Yoshimitsu et al. [49] synthesized polyamide TLCP from *p*-aminobenzoic acid, 4,4'-aminodiphenyl ether, and oligomer of 4-(6-methacryloyloxy hexyloxy)-4'-methoxy biphenyl terminated by thiomalic acid. Being heated in air conditions the polymer begins degradation at 332°C and follows a two-step process including the decomposition of the oligomer side chains at about 370°C and polyamide backbone at 559°C with two corresponding exotherms. The heating rate was not given. At a heating rate of 10°C min<sup>-1</sup> [50], the TLCP based on 2-chlorohydroquinone, 1,4-cyclohexanedimethanol, and terephthaloyl chloride has the onset of degradation at 300°C in air and 380°C in N<sub>2</sub>, and has less than 5% weight loss at 375°C in air. The 5% weight loss temperatures at 10°C min<sup>-1</sup> in air for TLCPs from 3-(4-hydroxyphenyl) propionic acid with *p*-HBA and 3-Cl-pHBA are in the range of 370–400°C [51].

## 2.2.4. TLCPs with Substitutes on the Aromatic Ring

The data of some TLCPs with substitutes on the aromatic ring are summarized in Table 4.1 [52,53]. The TLCPs from 4-hydroxy-2,3,5,6-tetrafluorobenzoic acid and 2,6-HNA were reported to decompose apparently after 320°C under

TABLE 4.1. The Temperatures of 5% Weight Loss at 20°C/min in N<sub>2</sub> of TLCPs with Substitute on the Aromatic Ring.

Monomer[52] Temperature (°C)	BrTA '+' (React with)			PhTA '+' (React with)		
	MPBP	DPBP	BND	MPBP	DPBP	BND
	470	473	445	450	485	463
Monomer [53] Temperature (°C)	Hydroquinone '+'			<i>p</i> -Phenylenediamine '+'		
	TA1	TA2	TA3	TA1	TA2	TA3
	482	480	467	489	492	474

BrTA—2-bromoterephthalic acid; PhTA—2-phenylterephthalic acid.

MPBP—3-phenyl-4,4'-biphenol; DPBP—3,3'-bis(phenyl)-4,4'-biphenol.

BND—1,1'-binaphthyl-4,4'-diol; TA1—2-phenyl terephthalic acid.

TA2—2-(4-biphenyl)terephthalic acid; TA3—2-(2-biphenyl)terephthalic acid.

'+'—React with.

$N_2$  at  $10^\circ\text{C min}^{-1}$  [54]. The introduction of 2-( $\alpha$ -phenylisopropyl) hydroquinone can lower the initial degradation temperatures of TLCPs of 4,4'-biphenol/TA and 2,6-HNA/TA to around  $460^\circ\text{C}$  from  $557$  and  $523^\circ\text{C}$ , respectively [55]. The initial decomposition temperatures in  $N_2$  at  $80^\circ\text{C min}^{-1}$  for TLCPs of 5-phenyl-2,6-HNA/pHBA and 3-phenyl-4,4'-hydroxybiphenyl carboxylic acid/pHBA are in the ranges of  $520$ – $550^\circ\text{C}$  and  $500$ – $520^\circ\text{C}$ , respectively [56]. Khan et al. [57] reported that for TLCPs with TA and phenyl hydroquinone as the major constituents and 1,4-naphthalenediol or 1,4-anthracene diol as the minority comonomer, they start to lose weight significantly above about  $450^\circ\text{C}$  under air at  $10^\circ\text{C min}^{-1}$ . When the polymers melt and are held for a fairly short time at  $400^\circ\text{C}$  between two glass plates, the plates lose the ability to be sheared, though they still show the nematic texture in optical observation. This indicates some form of degradation that involves crosslinking. Jackson [58] synthesized a series of polyester TLCPs with monosubstituted hydroquinone, and the solubility of the polymer films decreases after being heated in air at a temperature before decomposition. The thermal stability was evaluated according to the time required for the solubility to decrease. The result shows that the stability at  $150^\circ\text{C}$  decreases with various substitutes in the order of phenyl, *tert*-butyl, chloro, and methyl, and, at  $300^\circ\text{C}$ , the hydroquinone polyesters containing phenyl or *tert*-butyl substitutes are the most stable.

For the wholly aromatic TLCPs derived from TA, phenyl hydroquinone, and 3,4'-dicarboxyl phenylether [59], the thermal stability measured by TGA slightly decreases with the increasing ether content. All polymers exhibit good thermal stability up to about  $400^\circ\text{C}$  in  $N_2$  and  $25^\circ\text{C}$  lower in air, with a  $20^\circ\text{C min}^{-1}$  heating rate. The thermal stability of the TLCPs decreases when the phenyl hydroquinone is replaced by (1-phenylethyl) hydroquinone.

## 2.2.5. TLCP Blends

Blending TLCPs with the conventional engineering polymers has attracted much industrial and academic interest, due to the advantages brought by TLCPs, such as the in situ reinforcement and the viscosity reduction of the melts [10,11,60,]. Campoy et al. [61] have studied the thermal stability of the blends of Nylon 6 and Vectra A950 by TGA. All their tests were carried out in an oxygen atmosphere, and the heating rate in dynamic tests is  $20^\circ\text{C min}^{-1}$ . The thermal stability of Vectra A950 is much better than Nylon 6. The TGA and DTG curves of the blends with low Vectra A content are very similar to those of Nylon 6. However, the curves of blends with more than 15% of Vectra A indicate that the degradation behaviors of both individual polymers are retained in the blends. The TGA curves suggest that the thermal stability of the blends progressively improves with increasing Vectra A content. The theoretic values of the blend properties were calculated from the weight average method. For all

the blends, the experimental weight loss is higher than the theoretical one, and this effect is particularly evident for blends with low Nylon 6 content. When Nylon 6 content is high, the experimental and theoretical TGA curves are very similar to each other. The comparison of the characteristic degradation temperature between the experimental and the theoretical values also gives a similar conclusion. The  $(\partial W/\partial t)_m$  temperature corresponding to Vectra A decreases as Nylon 6 content increases. These results suggest that the less stable polymer Nylon 6 causes destabilization of the more stable polymer Vectra A. One possible reason for this kind of phenomenon is that some degradation fragments of the less stable polymer can be transferred to the phase rich in the more stable polymer. Lee et al. [62] have studied the thermal stability of the blends of Vectra B950 (VB) with poly(ether imide) (PEI). With  $10^\circ\text{C min}^{-1}$  heating rate in  $\text{N}_2$ , the thermal stability of VB is lower than that of PEI, and the thermal stability of the blend decreases with increasing VB content, with maximum instability occurring at 50% VB content. On DTG curves, the decomposition peak of VB appears when VB content arrives at 25%. The possible explanation is that when VB content is low, the thermal energy transferred to the dispersed VB phase should exceed the barrier of the PET phase, which is thermally very stable. However, when VB content is high, overcoming the energy barrier between different phases becomes easier due to the higher portion of VB. Similar results were obtained for the blends of the TLCP copolyester, poly[(phenylethyl-*p*-phenylene-terephthalate)-*co*-(cumyl-*p*-phenylene terephthalate)], with phenolphthalein poly(ether ether ketone) [63].

## 2.2.6. Others

Crosslinkable TLCPs derived from *p*-phenylene bis(acrylic acid) with methylhydroquinone and various aromatic hydroxycarboxylic acids were reported to have a 10% weight loss in the range of  $330\text{--}400^\circ\text{C}$  under  $\text{N}_2$  at  $10^\circ\text{C min}^{-1}$  [64]. TLCPs with a potentially biodegradable property were prepared from pHA, glycolic acid, and *trans-p*-hydroxycinnamic acid [65]. The newly synthesized polymers have 5% weight loss in the range of  $340\text{--}370^\circ\text{C}$  under  $\text{N}_2$  at  $10^\circ\text{C min}^{-1}$ , while the thermal stability decreases after treatment in buffer solution for a period of time due to the decrease of the molecular weight. Li et al. [66] collected the TGA data with a single heating rate for several aromatic polyester TLCPs with different chemical structure units. Determined by calculation, they estimated that, for most TLCPs, the initial decomposition temperatures are above  $420^\circ\text{C}$ , and the lifetimes were estimated to be longer than 26 days at  $200^\circ\text{C}$  or 2.3 hours at  $300^\circ\text{C}$ .

For the TLCPs with mesogenic triad units,  $[-\text{OOC}-\phi-\text{OOC}-\phi-\text{COO}-\phi-\text{COO}-\text{R}-]_m$ , with the FTIR spectroscopy on the solid residues [67], the thermal degradation mechanisms similar to that of the PET and PBT were proved to happen when R is a linear alkyl spacer. When R is a symmetrical substituted spacer, such as  $-\text{CH}_2\text{C}(\text{CH}_3)_2-\text{CH}_2-$  or  $-\text{CH}_2\text{C}(\text{C}_2\text{H}_5)_2-\text{CH}_2-$ , the

degradation related with the  $\beta$ -CH hydrogen transfer can be excluded, and the degradation rate can be lowered. However, when R is  $-\text{CH}(\text{CH}_3)\text{CH}_2\text{CH}_2\text{CH}(\text{CH}_3)-$  [68], the  $\beta$ -H can also be provided by the methyl substitution groups of the first and the fourth carbon atoms, so the thermal stability decreases compared to the  $-(\text{CH}_2)_4-$  spacer. Ellis et al. [69] have further proved the above conclusion by TG-MS. They explored the degradation mechanism by observing the MS evolution profile of  $\text{CO}_2$ , benzene, and phenol, as well as the fragments from the aliphatic spacers, against the DTG curves.

There are also many reports on the thermal decomposition behaviors of other aromatic polyesters, which are not necessarily TLCPs. It is necessary to introduce these studies here, because these polymers have almost the same chemical structures; subsequently, they have very similar thermal degradation behaviors as the aromatic polyester TLCPs [20,70–72].

Giuffrida et al. [73] have studied the thermal decomposition mechanism of the polyesters with structures similar to the aforementioned TLCPs with mesogenic triad units, and the intramolecular exchange reactions were found to occur at the pyrolysis stage, causing a reorganization of the copolymer sequences. Using direct Py-MS, Foti et al. [74] have studied a series of totally aromatic polyesters from m-m, m-p, p-m, and p-p couples of phthalic acid and hydroquinone. Poly(mHBA) was also investigated for comparison. The relative abundance of the cyclic oligomers formed in the pyrolysis is remarkably lowered with the meta units being replaced with para units. For p-p polyester, only the cyclic dimer is present in very low abundance; the other cyclic oligomers are completely absent. The formation of the cyclic monomer is observed only in m-m polyester. The formation of the cyclic oligomer is related to the meta structure of the repeating units, which induces an easier cyclization of the polymer chain. For the m-m polyester studied, the cyclic oligomers are formed first, and their intensities reach maximums at about 330–340°C, then decrease. Meanwhile, open-chain fragments are formed and become more intense at high temperature. This behavior is due to hydrolytic cleavage of the cyclic oligomers formed. This reaction should yield open-chain fragments containing phenolic and carboxylic end. However, fragments containing carboxylic end groups are absent, especially at high masses. This indicates that carboxylic end structures undergo a faster decarboxylation reaction once formed. For the thermal fragments with lower mass, the carboxylic structures are detected, but their abundance is much lower than decarboxylated structures. For m-p and p-m polyesters, the formation of the open-chain fragment  $\text{HO}-\Phi-\text{OH}$  is simultaneous with or even anticipates the formation of the cyclic oligomers. Therefore, the hydrolytic cleavage of ester bonds should occur directly on the polymer chain. The ester hydrolytic cleavage is temperature dependent, so that at sufficiently low temperatures the pyrolysis of the polyesters produces only cyclic oligomers. Foti et al. [75] have also studied the thermal fragmentation of aromatic-aliphatic polyesters by Py-MS. Their samples contained two series, one was from aliphatic acid and aromatic phenol while the other was formed from aromatic acid and aliphatic

glycol. The results indicate that the intramolecular exchange reactions in the primary fragmentation processes cause the formation of cyclic oligomers, followed by different secondary processes. Calahorra et al. [76] have studied the thermal degradation behavior of the blends of PET with polyarylate from bisphenol-A and equimolar mixture of mPA and TA.

### 3. THERMAL DEGRADATION KINETICS

#### 3.1. BACKGROUND OF DEGRADATION KINETIC MODELING

##### 3.1.1. Ozawa-Flynn Method

The degree of conversion in a thermal degradation process is defined as

$$\alpha = \frac{W_0 - W}{W_0 - W_f} \quad (1)$$

where  $W$ ,  $W_0$ , and  $W_f$  are the actual, initial, and final weight of the samples, respectively. Only when  $W_f = 0$ ,  $\alpha$  can be replaced by the weight loss percent [77]. The rate of degradation can be expressed as

$$\frac{d\alpha}{dt} = k(T) \cdot g(W) \cdot q(W, T) \quad (2)$$

where  $t$  and  $T$  are the reaction time and temperature, respectively, and  $k(T)$  is generally represented by Arrhenius equation,

$$k(T) = A \exp\left(-\frac{E_a}{RT}\right) \quad (3)$$

$$g(W) = \left(\frac{W - W_f}{W_0 - W_f}\right)^n = (1 - \alpha)^n \quad (4)$$

where  $A$  is the pre-exponential factor,  $E_a$  is the apparent activation energy of the degradation reaction, and  $R$  is the universal gas constant. The cross term  $q(W, T)$  takes into account the interactions between the weight and the reaction arising from factors such as the modifications of the sample physical properties during the decomposition.  $q(W, T)$  is generally assumed to be unity. Thus, Equation (2) becomes

$$\frac{d\alpha}{dt} = A \exp\left(-\frac{E_a}{RT}\right) (1 - \alpha)^n \quad (5)$$

Because the heating rate,  $r$ , is equal to  $dT/dt$ , Equation (5) can be rewritten as

$$\frac{r d\alpha}{dT} = A \exp\left(-\frac{E_a}{RT}\right)(1 - \alpha)^n \quad (6)$$

Equation (6) can be rearranged as

$$g(\alpha) = \int_0^a \frac{d\alpha}{(1 - \alpha)^n} = \frac{A}{r} \int_0^T \exp\left(-\frac{E_a}{RT}\right) dT = \frac{AE_a}{rR} h(x) \quad (7)$$

where  $x = \frac{E_a}{RT}$ ,  $h(x) = -\int_{\infty}^x \frac{\exp(-x)}{x^2} dx$ .

Ozawa [78] and Flynn [79] used Doyle's approximation [80] by assuming the integral  $h(x)$  can be expressed as  $\log h(x) \cong -2.315 - 0.457x$  or  $\ln h(x) \cong -5.330 - 1.052x$  if  $20 < x < 60$ . Thus, from Equation (7), we can get

$$\ln g(\alpha) = \ln \frac{AE_a}{rR} - 5.330 - 1.052 \frac{E_a}{RT} \quad (8)$$

In Equation (8),  $A$  and  $R$  are constant, and at a specific  $\alpha$  or weight loss percentage,  $g(\alpha)$  is also constant. Then, Equation (8) can be written as

$$\ln r = C - 1.052 \frac{E_a}{RT} \quad (9)$$

where  $C$  is a constant and is equal to  $\ln \frac{AE_a}{g(\alpha)R} - 5.330$ . Using this equation, the  $E_a$  value at any specific weight loss can be calculated from the linear dependence of  $\ln r$  vs.  $1/T$  at different heating rates.

### 3.1.2. Kissinger Method

Kissinger [81] deduced the following equation by taking a derivative of Equation (6).

$$\frac{d^2\alpha}{dT^2} = \frac{d\alpha}{dT} \left[ \frac{E_a}{RT^2} - \frac{An}{r} \exp\left(-\frac{E_a}{RT}\right)(1 - \alpha)^{n-1} \right] \quad (10)$$

If  $T_m$  is chosen as the temperature at the maximum of DTG (first derivative of thermo-gravimetric) curves with different heating rates, then  $\frac{d^2\alpha}{dT^2}$  is equal to zero at  $T_m$ . This relationship yields

$$\frac{E_a}{RT_m^2} - \frac{An}{r} \exp\left(-\frac{E_a}{RT_m}\right)(1 - \alpha_m)^{n-1} = 0 \quad (11)$$

or

$$\ln \frac{r}{T_m^2} = \ln \frac{nRA(1 - \alpha_m)^{n-1}}{E_a} - \frac{E_a}{RT_m} \quad (12)$$

The  $E_a$  value may be calculated from the linear dependence of  $\ln(r/T_m^2)$  on  $1/T_m$  at different heating rates by assuming that  $\alpha_m$  or weight loss percentage at  $T_m$  is constant.

### 3.1.3. Friedman Method [82]

After taking logarithm on the both sides, Friedman rewrote Equation (5) as

$$\ln \left( \frac{d\alpha}{dt} \right) = \ln A + n \ln (1 - \alpha) - \frac{E_a}{RT} \quad (13)$$

From a plot of  $\ln(d\alpha/dt)$  vs.  $1/T$  drawn with the points at a specific  $\alpha$  on TGA curves with different heating rates,  $E_a$  value can be calculated from the slope,  $-\frac{E_a}{R}$ .

### 3.1.4. Freeman and Carroll Method [15]

Kinetics data can also be calculated with only one heating rate, in other words, from only one TGA curve. By further processing on Equation (13), one can obtain

$$\frac{\Delta \ln \left( \frac{d\alpha}{dt} \right)}{\Delta \ln (1 - \alpha)} = n - \frac{E_a}{R} \frac{\Delta \left( \frac{1}{T} \right)}{\Delta \ln (1 - \alpha)} \quad (14)$$

Then, the kinetic parameter  $n$  and  $E_a$  can be calculated from the plot of

$$\frac{\Delta \ln \left( \frac{d\alpha}{dt} \right)}{\Delta \ln (1 - \alpha)} \text{ vs. } \frac{\Delta \left( \frac{1}{T} \right)}{\Delta \ln (1 - \alpha)}.$$

## 3.2. ANALYSIS RESULTS

### 3.2.1. Commercially Available and Research-Grade TLCPs

The thermal degradation kinetics of Ticona's Vectra, BP-Amoco's Xydar, DuPont's Zenite, and Mitsui's polyimide and polyamide LCPs are analyzed below.

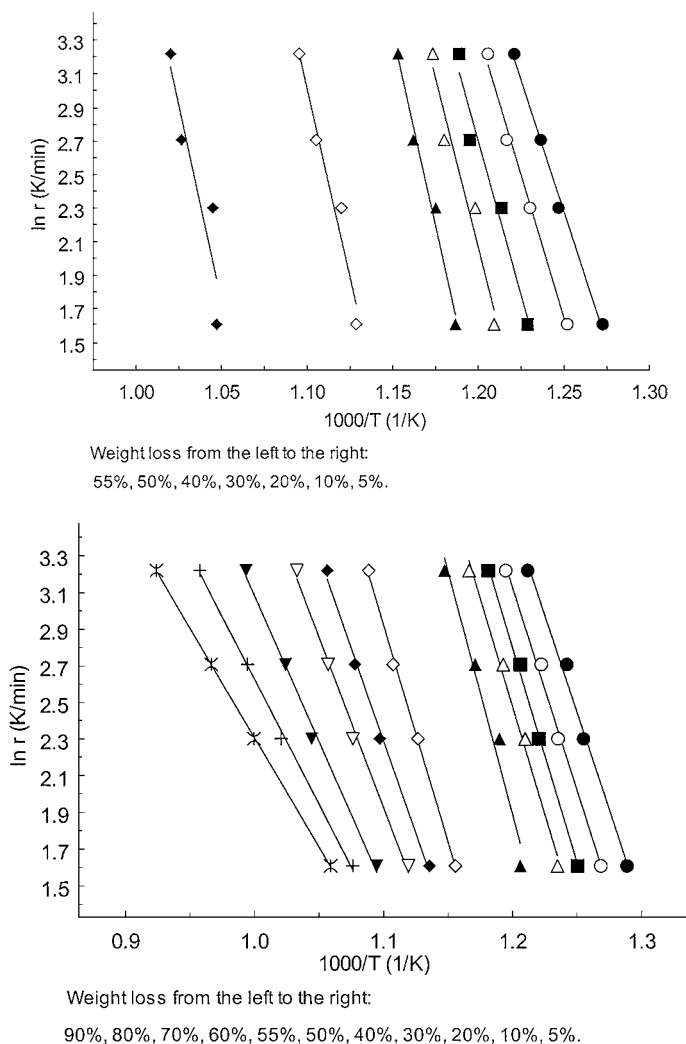


**Figure 4.10** The  $\ln r$  vs.  $1/T$  of TGA for Zenite 6000 in (a)  $N_2$  and (b) air.

According to Equation (9) of the Ozawa-Flynn method, the  $E_a$  value can be calculated from the linear dependence of  $\ln r$  vs.  $1/T$  at different heating rates,  $E_a = R \cdot \text{Slope}/1.052$ . Figure 4.10 shows the plots of  $\ln r$  vs.  $1/T$  at different weight loss percentages in TGA for Zenite 6000 under  $N_2$  and air conditions [30]. The plots for the other TLCPs are similar to this. Figure 4.11 shows the evolution of  $E_a$  at different degradation stages with different weight losses. It can be seen that the  $E_a$  curves of Xydar SRT-900 and Zenite 6000 have some

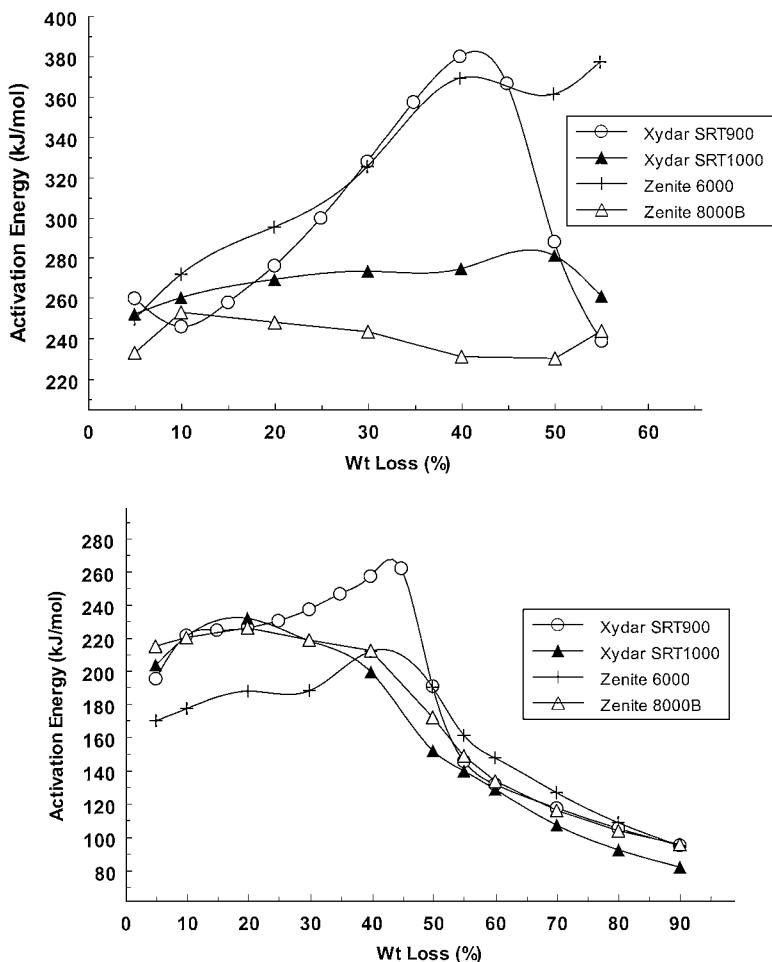


**Figure 4.11** Apparent activation energy of the thermal degradation for the Xydar and Zenite series in (a) N<sub>2</sub> and (b) air (calculated with the Ozawa-Flynn method).

similarities, and the curves reach a maximum at around 45% weight loss for the two LCPs both in air and in N<sub>2</sub>. For Xydar SRT-1000 and Zenite 8000B, their  $E_a$  values keep almost constant all through the decomposition process in N<sub>2</sub>. In an air environment, their  $E_a$  values do not change much before 40% weight loss. Then, they decrease apparently with the decrease in the extent of cross-linking and the amount of the char left. For all four LCPs, the  $E_a$  value in air atmosphere begins to decrease at a point after the first maximum of the DTG curve and close to the deflection point. The deflection points are at 48%,

50%, 47%, and 47% weight loss for Xydar SRT900, 1000, Zenite 6000, and 8000B, respectively.

In Equation (12) of the Kissinger method, if  $\alpha_m$  or the weight loss percentage at  $T_m$  is assumed to be constant, then the first term in the right hand side of Equation (12) becomes a constant. Thus, one can calculate  $E_a$  value from the linear dependence of  $\ln(r/T_m^2)$  on  $1/T_m$  at different heating rates following the relationship of  $E_a = -R \cdot \text{Slope}$ . The validity of this assumption is supported by the experiment result that the weight loss percentages for Zenite 6000 at  $T_m$  in an  $N_2$  atmosphere were 22.6%, 22.9%, 21.9%, and 24.3% at the heating rates of 5, 10, 15, and 25°C/min, respectively. They are 21.7%, 21.0%, 19.6%, and 16.8%, respectively, at the first  $T_m$  in air. The weight loss percentages at  $T_m$  are also very close at different heating rates for the other TLCPs. Therefore, it may be reasonable to take  $\alpha_m$  at the first  $T_m$  as a constant.

According to the method mentioned by Salin and Seferis [83], from Equation (10), we can get the intercept on the ordinate of a plot of  $\ln(r/T_m^2)$  vs.  $1/T_m$ :

$$I = \ln \frac{nRA(1 - \alpha_m)^{n-1}}{E_a} \quad (15)$$

We can solve for  $A$  and substitute it into Equation (6).

Then, we can get the reaction  $n$  as

$$n = \left( \frac{d\alpha}{dT} \right)_m^{-1} \frac{E_a e^I}{rR} (1 - \alpha_m) \exp\left( \frac{-E_a}{RT_m} \right) \quad (16)$$

The values of  $T_m$  for different experiments in air and  $N_2$ , the  $R^2$  (correlation coefficient) of  $\ln(r/T_m^2)$  vs.  $1/T_m$ ,  $E_a$ , and  $n$  and  $N_2$  results are listed in Table 4.2. It shows that the  $E_a$  values in Table 4.2 are in the same range as those at the same weight loss point from the Ozawa-Flynn method, and the order of the  $E_a$  values of different TLCPs are also the same from the two methods [30].

Calculated with the Kissinger method, the  $E_a$  of Vectra A950 and Vectra B950 were found to be 232 and 197 kJmol<sup>-1</sup> in  $N_2$ , and 222 and 159 kJmol<sup>-1</sup> in air, respectively. The results calculated with the Ozawa-Flynn method are in accordance with this [17].

### 3.2.2. Others

By regression analysis of the isothermal TGA data, Crossland et al. [31] got the overall  $E_a$  at different weight loss stages for homopolymer of pHBA and two copolyesters from pHBA, 4,4'-biphenol with TA and mPA, respectively. The  $E_a$  values of all three polymers showed an increase at the beginning stage of weight loss in  $N_2$ , and this increase was ascribed to the cross-linking and stabilization

TABLE 4.2. Thermal Data Calculated with Kissinger Method.

		Xydar SRT900		Xydar SRT1000		Zenite 6000		Zenite 8000B	
		N <sub>2</sub>	Air	N <sub>2</sub>	Air	N <sub>2</sub>	Air	N <sub>2</sub>	Air
$T_m$ (°C) <sup>a</sup>	5°C/min	548.0	519.0	529.0	516.4	545.8	528.1	518.9	493.7
	10°C/min	564.0	535.0	537.2	528.3	553.4	544.1	531.0	506.9
	15°C/min <sup>b</sup>	574.0	551.0	547.0	536.0	567.6	555.1	544.0	516.0
	25°C/min <sup>c</sup>	590.0	566.0	559.3	546.0	572.0	569.5	552.5	527.5
Correlation coefficient, $R^2$		0.9912	0.9989	0.9719	0.9999	0.9772	0.9979	0.9897	0.9987
$E_a$ (kJ/mol)		283.9	230.2	278.9	265.5	297.7	206.4	251.2	229.4
Weight loss at $T_m$ (%)		25.3	21.7	26.8	21.6	22.9	19.8	24.6	14.4
$n$		2.5	3.1	2.1	4.0	2.1	2.3	1.9	3.2
ln $A$ (min <sup>-1</sup> )		40.1	32.8	40.5	38.5	42.3	28.8	36.5	33.7

<sup>a</sup>  $T_m$  is the temperature at the degradation maximum. In the case of TG in air,  $T_m$  is the  $T_m$  at the first  $(\partial W/\partial t)_m$ .

<sup>b</sup> 20°C/min for Xydar SRT900.

<sup>c</sup> 40°C/min for Xydar SRT900.

www.Iran-mavad.com

مرجع دانشجویان و مهندسين مواد

that occurred at this stage. After arriving at a peak in the range of 25%–40% weight loss, the  $E_a$  values decreased rapidly, which signified the degradation of the stable chars. TGA data showed that the two copolyesters were more stable than the homopolymer. The peaks in the  $E_a$  plots occurred in the same order as the stability observed in TGA experiments. Before arriving at the peaks, the  $E_a$  values of the two copolyesters were higher than the homopolymer.

For TLCPs  $[-OOC-\phi-OOC-\phi-COO-\phi-COO-R-]_m$  [67], when R is line spacer,  $E_a$  was found to be similar to those of polyesters such as PET and PBT, and  $E_a$  decreases with increasing numbers of methylene groups in R. Li et al. [84–86] have reported some kinetic data of the X7G analogues, Vectra A with 58/42 molar ratio of pHBA/2,6-HNA, and Ekonol fiber with the same chemical structure units as Xydar. Kinetic data were also used to support the related conclusion about the thermal degradation behavior of the blends of Vectra A950 with Nylon 6 [61] and Vectra B950 with poly(ether imide), etc. [62].

### 3.2.3. Mitsui's Polyimide and Polyamide LCPs

The degradation trends for Mitsui's polyimide and polyamide LCP's are similar to other TLCPs, both in air and inert environments, with two-stage and single-stage decomposition processes, respectively. The residues left behind after decomposition are different under nitrogen for both TLC-PI and TLC-PA. While the residue left is about 42% in the case of TLC-PI, it is found to be 28% for TLC-PA. However, decomposition under air left negligible residues for both polymers. The first stage of the degradation reaction under air was observed to begin around 540°C and stop around 600°C with the maximum rate at 572°C. This initial reaction step is very close to the step observed in nitrogen. The second stage of the decomposition under air appears between 600 and 900°C with a maximum rate of weight loss around 820°C. This second stage, which leads to negligible residue, takes place around 950°C and appears to be oxidative in nature, as it is not observed in nitrogen. The decomposition temperature of the first step of degradation is 566°C for polyamide and is 572°C for the polyimide under air. Hence, the polyamide is thermally less stable than the polyimide.

The dynamic thermogravimetric analysis in air and nitrogen of the polyimide and polyamide was performed at various heating rates: 5°C/min, 10°C/min, 20°C/min, and 40°C/min. The relationship between the logarithm of heating rate ( $\ln \beta$ ) and  $1/T$  for different values of weight loss are straight lines during the thermal degradation of both polyimide and polyamide in nitrogen and air, respectively. The isoconversional plots are parallel straight lines in nitrogen but not in air, indicating a complex weight loss process with several mechanisms in the latter. Apparent activation energies are calculated according to Equation (9).

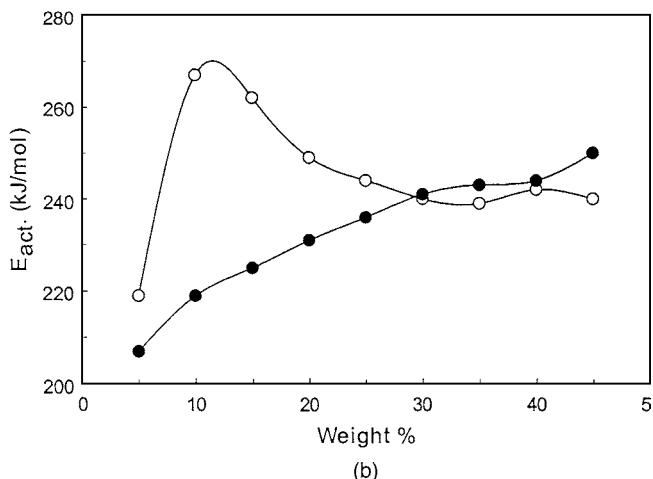
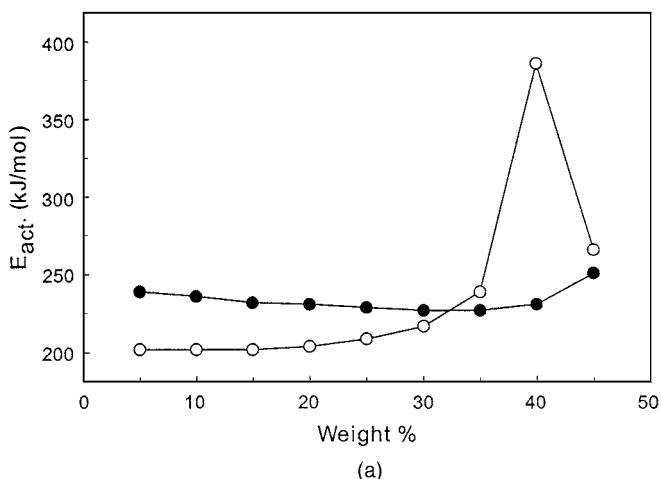


**Figure 4.12** Apparent activation energy of the thermal degradation for (a) polyimide and (b) polyamide in  $N_2$  and air (calculated with the Ozawa-Flynn method).

The values of activation energies for the degradation of polyimide in nitrogen and air environments vary with the percentage of weight loss as shown in Figure 4.12(a). Activation energies are approximately stable in nitrogen and air for initial weight loss and measure 236 and 201 kJ/mol, respectively. However, a jump in the activation energy is observed around 40% weight loss, beyond which it decreases. This may be due to the residue formed during the first step of degradation, which further reacts with oxygen to form an oxidized product.

The complex product thus formed is more stable and, therefore, requires higher activation energy for its decomposition.

Figure 4.12(b) represents the variation in apparent activation energy with the weight loss for a TLC-PA. An unusual observation was made during the degradation of TLC-PA. The apparent activation energy values are found to be higher under air than in the nitrogen. Similar behavior was observed by McNeill et al. [87] during the degradation of poly(acenaphthylene). In addition to thermal stability, they observed that the weight loss occurs in two stages under both air and nitrogen environments. Williams [88] calculated activation energies for the thermal decomposition of poly( $\alpha,\alpha,\alpha',\alpha'$ , - tetrafluoro-*p*-xylene) in nitrogen and air environments and found them to be equal. However, the apparent activation energy in the case of the TLC-PI is found to be higher than for the TLC-PA, although we found that the apparent activation energy in the case of the TLC-PA under air environment is higher than in nitrogen.

Based on Kissinger's method, the computation of the apparent activation energy is found to be 224 kJ/mol and 202 kJ/mol in nitrogen and air environments, respectively, for polyimide. The activation energies determined from the Ozawa and Kissinger methods are comparable.

#### 4. REFERENCES

1. T. S. Chung, The recent developments of thermotropic liquid crystalline polymers, *Polymer Engineering and Science*, 26, 901 (1986).
2. T. S. Chung, G. W. Calundann, and A. J. East, Liquid crystalline polymers and their applications, *Handbook of Polymer Science and Technology*, N. P. Cheremisinoff (Ed.), Marcel Dekker Publisher, New York, 2, 625 (1989).
3. M. Gordon and N. A. Plate (Ed.), *Liquid Crystal Polymers I, Advances in Polymer Science*, 59, Springer-Verlag, Berlin (1984).
4. J. L. White and S. Onogi (Eds.) U. S.-Japan seminar on polymer liquid crystals, *Applied Polymer Symposium 41, Journal of Applied Polymer Science*, John Wiley & Sons, New York (1985).
5. A. Blumstein (Ed.), *Polymeric Liquid Crystals*, Plenum Press, New York (1985).
6. H. Finkelmann, Liquid Crystal Polymers, *Thermotropic Liquid Crystals*, Chapter 6, G. W. Gray (Ed.), *Critical Reports on Applied Chemistry*, vol. 22, John Wiley & Sons, New York (1987).
7. R. A. Weiss and C. K. Ober, *Liquid Crystalline Polymers*, American Chemical Society, Washington, D.C. (1990).
8. A. M. Donald and A. H. Windle, *Liquid Crystalline Polymers*, Cambridge University Press, Cambridge (1992).
9. A. A. Collyer (Ed.), *Liquid Crystalline Polymers: From Structure to Applications*, Elsevier Applied Science, New York (1992).
10. D. Acierno and A. A. Collyer (Ed.), *Rheology and Processing of Liquid Crystal Polymers*, Chapman and Hall, London (1996).
11. F. P. La Mantia (Ed.), *Thermotropic Liquid Crystal Polymer Blends*, Technomic Publishing Co., Inc. Lancaster, PA (1993).
12. A. A. Collyer, Thermotropic liquid crystal polymers for engineering applications, *Materials Science and Technology*, 5, 309 (1989).

13. J. Economy and K. Goranov, Thermotropic liquid crystalline polymers for high performance applications, *Advances in Polymer Science*, 117, 221 (1994).
14. H. Han and P. K. Bhowmik, Wholly aromatic liquid crystalline polymers, *Prog. Polym. Sci.*, 22, 1431 (1997).
15. E. S. Freeman and B. Carroll, *J. Phys. Chem.*, 62, 394 (1958).
16. D. O. Hummel, U. Neuhoﬀ, A. Bretz, and H.-J. Dussel, Linear-temperature programmed pyrolysis of thermoresistant polymers—mass and FTIR spectrometries, 2, Aromatic polyesters and copolyesters, *Makromol. Chem.*, 194, 1545 (1993).
17. X. Jin and T. S. Chung, Thermal decomposition behavior of main-chain thermotropic liquid crystalline polymers, Vectra A-950, B-950, and Xydar SRT-900, *Journal of Applied Polymer Science*, 73, 2195 (1999).
18. H. Sato, T. Kituchi, N. Koide, and K. Furuya, Thermal degradation and combustion process of liquid crystalline polyesters studied by directly coupled thermal analysis—mass spectrometry, *Journal of Analytical and Applied Pyrolysis*, 37, 173 (1996).
19. P. R. Dufour, K. G. H. Raemaekers, and J. C. J. Bart, Simultaneous thermogravimetric and mass-spectrometric analysis of high temperature polyesters, *Thermochimica Acta*, 175, 263 (1991).
20. G. Montaudo and C. Puglisi, Thermal degradation mechanisms in condensation polymers, *Developments in Polymer Degradation*—7, Chapter 2, N. Grassie (Ed.), Elsevier Applied Science, New York (1987).
21. B. Immirzi, G. Lauria, M. Malinconico, and E. Martuscelli, Thermogravimetric studies of rigid rod-like polymers: Influence of solid phase structure and crystallinity on the degradation behavior, *Makromol. Chem., Rapid Commun.*, 12, 563 (1991).
22. J. R. Brown and A. J. Power, Thermal degradation of aramids: Part I—Pyrolysis/gas chromatography/mass spectrometry of poly(1,3- phenylene isophthalamide) and poly(1,4- phenylene isophthalamide), *Polymer Degradation and Stability*, 4, 379 (1982).
23. J. R. Brown and A. J. Power, Thermal degradation of aramids: Part II—Pyrolysis/gas chromatography/mass spectrometry of some model compounds of poly(1,3- phenylene isophthalamide) and poly(1,4- phenylene isophthalamide), *Polymer Degradation and Stability*, 4, 479 (1982).
24. Y. P. Khanna and E. M. Pearce, Aromatic polyamides. II. Thermal degradation of some aromatic polyamides and their model diamides, *Journal of Polymer Science: Polymer Chemistry Edition*, 19, 2817 (1981).
25. Y. P. Khanna and E. M. Pearce, Aromatic polyamides. III. Mechanistic studies on the role of substitute chlorine in flame retarding aromatic polyamides, *Journal of Polymer Science: Polymer Chemistry Edition*, 19, 2835 (1981).
26. D. A. Chatfield, I. N. Einhorn, R. W. Mickelson, and J. H. Futrell, Thermal decomposition products of a chlorinated aromatic polyamide, *Journal of Polymer Science: Polymer Chemistry Edition*, 17, 1353 (1979).
27. D. A. Chatfield, I. N. Einhorn, R. W. Mickelson, and J. H. Futrell, Analysis of the products of thermal decomposition of an aromatic polyamide fabric, *Journal of Polymer Science: Polymer Chemistry Edition*, 17, 1367 (1979).
28. A. K. Chaudhuri, B. Y. Min, and E. M. Pearce, Thermal properties of wholly aromatic polyamides, *Journal of Polymer Science: Polymer Chemistry Edition*, 18, 2949 (1980).
29. T. D. Greenwood, R. A. Kahley, and J. F. Wolfe, *N*-methyl-substituted aromatic polyamides, *Journal of Polymer Science: Polymer Chemistry Edition*, 18, 1047 (1980).
30. T. S. Chung and X. Jin, Studies on the phase transition and thermal stability of Xydar and Zenite series liquid crystalline polymers, *Polymer Engineering and Science*, 40, 841 (2000).
31. B. Crossland, G. J. Knight, and W. W. Wright, The thermal degradation of some polymers based upon *p*-hydroxybenzoic acid, *British Polymer Journal*, 18, 371 (1986).
32. K. Sueoka, M. Nagata, H. Ohtani, N. Naga, and S. Tsuge, Thermal degradation mechanisms of

- liquid crystalline aromatic polyesters studied by pyrolysis—gas chromatography/mass spectrometry, *Journal of Polymer Science: Part A: Polymer Chemistry*, 29, 1903 (1991).
33. A. A. Handlos and D. G. Baird, Extrusion blow molding of microcomposite based on thermotropic liquid crystalline polymers and polypropylene, *Polymer Engineering and Science*, 36, 378 (1996).
  34. M. I. van Eijndhoven-Rivera, N. J. Wagner, and B. Hsiao, Correlation of the minor-phase orientation to the flow-induced morphological transitions in thermotropic liquid crystalline polymer/ PBT blends, *Journal of Polymer Science: Part B: Polymer Physics*, 36, 1769 (1998).
  35. M. S. Connolly, U. S. Patent 4,664,972 (1987).
  36. M. R. Samuels and M. G. Waggoner, U. S. Patent 5,466,773 (1995).
  37. M. R. Samuels and M. G. Waggoner, U. S. Patent 5,525,700 (1996).
  38. I. Luderwald, Thermal degradation of polyesters in the mass spectrometer, *Developments in Polymer Degradation-2*, Chapter 3, N. Grassie (Ed.), Applied Science Publishers, London (1979).
  39. H. Zimmermann, Degradation and stabilisation of polyesters, *Developments in Polymer Degradation-5*, Chapter 3, N. Grassie (Ed.), Applied Science Publishers, London (1984).
  40. T. Suebsaeng and C. A. Wilkie, Solid products from thermal decomposition of polyethylene terephthalate: Investigation by CP/MAS13C-NMR and Fourier transform-IR spectroscopy, *Journal of Polymer Science: Polymer Chemistry Edition*, 22, 945 (1984).
  41. R. M. Lum, Thermal decomposition of poly(butylene terephthalate), *Journal of Polymer Science: Polymer Chemistry Edition*, 17, 203 (1979).
  42. D. Garozzo, M. Giuffrida, G. Montaudo, and R. W. Lenz, Mass spectrometric characterization of poly(ethylene terephthalate-co-*p*-oxybenzoate), *Journal of Polymer Science: Part A: Polymer Chemistry*, 25, 271 (1987).
  43. T. Asanuma, H. Oikawa, Y. Oikawa, W. Yamasita, M. Matsuo, and A. Yamaguchi, *J. Polym. Sci., Part A: Polym. Chem.*, 32, 2111 (1994).
  44. H. R. Kricheldorf, A. Domschke, and G. Schwarz, *Macromolecules*, 24, 1011 (1991).
  45. K. P. Pramoda, T. S. Chung, S. L. Liu, H. Oikawa, and A. Yamaguchi, *Polym. Deg. Stab.*, 67, 365 (2000).
  46. H. D. Kim and D. R. Paul, Preparation and properties of a series of thermotropic liquid crystalline copolyesters, *Journal of Applied Polymer Science*, 40, 155 (1990).
  47. X.-G. Li, M.-R. Huang, G.-H. Guan, and T. Sun, Synthesis and characterization of liquid crystalline polymers from *p*-hydroxybenzoic acid, poly(ethylene terephthalate), and third monomers, *Journal of Applied Polymer Science*, 66, 2129 (1997).
  48. T. K. Kim, S. O. Kim, and I. J. Chung, Synthesis and characterization of thermotropic liquid crystalline poly(ester-imide)s, *Polymers for Advanced Technologies*, 8, 305 (1997).
  49. Y. Yoshimitsu, K. Sugiyama, S. Shiraishi, T. Oda, and T. Ohashi, Synthesis and properties of aromatic polyamides and polyamide-smectic oligomer graft copolymer, *Polymer Journal*, 26, 551 (1994).
  50. S. Jenkins, V. Thammongkol, and M. B. Polk, Synthesis and spinning of a thermotropic liquid crystal copolyester containing a semirigid cycloaliphatic spacer, *Journal of Polymer Science: Part A: Polymer Chemistry*, 36, 1473 (1998).
  51. H. R. Kricheldorf and A. Conradi, New polymers synthesis 16. LC-copolyesters of 3(4-hydroxyphenyl) Propionic Acid and 4-hydroxy benzoic acids, *Journal of Polymer Science: Part A: Polymer Chemistry*, 25, 489 (1987).
  52. P. K. Bhowmik and H. Han, Fully aromatic liquid crystalline polyesters of phenyl-substituted 4,4'-biphenols and 1,1'-binaphthyl-4,4'-diol with either 2-bromoterephthalic acid or 2-phenylterephthalic acid, *Macromolecules*, 26, 5287 (1993).
  53. W. Hatke, H.-T. Land, H.-W. Schmidt, and W. Heitz, Influence of aryl substitutes on the thermal and solubility behavior of poly(*p*-phenylene terephthalate) and poly(*p*-phenylene terephthalamide), *Makromol. Chem., Rapid Commun.*, 12, 235 (1991).

54. K. Yonetake, M. Takahashi, T. Masuko, and M. Ueda, Synthesis and characterization of liquid crystalline copolyester of 4-hydroxy-2,3,5,6-tetrafluorobenzoic acid with 6-hydroxy-2-naphthoic acid, *Journal of Polymer Science: Part A: Polymer Chemistry*, 36, 413 (1998).
55. Y.-K. Yun, J.-I. Jin, and M. Lee, Wholly aromatic thermotropic liquid crystalline polyesters of 2-( $\alpha$ -phenylisopropyl) hydroquinone; copolymers with 1,1'-Biphenyl-4,4'-diol and 2,6-dihydroxynaphthalene, *Journal of Polymer Science: Part A: Polymer Chemistry*, 35, 2777 (1997).
56. J.-I. Jin and S.-M. Huh, Wholly aromatic polyesters derived from 6-hydroxy-5-phenyl-2-naphthoic acid and 4'-hydroxy-3'-phenylbiphenyl-4-carboxylic acid, *Macromol. Symp.*, 96, 125 (1995).
57. N. Khan, Z. Bashir, and D. M. Price, Liquid crystalline aromatic polyesters formed with terephthalic acid, phenyl hydroquinone, and naphthalene or anthracene diols, *Journal of Applied Polymer Science*, 58, 1509 (1995).
58. W. J. Jackson Jr., Liquid crystal polymers: VI. Liquid crystalline polyesters of substituted hydroquinones, In *Contemporary Topics in Polymer Science*, E. J. Vandenberg (Ed.), Plenum, New York, 5, 177 (1984).
59. M. H. B. Skovby, R. Lessel, and J. Kops, Thermal properties of some fully aromatic thermotropic liquid crystal polyesters, *Journal of Polymer Science: Part A: Polymer Chemistry*, 28, 75 (1990).
60. M. Jaffe, Paul Chen, E.-W. Choe, T.-S. Chung and S. Makhija, High performance polymer blends, *Advances in Polymer Science*, 117, 297 (1994).
61. I. Campoy, M. A. Gomez, and C. Marco, Thermogravimetric analysis of blends based on nylon 6 and a thermotropic liquid crystal copolyester, *Journal of Thermal Analysis*, 52, 705 (1998).
62. S. Lee, S. M. Hong, Y. Seo, T. S. Park, S. S. Hwang, and K. U. Kim, Characterization and processing of blends of poly(ether imide) with thermotropic liquid crystalline polymer, *Polymer*, 35, 519 (1994).
63. Y. Mi, S. Zheng, C.-M. Chan, and Q. Guo, Blends of phenolphthalein poly(ether ether ketone) and a thermotropic liquid crystalline copolyester, *Journal of Applied Polymer Science*, 69, 1923 (1998).
64. K.-Y. Hsu, T.-C. Chang, and C.-H. Li, Studies on thermotropic liquid-crystalline polymers: Part X. Synthesis and properties of crosslinkable aromatic copoly(ester)s containing conjugated double bonds, *Journal of Polymer Science: Part A: Polymer Chemistry*, 31, 971 (1993).
65. X.-M. Jin, C. Carfagna, L. Nicolais, and R. Lanzetta, Synthesis, Characterization, and *in vitro* degradation of a novel thermotropic ternary copolyester based on *p*-hydroxybenzoic acid, glycolic acid, and *p*-hydroxycinnamic acid, *Macromolecules*, 28, 4785 (1995).
66. X.-G. Li, M.-R. Huang, and H. Bai, Kinetics of thermal degradation of liquid-crystalline aromatic polymers, *Die Angewandte Makromolekulare Chemie*, 256, 9 (1998).
67. J. Lorente, G. Ellis, C. Marco, M. A. Gomez, and J. G. Fatou, The thermal decomposition of poly[alkyl-4,4'-(terephthaloyldioxy) dibenzoate]s, *Eur. Polym. J.*, 30, 621 (1994).
68. G. Ellis, J. del Pino, C. Marco, M. A. Gomez, and J. G. Fatou, Structural effects on the thermal degradation of main-chain thermotropic liquid crystal polyesters, *Vibrational Spectroscopy*, 9, 43 (1995).
69. G. Ellis, C. Marco, J. del Pino, and M. A. Gomez, Thermal stability and degradation mechanism for two main-chain liquid crystal polyesters: A TG-MS study, *Journal of Thermal Analysis*, 52, 683 (1998).
70. G. F. L. Ehlers, K. R. Fisch, and W. R. Powell, Thermal degradation of polymers with phenylene units in the chain. III. Polyarylates, *Journal of Polymer Science: Part A-1*, 7, 2969 (1969).
71. J.-P. Leblanc, J. Huang, A. B. Padias, and H. K. Hall Jr., Thermolysis of polyarylate model compounds, *Journal of Polymer Science: Part A: Polymer Chemistry*, 30, 2321 (1992).
72. M. Bounekhel and I. C. McNeill, Thermal degradation studies of terephthalate polyesters: 3.

- Diphenylene and phenylene terephthalate polymers, *Polymer Degradation and Stability*, 51, 35 (1996).
73. M. Giuffrida, P. Maravigna, G. Montaudo, and E. Chiellini, Thermal Decomposition mechanisms of sequential bipolyesters based on propeneglycol and hydroxybenzoic/phthalic diacid derivatives, *Journal of Polymer Science: Part A: Polymer Chemistry*, 24, 1643 (1986).
74. S. Foti, M. Giuffrida, P. Maravigna, and G. Montaudo, Direct mass spectrometry of polymers. X. Primary thermal fragmentation processes in totally aromatic polyesters, *Journal of Polymer Science: Polymer Chemistry Edition*, 22, 1201 (1984).
75. S. Foti, M. Giuffrida, P. Maravigna, and G. Montaudo, Direct mass spectrometry of polymers. XI. Primary thermal fragmentation processes in aromatic-aliphatic polyesters, *Journal of Polymer Science: Polymer Chemistry Edition*, 22, 1217 (1984).
76. M. E. Calahorra, J. I. Eguizabal, M. Cortazar, and G. M. Guzman, Thermal degradation of polyarate/poly(ethylene terephthalate) blends, *Polymer Communications*, 28, 39 (1987).
77. N. Regnier and C. Guibe, Methodology for multistage degradation of polyimide polymer, *Polymer Degradation and Stability*, 55, 165 (1997).
78. T. Ozawa, *Bull. Chem. Soc. Japan*, 38, 1881 (1965).
79. J. H. Flynn and L. A. Wall, *Polymer Letters*, 4, 323 (1966).
80. C. D. Doyle, *J. Appl. Polym. Sci.*, 15, 285 (1961).
81. H. E. Kissinger, Reaction kinetics in differential thermal analysis, *Anal. Chem.*, 29, 1702 (1957).
82. H. L. Friedman, *Journal of Polymer Science, Part C*, 6, 183 (1964).
83. I. M. Salin and J. C. Seferis, Kinetic analysis of high-resolution TGA variable heating rate data, *Journal of Applied Polymer Science*, 47, 847 (1993).
84. X.-G. Li, M.-R. Huang, G.-H. Guan, and T. Sun, Kinetics of thermal degradation of thermotropic poly(*p*-oxybenzoate-*co*-ethylene terephthalate) by single heating rate methods, *Polymer International*, 46, 289 (1998).
85. X.-G. Li and M.-R. Huang, Thermal decomposition kinetics of thermotropic poly(oxybenzoate-*co*-oxynaphthoate) vectra copolyester, *Polymer Degradation and Stability*, 64, 81 (1999).
86. X.-G. Li and M.-R. Huang, Thermal degradation kinetics of thermotropic poly(*p*-oxybenzoate-*co*-*p*',*p*'-biphenylene terephthalate) fiber, *Journal of Applied Polymer Science*, 71, 1923 (1999).
87. I. C. McNeill and M. H. Mohammed, *Polym. Deg. Stab.*, 55, 191 (1997).
88. K. R. Williams, *J. Thermal Anal.*, 49, 589 (1997).

# X-Ray Scattering from Liquid Crystalline Polymers

CHAOBIN HE

## 1. INTRODUCTION

**T**HERMOTROPIC liquid crystalline polymers exhibit some degree of molecular order in their liquid crystalline phases, or so-called mesophases, that denotes the intermediate states between crystalline solids, or amorphous solids in the case of non-crystalline polymers, and isotropic liquids. Due to the molecular order in their mesophases, liquid crystalline polymers provide us with an effective way to achieve high tensile strength and high modulus materials. In the past three decades, researches in the area of liquid crystalline polymers have attracted much attention.

Liquid crystalline phases are classified into many categories, such as nematic, smectic, and cholesteric, based on their distinct molecular orders. Many techniques have been employed to characterize structures of liquid crystalline polymers. For example, polarized light microscopy is commonly used to identify the phase behaviors of liquid crystalline polymers, and differential scanning calorimetry (DSC) is used to detect the thermal transitions associated with the different phases. In all the techniques used in the characterization of liquid crystalline polymers, X-ray scattering is by far the most useful one for probing the packing structures of liquid crystalline polymers. In particular, X-ray scattering study of oriented polymer samples enables us to obtain much important information on orientational and positional order of the molecular arrangements of liquid crystalline polymers, which is essential for understanding their packing structures.

The early X-ray scattering studies of liquid crystals can be dated back to the research work done by Kast [1] in 1924 and 1927 and Stewart [2] in 1931.

They found that, in solid and clear liquid states, a powerful magnetic field does not have any effect on the X-ray scattering of a small molecule liquid crystal, para-azoxyanisol, whereas in the liquid crystalline state, the X-ray scattering of para-azoxyanisol is strongly affected by the magnetic field. Apparently, the small molecule liquid crystal is oriented in the liquid crystalline phase under the magnetic field, which leads to the changes of its X-ray diffraction pattern. Ever since, X-ray scattering has been extensively used to study packing structures, orientation, and crystallization of liquid crystalline polymers.

This chapter does not intend to serve as a comprehensive review on X-ray scattering studies of liquid crystalline polymers. Instead, it focuses on the fundamental principles of X-ray scattering from liquid crystalline polymer systems, i.e., the basic background knowledge required for applying X-ray scattering techniques to the study of structures of liquid crystalline polymers. An introduction on numerical simulation of X-ray scattering patterns of nematic and smectic liquid crystalline polymers is given at the beginning. It serves as a theoretical basis for interpretation of the corresponding experimental X-ray diffraction patterns, which is described in the latter parts of the chapter. Important experimental techniques, which include both power and fiber diffraction methods, are also discussed.

## **2. NUMERICAL SIMULATION OF X-RAY DIFFRACTION PATTERNS OF NEMATIC SYSTEMS**

### **2.1. A PACKING MODEL FOR THE NEMATIC SYSTEMS—PARALLEL PACKED HARD RODS**

One characteristic of nematic liquid crystalline polymers is its long-range orientational order, i.e., polymer chains have a parallel packing arrangement. The molecular arrangement of a nematic liquid crystalline polymer in a monodomain is schematically presented in [Figure 5.1](#), in which the rods represent mesogenic groups that are all oriented in the direction of the nematic director. There is no regular side-to-side correlation between these rods. In the direction perpendicular to the director, these rods are randomly distributed as shown in [Figure 5.1\(b\)](#). This is a simplified model. In reality, the mesogens have a preferred orientation along the director, but not all of them are exactly aligned along the director.

### **2.2. X-RAY SCATTERING FROM A DILUTE SYSTEM OF PARALLEL PACKED HARD RODS**

Based on the above model, the X-ray diffraction patterns of nematic liquid

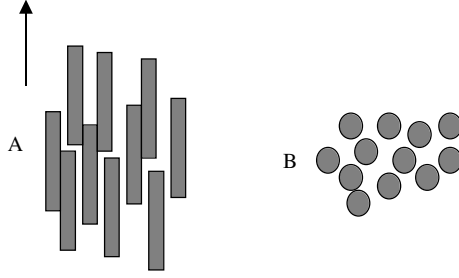


**Figure 5.1** Schematic illustration of a monodomain nematic liquid crystal. (a) Long-range orientational order of nematic liquid crystals and (b) projection of (a) in  $z$  (axis) direction.

crystalline polymers should resemble those of an array of uniaxially oriented hard rods. Assuming that the concentration of the rods is so low that interference among the rods can be ignored, the intensity of the X-ray scattering from a monodomain nematic liquid crystal can thus be written as

$$I(\alpha, \beta, \eta) = NF(\alpha, \beta, \eta)F^*(\alpha, \beta, \eta) \quad (1)$$

where  $F(\alpha, \beta, \eta)$  is the Fourier transform of electron density of a single rod, or so-called form factor,  $F^*(\alpha, \beta, \eta)$  is the conjugation of  $F(\alpha, \beta, \eta)$ ,  $\alpha$ ,  $\beta$ , and  $\eta$  are the three coordinates in  $Q$  space (scattering pattern) as shown in Appendix 1, and  $N$  is the number of the rods.

The Fourier transform  $F(\alpha, \beta, \eta)$  can be expressed as

$$F(\alpha, \beta, \eta) = \int \rho(\underline{r}) \exp(i\underline{r} \cdot \underline{Q}) d\underline{r}$$

where  $\underline{r}$  and  $\underline{Q}$  are the vectors in real space (scattering body) and  $Q$  spaces (scattering pattern) respectively, and  $\rho(\underline{r})$  is the electron density of a single rod.

The rods can be treated as cylindrically symmetric systems. If the electron density within a rod is a constant, an analytical solution of the Fourier transform can be derived. The result is shown in the following equation,

$$F(\alpha, \beta, \eta) = F(\xi, \eta) = \frac{2a\rho \sin\left(\frac{b\eta}{2}\right)}{\xi\eta} J_1\left(\frac{\xi}{a}\right) \quad (2)$$

in which  $a$  is the radius of the cylindrical rods,  $b$  is the length of the rods,  $\rho$

is the electron density of a single rod, and  $J_1$  is the first-order Bessel function. For more details, please refer to Appendix 1 for a discussion of the Fourier transform of electron density of a cylindrically symmetric rod in vacuum.

Assuming that there is no interference among the rods, which occurs in a very dilute system, the intensity of the X-ray scattering from an assembly of uniaxially oriented hard rods in vacuum can be written as

$$I(\alpha, \beta, \eta) = NF(\alpha, \beta, \eta)F^*(\alpha, \beta, \eta) = NF(\xi, \eta)F^*(\xi, \eta)$$

$$I(\xi, \eta) = N \left[ \frac{2ap \sin\left(\frac{b\eta}{2}\right)}{\xi\eta} J_1\left(\frac{\xi}{a}\right) \right]^2 \quad (3)$$

where  $N$  is the number of the rods in the system.

Given that the radius of the cylindrical rod ( $a$ ) is  $2.5 \text{ \AA}$ , which is roughly the radius of polymer chain, the simulated X-ray scattering pattern using Equation (3) from an array of parallel packed hard rods with length of  $100a$  is shown in Figure 5.2. An important feature of the pattern is the strong equatorial

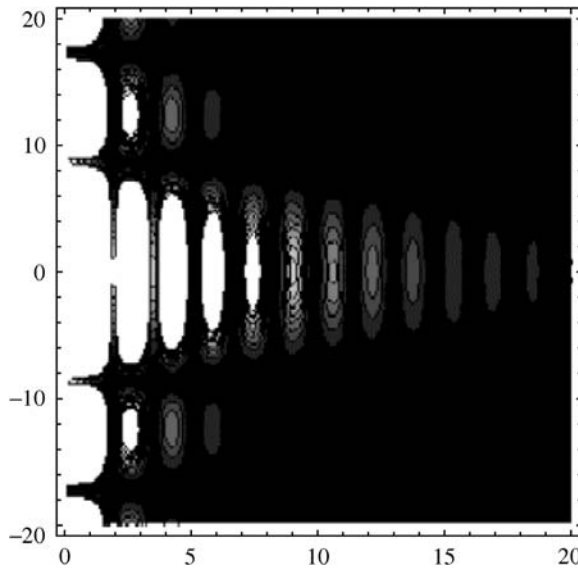


**Figure 5.2** Calculated X-ray scattering from  $N$  oriented rods (vertical direction) in vacuum without considering the interference function. The scattering vector is  $2qa$ , where  $q = 2\pi/d$  and the length of rod is  $100a$ ,  $a$  is the radius of rods.

scatterings, which are due to the electron density fluctuation between the rods and the surrounding media, i.e., vacuum.

### 2.3. INTERFERENCE AMONG THE RODS

The scattering patterns in Figure 5.2 represent the scatterings from the systems with very low concentrations of rods, as the interference among the rods has been ignored. A liquid crystalline polymer in its bulk state should, however, be treated as a condense matter. A more realistic X-ray scattering pattern from such a system can be obtained only when the interference function is included in the calculation, as shown in Equation (4) in which  $S(\alpha, \beta, \eta)$  is the interference function, or so-called structure factor of the system.

$$I(\alpha, \beta, \eta) = N S(\alpha, \beta, \eta) F(\alpha, \beta, \eta) F^*(\alpha, \beta, \eta) \quad (4)$$

If the analytical interference function were obtained, a more realistic X-ray scattering pattern could be generated using Equation (4). It is, however, very difficult, if not impossible, to derive an analytical solution for the interference function of such a complicated system. A successful example of deriving an analytical solution of the interference function is based on a much simpler system. Percus and Yevick have derived an analytical solution of the interference function for a hard-sphere liquid system through so-called “Direct Correlation Function.”

Numerical calculation of the X-ray scattering from a nematic system thus requires a simpler model than that presented in Figure 5.1. For further simplification, we can assume that the system consists of many very long hard rods, all of which are uniaxially oriented. Such a nematic system can be considered as a layer of oriented hard rods. As a result, a nematic system can be treated as a convolution of a hard rod with many randomly packed two-dimensional discs as shown in Figure 5.3. The form factor of such a simplified nematic system is that of the hard rod while the structure factor, i.e., interference function, is that of the two-dimensional randomly packed hard discs. An approximate analytical solution of the interference function of the two-dimensional randomly packed hard discs has been successfully derived by Ripoll and Tejero [3] in 1995 based on Percus and Yevick’s approach. This simplified model can therefore be used to calculate the scatterings from nematic liquid crystalline polymers.

Based on the approximate analytical solution of the interference function derived by Ripoll and Tejero, the X-ray scattering from a nematic liquid crystalline

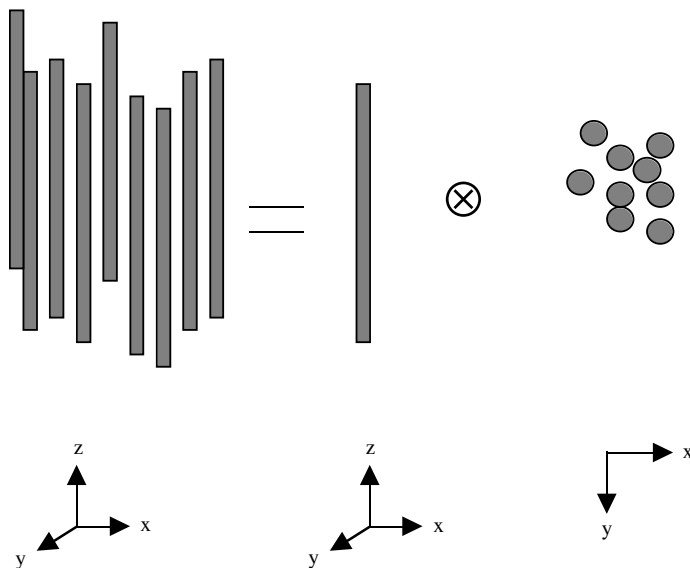


**Figure 5.3** The packing structure of nematic liquid crystals can be viewed as convolution of a long, hard rod with a layer of hard discs.

can be written as

$$\begin{aligned}
 I(\alpha, \beta, \eta) &= I(\xi, \eta) = NS(\xi)F(\xi, \eta)F^*(\xi, \eta) \\
 S(\xi) &= [1 - \nu \underline{C}(\xi)]^{-1} \\
 I(\xi, \eta) &= N[1 - \nu \underline{C}(\xi)]^{-1} \left[ \frac{2\rho a \sin\left(\frac{b\eta}{2}\right)}{\xi \eta} J_1\left(\frac{\xi}{a}\right) \right]^2 \quad (5)
 \end{aligned}$$

where  $\nu$  is the packing density of the hard discs,  $C(\xi)$  is the direct correlation function derived by Ripoll and Tejero, and  $\underline{C}(\xi)$  is the Fourier transformation of  $C(\xi)$ . For more details regarding the direct correlation function, please refer to Appendix 2.

Given that the radius of the cylindrical rod ( $a$ ) is  $2.5 \text{ \AA}$ , the length of the rods is  $100a$ , and the packing density is  $0.6$ , the simulated scattering pattern using Equation (5) is shown in Figure 5.4.

Comparing Figures 5.2 and 5.4, we can see that when the structure factor is included, the X-ray intensities at about  $2qa$  of 6 and 12 increase dramatically while intensities of other peaks decrease. The  $d$  spacings for these two scatterings are about  $5$  and  $2.5 \text{ \AA}$  respectively, which correspond to the first and second

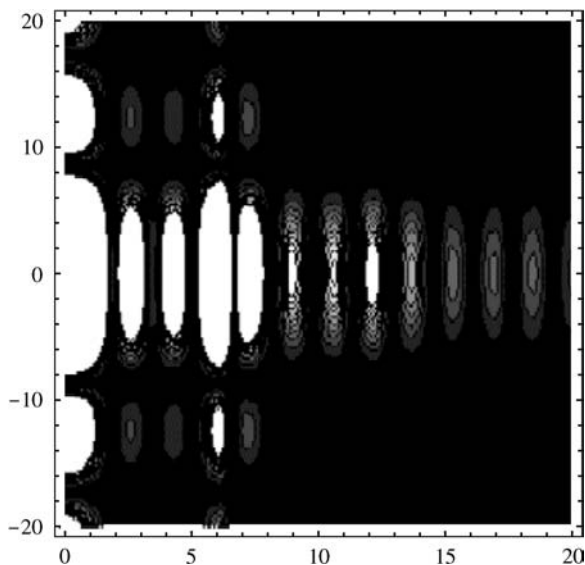


**Figure 5.4** Calculated X-ray scattering from  $N$  oriented rods (vertical direction) considering the interference function. The scattering vector is  $2qa$ , where  $q = 2\pi/d$  and the length of rod is  $100a$ ,  $a$  is the radius of rods.

order of side-by-side correlation of the long rods. By comparing the relative intensities of equatorial scatterings of these two calculated X-ray diffraction patterns quantitatively, the difference between them can be seen more clearly, as shown in Figure 5.5. When the structure factor is not included in the calculation, the strongest calculated equatorial scattering is at  $2qa = 2.8$ , whose intensity is about 10 times higher than that at  $2qa = 6$ . When the structure factor is included, the equatorial scattering is dominated by a peak at  $2qa = 6$ , which is about 10 times higher than other scatterings on the equator. This difference indicates that the scattering at  $2qa = 6$  ( $d \sim 5 \text{ \AA}$ ) represent the correlation between hard rods.

The calculated X-ray scattering patterns, however, still slightly deviate from the experimental X-ray scattering patterns. In experimental data, there is normally only one weak and diffused scattering on the equator. The appearance of additional scattering peaks on the equator in the calculated patterns is due to many simplifications made during calculation, e.g., it is assumed that all the rods are oriented exactly in the same direction and a simplified single layer model is used. Figure 5.5 indicates that the intensity of the inter-rod correlation is the strongest scattering on the equator, which is about 10 times higher than the rest of the equatorial scatterings. The only equatorial scattering observed

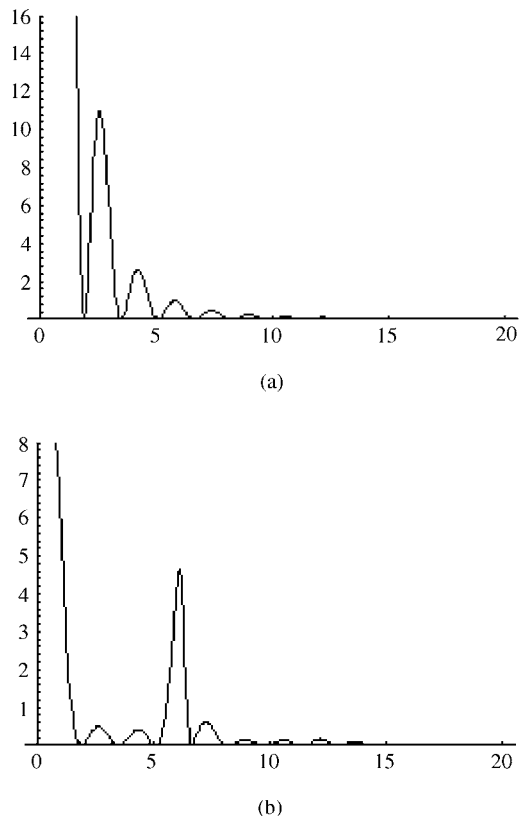


**Figure 5.5** Calculated equatorial scatterings from an assembly of hard rods. Y axis is the intensity while X axis is the scattering vector  $2qa$ . (a) Without structure factor and (b) with structure factor.

experimentally should, therefore, correspond to the inter-rod correlation. Nevertheless, the calculated X-ray scattering patterns clearly indicate that, for a nematic liquid crystalline polymer, the X-ray scattering is dominated by a diffused equatorial scattering, which represents the inter-rod correlation. During the calculation, the packing density is set to be 0.6, which is only slightly lower than that of a close packed two-dimensional body, which is about 0.78. The  $d$  spacing of the scattering corresponding to the inter-rod correlation is, therefore, close to the diameter of the hard rods.

It is noteworthy that, for an oriented nematic liquid crystalline polymer, the equatorial scattering provides important information regarding the interchain correlation, while the meridional scattering represents the correlation along the chains, which in general is featureless in the experimental X-ray diffraction patterns.

### 3. NUMERICAL SIMULATION OF X-RAY DIFFRACTION PATTERNS OF SMECTIC SYSTEMS

Smectic liquid crystalline polymers have more ordered structures than nematic liquid crystalline polymers, as their molecular arrangements have not only long-range orientational order, but also positional order. The positional order refers to the layer packing structures of the polymers. The less ordered smectic liquid crystals, such as smectic A, are true one-dimensional crystals. The packing structure of the smectic A is illustrated in Figure 5.6. The smectic A phase can be considered as convolution of a layer of two-dimensional liquid, i.e., a layer of randomly packed hard rods that are uniaxially oriented in the direction of the layer normal, and a one-dimensional lattice as shown in Figure 5.7.

The Fourier transform of electron density of such a smectic liquid crystal is expressed as

$$F(\underline{Q}) = \varphi(\underline{Q})\psi(\underline{Q}) \quad (6)$$

where  $\varphi(\underline{Q})$  and  $\psi(\underline{Q})$  are the Fourier transforms of the one-dimensional lattice and the two-dimensional liquid, respectively.

The intensity of the scattering from the smectic A liquid crystal can then be written as

$$I(\underline{Q}) = F(\underline{Q})F^*(\underline{Q}) = \varphi(\underline{Q})\varphi^*(\underline{Q})\psi(\underline{Q})\psi^*(\underline{Q}) \quad (7)$$

The Fourier transform of the one-dimensional lattice,  $\varphi(\underline{Q})$ , can be derived as [4]

$$\varphi(\underline{Q}) = \exp\{i(N-1)\underline{c} \cdot \underline{Q}/2\} \sin(N\underline{c} \cdot \underline{Q}/2) / \sin(\underline{c} \cdot \underline{Q}/2) \quad (8)$$

where  $\underline{c}$  is the vector of the lattice and  $N$  is the number of stacking lattice layer.

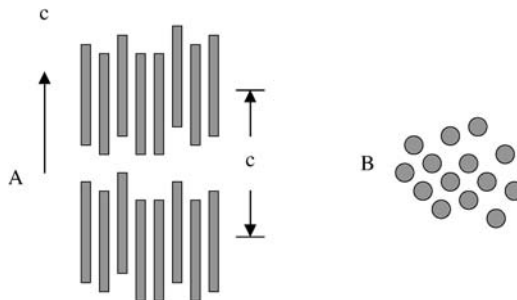


**Figure 5.6** Schematic illustration of a monodomain smectic liquid crystal. (a) Long-range orientational order and positional order of smectic liquid crystals and (b) projection of (a) in z (axis) direction.

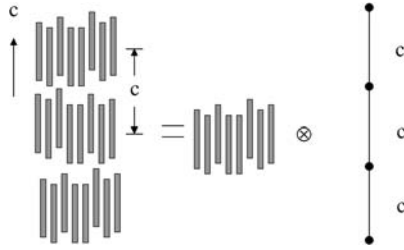


**Figure 5.7** The X-ray scattering from smectic A can be considered as convolution of a layer of two-dimensional liquid and a lattice.

If considering the first part in Equation (7) as a structural factor, i.e.,

$$S(\underline{Q}) = \varphi(\underline{Q})\varphi^*(\underline{Q}) = \sin^2(N\underline{c} \cdot \underline{Q}/2)/\sin^2(\underline{c} \cdot \underline{Q}/2) \quad (9)$$

we can have

$$I(\underline{Q}) = [\sin^2(N\underline{c} \cdot \underline{Q}/2)/\sin^2(\underline{c} \cdot \underline{Q}/2)]\psi(\underline{Q})\psi^*(\underline{Q}) \quad (10)$$

$$I(\underline{Q}) = F(\underline{Q})F^*(\underline{Q}) = S(\underline{Q})\psi(\underline{Q})\psi^*(\underline{Q}) \quad (11)$$

The structural factor represents the scattering from a one-dimensional crystal in the direction of the layer normal, which is a strong meridional scattering. Figure 5.8 shows the calculated meridional scatterings according to Equation (9). An increase in the number of layers,  $N$ , results in an increase of sharpness and intensity of the scattering peaks. The structure factor derived based on one-dimensional crystal lattice can be viewed as an amplifier. If a smectic liquid crystalline polymer has 50 layers stacked together, the intensities of the meridional scatterings would be about 80 times higher than that of a smectic liquid crystalline polymer of five layers.

In smectic A, the layer planes are spaced to each other by a distance of  $c$ . However, not all the hard rods in a layer lie exactly on the layer plane. Instead, they might have a displacement,  $r$ , above or below its plane along the layer normal direction with their average position being on the plane, as shown in Figure 5.7. If the displacements of the rods in the layer normal direction obey Gaussian distribution and the standard deviation of the displaced distances is  $\sigma$ , the distribution of the displacements is given by [4]

$$D(r) = (1/\sqrt{2\pi}\sigma) \exp(-r^2/2\sigma^2) \quad (12)$$

The lattice of an imperfect crystal can be considered as the convolution of the perfect one-dimensional lattice with  $D(r)$ . The Fourier transform of the

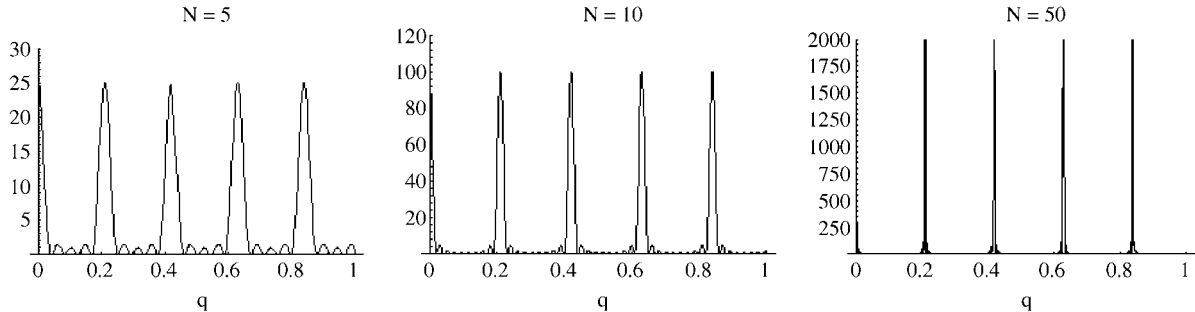


**Figure 5.8** Calculated structure factor with different  $N$ . Y axis is the intensity while X axis is the scattering vector  $2qa$ . The length of the layer is  $c = 30 \text{ \AA}$ , while  $q = 2\pi/d$ . The peak intensity and sharpness increase as  $N$  increases.

مرجع دانشجویان و مهندسين مواد

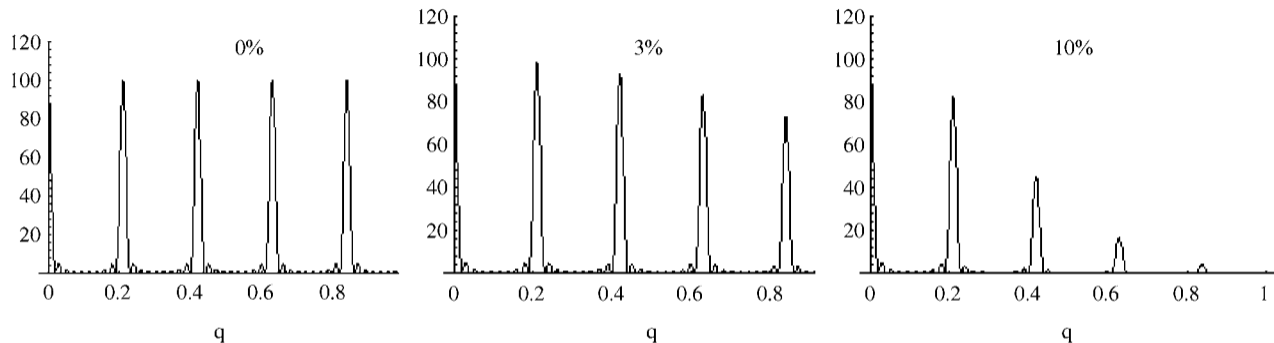


**Figure 5.9** Calculated meridional scattering of one-dimensional crystal with different root-mean-square displacement  $\sigma$ . Y axis is the intensity while X axis is the scattering vector  $2qa$ ,  $q = 2\pi/d$ . The percentage is derived from  $\sigma/l$ , and  $l$  is the length of layer that is 30 Å.

imperfect lattice is then obtained by multiplying the transform of perfect lattice by the transform of  $D(r)$ .

$$\tilde{D}(Q) = \exp(-Q^2\sigma^2/2) \quad (13)$$

$$S(\underline{Q}) = \{\tilde{D}(Q)\}^2 \varphi(\underline{Q}) \varphi^*(\underline{Q}) = \{\tilde{D}(Q)\}^2 \sin^2(N\underline{c} \cdot \underline{Q}/2) / \sin^2(\underline{c} \cdot \underline{Q}/2) \quad (14)$$

The addition of the Gaussian distribution function leads to a decrease in the intensity of the layer line at high  $Q$  without altering their sharpness, as shown in Figure 5.9. This is fairly different from the effect of disturbing the regular arrangement of layers in the layer normal direction. Fluctuation of the spacing between neighbor layers,  $c$ , could lead to a loss of intensity and an increase of width at high  $Q$ .

For the two-dimensional liquid, the scattering signature is similar to that of the nematic liquid crystalline polymers discussed in the previous section. It should have a diffuse equatorial scattering whose intensity is significantly lower than that of the meridional scatterings from the one-dimensional crystal.

The equations presented above are derived based on the least ordered smectic liquid crystalline polymers, i.e., the smectic A liquid crystals. The more ordered smectic systems may generate X-ray scattering patterns similar to those of crystal structures.

#### 4. MONODOMAIN AND POLYDOMAIN STRUCTURES

The equations derived above are only for X-ray scattering patterns from a single domain. Unoriented liquid crystalline polymers consist of many single domains. Within each domain, all the mesogenic groups have a preferred orientation along the director of the domain. The directors of these domains are, however, randomly distributed in the polymers so that mesophases usually display colorful textures under polarized microscope. The typical domain size of liquid crystalline polymers is in the range of micrometers, which is far smaller than the dimension of the samples used in X-ray experiments. Because an unoriented X-ray sample consists of many randomly distributed domains, their X-ray signatures in reciprocal space spread out into co-center scattering rings. In the case of nematic phase, the weak and diffuse equatorial scattering will spread out into weak and diffuse co-central rings, which resembles the X-ray scattering from isotropic liquid or unoriented amorphous polymers. This scattering mainly represents the interchain correlation for the main-chain liquid crystalline polymers. In the case of smectic phase, the sharp, intense meridional scattering spreads out, and the X-ray scattering displays one or more sharp co-center scattering rings in addition to a diffused outer scattering ring. These sharp scattering

rings are due to the positional order, or so-called layer structure, which is the intrachain correlation for main-chain liquid crystalline polymers.

The scattering patterns of monodomain liquid crystalline polymers represent those from oriented liquid crystalline polymers. Such orientation can be achieved either in the solid state by quenching the oriented polymers or in the melt state by shearing the melt at the mesophase temperatures. Under a force field, such as a tensile force, shear force, or magnetic field, all the domains are aligned in the direction of the external field so that the polydomain liquid crystalline polymers can effectively become monodomain liquid crystalline polymers. For oriented main-chain liquid crystalline polymers, the scattering on the equator is due to interchain correlation and the scatterings on meridian raised from intrachain correlation.

Having discussed the theory behind X-ray scattering from nematic and smectic liquid crystalline polymers, in the following sections, applications of X-ray scattering in studies of phase behavior, crystallization, and orientation of liquid crystalline polymers will be discussed.

## **5. X-RAY SCATTERING FROM UNORIENTED LIQUID CRYSTALLINE POLYMERS, POWDER DIFFRACTION METHOD**

Powder scattering method is commonly used as a starting point for investigating the structures of liquid crystalline polymers. Usually, the powder samples of liquid crystalline polymers have polydomain structures. Powder X-ray diffraction patterns of liquid crystalline polymers therefore contain one or more co-center scattering rings. For a nematic liquid crystalline polymer, the powder scattering pattern consists of a diffuse scattering ring representing the intermolecular correlation, which is not much different from the scattering of an amorphous solid or isotropic liquid. For a smectic liquid crystalline polymer, the powder scattering pattern consists of a diffuse outer scattering ring and a sharp inner ring representing the layer structure. The fact that the powder X-ray scattering from a polydomain nematic phase resembles scattering from amorphous solid polymers or isotropic polymer melts underlines the limitation of the powder X-ray scattering method in studying the structures of liquid crystalline polymers. Nevertheless, with the supplement of other methods, such as DSC and polarized light microscopy, powder X-ray scattering is still a powerful method in identifying the phase behavior and the packing structures of liquid crystalline polymers.

Quite often, room-temperature X-ray scattering data are used to characterize packing structures of mesophases by assuming that the mesophase structures can be frozen when the polymers are cooled down from mesophase temperatures to room temperature. However, liquid crystalline polymers normally crystallize at room temperature. The X-ray scatterings from liquid crystalline polymers at

room temperature thus are contributed by both liquid crystalline and crystalline components. It is difficult to separate these two portions of X-ray scatterings. Moreover, the packing structures of the mesophases may also change with temperature. One way to solve this problem is to use temperature-dependent X-ray scattering. By heating the polymer samples to the desired temperature range, i.e., to their mesophase temperatures while doing X-ray scattering measurements, the complication due to crystallization of the polymers can be eliminated, and direct information regarding the packing structures in the mesophases can be extracted.

Temperature-dependent X-ray scattering can be carried out using a conventional X-ray diffractometer fitted with a hot stage. A more advanced technique is in situ X-ray scattering technique using a synchrotron radiation source. Using this technique, the small angle scattering, wide-angle scattering, and DSC can be measured at the same time, which allows us to follow, in real-time, the phase evolution of the liquid crystalline polymeric materials as the temperature changes and to probe the corresponding packing structures. To demonstrate the capability of this advanced technique, an example of in situ X-ray scattering study of liquid crystalline polymers is introduced in the following.

Figure 5.10 is a schematic representation of a typical in situ X-ray scattering measurement using a synchrotron radiation source. The experiment was set up at Daresbury (Warrington, UK) Station 8.2, equipped with two linear detectors (one for small angle scattering and one for wide-angle scattering). The powder X-ray scattering can be represented by a 1-D plot rather than a 2-D plot as it has the same intensity in  $360^\circ$ . X-ray wavelength is monochromatized to  $1.54 \text{ \AA}$ . The small-angle X-ray scattering data were normalized by the detector response, background, and the incoming beam intensity. The DSC heating rate

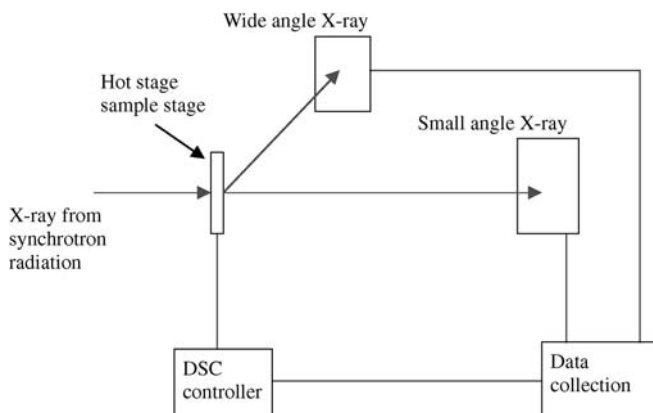


**Figure 5.10** Schematic representation of a typical in situ WAXS/SAXS/DSC X-ray scattering measurement using synchrotron radiation source.

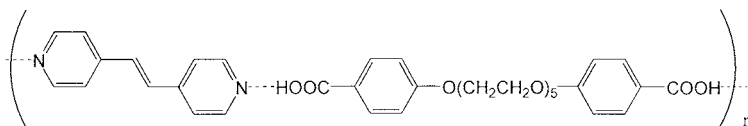


**Figure 5.11** Chemical structure of hydrogen-bonded association chain polymer.

was 10°C/min, and the X-ray collection frame time is 6 seconds. As a result, the X-ray data were collected at 1°C intervals. The polymer sample was placed into special aluminium DSC pans for X-ray experiments. One side of the DSC pan is made of aluminium, which faces the incoming X-ray beam, while the other side of the DSC pan is mica, which faces the outgoing X-ray beam.

The chemical structure of polymer used in this study is shown in Figure 5.11. The liquid crystalline polymer is an association chain polymer, i.e., polymer is formed through hydrogen bonding association rather than covalent bonding. Because it is a hydrogen-bonded association chain polymer, it is difficult to draw fiber from the polymer. Thus, powder X-ray scattering method is the only way to characterize the packing structure of the polymer. Polarized light microscopy shows that this hydrogen-bonded liquid crystalline polymer exhibits monotropic smectic and nematic phases on cooling. Though it is an association chain polymer, the X-ray scattering method employed in this study is the same as in other covalent-bonded liquid crystalline polymer systems.

The X-ray scattering data are showed in Figures 5.12–5.14, in which Figures 5.12 and 5.13 are the small-angle X-ray scattering data and Figure 5.14

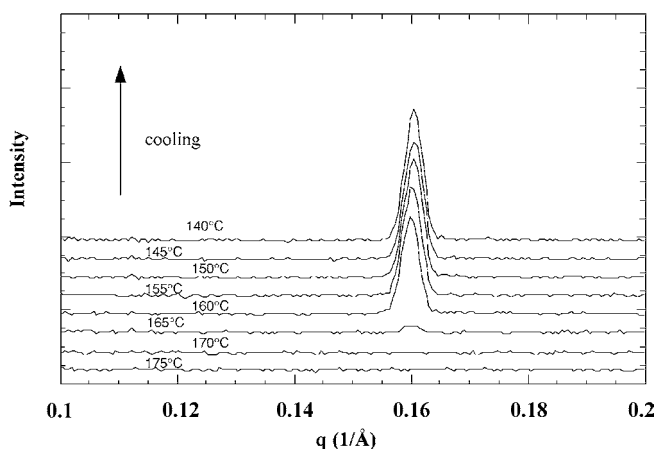


**Figure 5.12** Small-angle X-ray scattering of association chain liquid crystalline polymer on cooling,  $q = 2\pi/d$ . The appearance of small-angle scattering indicates polymer exhibits a smectic liquid crystalline phase.

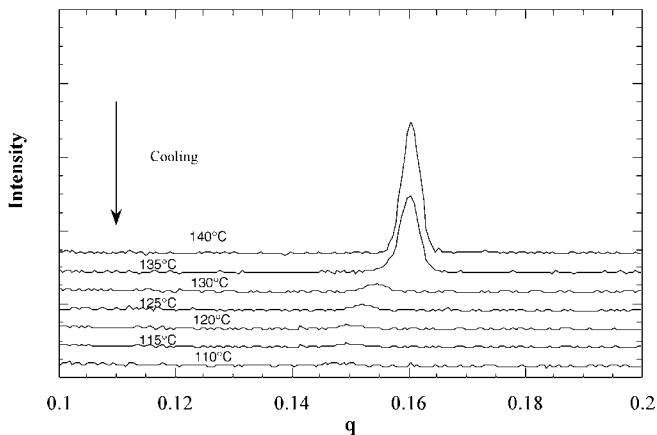


**Figure 5.13** Small-angle X-ray scattering of association chain liquid crystalline polymer on cooling,  $q = 2\pi/d$ . The disappearance of small-angle scattering indicates polymer becomes crystalline.

is the wide-angle X-ray scattering data. It is clear that when the polymer is cooled to its nematic phase temperature, X-ray scattering signature is hardly changed compared with that of the isotropic phase as shown in Figure 5.12. As discussed above, the X-ray scattering from the nematic phase only represents the side-by-side correlation among the hard rods, which is liquid-like, while the long-range orientational order of the nematic phase is not able to be picked up using powder X-ray scattering method, due to the polydomain nature of the system. When the cooling continues and polymer enters its smectic phase, X-ray signature shows a strong small-angle scattering.

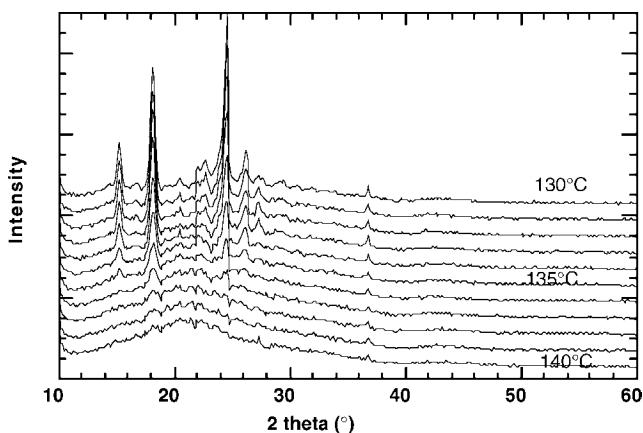


**Figure 5.14** Wide-angle X-ray scattering of association chain liquid crystalline polymer on cooling. The appearance of wide-angle scattering indicates crystallisation of polymer.

The low angle peak position was at  $0.159 \text{ \AA}^{-1}$ , which corresponds to a  $d$  spacing of  $39.5 \text{ \AA}$ . This small-angle peak is considered to be the scattering from the smectic layer of the polymer as it corresponds to the length of repeat unit A-B. Smectic A phase resembles a one-dimensional crystal. The strong low angle scattering corresponds to the motif of the one-dimensional crystal or the repeat length of the smectic A layer. The position of the small-angle peak hardly changed from the elevated temperatures when the polymer began to exhibit a smectic phase down to the temperature at which it displayed maximum small-angle scattering. If cooling was continued, the intensity of small-angle scattering decreased, and the peak position was shifted to a lower angle, which is about  $0.155 \text{ \AA}^{-1}$ , and corresponds to a length of  $40.5 \text{ \AA}$ , indicating polymer chain exhibit a more extended conformation. If the sample was cooled further, the small-angle scattering intensity was lost, while at the wide-angle region, X-rays scattering shows some sharp scatterings, indicating that the crystallization of polymer begins at about  $135^\circ\text{C}$  as shown in Figure 5.14.

The disappearance of the small-angle scattering indicates a reorganization of polymer chains when the polymer crystallizes. Looking at the higher angle region as shown in Figure 5.15, it can be seen that a weaker small-angle peak appears at  $0.34 \text{ \AA}^{-1}$ , which corresponds to a  $d$  spacing of  $18.5 \text{ \AA}$ . One possibility is that polymer chains form an interdigitated structure where the

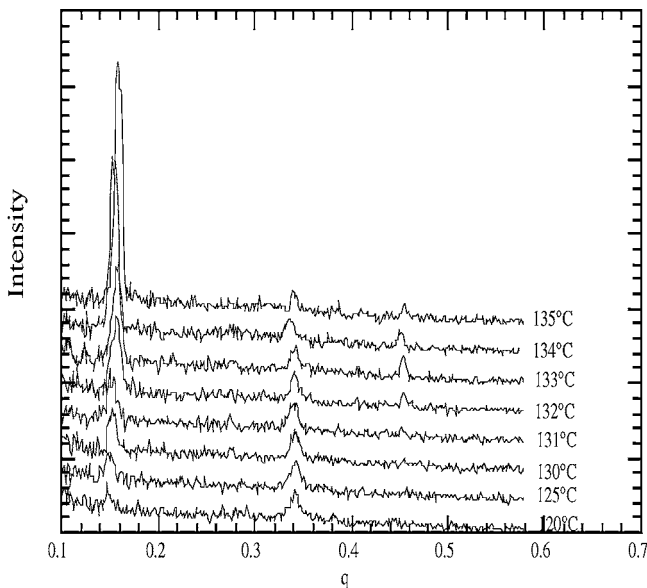


**Figure 5.15** Small-angle scattering of association chain liquid crystalline polymer. The appearance of scattering at about  $q = 0.35$  indicates a possible inter-digitized chain packing structure.

rigid part of one polymer chain is laterally associated with the ethylene oxide unit of neighboring chains during crystallization. This resulting interdigitated structure could minimize free volume in the packing structure and lead to a more stable structure. It is noteworthy that the scattering intensity at  $0.34 \text{ \AA}^{-1}$  is rather weak. This may be due to the highly distorted interdigitated packing structure.

The thermal stability of liquid crystalline polymers can also be studied using X-ray scattering method. The powder X-ray diffraction data for the above polymer system annealed at different temperatures are shown in Figures 5.16 and 5.17. Although the polymer is a monotropic liquid crystalline polymer, at  $145^{\circ}\text{C}$ , the liquid crystalline phase is fairly stable, while at lower temperature, the polymer crystallizes and loses its mesophase character within a few minutes of annealing.

## 6. X-RAY SCATTERING FROM ORIENTED LIQUID CRYSTALLINE POLYMERS—FIBER SCATTERING

The drawback of the powder X-ray scattering method is its inability to detect the long-range orientational structure of liquid crystalline polymers, as the powder X-ray scattering is a mixture of diffraction from many randomly distributed domains. One way to overcome this weakness is to transfer the polydomain liquid crystalline polymers into monodomain liquid crystalline polymers by applying external fields, such as shear force or magnetic field. Under orientation, the X-ray scattering patterns of the liquid crystalline polymers should resemble those calculated patterns discussed in the sections 2 and 3. For main-chain liquid crystalline polymers, the scattering along the equator represents the interchain correlation, while the meridian scattering represents the intrachain correlation. In the following, two examples of using fiber patterns to study packing structures are presented.

The first example is a random copolymer. The chemical structure of this polymer is shown in Figure 5.19. Polarized light microscopy and DSC studies show that the polymer is a nematic liquid crystalline polymer. A fiber X-ray scattering pattern from a single fiber of the polymer drawn at its mesophase temperature is shown in Figure 5.18. The fiber axis was tilted  $45^{\circ}$  to the left. We can see that the polymer chains are well oriented as indicated by the short arc of the equatorial scattering. In the pattern, there is a strong and diffuse equatorial scattering centered at about  $21^{\circ}$  of  $2\theta$ , which corresponds to a  $d$  spacing of about  $4.2 \text{ \AA}$ . As discussed in section 2, this scattering arises from the correlation among mesogenic groups in the lateral direction. The diffuse nature of this scattering indicates that the interchain distance between the polymer chains is somewhat randomized. There is also a weak four-point off-equatorial scattering in the fiber pattern. The position of this scattering is at about  $5.5^{\circ}$  of

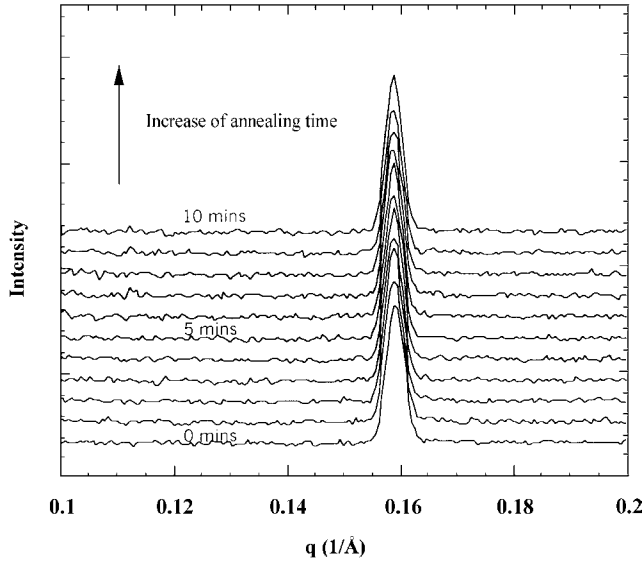


**Figure 5.16** Small-angle X-ray scattering of association chain polymer under annealing at 145°C.

$2\theta$ , corresponding to a  $d$  spacing of 16 Å, which does not appear in its powder scattering pattern. This weak four-point off-equatorial scattering is probably due to an interdigitated packing structure, which resulted from the orientation of polymer chains during the drawing process.

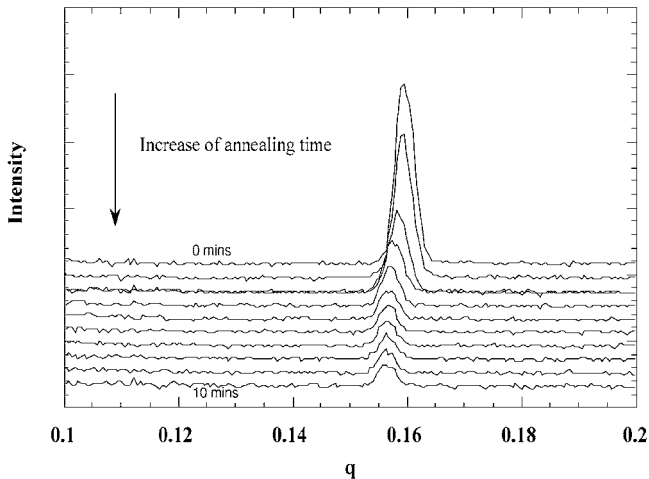


**Figure 5.17** Small-angle X-ray scattering of association chain polymer under annealing at 140°C.

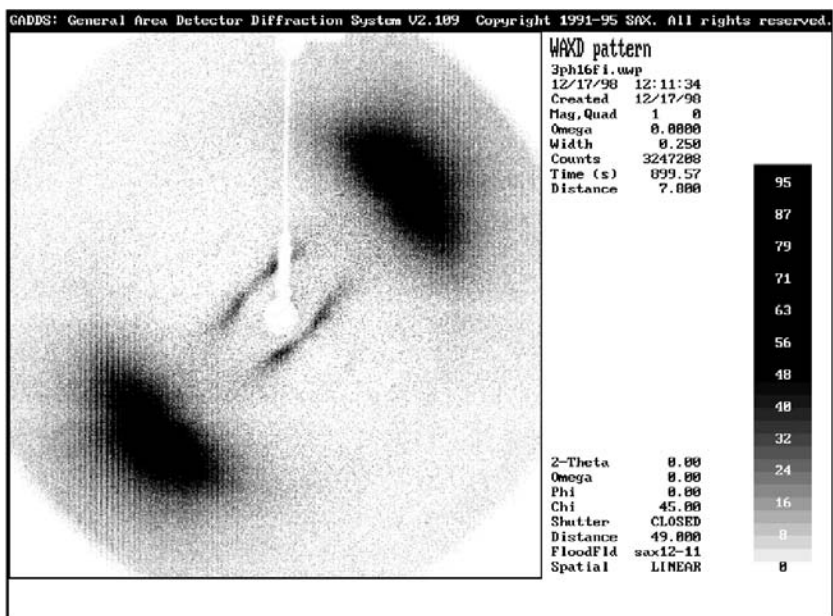


**Figure 5.18** X-ray fiber scattering pattern from oriented polymer sample. The chemical structure of the polymer is shown in [Figure 5.19](#) with  $x = 0.4n$ ;  $y = 0.6n$ .

The second example is an alternative copolymer. It has a regular chain structure rather than being a random copolymer. The chemical structure of the second polymer is shown in [Figure 5.19](#). The fiber pattern of this polymer is shown in [Figure 5.20](#). Similar to the first polymer, the pattern shows a strong but diffuse equatorial scattering, which, as discussed previously, arises from the correlation

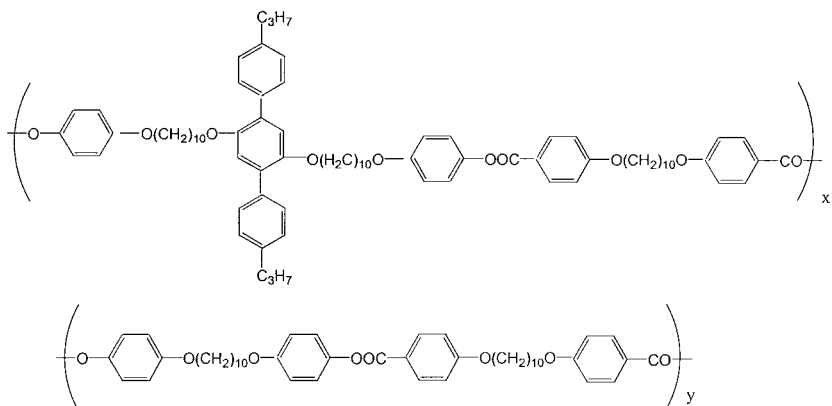


**Figure 5.19** Chemical structure of polymers in fiber scattering study.

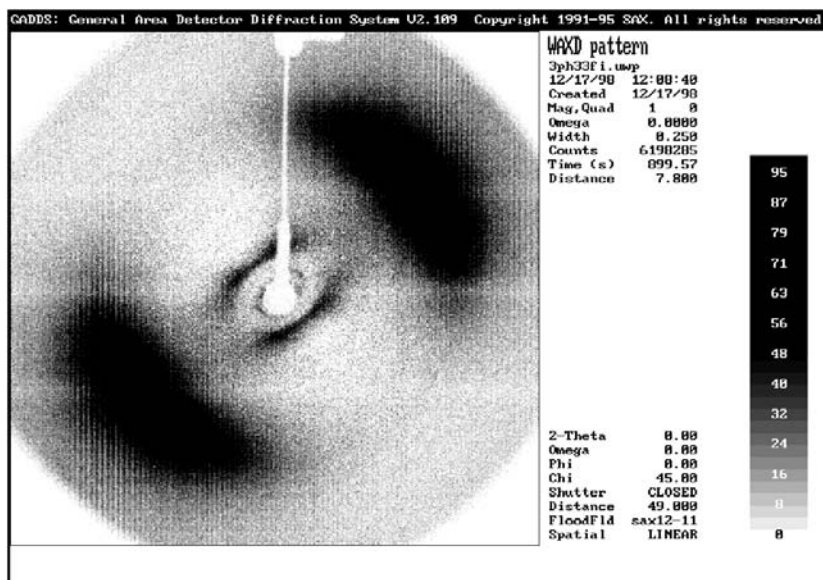


**Figure 5.20** X-ray fiber scattering pattern from oriented polymer sample. The chemical structure of the polymer is shown in Figure 19 with  $x = n$ ,  $y = 0$ .

between the polymer chains, and a weak four-point off-equatorial scattering. In addition to this, we can also see a strong meridional scattering superimposed by the four-point off-equatorial scattering. Although the signature of this scattering is similar to that from a smectic liquid crystalline polymer, the DSC study shows that the polymer exhibits only one phase transition, and polarized light microscopy indicates only a nematic phase. Here, it is worth noting that the arrangement of monomer in the second polymer is very different from that of the first polymer. The second polymer is a copolymer with a regular sequence distribution, while the first polymer is a random copolymer. As a result, the electronic density fluctuation along the polymer chain in the second polymer assumes a regular pattern.

## 7. SUMMARY

X-ray scattering is a powerful tool for the study of structures of liquid crystalline polymers. Theoretically, X-ray scattering from a given material can be treated as the Fourier transform of electron density of the material. For a nematic liquid crystalline polymer, the Fourier transform can be considered as the convolution of electron density of a long, hard rod and a layer of randomly

distributed two-dimensional discs, which results in a weak and diffuse equatorial scattering representing the inter-rod correlation. For a smectic liquid crystalline polymer, the Fourier transform can be considered as the convolution of electron density of a layer of oriented hard rods and a one-dimensional crystal lattice. The scattering from a layer of oriented hard rods is similar to that from nematic liquid crystalline polymers, while the one-dimensional crystal provides an additional strong scattering on the meridian. These theoretical models can be used to interpret the X-ray diffraction patterns obtained from oriented liquid crystalline polymer samples, i.e., the fiber X-ray patterns, directly because the oriented samples essentially are monodomain liquid crystalline polymers. The correct interpretation of the fiber X-ray diffraction patterns can provide unique information for gaining insight into the molecular arrangements of the liquid crystalline polymers. In X-ray scattering patterns obtained from unoriented liquid crystalline polymer samples, i.e., the powder X-ray patterns, the equatorial and meridional scatterings spread out into co-center scattering rings due to the polydomain characteristics of the unoriented liquid crystalline polymers. In this case, with the supplement of other experimental techniques, such as small-angle X-ray scattering, DSC, and polarized microscopy, useful information about the phase behaviors of liquid crystalline polymers can be obtained from temperature-dependent X-ray studies.

In the past two decades, a large number of novel liquid crystalline polymers have been created by polymer chemists around the world. X-ray scattering technique has been extensively used and proven to be a powerful tool in studying the structures of liquid crystalline polymers, while interpretation of X-ray diffraction patterns of liquid crystalline polymers remains a difficult task for many chemists. It is hoped that this chapter will help to fill the gap between polymer chemists and physicists.

## 8. APPENDIX 1

Here, the Fourier transformation of a cylindrically symmetric rod in vacuum is discussed.

Figures 5.21 and 5.22 represent the geometry of real space (the scattering body) and  $Q$  space (the scattering pattern). The relation between these two is given by the Fourier transform  $F(\alpha, \beta, \eta)$ .

$$F(\alpha, \beta, \eta) = \int_{\Omega} \rho e^{i\mathbf{r} \cdot \mathbf{Q}} d\mathbf{r} = \int_{\Omega} \rho e^{i(\alpha x + \beta y + \eta z)} dx dy dz \quad (15)$$

where  $\rho$  is the density of the rod, which is assumed constant. The integration will be within the rod.

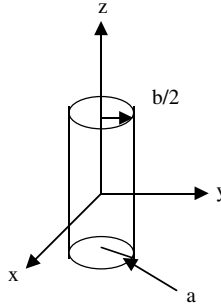


Figure 5.21

According to Figure 5.21, in real space, and using polar coordinates, we have

$$x = r \sin \theta; \dots y = r \cos \theta; \dots dxdy = r dr d\theta$$

$$F(\alpha, \beta, \eta) = \rho \int_{-b/2}^{b/2} dz \int_0^a r dr \int_0^{2\pi} e^{i\eta z} e^{ir\sqrt{\alpha^2 + \beta^2} \left( \frac{\alpha \sin \theta}{\sqrt{\alpha^2 + \beta^2}} + \frac{\beta \cos \theta}{\sqrt{\alpha^2 + \beta^2}} \right)} d\theta \quad (16)$$

In  $Q$  space as shown in Figure 5.22, we have

$$\xi = \sqrt{\alpha^2 + \beta^2}; \dots \frac{\alpha}{\sqrt{\alpha^2 + \beta^2}} = \sin \varphi; \dots \frac{\beta}{\sqrt{\alpha^2 + \beta^2}} = \cos \varphi$$

$$F(\xi, \theta, \eta) = \rho \int_{-b/2}^{b/2} e^{i\eta z} dz \int_0^a r dr \int_0^{2\pi} e^{ir\xi \cos(\theta - \varphi)} d\theta$$

$$= \rho \int_{-b/2}^{b/2} e^{i\eta z} dz \int_0^a r J_0(r\xi) dr \quad (17)$$

$$\int_0^a r J_0(r\xi) dr = \frac{a}{\xi} J_1\left(\frac{\xi}{a}\right) \quad (18)$$

$$F(\alpha, \beta, \eta) = F(\xi, \eta) = \rho \frac{a}{\xi} J_1\left(\frac{\xi}{a}\right) \int_{-b/2}^{b/2} e^{i\eta z} dz = \frac{2\rho a \sin\left(\frac{b\eta}{2}\right)}{\xi \eta} J_1\left(\frac{\xi}{a}\right) \quad (19)$$

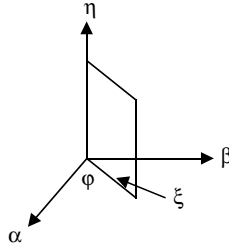


Figure 5.22

## 9. APPENDIX 2

Appendix 2 gives an approximate analytic solution of the interference function of two-dimensional randomly packed hard discs [3].

The direct correlation function for two-dimensional hard discs derived by Ripoll and Tejero is

$$C(x, \nu) = \Theta(1 - x)C(0, \nu)[1 - 4\nu + 4\nu\omega(x/2) + s_2(\nu)x] \quad (20)$$

where  $\nu$  is the packing fraction of the hard discs,  $\Theta(x)$  is the Heaviside step function,  $C(0, \nu)$  and  $s_2(\nu)$  are two constants depending on the packing density  $\nu$  and they are

$$C(0, \nu) = -\frac{1 + \nu + 3\nu^2 - \nu^3}{(1 - \nu)^3} \quad (21)$$

$$s_2(\nu) = \frac{3}{8}\nu^2 \frac{8(1 - 2p) + (25 - 9p)p\nu - (7 - 3p)p\nu^2}{1 + \nu + 3\nu^2 - \nu^3} \quad (22)$$

$$p = \frac{7}{3} - \frac{4\sqrt{3}}{\pi}$$

For two-dimensional hard disc systems, we have

$$\omega(x) = \frac{2}{\pi} [\arccos x - x(1 - x^2)^{1/2}] \quad (23)$$

The structure factor (interference function) of two-dimensional hard discs can then be calculated using Equations (20–23), and we have

$$S(Q) = \{1 - \nu \underline{C}(Q)\}^{-1} \quad (24)$$

$$\nu = \frac{\nu}{4\pi\Gamma(2)} \quad (25)$$

$S(Q)$  is the structure factor of the two-dimensional hard discs.  $\underline{C}(Q)$  is the Fourier transform of  $C(Q)$ . This approach has been successfully used to present the two-dimensional interference function of hard discs. For a packing density  $\nu$  of 0.6, this analytical solution only slightly overestimates the height of main peak by about 10% compared with the other prediction. Nevertheless, this approximation is good enough as we are more concerned about the qualitative than the quantitative result of the X-ray scattering.

## 10. REFERENCES

1. W. Kast, *Ann. D. Phys.* 73, 145, 1924; 83, 418, 1927.
2. G. W. Stewart, *Phys. Rev.* 38, 931, 1931.
3. M. S. Ripoll and C. F. Tejero, *Mol. Phys.* 85, 423–428, 1995.
4. D. W. L. Hukins, *X-ray Diffraction by Disorder and Order System*, Oxford, Pergamon, 1981, pp. 78.

# Surface Tension Investigations of Thermotropic Liquid Crystalline Polymers

KUI-XIANG MA  
TAI-SHUNG CHUNG

## 1. INTRODUCTION

**W**ITH the easy-processing properties in the liquid crystalline phase, main-chain TLCPs have been widely used as high-strength fiber, fiber reinforcement, in situ reinforcement additive, and injection molded articles, etc, [1–4]. The successful applications are quite dependent on the adhesion at interface of the liquid crystalline polymer and the conventional engineering resin, which is indeed affected by surface tension and/or interfacial tension between the two phases [1–2].

However, although polymer scientists are aware of the importance of surface tension of LCPs, only a few papers have been published on the subject of LCPs [5–9]. Uzman et al. [5] investigated the surface tensions ( $\gamma$ ) of a branched polyethylene and two side-chain liquid crystalline polyacrylate (LCPA) melts in isotropic, nematic, and smectic states, using the pendant-drop method. The relationship between surface tension and temperature of LCPA melts showed abnormal behavior when compared with normal polymer melts, which only vary negatively and linearly with temperature. When LCPA was in its isotropic state,  $\gamma$  increased with a decrease in temperature. This relationship changed near the isotropic-nematic transition. In the nematic state,  $\gamma$  again increased with a decrease in temperature until it reached the nematic-smectic transition, where  $\gamma$  jumped to higher values. Uzman et al. explained these phenomena were due to the fact that the mesogenic side groups governed the surface properties of LCPA.

Correia et al. also reported the surface tension [8] and temperature-dependent behavior [9] of a side-chain liquid crystalline polyacrylate (poly({3-[4-(4-

cyanophenyl)phenoxy] propyloxy carbonyl)ethylene)), provided by Merck. The  $\gamma$  was estimated from Neumann's equation, Owens and Wendt's equation (geometric-mean method), as well as Good and van Oss's equation (Lifshitz-van der Waals-acid-base method) (LWAB), by measuring contact angles. They found that  $\gamma$  were in the range of 40–45 mJ/m<sup>2</sup> from different approaches.

Liquid crystalline polymers with low surface tensions offer more interesting properties, such as low coefficient of friction, chemical inertness, low dielectric constant, etc. [10,11]. Low energy surfaces are useful for a number of applications, such as soil-resistant and breathable textiles, etc. To lower surface tension, it is generally understood to introduce a fluorinated group onto a polymer backbone in order to create a fluorinated surface. Wang and Ober recently found that a free-standing film of a semifluorinated side group ionene [12] possessed a low critical surface tension of 8 mN/m from contact angle measurement, due to its ability to arrange its fluorinated groups in a smectic layer structure. In these ionenes, the side groups were arranged in a highly ordered, liquid crystalline smectic B phase in which the —CF<sub>3</sub> end groups were arranged on the surface in a hexagonally organized layer.

From the same research group, Wang et al. [13] synthesized monodisperse poly(styrene-*b*-semifluorinated side chain) block copolymers by anionic polymerization of poly(styrene-*b*-1,2/3,4-isoprene), followed by the corresponding polymer analogous reaction. By controlling the block copolymer composition and the relative lengths of the fluorocarbon and hydrocarbon units in the side group, the authors investigated the effect of chemical structure on surface tension and the influence of liquid crystalline structure. They found that shorter fluorocarbon units (less than six —CF<sub>2</sub>— units) formed a smectic A phase with critical surface tension of 10.8 mN/m, and the polymer surface underwent reconstruction when immersed in water. However, more than eight —CF<sub>2</sub>— units formed a smectic B phase and exhibited a lower critical surface tension of 8 mN/m and negligible surface reconstruction.

In recent years, the increasing demand for lightweight, high-performance materials to substitute for heavyweight materials resulted in considerable progress of research in the field of reinforced polymers. The mixture of conventional polymers with liquid crystalline polymers is one of the choices, providing possibilities to facilitate the production as well as to improve the final properties. Most attention in the literature concerning TLCP-containing blends has been given to the relations between morphology, mechanical and rheological properties, and processing conditions [14–16]. However, the interfacial tension between TLCP and matrix is a key parameter governing the morphology and properties of a polymer blend, because it determines the formation of the TLCP domains and the compatibility between the components [17–21]. According to Machiels et al. [17], a small interfacial tension enables a fine dispersion generally, whereas a large interfacial tension leads to a coarse morphology. Furthermore, the interfacial tension also determines the interaction at the interface between the phases

of the blend components in the solid state. A small interfacial tension usually leads to diffuse phase boundaries with improved adhesion between phases and, hence, improved tensile properties because of a better stress transfer from one phase to the other.

Although the importance of surface tension and/or interfacial tension is obvious, most publications on LCPs are focused on the synthesis, phase transition, morphology, rheology, and mechanical property, etc., while comparatively few are reporting surface tension. Therefore this chapter will discuss surface tension of some main-chain TLCP, such as Hoechst Celanese's Vectra™ A950 and B950, and Amoco's Xydar™, etc. Moreover, the surface tension evolution during thin film polymerization will be discussed.

## 2. ESTIMATION OF SURFACE TENSION OF A SOLID

There are several approaches to the estimation of surface tensions of solids, but most are indirect measurements based on contact angle measurement. The measurement of contact angles of pure liquids, with known surface tension, on a given solid surface is the general way of estimating the surface tension of the solid material. Various approaches are summarized hereafter.

### 2.1. CONTACT ANGLE AND THE YOUNG'S EQUATION

When a liquid drop is in contact with an ideally smooth, undeformable, homogeneous solid (Figure 6.1), it exhibits an equilibrium contact angle that

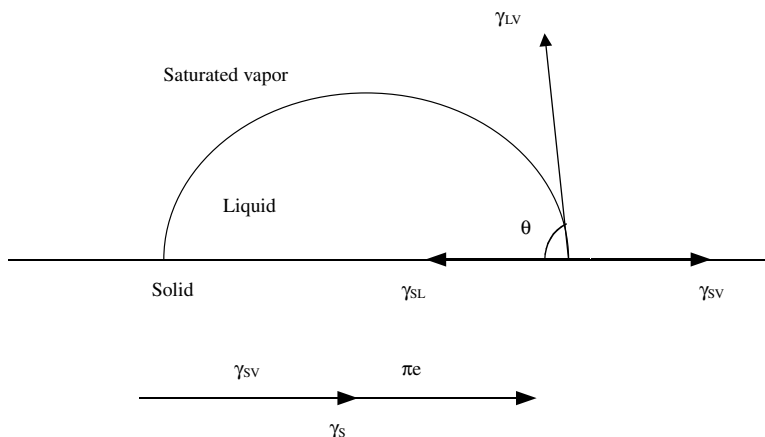


**Figure 6.1** A sessile drop of liquid on a solid showing three-phase force line.

can be expressed by the Young's equation:

$$\gamma_{LV} \cos \theta = \gamma_{SV} - \gamma_{SL} \quad (1a)$$

where  $\gamma_{LV}$  is surface tension of the liquid in equilibrium with its own vapor,  $\gamma_{SL}$  is the interfacial tension between liquid and solid,  $\gamma_{SV}$  is the surface tension of the solid in equilibrium with the saturated liquid vapor, and  $\theta$  is the contact angle. In terms of  $\gamma_S$  (surface tension of the solid), the Young's equation is rewritten as

$$\gamma_{LV} \cos \theta = \gamma_S - \gamma_{SL} - \pi_e \quad (1b)$$

where  $\pi_e \equiv (\gamma_S - \gamma_{SV})$ , equilibrium pressure. It is generally believed that, if the contact angle is greater than zero,  $\pi_e$  is negligible. Therefore, Equation (1b) can be rewritten as

$$\gamma_{LV} \cos \theta = \gamma_S - \gamma_{SL} \quad (1c)$$

## 2.2. ZISMAN'S METHOD

Zisman and co-workers showed [22,23] that contact angle measurements could be used to determine a criterion for wettability as well as surface tension of a solid. In their experiments, a series of testing liquids of known surface tension were used to measure contact angles against a solid. A linear or quasi-linear relationship was found between the cosine of the contact angle made by a liquid and the surface tension of the liquid. The linear relationship could be extrapolated to  $\cos \theta = 1$  (or  $\theta = 0$ ). The intercept of the line at  $\cos \theta = 1$  is considered to be the critical surface tension ( $\gamma_C$ ) of the solid, and the plot of  $\cos \theta$  versus  $\gamma_{LV}$  is known as the Zisman plot. When  $\cos \theta = 1$  and  $\gamma_C = \gamma_{LV}$ , Equation (1b) can be rewritten as

$$\gamma_C = \gamma_S - \gamma_{SL} - \pi_e \quad (2)$$

Equation (2) indicated that  $\gamma_C$  is always smaller than  $\gamma_S$  by  $(\gamma_{SL} + \pi_e)$ . Both the interfacial tension and the spreading pressure vary with the testing liquid; hence, the critical surface tension would vary depending on the choice of the testing liquids, as measured by Dann [24]. To minimize errors in interpreting results, Dann recommended that a testing liquid series be used in reporting values of critical surface tension of solid and that long extrapolations be avoided in determining  $\gamma_C$ .

## 2.3. NEUMANN'S METHOD

Neumann et al. [25–27] recommended that a relationship exist between  $\gamma_{SL}$ ,  $\gamma_{SV}$ , and  $\gamma_{LV}$ :

$$\gamma_{SL} = \gamma_{SL}(\gamma_{SV}, \gamma_{LV}) \quad (3)$$

This relationship was derived from the Gibbs-Durham relation [28] and from the phase rule [29]. Neumann developed an empirical equation from contact angle data [27] that is known as equation of state:

$$\gamma_{SL} = \gamma_{LV} + \gamma_{SV} - 2\sqrt{\gamma_{LV}\gamma_{SV}}\ell^{-\beta(\gamma_{LV}-\gamma_{SV})^2} \quad (4)$$

Combining with Young's equation yields

$$\cos \theta = -1 + 2\sqrt{\frac{\gamma_{SV}}{\gamma_{LV}}}\ell^{-\beta(\gamma_{LV}-\gamma_{SV})^2} \quad (5)$$

where  $\beta$  is  $0.001247 \text{ (m}^2/\text{mJ)}^2$ . Thus, the surface tension of solid can be determined from experimental contact angles and surface tensions of testing liquid by using Equation (5).

Some researchers [30–33] have challenged the validity of the equation of state. For example, to verify the equation of state experimentally, Spelt et al. [34] reported that the contact angles of two different testing liquids on a solid surface were identical when the liquid surface tensions were equal. On the contrary, van Oss et al. [31] showed that testing liquids of different surface tension values produced the same contact angle on the same solid, so that the results of Spelt et al. [34] could be completely explained by the theory of surface tension component. Johnson et al. [32] and Morrison [33] also criticized the method using Neumann's equation of state for its thermodynamic basis. However, Neumann et al. [35,36] rejected these criticisms and insisted on the thermodynamic validity of their approach.

## 2.4. FOWKES' METHOD

In the modern theory of surface science, Fowkes was the first to propose the theory of acid-base interfacial interaction [37–40].

It was suggested by Fowkes that the only significant interactions across an interface are those that are common to both phases in contact. Based on the additivity approach [37], the total thermodynamic work of adhesion between two substances in contact comprises contributions arising from various types

of interaction, i.e.,

$$W_A = W_A^d + W_A^{AB} \quad (6)$$

where  $d$  stands for dispersion part, while  $AB$  refers to nondispersion interactions, e.g., dipole-dipole, dipole-induced dipole, and hydrogen-bond interactions. In other words,  $AB$  also refers to acid-base interaction.

By using the geometric-mean expression, Fowkes [41] showed that the dispersion component of  $W_A$  is well predicted by

$$W_A^d = 2(\gamma_1^d \gamma_2^d)^{1/2} \quad (7)$$

However, according to Fowkes [40], the geometric-mean expression could not be applied to the acid-base component of  $W_A$ . To determine the strengths of acidic and basic sites of polymer, Fowkes suggested using spectroscopic or calorimetric methods.

## 2.5. OWENS, WENDT, AND KAEUBLE'S METHOD (TWO-LIQUID GEOMETRIC METHOD)

Although Fowkes has reservations, the geometric-mean approach proposed by Owens and Wendt [42], Schultz et al. [43], and Kaelble [44] is frequently employed to estimate surface tension of a solid. The technique is based on the use of testing liquids of known total surface tensions and their dispersive ( $d$ ) and nondispersive, e.g., polar ( $p$ ), components.

They extended Fowkes' equation [Equation (7)] to a more general form as follows:

$$W_A = 2(\gamma_S^d \gamma_{LV}^d)^{1/2} + 2(\gamma_S^p \gamma_{LV}^p)^{1/2} \quad (8)$$

Because the definition of  $W_A$  between a solid and a liquid is

$$W_A = \gamma_S + \gamma_{LV} - \gamma_{SL} \quad (9)$$

the following equation may be obtained:

$$\gamma_{SL} = \gamma_S + \gamma_{LV} - 2(\gamma_S^d \gamma_{LV}^d)^{1/2} - 2(\gamma_S^p \gamma_{LV}^p)^{1/2} \quad (10)$$

Combining Young's equation and Equation (10) yields

$$\gamma_{LV}(1 + \cos \theta) = 2(\gamma_S^d \gamma_{LV}^d)^{1/2} + 2(\gamma_S^p \gamma_{LV}^p)^{1/2} \quad (11)$$

where superscript  $d$  refers to dispersion (nonpolar) component and  $p$  refers to polar (nondispersion) component, including all the interactions established between the solid and liquid, such as dipole-dipole, dipole-induced dipole, and hydrogen bonding, etc.

Because  $\gamma_S$  is the sum of surface tension components contributed from dispersion and polar parts,

$$\gamma_S = \gamma_S^d + \gamma_S^p \quad (12)$$

Equations (11) and (12) provide a method to estimate the surface tension of solids. Using two liquids with known  $\gamma_L^d$  and  $\gamma_L^p$  for contact angle measurements, one could easily determine  $\gamma_S^d$  and  $\gamma_S^p$  by solving the following two equations:

$$\begin{aligned} \gamma_{LV1}(1 + \cos \theta_1) &= 2(\gamma_S^d \gamma_{LV1}^d)^{1/2} + 2(\gamma_S^p \gamma_{LV1}^p)^{1/2} \\ \gamma_{LV2}(1 + \cos \theta_2) &= 2(\gamma_S^d \gamma_{LV2}^d)^{1/2} + 2(\gamma_S^p \gamma_{LV2}^p)^{1/2} \end{aligned} \quad (13)$$

The values of  $\gamma_L^d$  and  $\gamma_L^p$  of testing liquids have been provided by Kaelble [45].

## 2.6. WU'S METHOD (TWO-LIQUID HARMONIC METHOD)

Based on “harmonic” mean and force addition, Wu proposed the following equations [46–48]:

$$\gamma_{SL} = \gamma_S + \gamma_{LV} - \frac{4\gamma_S^d \gamma_{LV}^d}{\gamma_S^d + \gamma_{LV}^d} - \frac{4\gamma_S^p \gamma_{LV}^p}{\gamma_S^p + \gamma_{LV}^p} \quad (14)$$

Equation (14) can be written as follows with the aid of Young's equation:

$$\gamma_{LV}(1 + \cos \theta) = \frac{4\gamma_S^d \gamma_{LV}^d}{\gamma_S^d + \gamma_{LV}^d} + \frac{4\gamma_S^p \gamma_{LV}^p}{\gamma_S^p + \gamma_{LV}^p} \quad (15)$$

Wu [46] claimed that this method applied accurately between polymers and between a polymer and an ordinary liquid.

## 2.7. LIFSHITZ-VAN DER WAALS-ACID-BASE METHOD (THREE-LIQUID ACID-BASE METHOD)

Van Oss et al. [49,50] have proposed a methodology that represents both Fowkes-Owens-Wendt-Kaelble and Wu. This methodology introduces a new meaning of the concepts “apolar” and “polar”; the latter cannot be represented by a single parameter such as  $\gamma^P$ .

Following Fowkes' approach [51,52], surface tension ( $\gamma$ ) can be separated into several components as

$$\gamma = \gamma^d + \gamma^{dip} + \gamma^{ind} + \gamma^h + \dots \quad (16)$$

where the superscripts,  $d$ ,  $dip$ ,  $ind$ , and  $h$  refer to (London) dispersion, (Keesom) dipole-dipole, (Debye) induction, and hydrogen-bonding forces, respectively. More generally,  $\gamma$  is composed of an apolar component and hydrogen-bonding component or acid-base interaction.

$$\gamma = \gamma^d + \gamma^{AB} \quad (17)$$

and the superscript  $AB$  refers to the acid-base interaction.

By regrouping components in Equation (16), van Oss and Good expressed the surface tension as

$$\gamma = \gamma^{LW} + \gamma^{AB} \quad (18)$$

$$\gamma^{LW} = \gamma^d + \gamma^{dip} + \gamma^{ind} \quad (19)$$

where  $LW$  stands for Lifshitz-van der Waals. Because a hydrogen bond is a proton-sharing interaction between an electro-negative molecule or group and an electro-positive hydrogen, hydrogen bonding is an example of Lewis acid (electron acceptor) and Lewis base (electron donor). Van Oss et al. [49–50,53–57] therefore treated hydrogen bonding as one of Lewis acid-base interactions. In addition, van Oss et al. [49,53] created two parameters to describe the strength of Lewis acid and base interactions:  $\gamma^+ \equiv$  (Lewis) acid parameter of surface tension;  $\gamma^- \equiv$  (Lewis) base parameter of surface tension.

$$\gamma_i^{AB} = 2\sqrt{\gamma_i^+ \gamma_i^-} \quad (20)$$

Based on these definitions, a material is classified as a bipolar substance if both its  $\gamma^+$  and its  $\gamma^-$  are greater than 0 ( $\gamma_i^{AB} \neq 0$ ). In other words, it has both non-vanishing  $\gamma^+$  and  $\gamma^-$ . A monopolar material is one having either acid or base characters, which means either  $\gamma^+ = 0$  and  $\gamma^- > 0$  or  $\gamma^+ > 0$  and  $\gamma^- = 0$ . An apolar material is neither an acid nor a base (both its  $\gamma^+$  and its  $\gamma^-$  are 0). For both monopolar and apolar materials, their  $\gamma_i^{AB} = 0$ . Therefore, according to the Fowkes notation, the criterion for a substance to be apolar is  $\gamma^{AB} = 0$ . This is not true in the van Oss and Good's methodology.

How do we calculate these surface tension parameters? Van Oss, Good, and their co-workers [49–50,53–57] have developed a “three-liquid procedure” [Equation (21)] to determine  $\gamma_S$  by using contact angle technique and a

traditional matrix scheme.

$$\begin{aligned}\gamma_{LV1}(1 + \cos \theta_1) &= 2\left(\sqrt{\gamma_S^{LW}\gamma_{LV1}^{LW}} + \sqrt{\gamma_S^+\gamma_{LV1}^-} + \sqrt{\gamma_S^-\gamma_{LV1}^+}\right) \\ \gamma_{LV2}(1 + \cos \theta_2) &= 2\left(\sqrt{\gamma_S^{LW}\gamma_{LV2}^{LW}} + \sqrt{\gamma_S^+\gamma_{LV2}^-} + \sqrt{\gamma_S^-\gamma_{LV2}^+}\right) \\ \gamma_{LV3}(1 + \cos \theta_3) &= 2\left(\sqrt{\gamma_S^{LW}\gamma_{LV3}^{LW}} + \sqrt{\gamma_S^+\gamma_{LV3}^-} + \sqrt{\gamma_S^-\gamma_{LV3}^+}\right)\end{aligned}\quad (21)$$

In short, to determine the components of  $\gamma_S$  of a polymer solid, it was recommended [58,59] to select three or more liquids from the testing liquids table, with two of them being polar, the other one being apolar. Moreover, the polar pairs, water and ethylene glycol, and water and formamide were recommended to give good results, while apolar liquids are either diiodomethane or  $\alpha$ -bromonaphthalene. Because the  $LW$ , Lewis acid, and Lewis base parameters of  $\gamma_{LV1}$ ,  $\gamma_{LV2}$ , and  $\gamma_{LV3}$  are available [58,59], one can determine the  $LW$ , Lewis acid, and base parameters of  $\gamma_S$  by solving these three equations simultaneously.

## 2.8. THEORETICAL ESTIMATION FROM GROUP CONTRIBUTION HYPOTHESIS

Surface tension of TLCPs can also be predicted using group contribution. Van Krevelen [60] has studied and summarized the hypotheses to estimate surface tension of a solid polymer by means of additive quantities, the parachor and the cohesive energy density. The parachor ( $P_S$ ), which was first introduced by Sugden [61], has the following additive quantity and is independent of temperature:

$$P_S = \gamma^{1/4} \frac{M}{\rho} = \gamma^{1/4} V \quad (22)$$

where  $\gamma$  refers to surface tension,  $M$  to molecular weight,  $\rho$  to density, and  $V$  to molar volume. Therefore, if group contributions of  $P_S$  and  $V$  per structural unit are known,  $\gamma$  can be calculated from the following equation:

$$\gamma = \left(\frac{P_S}{V}\right)^4 \quad (23)$$

where the dimensions of  $\gamma$ ,  $P_S$ , and  $V$  are dyne/cm ( $= \text{mJ/m}^2$ ),  $(\text{cm}^3/\text{mol} \cdot \text{mJ/m}^2)^{1/4}$ , and  $\text{cm}^3/\text{mol}$ , respectively.

It has also been suggested that surface tension of a polymer could be related to its cohesive energy density ( $e_{\text{coh}}$ ) as well as cohesive energy ( $E_{\text{coh}}$ ) by the

following empirical formulation [60]:

$$\gamma = 0.75 e_{\text{coh}}^{2/3} = 0.75 \left( \frac{E_{\text{coh}}}{V} \right)^{2/3} \quad (24)$$

where  $\gamma$  is expressed in  $\text{mJ/m}^2$ ,  $e_{\text{coh}}$  in  $\text{J/cm}^3$ , and  $E_{\text{coh}}$  in  $\text{J/mol}$ .

### 3. SURFACE TENSION OF COMMERCIAL THERMOTROPIC LIQUID CRYSTALLINE POLYMERS

#### 3.1. POLYMER MATERIALS

Three commercially available thermotropic liquid crystalline polymers (TLCPs) were presented as examples in this section. They are Hoechst Celanese Vectra™ A950 and Vectra™ B950 as well as Amoco Xydar™. Vectra™ A950 is a random copolymer of 73 mol% 4-hydroxybenzoic acid and 27 mol% 6-hydroxy-2-naphthoic acid, and Vectra™ B950 is a random copolyesteramide consisting of 60 mol% of 6-hydroxy-2-naphthoic acid, 20 mol% terephthalic acid, and 20 mol% *p*-aminophenol. Xydar™ is made from *p*-hydroxybenzoic acid, isophthalic acid and/or terephthalic acids, and 4,4'-biphenol. The repeating unit structures of the three LCPs are shown in Figure 6.2.

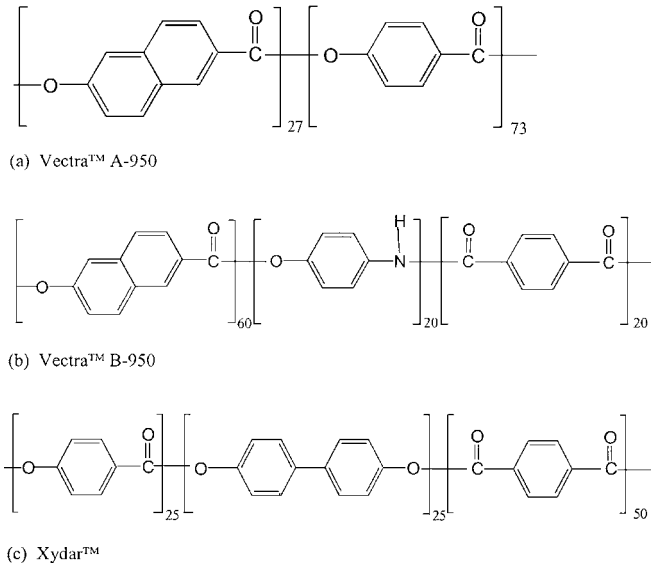


**Figure 6.2** Repeating unit structure of commercial liquid crystalline polymers.

### 3.2. FILM SAMPLE PREPARATION FOR CONTACT ANGLE MEASUREMENTS

These LCP polymers can be dissolved in bis-trifluoromethyl phenol (Bayer, 99%) with specific weight ratios (0.7 wt%) at  $50 \pm 5^\circ\text{C}$  in a water bath with a stirrer. Bis-Trifluoromethyl phenol is chosen because it is superior to pentafluorophenol for dissolving these LCPs and gives clearer solutions [62]. In addition, low concentrated solutions are preferred to yield smooth surfaces.

This is the recommended procedure. Before spin coating, a sufficient amount of solution is introduced onto alkali-treated (cleaned) glass slides. The spin coating can be conducted at 500 rpm for 1 minute using a Laurell™ Single Wafer Spin Processor (Model WS-200-4NPP). After coating, the fresh spun film sample should be immediately placed into a vacuum oven and heated from 70 to  $150^\circ\text{C}$  under vacuum overnight in order to remove the solvent. Spin coating has many advantages; one of them is to remove surface roughness that may cause complexity of contact angle measurement. The spin coating speed, which is 500 rpm, is much lower than the conventional speed for wafer coating (3000–7000 rpm). The low speed is chosen to minimize centrifugal force and, therefore, reduce radial orientation induced by spin coating.

### 3.3. CONTACT ANGLE MEASUREMENT

The contact angle measurements can be made on a Ramé-Hart Contact Angle Goniometer (Model 100-22) by the sessile drop method at  $25^\circ\text{C}$  using an environmental chamber. A built-in image system provided by Ramé-Hart is able to acquire the image, transmit it to a computer, and perform the image analysis. Liquid droplets should be laid by a Gilmont micro syringe or other precision syringe onto the surfaces of the films.

Advancing and receding contact angles can be obtained through a tilting base using the basic technique and principle developed elsewhere [63,64]. When a liquid drop resting on a solid surface is inclined, it deforms. The contact angle of the advancing edge of the drop increases while the angle of the receding edge decreases, as shown in Figure 6.3. The drop remains firmly adhered to

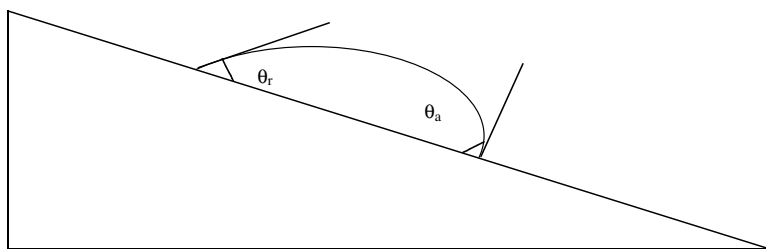


**Figure 6.3** A liquid drop on the tilting base showing the advancing and receding contact angles.

TABLE 6.1. Surface Tension Parameters (in mJ/m<sup>2</sup>) of Testing Liquids.

	Water	Glycerol	Formamide	Diiodomethane
$\gamma^+$	25.5	3.92	2.28	0.0
$\gamma^-$	25.5	57.4	39.6	0.0
$\gamma^{AB}$	51.0	30.0	19.0	0.0
$\gamma^{LW}$	21.8	34.0	39.0	50.8
$\gamma$	72.8	64.0	58.0	50.8
$\gamma^p$	51.0	26.4	18.7	2.3
$\gamma^d$	21.8	37.0	39.5	48.5
$\gamma$	72.8	63.4	58.2	50.8

the surface, stationary, until the advancing ( $\theta_a$ ) and receding ( $\theta_r$ ) angles exceed certain critical volumes.

Normally, at least five droplets at different regions of the same piece of film should be dispensed for contact angle measurement, and at least four pieces of film should be used to get reliable contact angle data. Thus, at least 20 advancing contact angles can be averaged for each kind of film as well as for each kind of testing liquid.

Deionized water (prepared in this laboratory), glycerol (from BDH), formamide (Unilab), and diiodomethane (from Nacalai Tesque) have been chosen as the testing liquids because there are significant data available for these liquids. Table 6.1 tabulates their basic surface tension parameters (in mJ/m<sup>2</sup>) [45,59].

### 3.4. RESULTS AND DISCUSSIONS

#### 3.4.1. Fabrication of Isotropic Liquid Crystalline Polymer Film

Following the procedures described in the experimental section, one may obtain transparent and ultra-thin films with a thickness of approximately 1  $\mu\text{m}$ . In order to be sure that there is no significant LCP orientation induced during spin coating, contact angles of the LCP films rotated 90° (i.e., films were turned 90° from previous position) should be measured. Both contact angles should be the same within experimental error, suggesting that there is no significant LCP orientation induced during the spin coating.

#### 3.4.2. Contact Angle and Surface Tension of Spin-Coated TLCP Films

Advancing contact-angle data as well as the standard deviations of the three main-chain TLCPs with different testing liquids are listed in Table 6.2. As expected, higher surface tension liquids give bigger contact angles for each of the TLCP films.

TABLE 6.2. Contact Angle (in Degrees) of Commercial Liquid Crystalline Polymers.

No. Liquids	1 Water	2 Glycerol	3 Formamide	4 Diiodomethane
Vectra™ A950				
Advancing angle	81.68	68.23	63.83	38.67
Standard deviation	1.46	1.08	1.29	1.33
Vectra™ B950				
Advancing angle	79.50	67.48	60.88	36.64
Standard deviation	1.28	1.14	1.18	1.71
Xydar™				
Advancing angle	78.17	65.54	60.07	36.57
Standard deviation	1.25	2.62	1.08	1.58

Two-liquid geometric and two-liquid harmonic methods are applied to calculate surface tension components of the TLCP films, as tabulated in [Tables 6.3](#) and [6.4](#). For both tables, calculated values from various pairs of liquids are shown in the third, fourth, and fifth columns, respectively. Columns 6, 7, and 8 give their corresponding average values. In [Table 6.3](#), it is found that three liquid pairs (water-diiodomethane, glycerol-diiodomethane, and formamide-diiodomethane) give comparable  $\gamma_s$  for each of the TLCPs by using the

TABLE 6.3. Surface Tensions (in mJ/m<sup>2</sup>) of Commercial Liquid Crystalline Polymers Using Two-Liquid Geometric Method.

	Liquid Pairs	$\gamma_S^d$	$\gamma_S^p$	$\gamma_S$	Mean $\gamma_S^d$	Mean $\gamma_S^p$	Mean $\gamma_S$
Vectra™ A950	Water-diiodomethane	37.11	3.43	40.54	39.2	1.5	40.7
	Glycerol-diiodomethane	39.30	1.07	40.37			
	Formamide-diiodomethane	41.12	0.14	41.26			
Vectra™ B950	Water-diiodomethane	37.64	4.06	41.70	39.8	1.8	41.6
	Glycerol-diiodomethane	40.37	1.02	41.39			
	Formamide-diiodomethane	41.35	0.43	41.78			
Xydar™	Water-diiodomethane	37.32	4.62	41.94	39.4	2.3	41.6
	Glycerol-diiodomethane	39.70	1.60	41.30			
	Formamide-diiodomethane	41.06	0.60	41.66			

TABLE 6.4. Surface Tensions (in mJ/m<sup>2</sup>) of Commercial Liquid Crystalline Polymers Using Two-Liquid Harmonic Method.

	Liquid Pairs	$\gamma_S^d$	$\gamma_S^p$	$\gamma_S$	Mean $\gamma_S^d$	Mean $\gamma_S^p$	Mean $\gamma_S$
Vectra <sup>TM</sup> A950	Water- diiodomethane	36.45	8.37	44.82	37.9	4.4	42.3
	Glycerol- diiodomethane	37.79	3.43	41.22			
	Formamide- diiodomethane	39.58	1.28	40.86			
Vectra <sup>TM</sup> B950	Water- diiodomethane	37.19	9.17	46.36	38.5	4.9	43.4
	Glycerol- diiodomethane	38.68	3.40	42.08			
	Formamide- diiodomethane	39.62	2.06	41.68			
Xydar <sup>TM</sup>	Water- diiodomethane	37.16	9.76	46.92	38.3	5.4	43.7
	Glycerol- diiodomethane	38.37	4.14	42.51			
	Formamide- diiodomethane	39.40	2.35	41.75			

two-liquid geometric method, though higher polar testing liquid, i.e., water, gives higher  $\gamma_S^p$  and lower  $\gamma_S^d$ . The average total  $\gamma_S$  is 40.7, 41.6, and 41.6 mJ/m<sup>2</sup> for Vectra<sup>TM</sup> A950, Vectra<sup>TM</sup> B950, and Xydar<sup>TM</sup>, respectively. Moreover, the mean  $\gamma_S^p$  values suggest that the polar components of these three TLCPs are very small, which seems structurally negligible. By defining the polarity ( $\chi^p$ ) of polymers ( $\chi^p = \gamma_S^p / \gamma_S$ ), Vectra<sup>TM</sup> A950, Vectra<sup>TM</sup> B950, and Xydar<sup>TM</sup> show identical polarity of 0.04, 0.04, and 0.05, respectively. In other words, these three main-chain TLCPs are actually nonpolar, although an amide group existed in Vectra<sup>TM</sup> B950 structure. Table 6.4 shows the relative results calculated from the two-liquid harmonic method, which tends to yield higher  $\gamma_S^p$  and, hence, overall  $\gamma_S$  values than the geometric method. The average total  $\gamma_S$  from the two-liquid harmonic method are 42.3, 43.4, and 43.7 mJ/m<sup>2</sup> for Vectra<sup>TM</sup> A950, Vectra<sup>TM</sup> B950, and Xydar<sup>TM</sup>, respectively.

To obtain valid results for the surface tension of LCPs, van Oss and Good's Lifshitz-van der Waals-acid-base theory (three-liquid acid-base method) was also utilized. We chose diiodomethane as the apolar liquid and either water-glycerol or water-formamide as polar liquids. Table 6.5 shows the calculated results using the three-equation method.

When using the three-equation method during the calculations, the Lewis acid parameters of surface tension,  $\gamma^+$ , for Vectra<sup>TM</sup> A950, Vectra<sup>TM</sup> B950, and Xydar<sup>TM</sup> are 0.08, 0.05, and 0.09 mJ/m<sup>2</sup>, respectively. Lewis base parameters of surface tension,  $\gamma^-$ , are 5.61, 6.44, and 6.95 mJ/m<sup>2</sup> and  $\gamma^{LW}$  are 40.27,

TABLE 6.5. Surface Tensions (in mJ/m<sup>2</sup>) of Commercial Liquid Crystalline Polymers Using Three-Liquid Acid-Base Method.

Liquid Pairs		$\gamma^+$	$\gamma^-$	$\gamma^{AB}$	$\gamma^{LW}$	$\gamma_S$
Vectra <sup>TM</sup> A950	Water-glycerol- diiodomethane	0.15	4.00	1.53	40.27	41.80
	Water-formamide- diiodomethane	0.00	7.21	0.00	40.27	40.27
	<i>Mean</i>	<i>0.08</i>	<i>5.61</i>	<i>0.77</i>	<i>40.27</i>	<i>41.04</i>
Vectra <sup>TM</sup> B950	Water-glycerol- diiodomethane	0.09	5.20	1.37	41.26	42.63
	Water-formamide- diiodomethane	0.00	7.68	0.00	41.26	41.26
	<i>Mean</i>	<i>0.05</i>	<i>6.44</i>	<i>0.68</i>	<i>41.26</i>	<i>41.94</i>
Xydar <sup>TM</sup>	Water-glycerol- diiodomethane	0.18	5.41	1.95	41.29	43.24
	Water-formamide- diiodomethane	0.00	8.49	0.00	41.29	41.29
	<i>Mean</i>	<i>0.09</i>	<i>6.95</i>	<i>0.98</i>	<i>41.29</i>	<i>42.27</i>

41.26, and 41.29 mJ/m<sup>2</sup>, respectively. Total  $\gamma_S$  are 41.0, 41.9, and 42.3 mJ/m<sup>2</sup> for Vectra<sup>TM</sup> A950, Vectra<sup>TM</sup> B950, and Xydar<sup>TM</sup>, respectively. Therefore, compared with Table 6.3, the best correlation between  $\gamma_S$  obtained from the Two-liquid geometric method and the three-liquid acid-base method occurred when diiodomethane is used as one of the testing liquids. Clearly, values of physicochemical parameters do match between two-liquid geometric method and three-liquid acid-base method if the correct combinations of testing liquid have been used, but three-liquid acid-base method provides much more information, e.g., acidity and basity of TLCP surfaces.

Hence some valuable information about the surface characteristics of LCP films can be yielded [66]:

- (1) All three LCPs have a monopolar Lewis base surface because their  $\gamma^+$  values are negligible. These results are consistent with Good and van Oss's conclusion and experimental data that ester groups are Lewis bases [59].
- (2) All three LCPs have very comparable values in terms of  $\gamma^P$ ,  $\gamma^d$ , and total  $\gamma_S$  obtained from the two-liquid geometric method,  $\gamma^+$ ,  $\gamma^-$ ,  $\gamma^{AB}$ ,  $\gamma^{LW}$ , and total  $\gamma_S$  obtained from the three-liquid acid-base method. This is probably due to the fact that the benzene group is the dominant factor governing the surface properties of the TLCP films.
- (3) The degree (intensity) of Lewis base (tendency to donate a pair of electrons to the formation of a covalent bond) for these three LCPs are as follows (with little difference):

$$\text{Xydar}^{\text{TM}} > \text{Vectra}^{\text{TM}}\text{B950} > \text{Vectra}^{\text{TM}}\text{A950}.$$

[www.iran-mavad.com](http://www.iran-mavad.com)

مرجع دانشجویان و مهندسين مواد

### 3.5. THEORETICAL ESTIMATION BY GROUP CONTRIBUTION METHOD

As introduced in [section 2.8](#), theoretical surface tension of a solid polymer can be estimated by means of additive quantities, the parachor, and the cohesive energy density. Van Krevelen [60] has summarized different group contributions to molar volume, parachor, and cohesive energy from previous literature, and they are tabulated in [Table 6.6](#). In short, the parachor ( $P_S$ ) is a summation term mainly based on atomic group contributions, while cohesive energy ( $E_{\text{coh}}$ ) is based on structural group contributions. Because  $E_{\text{coh}}$  values of *p*-naphthalene group are not available in the references, we can only estimate it using related structure units, and the approximated values are given in [Table 6.6](#). [Table 6.7](#) shows the calculated surface tensions of the three LCPs using Equations (6) and (7) and compare them with experimental data obtained from contact angle. In order to be sure that our calculations are correct, we also calculate the surface tensions of polyethylene, polystyrene, polyethylene terephthalate, and polymethyl methacrylate and find the results are in good agreement with Van Krevelen's data [60].

The second column of [Table 6.7](#) gives the  $\gamma_s$  values estimated from  $P_S$ . There is a rather large discrepancy from those obtained by contact angle experiments (which is in the last column). Clearly, the parachor approach is not suitable for the surface tension estimation of TLCPs. The third column summarizes the  $\gamma_s$  estimated from  $E_{\text{coh}}$ . In order to calculate  $E_{\text{coh}}$  values, three structural group contribution tables have been chosen and evaluated. They are Hoftyzer and Van Krevelen, Hayes, and Fedors' tables [60]. The  $E_{\text{coh}}$  value used for the *p*-naphthalene group is estimated from a combination of  $E_{\text{coh}}$  values of *p*-phenylene, ethylene, and other groups. For readers' information, Hoftyzer and Van Krevelen and Hayes do not provide  $E_{\text{coh}}$  value for the *p*-naphthalene group.

The results show that the estimated  $\gamma_s$  from Fedors for all three TLCPs are much higher than those obtained from contact angle measurement. However, the estimated  $\gamma_s$  values from Hoftyzer and Van Krevelen and Hayes are in quite close agreement to those from contact angle measurement. This is especially true for Vectra<sup>TM</sup> A950 and Xydar<sup>TM</sup> TLCP. In this case, the theoretically calculated values based on Hoftyzer and Van Krevelen and Hayes match very well with data obtained from contact angle, e.g., 42.2, 41.4, and 41.0 mJ/m<sup>2</sup> for Vectra<sup>TM</sup> A950, and 42.4, 41.8, and 42.3 mJ/m<sup>2</sup> for Xydar<sup>TM</sup>, respectively.

In the cases of Vectra<sup>TM</sup> B950, the agreement between theoretical calculations and experimental values obtained from contact angle measurement are reasonably good. However, the degree of agreement is inferior to the previous cases of Vectra<sup>TM</sup> A950 and Xydar<sup>TM</sup> LCP. This may be due to the fact that the  $E_{\text{coh}}$  values estimated for the amide group (—CONH—) vary significantly in Hoftyzer and Van Krevelen and Hayes' tables (60, 760 vs. 44, 750 J/mol). Moreover, both values estimated from Hoftyzer and Van Krevelen and Hayes exhibit

TABLE 6.6. Group Contributions to Molar Volume, Parachor, and Cohesive Energy.

Group Contributions	$V_a(298)^a$ (cm <sup>3</sup> /mol)	$P_S^b$ (cm <sup>3</sup> /mol · mJ/m <sup>2</sup> ) <sup>1/4</sup>	$E_{coh}$ (J/mol)			
			Hoftyzer and Van Krevelen <sup>c</sup>	Hayes <sup>d</sup>	Fedors <sup>e</sup>	
					$E_{coh}$ (J/mol)	$V_a$ (cm <sup>3</sup> /mol)
—COO—	23	64.4	13410	14160	18000	18.0
—CONH—	21	77.6	60760	44750	33490	9.5
<i>p</i> -Phenylene	65.5	172.9	25140	23880	31940	52.4
—CH=CH—			10200	7500		
>C=CH—			4860	4860 <sup>f</sup>		
—CH=					4310	13.5
>C=					4310	−5.5
Ring closure 5 or more atoms					1050	16
Conjugation in ring for each double bond					1670	−2.2
<i>p</i> -Naphthalene	112	313	40200	36240	53550	80

<sup>a</sup>Table 4.9 in reference [60] on page 87 ( $V_a$  is the molar volume in amorphous state at 298K).

<sup>b</sup>Table 8.1 in reference [60] on page 229.

<sup>c</sup>Table 7.1 in reference [60] on page 192.

<sup>d</sup>Table 7.1 in reference [60] on page 192.

<sup>e</sup>Table 7.3 in reference [60] on page 196.

<sup>f</sup>Hayes did not provide, so Hoftyzer and Van Krevelen data were used.

www.iran-mavad.com

مرجع دانشجویان و مهندسين مواد

TABLE 6.7. Comparisons of TLCP Surface Tensions Obtained from Different Approaches.

	$\gamma_s$ Estimated from $P_s$ (mJ/m <sup>2</sup> )	$\gamma_s$ Estimated from $E_{coh}$ (mJ/m <sup>2</sup> )			$\gamma_s$ Calculated from Contact Angle (mJ/m <sup>2</sup> )
		Hoftyzer and Van Krevelen	Hayes	Fedors	
Vectra <sup>TM</sup> A950	55.3	42.2	41.4	60.0	41.0
Vectra <sup>TM</sup> B950	61.1	46.7	43.7	63.2	41.9
Xydar <sup>TM</sup>	51.3	42.4	41.8	58.5	42.3

higher surface tension over experimental value from contact angle in Vectra<sup>TM</sup> B950, e.g., 46.7, 43.7, and 41.9 mJ/m<sup>2</sup>. It is assumed that the amide group in Vectra<sup>TM</sup> B950 should provide higher surface tension in terms of higher polar component of surface tension. However, probably due to surface reconstruction, benzene groups would be the dominant force governing the overall surface tension; hence, Vectra<sup>TM</sup> B950 shows similar surface tension with Vectra<sup>TM</sup> A950 and Xydar<sup>TM</sup> experimentally [65,66].

#### 4. SURFACE TENSION EVOLUTION DURING THIN-FILM POLYMERIZATION

In this part, we intend to investigate the surface tension evolution during the polymerization reaction for the wholly aromatic polymers prepared from acetoxibenzoic acid (ABA) and 2,6-acetoxynaphthoic acid (ANA) using our knowledge in thin-film polymerization [67,68]. In short, a thin layer of monomers was sandwiched between two glass slides with a steel ring as a spacer, and the thin-film polymerization was conducted on the heating stage of a microscope. The bottom slide contained a mixture of monomers that was solution cast on the slide and dried. Once the temperature reached a certain value, there was a sublimation (of monomers from bottom slide to upper slide)-recrystallization-melting-polymerization-LC domain formation-crystallization process at the upper slide during the preparation of polymer. The ring spacer provided space for easy removal or release of acetic acid during polymerization. Without the spacer, it was found that the reproducibility was quite low and the film quality was poor because the evaporation (or release) of acetic acid at elevated temperatures was vigorous.

##### 4.1. THIN FILMS WITH DIFFERENT DEGREES OF POLYMERIZATION FOR CONTACT ANGLE MEASUREMENTS

In this example, ABA and ANA monomers with specific mole ratios were co-dissolved in acetone. The solution was then deposited onto micro-glass slides,

[www.iran-mavad.com](http://www.iran-mavad.com)

مرجع دانشجویان و مهندسين مواد

and acetone evaporated in a few minutes. Another micro-glass slide was used to cover the one with monomer and was spaced about 0.5 mm by aluminum foil. The whole set was then wrapped with aluminum foil, followed by heating at  $270^{\circ}\text{C} \pm 1\%$  digital hot plate for 4 min, 8 min, 15 min, 30 min, 1 hour, and 2 hours, respectively. The whole package was removed from the thermostat hot stage immediately after a certain heating time and was cooled down under ambient temperature ( $\sim 25^{\circ}\text{C}$ ) for contact angle measurements.

Samples with different reaction times were scratched from the upper of the glass slides, mixed with KBr, and molded for FTIR (Perkin Elmer FTIR Spectrometer Spectrum 2000) study.

## 4.2. RESULTS AND DISCUSSION

### 4.2.1. Contact Angle of ABA/ANA Copolymers

Table 6.8 gives an example of the advancing and receding contact angles as well as the standard deviations of the 73/23 ABA/ANA copolymers with three different testing liquids and various reaction times. For each of the testing liquids, each mole ratio of copolymers, and each kind of reaction times, the difference between advancing and receding contact angles is less than  $10^{\circ}$ , and for most cases, the standard deviations are less than 2. Based on the previous work [69,70], it may be concluded that all copolymer surfaces obtained from thin-film polymerization have minor hysteresis, but they are suitable for contact angle measurements. Because the advancing contact angle is more precisely representing the equilibrium contact angle than the receding angles [71–73], only the advancing contact angles will be discussed hereafter.

Table 6.8 shows the contact angles with the most polar liquid, water; the less polar liquid, glycerol; and the apolar liquid, diiodomethane on 73/27 ABA/ANA copolymers under different reaction times. As expected, polar liquids give bigger contact angles than the apolar liquid. Moreover, it is quite obvious that water contact angle increases with an increase in the reaction time, e.g., from  $64^{\circ}$  at 4 minutes to  $82^{\circ}$  at 2 hours of reaction time. However, it is interesting to see that both glycerol and diiodomethane contact angles do not vary significantly compared to water. Same trends are also found in 50/50 and 27/73 ABA/ANA copolymers [68]. Clearly, with an increase in polymerization time, the polarity (in terms of Lewis acid and base interaction) of the copolymer surfaces decreases.

### 4.2.2. Surface Tension and Its Acid and Base Components of ABA/ANA Copolymers

In order to obtain surface tensions of ABA/ANA copolymers, van Oss and Good's Lifshitz-van der Waals-Acid-Base approach (3-liquid LWAB method) is used. We chose diiodomethane as the apolar liquid and water-glycerol as the

TABLE 6.8. Contact Angles of 73/27 ABA/ANA Copolymers.

No. Liquids	1 Water	2 Glycerol	3 Diiodomethane
ABA/ANA = 73/27, 270°C hot plate, 4 min.			
Advancing angle	64.6	64.4	39.6
Standard deviation	2.9	1.6	2.1
Receding angle	59.6	57.6	34.6
Standard deviation	2.9	0.4	1.8
ABA/ANA = 73/27, 270°C hot plate, 8 min.			
Advancing angle	71.4	64.0	40.0
Standard deviation	2.8	0.8	1.9
Receding angle	66.6	57.4	35.0
Standard deviation	3.4	1.8	2.2
ABA/ANA = 73/27, 270°C hot plate, 15 min.			
Advancing angle	75.9	64.4	35.3
Standard deviation	2.1	0.8	0.9
Receding angle	71.4	58.0	29.9
Standard deviation	1.5	0.9	0.9
ABA/ANA = 73/27, 270°C hot plate, 30 min.			
Advancing angle	77.0	65.6	35.4
Standard deviation	0.9	1.1	1.9
Receding angle	72.1	59.0	30.2
Standard deviation	1.0	1.5	1.6
ABA/ANA = 73/27, 270°C hot plate, 1 hour.			
Advancing angle	81.0	72.0	35.8
Standard deviation	1.1	1.9	1.8
Receding angle	74.8	64.3	29.2
Standard deviation	1.0	1.9	0.6
ABA/ANA = 73/27, 270°C hot plate, 2 hours.			
Advancing angle	82.1	66.7	35.7
Standard deviation	1.3	1.8	2.1
Receding angle	77.0	59.5	31.0
Standard deviation	1.3	2.0	2.6

polar liquid pair. Table 6.9 shows the calculated results. Table 6.9 tabulates all the surface tension components ( $\gamma^+$ ,  $\gamma^-$ ,  $\gamma^{AB}$ ,  $\gamma^{LW}$ ) as well as total surface tension ( $\gamma$ ) of 73/27 ABA/ANA copolymers under different reaction times.

The Lewis acid parameters ( $\gamma^+$ ) are very small, varying with reaction time from zero to 0.2 mJ/m<sup>2</sup>, resulting in quite small acid-base parameters ( $\gamma^{AB} = 2\sqrt{\gamma^+\gamma^-}$ ). Moreover, the Lifshitz-van der Waals parameters ( $\gamma^{LW}$ ) do not vary much with the reaction time. However, the Lewis base parameters ( $\gamma^-$ ) are absolutely and monotonously decreasing with an increase in the reaction time for all copolymers.  $\gamma^-$  decreases dramatically from 19.71 mJ/m<sup>2</sup> at 4

TABLE 6.9. Surface Tension Components of 73/23 ABA/ANA Copolymers (Calculated with 3-Liquid LWAB method).

Reaction Time	$\gamma^+$	$\gamma^-$	$\gamma^{AB}$ (mJ/m <sup>2</sup> )	$\gamma^{LW}$ (mJ/m <sup>2</sup> )	$\gamma$ (mJ/m <sup>2</sup> )
4 min.	0.00	19.71	0.28	39.79	40.07
8 min.	0.13	11.08	2.42	39.63	42.05
15 min.	0.15	6.69	2.03	41.87	43.90
30 min.	0.11	6.28	1.68	41.85	43.53
1 hr.	0.00	6.00	0.00	41.68	41.68
2 hrs.	0.21	3.12	1.63	41.71	43.34

minutes of reaction time to 3.12 mJ/m<sup>2</sup> at 2 hours of reaction time for 73/27 ABA/ANA copolymers. Similar results were obtained for 50/50 ratio and 27/73 ratio copolymers [68]. In other words, the strength of the Lewis base parameter decreases with the progress of ABA/ANA copolymerization. Figure 6.4 shows the monomer structure as well as the copolymerization formulation. With the progress of polymerization, more acetoxy and carboxyl groups combine to release the acetic acid; therefore, the decrease of  $\gamma^-$  of the surface is understandable.

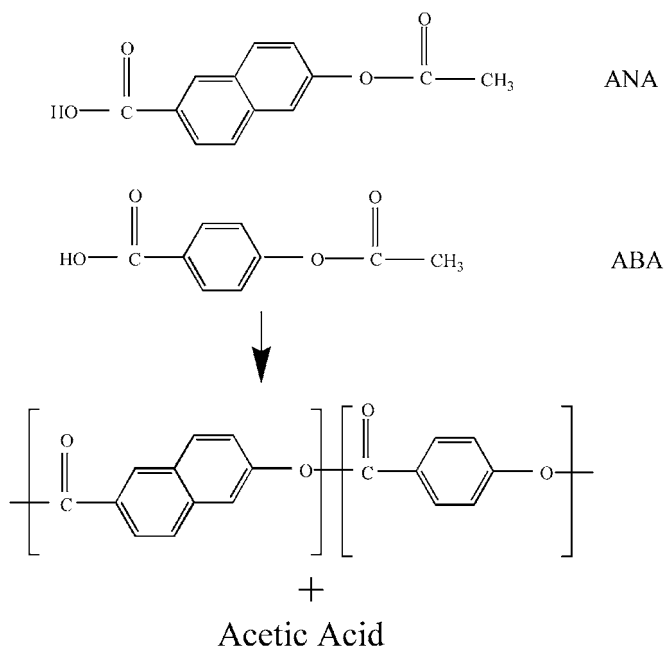
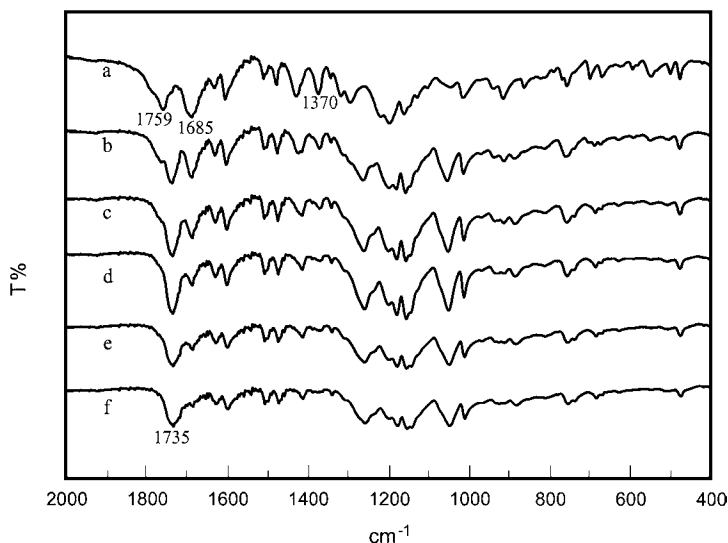


Figure 6.4 Monomer structures and polymerization formulation.



**Figure 6.5** FTIR spectra obtained by 73/27 ABA/ANA copolymers at different reaction times: (a) 4 min, (b) 8 min, (c) 15 min, (d) 30 min, (e) 1 hour, (f) 2 hours.

Figure 6.5 shows the FTIR spectra of thin-film 73/27 ABA/ANA copolymer as a function of the reaction time varying from 4 minutes to 2 hours. Generally, the peak at  $1685\text{ cm}^{-1}$  is the vibration of C=O bond in carboxyl, the peak at  $1370\text{ cm}^{-1}$  is C—H bond in acetoxy, and the peak at  $1759\text{ cm}^{-1}$  is the C=O bond in acetoxy. Moreover, the peak at  $1735\text{--}1740\text{ cm}^{-1}$  is the C=O bond in polymer ester. It is clear that the peaks of both carboxyl and acetoxy group are decreasing, while the peak of polymer ester is increasing with an increase in the reaction time. At the end of the reaction, as the spectrum shown in Figure 6.5f, the peaks at  $1370$ ,  $1685$ , and  $1759\text{ cm}^{-1}$  are almost indistinguishable compared to their original height, which indicates that nearly all of the acetoxy and carboxyl groups have been consumed. Meanwhile, a substantial number of polymer ester groups have formed as shown by the increment of the peak at  $1735\text{--}1740\text{ cm}^{-1}$ . Moreover, it is obvious that the condensation polymerization is much faster in the beginning stage (e.g., from 4 min to 15 min) than in the later stage (e.g., from 30 min to 2 hours) because both carboxyl and acetoxy peaks decrease significantly from 4 min to 15 min. These results coincide and well explain the trend of the Lewis base parameter ( $\gamma^-$ ) shown in the section A of Table 6.5, where  $\gamma^-$  decreases in a much greater magnitude from 4 min to 15 min of reaction time than that from 30 min to 2 hours of reaction time.

Table 6.10 compares the surface tension components of 73/27 ABA/ANA copolymer at 2 hours with those of commercial-grade Vectra<sup>TM</sup> A950 [75], which contains the same mole ratio of monomers. The table shows that all the surface tension components between our thin-film copolymer and Vectra<sup>TM</sup>

TABLE 6.10. Surface Tension Comparisons between 73/27 ABA/ANA Thin-Film Copolymers and Vectra™ A950 Spin-Coating Films.

(mJ/m <sup>2</sup> )	Polymerization Time	$\gamma^+$	$\gamma^-$	$\gamma^{AB}$	$\gamma^{LW}$	$\gamma$
Copolymer	2 hrs.	0.21	3.12	1.63	41.71	43.34
Vectra™ A950	Commercial	0.15	4.00	1.53	40.27	41.80

A950 are quite close. This excellent agreement strongly supports our previous hypothesis that the thin-film polymerization samples developed in this work are well suited for contact angle measurements and the surface tension calculation. In addition, this excellent agreement also suggests that the absorption of acetic acid vapor by the thin film during polymerization at elevated temperatures can be negligible.

In addition, the current data re-confirm our conclusions in the previous papers [65,66] that Vectra™ A950 has a monopolar Lewis base surface because its  $\gamma^+$  values are negligible, which is consistent with Good and van Oss’s conclusion that ester has Lewis-base character. This conclusion can also be extended to ABA/ANA copolymers obtained by thin-film polymerization with 73/27, 50/50, and 27/73 mole ratios with different polymerization times.

4.2.3. Effect of ANA Mole Ratio on the Surface Tension of LC Copolymers

4.2.3.1. Lewis Base Parameters of Surface Tension

Figure 6.6 not only exhibits that the Lewis base parameter ( $\gamma^-$ ) of ABA/ANA copolymers decreases with an increase in reaction time, but also shows that an

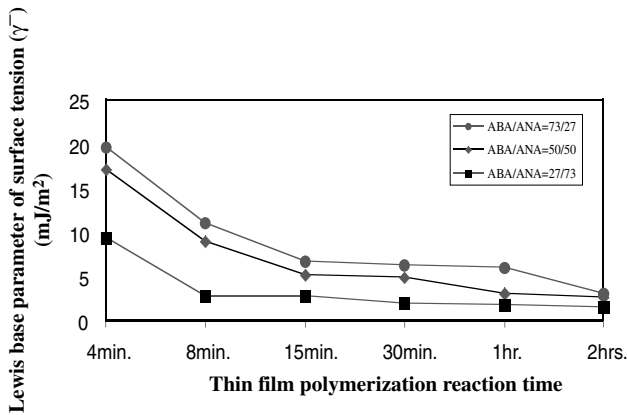


Figure 6.6 Lewis base parameter of surface tension of copolymers with different monomer ratio.

TABLE 6.11. Contact Angles of Poly(ABA) and Poly(ANA) Homopolymers.

No. Liquids	1 Water	2 Glycerol	3 Diiodomethane
Poly(ABA) homopolymer with 2-hour reaction			
Advancing angle	73.5	63.0	27.5
Standard deviation	2.4	2.5	1.7
Receding angle	69.0	57.4	18.0
Standard deviation	2.4	2.8	2.0
Poly(ANA) homopolymer with 2-hour reaction			
Advancing angle	90.7	78.1	39.7
Standard deviation	2.2	1.6	2.4
Receding angle	83.4	70.7	33.7
Standard deviation	2.1	1.5	2.7

increase in ANA ratio results in a decrease in the Lewis base parameter ( $\gamma^-$ ). The only difference between ABA and ANA is that the phenylene unit in ABA is replaced by the naphthalene unit in ANA. Because the activity of naphthalene is less than that of phenylene, an increase in the mole ratio of naphthalene (ANA) in copolymers should decrease the overall Lewis base parameter ( $\gamma^-$ ) (e.g., acid-base property), as presented in Figure 6.6.

#### 4.2.3.2. Surface Tension of Poly(ABA) and Poly(ANA) Homopolymers

For comparison and further understanding of the effect of ANA on surface tension properties, poly(ABA) and poly(ANA) homopolymer samples are prepared by the same thin-film polymerization method under 270°C hot plate for 2 hours. Table 6.11 summarizes their contact angle results, while Table 6.12 tabulates their surface tension components. Interestingly, the contact angles of all three testing liquids (e.g., water, glycerol, and diiodomethane) on poly(ANA) surfaces are much higher than those on poly(ABA) surfaces, and, hence, poly(ABA) exhibits a higher surface tension than poly(ANA). As shown in Table 6.12, the  $\gamma^-$  of both poly(ABA) and poly(ANA) are much larger than  $\gamma^+$ , which again indicates that these homopolymers are classified as Lewis base materials as well. The  $\gamma^-$  and  $\gamma^{LW}$  of poly(ANA) are much lower than

TABLE 6.12. Surface Tension Components of Poly(ABA) and Poly(ANA) Homopolymers.

(mJ/m <sup>2</sup> )	Polymerization Time	$\gamma^+$	$\gamma^-$	$\gamma^{AB}$	$\gamma^{LW}$	$\gamma$
Poly(ABA)	2 hrs.	0.06	7.86	1.32	45.21	46.53
Poly(ANA)	2 hrs.	0.00	2.02	0.00	39.78	39.78

those of poly(ABA), which strongly reconfirms our previous conclusion that the substitution of phenylene (ABA) units by naphthalene (ANA) units lowers the acid-base property (represented by the Lewis base  $\gamma^-$  in our case) as well as the apolar property ( $\gamma^{LW}$ ) of LCPs.

## 5. REFERENCES

1. A. A. Handlos and D. G. Baird, *J. M. S.-Rev. Macromol. Chem. Phys.*, C35, 183 (1995).
2. Y. Seo, S. M. Hong, S. S. Hwang, T. S. Park, and K. U. Kim, *Polym.*, 36, 525 (1995).
3. R. Lusignea, J. Piche, and R. Mathisen, in *Polymer Materials for Electronic Packaging and Interconnection*, ACS Symposium Series, 407, 446 (1989).
4. Hoechst Celanese Vectra<sup>TM</sup> technical brochure.
5. M. Uzman, B. Song, T. Runke, H. Cackovic, and J. Springer, *Makromol. Chem.*, 192, 1129 (1991).
6. T. Runke, B. Song, and J. Springer, *Ber. Bunsenges. Phys. Chem.*, 98, 508 (1994).
7. B. Song and J. Springer, *J. of Colloid and Interface Science*, 184, 64 (1996).
8. N. T. Correia, J. J. M. Ramos, B. J. V. Saramago, and J. C. G. Calado, *J. Colloid & Interface Sci.*, 189, 361 (1997).
9. N. T. Correia, J. J. M. Ramos, M. H. C. V. Adão, and B. J. V. Saramago, *Mol. Cryst. Liq. Cryst.*, 300, 45 (1997).
10. J. Brandrup and E. H. Immergut, *Polymer Handbook*, 3rd edition, Wiley, New York (1989).
11. R. F. Brady Jr., in *Encyclopedia of Polymer Science and Technology*, 2nd edition, by H. Mark, N. M. Bikales, C. G. Overberger, and G. Menges, Wiley, New York (1986).
12. J. Wang and C. K. Ober, *Macromolecules*, 30, 7560 (1997).
13. J. Wang, G. Mao, C. K. Ober, and E. J. Kramer, *Macromolecules*, 30, 1906 (1997).
14. D. Dutta, H. Fruitwala, A. Kohli, and R. A. Weiss, *Polym. Eng. Sci.*, 30, 1005 (1990).
15. O. Roetting and G. Hinrichsen, *Adv. Polym. Technol.*, 13, 57 (1994).
16. X. Jin and W. Li, *J. Macromol. Sci.-Rev. Macromol. Chem. Phys.*, C13, 1 (1995).
17. A. G. C. Machiels, R. J. Busser, J. Van Dam, and A. P. de Boer, *Polym. Eng. Sci.*, 38, 1536 (1998).
18. M. Uzman, K. Kühnpast, and J. Springer, *Makromol. Chem.*, 190, 3185 (1989).
19. S. Meretz, M. Kwiatkowski, and G. Hinrichsen, *Intern. Polymer Processing*, 3, 239 (1991).
20. Y. S. Lipatov, V. F. Shumsky, and V. F. Babich, *Int. J. Adhesion & Adhesives*, 16, 109, (1996).
21. B. B. Sauer and N. V. Dipaolo, *J. Adhesion*, 53, 245, (1995).
22. E. G. Shafrin and W. A. Zisman, *J. Phys. Chem.*, 64, 519 (1960).
23. W. A. Zisman, in *Contact Angle, Wettability and Adhesion*, ed. by F. W. Fowkes, ACS Symposium Series, Vol. 43, Washington, DC (1964).
24. J. R. Dann, *J. Colloid Interface Sci.*, 32, 302 (1970).
25. A. W. Neumann, R. J. Good, C. J. Hope, and M. Selpal, *J. Colloid Interface Sci.*, 49, 291 (1974).
26. O. Driedger, A. W. Neumann, and P. J. Sell, *Kolloid-Z. Z. Polym.*, 201, 52 (1965).
27. D. Li and A. W. Neumann, *Adv. Colloid Interface Sci.*, 39, 299 (1992).
28. C. A. Ward and A. W. Neumann, *J. Colloid Interface Sci.*, 49, 286 (1974).
29. D. Li, J. Gaydos, and A. W. Neumann, *Langmuir*, 5, 1133 (1989).
30. B. Janczuk and T. Bialopiotrowicz, *J. Colloid Interface Sci.*, 140, 362 (1990).
31. C. J. van Oss, R. J. Good, and M. K. Chaudhury, *Langmuir*, 4, 884 (1988).
32. R. E. Johnson Jr. and R. H. Dettre, *Langmuir*, 5, 293 (1989).
33. I. D. Morrison, *Langmuir*, 5, 540 (1989).
34. J. K. Spelt, D. R. Absolom, and A. W. Neumann, *Langmuir*, 2, 620 (1986).
35. D. Li, E. Moy, and A. W. Neumann, *Langmuir*, 6, 885 (1990).

36. J. Gaydos, E. Moy, and A. W. Neumann, *Langmuir*, 6, 888 (1990).
37. F. W. Fowkes, *J. Phys. Chem.*, 67, 2538 (1963).
38. F. W. Fowkes, *Ind. Eng. Chem.*, 56, 40 (1964).
39. F. W. Fowkes, in *Contact Angle, Wettability and Adhesion*, ed. by F. W. Fowkes, ACS Symposium Series, Vol. 43, Washington, DC (1964).
40. F. W. Fowkes, *J. Adhesion Sci. Tech.*, 1, 7 (1987).
41. F. M. Fowkes, *J. Adhes.*, 4, 155 (1972).
42. D. K. Owens and R. C. Wendt, *J. of Appl. Polym. Sci.*, 13, 1741 (1969).
43. J. Schultz, K. Tsutsumi, and J. D. Donnet, *J. Colloid Interface Sci.*, 59, 277 (1977).
44. D. H. Kaelble, *J. Adhesion*, 2, 66 (1970).
45. D. H. Kaelble, *Physical Chemistry of Adhesion*, Chapter 5, Wiley Interscience, New York (1970).
46. S. Wu, *J. Polymer Sci.: Part C*, 34, 19 (1971).
47. S. Wu, in *Adhesion and Adsorption of Polymers, Polymer Science and Technology*, Vol. 12A, ed. by L. H. Lee, p. 53, Plenum Press, New York (1980).
48. S. Wu and K. J. Brzozowski, *J. Colloid Interface Sci.*, 37, 686 (1971).
49. C. J. van Oss, M. K. Chaudhury, and R. J. Good, *Chem. Rev.*, 88, 927 (1988).
50. C. J. van Oss, L. Ju, M. K. Chaudhury, and R. J. Good, *J. Colloid Interface Sci.*, 128, 313 (1989).
51. F. M. Fowkes and M. A. Mostafa, *Int. Eng. Chem. Prod. Res. Dev.*, 17, 3 (1978).
52. F. M. Fowkes, D. C. McCarthy, and M. A. Mostafa, *J. Colloid Interface Sci.*, 78, 200 (1980).
53. C. J. van Oss and R. J. Good, *J. Macromol. Sci.-Chem.*, A26, 1183 (1989).
54. C. J. van Oss, *J. Dispersion Science and Technology*, 11, 491 (1990).
55. C. J. van Oss, K. Arnold, R. J. Good, K. Gawrisch, and S. Ohki, *J. Macromol. Sci.-Chem.*, A27, 563 (1990).
56. C. J. van Oss, R. J. Good, and H. J. Busscher, *J. Dispersion Science and Technology*, 11, 75 (1990).
57. C. J. van Oss, R. F. Giese Jr., and R. J. Good, *Langmuir*, 6, 1711 (1990).
58. R. J. Good and C. J. van Oss, in *Modern Approaches to Wettability*, Chapter 1, ed. by M. E. Schrader and G. I. Loeb, Plenum Press, New York (1992).
59. R. J. Good, Contact angle, wetting, and adhesion: A critical review, in *Contact Angle, Wetting, and Adhesion*, pg. 3, ed. by K. L. Mittal, VSP, The Netherlands (1993).
60. D. W. van Krevelen, *Properties of Polymers*, Chapter 4 and Chapter 8, Elsevier Science Publishers B. V., New York (1990).
61. S. Sugden, *J. Chem. Soc.*, 125, 1177 (1924).
62. R. Kuhn, A. Marhold, and H.-R. Dicke, U.S. Patent, 4,960,539 (1990).
63. G. MacDougall and C. Okrent, *Proc. R. Soc. London A*, 180, 151 (1942).
64. C. W. Extrand and Y. Kumagai, *J. Colloids & Interface Sci.*, 184, 191 (1996).
65. T. S. Chung, K. X. Ma, and M. Jaffe, *Macromol. Chem. Phys.*, 199, 1013 (1998).
66. K. X. Ma, T. S. Chung, and R. J. Good, *J. Polym. Sci.: Polym. Phys.*, 36, 2327 (1998).
67. S. X. Cheng, T. S. Chung, and S. Mullick, *Chem. Eng. Sci.*, 54, 663 (1999).
68. T. S. Chung and K. X. Ma, *J. Phys. Chem.*, 103, 108 (1999).
69. J. Drelich, J. D. Miller, and R. J. Good, *J. Colloid & Interface Sci.*, 179, 37 (1996).
70. J. Drelich, J. D. Miller, A. Kumar, and G. M. Whitesides, *Colloids and Surfaces A: Physico-chemical and Engineering Aspects*, 93, 1 (1994).
71. J. Drelich and J. D. Miller, *J. Colloid & Interface Sci.*, 164, 252 (1994).
72. R. J. Good and C. J. van Oss, in *Modern Approaches to Wettability*, Chapter 1, ed. by M. E. Schrader and G. I. Loeb, Plenum Press, New York (1992).
73. R. J. Good, in *Surface Colloid and Science II: Experimental Methods*, Chapter 1, ed. by R. J. Good and R. R. Stromberg, Plenum Press, New York (1979).

## LCP Blends

JIASONG HE  
JUN ZHANG

### 1. INTRODUCTION

**P**OLYMER blending is an effective and attractive way to obtain new polymer materials due to the effectively reduced cost and combined properties of neat component polymers for engineering purposes. In the past, most of the reported work and commercial developments of polymer blends have been concerned with conventional flexible-chain polymers. Along with the emerging liquid crystalline polymers (LCPs) composed of rigid (semi-rigid) rod-like molecules, LCP blends were investigated for producing blends of flexible and rigid rod-like chain polymers.

Liquid crystalline polymers are usually classified into two groups: lyotropic LCPs and thermotropic LCPs, based on the conditions for the formation of their liquid crystalline state. Lyotropic LCPs such as PPTA are processed to high-strength, high-modulus fibers by a solution spinning technique that has been briefly discussed in the previous chapters of this book. A group of so-called “molecular composites” was prepared by solution blending a lyotropic LCP and a flexible-chain matrix polymer in order to achieve molecular dispersion in coagulated blend [1–4], which was reviewed later by Pawlikowski et al. [5]. However, the aggregation of dispersed LCP phase and resulted phase separation in the blend system resulted in the dispersion of LCP phase at a scale of  $10^1$  to  $10^2$  nm, far from the molecular level dispersion. Because the rigid rod-like lyotropic LCP is not melt processable, the fabrication techniques are severely limited and usually require large amounts of strong acids to obtain the dilute solutions that are necessary to achieve good dispersion of the reinforcing phase. The fabrication of complex articles similar to what can be produced

by injection molding is impossible with the current state-of-the-art techniques, and usually “molecular composites” are prepared in the form of films or fibers. Although exceptional mechanical properties have been attained in “molecular composites,” the difficulties associated with processing these materials have thus far restricted the technology to the laboratory.

Thermotropic LCPs can be processed and molded to structural parts of different shapes by means of conventional processing techniques for thermoplastics, such as extrusion and injection molding. Due to the rigidity of the molecular chains of thermotropic LCPs, injection-molded parts of pure thermotropic LCPs usually show strong anisotropy, evidenced by higher strength and modulus along the flow direction and weak lateral adhesion transverse the flow direction. To overcome this deficiency, for injection-molded parts, thermotropic LCPs are blended with other thermoplastics to reduce the anisotropy of the performances of the final products and to widen their application areas.

In this chapter, our discussion will be confined to, and focused on, the blends of thermotropic LCPs with thermoplastics, where the thermotropic LCP is a minor fraction. Because both the thermotropic LCP and the thermoplastic are melts at processing temperatures and both melts show shear-thinning behavior, the fibrillation of the LCP occurs, and the rigidity of highly oriented LCP molecular chains forms a reinforcing phase in solidified parts. From an industrial viewpoint, thermotropic LCPs can function as a processing aid and a reinforcing agent to improve both the processibility and performance of thermoplastics. These advantages help to develop novel blends of advanced engineering plastics that have both acceptable processibility and excellent performance. For economic consideration, a minor fraction of the LCP in its blend is practical. LCP blends with an LCP as the minor fraction and a thermoplastic resin as the matrix have also received extensive research and development interests. From a scientific viewpoint, several aspects of basic understanding are involved in order to develop marketable technology: the rheological behavior of LCP blends, orientation and crystallization of blend systems, interfacial interaction and compatibilization in LCP blends, microstructure development, and the processing-structure-property relationship in these LCP blends.

The pioneering work on polymer blends containing LCP was reported in early 1980s by a number of research groups [6–8]. Siegmann blended a thermotropic liquid crystalline aromatic copolyester based on 6-hydroxy-2-naphthoic acid (HNA) and *p*-hydroxybenzoic acid (PHB) with an amorphous polyamide in the molten state. He found that the melt viscosity of the blend system was decreased by the addition of LCP, even just 5% LCP; that injection molded blends exhibited mechanical behaviors similar to that of composite materials; and that the phase morphology depended on their composition, changing from spherical to fibrillar with increasing LCP content. This was the first paper

reporting in detail the LCP blends that were named later as “in situ composites.” By following this investigation, more and more research works are concentrated on blending thermoplastics and thermotropic LCPs when thermotropic LCPs are available for further research and development.

## 2. IN SITU COMPOSITES

The research on polymer blends containing thermotropic LCPs received much more scientific and industrial interest after Hoechst-Celanese released more publications in 1987 [9,10]. He called polymer blends with thermotropic LCPs “in situ composites.” He emphasized that thermotropic LCP had sufficient chain stiffness to give extremely high stiffness and strength, and yet had sufficient flexibility to melt. Thermotropic LCPs formed fibers extremely readily, even in injection-molded and extruded parts. It was likely that LCPs would form fibrous domains of inclusions in a matrix polymer when melt blended. Given the inherent strength and stiffness of the thermotropic LCPs, these fibrous inclusions would then act as a reinforced element, much like chopped glass fibers. In short, thermotropic LCPs would act like “meltable chopped glass fibers.” Another extremely striking characteristic of thermotropic LCPs was their unusual rheology. Of great interest here was the extremely low viscosity they exhibited. So in situ composite blends were actually easier to process than the neat matrix polymer, a very different situation from that found for chopped-glass composites.

These widely cited papers contribute to dimming the boundary between the polymer blend and polymer composite. Blends of thermotropic LCPs with thermoplastic polymers are processed and molded by conventional techniques such as extrusion, injection molding, and spinning with related equipment. However, the resultant products have the characteristic reinforced structure and mechanical behaviors of fiber-reinforced plastics or composites. It is common where technical terms of LCP blends and in situ composites have the same meaning. LCP blends almost refer to blends with thermotropic LCPs as the minor portion so that in situ composites and newly invented in situ hybrid composites are the main content of this chapter on polymer blends.

From the viewpoint of composite mechanics, the better performances of composites come from the effective reinforcing effect of the reinforcements and effective stress transferring from the matrix to the reinforcements. The reinforcing LCP fibrils in in situ composites are generated during the melt processing of LCP blends, which is different from conventional glass or carbon fiber-reinforced composites. So the formation of LCP fibrils becomes one of the most important aspects in the preparation of in situ composites, except the common interfacial interaction in fiber-reinforced plastics.

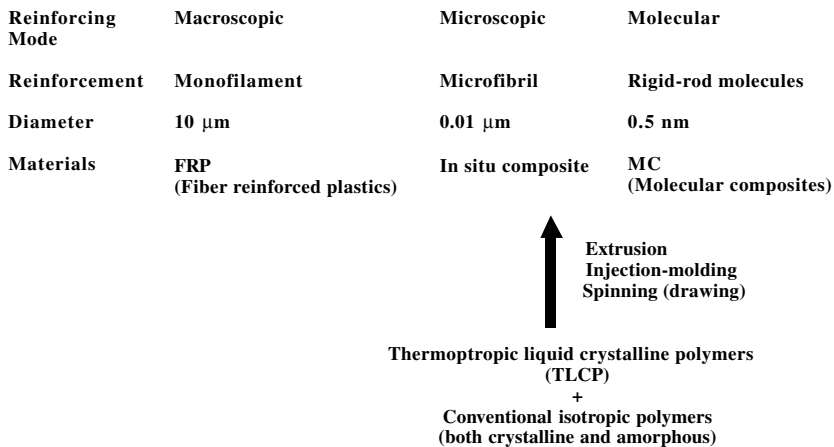


**Figure 7.1** Reinforcing modes for thermoplastic polymers.

At the early stage of research on in situ composites, most work has been conducted on the LCP microfibril formation connected with the melt viscosity or viscosity ratio, composition, and flow mode, etc. These results have been summarized and reviewed by several researchers [11–17]. In the aspect of fibrillation, the current work is only a supplement to those reviews, with additional new insights and results. We will summarize and review the recent work on the compatibility of LCP blends in this chapter.

## 2.1. FIBRILLATION

Figure 7.1 summarizes reinforcing modes for thermoplastic polymers. It shows that thermoplastics can be reinforced macroscopically by fibers such as carbon fiber, glass fiber, and aramid fiber (Kevlar) having their diameters of  $10^0$  to  $10^1 \mu\text{m}$ . In order to obtain a high-modulus and high-strength composite, a higher percentage of fiber content (up to 30%, 45%, and even 60%) is needed. Thermoplastics can also be reinforced at the molecular level by rigid rod-like molecules of microfibrils having their diameters of 0.5 nm, although achieved ones are 10–30 nm. Young's modulus of molecular composites increases significantly upon the addition of as little as 5% (by weight) of lyotropic LCPs. Now we have in situ composites reinforced by LCP fibrils. By assuming the diameters of reinforcements for macroscopic, microscopic, and molecular reinforcing form a geometric series, and the diameter of microfibrils of in situ composites could be the central term of this series and at the order of magnitude of  $0.01 \mu\text{m}$ , it is necessary to reach submicrometer order of magnitude for better reinforcing effect. It is well known that, as the diameter of reinforcements decreases, their reinforcing

effect will be more enhanced. The first step for the fabrication of in situ composites is to form LCP fibrils with as small of a diameter as possible and as large intrinsic aspect ratio (i.e.,  $L/D$  ratio) as possible. Several factors influence the fibrillation of LCPs in the thermoplastic matrix. Some are characteristics of thermotropic LCPs, while others are parameters relating to melt processing.

### 2.1.1. Characteristics of LCPs

With the development of the synthesis techniques and the application of thermotropic LCPs, there are now more than a dozen LCPs available for making in situ composites (Table 7.1). By using these LCPs, various results have been obtained by different researchers. However no papers discussing which LCP is suitable for making in situ composites have been published. In other words, the importance of the characteristics of thermotropic LCPs (may be characterized by other parameters, if any) for microfibril reinforcing is seldom discussed. However, the authors believe that some thermotropic LCPs are more suitable than others for generating fibrils and playing their reinforcing role.

The fibrillation of LCPs in thermoplastic melts is influenced by several parameters, including the thermal characteristics of the component polymers and their compatibility, and processing parameters such as viscosity ratio, melt temperature, flow mode, and shear rate. Among these parameters, thermal characteristics of LCPs are basic factors for the formation of LCP fibrils. They should have the matched “processing window” with the matrix resin, when the former is in the liquid crystal state. It has been found that the spinnability of LCPs can be taken as a prerequisite for the accomplishment of submicrometer reinforcing with LCP fibrils [18].

The spinnability of an LCP was defined as the ability of the LCP to be spun into a continuous fiber with the smallest average diameter under its optimized spinning conditions, such as melt temperature and spinning speed [18]. The spinnability was affected by structural parameters, such as bonding energy, spatial conformation, chain rigidity, molecular weight and molecular-weight distribution, as well as spinning parameters. Experimental results showed that LCPs could be divided into two groups. One group has good spinnability and yields small diameters and narrow diameter distribution of spun fibers, while the other group has poor spinnability with larger diameters and a broader diameter distribution. Under the same processing conditions, including low viscosity ratios of the dispersed LCP to the continuous matrix resin from 0.01 to 0.1, LCPs having good spinnability generated fibrils with small diameters, narrow diameter distribution, and large aspect ratio in resin melts, which showed a correlation between the spinnability of neat LCPs and the fibrillation of LCPs in blend resin melts.

La Mantia et al. [19] also noticed the importance of the spinnability, for mechanical properties of LCP blend fibers, although they did not emphasize

TABLE 7.1. List of TLCP Trade Names, Suppliers, and Possible Compositions from References Concerning TLCPs and Their Blends.

TLCP Trade Name	Supplier	Constituents	$T_g (^{\circ}\text{C})$	$T_m (^{\circ}\text{C})$
<b>Type I (HDT, 250–350°C)</b>				
Xydar SRT 300	Amoco	PHB + TA + BP		
Xydar SRT 900	Amoco	PHB + TA + BP		349
<b>Type II (HDT, 180–250°C)</b>				
Vectra A900/950	Hoechst-Celanese	73 mol% PHB + 27 mol% HNA	100	283
Vectra B900/950	Hoechst-Celanese	60% HNA + 20% TA + 20% aminophenol	145	285
Vectra RD500/501	Hoechst-Celanese	52% PHB + 28% HNA + 10% TA + 10% HQ	101	236
<b>Type III (HDT, 60–180°C)</b>				
Rodrun LC-3000	Unitika	60% PHB + 40% PET		
Rodrun LC-5000	Unitika	80% PHB + 20% PET		280
PCL Rhodester	Rhone-Poulenc	60% PHB + 40% PET		272
X7G	Eastman	60% PHB + 40% PET		
<b>Others</b>				
HX1000	DuPont	TA + HQ + other proprietary monomers	176	
HX4000	DuPont	TA + HQ + other proprietary monomers	179	311
HX6000	DuPont	TA + HQ + other proprietary monomers		332
HX8000	DuPont	TA + HQ + other proprietary monomers	110	272
Ultrax KR-4002	BASF	PHB + HQ + terephthaloy		
K161	Bayer	PHB + TA + HQ + IA + HBP		
Granlar	Granmont-Montedison	TA + PhHQ + StHQ		
SBH	Eniricerche	SA + PHB + BP		

www.iran-mavad.com

مرجع دانشجویان و مهندسين مواد

the characteristics of the LCP itself. The spinnability of flexible polymers with wholly aromatic or semi-aromatic LCPs was evaluated through the melt strength (MS) and the breaking stretching ratio (BSR). Their conclusions were that the LCP phase might actually play a considerable reinforcing effect only if good spinnability (granting the fibrillation of the LCP particles and the orientation of the matrix macromolecules) was accomplished by sufficient interphase adhesion in the solid state.

## 2.1.2. Influencing Factors

Even though LCPs used for blending have good spinnability, there are still some processing parameters controlling the formation of LCP fibrils in melt processing. They can be listed as the blend composition, viscosity ratio (and elasticity ratio) of the dispersed phase to the continuous phase, interfacial tension between the two phases, shear rate and shear stress, and processing conditions related to processing equipment (mixing time, type of mixer, rotational speed of rotor or screw). Among these, the melt viscosity ratio of the dispersed LCP phase to the continuous thermoplastic polymer phase is the first and decisive factor, based on the knowledge at this moment.

### 2.1.2.1. Viscosity Ratio

Detailed analysis of microstructure development within the extruder showed that, in the process of microstructure formation of extrudates, the deformation, coalescence, breakup, and relaxation of the dispersed phase were all involved. The process of deformation of LCP domains in the shear flow before the extruder die was controlled by the viscosity. The shear flow before the die could result in the deformation and fibrillation of LCP droplets, if the viscosity ratio (0.01 or smaller) favored the fibrillation. The coalescence and further deformation of the LCP domains in the die entrance lead to the increase in volume and aspect ratio of the fibrils [20].

Low viscosity ratios far below unity are necessary for the fibrillation of LCPs in resin melts, even for LCPs having good spinnability [18]. Furthermore, even for blends of flexible-/flexible-chain polymers, viscosity ratios far below unity (0.01) generated fibrils of a minor phase in an envelope of composition from 10% to 40% after different mixing times [21].

Table 7.2 lists results of the morphology in LCP blends reported in the literature [22–32]. It is shown that though in most cases, the viscosity of LCP is lower than that of matrix polymer, LCP cannot always form fibrils, so the condition of a viscosity ratio lower than unity is not sufficient for the LCP phase to form fibrils. Table 7.3 [33] shows the morphology of dispersed LCP phase related to viscosity ratios in LCP/polymer 10/90 (by weight). Combined with other results in that paper, it is concluded that the deformation of the LCP

TABLE 7.2. The Morphology in Polyblends Containing LCPs Reported in the Literature.

System	Extrusion Temp. °C	$\eta_{LCP}/\eta_m$	Morphology (with LCP Concentrations Indicated)	Ref.
P(PHB/HNA)/PC	310	<1	2.5%, 5%, 10% fibrils; 25%, 50% droplets	[22]
P(PHB/PET)/PC	240	<1	5%, 10% droplets	[23]
	260	<1	50% thick fibers	
P(PHB/HNA)/PET	280–288	<1	20%, 40%, 60% no fibril; 80% fibrils; at high shear rates, 30% fibrils	[24]
P(PHB/HNA)/PEEK	350	<1	2.5%, 5% no fibril; >10% fibrils	[25]
P(PHB/PET)/PET	280	<1	large L/D of die, no fibril; small L/D, lightly fibril	[26]
P(PHB/HNA)/PPO	310	<1	most fibrils in skin, >50% fibrils in core	[27]
Polyester/PC	270	<1	fibrils at very high shear rates and small L/D	[28]
P(PHB/PET)/PA66	275	<1	no fibril in stable shear	[29]
P(PHB/PET)/PC	260	<1	extruding, 10% droplets, 30% fibrils, >50% continuous	[29]
P(PHB/HNA)/PC	260	cross	fibrils at high shear rates	[30]
P(PHB/HNA)/PBT	260	>1	droplets	[30]
P(PHB/HNA)/PA66	260	>1	droplets	[30]
P(PHB/HNA)/PPS	285	>1	droplets	[31]
P(PHB/HNA)/PS	295	>1	spherical form	[32]
P(PHB/ PET)/PS	295	<1	fibrils	[32]

www.iran-mavad.com

مرجع دانشجویان و مهندسين مواد

TABLE 7.3. Morphology of Dispersed LCP Phase (LCP/Matrix, 10/90, by Weight), Related to Viscosity Ratios (Number in Parentheses) of LCP to Matrices (at a Shear Rate of  $57.6 \text{ s}^{-1}$ ).

Matrix	Extrusion Temperature ( $^{\circ}\text{C}$ )				
	270	300	320	340	360
PBT	Spheres (6.9)				
PC	Deformed Spheres (0.32)	Spheres (0.16)	Spheres (0.13)		
PES		Fibrils (0.0095)	Fibrils (0.0075)	Fibrils (0.0058)	
PSF			Fibrils (0.0096)	Fibrils (0.0041)	Fibrils ( $<0.0041$ )

dispersed phase needs a large viscous force, so the viscosity ratio of the LCP to the matrix is the decisive factor controlling the formation of LCP fibrils in the resin matrix. But, the effect of the viscosity ratio is related to the LCP content.

#### 2.1.2.2. LCP Content

The effect of LCP content is closely related to the viscosity ratio of the LCP to the matrix. Blizzard and Baird [29] concluded that at 10 wt% LCP (PHB/PET) with Nylon 66 and PC, the volume fraction of the minor LCP phase was too low to allow coalescence of the droplets necessary for fibril formation. The author has hypothesized when the LCP content is very low, such as 10%, the coalescence of the LCP phase is limited, the deformation of the dispersed phase is difficult, and the rather low viscosity ratio is not sufficient to make the LCP phase form fibrils; only at a much lower viscosity ratio can the deformation and coalescence of the LCP phase occur [33]. At a lower LCP content, significant LCP fibrillation takes place when the viscosity ratio is far below unity. The author found that even in extrudates of LCP [a copolyester polycondensed from *p*-hydroxybenzoic acid, naphthalene diphenol, terephthalic acid, and poly(ethylene terephthalate)]/polysulfone (PSF) 2/98 (by weight), LCP fibrils were generated when the viscosity ratio of LCP to PSF was smaller than 0.01 [34]. The purpose of developing in situ composites is to make strong materials at a reasonable cost. Practical formulations with lower LCP contents are readily accepted by the manufacturers, which will be accomplished only by viscosity ratios far below unity.

#### 2.1.2.3. Other Factors

The LCP content, the viscosity ratio, and the processing conditions (for example, stretching or drawing, extensional flow) are correlated to each other.

Blizard and Baird pointed out that when the LCP content is 30%, LCP can form fibrils for all values of the viscosity [29]. They also found that fibrils would form in elongational flow regardless of the viscosity ratio [16]. However, the final fibrous form of LCP blends limits the practical application. It is the authors' opinion that most results reported in the literature may be acceptable; however, the fibril formation of LCP in thermoplastic polymers is very complicated because of many factors. The techniques to maximize the LCP reinforcing function would be developed by matching and optimizing all the factors, and fabrication conditions affect the overall performance.

## 2.2. COMPATIBILIZATION

The in situ composite is a multi-phase system consisting of a dispersed LCP phase and a continuous polymer phase. For effective stress transferring from the matrix to the reinforcement, it is necessary to have a strong interfacial interaction between the reinforcing LCP fibrils and the reinforced thermoplastic resin. However, the enthalpy of mixing thermotropic rigid rod-like LCPs with thermoplastics of flexible chains is mostly positive. The small increase in entropy caused by mixing these two polymers is not large enough to compensate the enthalpy increase; thus, the change in the free energy because of mixing is usually not a negative value. Thermodynamically, this indicates that the mixing is not favorable. Almost all pairs of LCPs and thermoplastics, reported so far, are immiscible, which leads to weak interfacial interaction. The addition of LCPs to thermoplastics results in a significant increase in the modulus of the in situ composites, but the strengths are only slightly superior to those of the matrix polymers [35–38]. The weak interfacial interaction between LCP fibrils and the matrix polymers limits the wider application of in situ composites. Therefore, it is understandable that the compatibilization in in situ composites becomes one of the most important research topics, except the fibrillation just discussed above.

The compatibilization in in situ composites can be accomplished by introducing interactions between the two phases physically or chemically, including specific interactions, hydrogen bonding, chemical interaction, or a combination of these. In recent years, more and more attention has been paid to the compatibilization in in situ composites. In the following sections, several approaches and techniques to yield better compatibilization will be reviewed and classified.

### 2.2.1. Using a Third Component as a Compatibilizer

For immiscible polymer blends, using a third component as a compatibilizer is a common and effective method [39]. Many block or graft copolymers with functional groups offering specific interaction and/or chemical reaction with component polymers have been used as compatibilizers. They may be added

separately to the blend or formed in situ by reactive processing. It is expected that the compatibilizer stays at the interfacial region and reduces the interfacial tension like an emulsifier. Adhesion may be augmented through interpenetration and entanglements. This approach is also utilized for the compatibilization in in situ composites.

### 2.2.1.1. Functionalized Polymers

Baird et al. [40–42] used a functionalized polypropylene, MAH-g-PP, as a compatibilizer for in situ composites based on polypropylene reinforced by different thermotropic LCPs, such as Vectra A950 and B950 and Rodrun LC-3000. They reported that MAH-g-PP tended to improve the interfacial adhesion between the LCP and the matrix polymer, resulting in a finer and uniform distribution of the dispersed LCP fibrils. As a consequence, a significant enhancement in both tensile modulus and strength was achieved in LCP/PP blends. No direct evidence confirms the reaction between MAH-g-PP and the LCP; however, they suggested that some specific interactions, such as hydrogen bonding, are responsible for the compatibilization. More recently, Baird and his co-workers [43] investigated the compatibilization of a reactive terpolymer based on ethylene-acrylic ester-maleic anhydride in Nylon 11/LCP blends. Their results showed that a small amount of terpolymer added led to in situ composites with significantly higher modulus and strength along the machine/reinforcing direction and substantially higher strength and toughness along the transverse direction of injection-molded parts. Furthermore, compatibilized by the terpolymer, the final injection-molded articles displayed a smoother surface. These behaviors were attributed to enhanced fibrillation of the LCP and improved interfacial adhesion between the LCP fibrils and polymer matrix. It should be noted that there is an optimal amount of a compatibilizer for each LCP blend system. Adding too much MAH-g-PP to LCP blend samples may result in too small dispersed LCP droplets to form fibrils in the molding process followed. Therefore, the optimal amount of a compatibilizer is critical for overall enhancement of mechanical performances of in situ composites.

Seo reported the compatibilization of maleic anhydride-grafted ethylene-propylene-diene terpolymer (MAH-g-EPDM) in PA46/Vectra B950, PA6/Vectra B950, and PBT/Vectra B950 blends, etc. [44–48]. It is shown that a fine fibril structure of LCP could be developed by a shear flow in a thermoplastic matrix, even though the viscosity of the matrix was lower than the dispersed LCP. It was believed that this phenomenon resulted from the in situ compatibilization of MAH-g-EPDM, depicted as follows. Some chemical reactions between MAH groups and functional groups of the LCP were responsible for the compatibilization (as shown in Figure 7.2). The deformation scheme of a dispersed LCP phase in the compatibilized blend is shown in Figure 7.3 [46].

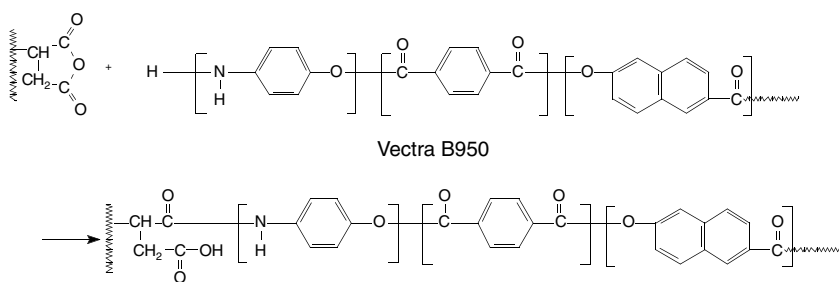
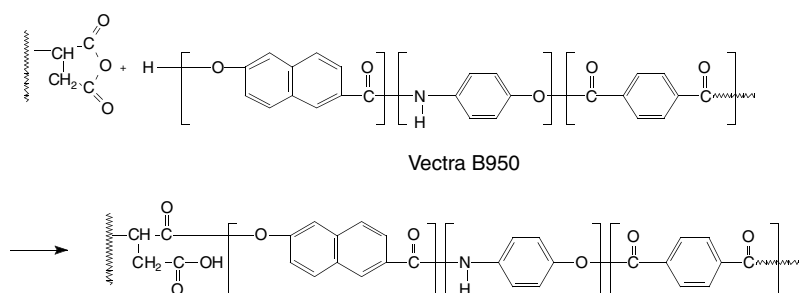
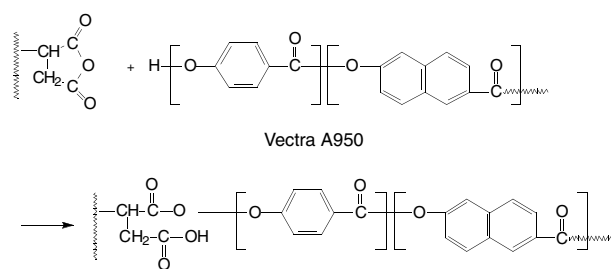
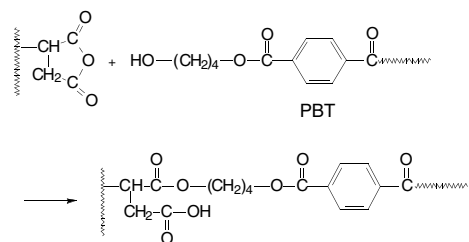
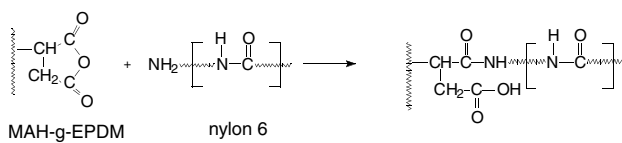


**Figure 7.2** Schematic representation of possible reactions in compatibilized in situ composites.

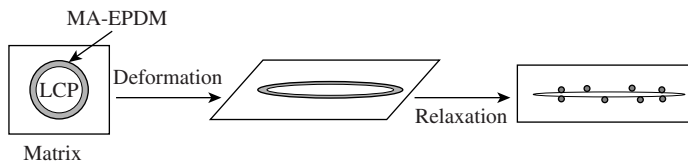


**Figure 7.3** The deformation scheme of a dispersed TLCP phase in the compatibilized in situ composites [46].

Chin and his co-workers conducted an interesting study on compatibilization of compatibilizers with epoxide functionalities in LCP/PET blends [49]. The addition of these compatibilizers resulted in higher stiffness, strength, and toughness of compatibilized LCP blends. It was suggested that an epoxy-*co*-PET-*co*-LCP mixed copolymer was formed in situ during the melt processing, which would reduce the interfacial tension between these phases and would enhance the fibril formation. However, the formation of this copolymer, or particularly the reaction of epoxy with the LCP, was not proven. Only the reduction of the amount of epoxide groups was proven by infrared spectroscopy. Chin et al. hypothesized that these epoxide groups might undergo hydrolysis and other unknown reactions.

#### 2.2.1.2. Ionomers

In recent years, ionomers, i.e., polymers containing a small amount of bonded ionic groups, have attracted more and more attention, because of their unusual compatibilization ability in many immiscible polymer blends. Ionic groups, especially acid groups and metal ionic groups, in ionomers can cause several interactions with polar groups when ionomers are blended with polar polymers. These possible interactions include dipole-dipole, ion-dipole, ion-ion, and hydrogen bond. These interactions can serve as physical crosslinks at the interface, reduce interfacial tension, and improve interfacial adhesion. Eisenberg and Hara [50] found that interactions between anions on one polymer and cations on the other resulted in miscibility of otherwise immiscible polymer pairs. Dutta and co-workers [51] observed an unusual phenomenon: zinc salt of sulfonated polystyrene (Zn-SPS) was miscible with an LCP (Vectra A950). The LCP/Zn-SPS blends exhibited only a single  $T_g$ , measured by DSC, which agreed well with the Fox equation prediction. In addition, Zn-SPS added to the blends of LCP/polycarbonate and LCP/PA66 acted as an effective compatibilizer for both blend systems. This work started the compatibilization of ionomers in in situ composites, i.e., polymer blends containing LCP. Following this, He and co-workers [52] found that lightly sulfonated PS was partially miscible with PSF, PC, and LCP. The specific interaction between the ionic groups of SPS

and the polar groups in PSF and PC led to the compatibilization of SPS in LCP/PSF, LCP/PC, and LCP/polyetherimide (PEI) blends. As a result, ternary blends of LCP/SPS/PSF, LCP/SPS/PC, and LCP/SPS/PEI have enhanced mechanical properties with acceptable processability. Using DSC and SEM, He [53] further found that chemically modified PS, sulfonated PS (SPS), and four of its salts were miscible with the LCP, a copolyester of *p*-hydrobenzoic acid and poly(ethylene terephthalate), although their molecular structures and the rigidity of their molecular chains differed greatly from each other. FTIR study revealed that miscibility enhancement was caused by specific interactions between the carbonyl groups of LCP and sulfonate groups of the acid form of SPS. Clearly, ionomers can act as an effective compatibilizer for various LCP blends, which is of practical interest.

### 2.2.1.3. Block and Graft Copolymers

Block or graft copolymers can be also used as a compatibilizer if the block or graft copolymers are composing the segments whose chemical structure and solubility parameters are similar to those of the polymers being blended. Magagnini and his co-workers [54–64] prepared a series of copolymers containing the monomer units of the polymers being blended, including PP-LCP, PE-LCP, and PET-LCP, and used them to compatibilize PP/LCP, PE/LCP, and PET/LCP blends, respectively. They found that the addition of a small amount of these copolymers led to a significant enhancement of interfacial adhesion between LCP and matrix polymers, and resulted in significant improvement of both tensile strength and elongation at break. For references, Table 7.4 lists various third components acting as compatibilizers in different in situ composites.

### 2.2.2. Transesterification

It is well known that polyesters can undergo acidolysis by acid-end groups, alcoholysis by hydroxyl-end groups, and inter-chain ester-ester interchange (transesterification) with itself or with other polyesters at elevated temperatures [85]. For high molecular weight polyesters and their blends, the probability of transesterification occurring is much higher than that of acidolysis or alcoholysis, because of relatively low end-group concentration. Therefore, transesterification usually dominates the reaction process. Transesterification has serious effects on the properties of polymers. For example, the molecular weight of polyester decreases with the increasing extent of transesterification. On the other hand, the miscibility of polyester blends could be enhanced by transesterification, due to the presence of the resultant hybrid chemical structure.

The compatibility between some thermotropic liquid crystalline copolyesters and other isotropic polyesters, such as poly(ethylene terephthalate) [86–90], poly(butylene terephthalate) [91–94], poly(ethylene naphthalate) [95],

TABLE 7.4. Various Third Components Acting as Compatibilizers and the Compatibilized in situ Composites.

Compatibilizer	Blend	Ref.
EGMA (ethylene-glycidyl methacrylate)	PP/Vectra A900	[65]
PP-g-MAH	PP/Vectra B950	[40–42]
	PP/Vectra A900	
	PP/LC-3000	
	PP/Vectra A950	[66–69]
	PA/Vectra A950	
	PA6/Vectra B950	[70]
	PA66/Vectra B950	[71]
Terpolymer (ethylene-acrylic ester- maleic anhydride)	PA11/HX8000	
	PA11/LC-3000	[43]
	PA6/HX8000	
	PA6/LC-3000	
EEAGMA (ethylene-ethyl acrylate- glycidyl methacrylate)	PP/LCP	[72]
LC-3000-g-MAH	PA6/LC-3000	[73]
EPDM-g-MAH	Nylon46/Vectra B950	[44–48]
	Nylon6/Vectra B950	
	PBT/Vectra A950	
S-GM	Noryl/Vectra A950	[74]
Styrene-glycidyl methacrylate		
Methyl methacrylate- <i>N</i> -methyl-dimethyl- glutarimide	PC/Vectra A950	[75]
PE-MAA	PE/Vectra RD501	[76,77]
PP-AA (Acrylic acid-functionalized PP)	PP/Rodrun LC-3000	[78–80]
DCTPPS Dicarboxyl-terminated PPS	PPS/ Vectra A950	[81]
Ionomer (sulfonated polystyrene)	PA66/ Vectra A950	[51]
	PC/ Vectra A950	
	PSF/PHB-PET	[52,53]
	PC/ PHB-PET	
	PEI/ PHB-PET	
PET-LCP (SBH)	PET/SBH	[54]
PE-LCP(SBH)	PE/SBH	[55–61]
PP-g-LCP(SBH)	PP/SBH	[62–64]
BP-b-PSF	PSF/BP-LCP	[82]
Polyhydroxyether	PET(modified with a dianhydride)/Vectra A900	[83,84]

polycarbonate [96–101], and polyarylate [102,103], can be enhanced by transesterification reactions under proper conditions. The first work concerning the miscibility of polymer blends containing LCP was conducted by Kimura and Porter [91] by studying the miscibility of PBT/PHB-PET blends by means of DSC, and they conjectured that reactions were created readily between the component PBT and PET-rich fraction of PHB-PET. Laivins [104,105] studied the interactions in an in situ composite (PHMT/X7G) and found that blending at an elevated temperature caused reactions between the components, with the confirmation of DSC, DMA, and NMR measurements. This reaction in the melt was the cause of the apparent miscibility of PHMT with X7G.

In the previous investigation [29,106–108] of the PET blends with the thermotropic liquid crystalline copolyesters (PHB-PET), several conclusions were drawn concerning the miscibility in these blends; however, no specific interchange reactions between the components were shown or confirmed. Perhaps this was confined by the limitation of instruments. But it is necessary to notice that the extent of transesterification in polymer blends strongly depends on their blending conditions, including mixing temperature and time, preparation method, viscosity ratio, and the presence of a catalyst and inhibitors. These conclusions were later confirmed by several researchers [90,95,97]. Ou et al. [86–89] studied transesterification occurring in blends of PET and a series of PHB-PET copolyesters having different PHB molar ratios. Their results showed that transesterification sometimes had some side effects on the properties of in situ composites. They claimed that, as the transesterification in blends was continuing, new amorphous miscible blends would form. This brought about the loss of the liquid crystalline characteristics and spoiled the starting purpose of blending with LCP. Thus, it is important to control a balance of enhancing the miscibility and maintaining the liquid crystalline character during transesterification.

Wei et al. [98–101] investigated the transesterification mechanism and reaction rate in blends of PC and an LCP (PHB/PET60/40). More recently, Guo [109–111] suggested experimentally that transesterification was a result of the compatibility, instead of a prerequisite of compatibility, e.g., transesterification was determined by the initial compatibility of polymer blends. This is an academic argument, but the presence of transesterification at least favors the compatibilization in in situ composites. Further investigation of the transesterification in LCP blends is needed in the coming years.

### 2.2.3. Ternary Polymer Blends

In general, two main problems are associated with binary blends containing LCP: a poor interfacial adhesion between the LCP and thermoplastic matrix and a difficulty in controlling the LCP fibrillation. Ternary polymer blends are gaining an important share in the field of polymer property diversification

through blending. Recently, the list of ternaries investigated has been considerably enlarged. In these blends, generally, a third polymer, either a homopolymer or copolymer, is added to an immiscible polymer pair. This action produces a miscible system in which the third polymer is miscible with respective component polymers and the modified interface improves the adhesion between these components.

Ternary blends containing LCPs also show an attractive approach to the development of reinforced systems. The differences between ternary polyblends and polyblends with a third component (a compatibilizer) added are that in the latter, usually the third component is a pre-made compound (or polymer) and its fraction in compatibilized blends is less than 10 wt%. The third polymer used in ternary blends is an as-received commercial product, and its content in ternary blends can be changed for tailoring the properties of blends.

Bretas et al. [112–115] first investigated a ternary blend containing an LCP, polyetherimide (PEI)/poly(ether ether ketone) (PEEK)/LCP (HX4000), because the blends of PEEK/HX4000 were miscible up to 50 wt% HX4000, but, were partially miscible above this value. The binary blends of PEI/PEEK were completely miscible in their amorphous state over the whole composition range. The PEI/HX4000 blends were partially miscible in the whole concentration range. Therefore, the ternary blends of PEI/PEEK/HX4000 were partially miscible. The morphology of partially miscible systems was quite different from that of an immiscible system. The ternary blends with high moduli could be obtained at high LCP loadings, while composites with high ultimate tensile strength could be obtained with high loadings of PEI or PEEK. This ternary blend has exhibited potential applications in the field of wear and lubrication [116].

Mai et al. [117,118] investigated properties of PC/PBT/LCP ternary in situ composite. Good LCP fibrillation was observed in injection-molded ternary blends. The addition of PBT to PC matrix improved skin-core distribution of LCP microfibrils, and the LCP (Vectra B950) with terephthalate acid groups enhanced the interfacial adhesion in the composite. The ternary blends also exhibited lower melt viscosity than PC/PBT blends and pure LCP. In a ternary system with 30 wt% of Vectra B950, the tensile modulus and tensile strength increased approximately threefold and twofold, respectively. The rule of mixtures for continuous reinforcement could accurately represent the strengthening effects for the ternary LCP in situ composites. Generally, LCP reduces the ductility and impact strength of thermoplastic blends. However, the relative loss in ternary systems is less than in binary systems. The multiphase matrix provides great flexibility in engineering composite design and manufacturing. Other ternary blends containing LCP, referred to as PET/PC/Vectra A950 [119], PPS/PSF/Vectra B950 [120], and PA6/ABS/Vectra A950 [121], were reported, too.

Wei et al. [122] added a second LCP (PHB-PET) to an originally immiscible blend of Vectra A950 and PEI, and this resulted in better interfacial adhesion

between A950 and PEI as evidenced by the morphological observation with SEM. The enhancement in the interfacial adhesion caused an increase in the ultimate tensile strength and impact strength of these ternary blends of Vectra A950/PHB-PET/PEI, as compared to those of the corresponding binary blends of Vectra A950 and PEI in an injection-molding process. Ternary blends of two LCPs with thermoplastics were also investigated by Lee et al. [123]. They found that, in ternary blends of LCP<sub>1</sub> (K161)/LCP<sub>2</sub> (PHB/PET60/40)/PET (or PC) systems, the presence of the second LCP (PHB/PET60/40) not only gave rise to a finer dispersion of the dispersed phase and very strong bonding between the phases, but also lowered the possible processing temperature, thus avoiding thermal degradation of the matrix. The shift of glass temperature of PET indicated an improved compatibility, compared to a binary blend. While with PC as the matrix, an improved wetting was suggested as being responsible for this compatibilization.

### 2.3. MECHANICAL PERFORMANCE OF IN SITU COMPOSITES

Compared to most isotropic polymers, thermotropic LCPs possess outstanding mechanical properties due to their rigid rod-like backbones. It has been reported that LCPs have tensile strength in a range of 150 to 400 MPa and tensile modulus from 13 to 25 GPa, while LCP fibers have tensile strength ranging from 500 to 650 MPa and tensile modulus from 50 to 100 GPa. When LCPs are blended with thermoplastics in a process where an elongational flow field exists, the LCP phase will deform into molecularly oriented fibers that reinforce the thermoplastic matrix. So, until now, many isotropic polymers have been blended with LCPs. Table 7.5 summarizes various in situ composites reported, with their machine direction mechanical properties.

From this table, several conclusions can be drawn. First, nearly all the isotropic polymers, including commodity plastics such as PP, PE, and PVC, engineering plastics such as PC, PET, PBT, and PA, and advanced engineering plastics (or high-performance plastics) such as PEEK, PSF, PES, PEI, and PPS, have been blended with various LCPs. Second, in almost all the in situ composites listed here, the tensile modulus is improved by the addition of an LCP, while the tensile strength is varied from system to system. In some cases, tensile strengths are improved due to the addition of LCPs, while, in other cases, tensile strengths are lower than that of a neat thermoplastic matrix. Based on the previous discussion in this chapter, these are mainly caused by the different interfacial adhesion in respective in situ composites. Third, through the compatibilization in in situ composites, the mechanical properties of original immiscible LCP blends can be increased significantly. Finally, compared to injection molding, fiber spinning and drawing after extrusion make in situ composites of the same composition possess higher tensile properties.

TABLE 7.5. The Mechanical Properties of in situ Composites (along Machine/Flow Direction).

TP	TLCP Content	Tensile Strength (MPa)	Tensile Modulus (GPa)	Elongation (%)	Izod Impact (J/m)	Processing Method	Ref.
PE	—	9.0	0.22			Cast film	[77]
	10% Vectra RD501	22.0	1.0				
	—	9.0	0.22			Blown film	
	10% Vectra RD501	25.0	1.2				
PP	—	31.2	1.369			Injection molded	[41]
	30% Vectra A950	36.6	3.759	1.64			
	30% Vectra A950 (com)	49.8	4.255	1.92			
	30% Vectra B950	23.1	3.69	1.04			[42]
	30% Vectra B950 (com)	25.3	3.99	0.96			
	30% LC3000	28.6	2.137	2.14			[41]
	30% LC3000 (com)	41.2	3.589	2.61			
PVC	—	44.52	1.365	26.35		Injection molded	[124]
	5% PHB-PET	48	1.8	3.5			
	10% PHB-PET	46	1.6	3			
	25% PHB-PET	40	1.6	2.8			
PS	—	28.0	1.41			Compression molded	[125]
	10% PHB-PET	22.5	1.67				
	—	32.0	1.82			Extrudates	
	10% PHB-PET	25.3	1.95				
	—	43.6	2.04			Spun fiber	
	10% PHB-PET	37.5	2.63				
PET	—	61	2.72	294		Injection molded	[126]
	30% Vectra A950	84	5.5	2.0			
	—	40	0.95			Injection molded	[127]

www.iram-mavad.com

مرجع دانشجویان و مهندسين مواد

TABLE 7.5. (continued).

TP	TLCP Content	Tensile Strength (MPa)	Tensile Modulus (GPa)	Elongation (%)	Izod Impact (J/m)	Processing Method	Ref.
	10% PHB/PET (60/40)	43	1.17				
	—	59.3	1.55			Compression molded	
	10% PHB/PET (60/40)	68.4	1.9				
	—	60.5	1.93			Extrudates	
	10% PHB/PET (60/40)	67.8	2.54				
	10% Vectra A950	200	7.3				
	20% Vectra A950	293	11.2			Spun fiber	[128]
	40% Vectra A950	483	16.8				
PBT	—	51.7	2.58	5.8		Injection molded	[9]
	30% Vectra A950	37.9	3.54	1.2			
PA	—	73.1	2.06	436	31.9	Injection molded	[9]
	30% Vectra A950	66.9	2.65	14.6	20.3		
	30% Vectra B950	60.7	3.16	2.5	11.6		
PA66	—	62	1.05	62		Extrudates, fiber or film	[51]
	20% Vectra A950	81.0	1.2	81.0			
	20% Vectra A950 (5% SPS)	107.0	1.31	107.0			
PA6	40% HX8000	63.6	4.70			Injection molded	[43]
	40% HX8000 (5% terpolymer)	85.7	5.74				
PA11	—	31.5	0.89			Injection molded	[43]
	35% HX8000	53.9	3.51				
	35% HX8000 (4% terpolymer)	63.9	4.45				
PA12	—	29	1.1	>100		Extruded rod	[129]
	20% Vectra A950	89	3.8	3			
	30% Vectra A950	165	9.3	2.1			

TABLE 7.5. (continued)

TP	TLCP Content	Tensile Strength (MPa)	Tensile Modulus (GPa)	Elongation (%)	Izod Impact (J/m)	Processing Method	Ref.
PC	—	66.9	2.32	100	462	Injection molded	[9]
	30% Vectra A950	121	5.72	3.49	14.8		
	30% Vectra B950	154	6.55	4.2	12.8		
	—	40	1.58	76			[51]
	20% Vectra A950	49.0	1.70	10.0			
	20% Vectra A950 (10% SPS)	58.5	1.90	4.8			
PEN	30% Vectra B950	146	12.5				[140]
	—	83		48.53		Injection molded	[130]
	10% Vectra A950	87		11.54			
	30% Vectra A950	112		6.22			
PPO	—	79.4	1.2			Injection molded	[27]
	10% Vectra A950	40	2.2				
	25% Vectra A950	60	2.8				
PPO/PS	—	69	3			Injection molded	[131]
	25% Vectra B950	63.7	6				
PAr	—	71.0	1.52	155	45.6	Injection molded	[9]
	30% Vectra A950	102	4.27	5.3	18.6		
	30% Vectra B950	51.7	3.28	2.0	8.4		
PEEK	—	84.1	3.5	48		Extrusion	[9]
	30% Vectra A950	71.7	4.3	2.5			
	—	116	5	83.7	60	Extrusion	[132]
	25% Vectra A950	123	16.5	1–2	50		
PES	—	64.3	2.52	74.7		Extrusion strand (shear rate = 240)	[9]
	30% Vectra A950	115.8	4.16	5.9			
	30% Vectra B950	139.9	11.8	1.9			
	—	63.6	2.50	122	42.1	Injection molded	

www.iran-mavad.com

مرجع دانشجویان و مهندسين مواد

TABLE 7.5. (continued).

TP	TLCP Content	Tensile Strength (MPa)	Tensile Modulus (GPa)	Elongation (%)	Izod Impact (J/m)	Processing Method	Ref.
PES-C	30% Vectra A950	125.5	4.99	3.8	19.2	Injection molded	[133]
	30% Vectra B950	172.4	8.82	2.6	19.2		
	—	100	16				
	10% Rhodester	90	19				
	25% Rhodester	85	20				
PSF	—	65				Spun fiber	[134]
	25% Vectra A950	200			DR = 2		
	25% Vectra A950	300			DR = 4		
	20% PHB-PET	50.2	0.75			Injection molded	
	19.6% PHB-PET (+2% SPS)	87.8	1.04				
PPS	—	82	3.697			Injection molded	[81]
	10% Vectra A950	84	3.987				
	10% Vectra A950 (com)	89	3.649				
	25% Vectra A950	87	4.803				
	25% Vectra A950 (com)	98	6.632				
new TPI	—	72	2.5	33		Injection molded	[135]
	30% Xydar SRT900	100	3.5	8			
PEI	—	91.0	3.05	59	24.7	Injection molded	[9,136]
	30% Vectra A	129	5.15	4.3	19.1		
	30% Vectra B	95.8	7.45	1.54	18.6		
	30% HX4000	152	9.7	2.28			
	30% K161	129	8.7				
	30% Granlar	129	9.0	2.05			

www.iran-mavad.com

مرجع دانشجویان و مهندسين مواد

However, there is a major drawback associated with in situ composites: the mechanical anisotropy that also occurs in neat thermotropic LCP products. Compared to glass fiber-reinforced plastics, the mechanical anisotropy observed for in situ composites is stronger. It has been recognized that this anisotropy is caused by fibrils being generated only in the direction of the elongational flow field developed at the advancing melt front. For example, the degree of anisotropy (ratio of machine to transverse direction properties) for glass fiber-reinforced thermoplastics ranges from about 1.1 to 1.7 due to the more random orientation of the reinforcing fibers in one plane. However, the degree of anisotropy in an in situ composite is higher. The degree of anisotropy of in situ composites may be affected by several factors including fibrillation of LCP, LCP concentration, process conditions, and interfacial adhesion between LCP fibrils and matrix resins. So, the degree of anisotropy of various in situ composites reported was different from system to system. In an investigation of the morphology of PC/LCP (Vectra) blends, Isayev and Modic [22,138] found that pure LCP has a high degree of anisotropy, whereas PC has little anisotropy. The ratios of anisotropy of blends containing different LCP contents were in a range of 1 to 2. In another study, Mehta and Isayev [25,139] found that PEEK/LCP (Vectra A950) blends retained isotropic behavior up to 5% LCP concentration. However, above 10% LCP concentration, a high degree of anisotropy of blends was observed, and the degree of anisotropy increased with the increasing LCP concentration. The high degree of anisotropy in thermoplastics/LCP blends has been reported by other researchers [140–143]. For example, Baird et al. [143] studied the anisotropy of blends of HX1000 and HX4000 with PEI. The degree of anisotropy of the in situ composites was found to increase from about 3 to 4.5 as the LCP content increased from 25 to 75 wt%.

Choy et al. [144] investigated the elastic modulus of an LCP (Vectra B950) and its in situ composites with PC as a function of draw ratio  $\lambda$  from 1 to 15 with the help of an ultrasonic method. Five independent elastic constants were used to describe the elastic behavior of LCP and PC/LCP in situ composites. The axial Young's modulus significantly increased with increasing  $\lambda$ , due to higher aspect ratios of the LCP domains in the composites and the improved molecular orientation within the domains. The reinforcing effect on other moduli was much weaker, with transverse Young's modulus and axial shear modulus of the composites only 5 to 30% higher than those of PC with a  $\lambda$  of 15. Because transverse shear modulus of the LCP decreased to a value below that of PC at  $\lambda > 2$ , so Choy and co-workers suggested that there was a positive reinforcement effect at a low  $\lambda$  but a negative effect at a high  $\lambda$ .

Many efforts have been undertaken to overcome the mechanical anisotropy of in situ composites through processing [145–156]. In recent years, pre-extruded thermoplastic LCP sheets, strands, and fibers have been used to produce composites with a good balance in machine direction and transverse direction. Bassett and Yee [145] used a method consisting of spinning composite fibers

from a melt blend of a thermoplastic with an LCP, followed by aligning and placing these composite fibers in a mold and heating to melt the thermoplastic matrix, but not to melt the LCP fibrils generated in situ during the spinning process. A finished composite structure reinforced by the LCP fibrils was obtained when the thermoplastic phase was consequently consolidated.

Isayev et al. [148] prepared self-reinforced prepregs of PP/Ultrax KR-4002, PPO/Vectra A950, and PS-PPO/VectraA950 by stretching sheets extruded through a coat hanger die. At this stage, processing was carried out at temperatures at which both components were melt processable. In the second stage followed, the prepared prepregs were laid up in multi-layers in the direction parallel to the stretching direction or in the direction  $+45^\circ/-45^\circ$ , and the lay-ups were compression molded into unidirectional or quasi-isotropic laminates at temperatures below the melt processing temperatures of the LCPs. The mechanical properties of these samples were dependent on sheet draw ratio and reduction ratio in the consolidation step. In this study, composites with biaxial properties were obtained. The highest tensile strength and secant modulus of the  $+45^\circ/-45^\circ$  composite, made of films of 50/50 w/w PP/Ultrax KR-4002, were 60MPa and 13GPa, respectively. However, one drawback of using in situ composite films with high mechanical properties was that a high LCP concentration was necessary.

Baird and co-workers [147,149,154,155] attempted to process pelletized in situ composite strands, or micro-composites, in injection molding and extrusion at temperatures below the melting temperature of LCPs. In a study on the processing of micro-composites, Baird et al. [154] attempted to produce LCP-reinforced composites at temperatures below the melting temperature of the LCP. With PP/30 wt% Vectra B, the composite, injection molded with the third zone barrel at  $250^\circ\text{C}$ , about  $35^\circ\text{C}$  lower than the melting temperature of Vectra B, showed a better balance between the machine and transverse direction properties, as compared to an in situ composite. However, this improvement in the balance of machine and transverse direction properties was the result of a 35% reduction in the machine direction properties, rather than an improvement in the transverse direction properties. This reduction in machine direction properties was believed to be the result of the loss of the fibrillar LCP structure by breakage and agglomeration in the screw of the injection-molding unit. The study by Baird et al. leaves a number of questions that still need to be answered about the processing and use of micro-composites.

In a further study, Handlos and Baird [155] investigated the mechanical properties of injection-molded composites using pellets of polypropylene containing pre-generated microfibrils of thermotropic LCPs, referred to as micro-composites. The LCPs used are HX6000 and Vectra A950. The micro-composites were produced by drawing strands of PP and LCPs generated by means of a novel mixing technique (using a dual extruder system), followed by pelletizing the strands. The work was undertaken in an effort to improve the

properties observed for in situ composites in which LCP fibrils were generated during molding filling. The influences of in situ composite strand properties, the temperature used in injection-molding, the LCP concentration, and the melt temperature of the LCP on the properties of the injection-molded composite were discussed. It is found that when the blend pellets were processed at appropriate temperatures, the LCP microfibrils were maintained through injection-molding, and the composites showed a good balance between machine and transverse direction properties (with ratios of the machine and transverse direction moduli ranging from 1.1 to 1.35), as shown in Table 7.6. The use of HX6000 rather than Vectra A allowed for higher processing temperatures to be used during injection molding. The moduli of the injection molded composites increased with both increasing LCP composition and in situ composite strand moduli. At 10 wt% LCP, the modulus of the injection-molded composite approached the prediction of composite theory, while at 20 and 30 wt% LCP, negative deviations from the theoretical values were found. They stated that this was a result of a loss of fiber aspect ratio from fiber breakage and agglomeration. It is believed that, with future studies on the effect of shear and elongational stresses on the aspect ratio of the fibrils during processing, a method to overcome this problem may be found. The modulus of a 20 wt% HX6000 composite was similar to that of a 20 wt% glass fiber composite (3.21 GPa versus 3.66 GPa), but the tensile strength of the HX6000 composite was about 28% lower than that of the glass fiber composite. The authors expected that, as the modulus and strength of the reinforcing LCP fibrils are improved, the properties of the injection-molded micro-composites should exceed those of glass fiber-reinforced composites.

### 3. IN SITU HYBRID COMPOSITES

Fabrication of in situ composites is an approach to reinforce thermoplastics. Although this approach has received much research attention for one decade, the prospect of these in situ composites containing LCP fibrils seems not as bright as previously expected. One of the main reasons is the limited improvement of mechanical performances achieved only by LCP fibrils. This limitation can be understood clearly by the analysis of the data shown in Table 7.7. Carbon/graphite fibers have quite high strengths and moduli up to 7 GPa and 800 GPa, respectively. Glass fibers have as high as 4 GPa of strength and 80 GPa of modulus with a very low price, compared to carbon fibers. Compared to these fibers, thermotropic LCP fibers, spun under their optimized conditions, have higher strengths and moduli than glass fibers, but with a higher cost for their raw materials. When LCPs are blended with thermoplastic polymers for making in situ composites, the formation of their fibrils in the blend melt (i.e., fibrillation) will be accomplished during melt processing, such as extrusion, injection molding, and spinning, where the fibrillation conditions are far from

TABLE 7.6. The Tensile Properties of Machine and Transverse Directions of in situ Composites.

Samples	Machine Direction			Transverse Direction			Ref.
	Modulus (GPa)	Strength (MPa)	Elongation (%)	Modulus (GPa)	Strength (MPa)	Elongation (%)	
PP/20% Glass	3.66	49.1	<2	2.78	33.2	<2	[155]
PP/20% Vectra A	2.31	37.6	4.53	2.18	21.6	2.44	
PP/20% HX6000	3.23	35.8	4.36	2.44	22.5	3.76	
PEI/10% Vectra A	3.1	109		2.6	91		[156]
PEI/20% Vectra A	4.6	142		2.6	58		

[www.iran-mavad.com](http://www.iran-mavad.com)

مرجع دانشجویان و مهندسين مواد

TABLE 7.7. Mechanical Properties of Fibers.

Fiber	Density (g/cm <sup>3</sup> )	Tensile Strength (GPa)	Tensile Modulus (GPa)
Carbon/Graphite			
T300	1.76	3.5	230
M40	1.81	2.7	390
T1000	1.72	7.2	220
M60	1.94	3.8	590
P120	2.18	2.1	810
Glass			
E-	2.53	3.7	77
S-	2.45	4.3	88
Thermotropic LCP			
Vectra	1.41	3.3	76
Ekonol	1.40	3.9	136

those of an optimized LCP spinning process. As a result, LCP fibrils formed in situ in the matrix have larger diameters, smaller aspect ratios, and lower mechanical properties, compared to the fibers spun from the same LCP. How can we demand LCPs to play a role in the reinforcement under such inferior conditions? This analysis leads to a new concept of the reinforcing, macroscopically and microscopically hybrid reinforcing [157].

### 3.1. CONCEPT AND MODEL OF IN SITU HYBRID COMPOSITES

A reinforced structure of thermoplastics, named as the in situ hybrid composite, consists of three components in principle: macroscopic fibers such as glass fiber, carbon fiber, or aramid fiber; microscopic LCP fibrils; and a matrix resin [157]. Macroscopic fibers are in their fibrous form before the fabrication of the reinforced composite, while LCP fibrils are generated in situ during the melt processing of the ternary composite.

It seems that, strictly speaking, the in situ hybrid composite is out of the range of LCP blends. But, it has to be discussed here due to the not-so-bright situation expected with in situ composites nowadays. Another reason for the discussion of in situ hybrid composites here is that it is almost impossible to fulfill practical tasks with only pure polymers or LCP blends. Nature and mankind need and produce hybrid materials and need and produce hierarchical structures. The structure of in situ hybrid composites is closer to that of the natural composites.

The characteristics of in situ hybrid composites can be found from their schematic structure (Figure 7.4). Take a composite of LCP/CF/PEEK15/30/55 (by weight) as an example. LCP, CF, and PEEK have their densities of 1.4, 1.8, and 1.3 g/cm<sup>3</sup>, respectively. By assuming carbon fibers with the diameter of

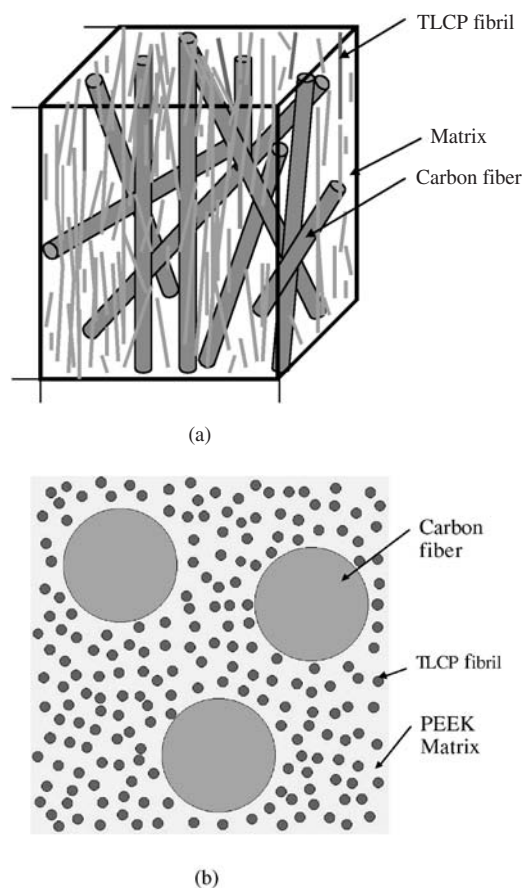


**Figure 7.4** Schematic structure of in situ hybrid composite: 3-D drawing ( $80 \times 80 \times 80 \mu\text{m}$ ) and cross-section ( $25 \times 25 \mu\text{m}$ ) of LCP/CF/PEEK15/30/55.

$8 \mu\text{m}$  and LCP fibrils of  $0.8 \mu\text{m}$ , and all of them in a continuous form, then in an area of  $25$  by  $25 \mu\text{m}$  of the cross-section, 3 carbon fibers and 192 LCP fibrils are dispersed in PEEK matrix (Figure 7.4). The number of LCP fibrils is 64 times of that of CF, the length of LCP fibrils is 64 times of that of CF, and the total surface area of LCP fibrils is 6.4 times of that of CF [158].

### 3.2. HYBRID EFFECT IN IN SITU HYBRID COMPOSITES

With this structure, in situ hybrid composites have their hybrid effects in several aspects: rheology, geometry, and mechanics.

### 3.2.1. Rheology

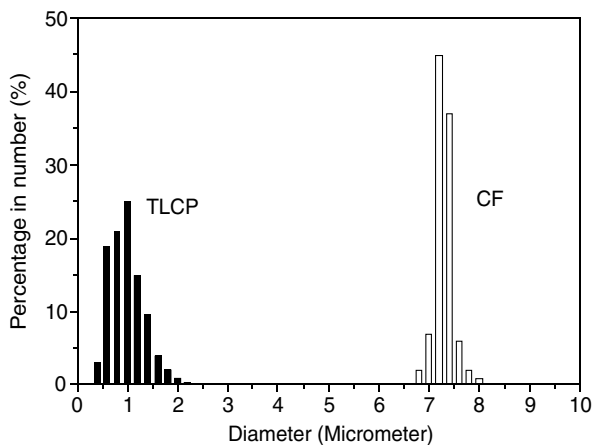
The hybrid effect in rheology means that the addition of macroscopic fibers and LCPs increase and decrease the melt viscosity of the whole material system, respectively. The apparent viscosity and torque for processing of CF/PES, CF/PEEK, and GF/PC reinforced plastics are high due to the existence of these macroscopic fibers in the melt. The addition of LCPs decreases the apparent viscosity and torque significantly, which favors the processing of in situ hybrid composites. The improvement of the processibility is very important for advanced engineering plastics, such as PES and PEEK.

### 3.2.2. Geometry

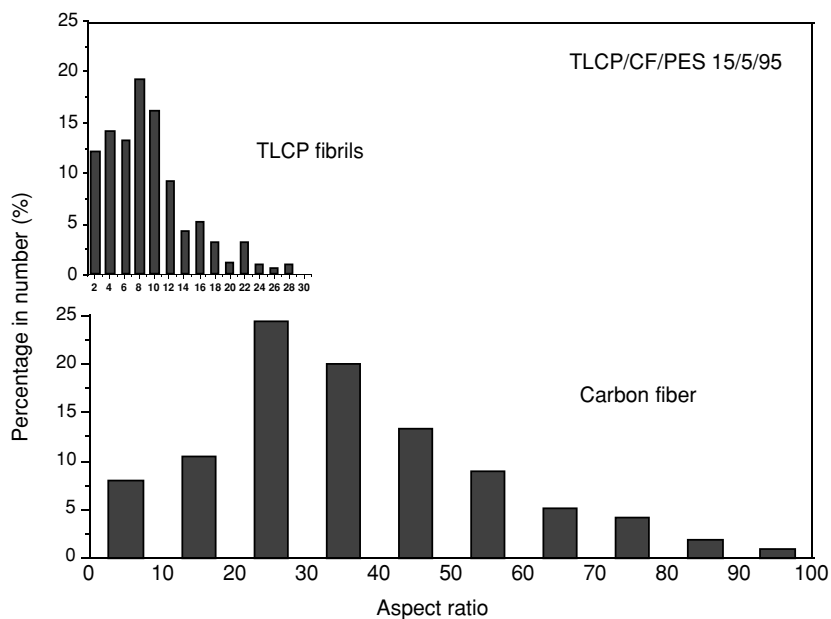
In the aspect of geometry, the in situ hybrid composite contains two groups of reinforcements at two orders of magnitude. Experimentally, the structure of in situ hybrid composites has been formed in injection-molded bars of polyether-sulfone (PES) reinforced by carbon fibers (CF) and liquid crystalline polymer fibrils, by matching the characteristics and processing conditions of the LCP and the matrix resin. Carbon fibers and in situ-generated LCP fibrils have their diameter distribution and intrinsic aspect ratio as shown in Figure 7.5. Their diameters are at two orders of magnitude: CFs with their diameters at the order of  $10^0$  to  $10^1$   $\mu\text{m}$  and LCP fibrils of  $10^{-1}$   $\mu\text{m}$ . CFs have a wide distribution of aspect ratio up to 100, and LCP fibrils have their aspect ratios up to 30. It is doubtless that carbon fibers act as the main load bearer, responsible for the strength and modulus of the composite, while LCP fibrils play the primary role to resist and block the propagation of microcracks in the composite.

Short fiber-reinforced plastics need fibers with large intrinsic aspect ratios, which are responsible for an effective load-bearing effect. But high melt viscosity of fiber/polymer blends leads to the breakage of fibers; otherwise, more energy is expended for processing at higher temperatures. The breakage of macroscopic fibers is minimized by the addition of LCPs, and, furthermore, the aspect ratios of these fibers increase with increasing content of LCPs.

It is also found that the orientation coefficient of these macroscopic fibers along the melt flow direction increases with the addition of LCPs. This can be attributed to the decrease of the melt viscosity. Favored orientation of reinforcing fibers leads to high anisotropy of final materials, which can be taken as a disadvantage if isotropy of the materials is needed. By working with in situ composites, novel technologies have been developed to decrease the anisotropy of final composites [151–156]. These approaches can also be utilized in the case of the in situ hybrid composite, due to their similarity to the in situ composite.



(a)



(b)

**Figure 7.5** The (a) diameter distribution and (b) aspect ratio distribution of LCP fibrils and CFs in an LCP/CF/PES 15/5/95 injection-molded bar [157].

TABLE 7.8. Mechanical Properties of Injection-Molded in situ Hybrid Composites.

Sample	Tensile Strength (MPa)	Tensile Modulus (GPa)
PES	96	0.92
CF/PES 5/95	113	1.38
TLCP/CF/PES 5/5/95	124	1.64
CF/PES 10/90	a	a
TLCP/CF/PES 5/10/90	167	1.90
PEEK	91	2.9
CF/PEEK 15/85	141	5.2
TLCP/CF/PEEK 15/15/70	154	5.6
CF/PEEK 30/70	a	a
TLCP/CF/PEEK 15/30/55	183	8.8

<sup>a</sup> These formulations could not be injection-molded by CS-183 due to their high viscosity.

### 3.2.3. Mechanics

The hybrid effect of mechanics results in the improvement and balance of mechanical properties of resultant in situ hybrid composites. Compared to short fiber-reinforced plastics with high enough mechanical properties, in situ hybrid composites have higher values up to 10%, even 20% (Table 7.8). Interestingly, some highly filled formulations of CF/PES and CF/PEEK become injection-moldable with the addition of LCP and have enhanced mechanical properties (Table 7.8). The main reinforcing effect of this composite comes from the fiber, while LCP fibrils block the propagation of microcracks, which is being revealed experimentally. The improved processability and enhanced properties are of importance for practical application of in situ hybrid composites, especially with advanced engineering plastics as the matrix.

### 3.3. TECHNIQUES FOR THE FABRICATION OF IN SITU HYBRID COMPOSITES

It should be noted that there is not simply an addition of thermotropic LCPs into fiber-reinforced plastics to get in situ hybrid composites. Bafna et al. used glass fibers to decrease the anisotropy of LCP fibril-reinforced polyetherimide [136]. He et al. improved the processability and mechanical performances of glass fiber-reinforced polypropylene by the addition of LCPs [159]. However, these two works did not actively and purposely generate a reinforced composite with the reinforcements having their diameters at two orders of magnitude. The key point for in situ hybrid composites is the formation of LCP fibrils in the material system. As a combination of in situ composite and hybrid fiber reinforcing, the fabrication of in situ hybrid composites utilizes fabrication

techniques for both in situ composites and fiber-reinforced composites. Except for the techniques involved in the fabrication of fiber-reinforced plastics, such as surface treatment of fibers, some important aspects should be taken into account. These are the formation of LCP fibrils with diameters as small as possible, aspect ratios as large as possible and strong enough interfacial interaction between TLCP fibrils and the matrix resin in the multi-phase system. As discussed in previous sections, these are common for in situ composites, due to the similarity between in situ composites and in situ hybrid composites.

Novel techniques have also been developed for the fabrication of in situ hybrid composites for different matrix polymers, such as PES [160], PEEK [161], and polycarbonate [162]. From the view-point of composite mechanics, the in situ hybrid composite has an ideal structure. It contains two reinforcements with their diameters at two orders of magnitude, that is carbon or glass fibers of about 10  $\mu\text{m}$  and liquid crystalline polymer fibrils of submicrometer, which are generated in situ in the fabrication of the composite. Macroscopic fibers act as the main load bearer for the strength and modulus of the material, and microscopic fibrils can block the propagation of microcracks. The TLCP, as one of the components, decreases the viscosity of the whole blend system, favors the orientation of the fiber, and minimizes the breakage of macroscopic fibers. Resulting from the hybrid effect of rheology, geometry, and morphology, in situ hybrid composites have excellent processability and balanced performances. By matching the characteristics of the TLCPs and the matrix resin and matching the processing parameters of ternary blends containing macroscopic fibers, the structure of in situ hybrid composites has been formed experimentally in injection-molded bars. All the conditions for the TLCP fibrillation and compatibilization in in situ composites are needed for the fabrication of in situ hybrid composites. New challenges are faced in experimental and theoretical aspects of material structure and composite mechanics.

#### 4. NOMENCLATURE

ABS	acrylonitrile-butadiene-styrene	PP	polypropylene
PA	polyamide	PPO	poly(phenylene oxide)
PAr	polyarylate	PPS	poly(phenylene sulfide)
PBT	poly(butylene terephthalate)	PS	polystyrene
PC	polycarbonate	PSF	polysulfone
PE	polyethylene	PVC	poly(vinyl chloride)
PEEK	poly(ether ether ketone)	MAH	maleic anhydride
PEI	polyetherimide	SPS	sulfonated polystyrene
PEN	poly(ethylene naphthalate)	HNA	6-hydroxy-2-naphthoic acid
PES	poly(ether sulfone)	HQ	hydroquinone

PET	poly(ethylene terephthalate)	StHQ	styryl hydroquinone
PHB	<i>p</i> -hydroxybenzoic acid	BP	4,4'-dihydroxybiphenyl
IA	isophthalic acid	SA	sebacic acid
PhHQ	phenyl hydroquinone	TA	terephthalic acid

## 5. REFERENCES

1. M. Takayanagi, T. Ogata, M. Morikawa, and T. Kai, *J. Macromol. Sci. Phys.*, B17, 591 (1980).
2. M. Takayanagi, *Pure Appl. Chem.*, 55, 819 (1983).
3. W. F. Hwang, D. R. Wiff, C. Verschoore, G. E. Price, T. E. Helminiak, et al., *Polym. Eng. Sci.*, 23, 784 (1983).
4. W. F. Hwang, D. R. Wiff, C. L. Benner, and T. E. Helminiak, *J. Macromol. Sci. Phys.*, B22, 231 (1983).
5. G. T. Pawlikowski, D. Dutta, and R. A. Weiss, *Annu. Rev. Mater. Sci.*, 21, 159 (1991).
6. E. G. Joseph, G. L. Wikes, and D. G. Baird, *Polym. Prep.*, 24, 304 (1983).
7. E. G. Joseph, G. L. Wikes, and D. G. Baird, *Polym. Prep.*, 25, 94 (1984).
8. A. Siegmann, A. Dagan, and S. Kenig, *Polymer*, 26, 1325 (1985).
9. G. Kiss, *Polym. Eng. Sci.*, 27, 410 (1987).
10. T. S. Chung, *Plastics Engineering*, 43, 39 (1987).
11. W. Brostow, *Polymer*, 31, 979 (1990).
12. D. Dutta, H. Fruitwala, A. Kohli, and R. A. Weiss, *Polym. Eng. Sci.*, 30, 1005 (1990).
13. A. I. Isayev and T. Limtasiri, Liquid-crystalline composites, in *International Encyclopedia of Composites*, Vol. 3, ed. by S. M. Lee, VCH, New York (1990).
14. F. P. La Mantia and A. Valenza, *Makromol. Chem., Macromol. Symp.*, 56, 151 (1992).
15. O. Roetting and G. Hinrichsen, *Advanc. Polym. Tech.*, 13, 57 (1994).
16. A. A. Handlos and D. G. Baird, *J. Macromol. Sci.-Rev. Macromol. Chem. Phys.*, C35, 183 (1995).
17. A. I. Isayev, in *Liquid-Crystalline Polymer Systems*, Chapter 1, ed. by A. I. Isayev, T. Kyu and S. Z. D. Cheng, *ACS Symp. Ser. 632*, ACS, Washington, D.C. (1996).
18. J. He and H. Zhang, *Polymer*, 37, 969 (1996).
19. F. P. La Mantia, A. Roggero, U. Pedretti, and P. L. Magagnini, in *Liquid Crystalline Polymer Systems*, Chapter 8, ed. by A. I. Isayev, T. Kyu, and S. Z. D. Cheng, *ACS Symp. Ser. 632*, ACS, Washington, D.C. (1996).
20. J. He and W. Bu, *Polymer*, 35, 5061 (1994).
21. W. Bu and J. He, *J. Appl. Polym. Sci.*, 62, 1445 (1996).
22. A. I. Isayev and M. Modic, *Polym. Compos.*, 8, 158 (1987).
23. M. R. Nobile, A. Amendola, L. Nicolais, D. Acierno, and C. Carfagna, *Polym. Eng. Sci.*, 29, 244 (1989).
24. C. U. Ko and G. L. Wilkes, *J. Appl. Polym. Sci.*, 37, 3063 (1989).
25. A. Mehta and A. I. Isayev, *Polym. Eng. Sci.*, 31, 971 (1991).
26. A. M. Sukhadia, D. Done, and D. G. Baird, *Polym. Eng. Sci.*, 30, 519 (1990).
27. T. Limtasiri and A. I. Isayev, *J. Appl. Polym. Sci.*, 42, 2923 (1991).
28. A. Kohli, N. Chung, and R. A. Weiss, *Polym. Eng. Sci.*, 29, 573 (1989).
29. K. G. Blizard and D. G. Baird, *Polym. Eng. Sci.*, 27, 653 (1987).
30. D. Deery and A. Siegmann, *Polym. Eng. Sci.*, 31, 451 (1991).
31. P. R. Subramanian and A. I. Isayev, *Polymer*, 32, 1961 (1991).
32. G. D. Choi, S. H. Kim, and W. H. Jo, *Polym. J.*, 28, 527 (1996).
33. J. He, W. Bu, and H. Zhang, *Polym. Eng. Sci.*, 35, 1695 (1995).

34. J. He, *Progress in Natural Science*, 4, 373 (1994).
35. Y. Oyanagi, *Plast. Mold. Technol.*, 4, 89 (1987).
36. F. P. La Mantia, A. Valenza, and P. L. Magagnini, *J. Appl. Polym. Sci.*, 44, 1257 (1992).
37. D. Beery, S. Kenig, and A. Siegmman, *Polym. Eng. Sci.*, 31, 459 (1991).
38. K. A. Khan, R. Kahraman, E. Z. Hamad, S. A. Ali, and S. H. Hamaid, *J. Appl. Polym. Sci.*, 64, 645 (1997).
39. C. Koning, M. van Duin, C. Pagnouille, and R. Jerome, *Prog. Polym. Sci.*, 23, 707 (1998).
40. A. Datta, H. H. Chen, and D. G. Baird, *Polymer*, 34, 759 (1993).
41. A. Datta and D. G. Baird, *Polymer*, 36, 505 (1995).
42. H. J. O'Donnel and D. G. Baird, *Polymer*, 36, 3113 (1995).
43. R. K. Krishnaswamy, S. E. Binwadud, and D. G. Baird, *Polymer*, 40, 701 (1999).
44. Y. Seo, S. M. Hong, S. S. Hwang, T. S. Park, K. U. Kim, S. Lee, and J. Lee, *Polymer*, 36, 515 (1995).
45. Y. Seo, S. M. Hong, S. S. Hwang, S. S. Hwang, T. S. Park, K. U. Kim, S. Lee, and J. Lee, *Polymer*, 36, 525 (1995).
46. Y. Seo, *J. Appl. Polym. Sci.*, 64, 359 (1997).
47. Y. Seo, S. M. Hong, and K. U. Kim, *Macromolecules*, 30, 2978 (1997).
48. Y. Seo, *J. Appl. Polym. Sci.*, 70, 1589 (1998).
49. H. C. Chin, K. C. Chiou, and F. C. Chang, *J. Appl. Polym. Sci.*, 60, 2503 (1996).
50. A. Eisenberg and M. Hara, *Polym. Eng. Sci.*, 22, 1306 (1984).
51. D. Dutta, R. A. Weiss, and J. He, *Polymer*, 37, 429 (1996).
52. J. He and J. Liu, *Polymer*, 40, 959 (1999).
53. J. He and J. Liu, *J. Appl. Polym. Sci.*, 67, 2141 (1998).
54. G. Poli, M. Paci, P. L. Magagnini, R. Scaffaro, and F. P. La Mantia, *Polym. Eng. Sci.*, 36, 1244 (1996).
55. L. I. Minkova, T. Miteva, D. Sek, B. Kaczmarczyk, P. L. Magagnini, M. Paci, F. P. La Mantia, and R. Scaffaro, *J. Appl. Polym. Sci.*, 62, 1613 (1996).
56. F. P. La Mantia, R. Scaffaro, P. L. Magagnini, M. Paci, D. Sek, L. I. Minkova, and T. Miteva, *Polym. Eng. Sci.*, 37, 1164 (1997).
57. P. L. Magagnini, M. Paci, L. I. Minkova, T. Miteva, D. Sek, J. Grobelny, and B. Kaczmarczyk, *J. Appl. Polym. Sci.*, 60, 1665 (1996).
58. J. Grobelny and D. Sek, *Polymer*, 39, 2143 (1998).
59. P. L. Magagnini, U. Pedretti, G. Perego, B. Bresci, S. Carrozzino, and A. Roggero, *U.S. Pat.*, 4,833,229 (1989).
60. F. P. La Mantia, R. Scaffaro, P. L. Magagnini, M. Paci, L. I. Minkova, and T. Miteva, *J. Appl. Polym. Sci.*, 71, 603 (1999).
61. D. Sek and B. Kaczmarczyk, *Polymer*, 38, 2925 (1997).
62. T. Miteva and L. Minkova, *Macromolecular Chem. Phys.*, 199, 597 (1998).
63. D. Sek and B. Kaczmarczyk, *Polymer*, 39, 3327 (1998).
64. P. L. Magagnini, M. Pracella, L. I. Minkova, T. Miteva, D. Sek, J. Grobelny, and F. P. La Mantia, *J. Appl. Polym. Sci.*, 69, 391 (1998).
65. Y. P. Chiou, K. C. Chiou, and F. C. Chang, *Polymer*, 37, 4099 (1996).
66. Y. Z. Meng and S. C. Tjong, *Polym. Compos.*, 19, 1 (1998).
67. S. C. Tjong, R. K. Y. Li, and Y. Z. Meng, *J. Appl. Polym. Sci.*, 67, 521 (1998).
68. S. C. Tjong, S. X. Chen, and R. K. Y. Li, *J. Appl. Polym. Sci.*, 64, 707 (1997).
69. S. C. Tjong and Y. Z. Meng, *J. Appl. Polym. Sci.*, 70, 1611 (1998).
70. Y. Seo, B. Kim, S. Kwak, K. U. Kim, and J. Kim, *Polymer*, 40, 4441 (1999).
71. Y. Seo, B. Kim, and K. U. Kim, *Polymer*, 40, 4483 (1999).
72. R. M. Holsti-Miettinen, M. T. Heino, and J. V. Seppälä, *J. Appl. Polym. Sci.*, 57, 573 (1995).
73. S. H. Kim, G. D. Choi, and W. H. Jo, *Polym. J.*, 32, 693 (1995).

74. D. Y. Chang and F. C. Chang, *J. Appl. Polym. Sci.*, 56, 1015 (1995).
75. M. Singer, G. P. Simon, R. Varley, and M. R. Nobile, *Polym. Eng. Sci.*, 36, 1038 (1996).
76. T. C. Hsu, A. M. Lichkus, and I. R. Harrison, *Polym. Eng. Sci.*, 33, 860 (1993).
77. W. Chinsirikul, T. C. Hsu, and I. R. Harrison, *Polym. Eng. Sci.*, 36, 2708 (1996).
78. M. M. Miller, J. M. G. Gowie, J. G. Tait, D. L. Brydon, and R. R. Mather, *Polymer*, 36, 3107 (1995).
79. M. M. Miller, D. L. Brydon, J. M. G. Gowie, and R. R. Mather, *Macromol. Rapid. Commun.*, 15, 857 (1994).
80. M. M. Miller, J. M. G. Gowie, D. G. Brydon, and R. R. Mather, *Polymer*, 38, 1565 (1997).
81. T. G. Gopakumar, S. Ponrathnum, A. Lele, C. R. Rajan, and A. Fradet, *Polymer*, 40, 357 (1999).
82. H. L. Yang, X. Q. Wu, and S. J. Li, *Polym. Eng. Sci.*, 36, 2781 (1996).
83. A. Bruggeman and A. H. A. Tinnemans, *J. Appl. Polym. Sci.*, 71, 1107 (1999).
84. A. Bruggeman and A. H. A. Tinnemans, *J. Appl. Polym. Sci.*, 71, 1125 (1999).
85. A. M. Kotlia, *J. Polym. Sci., Makromol. Rev.*, 16, 367 (1981).
86. C. F. Ou and C. C. Lin, *J. Appl. Polym. Sci.*, 59, 1379 (1996).
87. C. F. Ou and C. C. Lin, *J. Appl. Polym. Sci.*, 61, 1477 (1996).
88. C. F. Ou and C. C. Lin, *J. Appl. Polym. Sci.*, 61, 1455 (1996).
89. C. F. Ou, *J. Appl. Polym. Sci.*, 68, 1591 (1998).
90. S. M. Hong, S. S. Hwang, Y. Seo, I. J. Chung, and K. U. Kim, *Polym. Eng. Sci.*, 37, 646 (1997).
91. M. Kimura and R. S. Porter, *J. Polym. Sci. Phys. Ed.*, 22, 1697 (1984).
92. B. W. Jo, J. H. Chang, and J. I. Jin, *Polym. Eng. Sci.*, 35, 1615 (1995).
93. M. Paci, C. Barone, and P. L. Magagnini, *J. Polym. Sci., Part B: Polym. Phys.*, 25, 1595 (1987).
94. K. Engberg, M. Ekblad, P.-E. Werner, and U. W. Gedde, *Polym. Eng. Sci.*, 34, 1346 (1994).
95. S. H. Kim, B. J. Jeong, and H. O. Yoo, *Polym. Prep.*, 40, 619 (1999).
96. K. H. Wei, C. J. Jang, and J. C. Ho, *Polymer*, 38, 3521 (1997).
97. K. H. Wei, W. J. Hwang, and H. L. Tyan, *Polymer*, 37, 2087 (1997).
98. K. F. Su and K. H. Wei, *J. Appl. Polym. Sci.*, 56, 79 (1995).
99. K. H. Wei and K. F. Su, *J. Appl. Polym. Sci.*, 59, 787 (1996).
100. K. H. Wei and J. C. Ho, *J. Appl. Polym. Sci.*, 63, 1527 (1997).
101. K. H. Wei and J. C. Ho, *Macromolecules*, 30, 1587 (1997).
102. L. H. Wang and R. S. Porter, *J. Polym. Sci. Polym. Phys. Ed.*, 31, 1067 (1993).
103. K. H. Wei and H. L. Tyan, *J. Appl. Polym. Sci.*, 68, 1581 (1998).
104. G. V. Laivins, *Macromolecules*, 22, 3974 (1989).
105. J. F. Croteau and G. V. Laivins, *J. Appl. Polym. Sci.*, 39, 2377 (1990).
106. S. K. Battacharya, A. Tondonkar, and A. Misra, *Mol. Cryst. Liq. Cryst.*, 153, 501 (1987).
107. S. K. Sharma, A. Tondonkar, and A. Misra, *Mol. Cryst. Liq. Cryst.*, 157, 597 (1988).
108. A. M. Sukhadia, D. Done, and D. G. Baird, *Polym. Eng. Sci.*, 30, 519 (1990).
109. M. Guo and H. G. Zachmann, *Polymer*, 34, 2503 (1993).
110. M. Guo and H. G. Zachmann, *Polym. Prep.*, 36, 825 (1996).
111. M. Guo and H. G. Zachmann, *Polym. Prep.*, 36, 827 (1996).
112. R. E. S. Bretas and D. G. Baird, *Polymer*, 33, 5233 (1992).
113. R. E. S. Bretas, D. Collias, and D. G. Baird, *Polym. Eng. Sci.*, 34, 1492 (1994).
114. A. R. Morales and R. E. S. Bretas, *Eur. Polym. J.*, 32, 349 (1996).
115. A. R. Morales and R. E. S. Bretas, *Eur. Polym. J.*, 32, 365 (1996).
116. J. Hanchi and N. S. Eiss Jr, *Tribol. Trans.*, 40, 102 (1997).
117. Q. Xu, Y. Leng and Y. W. Mai, *Polym. Eng. Sci.*, 36, 769 (1996).
118. S. C. Wong, Y. W. Mai, and Y. Leng, *Polym. Eng. Sci.*, 38, 156 (1998).
119. S. K. Kwon and I. J. Chung, *Polym. Eng. Sci.*, 35, 1137 (1995).

120. B. C. Kim, S. M. Hong, S. S. Hwang, and K. U. Kim, *Polym. Eng. Sci.*, 36, 574 (1996).
121. G. Sawhney, S. K. Gupta, and A. Misra, *J. Appl. Polym. Sci.*, 62, 1395 (1996).
122. K. H. Wei and H. L. Tyan, *Polymer*, 39, 2103 (1998).
123. W. Lee and A. T. DiBenedetto, *Polymer*, 34, 684 (1993).
124. Y. Z. Meng and S. C. Tjong, *Polymer*, 40, 2711 (1999).
125. R. A. Weiss, W. Huh, and L. Nicolais, *Polym. Eng. Sci.*, 27, 684 (1987).
126. J. Seppälä, M. Heino, and C. Kapanon, *J. Appl. Polym. Sci.*, 44, 1051 (1992).
127. P. Zhuang, T. Kyu, and J. L. White, *Polym. Eng. Sci.*, 28, 1095 (1988).
128. M. Kyotani, A. Kaito, and K. Nakayama, *Polymer*, 33, 4756 (1992).
129. T. S. Chung, *Advances in Polymer Blends and Alloys Technology*, Vol.1, ed. by M. A. Kohudic, Technomic Publishing Company, Inc., Lancaster pa. (1988).
130. S. H. Jang, and B. S. Kim, *Polym. Eng. Sci.*, 35, 538 (1995).
131. G. Grevecoeur and G. Groeninckx, *Polym. Eng. Sci.*, 30, 532 (1990).
132. A. I. Isayev and P. R. Subramanian, *Polym. Eng. Sci.*, 32, 85 (1992).
133. G. Li, J. H. Yin, B. Y. Li, G. Q. Zhuang, Y. M. Yang, and L. Nicolais, *Polym. Eng. Sci.*, 35, 658 (1995).
134. S. M. Hong, B. C. Kim, K. U. Kim, and I. J. Chung, *Polym. J.*, 23, 1347 (1991).
135. K. G. Blizard, and R. R. Haghighat, *Polym. Eng. Sci.*, 33, 799 (1993).
136. S. S. Bafna, T. Sun, J. P. De Souza, and D. G. Baird, *Polymer*, 36, 259 (1995).
137. C. Carfagna, E. Amendola, L. Nicolais, D. Acierno, O. Francescangeli, B. Yang, and R. Rustichelli, *J. Appl. Polym. Sci.*, 43, 839 (1991).
138. A. I. Isayev and M. Modic, *SPE Technical Papers (ANTEC 86)*, 32, 573 (1986).
139. A. Mehta and A. I. Isayev, *Polym. Eng. Sci.*, 31, 963 (1991).
140. Q. H. Lin, J. Jho, and A. F. Yee, *Polym. Eng. Sci.*, 33, 789 (1993).
141. G. Grevecoeur and G. Groeninckx, *Polym. Eng. Sci.*, 33, 937 (1993).
142. D. Dutta, R. A. Weiss, and K. Kristal, *Polym. Compos.*, 13, 394 (1992).
143. D. G. Baird, S. S. Bafna, J. P. De Souza, and T. Sun, *Polym. Compos.*, 14, 214 (1993).
144. C. L. Choy, K. W. E. Lau, Y. W. Wong, and A. F. Yee, *Polym. Eng. Sci.*, 36, 1256 (1996).
145. B. R. Bassett and A. F. Yee, *Polym. Compos.*, 11, 10 (1990).
146. D. Dutta, R. A. Weiss, and D. Kristal, *SPE Technical Papers (ANTEC 92)*, 38, 224 (1992).
147. J. P. De Souza and D. G. Baird, *SPE Technical Papers (ANTEC 92)*, 38, 2236 (1992).
148. A. I. Isayev, Y. Holdengreber, R. Vismanathan, and S. Akhtar, *SPE Technical Papers (ANTEC 92)*, 38, 2654 (1992).
149. A. A. Handlos and D. G. Baird, *SPE Technical Papers (ANTEC 93)*, 39, 1170 (1993).
150. D. Dutta, R. A. Weiss, and K. Kristal, *Polym. Eng. Sci.*, 33, 838 (1993).
151. S. S. Bafna, J. P. De Souza, T. Sun, and D. G. Baird, *Polym. Eng. Sci.*, 33, 808 (1993).
152. M. Kyotani, A. Kaito, and K. Nakayama, *Polymer*, 35, 5138 (1994).
153. A. I. Isayev, Y. Holdengreber, R. Vismanathan, and S. Akhtar, *Polym. Compos.*, 15, 254 (1994).
154. E. A. Sabol, A. A. Handlos, and D. G. Baird, *Polym. Compos.*, 16, 330 (1995).
155. A. A. Handlos and D. G. Baird, *Intern. Polym. Proc.*, XI, 82 (1996).
156. W. Bu and A. I. Isayev, *J. Appl. Polym. Sci.*, 65, 329 (1997).
157. J. He, H. Zhang, and Y. Wang, *Polymer*, 38, 4279 (1997).
158. J. He, Y. Wang, and H. Zhang, *Compos. Sci. Tech.*, 60, 1919 (2000).
159. J. He, H. Zhang, and G. Li, *Acta Polymerica Sinica*, (1), 115 (1993).
160. J. He and H. Zhang, China Patent Application, 1996, CN1138604A.
161. J. He and Y. Wang, China Patent Application, 1997, CN1198453A.
162. J. He and Y. Wang, China Patent Application, 1997, CN1189517A.

# Rheology and Processing of Thermotropic Liquid Crystalline Polymers

K. S. SEO

## 1. INTRODUCTION

**T**HERMOTROPIC liquid crystalline polymers (TLCPs) have drawn much attention from researchers from both an industrial and a scientific point of view since the first TLCP, which showed an order of magnitude lower melt viscosity than its isotropic homologue, was introduced in the mid 1970s. TLCPs have outstanding flow behaviors and provide mechanical properties, thermal properties, and a chemical resistance all superior to those of flexible thermoplastic polymers. Despite such advantageous properties, commercialization of TLCPs has been hampered by the high manufacturing cost and the limited market size. Many commercial TLCPs are now available on the market, and their rheological properties have been studied extensively. In this chapter, the unique rheological behaviors of TLCPs and their effects on the processing and the end-use properties will be broadly reviewed.

## 2. MOLECULAR DIMENSION OF THERMOTROPIC LIQUID CRYSTALLINE POLYMERS

The molecular size of polymers is commonly expressed by the molecular weight, radius of gyration, intrinsic viscosity or inherent viscosity. The molecular weight is commonly determined by gel permeation chromatography (GPC) or light scattering. For relatively low molecular weight polymers, ebulliometry

Copyright © Eastman Chemical Company.

[www.iran-mavad.com](http://www.iran-mavad.com)

مرجع دانشجویان و مهندسين مواد

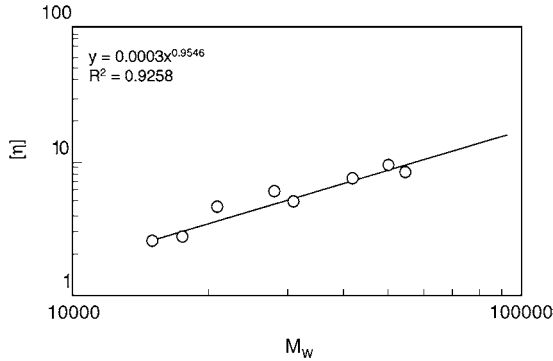


**Figure 8.1** The relationship between molecular weight,  $M_w$ , and intrinsic viscosity,  $[\eta]$ , for Thermx<sup>®</sup> LN001 [5].

or osmometry is also used. The radius of gyration is determined either by light scattering or neutron scattering. The dilute solution viscometry and GPC are based on the hydrodynamic volume of the polymer in a given solvent and at a given temperature. The hydrodynamic volume is a function of the molecular weight and the chain stiffness. The relationship between the intrinsic viscosity and the molecular weight is described by the Mark-Houwink equation:

$$[\eta] = K_{\theta} [M]^a \quad (1)$$

where  $[\eta]$  is the intrinsic viscosity,  $K_{\theta}$  is the front factor,  $M$  is the molecular weight, and  $a$  is the exponent. The stiffness of the polymer is reflected in both  $K_{\theta}$  and  $a$ . The Mark-Houwink exponent  $a$  is 0.5 for the random coil and approximately 2 for the rigid rod [1]. Illustrated in Figure 8.1 is a plot of  $M$  versus  $[\eta]$  in 60/40 (by weight) pentafluorophenol/1,2,4-trichlorobenzene for an all-aromatic liquid crystalline polyester composed of *p*-hydroxy benzoic acid (HBA), hydroquinone (HQ), terephthalic acid (TPA), and 2,4-naphthalene dicarboxylic acid (NDA) (Thermx<sup>®</sup> LN001 from Eastman Chemical Company). The Mark-Houwink exponent estimated from this plot is 0.95, which indicates that this TLCP is not a true rigid rod but is much stiffer than ordinary flexible polymers.

The chain stiffness is also evaluated from the persistence length,  $q$ , and the contour length,  $L$ , according to the Kratky-Porod criterion [2]:

$$L/2q \gg 1 \text{ for a random flight chain} \quad (2a)$$

$$L/2q \ll 1 \text{ for a rigid rod} \quad (2b)$$

The persistence length,  $q$ , may be determined from light scattering data using the Benoit-Doty relationship as proposed by Fetters and Yu [3]:

$$\langle S^2 \rangle = q^2 [(x/3) - 1 + (2/x) - (2/x^2)(1 - e^{-x})] \quad (3)$$

$$x = nh/q$$

where  $\langle S^2 \rangle$  is the mean square radius of gyration,  $n$  is the degree of polymerization, and  $h$  is the monomeric projection length.

The persistence length,  $q$ , can also be determined relatively easily from the intrinsic viscosity  $[\eta]$  (expressed in  $\text{cm}^3/\text{g}$ ) and the weight average molecular weight  $\langle M \rangle_w$  using the Bohdanecky equation [4]:

$$(\langle M \rangle_w^2 / [\eta])^{1/3} = A_n + B_n \langle M \rangle_w^{1/2} \quad (4)$$

$$A_n = A_o M_L \Phi^{-1/3} \quad (4a)$$

$$B_n = B_o \Phi^{-1/3} (2q / M_L)^{-1/2} \quad (4b)$$

where  $A_o$  and  $B_o$  are given as

$$A_o = 0.46 - 0.53 \log (d/2q)$$

$$B_o = 1.00 - 0.0367 \log (d/2q)$$

and  $\Phi$  is Flory's hydrodynamic constant ( $2.87 \times 10^{23}$ ),  $d$  is the diameter of the polymer chain, and  $M_L$  is the molecular weight per unit length.  $M_L$  can be determined from the molecular weight and the length of the repeat unit. Both  $q$  and  $d$  are estimated from the slope  $A_n$  and the intercept  $B_n$  of a plot of  $(\langle M \rangle_w^2 / [\eta])^{1/3}$  versus  $\langle M \rangle_w^{1/2}$  with a known value of  $M_L$ . Figure 8.2 is a plot of Equation (4) for Thermx<sup>®</sup> LN001. The estimated  $q$  and  $d$  from the slope and the intercept of the plot with a  $M_L$  value of 190 Å are approximately 97 Å and 7.4 Å, respectively [5]. The repeat unit length calculated from bond lengths and bond angles of this TLCP is about 7 Å [6]. The number average degree of polymerization of Thermx<sup>®</sup> LN001 is typically 100, which yields a contour length,  $L$ , of approximately 700 Å. Then,  $L/2q$  becomes approximately 3.5, which suggests, according to the Kratky-Porod criteria of Equation (2), that Thermx<sup>®</sup> LN001 is far from the rigid rod regime and instead has a semi-rigid "worm-like" chain conformation with some degree of flexibility. Listed in Table 8.1 are the persistence lengths of various liquid crystalline polymers (LCPs) [5–11]. The TLCPs of commercial interest have a persistence length in the range of 50 to 120 Å, while Kevlar<sup>®</sup>, a lyotropic aramid LCP that cannot be melt-processed due to its high melting point ( $T_m > 500^\circ\text{C}$ ), has a relatively long persistence length of 290 Å. The copolyester poly(hydroquinone-co-terephthalate), which

TABLE 8.1. Comparison of Persistence Lengths of Various LCPs.

Polymers	Composition	Persistence Length (Å)	Reference
Kevlar®	Poly(1,4 phenylene terephthalamide)	290	[8]
Vectra®	<i>p</i> -Hydroxy benzoic acid/ 2-Hydroxy 6-naphthoic acid	120	[9]
Thermx® LN001	<i>p</i> -Hydroxy benzoic acid/ 2,6-Naphthalenedicarboxylic acid/Terephthalic acid/ Hydroquinone	80–95	[5–6]
—	Terephthalic acid/ Hydroquinone	470	[10]
—	Terephthalic acid/ Phenylhydroquinone	60–150	[10]
—	32 Isophthalic acid 32 Hydroquinone 36 <i>p</i> -Hydroxy benzoic acid	44	[11]

has a long persistence length of 470 Å and a high melting point cannot be melt-processed either. When hydroquinone is replaced by phenylhydroquinone in the copolyester, its persistence length decreases substantially, but the modified copolyester forms the nematic melt phase over the temperature range of 350°C to 450°C, which is too high for normal melt processing without decomposition of the polymer [10]. Good mechanical properties, high thermal properties and good melt processability, which depend on the persistence length (in a sense of chain stiffness) and the melting point, are of prime importance for commercial TLCPs.

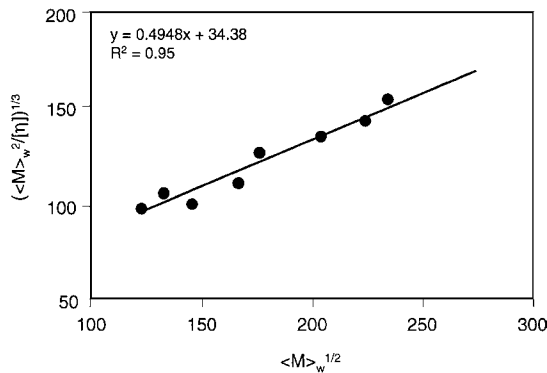


Figure 8.2 The plot of  $(\langle M \rangle_w^2 / [\eta])^{1/3}$  vs.  $\langle M \rangle_w^{1/2}$  for Thermx® LN001 [5].

### 3. DYNAMICS OF LIQUID CRYSTALLINE POLYMERS

Doi and Edwards developed the most extensive theory of dynamics of rod-like macromolecules in concentrated solutions [2,12]. As discussed in the previous section, the majority of commercial TLCPs are not perfect rigid rods but are semi-rigid rods having some degree of flexibility. Although several experimental results support the validity of the rigid rod approximation for both lyotropic [13–15] and thermotropic liquid crystalline polymers [16–18], there is no complete theory on the dynamics of TLCPs. To better understand the dynamics of TLCPs in the melt, the Doi-Edwards theory on the dynamics of rod-like polymers in solution is summarized here. Readers may find further details of the theory in the original reference [2,12].

Consider the number of polymer molecules per unit volume of solution,  $\nu$ , which is given as

$$\nu = \rho N_A / M \quad (5)$$

where  $\rho$  is the density of polymer solution,  $N_A$  is Avogadro's number, and  $M$  is the molecular weight of the polymer. Then, the average distance between polymers is approximately  $\nu^{-1/3}$ . In a dilute solution,  $\nu^{-1/3}$  is larger than the length of the polymer,  $L$ , so that no neighboring molecules are in contact with each other within an imaginary sphere having a diameter  $L$  [see Figure 8.3(a)]. The concentration at which the imaginary spheres, formed by individual rods, start to overlap is approximately equal to  $1/L^3$  [19]. This concentration is denoted by  $\nu_1$ . When the concentration is greater than  $\nu_1$ ,

$$\nu > \nu_1 \cong 1/L^3 \quad (6)$$

each rod is no longer independent of its neighboring rods [see Figure 8.3(b)]. Consequently, the lateral movement or rotation is highly restricted by the presence of surrounding rods, but the rod can still move freely along its long-axis,

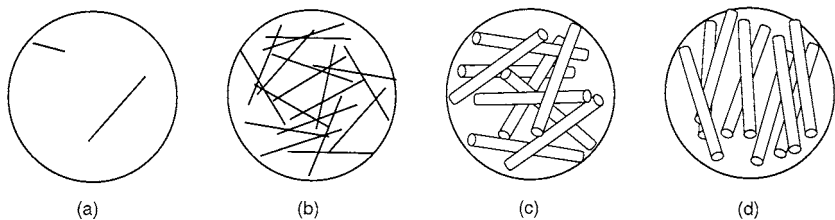


**Figure 8.3** Concentration regimes of rod-like polymers: (a) dilute solution, (b) semi-dilute solution, (c) isotropic concentrated solution, and (d) liquid crystalline solution (from Doi and Edwards [2], *The Theory of Polymer Dynamics*, 1986, reprinted with permission from Oxford University Press).

i.e., the excluded volume effect is negligible. This concentration regime is called the semi-dilute solution. In the semi-dilute solution, the intermolecular interaction has little effect on the static or equilibrium properties, but the dynamic properties completely change because the rods cannot move across each other. Such a constraint between rods is called “entanglement,” although they are not physically entangled.

As the concentration increases further, the excluded volume effect becomes important. The excluded volume of the rod is approximately  $bL^2$ , where  $b$  is the diameter of the rod. When the concentration is greater than  $1/(bL^2)$ , the excluded volume interaction increases, and, consequently, both the static and dynamic properties change substantially. Although the solution is well above the concentration regime where the excluded volume effect is significant, it remains isotropic until it reaches a critical concentration  $\nu^*$  [see Figure 8.3(c), and note that the rods are thicker to signify the excluded volume interaction]:

$$\nu^* > \nu > \nu_2 \cong 1/(bL^2) \quad (7)$$

where  $\nu_2$  is the concentration where the rods begin to experience the excluded volume effect. Doi and Edwards named this concentration regime the “concentrated isotropic solution.” Above the critical concentration  $\nu^*$ , which is also of the order of  $1/(bL^2)$ , the rods tend to align in the direction of the neighboring rods forming a liquid crystalline phase [see Figure 8.3(d)]:

$$\nu > \nu^* \cong 1/(bL^2) \quad (8)$$

To model the entanglement effect on the dynamics of rod-like macromolecules, Doi and Edwards chose the semi-dilute solution for the sake of simplicity. In the semi-dilute regime, the excluded volume effect is small, and the rods are randomly oriented. Because the polymers can freely move along their own axes in this concentration regime, the diffusion constant of the parallel motion of the rods,  $D_{//}$ , is the same as in the dilute solution,  $D_{//o}$ ;  $D_{//} \cong D_{//o}$ . On the other hand, the topological constraint of the rigid rods not being able to pass over neighboring rods results in almost no perpendicular motion but a limited rotation within the confined tube through a small angle. The rotational diffusion constant in semi-dilute solution is given as

$$D_r = D_{ro}\beta(\nu L^3)^{-2} \quad (9)$$

where  $\beta$  is a numerical factor in the range of  $10^3$  to  $10^4$  and  $D_{ro}$  is the rotational diffusion constant in dilute solution.  $D_{ro}$  is a strong function of the molecular weight:

$$D_{ro} \propto \log(M)/M^3 \quad (10)$$

Because  $\nu \propto \rho/M$  and  $L \propto M$ , Equation (9) becomes

$$D_r \propto \rho^{-2} M^{-7} \log(M) \quad (11)$$

The diffusion constant of the rods in semi-dilute solution decreases with the seventh power of molecular weight, which is a phenomenal difference from  $M^{-2}$  dependence for flexible entangled polymers [20]. Consequently, the zero shear viscosity of rigid rods depends strongly on the molecular weight [2]:

$$\eta_0 \propto \rho^3 M^6 / \log(M) \quad (12)$$

The zero shear viscosity scales with  $M^6$  to contrast  $M^3$  dependence for isotropic polymers [20]. So far, we have examined the dynamics of rod-like macromolecules in isotropic semi-dilute solution. For anisotropic LCP solutions in which the rods are oriented in a certain direction, the diffusion constant increases, and the viscosity decreases, but their scaling behavior with the molecular weight is expected to be unchanged [2,17]. Little experimental work has been reported on this subject. The dynamics of thermotropic liquid crystalline polymer melts may be considered as a special case of the concentrated solution with no solvent. Many experimental results [16–18] showed the strong molecular weight dependence of the melt viscosity as predicted by the Doi-Edwards theory. However, the complex rheological behaviors of TLCPs have not been well theorized.

## 4. RHEOLOGY OF THERMOTROPIC LIQUID CRYSTALLINE POLYMERS

### 4.1. THREE-REGION FLOW

One of the unique flow behaviors of LCPs is the three-region flow: shear thinning at low shear rates (Region I), reaching a Newtonian plateau at intermediate rates (Region II), and shear thinning again at high shear rates (Region III). The three-region flow was originally observed for lyotropic LCPs [21]. It has also been observed for some TLCPs [13,18,22–24]. The three-region flow behavior of Thermx<sup>®</sup> LN001 is illustrated in Figure 8.4. The three-region flow is not always observed for LCPs, but it depends on the polymers and experimental conditions, including melt temperature and shear history [13].

Many theoretical models have been suggested for the origin of three-region flow behavior. Some bases of the theories are discussed here. LCPs contain many disclinations in chain orientation, which are called “defects,” as they are commonly found in small molecule liquid crystals [25]. A good review for the defects in LCPs can be found in the literature [26]. The directional vector of

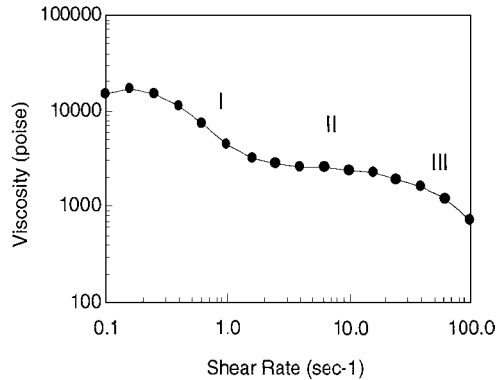
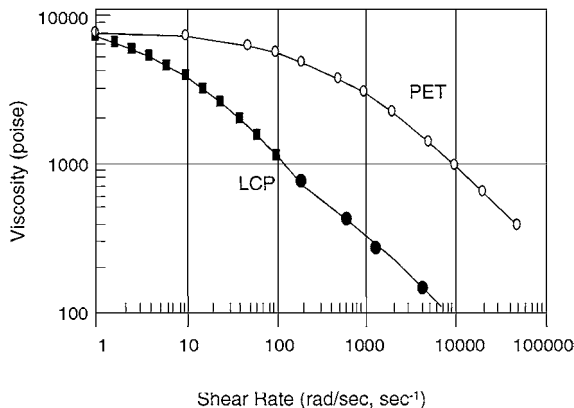


**Figure 8.4** Three-region flow behavior of Thermx® LN001 at 345°C (from Seo [18], reprinted with permission from Society of Plastics Engineers).

individual molecules or their segments in the liquid crystalline phase is called the “director.” The director varies from place to place in the liquid crystalline phase. The individual areas within which the molecules have the same director are called “domains.” The director within a domain can also vary as a defect structure. Thus, if no external stress is applied to the nematic liquids, the overall orientation of the molecules, which is called the “order parameter,” is zero on average [27]. When an external stress is applied to the LCP, its order parameter and the domain structure change easily for the system to reach the minimum energy state. As a result, LCP solutions or melts show complex rheological behaviors, depending on the previous shear history they experienced prior to the test. On the basis of the domain model, theories to predict Region I and Region II have been proposed. The shear-thinning Region I at low shear rates is considered to be due to changes in size or texture of the domains or of the defects in the nematic phase [28–30]. Onogi and Asada attributed Region I flow behavior to relative motion of the domains, Region II to flow of domains in the nematic medium resulting from Region I flow, and Region III to the oriented nematic structure [21]. A theoretical treatment of the dynamics of Region II and Region III based on the Doi theory has also been proposed [31]. Despite all these efforts to explain the observed three-region flow behavior of LCPs, more work is needed for complete understanding of this unique flow behavior.

## 4.2. MELT VISCOSITY CURVES

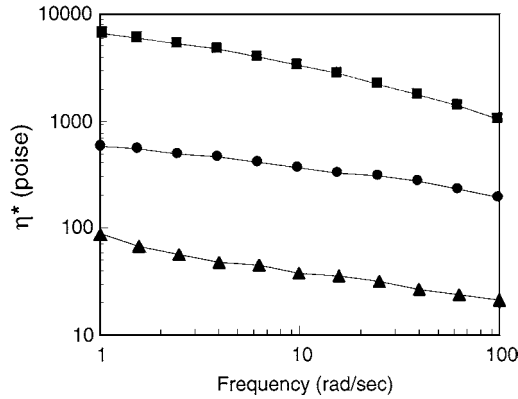
When a steady shear test is conducted on a rotational rheometer, the sample tends to fracture or run out of the gap between cone and plate or two parallel plates as the shear rate increases. LCP melts have a tendency to slip out of the gap more easily, and only limited shear rates can be applied to them for



**Figure 8.5** Comparison of shear-thinning behaviors of Thermx<sup>®</sup> LN001 at 345°C and PET at 285°C. The high shear rate data ( $>100 \text{ sec}^{-1}$ ) for LCP were measured by a capillary rheometer, and those for PET were extrapolated from the dynamic data at low shear rates using the Cross model (from Seo [18], reprinted with permission from Society of Plastics Engineers).

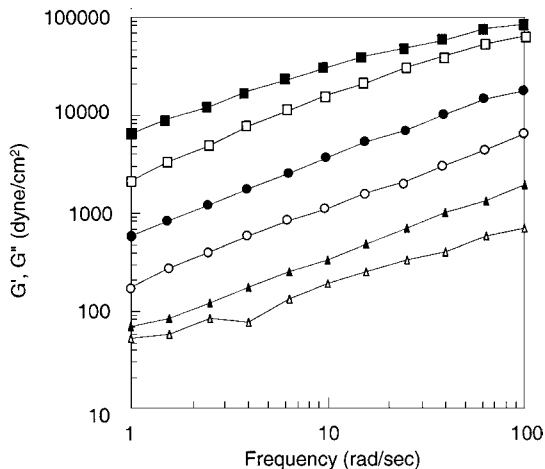
steady shear experiments on the rotational rheometer. The dynamic oscillatory test with a small strain would reduce this problem and provide relatively higher shear rates (in the unit of angular frequency, radians/sec, which is equivalent to the shear rate if the Cox-Merz rule applies). A capillary rheometer is normally used to measure the high shear rate viscosity. However, the capillary viscosity of TLCPs is very sensitive to the capillary dimension, especially to the diameter [32], so that care must be taken when the capillary viscosity data for TLCPs are compared. Due to their characteristically rigid molecular structure, TLCP molecules orient easily in the shear direction, exhibiting high shear-thinning behavior. Figure 8.5 compares the shear-thinning behavior of Thermx<sup>®</sup> LN001 and PET over a wide range of shear rates. The high shear-thinning characteristic of TLCP is the greatest advantage over the ordinary thermoplastics from a processing point of view. The ease of flow is especially beneficial for injection molding of thin walled parts such as computer connectors, miniature communication devices, or medical devices.

Figure 8.6 shows the dynamic complex viscosity curves of Thermx<sup>®</sup> LN001 with various molecular weights. The dynamic viscosity curves with the high shear-thinning behavior are generally observed for many TLCPs. The upward concavity or yielding behavior of the low molecular weight sample at low frequencies is often found for other TLCPs and is considered analogous to Region I flow in the steady shear experiment. TLCPs that show the upward concavity include 60/40 *p*-hydroxybenzoic acid (HBA)/poly(ethylene terephthalate) (PET) [22], 80/20 HBA/PET [33], and 73/27 HBA/2,6-hydroxy naphthoic acid (HNA) [34].



**Figure 8.6** Complex viscosities of Thermx® LN001 at 345°C for various molecular weights;  $M_w = 15,000$  ( $\blacktriangle$ ),  $M_w = 31,000$  ( $\bullet$ ), and  $M_w = 55,000$  ( $\blacksquare$ ) (from Seo [18], reproduced with permission from Society of Plastics Engineers).

Figure 8.7 shows plots of the storage modulus ( $G'$ ) and the loss modulus ( $G''$ ) of Thermx® LN001. The  $G'$  and  $G''$  curves are almost parallel to each other, and their slopes are much less than unity. This curve shape of  $G'$  and  $G''$  is also found for glass-fiber filled flexible polymers. The high  $G'$  value (i.e., lower slope) in the low shear rate region reflects the long relaxation time of the



**Figure 8.7** Storage modulus ( $G'$ ) and loss modulus ( $G''$ ) of Thermx® LN001 at 345°C for various molecular weights.  $M_w = 15,000$  (triangle),  $M_w = 31,000$  (circle), and  $M_w = 55,000$  (square). Filled symbols represent  $G''$  and open symbols represent  $G'$  (from Seo [18], reproduced with permission from Society of Plastics Engineers).

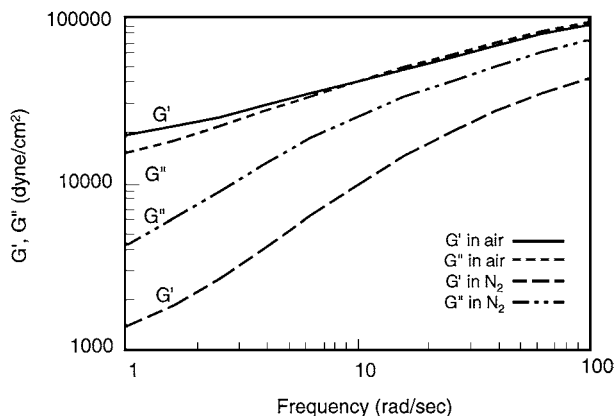


**Figure 8.8** Effects of air and nitrogen environments on  $G'$  and  $G''$  of Thermx® LN001, after 10 minutes melting time at 345°C.

TLCP associated with their rigid chain structure and the domains in the nematic phase. The curve shape of  $G'$  and  $G''$  varies greatly depending on the polymer and the melt temperature. In some cases,  $G'$  and  $G''$  curves tend to level off with  $G'$  being higher than  $G''$  in the low frequency region [35]. Branching or cross-linking, or residual crystallinity in the melt (“unmelt”), also change the curve shape of  $G'$  and  $G''$ . Figure 8.8 shows the effect of the thermooxidative degradation on  $G'$  and  $G''$  during the test. The dramatic differences in both the curve shape and the values of  $G'$  and  $G''$  in the presence of air are presumably due to branching by the thermooxidative degradation.

#### 4.3. EFFECTS OF MOLECULAR WEIGHT

The zero shear viscosity of flexible linear polymers varies experimentally with  $M^{3.4}$  and theoretically with  $M^3$  [20]. Due to the highly restricted rotational diffusion, the viscosity of TLCPs is much more sensitive to the molecular weight than that of ordinary thermoplastics as discussed in section 3. Doi and Edwards predicted that the viscosity of rod-like polymers in semi-dilute solutions scales with  $M^6$  [see Equation (12)] [2]. Such a high power dependence of viscosity on the molecular weight has been experimentally observed both for lyotropic LCPs [14,15] and for TLCPs [16–18]. The experimental values of the exponent range from 4 to 7 depending on the chemical structure, the chain stiffness, and the domain or defect structure of the liquid crystalline solution or melt. The anisotropy of the liquid seems to have little effect on the exponent. A slightly smaller exponent for the nematic phase than for the isotropic phase (6 in the nematic phase versus 6.5 in the isotropic

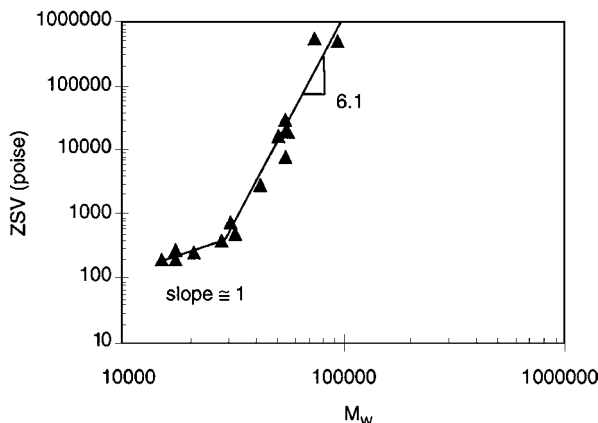


**Figure 8.9** The effect of molecular weight on the zero shear viscosity (ZSV) of Thermx® LN001 [5].

phase) has been reported for a TLCP poly[(phenyl sulfonyl)-*p*-phenylene-1,10-decamethylenebis(4-oxybenzoate)] [17]. Although most of the reported exponents in the literature are in reasonably good agreement with the Doi-Edwards theory, there seems to be a large uncertainty in the exponent that was determined with the limited range of molecular weights. Due to the high shear-thinning behavior of TLCPs at low shear rates, the uncertainty in the predicted zero shear viscosity from a viscosity model such as the Cross or the Carreau models should also be large. Figure 8.9 illustrates the effect of molecular weight on the zero shear melt viscosity. Despite the experimental error anticipated in both molecular weight and melt viscosity measurements, the estimated exponent of 6.1 from the curve fit is in good agreement with the theoretical prediction of 6 by Doi and Edwards [2]. However, considering the fact that the TLCP is not a perfect rod but a semi-rigid chain with some degree of flexibility, the observed result of 6 for the exponent is somewhat surprising.

It is of interest to note that the plot of the molecular weight versus the viscosity shown in Figure 8.9 changes its slope at a molecular weight of about 30,000 g/mol. For flexible polymers, this slope change is associated with the onset of entanglement coupling between molecules. The molecular weight at which the slope changes is called the critical molecular weight for entanglement ( $M_c$ ) and is usually twice the entanglement molecular weight ( $M_e$ );  $M_c \cong 2M_e$ .  $M_e$  is related to the plateau modulus  $G_n^o$  by the following equation of the rubber elasticity:

$$M_e = \rho RT / G_n^o \quad (13)$$

where  $\rho$  is the density of the melt,  $R$  is the gas constant, and  $T$  is the absolute temperature. For LCPs, the entanglement molecular weight is not well defined

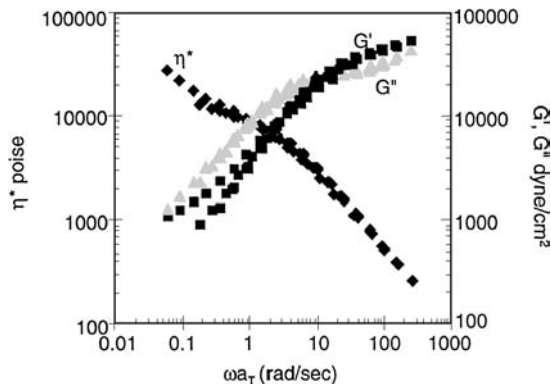


**Figure 8.10** The time-temperature superposition data at the reference temperature of 345°C for Thermx® LN0001. Complex viscosity (◆),  $G'$  (▲), and  $G''$  (■) [5].

because actual entanglement between the rigid rods other than topological constraint would be rare. Therefore, applicability of Equation (13) for LCPs is somewhat unclear. A very high entanglement molecular weight in the order of  $10^5$ – $10^6$  g/mol has been estimated from the plateau modulus for a side-chain liquid crystalline polymer by Rubin et al. [36]. They reported that  $M_e$  of the LCP in the nematic phase is even larger than that in the isotropic phase. Figure 8.10 illustrates the time-temperature superposition data for Thermx® LN001. Although the super position is poor, a plateau modulus of ca 40,000 dyne/cm<sup>2</sup> was crudely estimated at the inflection point of  $G''$ , or at the minimum  $\tan \delta$  ( $G''/G'$ ). The melt density of this TLCP is about 1.2 g/cm<sup>3</sup> at 345°C. Then, Equation (13) estimates  $M_e$  of ca 600,000 g/mol. This value is more than an order of magnitude larger than the molecular weight of 30,000 g/mol where the slope changes as shown in Figure 8.9.

Fetters et al. suggested that  $M_e$  can be estimated from the ratio  $\langle R^2 \rangle_o / M$  [37]:

$$M_e = B^{-2} (\langle R^2 \rangle_o / M)^{-3} \rho^{-2} N_A \quad (14)$$

where  $\langle R^2 \rangle_o$  is the mean square end-to-end distance in a  $\theta$ -solvent and  $M$  is the molecular weight. The ratio  $\langle R^2 \rangle_o / M$  for Thermx® LN001 determined by light scattering in pentafluorophenol is about 13 Å<sup>2</sup> mol g<sup>-1</sup> on average [5]. This value predicts an unusually low  $M_e$ , which is close to zero. Another approach to estimate the entanglement molecular weight based on the assumption that  $M_e \propto (C_\infty)^2$  where  $C_\infty$  is the characteristic ratio has been proposed [38]. This latter approach, which is in an opposite sense of Equation (14), gives  $M_e$  of  $1.4 \times 10^6$  g/mol for the same TLCP. Although this value for  $M_e$  is comparable to the result of the plateau modulus and Equation (13), the validity of the estimated  $M_e$  is not known. Therefore, it is unclear whether the slope change observed

in Figure 8.9 is associated with the same type of entanglement coupling as defined for ordinary flexible polymers. The low molecular weight TLCPs made by the condensation polymerization can differ from their high molecular weight homologues in many factors that may influence the zero shear viscosity, which includes blockiness in the backbone, broadness of melting point distribution, and polydispersity. The profound effect of polydispersity on the melt viscosity of entangled, rod-like polymers has been theorized by Marrucci [39]. According to his theory, the melt viscosity of the polydisperse LCP is about 10 times higher than that of the monodisperse one at the same weight-average molecular weight. For the samples in Figure 8.9, no significant differences in polydispersity were found by GPC between low and high molecular weight samples. Obviously, the complicated effects of the structural variables in TLCPs on the melt rheology are not well understood, and the origin of the slope change is open to further investigation.

#### 4.4. EFFECTS OF TEMPERATURE

Temperature influences the melt rheology of TLCPs in many different ways. The friction coefficient or the diffusion coefficient of molecules, the liquid crystallinity or nematicity of the melt, and three-dimensional crystallinity in the melt may change as the temperature changes. When the melt temperature is below the nematic-to-isotropic transition temperature ( $T_{ni}$ ), the melt viscosity of TLCPs decreases as the temperature increases due to the increased Brownian motion. Above  $T_{ni}$ , the melt viscosity increases with the temperature as the liquid crystallinity decreases, which prevails over the effect of increased Brownian motion on the melt viscosity. Such behavior is not always observable for high melting temperature TLCPs. At higher temperatures, the thermooxidative degradation of the polymer can cause molecular weight loss, lowering the melt viscosity. In more severe cases, branching or cross-linking in the melt can occur, which will increase the melt viscosity. In general, TLCPs have broad melting peaks. Thus, TLCPs often do not melt completely even after being heated above the peak melting temperature. Another possibility is that TLCPs may undergo crystallization, annealing, or changes in the nematic structure upon heating. As a result, completely different melt viscosity data can result for TLCPs depending on the thermal history. For example, the melt viscosity of a directly heated sample could be substantially higher than that of a super-cooled sample at the same test temperature. The practical significance of this thermal history dependence of the melt viscosity is that the viscosity data obtained by direct heating fail to predict the injection-molding behaviors of the TLCP. On the other hand, data obtained from the super-cooled sample predict the injection-molding behavior more accurately [40].

Estimation of the activation energy of flow for TLCPs is not straightforward because it largely depends on the experimental condition and the sample

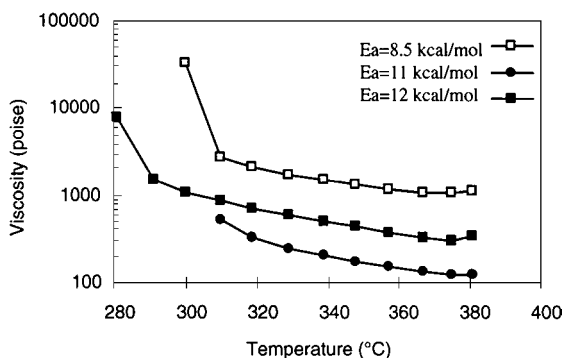


**Figure 8.11** The effect of temperature on the melt viscosity of Thermx® LN001 with different molecular weights (from Seo [18], reproduced with permission from Society of Plastics Engineers).

handling. In general, two activation energies are observed for TLCPs depending on the range of temperature examined. For some TLCPs, however, the viscosity is almost independent of temperature [41]. The effect of temperature on the dynamic melt viscosity measured by cooling the sample stepwise is illustrated in Figure 8.11. The Arrhenius activation energy estimated for the temperature range of 325–375°C is 9–12 kcal/mol, which is slightly lower than that of PET (13.5 kcal/mol) [42]. The fast increase in melt viscosity at lower temperatures is believed to be due to crystallization of the sample. Although there appears to be a minimum in viscosity at 375°C, the exact cause of the viscosity minimum shown in Figure 8.11 is not known. Due to the thermal degradation at high temperatures, it is difficult to examine the nematic-to-isotropic phase transition temperature (e.g., by microscopy) for the high melting TLCP. A similar activation energy of 11 kcal/mol above 300°C has been reported for Vectra® A900 (from Hoechst-Celanese), a thermotropic copolyester of 2-hydroxy-6-naphthoic acid (HNA) and para-hydroxy benzoic acid (HBA). The activation energy of Vectra® A900 sharply increases when the temperature drops below 300°C, which is about 20°C above the peak melting point [32]. A somewhat higher activation energy (25 kcal/mol) above its melting point has been reported for Vectra® B950, a TLCP composed of 60% HNA and 20% TPA and 20% *m*-aminophenol. Its activation energy jumps to 90 kcal/mol at temperatures below the melting point [43]. Although the increase in activation energy near the melting point is believed to be associated with crystallization, the possible change in liquid crystallinity or nematic phase structure would also be responsible for the observed strong temperature dependence at low temperatures. It should be noted that for amorphous polymers, the activation energy near the glass transition temperature  $T_g$ ; (typically below  $T_g + 100^\circ\text{C}$ ) is also much higher than that at higher temperatures.

## 4.5. EFFECTS OF GLASS FIBERS

The rheology of filled polymers has been reviewed extensively [44,45]. In general, viscosity curves of highly filled polymers show a yielding behavior at low shear rates followed by a power-law behavior at high shear rates [44]. For most of the filled thermoplastics with small particles such as glass beads, calcium carbonate, talc, and carbon black, etc., the viscosity increases with the filler concentration. For some filled systems, however, the viscosity increases with the filler content up to the critical concentration, then decreases [46] or becomes little dependent on the filler concentration [47]. This is particularly true for glass fiber-filled polymers.

Studies on the effects of fillers on the melt viscosity of TLCPs have also been reported [48,49]. The rheology of glass fiber-filled TLCPs is similar to that of glass fiber-filled, ordinary thermoplastics. Figure 8.12 illustrates the effect of glass fibers on the melt viscosity of TLCP. Unlike the case of ordinary flexible polymers, the glass fibers appear to reduce the melt viscosity of the TLCP composite. Caution needs to be taken, however, in interpreting the effect of glass fiber on melt viscosity because other factors such as molecular weight of the matrix polymer and glass fiber length also influence the viscosity of glass fiber-filled TLCPs. Despite their high processing temperatures, retention of the molecular weight and mechanical properties of TLCPs after processing is generally very good. However, liquid crystalline copolyesters may undergo hydrolysis, causing molecular weight loss during the melt process when they are not properly dried. The molecular weight loss is significant, particularly when TLCPs are compounded with glass fibers, which generate high mechanical shear and high dissipated heat. Typical molecular weight loss during the compounding is about 20%, and an additional 10% loss can occur during the

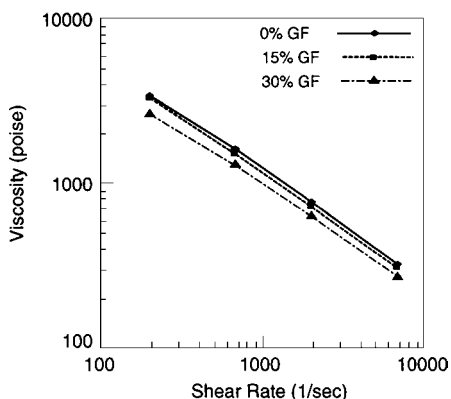
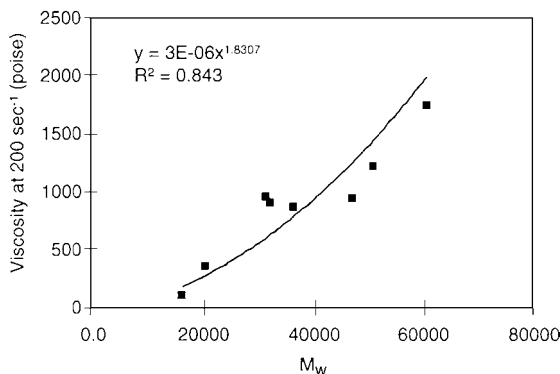
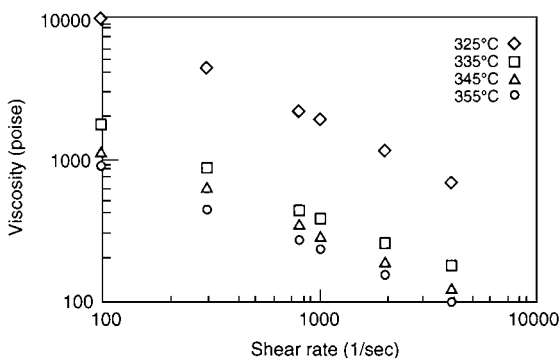


Figure 8.12 The effect of glass fiber on the melt viscosity of Thermx® LCP at 345°C.



**Figure 8.13** Effect of the molecular weight of the matrix LCP (Thermx® LN001) on the melt viscosity of glass fiber-filled LCP.

injection-molding process. The effect of the molecular weight of the matrix TLCP on the melt viscosity of the glass fiber-filled system is illustrated in Figure 8.13. Although the slight decrease in melt viscosity with increasing glass fiber content (see Figure 8.12) is partially due to the molecular weight loss of the TLCP during compounding, breakage of the glass fibers, deformation of the domain structures, and homogenization (reduction of the high molecular weight tail) of the molecular weight distribution during the compounding could also be responsible for the decrease in the melt viscosity. The effect of temperature on the melt viscosity measured on a capillary viscometer for a glass fiber-filled TLCP (Thermx® LG431 from Eastman Chemical Company) is shown in Figure 8.14 [50]. The rapid jump in the melt viscosity at 325°C, which is close to the melting point of this TLCP, is due to crystallization.



**Figure 8.14** The effect of temperature on the melt viscosity of glass fiber-filled Thermx® LG431 [50].

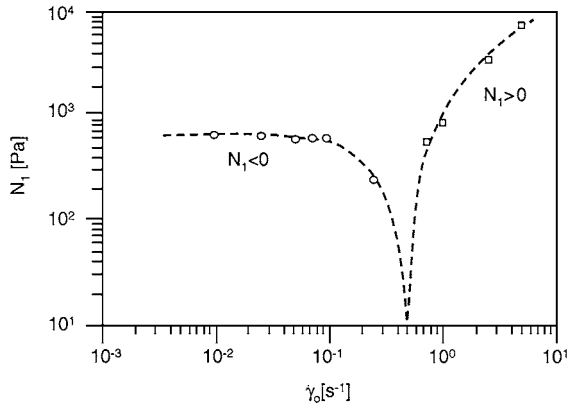


**Figure 8.15** Steady shear,  $N_1$ , vs. shear rate,  $\dot{\gamma}_o$ , at 290°C.  $N_1$  is negative for  $\dot{\gamma}_o < 0.5 \text{ s}^{-1}$  and positive for  $\dot{\gamma}_o > 0.5 \text{ s}^{-1}$  (from Guský and Winter [35], reprinted with permission from *J. of Rheology*).

#### 4.6. NEGATIVE NORMAL STRESS DIFFERENCE

The first and second normal stresses generated under the shear stress are non-linear viscoelastic properties of polymer melts. Particularly, the first normal stress difference ( $N_1$ ) is closely related to various processing and manufacturing behaviors of polymers, including die swell, entrance pressure drop of capillary flow, and reactants climbing the agitator shaft during the melt-phase polymerization. For ordinary isotropic polymers,  $N_1$  is positive and increases with the square of the shear rate [51]. In contrast, LCPs often show negative first normal stresses at low or intermediate shear rates [35,52–55]. Figure 8.15 illustrates the negative  $N_1$  of a TLCP composed of HBA/HNA. The negative  $N_1$  is another unusual rheological behavior of LCPs that is not predicted by the current continuum theory. The Doi-Edwards theory of nematic liquids predicts only positive  $N_1$  which varies linearly with the shear rate, in contrast to the square dependence of  $N_1$  on the shear rate for the flexible polymers [19]. Marrucci attributed the negative  $N_1$  to switching molecular motion of rigid rods from tumbling mode at very low shear rates to flow-aligning mode, i.e., rearrangement of the distribution of molecular orientation at high shear rates [56]. The sudden increase in  $N_1$  from negative to positive values at high shear rates has not been explained well.

The negative  $N_1$  is not always evident for many LCPs. As shown in Figure 8.16, Thermx<sup>®</sup> LN001 shows a very small negative  $N_1$  at low shear rates; but  $N_1$  increases sharply to positive values as the shear rate increases. In contrast, PET (polyethylene terephthalate) shows little  $N_1$  at shear rates up to  $20 \text{ s}^{-1}$ . Beekmans et al. have reported that the normal stress of Vectra<sup>®</sup> B950 is positive over the entire range of the observed shear rate ( $0.1\text{--}60 \text{ s}^{-1}$ ) [24]. Baek et al.

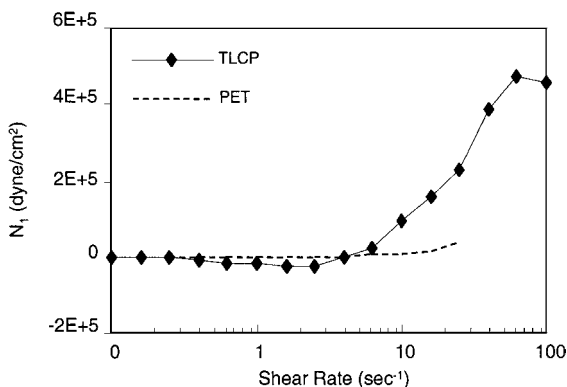


**Figure 8.16** The first normal stress differences of Thermx® LN001 and PET.

have also reported that hydroxypropyl cellulose (HPC) melts did not show the negative  $N_1$  [57]. An interesting observation is that presence of particles in the liquid crystalline solution or melts influences  $N_1$ . A small amount of polystyrene particles in a lyotropic LCP 55% HPC/water solution eliminates negative  $N_1$  or shifts the region of the negative  $N_1$  to the positive direction [58]. This is in contrast with the observation that a TLCP 80/20 HBA/PET exhibits the negative  $N_1$  only when crystallites are present in the melt [54]. Despite all these intriguing experimental observations, the normal stress behaviors of LCPs have not been explained very well by the existing theories.

#### 4.7. ELONGATIONAL VISCOSITY

The elongational viscosity is directly related to the polymer processing, including fiber spinning, film blowing, and fibrillation of TLCPs in isotropic flexible polymers. Numerous methods have been proposed to measure the elongational viscosity of polymers. Dealy and Wissbrun have given a good review of the individual techniques [59]. Although improvements of the experimental methods are being made, each method has limitations and does not characterize the true elongational property of polymers. A direct way to measure the elongational viscosity is to use the clamp-and-pull type extensional rheometer designed by Munstedt [60] or the rotary clamp apparatus designed by Meissner [61]. This type of extensional rheometer is, however, limited to low strain rates typically around 10 sec<sup>-1</sup>. Only limited work has been reported on the elongational viscosity of TLCPs measured by this method [62]. Another way to estimate the elongational property at relatively higher strain rates is spinning fibers with a proper tension-meter attached to the spin line. This spinning method has the drawback of causing non-uniform deformation of the thread along the spin line. The most widely used method in polymer processing simulation, and

probably the most convenient way to estimate an approximate elongational viscosity, is Cogswell's method. This method is based on the entrance pressure drop that is associated with the development of the elongational flow at the converging die entrance [63]:

$$\eta_e = [9(n + 1)^2(P_o)^2]/[32\eta\dot{\gamma}^2] \quad (15)$$

where  $\eta_e$  is the average elongational viscosity,  $n$  is the power law index,  $P_o$  is the entrance pressure loss,  $\eta$  is the shear viscosity, and  $\dot{\gamma}$  is the apparent shear rate. Despite the simplicity of the measurement,  $\eta_e$  estimated by Equation (15) is not the true elongational viscosity because the nature of the flow at the die entrance is not 100% elongational but mixed with non-steady transient shear flow.

Depending on the experimental methods employed, the measured elongational viscosity varies for LCPs. The transient elongational viscosities of hydroxypropyl cellulose (HPC) and Vectra® A900 (73 HPA/27 HNA) melts were measured on a Meissner-type extensional viscometer with rotary clamps by Wilson et al. [62]. They reported that both polymers showed a linear viscoelastic behavior, i.e., the ratio of the elongational viscosity and the shear viscosity is 3, at low strains (<0.5 strain unit) followed by a strain hardening at high strains. Their maximum strain was limited to 2 due to the breakage of sample at the high strain. Metzner et al. used the fiber spinning method to measure the elongational viscosity of a lyotropic 40% HPC solution in acetic acid. They observed a high elongational viscosity with Trouton's ratio of about 10, which is strikingly independent of the strain rate up to  $10 \text{ sec}^{-1}$  [64]. La Mantia et al. used Cogswell's method for Vectra® A900, Vectra® B950, and their Nylon 6 blends. They reported two orders of magnitude higher elongational viscosities than expected from Trouton's rule;  $\eta_e = 3\eta$ . This high elongational viscosity measured by Cogswell's method was attributed to the large energy barrier to overcome by the rigid LCP entering the converging flow at the die entrance [65]. The entrance pressure is determined by the Bagley plot: the linear plot of the pressure drop versus the capillary length-to-diameter ratio,  $L/D$ . It is often found that Bagley plots for LCPs are not linear but tend to have an upward concavity at high  $L/D$ s [66]. This nonlinearity is postulated to be due to loss of molecular orientation by director tumbling under the shear field during transit of the LCP inside the die [67,68]. A "two-fluid" model based on the inner and the outer layers of the fluid inside the die has been proposed to account for the non-linearity in the Bagley plots [67]. This two-fluid layer model has been extended to explain the unusual negative die swell behavior of TLCPs [68], as will be discussed in the next section.

#### 4.8. DIE SWELL

Unlike isotropic flexible polymers, LCPs have very small or even negative die swells. The die swell or the extrudate swell is the result of the stored elastic

energy in the liquid inside the die that is recovered when the liquid leaves the die exit. Based on this idea of Hookian elasticity, a die swell equation that correlates the first normal stress difference ( $N_1$ ) and the die swell ( $DS$ ) has been developed by Tanner [69]:

$$DS = d_f/d_o = 0.1 + [1 + 0.5(S_o)^2]^{1/6} \quad (16)$$

$$S_o = N_1/2\tau_{yx}$$

where  $d_f$  is the extrudate diameter,  $d_o$  is the die diameter, and  $\tau_{yx}$  is the shear stress. Although the Tanner equation provides a qualitative estimation of die swell, the predicted die swell deviates significantly from the measured die swell for many polymers [70]. Furthermore, it would not predict the negative die swell observed for many TLCPs due to the square term of  $S_o$ , which is positive regardless of the sign of  $N_1$ . The Doi theory predicts a range of  $S_o$  for LCPs,  $1.5 < S_o < \infty$ , which depends on the concentration. A small  $S_o$  of 0.75, which is half the predicted minimum value of 1.5 by the Doi theory, has been reported for poly ( $\gamma$ -benzyl-L-glutamate) (PBLG) [19]. According to Equation (16), this  $S_o$  value would yield a  $DS$  of 1.19 or 19%, which is positive.

To account for the negative die swell of LCPs, an improved model based on Tanner's two fluid layer model has been proposed [68]. This model predicts both positive and negative die swells depending on the relative elongational viscosity of the inner and the outer layers of the capillary flow at the die exit:

$$DS = \{V[1 - (R_i/R_o)^2(1 - 1/V)]\}^{1/2} \quad (17)$$

$$V = \eta_o/\eta_i$$

where  $R_i$  is the radius of interface between the two layers at the die exit,  $R_o$  is the radius of the die,  $\eta_o$  is the elongational viscosity of the outer layer, and  $\eta_i$  is the elongational viscosity of the inner layer. When  $V$  is less than unity, i.e., the elongational viscosity of the outer layer is lower than that of the inner layer,  $DS$  should be less than unity (a negative die swell). It was hypothesized that loss of orientation by the director tumbling under the shear field inside the capillary can reduce the elongational viscosity of the outer layer [68]. Occurrence of such a case does not seem to be confirmed either experimentally or theoretically. The direct measurement of the elongational viscosity of the layers, however, would not be trivial, and no measured data have been reported. Measurement of  $R_i$  or the ratio  $R_i/R_o$  would not be trivial either, although they are expected to be an increasing function of  $L/D$  in view of the experimental result that the die swell decreases with increasing  $L/D$  [66].

For ordinary flexible polymers, the die swell increases with the shear rate [71]. The dependence of the die swell on the shear rate is implicitly described in Equation (16). Because  $N_1$  varies with the square of the shear rate and  $\tau_{yx}$  has a power-law relationship with the shear rate,  $S_o$  in Equation (16) will be a power

TABLE 8.2. Effect of Shear Rate on Die Swell of Neat and Glass Fiber-Filled TLCP.

Sample	Glass Fiber (%)	Shear Rate (sec <sup>-1</sup> )	Die Swell Ratio
Thermx® LN001	0	15	1.49
		75	1.40
		750	0.63
Thermx® LG431	30	240	0.81
		600	0.92
		940	1.00

function of the shear rate, with the power less than 2 but greater than 1. Therefore, the die swell should increase with the shear rate. This does not appear to be the case for TLCPs, i.e., the die swell of TLCPs often decreases with increasing shear rate [68]. Table 8.2 shows the decreasing die swell with increasing shear rate for Thermx® LN001. The decreasing die swell with increasing shear rate was attributed to lack of deformability of the rigid LCPs resulting in a minimal stored elastic energy even at high shear rates [65]. Very little theoretical work has been reported on this subject for TLCPs.

Unlike the neat TLCP, the die swell of the glass fiber-filled TLCP increases with the shear rate (see Table 8.2). It should be noted that the glass fiber-filled TLCP also shows negative die swells at the intermediate shear rates. Filled polymers generally show less die swell than the unfilled neat polymers [72–76]. The die swell decreases with the filler concentration presumably due to enhanced rigidity and reduced stored elastic energy of the system in the presence of the fillers [46]. The die length, the shear rate and the filler concentration influence the die swell of the filled polymers. For example, acrylonitrile-butadiene-styrene filled with glass beads or glass fibers shows a maximum die swell at the intermediate shear rate, but the die swell decreases at high shear rates. This behavior was attributed to the order-disorder transition of the fillers at the intermediate shear rate [77]. The lack of die swell can result in insufficient wetting of the gate area of the mold by the polymer, causing the jetting problem during injection molding [32,78]. However, the small or negative die swell does not seem to be a major concern in the processing of TLCPs.

## 5. PROCESSING OF THERMOTROPIC LIQUID CRYSTALLINE POLYMERS

The high orientability and the high shear-thinning behavior of liquid crystalline polymers provide a number of benefits in polymer processing, including the fiber spinning, injection molding, and fibrillation of TLCPs in

TLCP/isotropic polymer blends. Ironically, many rheological and processing behaviors of TLCPs are opposite to what is expected from ordinary thermoplastics. All these unusual behaviors of LCPs are not well understood. In this section, some processing behaviors of TLCPs, their morphologies, and their mechanical properties in relation to the processing conditions will be reviewed.

## 5.1. INJECTION MOLDING

The high shear-thinning behavior of TLCPs is the main advantage for injection-molding applications, especially for thin-walled parts. The high orientability of TLCPs in shear or elongational flow yields a variety of properties which depend on the distribution of the molecular orientation in the molded parts. The orientation distribution depends on the materials, the processing condition, and the mold design. The selection of proper injection-molding conditions and mold designs is particularly important to obtain desired mechanical properties of TLCPs. Another advantage of TLCPs is that they make little or no flashing in the injection-molded parts [79].

### 5.1.1. Morphology of Injection-Molded Parts

A variety of models have been proposed for the morphology of melt processed TLCPs based on microscopy and X-ray studies. Although there is some generality, the actual morphology varies with the type of polymer and the processing conditions. Some typical models proposed in the literature are listed below.

- (1) Hierarchical fibrillar model [80]: This model was proposed for drawn TLCP fibers. They are composed of bundles of macro fibrils ( $5\text{ }\mu\text{m}$ ), fibrils ( $0.5\text{ }\mu\text{m}$ ), and micro fibrils ( $0.05\text{ }\mu\text{m}$ ) in a hierarchical order (see [Figure 8.17](#)). This type of highly oriented fibrillar morphology is also found in the inner skin region of the injection-molded parts, as illustrated in [Figure 8.18](#).
- (2) Hierarchical sheet model [81]: The morphology of injection-molded bar of a HBA/HNA TLCP consists of a skin layer, a boundary layer, and the core region (see [Figure 8.19](#)). The skin layer is divided again into three sublayers: a top layer ( $20\text{ }\mu\text{m}$ ), sublayers ( $30\text{--}50\text{ }\mu\text{m}$ ) that consist of micro layers ( $0.4\text{--}0.6\text{ }\mu\text{m}$ ), and less ordered micro layers. The top layer is oriented in the flow direction, while the core region is oriented perpendicular to the flow direction. The orientation in the flow direction gradually decreases from the surface layer to the core region.
- (3) Four-layer model [82]: The morphology of the injection-molded bar of Ultrax KR 4002 (all-aromatic TLCP from BASF) is composed of four distinct layers: highly oriented skin layer, weakly oriented sub-skin layer, highly

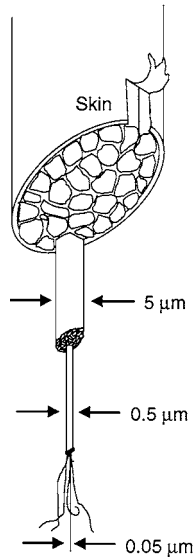


**Figure 8.17** The LCP structural model shows the hierarchical, fibrillar texture of LCP materials (from Sawyer and Jaffe [80], reproduced with permission from *J. Materials. Sci.*).

oriented transition zone, and weakly oriented core zone. The thickness of individual layers varies with the injection speed (see Figure 8.20).

- (4) Five-layer model [83]: The morphology of injection-molded bars of a TLCP, para-acetoxybenzoic acid and para-acetoxynaphthoic acid (70/30),

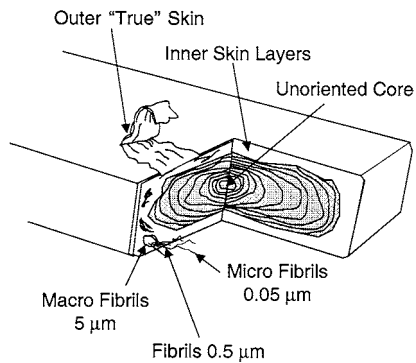


**Figure 8.18** The LCP polymer structure of moldings (from Sawyer and Jaffe [80], reproduced with permission from *J. Materials. Sci.*).

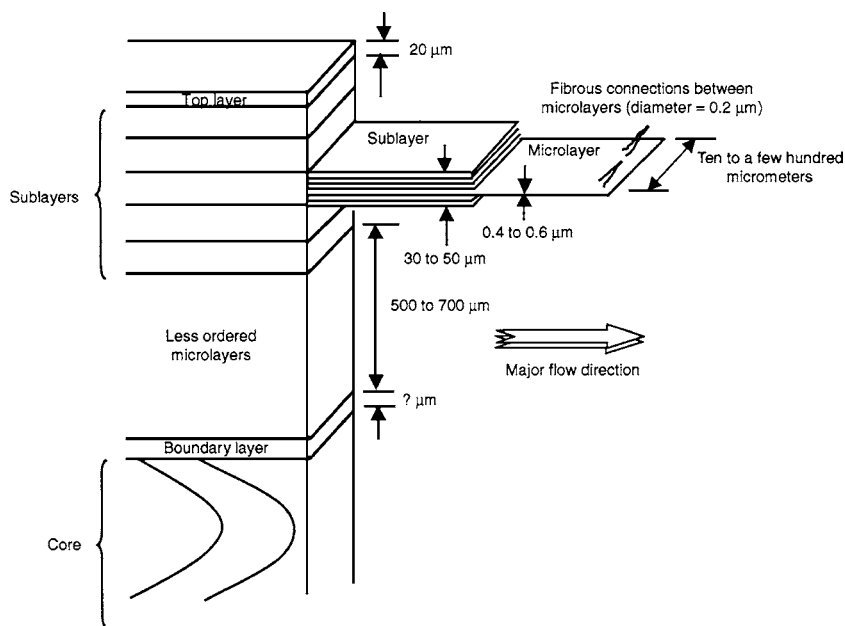


**Figure 8.19** Schematic illustration of the proposed hierarchical model (not drawn to scale) (from Weng, Hilmer, and Baer [81], reproduced with permission from *J. Materials. Sci.*).

is composed of the skin, nodules, a mixture of nodules and fibrils, tightly packed fibrils, and the parabolic core. Both the skin and the core layers have sheet-like structures composed of fibrils. The sheets in the skin have orientation in the flow direction, while those in the core region have orientation

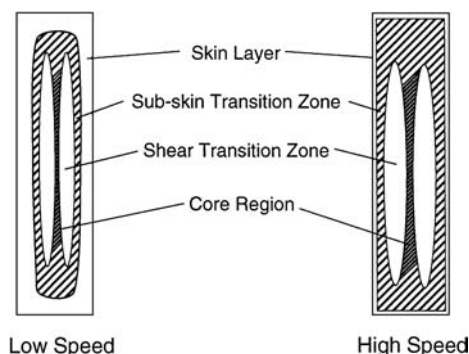


**Figure 8.20** Schematic of four-layer model of injection-molded LCP at low and high injection speeds (from Hshuing, Tian, and Cakmak [82], *Intern. Polymer Processing*, reproduced with permission from Hanser Publishers).

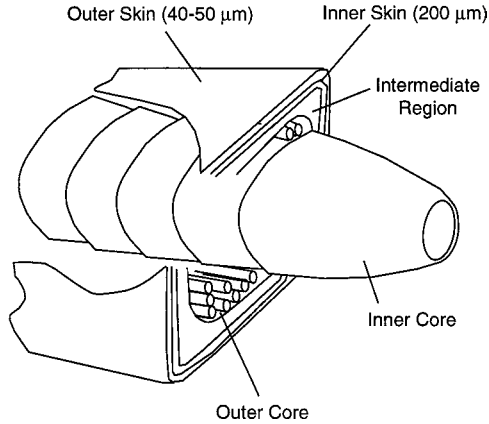


**Figure 8.21** Five-layer morphology with conical core of injection-molded TLCP (from Plummer [84], *Advanced Thermoplastic Composites*, 1993, reproduced with permission from Hanser Publishers).

perpendicular to the flow direction. This model is similar to the hierarchical sheet model. The cavity thickness controls the thickness of the skin layer. For a 1-mm thick sample, approximately 90% of the section is the skin layer, while for a 4-mm thick sample, only 60% of the section is occupied by the skin layer.

- (5) Five-layer model with conic flow surfaces in the inner core [84]: The morphology of Vectra® 900, 73/27 HBA/HNA injection-molded into a dumbbell-shaped tensile bar, is composed of a highly birefringent outer skin (40–50  $\mu\text{m}$ ), a birefringent inner skin (200  $\mu\text{m}$ ), an intermediate region that is weakly birefringent, an outer core with a fibrillar structure (fibril diameter of 5  $\mu\text{m}$ ), and an inner core composed of conic flow surfaces pointing along the sample axis and concentric with the core center. The conic flow surface attenuates toward the center of the inner core, but its fracture surface reveals that it is predominantly fibrillar (see Figure 8.21).

The morphology of the fabricated articles is closely related to the injection speed. As the injection speed increases, the thickness of the skin layers decreases substantially, while the thickness of less oriented sub-skin transition layers increases (see Figure 8.20) [82]. Consequently, the tensile modulus and the tensile strength of TLCPs increase with decreasing injection speed or injection pressure due to the higher orientation of the skin layer in the flow direction [83,85,86]. The increase in orientation of the TLCP with decreasing injection speed is not normally expected because the orientation increases with the injection speed for ordinary thermoplastics. The processing temperature also influences the morphology of molded parts. Normally, the barrel temperature increases the orientation, resulting in better mechanical properties [83].

The mold temperature, on the other hand, affects the thickness of skin layers [82,83,87]. In general, the effect of temperature on the mechanical properties is relatively small compared to the injection speed. Mathematical modeling and computer simulations based on Doi's molecular theory for the motion of rigid rods were recently used in an attempt to predict the orientation and flow behavior of TLCPs in the mold as a function of processing conditions. A reasonably good agreement between the simulation and the experiment was reported [88].

### 5.1.2. Mechanical Properties of Injection-Molded Parts

The effect of orientation on the mechanical properties of injection-molded bars is phenomenal for TLCPs. A list of tensile properties of both a thermoplastic poly(1,4-cyclohexylene dimethylene terephthalate) (PCT) and Thermx<sup>®</sup> LN001, which were injection-molded in end-gated molds with different wall thicknesses, is shown in Table 8.3. The tensile properties of the TLCP increase straightforwardly with decreasing thickness, while the thickness effect is negligible for the thermotropic PCT. The enhanced tensile properties of thinner parts are due to the molecular orientation of the polymer as indicated by the Hermans orientation function. It is not feasible to obtain the Hermans orientation function for PCT due to lack of crystallinity. For the filled TLCP, the glass fibers may interfere with the X-ray diffraction causing poor resolution. The effect of orientation on the mechanical properties ( $E'$ ) can also be examined by dynamic mechanical analysis (DMA) [89]. Figures 8.22 and 8.23 show the DMA data of PCT and Thermx<sup>®</sup> LCP, respectively. No thickness effect on the modulus ( $E'$ ) is seen for PCT [see Figure 8.22(a)], while the thickness effect is substantial

TABLE 8.3. Effect of Mold Thickness on the Mechanical Property of LCP and Thermoplastic PCT.

	Glass Fiber (%)	Thickness (mm)	Tensile Strength (MPa)	Young's Modulus (MPa)	Break Elongation (%)	Hermans Orientation Function
Thermx <sup>®</sup> LN001	0	3.2	125	7066	3.1	0.42
		1.6	196	12215	2.4	0.59
		0.8	239	14763	2.4	0.61
Thermx <sup>®</sup> LG431	30	3.2	105	8655	4.2	—
		1.6	119	13478	2.3	—
		0.8	166	17671	2.1	—
PCT	0	3.2	33	1784	34	—
		1.6	30	1722	51	—
		0.8	28	1827	43	—
PCT with glass fibers	30	3.2	90	8752	1.4	—
		1.6	87	9295	1.3	—
		0.8	83	9345	1.2	—

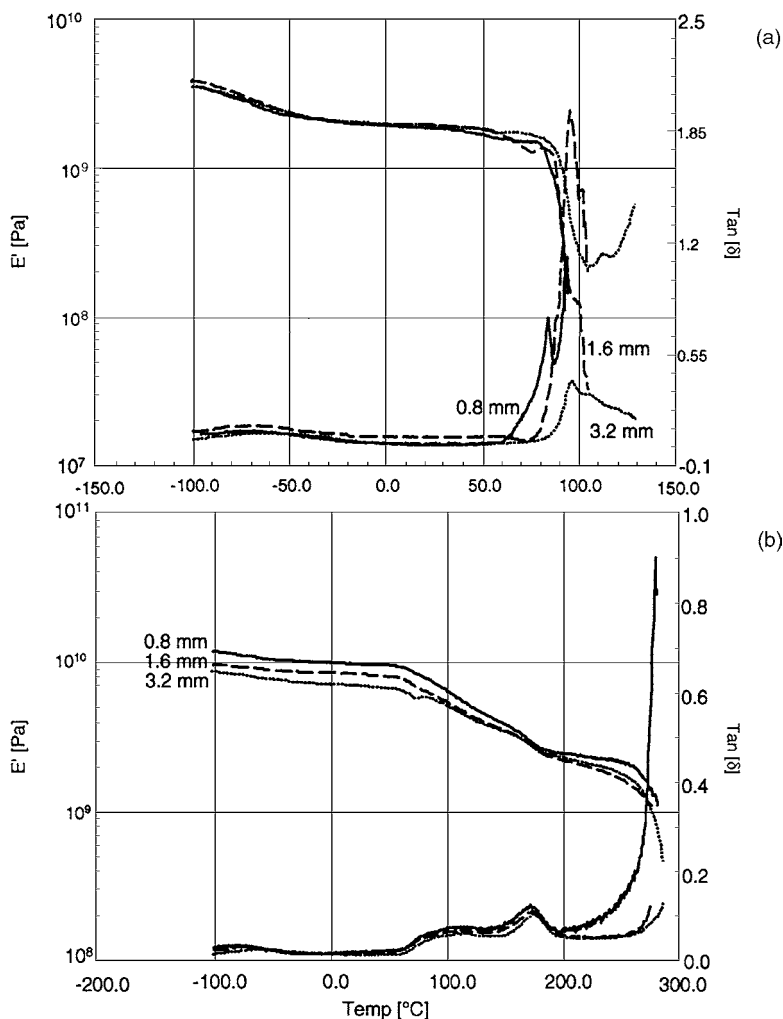


**Figure 8.22** Effect of mold wall thickness on the dynamic mechanical properties of injection-molded bars of PCT; (a) unfilled and (b) filled with glass fibers.

for the TLCP [see Figure 8.23(a)]. The negligible effect of the thickness on the mechanical properties of the unfilled flexible PCT suggests that the molecular orientation developed during the injection is rapidly relaxed out before the melt solidifies. Due to the fast relaxation time, the molecular orientation in injection-molded parts of ordinary thermoplastics is greatly controlled by the mold temperature and the cooling rate of the mold. On the other hand, TLCPs have characteristically long relaxation times, so that the orientation developed

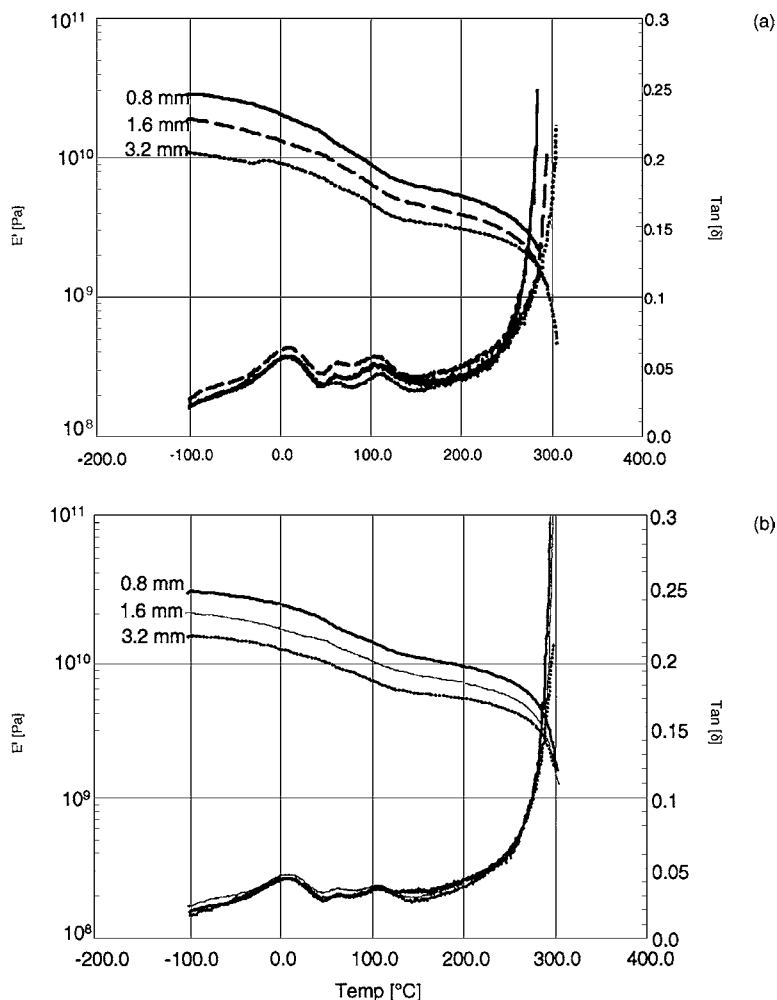


**Figure 8.23** Effect of mold wall thickness on the dynamic mechanical properties of injection-molded bars of Thermx® LCP; (a) unfilled and (b) filled with glass fibers.

in the mold is retained during the cooling cycle. The orientation in the molded part is also influenced by the molecular weight of TLCPs, so that there is an optimum molecular weight that yields the maximum tensile property [18]. Above the critical molecular weight, the sluggish large molecules may not easily orient under the applied shear and within the processing time.

In many commercial thermoplastics, glass fibers are added to enhance tensile properties, heat deflection temperature, dimensional stability, and flame

retardancy. The tensile strength of the composite material has two contributions: one from the glass fiber and the other from the matrix, and may be expressed by the Kelly-Tyson equation [90–92]:

$$\sigma_c = \tau_i(L/D)C_oV_f + \sigma_mV_m \quad (18)$$

where  $\sigma_c$  is the tensile strength of the composite,  $\sigma_m$  is the tensile strength of the matrix polymer,  $\tau_i$  is the interfacial shear strength,  $L$  is the average fiber length,  $D$  is the fiber diameter,  $C_o$  is the orientation function of the fiber in the test direction,  $V_f$  is the volume fraction of the fiber, and  $V_m$  is the volume fraction of the matrix polymer. The strong effect of glass fiber on the tensile property of the isotropic PCT is clearly seen in Table 8.3 and Figure 8.22, that is expected from Equation (18).

The contribution of the glass fiber [the first term in Equation (18)], estimated with known values of  $\tau_i$  and  $C_o$ , was about 30% for a Thermx<sup>®</sup> LG 431 [93]. As shown in Table 8.3 and Figure 8.23, the observed glass fiber contribution to the tensile property of the TLCP is small or even negative. Although it appears that the Kelly-Tyson equation would not predict the tensile property of the TLCP, accurate estimates of  $\tau_i$  and  $C_o$  will be necessary to verify the validity of the equation for glass fiber-filled TLCPs. It was postulated that the improperly dispersed glass fibers may form weak slip boundaries between glass fibers not in contact with the matrix, causing the lower properties of the glass fiber-filled TLCP [93].

The negligible effect of glass fibers on the mechanical properties of the glass fiber-filled TLCP suggests that the mechanical properties of glass fiber-filled TLCPs are mainly controlled by the molecular orientation of the TLCP. The role of the glass fibers in the filled LCP is then to alter the molecular orientation in the lateral direction, which improves the strength of the composite in the transverse direction such as heat-deflection temperature. In contrast, glass fibers significantly enhance the mechanical properties of flexible polymers such as PCT. Furthermore, the effect of wall thickness on the mechanical properties of the flexible polymer becomes significant only when glass fibers are present in the polymer, suggesting that the properties of glass fiber-filled flexible polymers are predominantly controlled by the glass fiber orientation.

### 5.1.3. Weld Line Strength

The strength of weld lines in injection-molded articles is generally weaker than that of the bulk. This is due to the incomplete entanglement of polymer chains at the two impinging fountain flow fronts in the mold cavity. When the two flow fronts meet in the cold cavity, the molecular orientation at the interface remains parallel to the weld line as evidenced by the frozen-in molecular orientation found in the molded article under proper injection-molding conditions

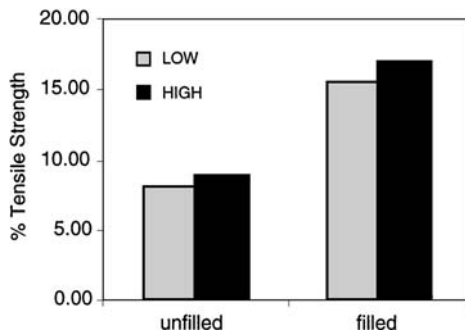


**Figure 8.24** Weld line strengths of unfilled and filled Thermx<sup>®</sup> LCP at two different conditions. HIGH means high temperature, high pressure, and high injection speed; LOW means low temperature, low pressure, and low injection speed [100].

[94]. The entanglement of the polymer chains at the weld line is related to their diffusion rate, which is a function of temperature and melt viscosity of the polymer [95]. The holding pressure in the cavity and the injection speed can also affect the weld line strength [96]. Many predictive models for the weld line strength of thermoplastic amorphous polymers in relation to the viscoelastic properties and processing conditions such as the melt temperature, the mold temperature, and the holding time, have been proposed [97–99].

Due to the low rotational diffusion coefficient and high orientability, the weld line strength of rigid LCPs is very poor. Figure 8.24 shows the weld line strengths of Thermx<sup>®</sup> LCP (the neat and the 30% glass fiber filled) as a percentage of the bulk strength. Although the glass fiber improves the weld line strength significantly, it is still below 20% of the bulk strength. The combination of high temperature, high pressure, and fast injection speed has a relatively small effect on the weld line strength [100]. The typical weld line strength of ordinary thermoplastics is 25–98% of the bulk strength depending on the materials and processing conditions [96].

The weak weld line strength could be detrimental for some applications. Numerous studies have been reported on how to improve the weld line strength by either changing the processing conditions or modifying the mold design. Gardner et al. demonstrated a significant improvement of the weld line strength for a polypropylene with 40% glass fibers using a special mold in which pins reciprocate back and forth vertically to the cavity wall, which promotes the localized mixing across the weld zone near the pins [101]. Similar approaches have been reported for TLCPs [86,102,103]. It has been reported that a controlled shear orientation can improve the weld line strength by as much as 90% [102]. Kawaguchi et al. have claimed in their patents that incorporation of branched flows, which remobilize the melt at the weld line, improves the weld line strength [103]. Relocation of the weld line to the less critical region

of the part can be another option to avoid the weak weld line problem [86]. Modification of the material, e.g., improving interfacial strength for blends, has been also suggested to improve the weld line strength of thermoplastics [104]. Obviously, the choice of methods to improve the weld line strength depends on the materials and the applications.

## 5.2. EXTRUSION AND COMPOUNDING

Blending a small amount of LCP to the conventional flexible thermoplastic polymer to enhance the tensile modulus of blown films [105–107] or to develop in situ composite structures with fibrillated LCPs [108–111] has drawn much attention. The strength enhancement of the LCP blends is normally achieved by having the LCP fibers elongated with the aspect ratio greater than 40 [111]. A significant but not dramatic increase of modulus by employing multiple drawing stages at various temperatures has also been reported [112]. Poorly dispersed LCP droplets tend to show up on the surface of extruded films. Fibrillation of the LCP under proper elongational flow improves the appearance of the surface by reducing the LCP droplets. A special jet to break the LCP droplets for a more uniform surface has also been suggested [113,114]. The extensive work on LCP blends and their rheology and processing has been reviewed by Utracki [115] and Acierno et al. [116].

Various defects on the surface of the extrudate can result depending on the process conditions, including the temperature profile of the extruder at various zones. One major concern with the extruded films or parts from neat TLCPs for high performance applications, such as flight balloons, is poor surface appearance. A typical surface defect is the grainy texture, which is believed to be caused by the change in molecular orientation of the LCP. Setting the die temperature close to the extruder temperature or conducting a multiple pass operation normally improves the surface uniformity [105]. One of the big advantages of TLCPs over thermoplastics in melt processing is that they have an excellent thermal stability, which allows a multiple pass operation without significant molecular weight loss. For ordinary thermoplastics, high melt elasticity and high extrusion speed tend to cause irregular surface “melt fractures” on the extrudate. As discussed earlier, TLCPs have high normal stresses at moderate or high shear rates (see Figures 8.15 and 8.16) that may cause melt fracture at certain conditions. Unlike ordinary thermoplastics, however, the surface of TLCP becomes smoother as the extrusion speed increases. This is particularly true when the TLCP is compounded with glass fibers. Proper controls of the barrel temperature, the die temperature, and the extrusion speed will be necessary to alleviate the melt fracture or the surface defect. Due to the low melt viscosity of TLCPs at high shear rates (high shear thinning), glass fibers often would not mix well with TLCPs during compounding. Modification of screw design is the normal practice to obtain good dispersion of the glass fibers with proper fiber lengths without having a significant breakdown of molecular weight in the matrix polymer.

### 5.3. FIBER SPINNING

It is well known that the fibers from lyotropic LCPs such as Kevlar® and poly(*p*-benzamide) (PBA) have much higher modulus and tensile strength than conventional thermoplastic fibers. They are spun by dry spinning (for PBA) or by dry-jet-wet spinning (for Kevlar®) [117]. The enhanced properties are inherited from their rigid molecular structure and the high molecular orientation. Such high modulus fibers with high levels of orientation can also be melt-spun from TLCPs. The highly oriented fibrillar structure constructed in a hierarchical manner, which is the common structure of lyotropic fibers, has also been observed for TLCP fibers (see Figure 8.17) [80].

In conventional melt spinning, the molecular orientation in the spun fibers is achieved by spin drawing. The extent of drawing is controlled by the extrusion throughput and the take-up speed. Due to the short relaxation time in the case of ordinary thermoplastics, the orientation developed at the entrance or inside of the spinneret will be lost very rapidly at the spinneret exit. As a result, the molecular orientation in the undrawn fibers of flexible polymers is normally small. For TLCPs, on the other hand, high orientation is developed even in undrawn fibers, and further drawing provides only a marginal increase in orientation [18,118]. Figure 8.25 shows the plot of Hermans orientation function (HOF) versus the take-up speed of Thermx® LN001. The tensile moduli of the fibers are shown in Figure 8.26. The low modulus value at 200 ft/min is probably due to the imperfection of the fiber samples. A very rapid increase in modulus at the low draw ratio followed by a gradual increase has been reported for 40PET/60PHB fibers [119]. It is believed that the elongational flow at the die entrance creates a significant amount of molecular orientation, which is maintained both inside the die and after the die exit due to the long relaxation

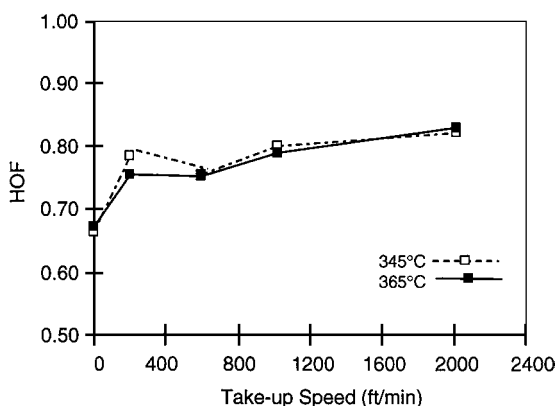


**Figure 8.25** Hermans orientation function of Thermx® LN001 fibers spun at different take-up speeds (from Seo [18], reproduced with permission from Society of Plastics Engineers).

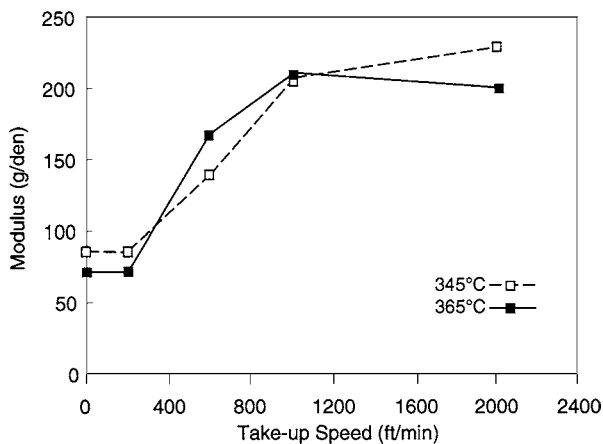


**Figure 8.26** Moduli of Thermx® LN001 fibers spun at different take-up speeds.

time of TLCPs. It has been observed that the modulus of spun fibers increases with the capillary L/D, while the effect of drawing is more prominent when a short die is used [118]. This result was attributed to the improved orientation due to more shear with longer residence time in the long capillary. This conclusion appears contrary to the two-fluid layer model [Equation (17)] where the shear inside the capillary is assumed to reduce the orientation of LCPs, resulting in a little or negative die swell. Another interesting observation of TLCPs is the effect of shear rate on the melt fracture. The melt fracture of extruded rods or fibers of flexible thermoplastics normally occurs when the shear stress is increased above the critical shear stress and becomes more severe as the shear rate increases. For TLCPs, the melt fracture disappears and better fibers are produced when the shear stress at the die wall exceeds the critical shear stress [119,120].

It has been reported that higher melt temperatures tend to improve the molecular orientation and the modulus of glass fiber-filled TLCPs [119]. This does not seem to always be the case (see Figures 8.25 and 8.26). Although better liquid crystallinity or fewer defects in the fiber may result with increasing temperature, the main effect of high temperature appears to be better melting of the crystallites. Imperfectly melted crystallites or unmelts at lower temperatures are expected to interrupt the orientation of the neighboring molecules. Heat treatment (annealing) of fibers, which is controlled by fiber diameter, time, and temperature, often improves the fiber properties, particularly for liquid crystalline copolyesters. The main effect of annealing on the fiber properties of the liquid crystalline copolyesters is from the molecular weight enhancement by solid-state polymerization upon heating.

TABLE 8.4. Tensile Properties of Various Fibers.

Fibers	Strength (g/d)	Elongation (%)	Modulus (g/d)	References
Kevlar®	25	5	850	[117]
PBA	15	3	1050	[117]
Nomex®	5.5	35	82	[117]
PET	9	7	160	[117]
PP (iso)	9	15	120	[117]
PE	9	8	100	[117]
Nylon 6	9.5	16	50	[117]
HBA/HNA/HQ/TPA	7	2–4.5	400	[120]
HBA/HNA (75/25)	9	2	400–600	[119,121]
HBA/HNA/TPA/ 4,4'-biphenol (60/10/15/15)	—	—	1080	[121]

A list of tensile properties of various LCP fibers in comparison with those of typical thermoplastic fibers is made in Table 8.4. It should be noted that the fiber properties of TLCPs in Table 8.4 are not for commercial fibers and should be used only for a comparison purpose. The fiber spinning, orientation, and properties of TLCP fibers have been well reviewed in the literature [121,122].

## 6. REFERENCES

1. H. Yamakawa, *Modern Theory of Polymer Solutions*, Ch. 6, Harper & Row, New York (1971).
2. M. Doi and S. F. Edwards, *The Theory of Polymer Dynamics*, Ch. 9, Oxford Science Publications, Oxford (1986).
3. L. J. Fetters and H. Yu, *Macromolecules*, 4, 385 (1971).
4. M. Bohdanecky, *Macromolecules*, 16, 1483 (1983).
5. K. S. Seo and G. B. Caflisch, submitted to *J. Polym. Sci., Polym. Phys.*
6. G. B. Caflisch, Paper presented at *International Symposium on Polymers and Complex Fluids*, Seoul, Korea, Korean Chemical Society (1993).
7. G. L. Brelsford and W. R. Krigbaum, in *Liquid Crystalline in Polymers*, Ch. 2, ed. by A. Cifferi, VCH, New York (1991).
8. A. Ying, B. Chu, R. Qian, J. Bao, J. Chang, and C. Xu, *Polymers*, 26, 1401 (1985).
9. H. Kromer, R. Kuhn, H. Pielartzik, and W. Siebke, *Macromolecules*, 24, 1950 (1991).
10. W. R. Krigbaum and T. Tanaka, *Macromolecules*, 21, 743 (1988).
11. W. A. MacDonald, A. D. McLennaghan, and R. W. Richards, *Macromolecules*, 25, 826 (1992).
12. M. Doi and S. F. Edwards, *J. Chem. Soc. Farad. Trans. II*, pp. 560, 918 (1978).
13. K. F. Wissbrun, *J. Rheol.*, 25 (6), 619 (1981).
14. D. G. Baird and R. L. Ballman, *J. Rheol.*, 23, 505 (1979).
15. D. R. Wiff, S. Timms, T. E. Helminiak, and W. Hwang, *Polym. Eng. Sci.*, 27 (6), 424 (1987).
16. A. Romo-Uribe and A. H. Windle, *Macromolecules*, 28, 7085 (1995).
17. S. S. Kim and C. D. Han, *Macromolecules*, 26, 24, 6633 (1993).
18. K. S. Seo, *SPE ANTEC 98*, 45, 1566 (1998).

19. R. G. Larson, *Constitutive Equations for Polymer Melts and Solutions*, Ch. 10, Butterworths Series in Chemical Engineering, Butterworth, Boston (1988).
20. P. G. de Gennes, *Scaling Concepts in Polymer Physics*, Cornell Univ. Press, Ithaca, NY (1979).
21. S. Onogi and T. Asada, in *Rheology*, Vol. 1, ed. by G. Astarita, G. Marrucci, and L. Nicolais, Plenum Press, New York (1980).
22. K. F. Wissbrun, *British Polym. J.*, 12, 4, 163 (1980).
23. D. W. Giles and M. M. Denn, *J. Rheo.*, 38, 617 (1994).
24. G. Beekmans, A. D. Gotsis, and B. Norder, *J. Rheo.*, 40 (5), 947 (1996).
25. D. Demus and L. Lichter, *Textbook of Liquid Crystals*, Verlag Chemie, New York (1978).
26. C. Noel, *Acta Polymer.*, 48, 335 (1997).
27. G. Marrucci, in *Rheology and Processing of Liquid Crystalline Polymers*, Ch. 2, ed. by D. Acerino and A. A. Collyer, Chapman & Hall, London (1993).
28. G. Marrucci, *Proceedings of the 9th International Congress on Rheology*, Acapulco, Mexico, Oct. 8–13 (1984).
29. G. Marrucci, in *Advance in Rheology*, Vol. 1, 441, ed. by B. Mena, A. Garcia-Rejon, and C. Rangel-Nafaile, Elsevier, Amsterdam (1984).
30. K. Wissbrun, *Faraday Discuss. Chem. Soc.*, 79, 161 (1985).
31. D. Dorraishwamy and A. B. Metzner, to be published in *Rheological Acta* (1987).
32. F. N. Cogswell and K. F. Wissbrun, in *Rheology and Processing of Liquid Crystalline Polymers*, Ch. 4, ed. by D. Acierno and A. A. Collyer, Chapman and Hall, London (1996).
33. D. S. Kalika, D. W. Giles, and M. M. Denn, *J. Rheo.*, 34 (2), 132 (1990).
34. D. S. Kalika, L. Nuel, and M. M. Denn, *J. Rheo.*, 33 (7), 1059 (1989).
35. S. M. Guskey and H. H. Winter, *J. Rheo.*, 35 (6), 1191 (1991).
36. S. F. Rubin, R. M. Kannan, J. A. Kornfield, and C. Boeffel, *Macromolecules*, 28, 10, 3521 (1995).
37. L. J. Fetters, D. J. Roshe, D. Richter, T. A. Witten, and A. Zirkel, *Macromolecules*, 27, 17, 4639 (1994).
38. S. Wu, *Polym. Eng. Sci.*, 32 (12), 823 (1992).
39. G. Marrucci and N. Grizzuti, *J. Polym. Sci. Polym. Letter ed.*, 21, 83 (1983).
40. A. Mekkaoui and H. Lobo, *ANTEC 92*, 1368 (1992).
41. D. A. Simoff and R. S. Porter, *Mol. Cryst. Liquid Cryst.*, 110, 1 (1984).
42. D. R. Gregory, *J. Appl. Polym. Sci.*, 12 (40), 1479 (1972).
43. F. P. La Mantia and A. Valenza, *Polym. Eng. Sci.*, 29, 625 (1989).
44. C. D. Han, *Multiphase Flow in Polymer Processing*, Ch. 3, Academic Press, New York (1981).
45. M. J. Folkes, *Short Fiber Reinforced Thermoplastics*, John Wiley & Sons, New York (1982).
46. S. N. Maiti and P. K. Mahapatro, *Polymer Composites*, 9, 4, 291 (1988).
47. J. M. Charrier and J. M. Rieger, *Fiber Sci. Technol.*, 7, 161 (1974).
48. L. Nuel and M. Denn, *Rheo. Acta*, 30, 65 (1991).
49. V. G. Kulichikhin, V. F. Shumskii, and A. V. Semakov, in *Processing and Properties of Liquid Crystalline Polymers*, Ch. 5, ed. by D. Acerino and F. P. La Mantia, Chem Tech Publishing, London (1993).
50. G. M. Stack, data presented at 31st Ann. Connector and Interconnection Sympo. and Trade Show, International Institute of Connector and Interconnection Technology, Inc., Boston, October (1998).
51. J. M. Dealy and K. F. Wissbrun, *Melt Rheology and Its Role in Plastic Processing*, Ch. 5, Van Nostrand Reinhold, New York (1990).
52. G. Kiss and R. S. Porter, *J. Polym. Sci., Polym. Symp.*, 65, 193 (1978).
53. G. Kiss and R. S. Porter, *Mol. Cryst. Liq. Cryst.*, 60, 267 (1980).
54. A. D. Gotsis and D. G. Baird, *J. Rheol.*, 29, 538 (1985); *Rheol. Acta*, 25, 275 (1986).
55. J. J. Magda, S. G. Baek, and L. deVries, *Macromolecules*, 24, 4460 (1991).
56. G. Marrucci and P. L. Muffettone, *Macromolecules*, 22, 4076 (1989).

57. S. G. Baek, J. J. Magda, R. G. Larson, and S. D. Hudson, *J. Rheol.*, 38, 1473 (1994).
58. P. Moldinaers, J. Vermant, E. Heinrich, and J. Mewis, *Rheol. Acta*, 37, 463 (1998).
59. J. M. Dealy and K. F. Wissbrun, *Melt Rheology and Its Role in Plastic Processing*, Ch. 6, Van Nostrand Reinhold, New York (1990).
60. H. Munstedt, *J. Rheol.*, 23, 421 (1979).
61. J. Meissner, *Polym. Eng. Sci.*, 27, 537 (1987).
62. T. S. Wilson and D. G. Baird, *J. Non-Newtonian. Fluid Mech.*, 44, 85 (1992).
63. F. N. Cogswell, *Polym. Eng. Sci.*, 12, 1, 64 (1972).
64. A. B. Metzner and G. M. Prilutski, *J. Rheol.*, 30 (3), 661 (1986).
65. F. P. La Mantia, M. Paci, and P. Magagnini, *Rheol. Acta*, 36 (2), 152 (1997).
66. D. E. Turek, G. P. Simon, and C. Tiu, *J. Rheol.*, 36 (6), 1057 (1992).
67. K. F. Wissbrun, *J. Rheol.*, 37 (5), 777 (1993).
68. K. F. Wissbrun, *J. Rheol.*, 38 (2), 247 (1994).
69. R. I. Tanner, *J. Appl. Polym. Sci.*, A-2, 8, 2067 (1970).
70. D. G. Baird and D. I. Collias, *Polymer Processing—Principle and Design*, Ch. 7, John Wiley & Sons, New York (1998).
71. J. L. White and J. F. Roman, *J. Appl. Polym. Sci.*, 20, 1005 (1976).
72. N. Minagawa and J. L. White, *J. Appl. Polym. Sci.*, 20, 501 (1976).
73. Y. Chan and J. L. White, *Polym. Eng. Sci.*, 18, 25 (1978).
74. T. Nishimura and T. Kataoka, *Rheol. Acta*, 23, 401 (1984).
75. A. B. Metzner, *J. Rheol.*, 29, 739 (1985).
76. A. Wagner, R. Yazici, and D. M. Kalyon, *Polymer Composites*, 17, 6, 840 (1996).
77. U. Yilmazer, *Polymer Composites*, 10, 1, 1 (1989).
78. K. Oda, J. L. White, and E. S. Clark, *Polym. Eng. Sci.*, 16 (8), 585 (1976).
79. K. F. Wissbrun, *Polym. Eng. Sci.*, 31 (15), 1130 (1991).
80. L. C. Sawyer and M. Jaffe, *J. Mater. Sci.*, 21, 1987 (1986).
81. T. Weng, A. Hilmer, and E. Baer, *J. Mater. Sci.*, 21, 744 (1986).
82. C. M. Hsuing, J. Tian, and M. Cakmak, *Intern. Polym. Process.*, 2, 164 (1993).
83. H. Thapar and M. Bevis, *Plastics and Rubber Processing Applications*, 12, 39 (1989).
84. J. G. Plummer, in *Advanced Thermoplastic Composites*, Ch. 8, ed. by H. Kausch, Hanser Publisher, Munich (1993).
85. O. Khennache and M. R. Kamal, *SPE ANTEC 89*, 35, 1721 (1989).
86. Z. Ophir and Y. Ide, *Polym. Eng. Sci.*, 23 (14), 792 (1983).
87. P. G. Hedmark, J. M. R. Lopez, M. Westdal, P. E. Werner, J. F. Janson, and U. W. Gedde, *Polym. Eng. Sci.*, 28, 1248 (1988).
88. C. Lekakou, *Polym. Eng. Sci.*, 37 (3), 529 (1997).
89. J. C. Scanlan, *SPE ANTEC 98*, Vol. II, 1575 (1998).
90. P. A. Templeton, *J. Reinforced Plastics and Composites*, 9, 210 (1990).
91. H. Fukuda and T. Chou, *J. Materials Sci.*, 17, 1001 (1982).
92. Y. Termonia, *J. Polym. Sci., Part B, Polym. Phys.*, 32, 969 (1994).
93. G. M. Stack and R. A. Knowels, *SPE ANTEC 98*, Vol. II, 1187 (1998).
94. Z. Tadmor, *J. Appl. Polym. Sci.*, 19, 558 (1979).
95. W. W. Graessley, *J. Polym. Sci., Polym. Physics*, 18, 27 (1980).
96. R. Seldon, *Polymer Eng. Sci.*, 37 (1), 205 (1997).
97. S. Kim and N. P. Suh, *Polym. Eng. Sci.*, 26 (17), 1200 (1986).
98. T. J. Pecorini and K. S. Seo, *Plastics Eng.*, 52 (6), 31 (1996).
99. A. Haufe and G. Menning, *Angew. Makromol. Chem.*, 265, 75 (1999).
100. G. M. Stack, unpublished data.
101. G. P. Gardner and R. A. Molloy, *ANTEC 96*, Vol. I, 685 (1996).
102. L. Wang, P. S. Allan, and M. J. Bevis, *Plas., Rubber Compos. Process. Appl.*, 23 (3), 139 (1995).

103. A. Kawaguchi and N. Wakita, Japanese Patents 90-417782 901228, 90417781 901228 (1994).
104. S. Fellahi, B. Fisa, and B. D. Favis, *J. Appl. Polym. Sci.*, 57 (11), 1319 (1995).
105. T. C. Hsu and I. R. Harrison, *SPE ANTEC* 93, 39, 1183 (1993).
106. A. M. Lichkus and I. R. Harrison, *SPE ANTEC* 92, 38, 2257 (1992).
107. A. Siegmman, A. Dagan, and S. Kenig, *Polymer*, 26, 1325 (1985).
108. G. Kiss, *Polym. Eng. Sci.*, 27, 410 (1987).
109. K. G. Blizard and D. G. Baird, *Polym. Eng. Sci.*, 27, 653 (1987).
110. M. A. McLeod and D. G. Baird, *Polym. Composites*, 20 (1), 3 (1999).
111. W. Huh, PhD Thesis, U. of Connecticut (1986).
112. Y. Quin, D. L. Brydon, and R. R. Mather, *Polymer*, 341203 (1993).
113. M. Pracella, E. Chillinie, and G. Galli, *Mol. Cryst. Liquid Cryst.*, 153, 525 (1987).
114. A. M. Sukhadia, A. Datta, and D. G. Baird, *SPE ANTEC* 91, 37, 913 (1991).
115. L. A. Utracki, *Commercial Polymer Blends*, Ch. 21, Chapman & Hall, New York (1998).
116. D. Acierno and F. P. La Mantia, in *Processing and Properties of Liquid Crystalline Polymers and LCP Based Blends*, ed. by D. Acerino and F. P. La Mantia, ChemTech, Toronto (1993).
117. H. H. Yang, in *Handbook of Fiber Science and Technology*, Vol. III—*High Technology Fibers*; Part C, Ch. 2, ed. by M. Lewin and J. Preston, Marcel Dekker, Inc., New York (1993).
118. K. Shimamura, J. L. White, and J. F. Fellers, *J. Appl. Polym. Sci.*, 26, 2165 (1981).
119. W. R. Krigbaum, in *Spinning Thermotropic Polymers, Handbook of Fiber Science and Technology*, Vol. III—*High Technology Fibers*; Part B, Ch. 9, ed. by M. Lewin and J. Preston, Marcel Dekker, New York (1989).
120. K. S. Seo, unpublished data.
121. M. Jaffe, G. Calundann, and H. Yoon, in *Spinning Thermotropic Polymers, Handbook of Fiber Science and Technology*, Vol. III—*High Technology Fibers*; Part B, Ch. 3, ed. by M. Lewin and J. Preston, Marcel Dekker, New York (1989).
122. J. Nakagawa, in *Advanced Fiber Spinning Technology*, Woodhead Publishing, Cambridge, UK, 160–71 (1994).

# Liquid Crystal Elastomers, Networks, and Gels

PING XIE  
RONGBEN ZHANG

## 1. INTRODUCTION

**N**UMEROUS publications [1–3] and review articles [4,5] have described liquid crystalline polymers, including main-chain and side-chain types. Side-chain liquid crystalline polymers (SCLCPs) could be synthesized via either macromolecular reaction or polymerization of mesogenic vinyl monomers. Polymers show the liquid crystalline behavior similar to precursor monomers and also make the liquid crystalline phase stable [6]. Meanwhile, main-chain liquid crystalline polymers synthesized from bifunctional monomers also show similar liquid crystalline behavior to those of low mass model compounds. Above the glass transition ( $T_g$ ), segments in polymer chains can freely move due to the micro-Brownian movement, and the orientation of decoupled mesogens induces the optical anisotropy, which is characteristic of the liquid crystalline compounds. Crosslinkage among the polymer chains results in the network polymers. In this case, macro-Brownian movement, that is the motion of entire molecules, is prevented by crosslinking reactions, but micro-Brownian motion of segments is not essentially influenced. Theoretically, liquid crystal polymers could be crosslinked to form elastomers in which properties arising from the liquid crystalline behavior could be greatly immobilized to give anisotropic solids with unusual properties. Therefore, it is possible to realize a form-retaining liquid crystalline material of any desired shape. So, the liquid crystalline polymer with rubber elasticity (liquid crystalline elastomer, LCE) can be developed as a new functional material. By using various liquid crystalline polymers (main-chain, side-chain, and combined polymers) with reactive groups, the

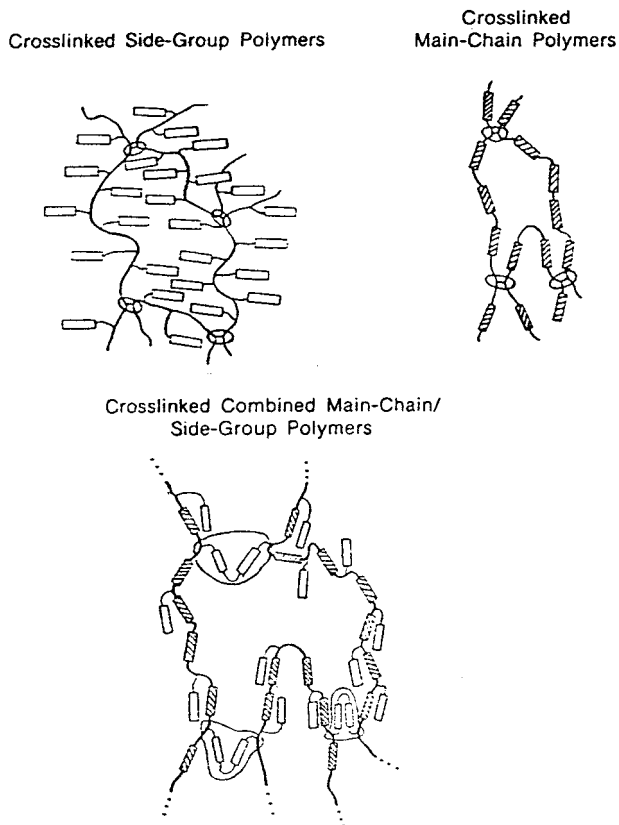


**Figure 9.1** Schematic representation of different types of LC elastomers (LCE) from (a) side chain, (b) main chain, and (c) combined (main chain/side chain) LCPs; crosslinking points are circled.

anisotropic network can be formed via crosslinking. The schematic representation of the LC elastomers prepared in this way is given in [Figure 9.1](#).

During recent years, SCLCPs have been developed as the materials for electric-optics (nonlinear optics, NLO), integrated optics, and storage devices. For all of these applications, it is necessary to have samples with the optical axis of the mesogens being macroscopically and uniformly aligned; in this case, liquid crystal polymers can perform like single crystal with respect to their optical properties. Under an external field, uniformly aligned mesogenic monomers containing two reactive groups, or prepolymers incorporating reactive groups, can be photo or thermally polymerized or crosslinked by one or two steps with the addition of a non-mesogenic crosslinking agent. As a result, macroscopically aligned elastomer (liquid single crystal elastomer, LSCE) and anisotropic network with different crosslink density can be prepared, and also macroscopic

orientation in the liquid crystalline state can be fixed in the solid sample. Anisotropic gels consist of a swollen anisotropic network and non-covalently bonded, but strongly oriented, domains of low molar mass liquid crystals.

The main objective of this chapter is to review and outline the research studies and perspectives on liquid crystalline elastomers and LC anisotropic networks, with emphasis on recent interesting innovations on network-stabilized ferroelectric LC (FLC) gels, discotic columnar networks, and self-assembly hydrogen-bonded LC network. We will also present hybrid networks based on ladderlike polysiloxanes that have been developed in our group as advanced functional film materials.

Recently, polymer networks by in situ polymerization of aligned low molar mass liquid crystalline monomers have been reported. By this technique, some interesting materials with molecular “memory” in the anisotropic state where the crosslinking took place can be made. This technique will be discussed in detail in [Chapter 10](#).

## 2. LIQUID CRYSTALLINE ELASTOMERS (LCEs) [7–19]

### 2.1. SYNTHESIS AND PHASE BEHAVIOR OF LCE

The first example of a neat liquid crystalline elastomer appeared in the literature in 1981 (Finkelmann et al.) [7] and was based upon side-chain LCPs. Semi-flexible main-chain-based LC networks were also reported later in 1986 by Zental and Reckert [8].

#### 2.1.1. Side-Chain Type LCEs

Finkelmann et al. [7] first synthesized a side-chain type liquid crystalline elastomer using a liquid crystalline polysiloxane with flexible main chains as a precursor; the crosslinkage between the chains produced the LCE with liquid crystallinity at room temperature. The synthesis of an LCE is illustrated in [Figure 9.2](#) through the hydrosilylation reaction, which is the same as the synthesis of a side-chain liquid crystalline polysiloxane. These early elastomers were prepared by a one-step process in which monofunctional liquid crystal monomers and bifunctional crosslinking agents, such as divinyl derivatives of dimethyl-siloxane oligomers, were simultaneously attached to the polymer backbone. These liquid crystalline elastomers display liquid crystalline behavior similar to common liquid crystalline compounds. Not only are they identified based on the white turbid mesophase, but they also can be simply detected by the transition from a white turbid state to a transparent state due to the orientation of the mesogenic groups, which is induced by mechanical deformation.

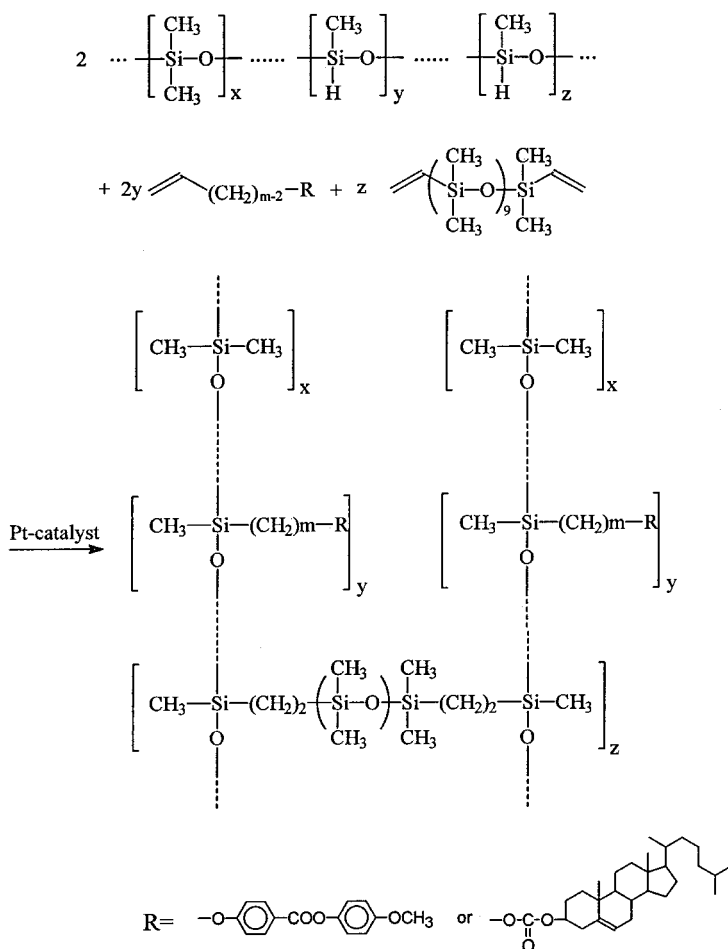


**Figure 9.2** Schematic of synthesis of side-chain LC elastomers based on LC polysiloxanes (adapted from Reference [7]).

Zental and Reckert [8] synthesized chained copolymer of acrylate or methacrylate esters containing mesogenic and hydroxy groups by radical copolymerization. The copolymers containing 5~8 mole percent of hydroxy groups were used as a precursor and were crosslinked using hexamethylene diisocyanate or 4,4'-diphenylmethane diisocyanate as crosslinking agents (Figure 9.3). The liquid crystalline behavior of these elastomers is also similar to that of chained polymers.

Dichromatic dyes included in the liquid crystalline elastomers can be used to investigate the LC orientation behavior. The stress-induced orientational

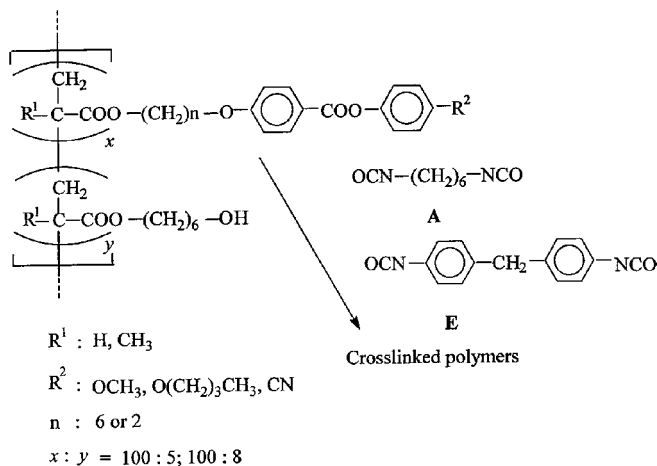


**Figure 9.3** Schematic of synthesis of side-chain LC elastomers using diisocyanates as crosslink agents (adapted from Reference [8]).

elastomers could be developed to form color polarizer. Ringsdorf et al. synthesized the liquid crystalline polymers containing dye moieties in side chains [20]. And then, Canessa et al. [10] synthesized dichromatic dye-containing liquid crystalline elastomers by reacting a terpolymer shown in Figure 9.4 as a precursor with hexamethylenediisocyanate. Crosslinked polymers display the same liquid crystalline behavior as their precursors—chained LCPs. The elastomers even with 10 mole percent of crosslinking still remain nematic liquid crystallinity.

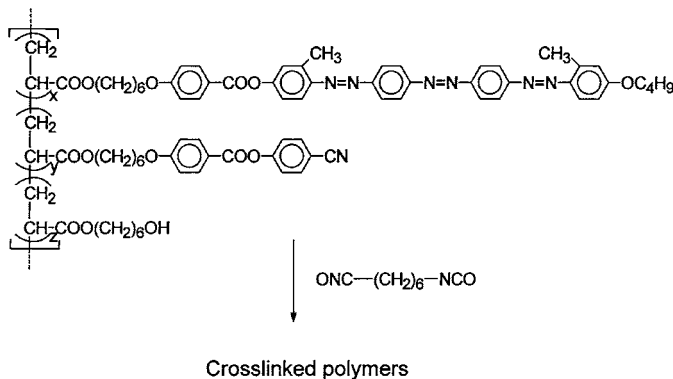


**Figure 9.4** Schematic of synthesis of side-chain LC elastomers containing dichromatic dyes (adapted from Reference [10]).

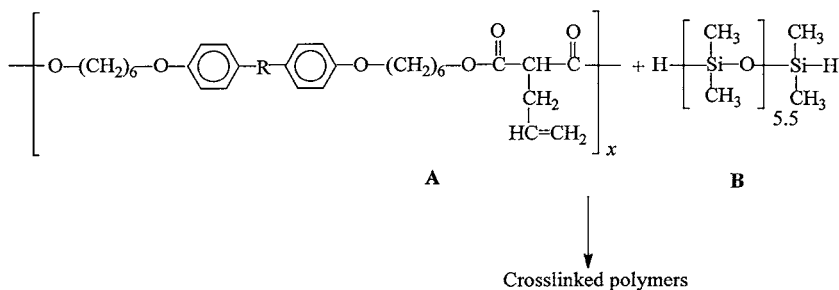


**Figure 9.5** Schematic of synthesis of main-chain LC elastomers (adapted from Reference [8]).

### 2.1.2. Main-Chain Type LCEs

Zental et al. prepared linear main-chain liquid crystalline polymers as shown in [Figure 9.5](#) either by solution polycondensation of diols with allylmalonic acid or by melt polycondensation of the diols and diethyl allylmalonate. The chained polymers as a precursor were crosslinked by the addition of Si-H groups of  $\alpha$ -dimethylsilyl- $\omega$ -hydro-oligo(dimethylsiloxane) to the allyl groups [8]. The phase transition temperatures of the elastomers are lower than those of the precursor chained polymers due to the presence of the flexible oligo (dimethylsiloxane) units. Bhadani and Gray [21] prepared heavily crosslinked cholesteric networks by reacting hydroxypropyl cellulose with acryloyl chloride and stimulating crosslinking further between the adjacent side groups using ultraviolet radiation. The resultant films retained their static cholesteric structure. Following a different route that allows the level of crosslinking to be controlled through competitive esterification, Mitchell et al. prepared liquid crystal elastomers displaying both thermotropic and lyotropic liquid crystalline phases [22]. The phase transitions from the liquid crystal to the isotropic state are reversible for materials with moderate levels of crosslinkage. A lyotropic mesophase was preserved even if the level of swelling was in excess of 500%. A reversible transition of liquid crystalline to isotropic phase was observed with the swollen materials as the fraction of swellant was adjusted. The elastomers showed marked macroscopic orientation effects when mechanically deformed, but, surprisingly, the response was less dramatic than that in some side-chain liquid crystal elastomers.

### 2.1.3. Combined LCEs

Combined (mesogenic groups are contained both in main chain and side chain) LC chained polymers and elastomers are shown in [Figure 9.6](#), and were also first prepared by Zental and Reckert [8]. The linear “combined” liquid

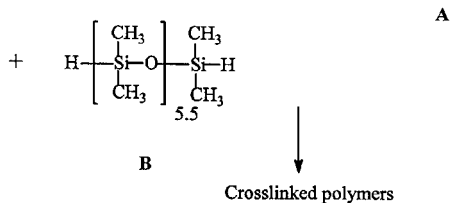
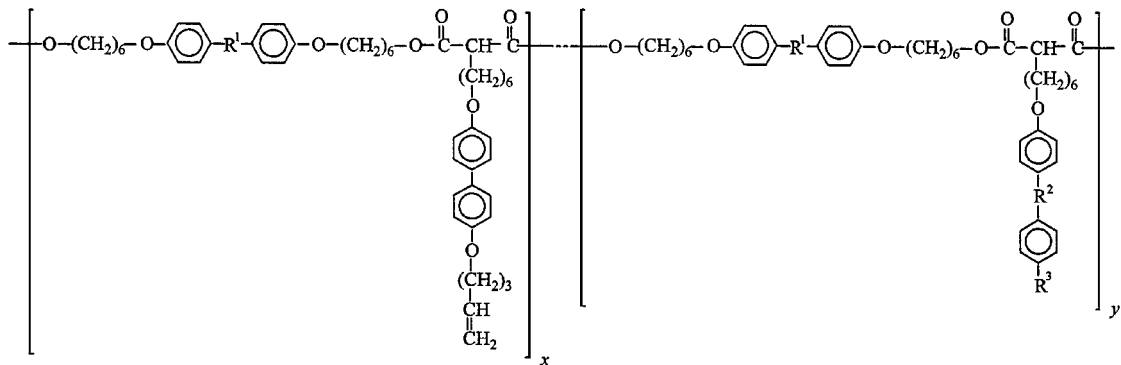


**Figure 9.6** Schematic of synthesis of combined LC elastomers (adapted from Reference [8]).

crystalline polymers were prepared by melt polycondensation or copolycondensation of the diols and the diethyl malonates. The chained homo- or copolyesters were crosslinked by hydrosilylation of  $\alpha,\omega$ -di(hydrodimethylsilyl)-oligo (dimethylsiloxane) with the olefinic double bonds in pendant groups in the same way as main-chain type LCEs. The phase transition temperatures are lower than the chained precursor polymers due to the presence of the flexible oligo(dimethylsiloxane) as crosslinkage units.

## 2.2. PHYSICAL PROPERTIES OF LCE

The liquid crystalline elastomers simultaneously exhibit properties associated with low molar mass LCs and standard elastomers. Therefore, the mechanical and optical properties of such networks are anisotropic below the clearing point ( $T_c$ ) and also are dependent upon stress/strain field caused by mechanical deformation.

### 2.2.1. Thermal Properties

It was found that the mesophase of chained polymer precursors remained after crosslinking. In other words, the crosslinked liquid crystalline polymers showed the same mesophase as that of their mother polymers [15,16,23]. If the degree of crosslinking is only a few percent, no significant change of transition temperatures was observed [8,13,23]. As the degree of crosslinking increases, the clearing temperature ( $T_c$ ) shifts a few degrees to a lower temperature. On the other hand, the melt points ( $T_m$ ) or the glass transition temperature ( $T_g$ ) could be increased or decreased depending on the flexibility of introduced crosslinking units.

### 2.2.2. Mechanical Properties

Above  $T_c$ , i.e., at the isotropic phase, LCE behaves like a conventional elastomer, but at the mesophase, its mechanical properties are highly temperature and time dependent [13]. In the vicinity of  $T_c$ , a drastic change in the mechanical behavior is observed. In the case of constant deformation, the true stress decreases rapidly by decreasing the temperature below  $T_c$  as shown in Figure 9.7. This is caused by a spontaneous change of the geometrical dimensions, which can only be explained by an anisotropic ordering of the mesogenic side chains below  $T_c$ .

The temperature dependence of the sample length of an elongated strip at constant load is shown in Figure 9.8. It is remarkable that the length of the sample increases by decreasing the temperature below  $T_c$  until reaching the glass transition temperature  $T_g$ . This unusual temperature dependence is caused by

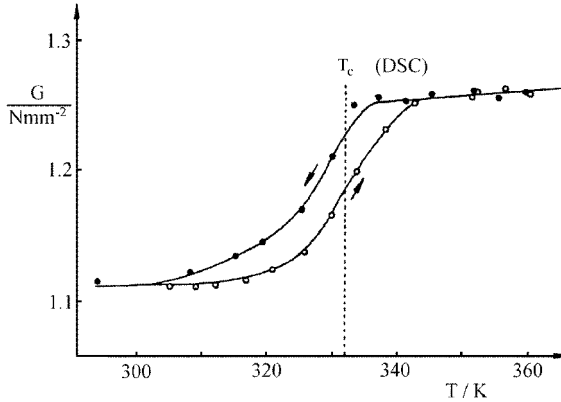


**Figure 9.7** Temperature dependence of true stress  $\sigma(T)$  at constant deformation ( $\lambda = 0.78$ ;  $T > T_c$  : isotropic rubber;  $T < T_c$  : anisotropic rubber) (adapted from Reference [24]).

rising orientation of the mesogenic groups in the nematic phase and consequently by a higher anisotropic deformation of the polymer chains. This means that the linear thermal expansion coefficients are anisotropic.

The mechanical properties of a series of main-chain and side-chain LC elastomers that possessed  $S_c$ ,  $S_c^*$ , N, cholesteric, and isotropic phases were studied using dynamic mechanical spectroscopy [25]. Around  $T_g$ , the polymers exhibit value's variation for storage modulus above and below the transition. In the nematic state,  $G'$  is below the value observed in the isotropic state. In the smectic phase, the layered organization produces a kind of network that causes a  $G'$  plateau. A summary of this behavior is shown in Figure 9.9.

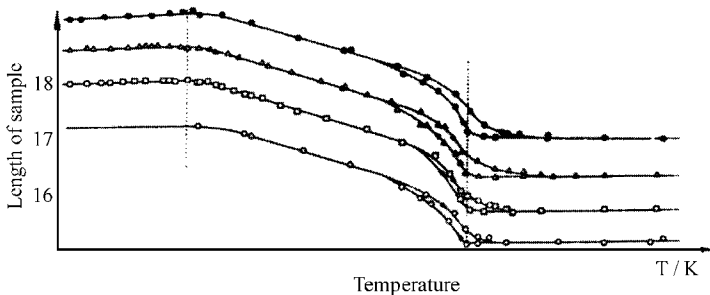


**Figure 9.8** Temperature dependence of sample length at constant load  $F$  ( $\circ$ :  $F = 0$ ,  $\square$  :  $F = 0.058$  N,  $\triangle$ :  $F = 0.121$  N,  $\bullet$ :  $F = 0.183$  N) for LC elastomer; uniaxial elongation (adapted from Reference [24]).

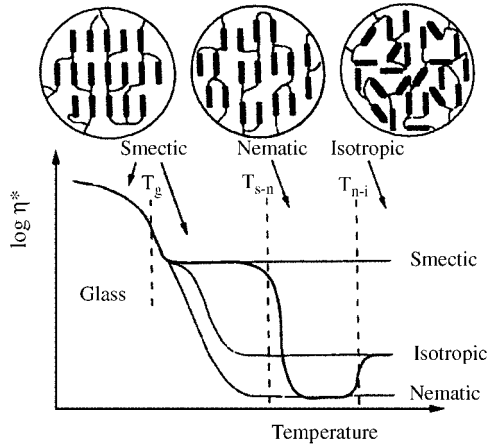


**Figure 9.9** Schematic of mechanical behavior of LC elastomers (adapted from Reference [25]).

### 2.2.3. Optical Properties

A question to be asked is whether the macro-mechanical deformation of liquid crystal elastomers or stress fields can produce effects similar to those observed in conventional liquid crystals under external fields. Studies using the stress optical properties, conoscope, and X-ray diffraction have shown that applied mechanical fields do have a profound effect on the arrangement of the mesogenic groups in LC network [26].

The quotient of orientational birefringence,  $\Delta n$ , and stress,  $\sigma$ , is defined as the stress optical coefficient  $C$ , i.e.,  $C = \Delta n / \sigma$ ;  $\Delta n = n_{//} - n_{\perp}$ . From the simple model of the network chains, the product  $CT$  [Equation (1)] should be independent of  $T$  if a slight temperature dependence of  $n$  is neglected.  $CT$  is proportional to the optical anisotropy of the statistical segment.

$$CT = \frac{2\pi}{45k} \frac{(\bar{n}^2 + 2)^2}{\bar{n}} \Delta\alpha \quad (1)$$

$\bar{n}$  is the mean refractive index of the sample, and  $\Delta\alpha$  is optical anisotropy.

The  $CT(T)$ -curves of all samples can be divided into two regions: one is high above  $T_c$ , showing constant values, and the other is near  $T_c$  with significant temperature dependence. For an LC-elastomer with a spacer length of  $m = 3$ , the negative values of  $CT$  (Figure 9.10) indicate that the mesogenic side chains orient more or less perpendicular to the deformed network chain; while they are positive in the pre-transformational region for the LC-elastomers with  $m = 4$ , this means that the mesogenic side chains are oriented parallel to the axis of deformation.

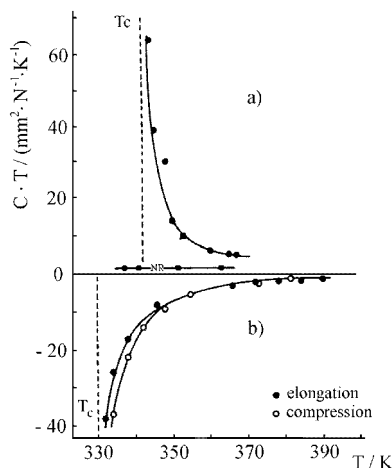


**Figure 9.10** Stress-optical properties of LC elastomers: (a) spacer  $m = 4$ ; (b)  $m = 3$  (adapted from Reference [26]).

The transition from the isotropic to the LC state is a first-order transformation, which causes a jump of  $CT$ -values at the transformation temperature,  $T_c$ . So, it is not possible to draw conclusions with respect to the orientation of mesogenic groups in both isotropic and LC states only from the stress optical results. To get information on their orientation in the LC-state, additional conoscopic and X-ray experiments have been performed.

The imagined model for the orientation state of these LC elastomers is shown at the bottom of Figure 9.11. X-ray diffraction results supported this model. The X-ray diffraction measurements were taken with samples oriented above  $T_c$  and then cooled below  $T_c$  by fixing the length of the sample. Two different positions, achieved by turning the sample around the axis of deformation, have been investigated. The resulting X-ray photographs are shown schematically in the top of Figure 9.11.

These networks exhibit a nematic mesophase. Clearly, the type of response to the mechanical field is extremely structure dependent. The effect of spacer length on elastomer behavior was examined [27]. The reported work showed that the coupling between the mechanical stress and polymer backbone can greatly influence the mesomorphic order. This effect can be enhanced by coupling the mesogenic group more tightly to the polymer backbone.

### 2.3. LC THERMAL-PLASTIC ELASTOMERS [28]

Different from the cured rubber containing strong chemically bonded network, thermoplastic elastomers possess elastic properties similar to those of

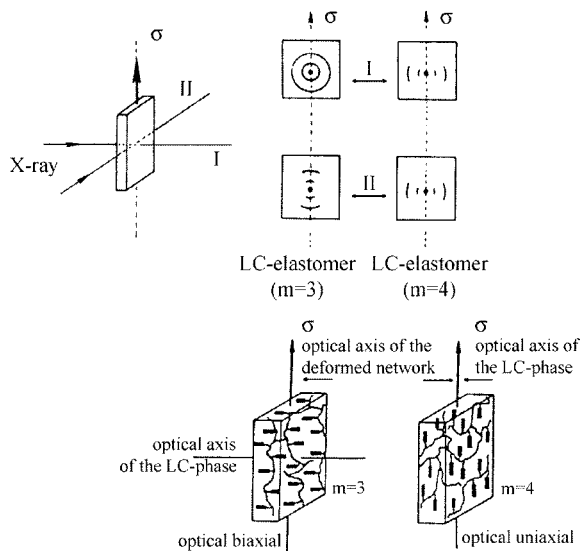


**Figure 9.11** XRD measurements of stretched LC elastomers (adapted from Reference [26]).

cured rubber at lower temperatures due to physical crosslink between polymer molecules. Thermal-plastic elastomers are a combination of soft segments (flexible components that display rubbery elasticity) and hard segments (constraining components). Aggregation of the hard segments arose from hydrogen bonding, and formation of crystal phases results in the physical crosslinking. Among general thermal-plastic elastomers, physical crosslinking for urethane-type elastomers is constructed by hydrogen bonding between polyurethane segments, while polybutylene terephthalate (PBT) serves as hard segments for ester-type elastomers. The micro-phase separation of two kinds of segments has great influence on the properties of thermal-plastic elastomers. Thermotropic LC thermal-plastic elastomers with liquid crystallinity at room temperature were synthesized by introducing rigid plate-like mesogen units as hard segments and flexible spacers as soft segments. These thermotropic LC thermal-plastic elastomers possess both liquid crystallinity and thermal plastic properties, which is different from the chemical-bonded elastomers mentioned above. Thus, they are prospective materials because of easy-processing and reproducibility.

### 3. LIQUID SINGLE CRYSTAL ELASTOMER (LSCE), ANISOTROPIC NETWORK, AND GELS

Anisotropic elastomers, network, and gels with liquid crystal properties represent an area of research in the general domain of self-assembling materials

and receive rapidly growing scientific interest because of technological potential. They have many potential applications, such as color filter, polarizers, piezoelectric sensors, NLO film, orientation layers for LCDs, etc. The variety of structures for building an LC network is large, ranging from the entirely rigid networks that may be obtained by dense crosslinking of appropriate low molecular weight mesogens (for example rigid-rod diacrylates) to elastomers containing the mesogenic moieties as pendants in a highly flexible, lightly crosslinked polymer matrix.

Starting either from preformed linear LC polymers or from low molecular weight LC compounds, any ordinary crosslinking reaction can produce LC networks having a polydomain structure. Stable orientation on the macro-scale has been obtained by crosslinking pre-aligned systems. This may be achieved by magnetic-field-induced orientation of low molecular weight mesogens or by mechanical orientation of the polymer in the bulk.

### 3.1. CONCEPT FOR LSCE

The ability to form monodomain structures makes LC elastomers of interest for a number of optical applications where the optical axis of the polymer must be macroscopically and uniformly aligned. Kuepfer and Finkelmann have reported in detail the formation of what was termed “nematic liquid single crystal elastomers” [29], which are optically similar to organic or inorganic single crystals.

### 3.2. SYNTHESIS AND CHARACTERIZATION OF LSCE

To make anisotropic networks, the linear chains have to be ordered prior to the crosslink reaction. This orientation can be achieved in the melt state under strain by simple extension. The crosslinking reaction is performed in a two-step process. In the first step, a well-defined weak network is synthesized, which is deformed with a constant load to induce the network anisotropy. The load has to exceed the threshold load  $\sigma_{th}$ , which is necessary to obtain a uniform director orientation. In the second step, a second crosslinking reaction occurs and locks in the network anisotropy. This procedure is shown schematically in Figure 9.12.

The LSCE has optical behavior similar to a single crystal. X-ray measurements prove this structure and confirm the concept of LSCE. The conventional LC elastomer is turbid and shows an X-ray pattern typical of non-ordered nematic: small- and wide-angle halos. The LSCE, on the other hand, is completely clear or translucent and with an X-ray pattern: short arcs characteristic of highly ordered nematics. Such materials appear to have tremendous potential for optical and possibly mechanical memory applications.

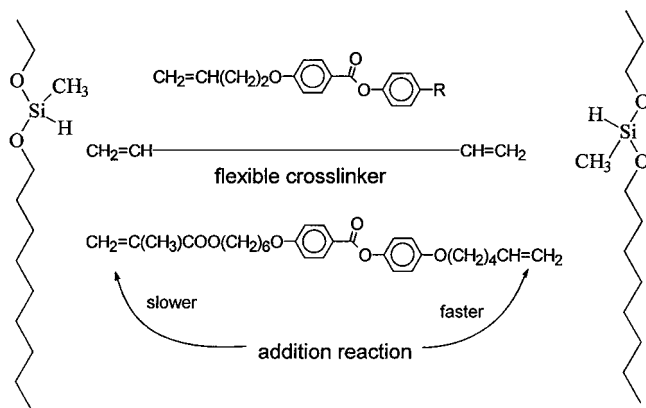


**Figure 9.12** Chemical route to a macroscopically oriented liquid crystalline network (adapted from Reference [29]).

### 3.3. ANISOTROPIC NETWORK AND GELS

The LSCEs represent a new class of macromolecular systems distinguished by macroscopically uniform anisotropy. The concept of LSCE can be further extended to other synthesis routes and to the densely crosslinked systems. Macroscopic uniaxially oriented films can be formed by mechanical force, alignment surface [30], magnetic and electric fields [31], polarized light [32], etc., and then crosslinked to form an anisotropic network (LC network is abbreviated as LCN) if the mixture components contain polymerizable or crosslinkable bifunctional monomers (Figure 9.13). Alternatively, amorphous or liquid crystalline side-group and/or main-chain polymers incorporating additional

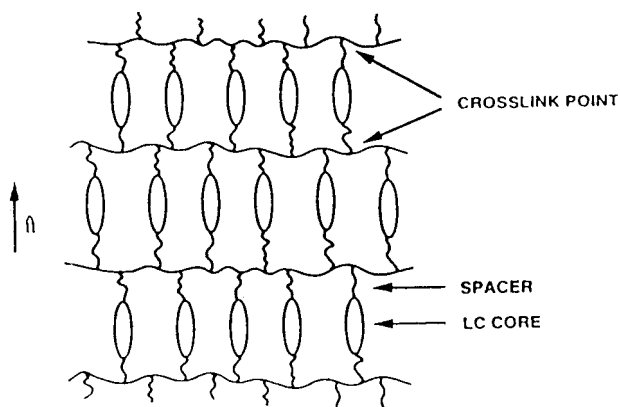


**Figure 9.13** A simple schematic representation of the supra-molecular structure of anisotropic network.

reactive groups can be transferred onto a suitable substrate, macroscopically oriented by mechanical force, and then crosslinked.

Anisotropic gels are a mixture of a solid crosslinked LC network and non-reactive low molar mass LCs [33] produced by the in situ polymerization of LC monomers with two polymerizable groups, such as diacrylates, in the presence of low molar mass LCs without reactive units. The resultant solid polymer network incorporates the three-dimensional structure of the original LC mixture. Main aspects around LC networks, especially those involving densely crosslinked solids, that arose from low molar mass bifunctional LC monomers are stated in [Chapter 10](#). Here the description focuses only on some specific and innovative system, especially for the networks formed by the moderate crosslinking of preformed linear polymers.

### 3.4. COUPLING EFFECT BETWEEN MESOGENS AND POLYMER NETWORK

Early studies on side-chain LC polymers showed the possibility of a decoupling between the mesogenic units and polymer backbone by flexible spacers. This is clearly not the case, because many of the observed properties and phenomena are related to the nature of the coupling between mesogens and polymer backbone, especially in LCE and LCN systems. As mentioned in [sections 2.2.2 and 2.2.3](#), the elastic and stress-optical properties of LC networks have been investigated mostly for side-chain polymers. With these structures, a mechanical deformation of the network matrix is coupled with a change in the orientation of the mesogenic side groups. Conversely, a change in the orientation of the mesogenic groups driven by a force field is reflected in the deformation of the network. In order to elucidate the relationship between network deformation and mesogen orientation at the molecular level, a relevant step is the definition of the sense of the coupling, i.e., the relation of the order parameters of backbone network matrix and mesogens. Mitchell and co-workers [34] have applied small-angle neutron scattering techniques to attack this problem for a side chain, polyacrylate-based, moderately crosslinked network and for its corresponding linear polymer. For the network polymers, a substantial macroscopic orientation of the mesogenic units could be induced by small mechanical extensions. The assembled nematic structure of side-chain mesogens influences the network deformation. Various peculiar phenomena, such as electrically induced shape changes [20], mechanical and electrical molecular switching [20,35], memory effects [36,37], and variations in phase behavior [36,38], have been observed, which mainly arise from these interactions.

The nature of the relative dispositions of the backbone and the mesogenic unit are controlled by the strengths of the interactions between the mesogenic units and polymer backbones. The latter term may be resolved into two components: one component favors parallel alignment between the mesogenic units and the polymer chains simply because of the nematic field, and another component

is related to the nature of the coupling. Gleim and Finkelmann observed both perpendicular and parallel arrangements of the mesogenic units with respect to the extension direction for liquid crystalline elastomers with spacers (coupling chains) of different lengths [39]. Shortening the coupling spacer is expected to enhance the probability of the perpendicular configuration. Mitchell and Zental reported the intriguing electrically induced macroscopic shape changes that are observed in swollen samples of liquid crystal polymers with low mass liquid crystals [22, 40]. These observations show an extension of the sample along the axis of the applied electric field. One explanation for such shape changes is that reorientation of the liquid crystal directors by electric field from a polydomain to a monodomain texture parallel to the electric field results in coupled reorientation of the backbone chains.

### 3.5. MEMORY EFFECTS OF LC NETWORK

Memory effects of LC networks display in two way: macroscopic shape and/or dimension memory, and memory on configuration. The phase state at the time of crosslinking determines the organization of the LC elastomeric network [37]. Free-standing monodomain LC elastomers (i.e., liquid single crystal elastomers) showed a complete memory of the orientational configuration at the time of crosslinking. The precursor polymer was first aligned in an external field prior to crosslinking. After crosslinking, the oriented network could be heated above the clearing transition for a long period of time to produce a network with no evidence of orientation. Very large shape changes occur while passing into the isotropic state—the changes occur in the absence of an applied external field. These changes in dimension are qualitatively identical to the dimensional changes that occur to nematic elastomers under stress. However, once the elastomer was cooled into the mesophase, a highly aligned network could be recovered. This memory is particularly interesting because it arises from an equilibrium situation and is not due to kinetic factors.

Anisotropic gels were produced by using an LC mixture containing reactive and non-reactive molecules [41–50]. The long-range orientation of the molecules can be frozen in the structure by the creation of a three-dimensional anisotropic network. After the extraction of the non-reactive LC from the gel containing moderate concentration of polymer network, the anisotropic configurations similar to that in the LC gels remained in the solid network. Of particular interest, the cholesteric phase can be retained after removing the chiral dopant by extraction.

The birefringence of the LC gel observed above the clearing temperature of the non-reactive LC is attributed to the thermally stable network that remains oriented at elevated temperatures. However, this birefringence of the gels measured above the clearing temperature is higher than what is expected from the network alone, indicating that part of the non-reactive LC molecules

also remains oriented above their clearing point. This large influence of the network on the behavior of the LC molecules in fact forms the basis for some applications of anisotropic gels.

### 3.6. SPECIFIC ANISOTROPIC NETWORKS AND GELS

#### 3.6.1. Network-Stabilized FLC gels

The interest in low-molar-mass ferroelectric liquid crystals (FLC) stems from their short switching times in electric fields. A much better orientation of the pure FLC could be obtained in much thinner ( $2\text{ }\mu\text{m}$ ) cells in which surface stabilization could be induced. But the mechanical shock instability of surface-stabilized ferroelectric liquid crystal displays (SSFLCDs), in which the molecular orientation is determined by alignment layers on the cell walls, is a major factor hindering their successful commercialization. These problems can be alleviated by using ferroelectric gels, in which the orientation of the non-attached molecules is determined by the network instead of surface forces [51,52]. Anisotropic network stabilized ferroelectric liquid crystal displays (ANSFLCDs) exhibit continuous switching over a range of voltages in thick cells ( $d \approx 8\text{ }\mu\text{m}$ ) without interference color. In contrast to SSFLCDs, the switching behavior of ANSFLCDs allows full-color LCDs to be produced by the use of gray scale.

#### 3.6.2. LC Networks Consisting of Discotic Mesogens

LC network consisting of discotic mesogens as building units is an interesting innovation as a promised low-dimensional conductive material [53]. The discotic mesogens are assembled to an ordered columnar phase, which is fixed in an anisotropic network.

Columnar discotic liquid crystals are becoming more and more of interest as organic molecular wires for rapid charge mobility [54,55]. Especially for the columnar liquid crystals with triphenylene cores, on illumination with a defined wavelength of light, the charge mobility reaches sometimes up to two orders of magnitude higher than that observed for the amorphous organic polymers currently used in most photocopies and laser printers, e.g., polyvinylcarbazole, PVK. For technical applications, a mechanically stable arrangement of the columnar assembly is necessary, preferably involving a macroscopically uniform director alignment. Although stabilization of the fluid columnar photoconducting layer can be achieved by polymerization of monomers in the columnar liquid crystalline state to produce a stabilized network as a thin solid film, the charge mobility decreases by more than an order of magnitude. The major practical issue is the formation of uniformly oriented columnar phases without defects. Columnar LSCEs provide the prospect of achieving this goal by utilizing

mechanical forces to overcome the high viscosity of the non-crosslinked side-chain polymer precursor to induce uniform director alignment.

### 3.6.3. Hydrogen-Bonded and Other Reversible LC Networks

The hydrogen-bonding interaction between aromatic carboxylic acids and pyridines has been described before in the formation of small molecule dimeric complexes [56]. The construction of mesogenic molecules [57,58] in such a manner and the relation between hydrogen bonding and liquid crystallinity involved in low molar mass materials has also been extensively investigated [59–61].

Most reversible networks have been made by using the non-covalent hydrogen bond [62–64] as the reversible crosslinking unit, and the first thermotropic systems of this type were based on hydrogen-bond crosslinks between side-group polymers of benzoic acids with long spacers. Related reversible networks are formed from either side-chain or main-chain LCPs with carboxylic acid groups and nitrogen-containing crosslinking units, such as stilbazole or bipyridyl derivatives. Anisotropic networks consisting of a poly(methacrylate) backbone, stilbazole side groups, and bipyridyl crosslinking units can be mesomorphic across the complete phase diagram. The coordination of mesogenic ligands with metals as crosslinking units has also been used to prepare non-covalently bonded anisotropic network [65]. The 4-cyano-4'-biphenyl side groups of poly(acrylic esters) have been found to coordinate with dichlorobis(benzonitrile) platinum (II) to produce a non-covalently bonded anisotropic network. A smectic phase is observed at low platinum concentrations, and a nematic phase is then observed as the concentration is further increased. At a critical value, the crosslinking density is so high that LC properties can no longer be observed.

### 3.6.4. Non-LC Anisotropic Networks for Non-Linear Optics

The first attempt to produce second harmonic NLO polymers involved guest-host systems with a chromophore simply dissolved in an amorphous polymer stabilized below the glass transition temperature ( $T_g$ ). However, such systems suffer from low solubility of the chromophore in the polymer matrix leading to phase separation and low NLO efficiency. Side-chain copolymers incorporating mesogenic groups and dye groups chemically bonded to the polymer backbone enable high chromophore concentration and improve dipolar alignment, but the signal decay time even at room temperature is still too short for device application due to the relaxation of polymer backbone. The improved stability was achieved with anisotropic network derived from side-chain polymers incorporating chemically bonded NLO chromophores and crosslinkable units [66,67]. They can be ordered using high field strength of corona poling,

and the resultant dipolar ordering can be fixed by in situ crosslinking. Further improvements were achieved with hybrid networks containing designed rigid-rod bridges according to the size of chromophore molecules (also see [Chapter 10, section 2.6](#)), so that the chromophore molecules can be trapped within the “cages” at the molecular level [68,69].

### 3.6.5. Hybrid Networks and Optical Films Based on Ladderlike Polysiloxanes

Intrinsic unique properties of ladderlike polysiloxane (LPS) [70,71], such as excellent optical transparency, high thermal and irradiation resistance, good film-forming ability, and fair mechanical properties, arise from its hybrid nature containing inorganic and one-dimensional ordered network main chain. Various LPSs including reactive polyhydrosilsesquioxane (H-T), polyvinyl (Vinyl-T), or polyallylsilsesquioxanes (Allyl-T) have been synthesized in Zhang’s group via “stepwise coupling polymerization reactions” [72–74]. As parent polymers, H-T and its copolymers can be further functionalized by hydrosilylation reaction with vinyl-terminated LC or photosensitive monomers and, as a result, make so-called “fishbone-like” or “rowboat-like” mesogenic polymers and corresponding metal complexes, which can be used as promising skeleton materials for highly stable optical films. For example, low decay-nonlinear optical (NLO) films were prepared from “rowboat-like” mesogenic polymers with laterally fixed stilbene units on the LPS backbone, and the orientation of dipole director was induced by corona-poling and in situ fixed in a sol-gel process [75,76]. Anisotropic LPP alignment films for LCD were produced by illumination with linear polarized UV-light of cinnamate-grafted LPS. Unique high stability of orientation state is attributed to the inherent properties of the material [77].

## 4. POTENTIAL APPLICATION OF LCE, ANISOTROPIC NETWORK, AND GELS

An interesting example of the application of LC elastomers has been investigated for gas permeation membranes [78]. A distinct change in the transport behavior of the material was observed at a given phase transition. The diffusion was also found to be stress dependent. A recent focus on the development of LC elastomers has been in the preparation of networks that exhibit ferroelectric properties because they have the potential to make interesting bistable display devices. Using dielectric spectroscopy in the  $10^{-1}$ – $10^9$  Hz frequency range, the ferroelectric properties of some combined (side chain and main chain) LC networks containing chiral smectic C phase were confirmed [79]. Similar features were observed in a side-chain LC network with a siloxane backbone [80].

More recently, it has been theoretically predicted by Brand [81] that elastomeric networks that have chiral nematic or smectic C\* mesophases should have piezoelectric properties. The non-centro-symmetric material responds to the deformation via a piezoelectric response. Following this prediction, both Finkelmann and Zental have reported the observation of piezoelectricity. In one case, a nematic network was converted to the cholesteric form with the addition of CB15, 2'-(2-methylbutyl)biphenyl-4-carbonitrile [82]. By producing a monodomain, it is possible to measure the electro-mechanical or piezoelectric response. Compression leads to a piezoelectric coefficient parallel to the helical axis. Elongation leads to the perpendicular piezoelectric response. As another example, a network with a chiral smectic C phase that possesses ferroelectric properties can also act as a piezoelectric element [83]. Larger values of this response might be observed if crosslinked in the  $S_c^*$  state.

One of the most pressing issues in the use of organic materials for nonlinear optics (NLO) is the loss of response due to aging phenomena. Several attempts have been made to lock-in the orientation by producing ordered networks using liquid crystalline and glassy polymers with NLO dye chromophores incorporated into structure. It has been suggested that if an NLO chromophore could be poled in a liquid crystalline environment, a five-fold increase in NLO response could be produced. One of the first reported studies [84] incorporated a diamino chromophore into an epoxy network, and the network was partially pre-cured to 100°C to enable good film formation. It was then cured for several hours in an electric field using corona poling. Both the reaction temperature and the inherent rigidity of the molecular structure set the  $T_g$  of the final network. In order to improve these properties, new epoxy chromophores based on nitroaniline [85] and tolane structures were developed. These materials, due to their high overall concentration of chromophores, gave very favorable results. In another approach, a diepoxy compound reacted with a diamine to produce a prepolymer, in which NLO chromophores were incorporated. Then, cinnamate groups were attached to the hydroxy groups, and the prepolymer was subsequently crosslinked in an electric field using UV radiation [86].

As mentioned above, LC elastomers, especially LSCE with monodomain order, anisotropic LC networks, and gels, may be optimized to make a kind of smart material for molecular switching and piezoelectric or pyroelectric sensors, because of their sensitivity to environmental conditions (electric or stress fields, temperature, and radiation, etc.) and memory effect. Other applications include wave-guide, polarizers, optical filters, alignment, and compensation films for LCD displays.

## 5. REFERENCES

1. *Polymeric Liquid Crystals*, ed. by A. Blumstein, Polym. Sci. Tech. 28, Plenum Press, New York and London (1985).

2. *Side Chain Liquid Crystal Polymers*, ed. by C. B. McArdle, Blakie, Glasgow and London (1989).
3. *Liquid Crystal Polymers*, ed. by N. A. Plate, Plenum, New York (1993).
4. C. K. Ober, J.-I. Jin, and R. W. Lenz, *Adv. Polym. Sci.*, 59, 103 (1984).
5. V. P. Shibaev and N. A. Plate, *Adv. Polym. Sci.*, 60/61, 173 (1984).
6. H. Finkelmann and G. Rehage, *Makromol. Chem. Rapid Commun.*, 1, 31 (1980).
7. H. Finkelmann, H.J. Kock, and G. Rehage, *Makromol. Chem. Rapid Commun.*, 2, 317 (1981).
8. R. Zental and G. Reckert, *Makromol. Chem.*, 187, 1915 (1986).
9. R. Zental and M. Benalia, *Makromol. Chem.*, 188, 665 (1987).
10. G. Canessa, B. Reck, G. Reckert, and R. Zental, *Makromol. Chem. Macromol. Symp.*, 4, 91 (1986).
11. F. Hessel, R. P. Herr, and H. Finkelmann, *Makromol. Chem.*, 188, 1597 (1987).
12. F. J. Davis, A. Gilbert, J. Mann, and G. R. Mitchell, *J. Chem. Soc., Chem. Commun.*, 1333 (1986).
13. G. R. Mitchell, F. J. Davis, and A. Ashman, *Polym*, 28, 639 (1987).
14. J. Achaetzie, W. Kaufhold, and H. Finkelmann, *Makromol. Chem.*, 190, 3269 (1989).
15. S. Bualek, H. Kapitza, J. Meyer, G. F. Schmidt, and R. Zental, *Mol. Cryst. Liq. Cryst.*, 155, 47 (1988).
16. R. Zental, G. Reckert, S. Bualek, and H. Kapitza, *Makromol. Chem.*, 190, 2869 (1989).
17. R. Zental, H. Kapitza, F. Kremer, and S. U. Vallerian, in *Functionalized Liquid Crystalline Polymers*, Am. Chem. Soc., Washington, D.C. (1990).
18. P. Keller, *Chem. Materials*, 2, 3 (1990).
19. R. V. Talroze, T. I. Gubana, V. P. Shibaev, and N. A. Plate, *Makromol. Chem. Rapid Commun.*, 11, 67 (1990).
20. H. Ringsdorf, H.-W. Schmidt, G. Bauer, and R. Kiefer, in *Recent Advances in Liquid Crystalline Polymers*, ed. by L. L. Chapoy, Els. Appl. Sci. Publ., London & New York (1985), p. 253.
21. S. N. Bhadani and D. G. Gray, *Mol. Cryst. Liq. Cryst. Lett.*, 102, 255 (1984).
22. G. R. Mitchell, W. Guo, and F. J. Davis, *Polymer*, 33, 68 (1992).
23. N. R. Barnes, F. J. Davis, and G. R. Mitchell, *Mol. Cryst. Liq. Cryst.*, 168, 13 (1989).
24. H. J. Kock, H. Finkelmann, W. Gleim, and G. Rehage, in *Polymeric Liquid Crystals*, ed. by A. Blumstein, Plenum Press, New York and London (1985), p. 275.
25. T. Pakula and R. Zental, *Makromolek. Chem.*, 192, 2401 (1991).
26. H. Finkelmann, H.-J. Koch, W. Gleiss, and G. Rehage, *Makromolek. Chem., Rapid Commun.*, 5, 287 (1984).
27. W. Kaufhold, H. Finkelmann, and H. R. Brand, *Makromolek. Chem.*, 192, 2555 (1991).
28. M. Sato, *Polymer-Digest*, 43 (12), 45 (1991).
29. J. Kuepfer and H. Finkelmann, *Makromolek. Chem. Rap. Commun.*, 12, 717 (1991).
30. R. A. M. Hikmet, *Adv. Mater.*, 4, 679 (1992); *Mol. Cryst. Liq. Cryst.*, 198, 357 (1991).
31. S. B. Clough, A. Blumstein, and E. C. Hsu, *Macromolecules*, 9, 123 (1976).
32. M. Schadt, H. Seiberle, A. Schuster, and S. M. Kelly, *Jpn. J. Appl. Phys.*, 34, 3240, L764 (1995).
33. H. Finkelmann, *Trends Polym. Sci.*, 2, 222 (1994).
34. G. R. Mitchell, F. J. Davis, W. Guo, and R. Cywinski, *Polymer*, 32, 1347 (1991).
35. F. J. Davis and G. R. Mitchell, *Polym. Commun.*, 28, 8 (1987).
36. F. J. Davis, *J. Mater. Chem.*, 3(6), 551 (1993).
37. C. H. Legge, F. J. Davis, and G. R. Mitchell, *J. Phys. II*, 1(10), 1253 (1991).
38. J. Schatzle and H. Finkelmann, *Mol. Cryst. Liq. Cryst.*, 142, 85 (1987).
39. W. Gleim and H. Finkelmann, in *Side-Chain Liquid Crystal Polymers*, Chapter 10, ed. by C. B. McArdle, Blackie, Glasgow (1989).
40. R. Zental, *Liq. Cryst.*, 1, 589 (1989).
41. R. A. M. Hikmet, in *Liquid Crystals in Complex Geometries*, Chapter 3, ed. by G. P. Crawford and S. Zumer, copyright © Taylor & Francis, Ltd., London, New York (1996).

42. R. A. M. Hikmet, *Liq. Cryst.*, 9, 405 (1991).
43. R. A. M. Hikmet, *Adv. Mater.*, 4, 679 (1992 b).
44. R. A. M. Hikmet, *Macromolecules*, 25, 5759 (1992 c).
45. R. A. M. Hikmet and H. M. J. Boots, *Phys. Rev. E51*, 5824 (1995).
46. R. A. M. Hikmet and M. Michiels, *Adv. Mater.*, 7, 300 (1995).
47. R. A. M. Hikmet and C. De Witz, *J. Appl. Phys.*, 70, 1265 (1991).
48. R. A. M. Hikmet and B. H. Zwerver, *Liq. Cryst.*, 13, 561 (1993).
49. R. A. M. Hikmet, H. M. Boots, and M. Michiels, *Liq. Cryst.*, 19, 65 (1995a).
50. D.-K. Yang, J. I. West, L.-C. Chien, and J. W. Doan, *J. Appl. Phys.*, 76, 131 (1994).
51. R. A. M. Hikmet, H. M. Boots, and M. Michielson, *Liq. Cryst.*, 19, 65 (1996).
52. R. A. M. Hikmet, H. M. J. Boots, and M. Michielson, *J. Appl. Phys.*, 79, 8098 (1996).
53. S. Disch, H. Finkelmann, H. Ringsdorf, and P. Schuhmacher, *Macromolecules*, 28, 2424 (1995).
54. D. Adam, F. Closs, D. Funhoff, D. Haarer, H. Ringsdorf, P. Schuhmacher, and K. Siemensmeyer, *Phys. Rev. Lett.*, 70, 457 (1993).
55. D. Adam, P. Schuhmacher, J. Simmerer, L. Haussling, K. Siemensmeyer, K. H. Etzbach, H. Ringsdorf, and D. Haarer, *Nature*, 371, 141 (1994).
56. S. L. Johnson and K. A. Rumon, *J. Phys. Chem.*, 69, 74 (1965).
57. T. Kato and J. M. J. Frechet, *J. Am. Chem. Soc.*, 111, 8533 (1989).
58. J. L. Yu, J. M. Wu, and L. S. Wu, *Mol. Cryst. Liq. Cryst.*, 198, 407 (1991).
59. T. Kato, A. Fujishima, and J. M. J. Frechet, *Chemistry Lett.*, 919 (1990).
60. T. Kato, P. G. Wilson, A. Fujishima, and J. M. J. Frechet, *Chemistry Lett.*, 2003 (1990).
61. T. Kato, H. Adachi, A. Fujishima, and J. M. J. Frechet, *Chemistry Lett.*, 265 (1992).
62. T. Kato, H. Kihara, U. Kumar, T. Uryu, and J. M. J. Frechet, *Angew. Chem.*, 106, 1728 (1994).
63. C. G. Bazuin, F. A. Brandys, T. M. Eve, and M. Plante, *Makromol. Chem. Makromol. Symp.*, 84, 183 (1994).
64. L. M. Wilson, *Liquid Crystals*, 18(3), 381 (1995).
65. K. Hanabusa, T. Suzuki, T. Koyama, H. Shirai, N. Hojo, and A. Kurose, *Makromol. Chem.*, 191, 489 (1990).
66. S. Muller, P. Le Barny, E. Chastaing, and P. Robin, *Mol. Eng.*, 2, 251 (1992).
67. B. K. Mandai, Y. M. Chen, J.-C. Huang, and S. Tripathy, *Makromol. Chem., Rapid Commun.*, 12, 63 (1991).
68. D. S. Liu, D.-R. Dai, C. Ye, P. Xie, Z. Li, and R. B. Zhang, *Solid State Communication*, 94 (3), 169 (1995).
69. D. S. Liu, Y. X. Tang, D.-R. Dai, and R. B. Zhang, *Science in China (ser. B )*, 27(4), 314 (1997).
70. P. Xie and R. B. Zhang, *Polym. Adv. Tech.*, 8, 649 (1997).
71. R. B. Zhang, D. R. Dai, L. Cui, H. Xu, C.-Q. Liu, and P. Xie, *Supramol. Chem.*, 1999 (in press).
72. Z. S. Xie, Z.-Q. He, D.-R. Dai, and R. B. Zhang, *Chinese J. Polym. Sci.*, 7(2), 183 (1989).
73. Z. S. Xie, Z.-Q. He, D.-R. Dai, and R. B. Zhang, *Chinese J. Polym. Sci.*, 9(3), 266 (1991).
74. Z. Li, X.-Y. Cao, H. Xu, P. Xie, M. Cao, and R. B. Zhang, *Reactive Polymers*, 39(1), 1 (1998).
75. P. Xie, J.-S. Guo, and R. B. Zhang, *Mol. Cryst. Liq. Cryst.*, 289, 45 (1996).
76. P. Xie, J.-S. Guo, and R. B. Zhang, *Polym. Adv. Tech.*, 7, 662 (1996).
77. L. Cui, W. Jin, P. Xie, and R.-B. Zhang, *Liq. Cryst.*, 25(6), 757 (1998).
78. H. Modler and H. Finkelmann, *Ber. Bunsenges. Phys. Chem.*, 94, 836 (1990).
79. S. U. Vallerien, R. Zental, F. Kremer, H. Kapitza, and E. W. Fischer, *Makromolek. Chem., Rapid Commun.*, 10, 333 (1989).
80. A. Schönfeld, F. Kremer, S. U. Vallerien, H. Poths, and R. Zental, *Ferroelectrics*, 121, 69 (1991).
81. H. Brand, *Makromolek. Chem., Rapid Commun.*, 10, 441 (1989).
82. W. Meier and H. Finkelmann, *Makromolek. Chem., Rapid Commun.*, 11, 599 (1990).
83. S. U. Vallerien, F. Kremer, E. W. Fischer, H. Kapitza, R. Zental, and H. Poths, *Makromolek. Chem., Rapid Commun.*, 11, 593 (1990).

84. M. Eich, B. Reck, D. Y. Yoon, C. G. Willson, and G. C. Bjorclund, *J. Appl. Phys*, 66(7), 3241 (1989).
85. D. Jungbauer, B. Reck, R. Twieg, D. Y. Yoon, C. G. Willson, and J. D. Swalen, *Appl. Phys. Lett.*, 56, 2610 (1990).
86. B. K. Mandal, R. J. Jeng, J. Kumar, and S. K. Tripathy, *Makromolek. Chem. Rapid Commun*, 12, 607 (1991).

# Thermosetting Liquid Crystal Polymers

PING XIE  
RONGBEN ZHANG

## 1. INTRODUCTION

**C**ROSSLINKED liquid crystalline polymers may be divided into two categories: thermosetting LCP or LC thermosets (Ts-LCP or LCT) and LC elastomers (LCE) [1–3]. Among them, LC elastomers are lightly crosslinked LC polymers with a relatively high degree of elasticity in which the LC domains can be oriented by mechanical strains. Potential applications of these materials include waveguides and mechanically switched optical devices. In contrast, LC thermosets are rigid, highly crosslinked LC polymer networks with a relatively low degree of elasticity.

There is no definite division line between Ts-LCP and LCE. In general, the thermosetting LCPs, including rigid-rod network and semi-rigid-rod network, are defined as almost completely crosslinked solids, whose monomers are low molar mass liquid crystals or rigid-rod compounds possessing two reactive groups at both ends; LC elastomers are designated as deformable solids derived in one or two steps of crosslinking reactions from LC polymers or monomers with a small amount of di-reactive crosslinker.

In fact, the idea of utilizing a mesomorphic phase to create an organized network was reported as early as in 1964, when Herz “froze-in” the molecular organization of the 11-sodium styrylundecanoate-water system using the free radical polymerization of divinyl benzene as the crosslinking agent [4]. Similarly, in 1969, Blumstein “froze-in” the quasi-smectic organization of monolayers of polar molecules using tetraethylene glycol dimethacrylate as a crosslinking agent to stabilize the two-dimensional arrangement of molecules [5]. However,

the first “true” liquid crystalline thermosets were prepared by Liebert and Strzelechi in 1973, who crosslinked diacrylate schiff base monomers within the liquid crystal state [6]. The resulting highly crosslinked networks had the “frozen-in” molecular organization of the LC phase. Further work by Blumstein on the polymerization of similar diacrylate schiff base from nematic state in a 4,5 KG magnetic field resulted in a well-oriented crosslinking network [7].

After these early works on crosslinked liquid crystalline systems, subsequent research on LC polymer systems concentrated on the side-chain and main-chain LCPs. Until the past decade, there has been an increasing interest in the investigation of densely crosslinked networks based on rigid rod molecules and creation of organized polymer networks. Interest in such materials arises from their unique properties, for example, low shrinkage during the solidification process, increased reaction rate due to the proximity of the reactive groups, highly bulk orientation, and increased thermal stability. There are a number of possible applications for such ordered anisotropic networks, ranging from thin films for micro-electric packaging to matrix materials for advanced composites. This chapter aims to briefly review the main aspects on the research of thermosetting LCPs, including synthesis and phase behavior of some main types of LC thermosets, reaction kinetics in its preparation process, physical properties, and potential application. A special substance about LC network based on hybrid organic-inorganic designs is also introduced in a special section. More information can be found in recent review articles [8–11] and papers listed in the [reference section](#).

## 2. SYNTHESIS AND PHASE BEHAVIOR OF TS-LCP

Typical monomers of thermosetting LCPs described in this chapter comprise different reactive groups, such as epoxy, cyanate, maleimide, acrylate, and ethynyl attached directly or by spacers to two sides of rigid-rod components, such as the biphenyl, phenyl benzoate, methyl stilbene, or naphthyl structures.

Thermal or photo-polymerization of multi-functional low molar mass monomer results in a high, densely crosslinked network. Liquid crystallinity of monomers or precursors can be “frozen in” after in situ polymerization. Interestingly, some monomers are not liquid crystalline themselves; however, as the curing reaction proceeds, a nematic phase is developed and finally remained. Photopolymerization is divorced from the thermal properties of the material, while thermal polymerization is limited by the finite temperature range over which the liquid crystal phase can exist. But photopolymerization can be only suitable for thin film sample due to the limitation of the penetrating ability of the light used.

## 2.1. EPOXY RIGID AND SEMIRIGID-ROD THERMOSETS

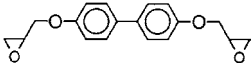
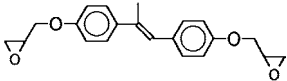
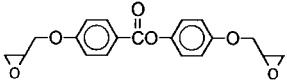
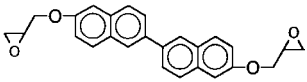
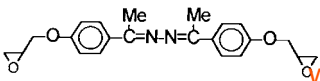
Rigid-rod epoxy thermosets have been investigated more extensively than other rigid-rod thermosets, with more than 20 papers and patents published to date. Epoxy LC networks were first claimed in a Japanese patent issued in 1984 [12]. Following that, Bayer AG and the Dow Chemical Company were issued a number of patents on thermosets based on glycidyl end-capped mesogenic structures. Recently, these materials were initially developed and intensely studied commercially for structure materials with improved performance [13–16].

Table 10.1 displays the structure and thermal properties of rigid epoxy monomers [17–29]. The five kinds of rigid rod epoxy monomers shown in Table 10.1 display a mesophase network structure when they react with the curing agents listed in Table 10.2. Table 10.3 displays the final phase of the networks obtained from the combination of a rigid-rod epoxy compound and a curing agent. Most of them show a nematic-like phase even if they are densely crosslinked. A bulky diamine compound such as DAE does not give a nematic structure to the network. When a rigid-rod epoxy compound was reacted with a curing agent having two groups with unique reactivity such as sulfanilamide (SAA), a smectic-like structure formed. The higher reactive group of the “dual reactive” curing agent performs as a chain extension agent, while the group with lower reactivity subsequently completes the crosslinking reaction. The resulting smectic-like structure suggests that these “dual reactive” curing agents allow sufficient chain extension before crosslinking occurs [20].

An isotropic–liquid crystalline, time-temperature transformation (TTT) diagram (Figure 10.1) is useful in understanding the evolution of the LC phase during an isothermal curing reaction. Lin et al. [21] revealed that the difunctional curing agent leads to faster formation of the LC phase than the tetrafunctional crosslinker. Two factors may contribute to this phenomenon: (1) increased reaction rate and/or (2) more extended chain conformations. It is well known that the latter is responsible for the increase in the clearing transition and broadened LC phase temperature range. For both factors (1) and (2), the initial chain extension reaction plays an important role in stabilizing the LC mesophase. Figure 10.2 shows a non-equilibrium phase diagram for the BOMS/DDM (as shown in Tables 10.1 and 10.2) system [30] and illustrates that the curing process can induce an additional degree of order in the network. In other words, the monomer cured from the nematic melt (80–85°C) leads to the development of a smectic-like network. Similarly, the monomer cured from an isotropic melt (85–150°C) results in a nematic-like network. However, if the reaction is carried out at a sufficiently high temperature, an isotropic network is formed. So, a variety of different networks can be obtained by simply changing the curing temperature.

Semirigid-rod LC monomers contain spacers consisting of methylene units with five to 10 carbons or oxyethylene units between mesogen and reactive

TABLE 10.1. Rigid Rod Epoxy Thermoset Monomers.

		LC Phase	$T_m T_n$ (°C)	CAS RN	References
BPBO		non LC	155	2461-46-3	[17–19,27]
BOMS		monotropic LC	131 (115)	131090-75-0	[17,20–22,27,29]
OPOB		monotropic LC	119 (92)	114815-57-5	[18,23,24,27]
BOBN		enantiotropic LC	240 270	156880-27-2	[25]
FE3		no data	176	153005-52-8	[26]

[www.iran-mavad.com](http://www.iran-mavad.com)

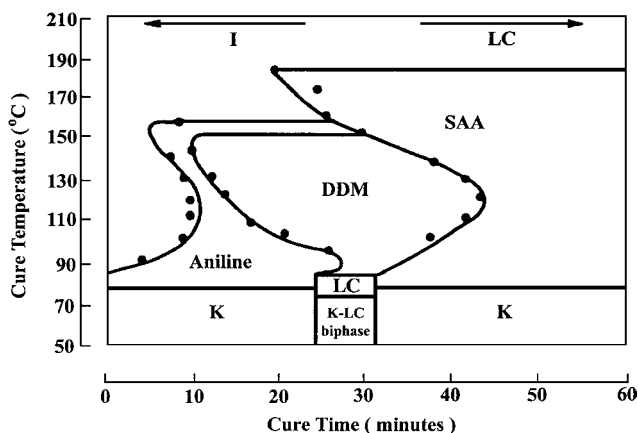
مرجع دانشجویان و مهندسين مواد

TABLE 10.2. Curing Agents for Rigid-Rod LC Epoxy Compounds.

	Abbreviation	$T_m$ (°C)
	DAE	76
	DAT	98
	DDM	90
	Epikure 1061	162
	PDA	144
	BPA	131
	t-DAC	70
	SAA	166
	DDS	176
	NA2	167
	FA	133

TABLE 10.3. Combination of Rigid Rod LC Epoxy Monomers and Curing Agents.

Curing System	Process Temperature (°C)	Network Phase	$T_g$ (°C)	References
BOMS/DAT	110–180	Nematic		[17,20,27]
BOMS/DAE		Isotropic		[17]
BPMS/DDM	90–150	Nematic	150	[29]
BOMS/SAA	75–180	Smectic		[21,22]
BPBO/DAT	110–180	Nematic		[17]
BPBO/na2	100–160	Nematic		[27,28]
OPOB/t-DAC	95	Nematic	127	[23]
BOBN/DDS	250	Nematic	254	[25]
BOBN/FA	230		150	[25]
EF3/NA2	170	Nematic	220	[26]



**Figure 10.1** TTT diagram for LC diepoxy monomer 2,2'-((1-methyl-1,2-ethenediyl)bis(4,1-phenyleneoxymethylene))bisoxirane (BOMS) when reacting with diamine compounds (adapted from Reference [21]).

end group. The spacer leads to better orientation and produces a higher order liquid crystalline phase, with an order parameter as high as 0.8 in a densely crosslinked network [31]. But the long spacer group can deteriorate the thermal and mechanical properties, which makes the semirigid-rod LC thermosets unsuitable for extremely high temperature use and unattractive for structural applications.

Five kinds of semirigid-rod diepoxy compounds with general structures illustrated in Table 10.4 were reported [32–37], displaying a nematic phase

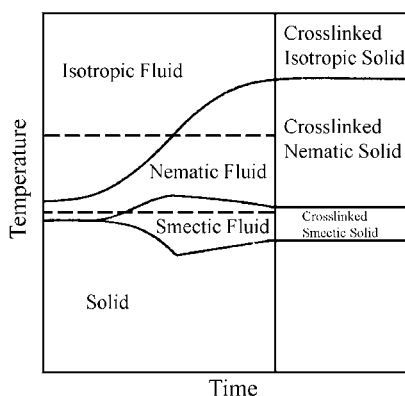


**Figure 10.2** Non-equilibrium phase diagram describing the behavior of liquid crystalline thermosets (adapted from Reference [29]).

TABLE 10.4. Chemical Structure and Transition Temps of Semirigid-rod LC Epoxy Monomers.

		$n$	$T_m$	$T_c$	References
PEHB		4	107	190	[32]
PEOB		6	114	213	[33]
PEEB		—	124	186	[33–36]
EPBP		3	124	Non-LC	[33]
EHBP		4	107	Non-LC	[33]
EOBP		6	111	Non-LC	[33]
EHAB		6	84 71.4	Monotropic LC 84.2	[37]
Twin8		8	152	182	[32]
Twin9		9	127	149	[32]

مرجع دانشجویان و مهندسين مواد

except for the diepoxy compounds containing a biphenyl mesogen (EPBP, EHBP, EOBP). Diepoxy compounds containing a 1,4-bis(benzoyloxy-phenylene mesogen (PEHB, PEOB, PEEB) have been extensively investigated because they show a stable nematic phase over a 60 to 100°C temperature range in the presence of aromatic diamine compounds as the curing agents. The networks from a diepoxy compound having a 1,4-bis(benzoyloxy) phenylene mesogen (PEHB, PEOB, and PEEB) and an aromatic diamine compound retain the LC properties of the diepoxy monomer and tend to form stable nematic LC networks.

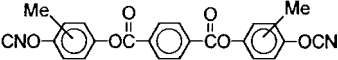
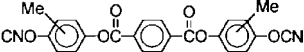
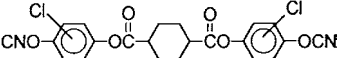
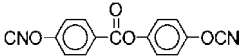
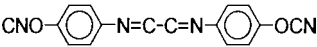
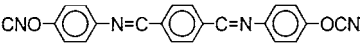
## 2.2. CYANATE ESTER RIGID-ROD THERMOSETS

The first LC cyanate ester thermoset material was reported by G. G. Barclay et al. in 1992 [38]. Since then, several new LC cyanate ester materials have been reported [39–41]. Table 10.5 illustrates the cyanate ester monomers that show a liquid crystallinity during the curing reaction. Monomers C1, C2, and C3 are not liquid crystalline themselves; however, as the curing reaction proceeds, a nematic phase is developed. Other monomers show a nematic phase above the melting point. It is noticed that some cyanate or isocyanate monomers display a much broader and stable mesophase [42] due to the end capped with three atoms groups. The liquid crystalline rigid-rod thermosets with triazine crosslinks were prepared by thermal cyclotrimerization of dicyanate compounds incorporating a rigid-rod segment as shown in Figure 10.3, which can be monitored by the reduction of the characteristic nitrile stretching absorption at  $2260\text{ cm}^{-1}$  and appearance of triazine ring stretching at  $1564\text{ cm}^{-1}$  and  $1370\text{ cm}^{-1}$  using FTIR.

The formation of networks via the cyclotrimerization of the cyanate group to the 1,3,5-triazine crosslink site is unique, because the reaction forming the triazine ring undergoes very few side reactions [43]. The cyclotrimerization reaction of the cyanate group results in nearly quantitative triazine ring formation [44,45]. It is unlikely that linear chain extension through the formation of dimeric intermediate products could occur. One possible feature enabling mesophase formation was that the ether linkages connecting the rigid-rod units to the 2,4,6- positions of the triazine crosslink site were flexible enough to accommodate the formation of elongated rigid-rod species during the initial stages of the curing process, involving the rotation of rigid segments to lie parallel to one another.

The thermal cyclotrimerization of these dicyanates could be carried out using a transition metal catalyst (e.g., Zn, Co, or Cu) to reduce the temperature at which the crosslinking reaction occurred [46,47]. The use of a catalyst facilitates the preparation of highly crosslinked samples at lower, more convenient temperatures. Oriented triazine rigid-rod networks aligned during the curing process under the influence of a magnetic field showed a layered molecular organization indicating an aligned smectic-like network [38]. The dimension derived

TABLE 10.5. Structures and Thermal Properties of Liquid Crystalline Cyanate Ester Monomers.

Monomer		$T_m$	$T_n^a$	$T_c$	Texo	References
C1		151,162,181 <sup>b</sup>	230	—	323	[38]
C2		165,187 <sup>b</sup>	206	—	275	[40]
C3			155,160 <sup>c</sup>	—	245	[39]
C4		140	n/a	n/a	310	[40]
C5			215	215	237	[41]
C6			216	216	280	[41]

<sup>a</sup>Temperature where nematic droplets appear due to cyclotrimerization reaction on POM when heating at 10°C/min.

<sup>b</sup>Polymorphic melting point behavior due to mixture of isomers.

<sup>c</sup>After melting the molecule shows nematic phase.

[www.Iran-mavad.com](http://www.Iran-mavad.com)

مرجع دانشجویان و مهندسين مواد

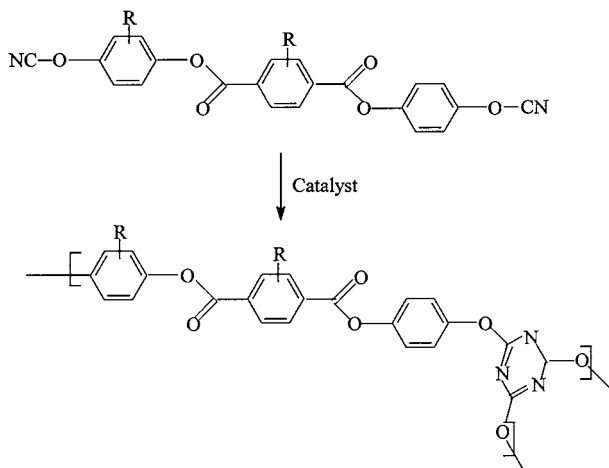


**Figure 10.3** The formation of network via the cyclotrimerization of the cyanate group to the 1,3,5-triazine crosslinks (adapted from Reference [37]).

from computer modeling of a rigid-rod mesogen between triazine crosslinking sites were in close agreement with the X-ray data for the layered structure (Figure 10.4).

The orientation parameter ( $f \sim 0.50$ ) achieved for the aligned triazine networks is comparable to orientation parameters reported for the magnetic field alignment of diacrylate [7,48,49] and epoxy [29] LC network. The inherent anisotropy of the magnetically aligned rigid-rod networks prepared from the dicyanate of di-(4-hydroxy-methylphenyl) terephthalate showed as apparent difference in thermal expansion parallel (17 ppm/°C) and perpendicular (94 ppm/°C) to the direction of the applied field. These values are similar to those observed for the magnetically aligned epoxy networks.

Koerner et al. reported that cyanate ester monomer C1 and C3 could be oriented and polymerized in an a-c electric field [39] and that the orientation of the molecules was controllable by changing the frequency of the field. The cyanate ester LC monomer could self-organize in such a dynamic environment. This “orientation-on-demand” technique will provide a new method to control and modify high performance materials. It is claimed that triazine systems based on 2,4,6-tris[4-aminophenyl]-alkoxybenzylidene]-1,3,5-triazine form a discotic liquid crystalline phase [50]. This report made the investigation of such networks of even more interest.

### 2.3. BISMALEIMIDE RIGID-ROD THERMOSETS

Investigations of bismaleimide rigid-rod thermosets were initiated by Hoyt et al. [51,52]. The investigations involved both rigid-rod amide and rigid-rod

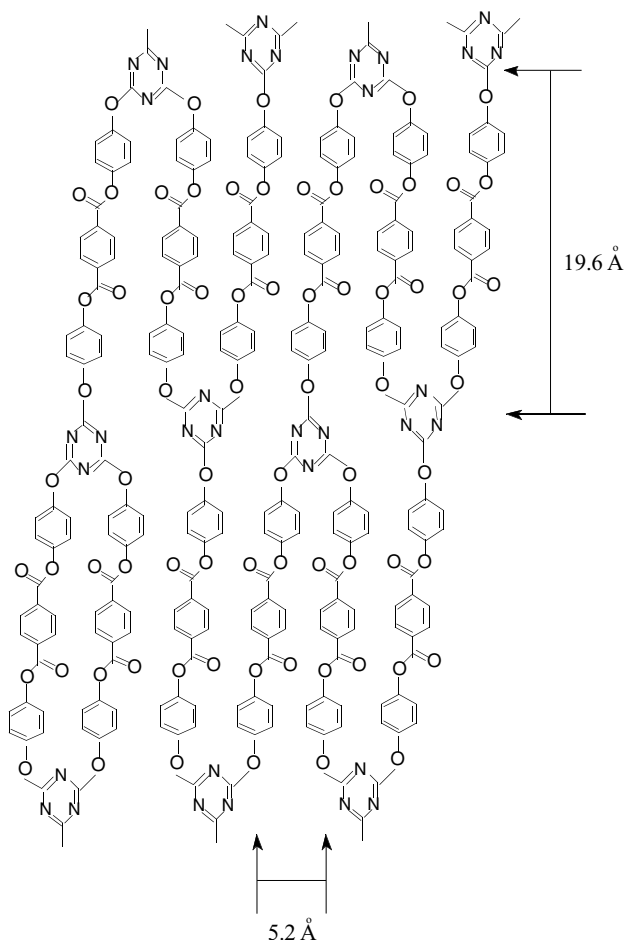


**Figure 10.4** Molecular dimensions of triazine network (adapted from Reference [37]).

ester monomers end-capped with maleimide, nadimide, and methylnadimide crosslinking functionalities of the general structure in Figure 10.5.

Due to the high melting temperatures of these amide monomers, it was difficult to control or study their curing process within the LC phase. To overcome this problem, Hoyt and Benicewicz replaced the amide rigid-rod units with an ester unit. In general, esters have lower melting temperatures than amides. It must be noted that these monomers are more reactive, and sometimes fast heating rates are needed to define the general phase behavior of the monomer before substantial crosslinking reaction occurs. The bismaleimides and bisnadimides could be supercooled after melting in to the nematic phase. The nematic texture was usually maintained after solidification.

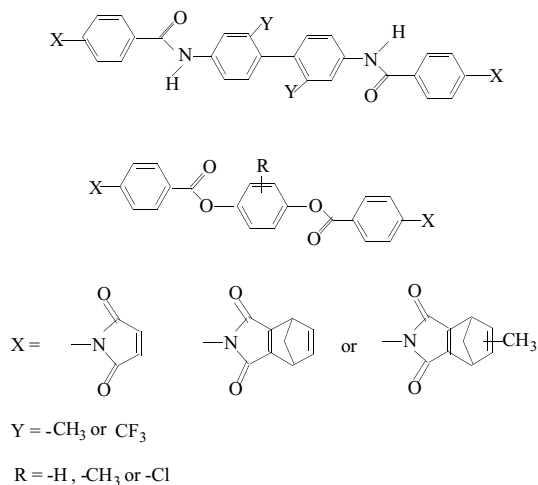


**Figure 10.5** Schematic of general structures of rigid amide and ester monomers for maleimide LC thermosets.

An interesting phenomenon was observed during the isothermal heating of the sample in the isotropic phase: an LC texture could be formed that would coalesce into a continuous phase. This observation is similar to the work on the curing of diester cyanates in an isotropic phase to produce LC triazine networks. Possible mechanisms for the formation of the LC phase involved the chain extension during the initial stage of the reaction, and the growing oligomers would have a higher length-to-diameter ratio than the initial monomer and result in phase separation. As the reaction proceeded, continuous nematic phase was formed and frozen into the final network.

The mechanisms postulated for the curing of nadimide resins involve reverse Diels-Alder reactions and the formation of cyclopentadiene. The release of some cyclopentadiene causes bubble formation, and a distinctive odor is detected concurrently with bubble formation.

## 2.4. DIACRYLATE SEMIRIGID-ROD NETWORK

As stated in the introduction, the first LC thermosets were prepared in 1973 by Blumstein and Strzelecki et al. [6,53–56] via the thermal polyaddition of acrylate-terminated schiff-base mesogens within the mesophase. Strzelecki et al. also reported the first preparation of networks with a helicoidal structure. Copolymerization of the mixture of LC diacrylate, LC monoacrylates having a mesogen, and/or a chiral group within the cholesteric mesophase resulted in the LC networks with a characteristic cholesteric texture.

Blumstein and co-workers prepared anisotropic networks under the influence of a magnetic field. The thermal expansion of these oriented networks was found to be very anisotropic. The initial work of Strzelecki, Blumstein, and their co-workers on the homopolymerization of diacrylate mesogens and copolymerization of diacrylate and monoacrylate mesogens first proved the concept of creating densely crosslinked and highly organized networks in which the LC mesophase was frozen. The three main types of mesophase structures (nematic, smectic, and cholesteric) were observed in these highly crosslinked LC networks. Blumstein et al. [7] also proved the concept of creating highly anisotropic LC networks by crosslinking under the influence of an aligning field.

Recently, semirigid-rod diacrylate compounds were investigated by Hikmet et al. in order to obtain densely crosslinked LC network materials [57] as well as loosely crosslinked anisotropic gel [58–60]. Copolymerization of an LC monoacrylate having a chiral group and LC diacrylate led to a ferroelectric LC network. In a series of papers by Broer et al. [48,49,61,62], highly crosslinked LC networks were prepared by the photopolymerization of diacrylate LC monomers. Photo-polymerization allowed control of the initiation of polymerization and, therefore, the temperature of polymerization. Orientation was induced using surface treatment technique as applied in liquid crystal display, such as a rubbed polyimide film. The resulting ordered networks showed anisotropic behavior in a number of physical properties, such as coefficient of thermal expansion, modulus of elasticity, and refractive index.

Flexible spacers in the semirigid-rod molecule allow the molecule to orient with order parameter greater than 0.8 when coated and cured upon a rubbed polyimide layer. Kinetics of the photo-polymerization [62,63] and surface-induced orientation [49] as well as mechanical [64,65], optical [59,66,67], and ferroelectric properties [68–70] of the anisotropic networks were thoroughly examined. These investigations were mainly carried out by the Philip's research group and were applied to develop liquid crystalline display devices [58,69].

## 2.5. BISACETYLENE RIGID-ROD NETWORK

As mentioned before, in the mid 1980s, industrial research rediscovered LC polymer networks. The Celanese corporation issued a number of patents on anisotropic heat-curable acetylene-terminated mesogens and the LC thermoset resins produced from this type of materials [71–74]. Melissaris and his co-workers [75,76] studied the solid-state polymerization of the acetylene end-capped monomers, while Douglas et al. [30] focused on the curing behavior of the bisacetylene compounds in the LC state. The general structures of the bisacetylene compounds that Melissaris et al. and Douglas et al. investigated are shown in [Figure 10.6](#). [Table 10.6](#) lists 16 kinds of these *p*-ethylbenzoyl ester monomers.

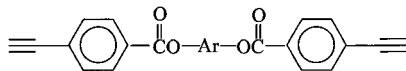


**Figure 10.6** General structure of the bisacetylene monomers; -Ar- is an aromatic group.

Because the polyaddition reaction of the bisacetylene monomers occurred around 200°C, a crosslinking reaction will occur in the solid state if the molecule does not melt above 200°C. The bisacetylene monomers that have small substituents like methyl, methoxy, and chloro group exhibit LC behavior.

Combining X-ray diffraction data with molecular modeling, Melissaris et al. suggested that bisacetylene monomers were inter-digitated in the crystalline state. This plays an important role in the solid-state polymerization enabling high conversion to be achieved, because the reactive ends of the bisacetylene monomers do not need to diffuse much to reach other reactive sites (Figure 10.7). These bisacetylene monomers shrink only 0–2.4% when polymerized, which is much lower than that observed for the epoxy-aromatic amine systems (8–9%) or acrylate networks (11–15%).

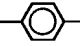
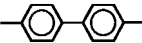
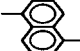
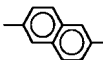
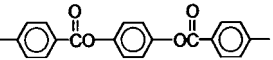
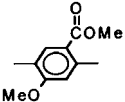
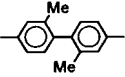
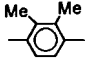
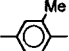
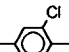
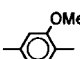
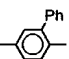
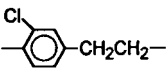
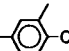
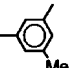
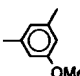
Melissaris et al. developed a medium pressure (500–1000 psi) molding process for these monomers and successfully produced a void-free polymer sample made from the monomer powder. Hardened samples have a flexural storage modulus of 4.5 to 4.8 GPa. The coefficient of thermal expansion was  $2.0 \times 10^{-5} \text{ } ^\circ\text{C}^{-1}$ . Cured samples had good thermal stability with 5% weight loss temperatures above 400°C in air.

Some bisacetylene monomers exhibited an LC state in which they could be polymerized; however, the monomers showed only a nematic phase. Some monomers started to cure in the isotropic state and transformed to a nematic phase as the reaction proceeded. Similar behavior was also observed in an LC epoxide/diamine system. Hardened samples exhibit  $T_g$ s above 350°C, more than 100°C above their processing temperatures. The coefficient of thermal expansion of the thermosets was  $5.0 \times 10^{-5}$  to  $6.9 \times 10^{-5} \text{ } ^\circ\text{C}^{-1}$ .

## 2.6. RIGID AND SEMIRIGID-ROD NETWORKS BASED ON HYBRID ORGANIC-INORGANIC DESIGNS

In addition to networks based on organic materials, rigid structures based on hybrid organic-inorganic designs are being developed, in which structure aromatic rigid groups, such as phenyl, biphenyl, and terphenyl, were capped with reactive siloxy groups. The formation of a silicate network in which organic bridges were present between the crosslink sites resulted in a porous gel structure [77]. Small functional molecules embedded within the pores of the polymer network can show interesting properties. In the authors' laboratory, a novel self-assembled NLO polymer film constructed from a structurally

TABLE 10.6. Structure and Thermal Transitions of Biacetylene Monomers.

Monomer	-Ar-	Endo(°C)	Phase Behavior	Exo (°C)	References
A1		None	Crystalline	211	[75,30]
A2		None	Crystalline	217	[75,76,30]
A3		None	Crystalline	258	[75,76]
A4		None	Crystalline	207	[75,30]
A5		None	Crystalline	249	[75]
A6		None	Crystalline	229	[30]
A7		168	k → n	182	[30]
A8		176	k → n	181	[30]
A9		183	k → n	189	[75,30]
A10		164	k → n	178	[75,30]
A11		154 164	k → n → i n	178	[30]
A12		182	k → i	192	[30]
A13		113	k → i	187	[30]
A14		157	k → i	192	[30]
A15		177	k → i	194	[30]
A16		139	k → i	185	[30]

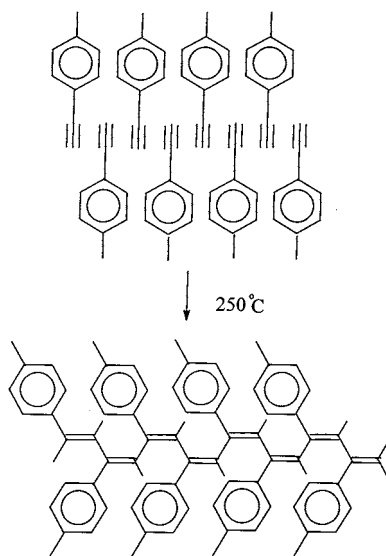


**Figure 10.7** Schematic representation of interdigitation of the ethyl groups and their polymerization (adapted from Reference [74]).

controlled, cage-like crosslinking polymer (SCCP) and chromophore molecules embedded in it (Figure 10.8) has been prepared by a “sol-gel” process [78,79]. The rigid organic bridge was designed according to the size of the chromophore molecules, so that they can be consequently trapped within the “cages” at the molecular level.

Another innovation based on hybrid organic-inorganic designs is mesogenic ladderlike polysiloxanes (LPSs). One-dimensional ordered network is inherent skeleton structure in these ladder polymers (Figure 10.9), which enables this polymer material possessing unique optical and mechanical properties. Reactive polyhydro-silsesquioxane and its copolymers were first prepared in our group by a new route named “stepwise-coupling polymerization” [80,81]. As parent polymers, they were further functionalized mainly by hydrosilylation reaction with vinyl-terminated mesogenic or photosensitive monomers. Various functionalized optical films can be prepared from them. For example, the orientation of dipole director of the chromophores connected on the LPS backbone induced by corona-poling can be in situ fixed in the sol-gel process and results in high temporally stable nonlinear optical SHG films [82,83]. Anisotropic LPP alignment film for LCD was produced by illumination with linear polarized UV-light of cinnamate-grafted LPS. The unique, high stability of the orientation state is attributed to the inherent material properties [84]. Especially, the alignment film with high pretilt angle or patterned characters can be prepared by

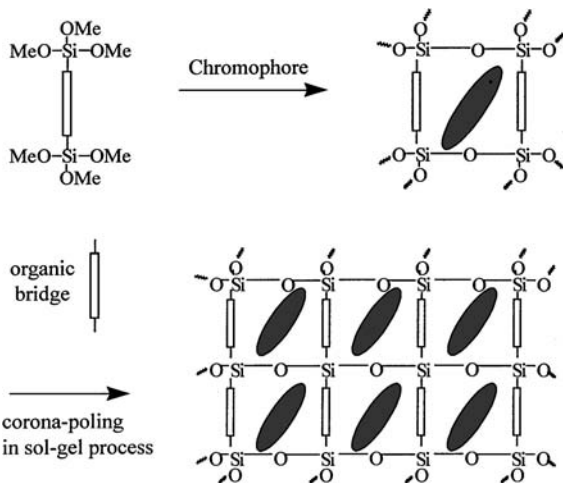


**Figure 10.8** A proposed depiction for preparing SCCP/NPP self-assembly polymer film.

combined technique of rubbing and UV-modification from photosensitive ladderlike polysiloxanes [85]. The generation of high pretilt state can be attributed to the isomerization of azobenzene groups, and it can be fixed by cycloaddition of adjacent cinnamate groups.

### 3. REACTION KINETICS OF LC NETWORKS

Reaction kinetics in LC phase is greatly different from that in an isotropic phase. For example, in a curing process of LC diepoxy with aromatic diamine, the reactive mixtures are not liquid crystalline in the initial stage. As the reaction proceeds, the formation of molecular segments of critical length and stiffness

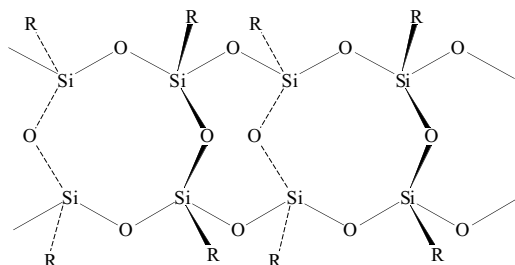


**Figure 10.9** Schematic representation of ladderlike polysiloxanes.

is responsible for the transition from an isotropic to a nematic phase under an isothermal condition [17,25–27]. Accompanying the transition to a nematic phase, the curing reaction usually shows auto-acceleration [20,86]. In the cases of photo-radical polymerization of LC diacrylate [87] and photo-cation polymerization of LC epoxies [88], the reaction rates in the nematic phase were remarkably higher than that in the isotropic phase, and the same phenomenon was also reported for bisacetylene systems [30]. This higher reactivity is attributed to the higher frequency factor evaluated for the reaction occurring in the nematic state. The higher frequency factor is attributed to the lower viscosity and the ordered structure between molecules. Especially, for radical polymerization systems, lower rates of terminating reaction also could be explained by the ordered structure.

As the reaction proceeds further, the onset of crosslinking reaction results in the increase in viscosity pertinent to an infinite network. However, the short-range Brownian motion of molecular segments and the diffusion of low molecules undergo further phase transition after reaching the gel point. So, the curing reaction with a crosslinking agent should be carried out in a temperature range compatible with the presence of the nematic phase of the growing prepolymer. Once the nematic phase appears, the curing reaction proceeds up to the development of a three-dimensional network with a permanent liquid crystalline structure. A non-equilibrium phase diagram as in Figure 10.1 was proposed to explain the melting behavior of these reactive liquid crystal thermoset materials [30].

#### 4. PHYSICAL PROPERTIES AND POTENTIAL APPLICATION

The main reason for the current and future ever-growing interest in liquid crystalline polymers lies in their unusual properties [89]. The effective alignment of molecular backbones in LCP is claimed to produce properties even superior to engineering thermoplastics. The long-range orientational ordering of the liquid crystalline polymers leads to anisotropic mechanical, optical, magnetic, and electrical properties.

The discovery of mesophase order in densely crosslinked networks has led to some innovative concepts in designing and processing thermoset materials, for example, these networks could be oriented under external fields during curing reaction and result in highly anisotropic materials. These LC thermosets exhibit unique properties that show promise for applications in the aircraft, aerospace, and electronic packaging fields as well as for surface coatings with superior impact resistant properties.

Because LC thermosets are highly ordered and densely crosslinked network polymers, it is self-evident that they possess unique thermal and mechanical properties [90]. In general, their  $T_g$ s are very high or even cannot be

TABLE 10.7. Comparison of Thermal and Electrical Properties between Liquid Crystal Epoxy and Bisphenol A Epoxy (Epon 828), Both Cured with Molar Equivalents of Trimellitic Anhydride (TMA).

Sample	( $T_g$ , °C)	Dielectric Strength (kV/10 mil)	Dissipation Factor (@ 1 MHz)
LC Epoxy/TMA	183	12.38	0.0319
Epon 828/TMA	127	10.89	0.0372

observed. Meanwhile, the high tensile modulus can be maintained at high temperatures, even above  $T_g$ , because the micro-Brownian motion of segment between crosslinking sites is suppressed due to the orientation of LC units in the network. This nature greatly broadens the application temperature range of Ts-LCPs.

Compared with cured samples of conventional bisphenol A epoxy (Epon 828), the liquid crystal epoxy with the same curing condition exhibits better thermal and electric properties as shown in Table 10.7 [91]. The results are expected because of the highly ordered rigid-rod structure of the liquid crystal epoxy, and a shorter gel time than that of bisphenol A epoxy was observed.

High dielectric strengths, low dielectric loss, low thermal expansion coefficients, and the low viscosity of LC monomers and precursor-oligomers enable LC epoxy resins to be promised as micro-electronic packing materials. Moreover, ordered thermosets are expected to exhibit better mechanical properties than ordered thermoplastics due to the presence of permanent interchain linkage in the cured LC thermosets. High fracture toughness of Ts-LCP is mainly attributed to the presence of multiphase structure and retained LC anisotropic structure [27]. X-ray diffraction investigation indicated that oriented LC domain was surrounded by isotropic domains, which was similar to fiber-reinforced composite material, and oriented segments in LC domain interrupted the craze development in isotropic domains and thus led to high fracture toughness.

Oriented and liquid crystalline precursor oligomers produced in the early stage of Ts-LCPs syntheses make the manufacture of composites convenient and are utilized to solve the rheological problem. Liquid crystallinity of the precursor oligomer leads to the dense alignment and results in low bulk shrinkage in the curing process, that not only is helpful to simplify the manufacture, but also can improve the mechanical properties of composite materials.

## 5. REFERENCES

1. R. A. Weiss, and C. K. Ober, in *Liquid Crystalline Polymers*, ACS Symposium Ser. 435, ed. by ACS, Washington, D.C. (1990), p. 7–8.
2. R. Zental, *Angew. Chem., Int. Ed. Engl. Adv. Mater.*, 28, 1407 (1989).

3. H. Finkelmann, H.-J. Kock, and G. Rehage, *Makromol. Chem. Rapid. Commun.*, 2, 317 (1981).
4. J. Herz, F. Reiss-Husson, P. Rempp, and V. Luzzati, *J. Polym. Sci.*, Part C, 1275 (1963).
5. A. Blumstein, R. B. Blumstein, and T. H. Vanderspurt, *J. Colloid Interface Sci.*, 31(2), 236 (1969).
6. L. Strzelecki and L. Liebert, *Bull. Soc. Chem.*, (France) 597 (1973).
7. S. B. Clough, A. Blumstein, and E. C. Hsu, *Macromolecules*, 9(1), 123 (1976).
8. W. Mormann, *Trends Polym. Sci.*, 3, 255 (1995).
9. G. G. Barclay and C. K. Ober, *Prog. Polym. Sci.*, 18, 899 (1993).
10. A. Shiota and C. K. Ober, *Prog. Polym. Sci.*, 22, 975 (1997).
11. D. Coates and M. Verrall, in *Specialty Polymers*, Chapter 7, ed. by R. M. Dyson, Blackie Academic & Professional, London, Second Ed (1998), pp.192–197.
12. Jpn. KoKKyo Koho Jp 58, 206,579[83,206,579], Agency of Industrial Science and Technology; Chem. Abstr., 100, 138934x (1984).
13. R. Dhein, H.-M. Meier, H.-P. Muller, and R. Gipp, Ger. Offen, 3622613 A1 (1988).
14. J. D. Earls and R. E. Hefner Jr., Eur. Pat. Appl. 379057A2 (1990).
15. R. E. Hefner and J. D. Earls, Eur. Pat. Appl. 475238A2 (1992).
16. S. Eirchmeyer, H.-P. Muller, and A. Karbach, Eur. Pat. Appl. 445401 (1991).
17. C. Carfagna, E. Amendola, M. Giamberini, A. G. Filiprov, and R. S. Bauer, *Liq. Cryst.*, 13, 571 (1993).
18. W. Mormann, J. Zimmermann, and C. Irle, *Pom. Prepr.* (Am. Chem. Soc.), 34, 704 (1993).
19. J. T. Guthrie, A. Morton, and E. Nield, *Surf. Coat. Int.*, 75, 212 (1993).
20. E. Amendola, C. Carfagna, M. Giamberini, and G. Pisaniello, *Macromol. Chem. Phys.*, 196, 1577 (1995).
21. Q. Lin, A. F. Yee, J. D. Earls, R. E. Hefner Jr., and H.-J. Sue, *Polymer*, 35, 1682 (1994).
22. A. A. Robinson, S. G. McNamee, Y. S. Freidzon, and C. K. Ober, *Polym. Prepr.* (Am. Chem. Soc.), 34, 743 (1993).
23. C. Carfagna, E. Amendola, and M. Giaberini, *J. Mater. Sci. Lett.*, 13, 126 (1994).
24. S. M. Kirchmeyer, H.-P. M. R. Muller, and H.-M. Dhein, Meier, *Angew. Makromol. Chim.*, 211, 61 (1993).
25. C. Carfagna, E. Amendola, and M. Giamberini, *Macromol. Chem. Phys.*, 195, 2307 (1994).
26. C. Carfagna, E. Amendola, and M. Giamberini, *Macromol. Chem. Phys.*, 195, 279 (1994).
27. C. Carfagna, E. Amendola, and M. Giamberini, *Composite Struct.*, 27, 37 (1994).
28. C. Carfagna, E. Amendola, and M. Giamberini, in *Liquid Crystalline Polymers: Proceedings of the International Workshop on Liquid Crystalline Polymers*, WLCP 93, Capri, Italy, ed. by C. Carfagna, Pergamon Press, Oxford, pp. 69–85 (1994).
29. G. G. Barclay, S. G. McNamee, C. K. Ober, K. I. Papathomas, and D. W. Wang, *J. Polym. Sci., Part A: Polym. Chem.*, 30, 1845 (1992).
30. E. P. Douglas, D. A. Langlois, and B. C. Benicewicz, *Chem. Mater.*, 6, 1925 (1994).
31. S. Jahromi, *Macromolecules*, 27, 2804 (1994).
32. A. Shiota and C. K. Ober, *J. Polym. Sci., Part A: Polym. Chem.*, 28, 3403 (1990).
33. J. J. Mallon and P. M. Adams, *J. Polym. Sci., Part A: Polym. Chem.*, 31, 2249 (1993).
34. S. Jahromi, J. Lub, and G. N. Mol, *Polymer*, 35, 622 (1994).
35. S. Jahromi and W. Mijs, *Mol. Cryst. Liq. Cryst. Sci. Tech.*, Sect. A., 250, 209 (1994).
36. S. Jahromi, W. A. G. Kuipers, B. Norder, and W. J. Mijs, *Macromolecules*, 28, 2201 (1995).
37. B. Koscielny, A. Pfitzman, and M. Fedtke, *Polym. Bull.*, 32, 529 (1994).
38. G. G. Barclay, C. K. Ober, K. I. Parathomas, and D. W. Wang, *Macromolecules*, 25, 2947 (1992).
39. K. Koerner and C. K. Ober, *Polym. Mater. Sci. Eng. Prepr.*, 73, 456 (1995).
40. W. Mormann and J. Zimmermann, *Macromol. Symp.*, 93, 97 (1995).
41. Y. H. Wang, Y. L. Hong, F. S. Yang, and J. L. Hong, *Polym. Mater. Sci. Eng. Prepr.*, 71, 678 (1994).

42. W. Mormann and J. Zimmerman, *Liq. Cryst.*, 19, 227 (1995).
43. V. V. Korshak, V. A. Pankratov, A. A. Ladovskaya, and S. V. Vinogradova, *J. Polym. Sci., Polym. Chem.*, 16, 1697 (1978).
44. V. V. Korshak, V. A. Pankratov, A. A. Ladovskaya, and S. V. Vinogradova, *J. Polym. Sci., Chem.* 16, 1697 (1978).
45. V. A. Pankratov, S. V. Vinogradova, and V. V. Korshak, *Russ. Chem. Rev. (Engl.)*, 46, 278 (1977).
46. D. A. Shimp, J. R. Christenson, and S. J. Ieing, *SAMPE Symp.*, 34(1), 222 (1989).
47. D. A. Shimp and W. K. Craig, *SAMPE Symp.*, 34, 1336 (1989).
48. D. J. Broer, R. A. M. Hikmet, and G. Challa, *Makromolek. Chem.*, 190, 3201 (1989).
49. D. J. Broer, G. N. Mol, and G. Challa, *Makromolek. Chem.*, 192, 59 (1991).
50. S. J. Huang, J. A. Feldman, and J. L. Cercena, *Polym. Prepr. (Am. Chem. Soc., Div. Polym. Chem.)*, 29 (2), 348 (1988).
51. A. E. Hoyt and B. C. Benicewicz, *J. Polym. Sci., Part A: Polym. Chem.*, 28, 3403 (1990).
52. A. E. Hoyt and B. C. Benicewicz, *J. Polym. Sci., Part A: Polym. Chem.*, 28, 3417 (1990).
53. A. Blumstein (Ed), *Mesomorphic Order in Polymers and Polymerization in Liquid Crystalline Media*, ACS Symposium Series, Vol 74, ACS, Washington D.C. (1978).
54. L. Liebert and L. Strzelecki, *Bull. Soc. Chem. (France)*, 603 (1973).
55. L. Strzelecki and L. Liebert, *Bull. Soc. Chem. (France)*, 605 (1973).
56. Y. Bouligand, P. E. Cladis, L. Liebert, and L. Strzelecki, *Mol. Cryst. Liq. Cryst.*, 25, 233 (1974).
57. R. A. M. Hikmet, J. Lub, and A. J. M. Tl, *Macromolecules*, 28, 3313 (1995).
58. R. A. M. Hikmet, *Adv. Mater.*, 4, 679 (1992).
59. R. A. M. Hikmet, *Liq. Cryst.*, 12, 319 (1992).
60. R. A. M. Hikmet and R. Howard, *Phys. Rev. E*, 48, 2752 (1993).
61. D. J. Broer and I. Heynderickx, *Macromolecules*, 23, 2474 (1990).
62. D. J. Broer, R. G. Gossink, and R. A. M. Hikmet, *Angew. Makromol. Chem.*, 183, 45 (1990).
63. C. E. Hoyle, C. P. Chawla, D. Kang, and A. C. Griffin, *Macromolecules*, 26, 758 (1993).
64. R. A. M. Hikmet and D. J. Broer, *Polymer*, 32, 1627 (1991).
65. M. H. Litt, W.-T. Whang, K.-T. Yeh, and X.-J. Qian, *J. Polym. Sci., Part A: Polym. Chem.*, 31, 183 (1993).
66. R. A. M. Hikmet and A. H. Zwerver, *Liq. Cryst.*, 13, 561 (1993).
67. H. S. Kitzerow, H. Schmid, and A. Ranft, *Liq. Cryst.*, 14, 911 (1993).
68. R. A. M. Hikmet and J. Lub, *J. Appl. Phys.*, 77, 6234 (1995).
69. R. A. M. Hikmet and D. J. Broer, *Liq. Cryst.*, 19, 65 (1995).
70. R. A. M. Hikmet, *Macromolecules*, 25, 5759 (1992).
71. A. B. Concliatori, E. W. Choe, and G. Farrow, US Pat. 4,440,945 (1984).
72. A. B. Concliatori, E. W. Choe, and G. Farrow, US Pat. 4,452,993 (1984).
73. A. B. Concliatori, E. W. Choe, and G. Farrow, US Pat. 4,514,553 (1985).
74. R. W. Stackman, U.S. Pat. 4,683,327 (1987).
75. A. P. Melissaris and M. H. Litt, *Macromolecules*, 27, 2675 (1994).
76. A. P. Melissaris, J. K. Sutter, M. H. Litt, D. A. Scheiman, and M. Scheiman, *Macromolecules*, 28, 860 (1995).
77. K. J. Shea, D. Loy, and O. W. Webster, *Chem. Mater.*, 1, 572 (1989).
78. D. S. Liu, D.-R. Dai, C. Ye, P. Xie, Z. Li, and R. B. Zhang, *Solid State Commun.*, 94 (3), 169 (1995).
79. D. S. Liu, Y. X. Tang, D.-R. Dai, and R. B. Zhang, *Science in China (Ser. B)*, 27 (4), 314 (1997).
80. P. Xie and R. B. Zhang, *Polym. Adv. Tech.*, 8, 649 (1997).
81. R. B. Zhang, D. R. Dai, L. Cui, H. Xu, C. Q. Liu, and P. Xie, *Supramol. Chem.*, 1999, 5 (in press).
82. P. Xie, J. S. Guo, and R. B. Zhang, *Mol. Cryst. Liq. Cryst.*, 289, 45 (1996).

83. P. Xie, J. S. Guo, and R. B. Zhang, *Polym. Adv. Tech.*, 7, 662 (1996).
84. L. Cui, W. Jin, P. Xie, and R. B. Zhang, *Liq. Cryst.*, 25 (6), 757 (1998).
85. L. Cui, W. Jin, Y. B. Liu, P. Xie, and R. B. Zhang, *Mol. Cryst. Liq. Cryst.*, (in press, 1999).
86. J. Liu, C. Wang, G. A. Campbell, J. D. Earis, J. Ralph, and D. Priester, *J. Polym. Sci., Part A: Polym. Chem.*, 35, 1105 (1997).
87. C. E. Hoyle and T. Watanabe, *Macromolecules*, 27, 3790 (1994).
88. D. J. Broer, J. Lub, and G. N. Mol, *Macromolecules*, 26, 1244 (1993).
89. H. N. Yoon, L. F. Charbonneau, and G. W. Calundann, *Adv. Mater.*, 4, 206 (1992).
90. S. M. Aharoni, in *Synthesis, Characterization and Theory of Polymeric Networks and Gels*, Plenum Press, New York (1992), p. 147.
91. W. F. A. Su, *J. Polym. Sci., Part A: Polym. Chem.*, 31, 3251 (1993).

# LCP Extrusion and Applications

RICHARD W. LUSIGNEA

## 1. INTRODUCTION

**A**FTER more than 15 years of commercial use in injection-molded parts, liquid crystal polymers (LCPs) are being extruded and used commercially for tubing, film, and blow-molded containers. Why has it taken so long for LCPs to find uses in extruded parts? The primary reason is that conventional plastic processing does not work well with LCP, resulting in products with mechanically weak directions, uncontrolled thermo-mechanical strain, and other undesirable properties. Now, processing methods such as the counter-rotating extrusion die have been developed and are being commercially exploited to produce extruded LCP parts that meet market demands for performance and price. For example, LCPs are now being used in tubing for endoscopic surgical instruments and in film-foil laminates for electronic circuit boards.

This chapter will briefly describe LCPs, why they are useful, and how processing methods can make effective use of their properties. Next, new processing methods will be discussed that unlock the mechanical, electrical, barrier, and chemical resistance properties of extruded LCP. Later, we will look at applications of tubing, film, and molded containers, along with new work in processing and using LCP-thermoplastic blends.

## 2. LCP BACKGROUND

Liquid crystal polymers (LCPs) are so called because their molecules can be mutually aligned and organized (crystal), yet the bulk LCP can flow (liquid)

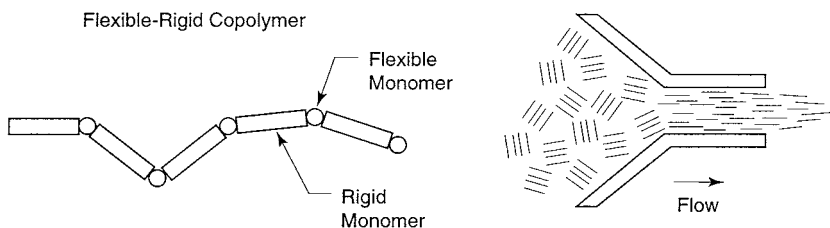


**Figure 11.1** Liquid crystal polymers have rigid segments that tend to align in shear flow.

in the molten state for thermotropic LCPs, or the solvated state for lyotropic LCPs [1–4]. This behavior is unlike ordinary “random coil” polymers, which are isotropic in the melt or in solution and can be oriented by stretching at proper temperatures [5]. The liquid crystal state results from the rigid nature of segments of the LCP molecules (see Figure 11.1). When the LCP flows in the liquid crystal state, the rigid segments of the molecules align next to one another in the shear flow direction, creating anisotropic-oriented regions. Once the oriented regions are formed, their direction and structure persist, even when the LCP approaches the melt temperature, because of the long relaxation time of the stiff chain LCP molecules. This can present problems if the orientation produces weak areas, such as the uniaxial film shown in Figure 11.2(a), which tends to split under transverse load. However, LCPs can be used to great advantage if the orientation is biaxial or multiaxial and in line with the directions of maximum stress. In this case, the LCP structure will be efficient with regard to strength-to-weight and strength-to-cost ratios. Figure 11.2(b) shows a biaxially

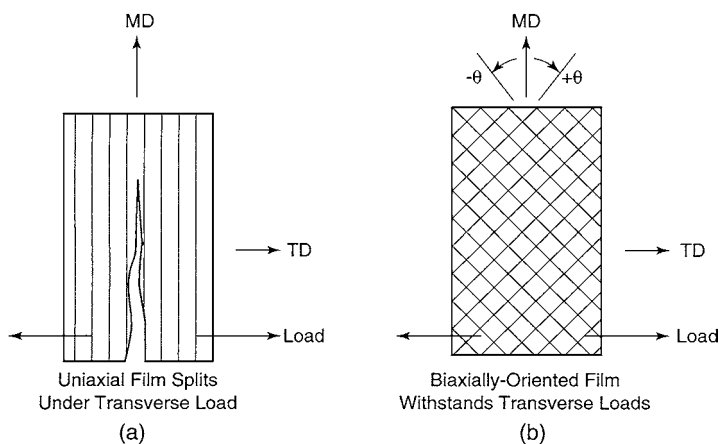


**Figure 11.2** Molecular orientation of uniaxial LCP film results in weak transverse strength. Biaxially-oriented film has equal transverse and machine direction strengths.

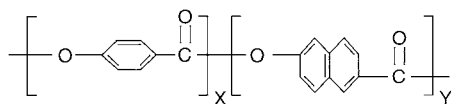


**Figure 11.3** Ratio of rigid monomer, X, to flexible monomer, Y, determines the properties of Vectra® A950.

oriented film with equally good transverse and machine direction (isotropic) properties as opposed to the anisotropic properties of the film in Figure 11.2(a).

All commercial LCPs are copolymers composed of molecules with rigid and flexible monomeric units. The rigid part (often called the mesogenic monomer) imparts high temperature capability and high mechanical properties, while the “flexible” monomer contributes processibility. For example, Vectra® (Ticona) consists of hydroxybenzoic acid, HBA, as the mesogenic monomer and hydroxynaphthoic acid, HNA, as the “flexible” monomer, as shown in Figure 11.3. Each commercial type of LCP has its own combination of components, and within each type, the ratio of the components can be changed to produce grades with different melt temperatures and cost-performance tradeoffs.

In general, LCP molecules with more rigid segments result in polymers with higher thermal and mechanical properties than those with more flexible segments, but the greater the molecular stiffness, the more difficult it is to process the LCP.

LCPs, with some flexible segments, are of great commercial interest because they can be processed thermoplastically, opening up a rich variety of processing methods to make parts that exploit the properties of LCPs. Copolyesters with rigid and flexible moieties, such as in Figure 11.3, have sufficient chain mobility that they can be melt processed at temperatures from 200 to 400°C [6,7], and they are commercially available. Such thermotropic LCPs are currently being used for injection-molded parts, such as electrical connectors and connectors for fiber optic devices. The current world production of these LCPs is approximately 10,000 tons per year at a value of \$200 million. These commercial LCPs are currently priced at about 15 to 33 U.S. dollars per kg in pure form and from 13 to 28 U.S. dollars per kg with 30 to 50% glass or mineral fillers. While the use of fillers decreases the price and anisotropy of molded parts, it also decreases the inherent mechanical properties of LCPs, makes parts heavier, and cannot be used for thin films.

The first LCP films were extruded through conventional slot dies and had tremendous strength in the extrusion direction, but only one-tenth that strength transversely, thereby severely limiting the usefulness and widespread application of LCP films. Now, through new processing methods, LCP film can be made with controlled orientation, placing the LCP molecules where they carry the greatest load, often providing higher performance to cost than conventional

TABLE 11.1. Tensile Test Results on LCP Film Made with TRD.

Orientation Angle	Tensile Strength		Tensile Modulus	
	MD Mpa (ksi)	TD Mpa (ksi)	MD Gpa (Msi)	TD Gpa (Msi)
30°	270	130	12.9	5.40
Superex #101394	(39)	(19)	(1.87)	(0.78)
45°	166	193	9.0	7.6
Superex #120695	(24)	(28)	(1.3)	(1.1)
0°	793	83	42.8	3.4
Superex #103096	(115)	(12)	(6.2)	(0.5)

thermoplastics. This is analogous to using fibers in a composite material to make parts that are lighter in weight and cost less than those made of less efficient isotropic materials.

## 2.1. CONVENTIONAL EXTRUSION OF LCP

Generally, conventional processing such as extrusion through slot dies and injection molding produces high shear and other flow patterns in the LCP that cause undesirable orientation and familiar problems, including weld lines and weak strength directions where parts will split. As noted before, some of the problems can be alleviated by fillers, but this reduces mechanical properties and is not applicable to films.

Figure 11.4 shows the type of orientation in two films, one a uniaxial film extruded through a slot die and the other with biaxial orientation [8–11]. Table 11.1 shows the tensile properties of LCP film made by conventional processing for 0° orientation. We note that MD tensile properties are about 10 times higher than TD properties.

## 2.2. CONTROLLED ORIENTATION OF LCP FILM

The reason for the uniaxial LCP film in Figure 11.4 is that the flow within the die created longitudinal orientation in the melt. As the LCP melt flowed over the fixed land area of the die, the liquid crystal domains were further aligned in the flow direction. To counteract this longitudinal flow-induced orientation, one or both surfaces of the die are moved transversely with respect to one another. This is most easily accomplished by using two coaxial cylinders, rotating in opposite directions, producing transverse shear between the walls of the cylinders, as shown in Figure 11.5.

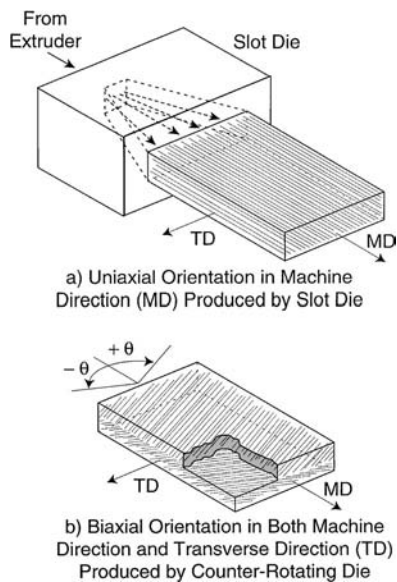


**Figure 11.4** Uniaxial and biaxial orientation of LCPs.

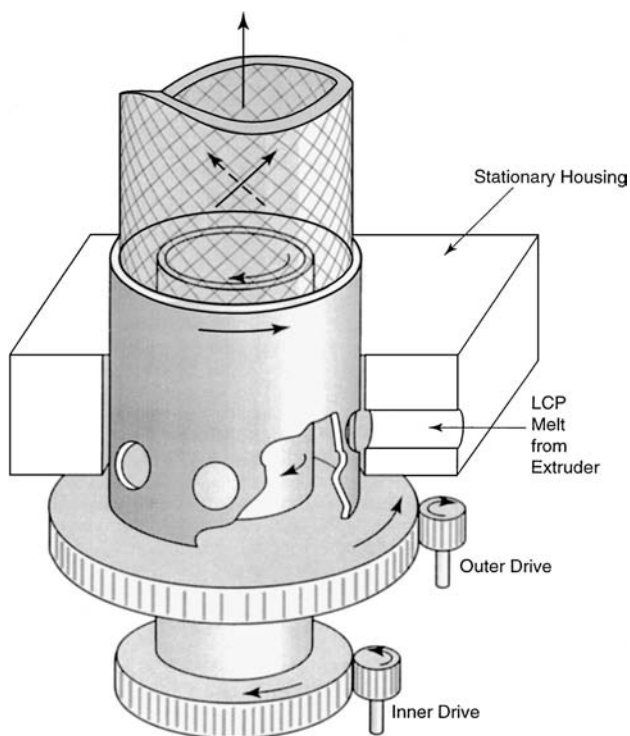


**Figure 11.5** Schematic representation of counter-rotating die.

The counter-rotating die of [Figure 11.5](#) can be used for film, tubing, and blow-molded containers, as well as multilayer coextruded products. The machinery, processing, and applications are described in subsequent sections of this chapter. Specifically, [section 3](#) will describe the importance of stretching, combined with shear, to control orientation.

Although LCPs were developed 25 years ago and have been commercially available for more than 15 years, their use is almost exclusively limited to injection-molded parts [12]. There are two major reasons for this: (1) the processing methods for making multiaxially oriented extruded parts are just now being introduced, and (2) the price of LCP has been relatively high, but is now dropping as more suppliers enter the market and volumes increase. The major suppliers of LCP are Ticona and affiliate Polyplastics (Vectra®), Amoco Performance Products (Xydar®), Dupont (Zenite®), Eastman (Thermx®), and Sumitomo Chemical (Sumikasaper®). The various LCPs have different chemical constituents, melt temperatures, and other physical properties. However, all share the same rigid-flexible polymer structure.

LCPs are useful in many applications because they possess a combination of properties not found in other plastics [12,13]. This balance of properties, combined with processing to provide orientation, results in LCP parts that are more cost-effective than the same parts made from other polymers.

### 3. COUNTER-ROTATING DIES FOR EXTRUSION

This section will describe the process and machinery for making multiaxially oriented film from LCP. As summarized in [section 2](#), the extruded LCP melt can be oriented through axial and transverse shear forces. Now, we will consider the use of stretching, or elongational forces, to improve and control the orientation.

#### 3.1. ORIENTATION IN LCP FILM

Orientation of typical “random coil” polymer films, such as polypropylene and polyethylene terephthalate, involves stretching the film at a temperature above the glass transition temperature ( $T_g$ ) and below the melt temperature ( $T_M$ ) [5]. This allows the polymer chains sufficient mobility to be aligned in the strain directions, but not so much mobility that they will relax to a random state. With LCP films, the development of orientation is quite different.

We saw previously in [Figures 11.2 and 11.3](#) how a uniaxial film is produced by extruding LCP through a fixed slot die. Unlike random coil polymers, if the uniaxial LCP film is heated above  $T_g$  and below  $T_M$ , then transverse stress is applied, and the LCP film will tear, as in [Figure 11.2\(a\)](#). The reason for this is that the rigid rod molecular segments remain aligned, even near the melt temperature, and, therefore, the LCP film remains weak in the transverse direction

and fractures before transverse stretching and orientation can occur. Moreover, because almost all of the molecular segments of a uniaxial LCP film are oriented in the machine direction, any transverse strain that occurs before fracture will merely cause the uniaxial film to become thinner without imparting transverse orientation. All of this points to the need to have transverse orientation in the LCP *before* transverse stretching is applied. Figure 11.6 shows the effect of

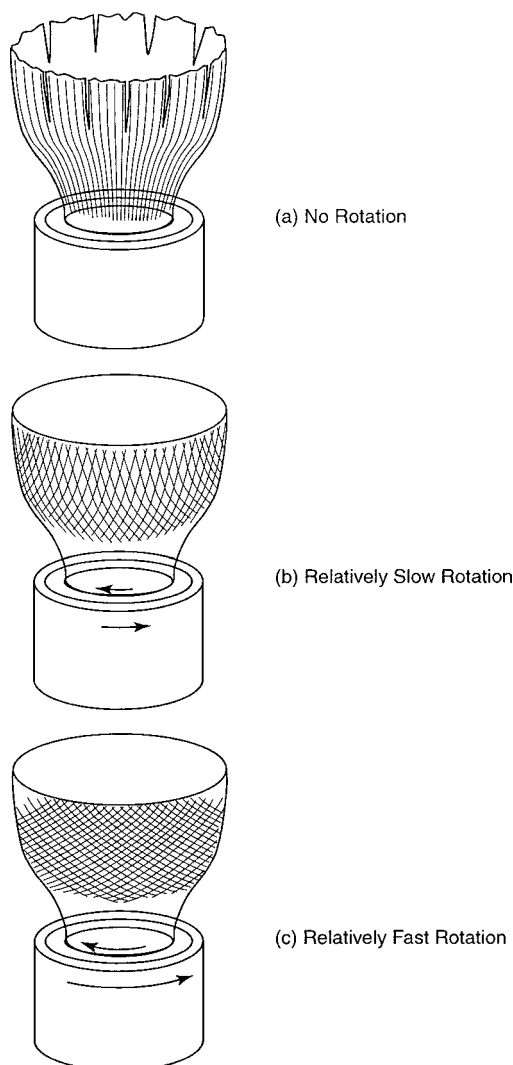


**Figure 11.6** Effect of rotation rate on orientation.

transverse stretching with various degrees of orientation imparted by a counter-rotating die. In Figure 11.6(a), the die is not rotating, no transverse orientation is imparted by the die prior to extrusion, and the film tube splits longitudinally after extrusion. In Figure 11.6(b), the die is rotating relatively slowly, so some transverse orientation is imparted, and the film has greater strength in the machine direction than in the transverse direction. In Figure 11.6(c), the die is rotating relatively quickly, and a high degree of transverse orientation is imparted so that the strength in the transverse direction is approximately equal to that in the machine direction.

### 3.2. CALCULATION OF ORIENTATION ANGLES

The transverse shear stress through the melt will be equal through the thickness and will be proportional to the applied rotation rate for a constant viscosity. Polymer melts are not “ideal” fluids (i.e., Newtonian and constant temperature), so in actual conditions, the transverse shear rate will not be constant through the thickness of the extrudate between the cylinder walls, but this is a good approximation.

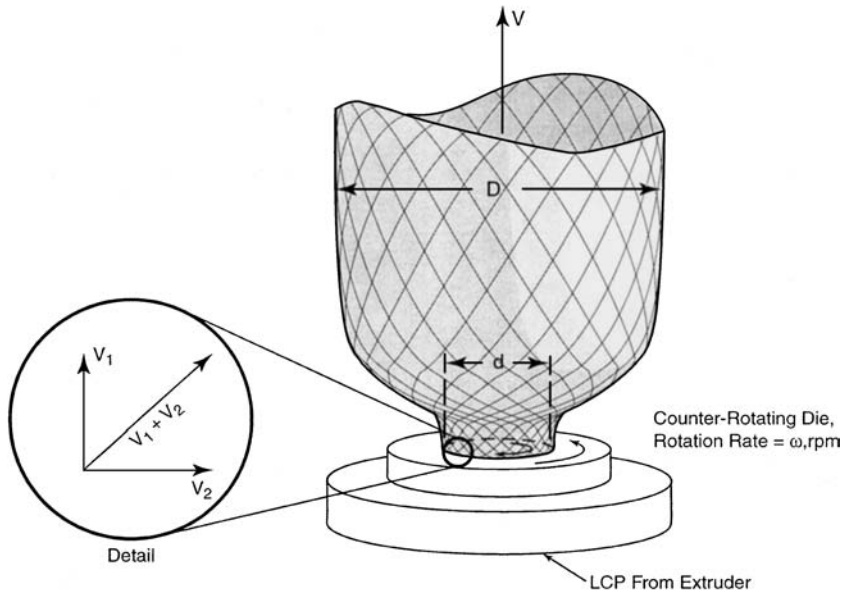
The longitudinal shear will be highest at the walls of the die and zero in the center, between the cylinder walls. For an ideal fluid, the shear stress profile would form a parabola, but under actual conditions, it is closer to “plug flow” where melt near the center moves at the same velocity, hence, with no longitudinal shear stress. Once again, as a good approximation, one can treat the LCP melt as an ideal fluid. From this, one might predict that the LCP molecules or fibrils in the die would align with the local direction of shear stress, if given enough time or total strain; but this has not been proven.

The orientation at the outer layers of the LCP film as it exits the die can be predicted fairly well as the vector sum of the transverse die lip velocity and the average longitudinal velocity of the melt, as indicated by the detail in Figure 11.7. The orientation of the film, after it goes through the elongation forces of draw in the machine direction and blow up in the transverse direction, will be the vector sum shown in Figure 11.8. For thin LCP films less than about 100  $\mu\text{m}$ , this is a good approximation of orientation direction. For thicker films, the orientation in the center of the film is complex, and this begins to have an effect on the tensile properties of the film.

The orientation angle is given by

$$\theta = \tan^{-1}(v_2 \times \text{BUR} / V)$$

where  $v_2$  is the transverse velocity at the die lip and BUR is the blow up ratio  $[(D/d) D = \text{the bubble diameter}, d = \text{the die diameter}, \text{and } V = \text{the take-up speed}]$ .



$V$  = Take Up Speed

$D$  = Bubble Diameter

$V_1$  = Axial Velocity of Melt Out of the Die

$V_2$  = Transverse Speed at the Die Lip,  $\pi d\omega$

$d$  = Die Diameter

**Figure 11.7** Extrusion parameters for counter-rotating die.

The transverse velocity at the lip,  $v_2 = pdv$ , where

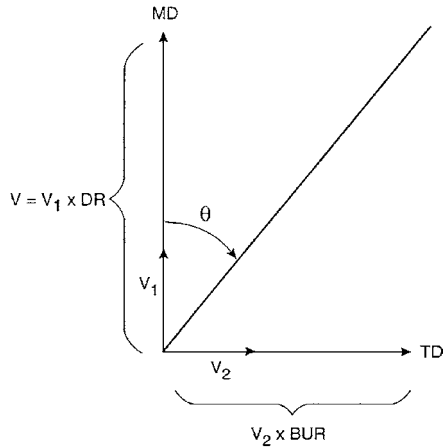
$v$  = the rotation rate of the die, rpm

Substituting in the earlier equation,

$$\theta = \tan^{-1}(pDv/V).$$

Thus, for a bubble diameter of 40 cm, rotation rate of 4 rpm, and take-up speed of 503 cm/min, the orientation angle will be  $45^\circ$ .

For a given orientation angle, a “map” of extrusion conditions can be made, as shown in Figure 11.9. From the “map,” we see that a throughput rate of 28 kg/h is required for the conditions above. The throughput is calculated



MD = Machine Direction  
 TD = Transverse Direction  
 DR = Draw Ratio,  $V/V_1$   
 BUR = Blow Up Ratio  $D/d$

$$\theta = \tan^{-1} \left( \frac{V_2 \times \text{BUR}}{V} \right)$$

**Figure 11.8** Vector diagram of orientation angle.

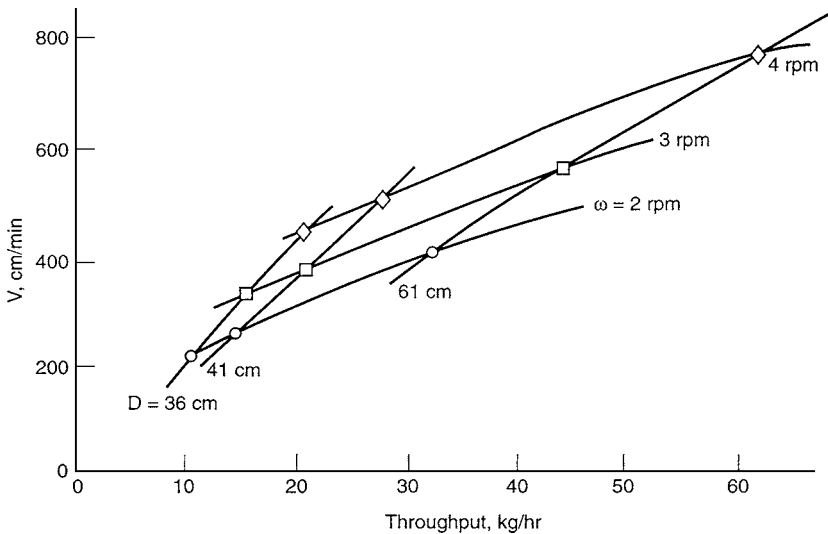


**Figure 11.9** “Process map” for  $q = 45^\circ$ , film thickness = 50  $\mu\text{m}$ .

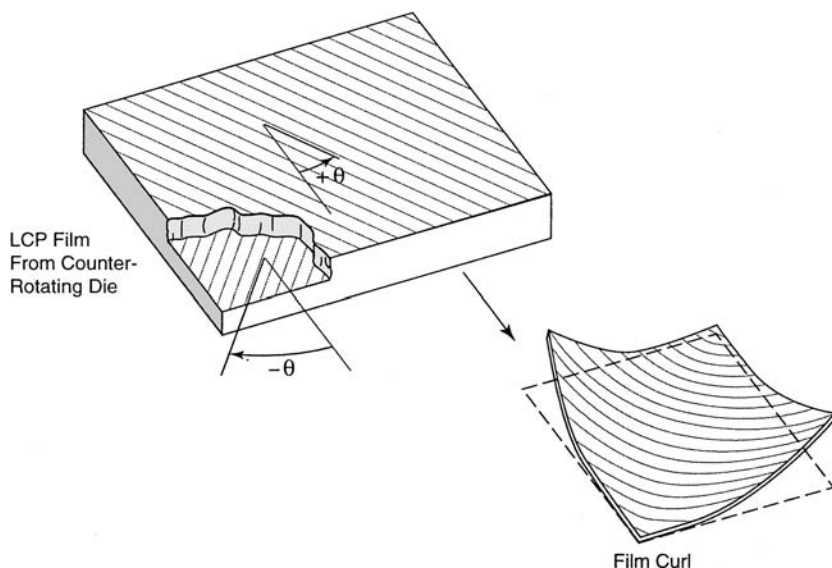


**Figure 11.10** Orientation of film made from counter-rotating die results in curl.

directly from the product of take-up speed, the cross-sectional area of the film, and the density.

LCP film produced by the counter-rotating die tends to curl because of thermally induced stresses in the upper and lower surfaces of the film during melt cooling and solidification. In Figure 11.10, the top is oriented at  $+\theta$  and the bottom at  $-\theta$  due to the action of the counter-rotating die on the melt. As the LCP film cools, the orientation persists, and the top layer will tend to shrink most in the direction perpendicular to  $+\theta$ , while the bottom will shrink most perpendicular to  $-\theta$ . The top surface will be in compression in the  $+\theta$  direction because of the shrinkage in the bottom surface in that direction. Thus, there are unbalanced residual stresses about the midplane of the film that cause curl. The curl is most pronounced when  $\theta = 45^\circ$ .

Curl due to residual stresses is well known in the production of fiber-reinforced composites where uniaxially oriented plies are laminated together to form a sheet. If two such fiber plies are laminated at a relative angle to one another, the sheet will curl just as the LCP film produced by the counter-rotating die. There is no effective way to cause the residual stresses in the LCP film to relax by heating the film, because the orientation in the LCP persists and will not relax to a random state. Near the melt temperature, the LCP film will lie flat because the stresses are balanced, but upon cooling, no matter how fast or slow, the curl will return.

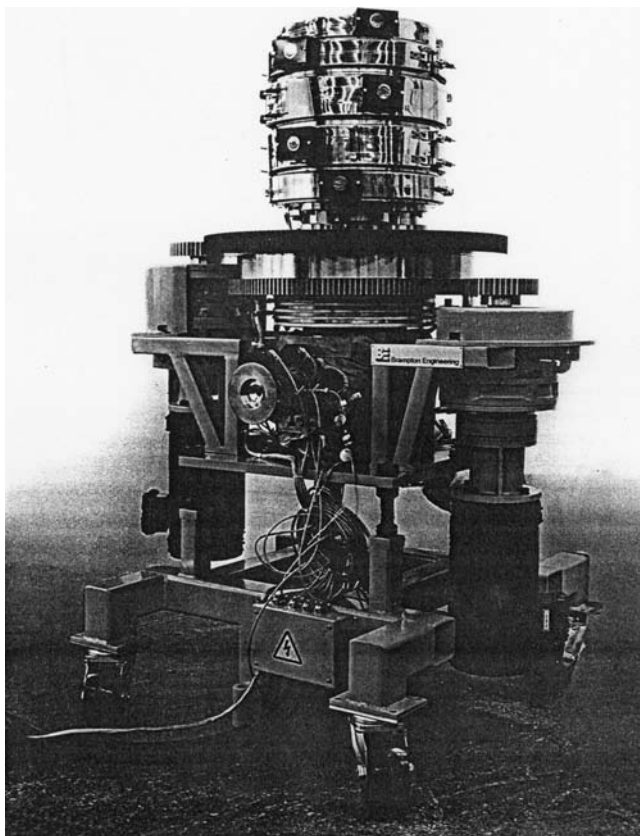


**Figure 11.11** Brampton-Superex tri-rotating die.

A new type of film extrusion die has been developed [8] and is being used by Superex and Brampton Engineering to produce flat LCP film, as shown in [Figure 11.11](#). The die uses three rotating cylinders, rather than two, and is called the tri-rotating die (TRD). The orientation produced by the TRD is symmetrical about the midplane, so that the residual stresses are completely balanced. The tendency for the top to curl is equal and opposite to curl in the bottom. Although there are oriented internal layers in the LCP film, they do not delaminate because there is sufficient bonding through the thickness of the film. The TRD produces this orientation in one single extrusion step, producing continuous lengths of film.

[Figure 11.12](#) schematically shows the orientation in TRD film: in this idealized representation, the top 25% is oriented at  $+45^\circ$ , the middle 50% at  $-45^\circ$ , and the bottom 25% is at  $+45^\circ$ . [Figure 11.13](#) shows a simplified view of the

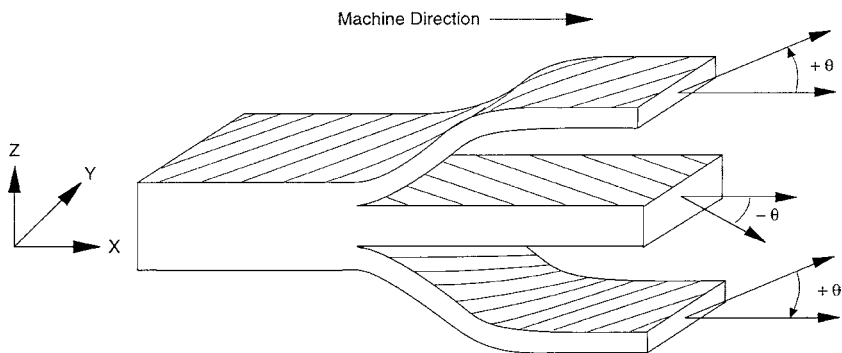


**Figure 11.12** Orientation of film made with the tri-rotating die.

TRD with two flow channels: one between the outer and middle rotors, and the other between the inner and middle rotors. The film in [Figure 11.12](#) is produced by rotating the middle rotor in the opposite direction and at the same speed as the outer and inner rotors. Referring again to [Table 11.1](#), we can see the effect of orientation angle on tensile properties in the film.

[Figure 11.14](#) shows LCP film being extruded on the tri-rotating die at Brampton Engineering.

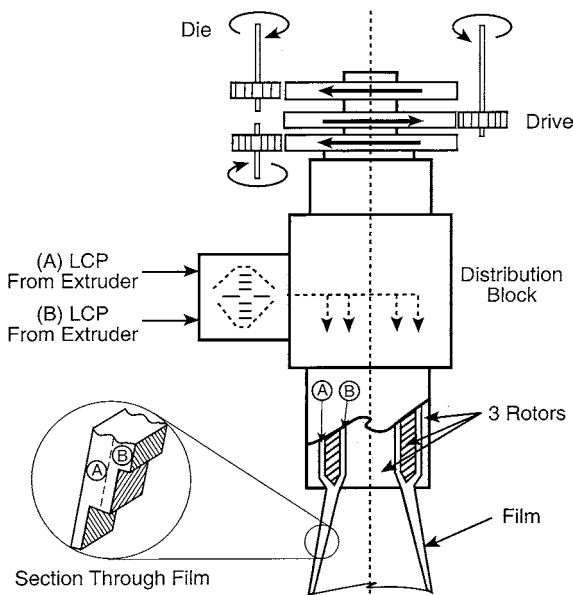


**Figure 11.13** Tri-rotating die provides two-layer coextrusion.

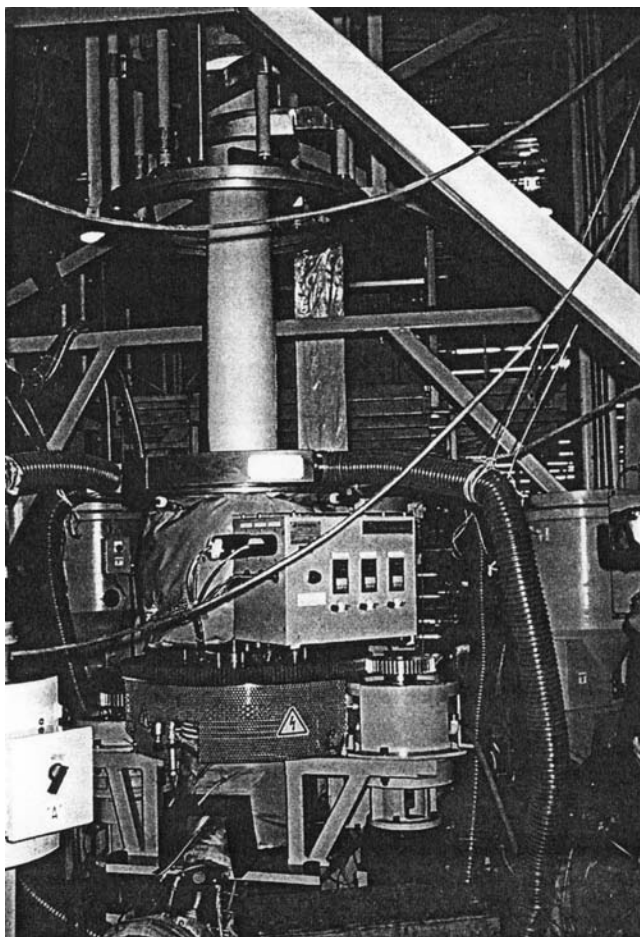


**Figure 11.14** Film extrusion on tri-rotating die for LCP film.

### 3.3. MULTILAYER COEXTRUSION

The die shown in [Figure 11.11](#) can be used to coextrude multilayer films with oriented LCP layers.

Oriented LCP layers can be coextruded with other thermoplastics, such as polyethylene terephthalate, nylon, polycarbonate, and high-density polyethylene. The primary benefit of the LCP layer is to improve the barrier properties of the container. For example, using an LCP layer comprising 5% of the wall thickness of a container along with PET and tie layer in the other 95% will increase the oxygen barrier by more than 20 times compared with a pure PET

container. A further example, below, compares the barrier properties of LCP with another barrier material, ethylene vinyl alcohol (EVOH).

Various types of multilayer dies, such as the TRD, have successfully produced coextruded LCP-thermoplastic film, sheet, and thermoformed articles. These products are expected to penetrate the high barrier plastics market valued at more than \$700 million per year for a variety of food, beverage, medical, and industrial packaging applications. Because of their very low permeability to oxygen and water vapor combined with high temperature and chemical resistance, coextruded LCP films should find applications in this market. The process for coextruded LCP thermoplastic multilayers overcomes the key problems previously limiting LCP coextrusion:

- (1) Biaxial orientation is imparted to the coextruded LCP layer, greatly improving transverse properties and eliminating splitting and thinning of the LCP layer.
- (2) Uniform and thin LCP layers are produced, resulting in cost-effective use of high-performance LCP resins. Coextruded multilayers may contain small fractions of high barrier LCP with impressive barrier properties at competitive cost compared to EVOH and PVDC multilayers.

## 4. TUBE EXTRUSION AND APPLICATIONS

This section will discuss the use of the counter-rotating die for LCP tubing with controlled orientation to maximize properties.

### 4.1. APPLICATIONS AND PROPERTIES OF LCP TUBE

Rigid tubing that overcomes the tendency of thick LCP to have uncontrolled orientation has been developed using a counter-rotating die coupled with a conventional take-up system. The tubing is made from commercially available LCPs and is being used for important new products in the health care market, automotive applications, industrial tubing, cryogenic pipe, flame retardant conduit, and structural tubing.

A significant application for LCP tubing is in minimally invasive surgery, including laparoscopic surgical instruments and other types of endoscopic surgical devices, such as cannulae, aspiration-irrigation tubes, and electrosurgical “pencils” [11,14]. LCP tubing provides the features and benefits for these applications, as shown in [Table 11.2](#).

These benefits provide favorable performance-cost tradeoffs for LCP tubing compared with other candidates, such as fiber-reinforced composite and Teflon-coated, stainless-steel tubing. In the near future, LCP tubing should find significant applications in the field of minimally invasive surgery where

TABLE 11.2. Superex Tubing Provides Benefits for Medical Applications.

Features of Superex Tube	Benefits of Superex Tube
High stiffness and strength; excellent rigidity	Large lumens, thin walls; wall thickness reduction of over 50% compared to other plastics.
Excellent electrical properties, superior high-voltage strength	High reliability, simple design with one type of material; no insulation coating needed.
High chemical and thermal durability	Broad sterilization and re-sterilization capability with eto, gamma, or autoclave.
Manufactured by a one-step extrusion process	Low cost, 30% lower than fiber reinforced composite tubing.
Orientation is controlled	Efficient use of this material, adaptability to different user requirements; one type of tube for many uses.

more than two million such procedures are performed annually in the United States.

The key to maximizing the properties of LCP tubing is the unique, controlled orientation built into the tube wall and aligned with the principal load directions for maximum mechanical properties and minimum amount of material. This efficient structure, combined with the inherent high strength and stiffness of LCP, results in tubing with five to 10 times higher stiffness than conventional plastic tubing, such as polycarbonate, PET, PVC, and polyimide. Accordingly, LCP tubing provides wall thickness reduction of more than 50%.

The flexural modulus of LCP tubing is typically 1.5 to 2.0 million psi (10 to 14 GPa), which is equivalent to higher cost glass fiber-reinforced epoxy tubes. Because LCP's tubing is made by a one-step extrusion process that is suited to high-volume production, the price of LCP tubing is 30 to 50% lower than glass fiber composite tubes. LCP tubes may provide high yield and reliability benefits over composite tubes because melt-extruded LCP tube has substantially no voids that could cause electrical breakdown. Composite tubes need to be "prepregged" then cured to solidify the epoxy polymer matrix, and these processes have been identified as causes of voids in composite tubes. Also, composite tubes cannot be steam sterilized in an autoclave because they tend to delaminate.

LCP tube replaces plastic-coated metal tubing based upon the excellent electrical insulative properties of LCP and the potential reliability and operational concerns with electrically conductive stainless-steel tubes.

Typical LCP tube properties are shown in Table 11.3. The LCP tube properties of Table 11.3 are for isotropic, biaxially oriented tube, processed as described below. Table 11.4 shows the trade names and temperature capabilities for the commercially available LCPs.

TABLE 11.3. Typical LCP Tube Properties.

	LCP Tube
Tensile strength, psi (MPa)	20,000 (138)
Tensile modulus, Msi (GPa)	1.8 (12.4)
Upper use temperature °F	over 400
Upper use temperature °C	over 200
Density gm/cc	1.4

## 4.2. PROCESSING AND PERFORMANCE OF LCP TUBING

Figure 11.15 shows how biaxial orientation can be achieved with a counter-rotating circular die for tubing, in a similar way to the film die described previously. By controlling the rotation rate of the die along with other processing parameters, this extrusion machinery can produce LCP tubing with a wide range of orientation, diameters, and thicknesses. When the rotation rate is relatively slow, the orientation angle will be small, and the tube will have higher longitudinal properties than hoop direction properties. At higher rotation rates, the orientation angle increases, and the hoop direction properties approach those in the longitudinal direction. At even higher rotation rates, the hoop direction properties will exceed longitudinal properties. Figure 11.16 shows how the crush strength and modulus of tubing are controlled by the angle of orientation. The type (a) tube has a low angle of orientation, type (b) is higher, and type (c) is the highest angle. The most efficient type of tubing can be selected for the needs of specific applications.

The counter-rotating extrusion die for LCP has been used with a conventional vacuum tank, tube puller, and cutter to make high-quality LCP tube. Tubing from 2 mm OD to 50 mm OD has been extruded with wall thickness ranging from 0.25 mm to 6 mm.

## 4.3. MEDICAL APPLICATIONS OF LCP TUBING

Figure 11.17 shows a typical endoscopic surgical instrument with an LCP tube connecting the handle actuator to the surgical device. A wide range of

TABLE 11.4. Commercial LCPs.

Trade Name	Melt Temperature	Approximate Use Temperature
Vectra® (Ticona)	277°C	250°C
Sumikasuper® (Sumitomo)	330°C	300°C
Xydar® (Amoco)	420°C	390°C
Zenite® (DuPont)	320°C	290°C

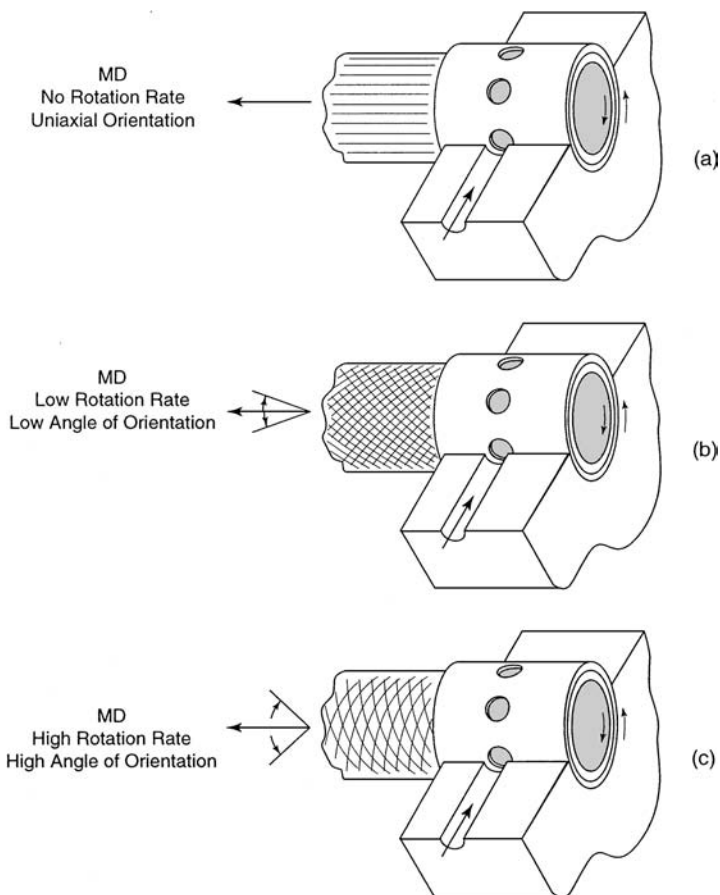


**Figure 11.15** Counter-rotating die provides orientation.

devices can be built using this type of design or related designs. Other endoscopic surgical instruments that use tubes include

- cannulae through which cameras and other instruments can be inserted
- aspiration-irrigation tubes for introducing or removing fluids during surgical procedures
- electrosurgical “pencils,” which are small diameter (approximately 5 mm) tubes with high-voltage electrodes in them for cutting and cauterizing tissue.
- sheaths from 1 mm to 2 mm diameter that enclose wires for manipulating the surgical instruments

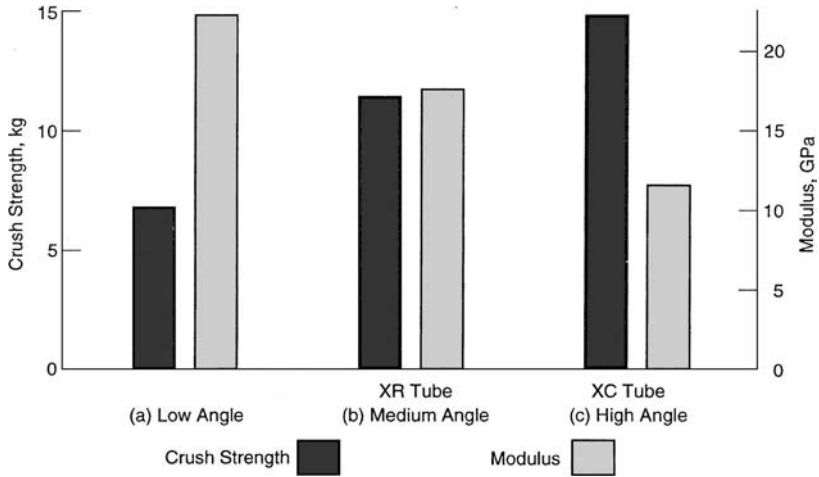


**Figure 11.16** Crush strength and modulus of Superex LCP tube (5 mm outside diameter) are controlled.

These various types of devices have their own set of requirements for rigidity, strength, electrical properties, disposability or reuseability, and cost. [Table 11.5](#) shows some of the general properties and tradeoffs for LCP tube versus the other candidates.

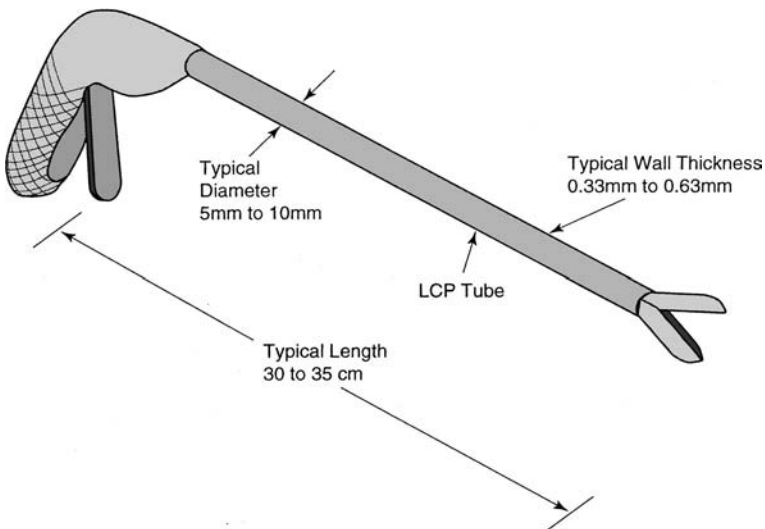


**Figure 11.17** Typical endoscopic surgical instrument with stiff, nonelectrically conducting tube.

TABLE 11.5. Superex Tube Provides the Best Combination of Properties.

Property	Superex Tube	Fiberglass-Epoxy Composite	Polycarbonate or Other Plastic	Stainless Steel
Flexural modulus	High (15 to 25 GPa)	Medium (7 to 12 GPa)	Low (2 GPa)	High
Electrical insulating properties (dielectric strength)	Excellent (1000 V/mil)	Fair (200 V/mil)	Good (400 V/mil)	Poor (conductor)
Sterilizable by autoclave	Yes	No	Possibly	Yes
Approximate price	Low \$1 to 2.50/ft	High \$3/ft	Low \$1/ft	Moderate to high \$2 to 5/ft

The flexural and tensile modulus of LCP tubing are high because the LCP material itself is high stiffness, and the process described above orients the LCP efficiently. Metal tubes are much higher modulus than LCP tubes, but because they are electrically conducting, their use in instruments for minimally invasive surgery may be limited.

The electrical insulation properties of LCP are excellent, and because the LCP is homogeneous material, it is not prone to void formation as in fiberglass epoxy composite. The electrical breakdown strength of LCP is higher than polycarbonate—a plastic that is well-known for its good electrical properties.

LCPs are processed at temperatures of 270 to 325°C and can withstand temperatures more than 200°C for long periods of time without noticeable change in properties. Also, LCPs have excellent resistance to chemicals and to ionizing radiation. Thus, tubing made from LCP can be sterilized and re-sterilized by a range of methods, including ethylene-oxide (eto), gamma radiation, and steam autoclave.

The LCP tube process is a single-step extrusion process that uses pellets of LCP compound and results in oriented tubing. By comparison, fiberglass epoxy composite requires many steps, including fiber braiding or winding, fiber impregnation (prepregging), curing, and coating. These multiple steps add cost to the processing. Metal tubing must be coated with an insulation layer, which increases material and production costs.

#### 4.4. OTHER APPLICATIONS OF LCP TUBE

Figure 11.18 shows commercial LCP tube made by Superex Polymer, Inc., from Vectra® B-130, Zenite® 6130, and Xydar® G-930 resins. Table 11.6 shows properties of the tubes.

TABLE 11.6. Superex LCP Tube Properties.

Property for Superex Tube, 5 mm (0.197 in.) OD, 3.75 mm (0.148 in.) ID	Vectra® B-130 (Some Data from Hoechst-Celanese)	Zenite® 6130 (Some Data from DuPont)	Xydar® G-930 (Some Data from Amoco)
Density, gm/cc	1.61	1.67	1.6
Water absorption, 24 hr 23°C immersion, weight percent	0.02	0.002	<0.1
Tensile strength, 10 <sup>3</sup> psi (MPa)	20 (138)	20 (138)	19 (135)
Tensile modulus, 10 <sup>6</sup> psi (GPa)	1.8 (12.4)	1.5 (10.4)	2.0 (13.9)
Flexural modulus, 10 <sup>6</sup> psi (GPa)	2.5 (17)	2.3 (16)	2.7 (18.8)
Crush strength, lb (kg)	26 (12)	26 (12)	24 (11)
Melting point, °F (°C)	536 (280)	635 (335)	788 (420)
UL flammability at thickness, in. (mm)	V-0	V-0	V-0
Dielectric strength, volt/mil (kV/mm)	0.017 (0.43)	0.016 (0.41)	0.031 (0.8)
	—	1020 (40)	—

Other applications of LCP tubing include

- lightweight conduit that is inherently flame retardant
- tubing for cryogenic fluids, corrosive chemicals, and other industrial pipe applications
- rigid tubing for automotive fluid systems
- structural tubing for sporting goods and recreational equipment

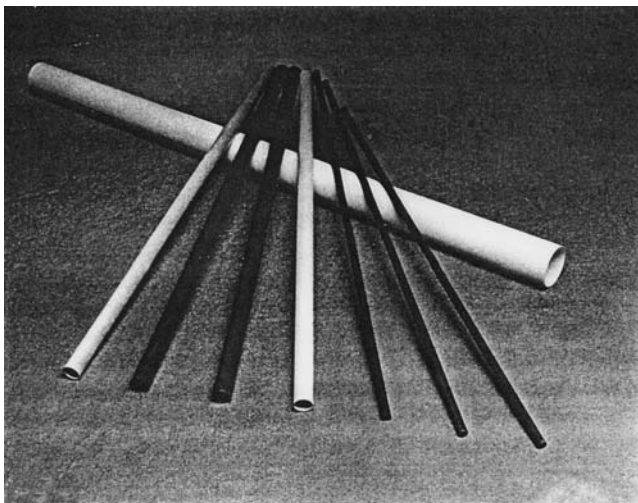


Figure 11.18 Superex LCP tube.

[www.iran-mavad.com](http://www.iran-mavad.com)

مرجع دانشجویان و مهندسين مواد

## 5. FILM EXTRUSION AND APPLICATIONS

This section will discuss the overall blown film process for LCP, together with properties and applications of various LCP films.

### 5.1. THE LCP BLOWN FILM PROCESS

Films made from LCP and LCP-thermoplastic blends have been made using the blown film process [6,10,11,15–17], combined with a counter-rotating die. This process provides for multiaxial orientation of the LCP through controlled shear forces in the die prior to extrusion from the lips. Then, after extrusion from the die, the semi-molten LCP film tube is simultaneously stretched in the longitudinal (machine) direction and the circumferential (transverse) direction. The die shear and stretching were discussed previously in [section 3](#).

The blown film take-up system for LCP film must be capable of handling stiff film so that creases and folds do not form in the film as the bubble is flattened and pulled through the pinch rollers in the blown film process, shown schematically in [Figure 11.19](#). A desiccant dryer is used to remove moisture from the LCP resin. As with any polyester, even small amounts of moisture can cause reduction in molecular weight, decreased melt strength, and other conditions that will adversely affect the quality of the film. Most LCP manufacturers recommend drying to less than 50 ppm, or dew point of  $-40^{\circ}\text{C}$  [18].

From the dryer, pellets are fed to the extruder, then to the tri-rotating die (see [section 3](#) for a complete description of this machine).

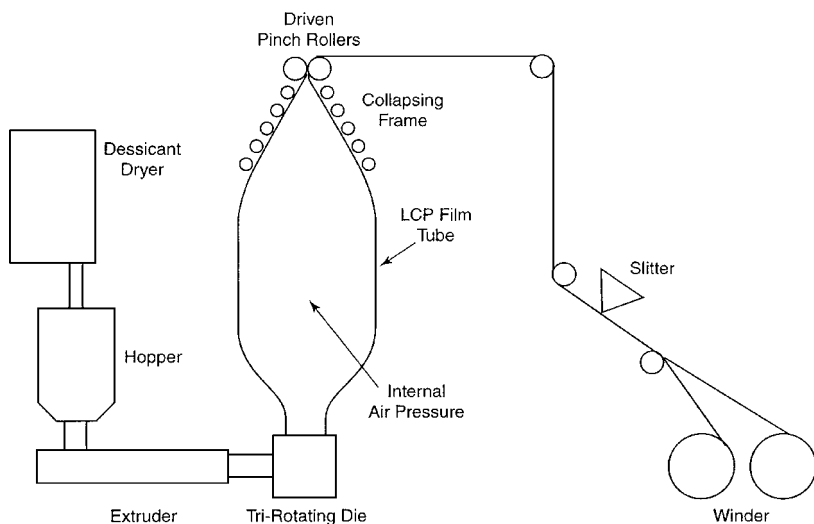


**Figure 11.19** Diagram of blown film process for LCP film.

TABLE 11.7. Properties of Thermotropic Liquid Crystal Polymer Films.

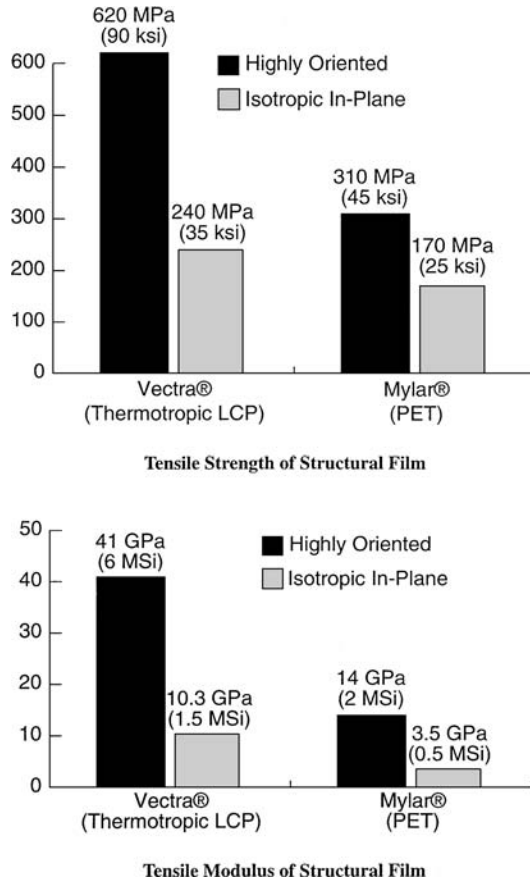
• High strength	240 MPa, isotropic 430 MPa, oriented
• High modulus	10.3 GPa, isotropic 41 GPa, oriented
• Low, tailorable CTE	0 to 5 ppm/°C
• High dielectric strength	Over 7000 V/25 $\mu\text{m}$
• Low dielectric constant	Less than 3.0
• Low oxygen permeability	Less than 0.31 cc-25 $\mu\text{m}/\text{m}^2$ -24 hr-atm
• Low water vapor permeability	Less than 0.10 gm-25 $\mu\text{m}/\text{m}^2$ -24 hr-atm
• Low thermal conductivity	Less than 0.05 W/M-°K
• High degradation temperature	Over 400°C
• Low flammability, no flame-retardant additives needed	V-0 at 0.031 in. (UL-94)

Immediately upon extrusion from the die, the film tube is expanded by internal air pressure, which is supplied by air fittings and controls in the center of the die. An air ring may be used on the die to control the cooling and stabilize the semi-molten LCP film tube. The driven pinch rollers are controlled so that the total take-up speed will produce stretching, or draw, in the machine direction.

As noted earlier in sections 2 and 3, LCPs are different from typical random coil polymers, in that the orientation that is produced in the die does not relax quickly. For this reason, the transverse stretch from internal air pressure and the longitudinal stretch from the take-up speed enhance the orientation from the die, and do so within a relatively short distance from the die lips. Typical blown film conditions would be 2 to 1 blow-up ratio, with the bubble reaching full diameter within a height equal to one to two times the die diameter. Typical LCP film thickness is 12 to 75 micrometers (0.0005 to 0.003 in.).

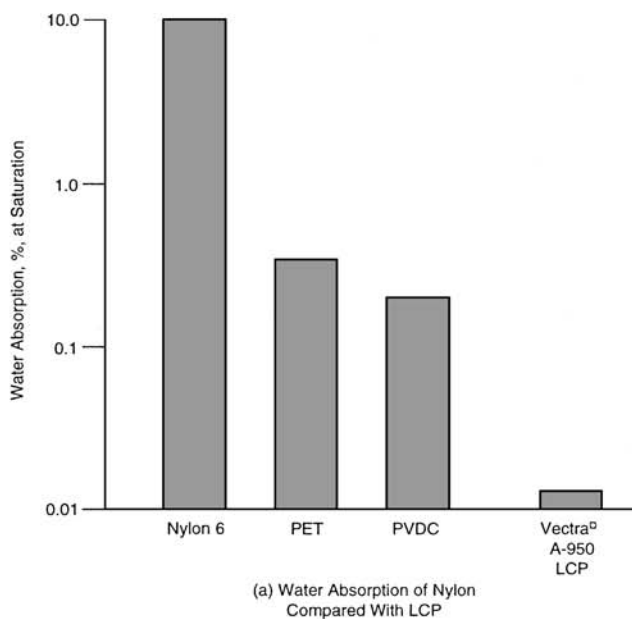
In order for an LCP to be extruded, it must have sufficient melt strength to be drawn in the zone just after extrusion from the die. To form good extruded film, the LCP should be filtered and free from gels. The melt viscosity should be above 200 Pa-sec at a shear rate of  $100 \text{ sec}^{-1}$ . Of course, the temperature of the melt must be controlled to maintain proper extrusion conditions.

Table 11.7 lists some key properties of LCP film. Tensile strength and modulus of films made from Vectra® are typically about 1.5 to two times greater than oriented polyethylene terephthalate film, as shown in Figure 11.20. The service temperature of films made from LCPs exceeds that of polyamide films by 50°C. As shown in Figure 11.21, the water absorption to LCP film is more than 100 times lower than that of polyamide, a major benefit for food and beverage packaging. The coefficient of thermal expansion (CTE) of the film can also be controlled by orienting the film, resulting in much better control of printed circuit features than is possible with other plastic films [19]. The

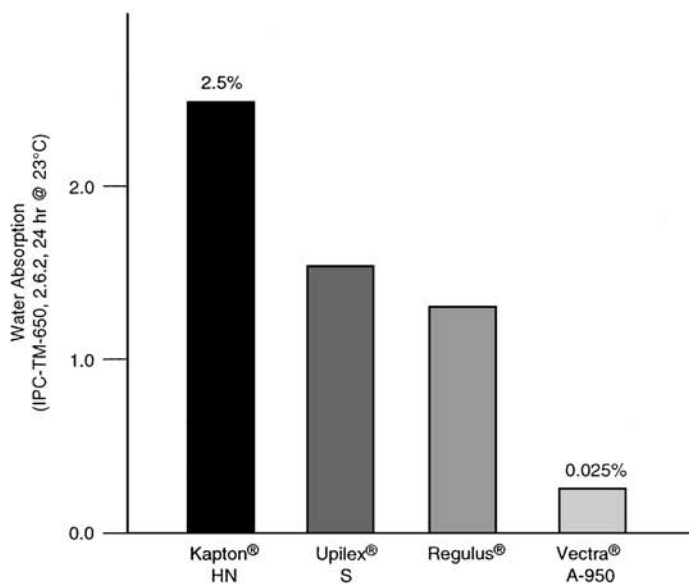


**Figure 11.20** Tensile properties of LCP film compared to PET film.

low dielectric constant, high dielectric strength, and low moisture absorption of the LCP films make them useful for electronic and electrical applications [20–23], such as circuit substrates and insulation, in addition to their current use as connectors. The permeability of LCP films is extremely low [24–26], as shown in Figure 11.22, making them ideal high barrier materials for gases and water vapor. No other polymer film has this combination, which is important for packaging food, beverages, pharmaceuticals, and specialty chemicals, for liners in fuel storage tanks, and as a barrier layer in vacuum insulation, to name a few applications. LCPs are among the most thermally stable thermoplastics, with upper use temperature of more than 250°C and excellent inherent flame retardancy. The following sections will discuss these and other applications in more detail.



**a) Water Absorption of Nylon Compared with LCP**



**b) Water Absorption of Polyimides Compared with LCP**

**Figure 11.21** LCPs are more than 100 times lower in water absorption than polyamides and polyimides.

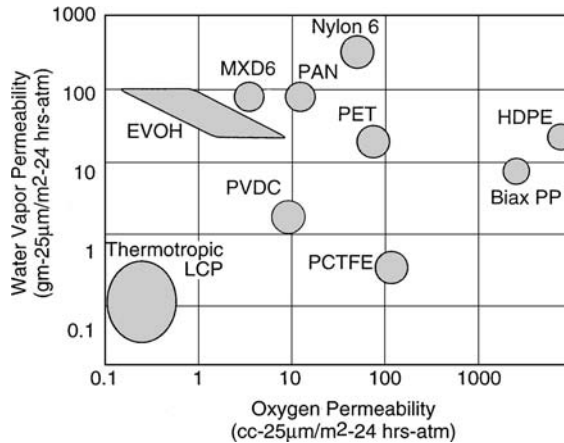


**Figure 11.22** LCPs provide outstanding barrier properties.

## 5.2. LCP FILM IN PRINTED CIRCUIT BOARDS

By processing LCP films, as described above, circuit substrates have been made with controlled CTE over the range from 3 ppm/°C to match silicon to 16 ppm/°C to match copper [27]. Because the dielectric constant of LCPs is low (2.7 to 3), and moisture has a negligible effect, LCPs can be used as thin dielectric layers less than 50 µm thick, placing the signal lines close to the ground plane at the required impedance of 50 to 70 Ω. With a dielectric this thin, the signal lines can be placed closer together at 25 to 75 µm without cross talk, resulting in more densely packed circuits. Further use of thin LCP substrates should lead to an interconnection density 100 times greater than currently possible with epoxy and polyimide-based boards, and with four to five times fewer layers than ceramic boards, which are costly to produce. There are major applications for LCP circuit substrates in multilayer boards, multichip modules, PCMCIA cards, and flexible printed circuits [28–30].

Workers at Foster-Miller, Inc., have recently constructed a board containing 10 layers—two internal plane layers, six signal layers, and two external bonding layers [22,23,28], as shown in Figure 11.23. The copper is one ounce throughout, with dielectric thicknesses in the 0.0035 in. to 0.004 in. range. For the bonding layer, two approaches were used. The first boards were fabricated with random aramid-reinforced epoxy resin, using lamination cycles developed for all aramid products. Because the aramid materials are only slightly higher in CTE than the LCP dielectrics, the overall board in-plane CTE had the desired value. The second set of boards were fabricated with an LCP bonding layer that melts at a lower temperature than the copper-clad LCP. This difference in melt

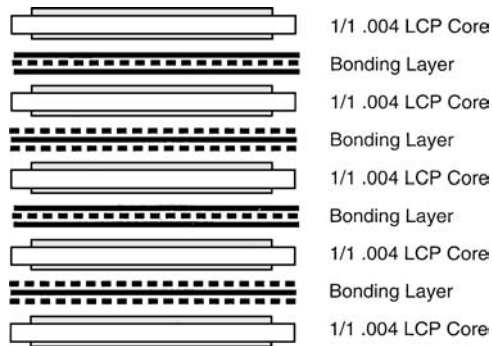


**Figure 11.23** Layup of Foster-Miller test board.

temperatures is necessary to prevent the copper clad cores from softening and distorting during the lamination cycle.

#### 5.2.1. Test Results of the LCP Circuit Board

Figure 11.24 shows one of the completed PWBs after surface mount assembly. Table 11.8 shows the fabrication steps for making the LCP film multilayer board. The board has been coated with a conventional solder mask with good

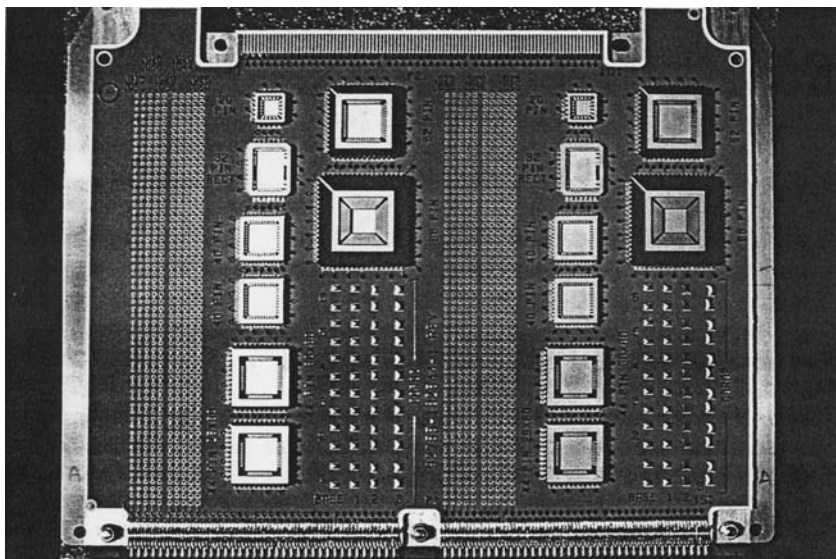


**Figure 11.24** Photo of CTE controlled surface mount PWB.

TABLE 11.8. Fabrication Steps for LCP Printed Circuit Board.

Step	Current Status
1. Produce LCP dielectric layer	1. One-step biaxially oriented film extrusion
2. Produce copper-LCP laminate	2. Vacuum press for adhesiveless copper bond
3. Etch laminate	3. Standard image and etch process
4. Multilayer fabrication	4. Lay-up with epoxy/aramid or FR-4 bonding layers, standard press cycle
5. Drilling, cleaning, plating	5. Standard processes demonstrated
6. Surface mount components	6. Standard SMT methods demonstrated

bonding of the mask to the LCP surface. A matrix of testing was performed to develop drilling parameters suitable for the material, followed by plasma and chemical hole cleaning experiments. Figure 11.25 shows a cross section of one of the 0.013 in. diameter holes after solder floating. The drilling and plating processes were optimized to provide good quality of the plated through hole with no evidence of cracks, pad lifting, or separation of plated wall. This has been of concern with unreinforced materials because their z-axis expansion is higher than some glass-reinforced materials. However, because the LCP material does not go through a significant glass transition temperature, the overall expansion from room temperature to solder temperature is still significantly lower than a typical FR-4 PWB. This type of board will also be thinner than typical reinforced resin-based boards, which also minimizes the stress effects on the plated hole barrel.

As shown in this Figure also, the layers line up with virtually no misregistration. Because of the low CTE of the LCP, the lack of shrinkage due to moisture desorption, and their high modulus compared to the bonding material used, the layers did not distort during processing, and X-ray analysis of the entire board shows that the pads line up on all parts of the panel. This is a key advantage of this material system for substrates that require much higher density, such as MCM-LS, where board real estate cannot be dedicated to large pads to accommodate inner layer registration. Combining thinner dielectrics, very small holes, and the fine lines possible with a flat, unreinforced substrate, these materials will support the merging thin board requirements.

The 10-layer board was subjected to thermal cycling from 0 to 100°C, in accordance with NASA specification NHB-5300.4. No failures in electrical continuity were observed after more than 500 cycles, indicating that the high z-direction CTE does not cause fatigue failure in the plated through holes.

One concern expressed about LCP films in multilayer circuit boards is the relatively high CTE in the thickness direction. Values of 100 to 140 ppm/°C have been reported [21,23]; however, the stiffness in the thickness direction is

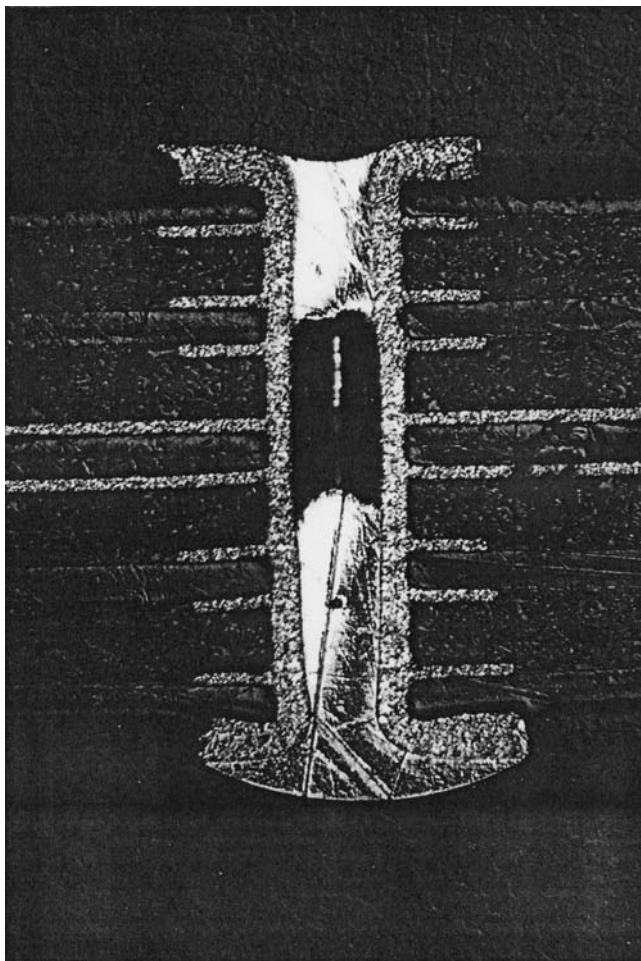


**Figure 11.25** Cross section after thermal stress (288°C solder float).

relatively low. This means that the effect on stress in the copper plating used for interconnection through the thickness (called “vias”) will be low enough to avoid fracture. The stress in the copper is based on the product of CTE times stiffness, so low stiffness means low stress. Calculations show that LCP multilayer boards will have better thermal cycle performance than equivalent boards made from polyimide film or fiberglass-epoxy [23].

LCP-copper foil laminates and circuit boards made from these laminates offer high performance at moderate price, as shown in Figure 11.26. On a price per volume basis, LCPs are less expensive than polyimides and fluoropolymers;

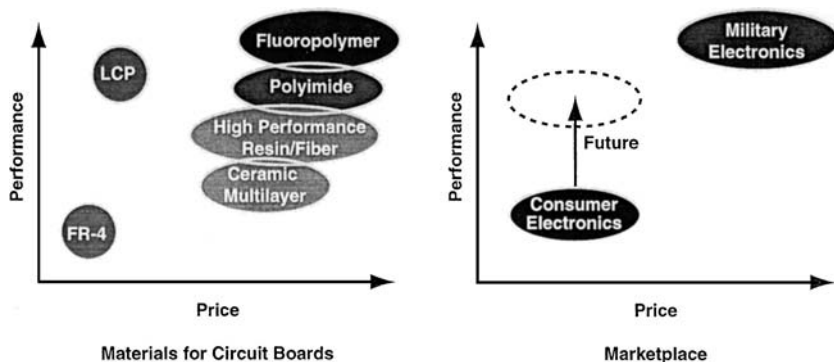


**Figure 11.26** LCP-based circuit boards can meet future performance and price for consumer electronics.

therefore, the resulting films and laminates will be less expensive. The electrical properties of LCP are better than polyimide, as shown in [Figure 11.27](#) and [Tables 11.9](#) and [11.10](#), and actually rival those of fluoropolymers having very low dielectric constant and loss factor at GHz frequencies. The strength, stiffness, and dimensional stability of LCP laminates are superior to fluoropolymers. Therefore, LCP should compete well with polyimide film for flexible printed circuit board applications and with fluoropolymers for high-frequency digital and microwave circuit boards. LCP laminates are currently finding application in multichip modules (MCMs), such as the one shown in [Figure 11.28](#). In relatively new developments, LCP laminates are being used for very small chip packaging (see [Figure 11.29](#)) and are expected to be used in place of polyimide film and thin fiberglass-epoxy for chip scale packaging.

- CTE of PWBs Tailorable
- Low Weight because Thinner Dielectrics Can Provide Same Performance
- No Solvents, Virtually No Moisture Absorption
- Processible With Standard Equipment
- Excellent Electrical Properties for Next Generation Designs
  - Low Dielectric Constant
  - Low Loss

**Figure 11.27** Liquid crystal polymers meet requirements for low cost, reliable packages.

TABLE 11.9. Comparison of Electrical Properties LCP and Polyimide Film.

Flexible Film 0.002 in. Thick	Dielectric Constant @ 1 MHz ASTM D-150	Dielectric Constant @ 1 GHz ASTM D-2520, B	Loss Tangent @ 1MHz ASTM D-150	Loss Tangent @ 1 GHz ASTM D-2520, B	Permeability to Moisture (Mocon)	Melt Temperature
LCP, Vectra® A-950	2.7	3.0 to 3.5	0.006	0.002	0.006 gm-mil/100 in. <sup>2</sup> –24 hr-atm	280°C
LCP, Xydar® SRT 900	2.9	3.5	0.011	0.004	0.013	350°C
LCP, Zenite® HX 600	3.0	3.1	0.014	0.005	0.016	345°C
Polyimide, Kapton®	3.2	a	0.002	a	2.25	N/A
Polyimide, Upilex®	3.1	a	0.002	a	0.040	N/A
Polyimide, Aurum® Regulus®	3.2	3.2 <sup>b</sup>	0.002	0.004 <sup>b</sup>	4.91	400°C

<sup>a</sup>Data not available.<sup>b</sup>From manufacturer's data.[www.iran-mavad.com](http://www.iran-mavad.com)

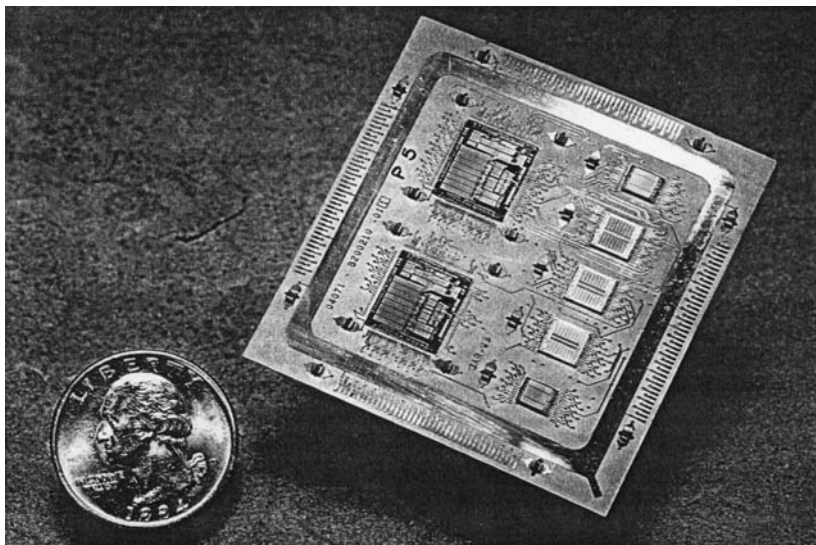
مرجع دانشجویان و مهندسين مواد

TABLE 11.10. Comparison of Other Properties of LCP and Polyimide Film.

Flexible Film 0.002 in. Thick	Bare Film Price	Moisture Absorption IPC Test Method 2.6.2	Copper Adhesion	Coefficient of Thermal Expansion, In-Plane
LCP, Vectra® A-950	\$0.50 to \$0.80/ft <sup>2</sup>	0.075%	4 to 6 lb/in. no additional adhesive	Less than 5 ppm/°C
LCP, Xydar® SRT 900	\$0.50 to \$0.80/ft <sup>2</sup>	0.069%	4 to 6 lb/in. no additional adhesive	Less than 5 ppm/°C
LCP, Zenite® HX 600	\$0.50 to \$0.80/ft <sup>2</sup>	0.014%	4 to 6 lb/in. no additional adhesive	Less than 5 ppm/°C
Polyimide, Kapton® HN	\$0.93/ft <sup>2a</sup>	2.50%	8 to 10 lb/in. with adhesive <sup>a</sup>	More than 17 ppm/°C <sup>a</sup>
Polyimide, Upilex® S	\$1.37/ft <sup>2a</sup>	1.46%	Adhesive needed <sup>b</sup>	12 ppm/°C <sup>a</sup>
Polyimide, Aurum® Regulus®	\$1.08/ft <sup>2a</sup>	1.26%	<sup>b</sup>	30 ppm/°C (estimate)

<sup>a</sup>Manufacturer's data.<sup>b</sup>Data not available.[www.iran-mavad.com](http://www.iran-mavad.com)

مرجع دانشجویان و مهندسين مواد



**Figure 11.28** MCM-L built by Foster-Miller and Teledyne.

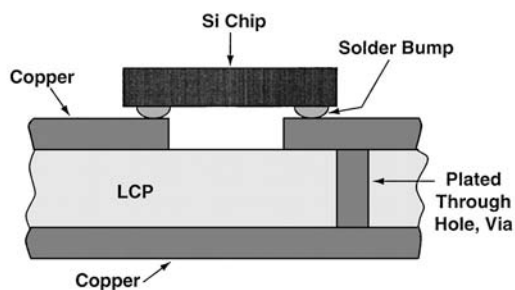
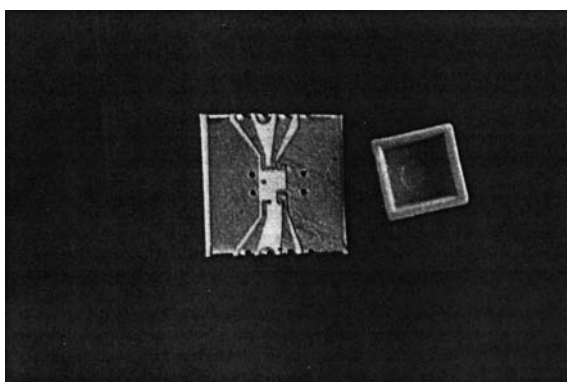


**Figure 11.29** “Flip chip” mounting on LCP film—copper circuit.

### 5.3. LCP FILM IN HIGH BARRIER PACKAGING APPLICATIONS

LCPs are highly effective barrier materials, as noted previously in [section 3.3](#). When used with less costly plastics, LCP barrier layers provide cost-effective multilayer films, trays, and containers with high barrier performance.

Demands on barrier packaging are exceeding the capabilities of today's materials, particularly where both high performance and low cost are needed, such as retortable containers and pouches, moisture-resistant medical packaging, and high temperate, chemically resistant containers [31]. Liquid crystal polymers (LCPs) are new to the packaging market and are currently being developed into applications that meet tomorrow's packaging needs. Based on initial results, LCPs should play an increasingly important role in packaging as super barrier materials with oxygen transmission on a par with dry EVOH and water vapor barrier better than many fluoropolymers. The key to using LCP in packaging is processing that makes efficient use of barrier properties. Thin, multiaxially oriented layers of LCP can be combined with structural layers of relatively inexpensive plastic. [Figure 11.30](#) shows the barrier properties of films made by Superex Polymer, Inc., from commercial LCPs.

Commercial use of LCP in packaging will have a significant effect on prices for LCP because the volume demand will be much larger than current injection-molded LCP applications, and economics of scale can bring the price down.

Applications targeted for LCP include

- multilayer films for all plastic retort pouches and bag-in-box with long shelf life (see [Figure 11.31](#))

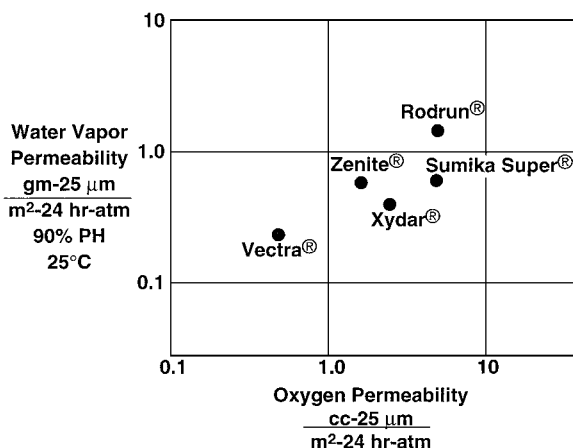
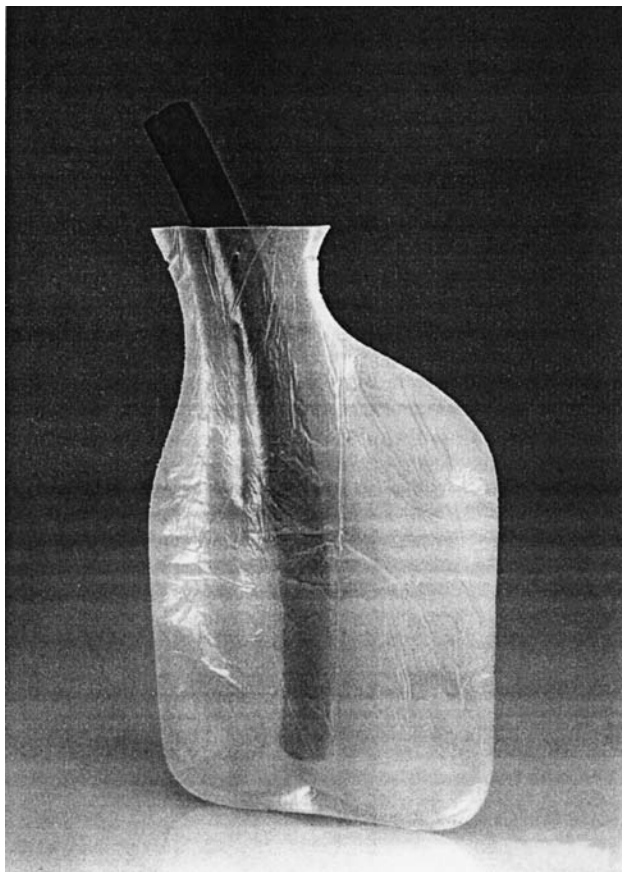
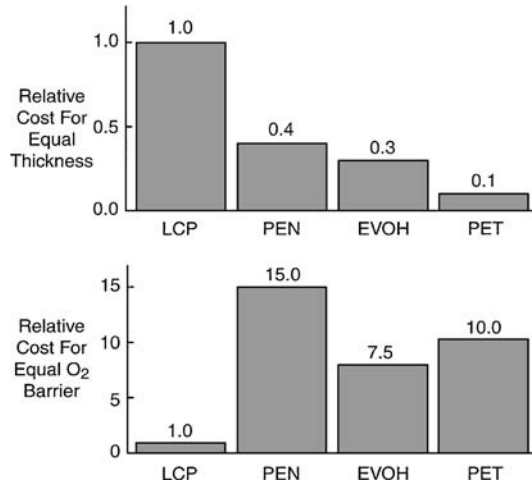


Figure 11.30 Barrier properties of films made from LCP.



**Figure 11.31** Superex PE-LCP multilayer pouch (3 mil PE, 0.5 mil LCP).

- multilayer bottles and jars with improved oxygen and flavor barrier over PET and other barrier layers
- multilayer food trays with one year shelf life and lower cost than EVOH
- multilayer LCP-HDPE automotive fuel tanks with lower cost than EVOH designs
- LCP barrier layers for disposable medical bags to replace PVDC
- LCP laminates for use in high barrier bags for industrial chemicals
- LCP-based all-plastic lids for snack food cups and trays to replace metal lids that have sharp edges
- LCP laminates for protective gloves and clothing for use against corrosive chemicals



**Figure 11.32** LCP cost comparison.

In order to tap the commercial applications of LCP in packaging, processing must achieve efficient use of the high-performance polymer. There are many high value polymers and other materials that are used in thin layers. A prime example is ethylene vinyl alcohol (EVOH), a “super barrier” material used as a thin layer in coextruded film and multilayer containers such as ketchup bottles. Other examples are coatings, such as metal, glass, and polymeric coatings. LCP used in thin multilayer constructions should compete well with these other materials.

As an example of performance-cost tradeoffs, the high barrier properties of LCP outweigh the price differential for certain types of packaging, as shown graphically in Figure 11.32. Based on the cost per barrier, LCP is actually the lowest price material. The oxygen barrier of LCP is six to eight times higher than EVOH at relative humidity of more than 85%, but the price of LCP is three to four times higher. This results in a net materials cost savings of 33 to 50% for use of the LCP. The key to achieving the savings is making the LCP layer very thin, about 6  $\mu\text{m}$ , which is where film-processing technology is very important, as discussed earlier.

Special extrusion dies have been built to coextrude and orient LCP with other thermoplastics. Recently, three-layer structures have been coextruded with such a die, resulting in PET-tie layer-LCP structures with a total thickness of 25 to 50  $\mu\text{m}$  and 10 to 30% LCP thickness [32]. These films have excellent oxygen and water vapor barrier properties as expected from the properties of LCP. Also, because only a thin layer of LCP is used, this multilayer film has very good performance-cost figures. In the future, it will be possible to coextrude

TABLE 11.11. Properties of Coextruded PET-LCP Film.

Total thickness	0.05 mm
Structure	3 layer, PET-tie-LCP
Tensile strength	MD: 90 MPa, TD: 55 MPa
Oxygen permeability	1.1 cc/m <sup>2</sup> -24 hr-atm (24 hr exposure to water, no change from dry)
Water vapor permeability	0.54 gm/m <sup>2</sup> -24 hr-atm at 90% RH, 25°C
Optical transparency	Hazy

LCP layers with other thermoplastics to make high-performance, cost-effective films.

Figure 11.33 shows a schematic representation of coextruded LCP-tie-PET film. The properties of the film are listed in Table 11.11.

LCPs are finding applications in an increasingly wide variety of products. As pointed out earlier, the price of LCP is currently high, about \$22 per kg, but the barrier performance is also very high, meaning that thinner layers of LCP provide equivalent performance to thick layers of other barrier materials. Importantly, this means LCP can be used with cost advantages in high-volume commercial uses, such as food packaging, where LCP can be used as a thin high barrier layer to prevent oxygen from deteriorating the taste of precooked and packaged food. LCP is about three times more expensive than an equal thickness of EVOH. However, to provide an equivalent oxygen barrier to EVOH at 80% RH, the raw material cost of LCP will be about three times less. To achieve these cost benefits, thin LCP layers had to be created.

Because the barrier properties of the LCP are so good, a little bit goes a long way, meaning that a layer of LCP less than 1/4 the thickness of PVDC

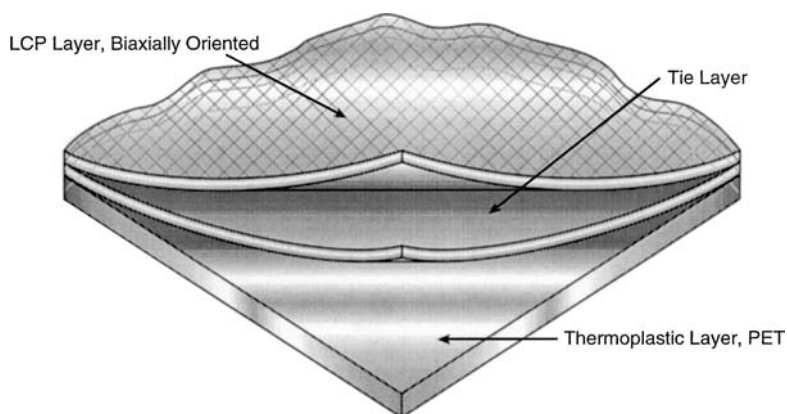


Figure 11.33 Schematic representation of coextruded LCP-thermoplastic multilayer.

TABLE 11.12. Cost Comparison of Materials in Polypropylene Barrier Multilayers at Equal Barrier.

Barrier Polymer	O <sub>2</sub> Permeability of Barrier (cc-mil/100 in. <sup>2</sup> ) at 80% RH	Volume of Barrier (in. <sup>3</sup> /1000 in. <sup>2</sup> )	Cost (\$/1000 in. <sup>2</sup> )
LCP-PP	0.02	0.2	0.07
EVOH-PP	0.09	0.9	0.09
PVDC-PP	0.16	1.6	0.11

or EVOH can do a better job, providing economic and performance benefits in shelf-stable, retortable food packaging. Cost savings of 30% are possible even at today's high prices for LCP, and as the price drops because of increased volume, supplier competition, and lower cost monomers, even more applications and uses of LCP will emerge. Table 11.12 compares material costs for three types of multilayer barriers of equal performance.

LCPs can be used in thin layers or at low concentrations in blends to make cost-effective high barrier films and containers. LCP barriers have advantages over aluminized plastics and metal foil because the LCP layers can be thermoformed, they are microwavable, recycling is easier, and metal detection systems can be used to inspect packaged foods.

Using biaxial film processing, LCPs can be made into thin liners for compressed and liquefied natural gas tanks, replacing thick and heavy high-density polyethylene (HDPE) liners or costly aluminum liners. An LCP liner only 0.051-mm thick provides 10 times more barrier than an HDPE liner 9 to 13 mm thick, and does so at 1% of the weight and with a 30% savings in material costs compared to the HDPE liner. Packaging manufacturers are actively engaged in development of thin LCP liners, including blow molding and thermoforming to make the liner and filament winding to make the composite structure.

High barrier film users are currently looking for alternatives to polyvinylidene chloride as a barrier layer because of problems cited in melt recycling or burning PVDC. LCP laminates and coextruded films are being evaluated because evidence suggests they can be burned as easily as PET, and their high barrier properties mean that LCP layers will be four to five times thinner than PVDC for equivalent barrier performance.

Although ethylene vinyl alcohol (EVOH) is a very good oxygen barrier when dry, it has poor resistance and barrier to water vapor, and does not retain much strength at high temperatures used for food sterilization. For these reasons, manufacturers of packaged foods are looking into multilayer LCP film, sheet and tubes for pouches and trays and lids used in packaging, particularly for retorted pouch applications.

LCP coatings are being developed for tube, cable, and fiber barrier layers, where the LCP layer provides improved performance to more permeating

materials and over a wider range of conditions than alternative coatings. With regard to plastic water pipe, a thin LCP coating can replace thicker EVOH coatings, preventing water vapor from leaving the pipe and oxygen from entering it. LCP coatings are being applied to electric cables to increase the barrier to water vapor, which causes premature electrical failure of the insulation. LCP coatings for optical fibers provide a combination of barrier to water vapor and increased tensile properties.

## 6. BLOW MOLDING LCPs AND APPLICATIONS

LCPs have recently been blow molded into containers by extrusion blow molding, and they have been used in multilayer containers made by coextrusion blow molding [33,34]. As in high barrier multilayer films, the LCP provides a thin high barrier layer, and a less costly plastic, such as PET, is used to provide strength and stiffness.

High barrier plastic containers are currently made from multiple layers of a relatively thick economical polymer such as polyethylene terephthalate (PET) or polyethylene, combined with a thin layer of a barrier polymer such as ethylene vinyl alcohol (EVOH). In a similar way, multilayer barrier containers can be made with a thin layer of liquid crystal polymer (LCP), as an excellent barrier to oxygen, water vapor, and other gases.

The motivation for using LCP as the barrier layer stems largely from the fact that LCP is impermeable to both oxygen and water vapor, not like EVOH, which has poor water vapor barrier properties. This results in a simpler three-layer structure for an LCP barrier container, or opposed to a five (or more) layer structure with EVOH. Thus, although LCP is currently more expensive than EVOH, less volume of material is needed, fewer layers are needed, and manufacturing costs can be reduced, resulting in an overall savings per container.

Oriented LCP layers can be coextruded with other thermoplastics such as polyethylene terephthalate, nylon, polycarbonate, and high-density polyethylene. The primary benefit of the LCP layer is to improve the barrier properties of the container, especially under conditions of high heat and humidity, such as retorted bottles and trays. For example, using an LCP layer comprising 5% of the wall thickness of a container along with PET and tie layer in the other 95% will increase the oxygen barrier by more than 20 times compared with a pure PET container. A further example, below, compares the barrier properties of LCP with another barrier material, EVOH.

Once the coextruded LCP-thermoplastic multilayer parison is formed, it can be blow molded into bottles and other containers. The orientation in the LCP layer is controlled by the counter-rotating action of the cylinders in the die, and the LCP orientation remains in the finished bottle because of the very long relaxation time of LCP. While other polymers being coextruded with LCP may

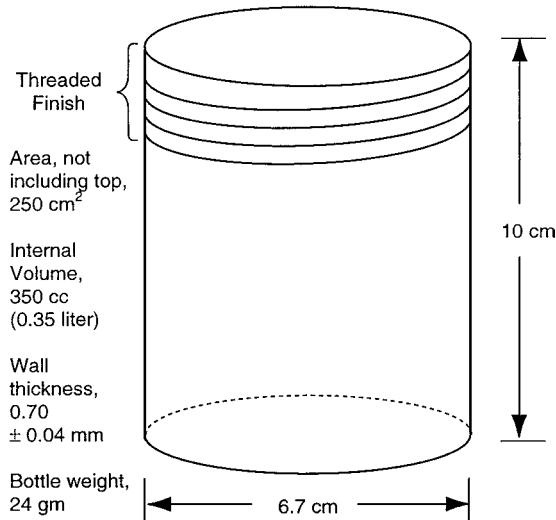


**Figure 11.34** Superex test container.

be partially oriented by shear flow, such orientation will typically relax before the polymer is cool.

A multilayer container (see [Figure 11.34](#)) was made using Eastman 13339 PET, Vectra<sup>®</sup> A950 (Ticona) LCP, and a proprietary Superex adhesive tie layer. [Figure 11.35](#) shows the blow molding system schematically, with three extruders feeding a special multilayer rotating coextrusion die attached to a single-cavity, continuous blow molding machine. The average LCP layer thickness was approximately 0.09 mm, or about 13% of the total wall thickness.

The barrier properties of the container were measured, as shown in [Table 11.13](#). The oxygen barrier improvement is in good agreement with the calculated result. Because the oxygen permeability of LCP is approximately 200 times lower than PET and LCP comprises 13% of the total thickness, the LCP-PET container should be 15 times better in barrier than the PET container of the same dimensions. The result for water vapor permeability shows a higher barrier improvement than calculated. The water vapor permeability of LCP is approximately 400 times lower than PET, so the multilayer LCP-PET container should be 30 times better in barrier than PET. The discrepancies in calculated versus observed barrier improvements could be due to variation in the LCP layer thickness, or in the measurement of the permeability of pure LCP and PET. In any event, the barrier improvement of the LCP-PET multilayer container versus the same dimension PET container is quite good and shows that thin layers of high barrier LCP can be used cost effectively in plastic packaging.

TABLE 11.13. Permeability Test Results for Superex Bottle  
(0.35 Liter, 0.7 mm Thick).

	LCP-PET Multilayer Bottle 13% LCP	100 PET Bottle	Barrier Improvement
Oxygen permeability (cc/24 hr) 25°C, 100% RH	0.022	0.24	11X
Water vapor permeability (gm/24 hr) 38°C, 90% RH	0.0014	0.080	57X

The hot fill shrinkage of the LCP-PET container was measured and compared with the pure PET container. Two multilayer containers and two monolayer PET containers were hot filled with water at 85°C, then allowed to cool. The volumetric change from before filling compared with after cooling is the shrinkage. The average shrinkage for the PET container was 2.2%, while the average shrinkage for the LCP-PET container was only 0.34%. The improvement in shrinkage of the LCP-PET multilayer containers is likely due to the relatively high stiffness and low thermal expansion of the LCP layer.

The containers were also tested for absorption and permeation of *d*-limonene, a stimulant for flavor. The results showed that the LCP-PET multilayer container retained more than five times the amount of *d*-limonene as the PET container. Furthermore, tests on LCP and PET film show that the absorption of *d*-limonene

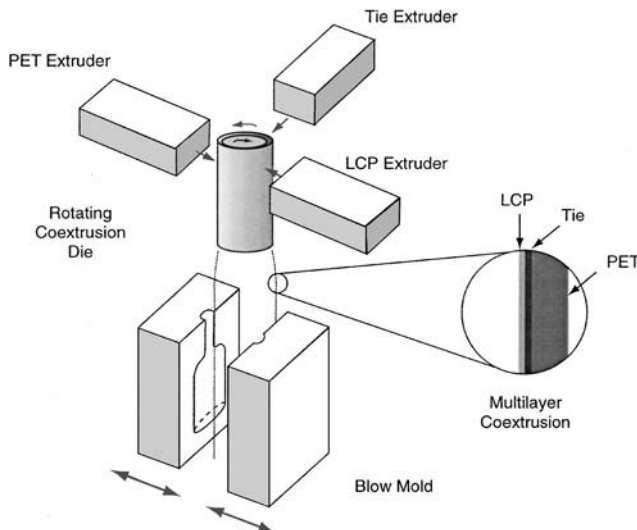


Figure 11.35 Schematic diagram of multilayer blow molding.



**Figure 11.36** Multilayer LCP tray and bottle.

is approximately 50 times lower for LCP than for PET. Together, these results suggest that the LCP-PET container should be very good for low flavor scalping and should also resist loss of fragrances.

The multilayer coextrusion blow molding technology can be used for a wide variety of containers made from LCP and other thermoplastics. [Figure 11.36](#) shows a multilayer bottle and tray made from LCP and PET by coextrusion blow molding. [Figure 11.37](#) shows high barrier bottles made with LCP and PET.

Although not yet developed to a commercial stage, LCP multilayer containers should provide performance and cost benefits for certain high barrier applications.



**Figure 11.37** Superex LCP-PET high barrier bottles.

## **7. LCP—THERMOPLASTIC BLENDS AND ALLOYS, PROCESSING, AND APPLICATIONS**

LCP blends and alloys are mixtures of thermoplastic resins and LCP [35]. In general, an alloy involves addition of “compatibilizers” and results in better chemical interaction between the two heterogeneous phases of LCP and thermoplastic [36–43].

The goal of LCP-thermoplastic blends and alloys, also referred to as “molecular composites” [37], is to achieve a disproportionately large increase in performance compared to the attendant increase in cost. Performance can mean

- improved processibility and reduced viscosity of high temperature thermoplastics, for example
- higher strength and stiffness, with the LCP acting as a reinforcing material
- improved gas barrier properties, owing to the excellent low permeability of LCP
- increased upper use temperature
- lower coefficient of thermal expansion

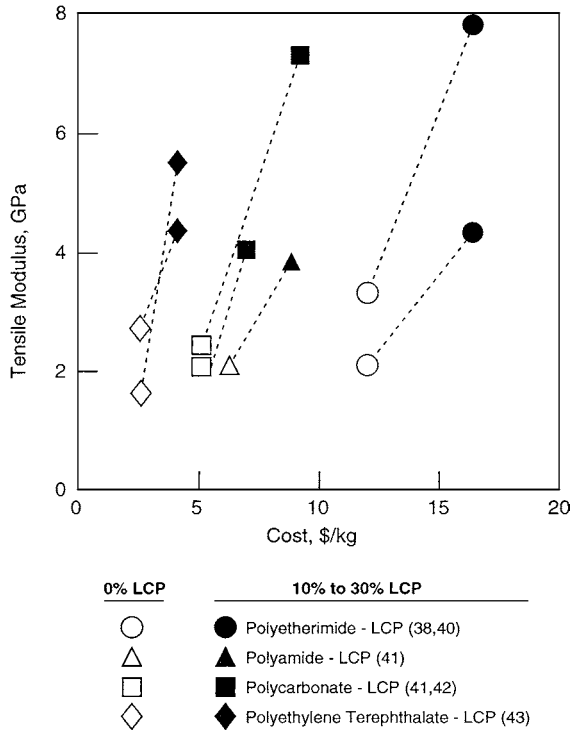


**Figure 11.38** Cost-effective LCP blends increase modulus [27].

## 7.1. TENSILE PROPERTIES OF LCP BLENDS

Over the past 15 years, many workers have reported on LCP blends and alloys with limited success at meeting the goal of improved performance-to-cost ratio. Figure 11.38 shows the tensile modulus of a number of LCP blends as a function of material cost [27]. Baird et al. [38] report that at LCP concentrations of greater than 40% and less than 90% in the polyetherimide Ultem<sup>®</sup>, the tensile modulus of the blend is actually higher than the pure LCP. This synergistic effect was noted for one particular type of blend and is attributed to partial miscibility and final blend morphology.

Table 11.14 presents the data of Figure 11.38 in terms of relative cost and weight savings for structures designed for equivalent stiffness. Of course, this is a simplification because designs must include other factors, such as strength and toughness. However, for structures such as thin shells and slender columns that are designed based on stiffness, the analysis of Table 11.14 points to significant cost and weight savings for the LCP blends.

TABLE 11.14. Cost and Weight Savings of LCP Blends.

Base Resin	With LCP Reinforcement			
	Modulus Increase	Apparent Cost Increase	Performance Cost Savings (%)	Weight Savings (%)
PET	2.2	1.6	30	65
PA	2.3	1.4	37	50
PC	3.0	1.8	42	72
PEI	2.1	1.4	33	50

## 7.2. PROCESSING LCP BLENDS AND ALLOYS

The anisotropy of LCP blends and alloys is less pronounced than pure LCP, as expected. At LCP concentrations of about 10 to 15%, conventional processing machinery can produce extruded and injection-molded parts that are nearly isotropic. At higher LCP concentrations, more than 40% LCP, some means are necessary (such as the counter-rotating die) to orient the extruded film, sheet, or tube to control anisotropy. One group has succeeded in processing a polyethylene/LCP blend through a counter-rotating die [17], and another group has focused on polyimide/LCP blends processed with a counter-rotating die [36,44].

Processing will have a direct effect on the morphology of the heterogeneous LCP-thermoplastic blend or alloy. When the LCP is in the minor phase, at concentrations below 40% by volume, it will exist as spherical particles, elongated fibrils, or planar regions depending on the type of blend and the process. Generally, higher mixing will produce smaller particles, and elongational strain will produce fibrils. When the LCP is in the major phase, more than 50% by volume, the LCP blend will behave much as the pure LCP.

The effects of processing conditions, melt temperatures of the components, viscosity, and chemical interaction with and without compatibilizer are complex and beyond the scope of this chapter. Processing and use of LCP blends will continue to be an active area of research and product development.

## 8. CONCLUSIONS

LCPs are now being extruded into films, tubes, and blow molded products, in addition to their use in injection-molded parts. These new applications should significantly increase the current market volume from 7000 to 10,000 tons per year to more than 50,000 tons per year. As LCP volume increases, LCP prices should fall. Also, new synthesis methods and the availability of low-priced intermediate chemicals should reduce prices [45,46].

Before they will find widespread applications in extruded products, more development is needed in the following areas for LCPs:

- (1) Extrusion-grade LCPs need to be formulated with higher melt strength and purity than the current injection-molding grades.
- (2) LCPs with lower melt temperature, in the range of 180 to 220°C, and having excellent barrier properties need to be developed.
- (3) More development is needed on the LCP coextrusion process.
- (4) Optically transparent LCP should be developed.
- (5) FDA approval of LCP for food contact should be obtained.
- (6) The toughness of LCP should be improved, as measured by elongation at break.

Other performance improvements will be needed as LCPs find applications in extruded products, such as the current LCP tubes for surgical instruments and LCP films for laminates used in printed circuit boards.

## 9. REFERENCES

1. T. S. Chung, G. W. Calundann, and A. J. East, Liquid crystal polymers and their applications, published in *Handbook of Polymer Science and Technology*, vol. 2, edited by N. P. Cheremisinoff, pp. 625–675, Marcel Dekker, New York (1989).
2. A. Ciferri, W. R. Krigbaum, and R. B. Meyer, *Polymer Liquid Crystals*, Academic Press, San Diego (1982).
3. L. L. Chapoy, *Recent Advances in Liquid Crystal Polymers*, Elsevier, New York (1985).
4. A. M. Donald, and A. H. Windle, *Liquid Crystalline Polymers*, Cambridge University Press, Cambridge, U.K (1992).
5. K. R. Osborn, and W. A. Jenkins, *Plastic Films Technology and Packaging Applications*, Technomic Publishing Co., Inc., Lancaster, PA (1992).
6. R. W. Lusignea, Film processing and applications for rigid-rod polymers, *Mat. Res. Soc. Symp. Proc.*, vol. 134, 265–276.
7. Y. Ide and Z. Ophir, *Polym. Engr. and Sci.*, 23, No. 5, 261–265 (1983).
8. Harvey et. al., U.S. Patent 5,288,529.
9. M. Meier, The Extrusion of Liquid Crystal Polymers, *SPE Symposium, ANTEC*, 200–202 (1989).
10. G. W. Farrell and J. F. Fellers, *J. Polym. Engr.*, 6, 263–289 (1986).
11. R. W. Lusignea, Extrusion of oriented LCP film and tubing, published in *Applications of High Temperature Polymers*, edited by R. R. Luise, pp. 25–40, CRC Press, Inc., New York (1997).
12. L. C. Sawyer, H. C. Linstid, and M. Romer, Emerging applications for neat LCPs, *Plastics Engineering*, December 1998, 37–41.
13. A. Kaslusky, Liquid crystal polymers, *Advanced Materials and Processes*, December 1993, pp. 38–41.
14. R. W. Lusignea, *Fabrication of LCP Tubing for Medical Applications*, Specialty Polyesters '95, Schotland Business Research, Brussels, pp. 71–82 (1995).
15. K. G. Blizard et al., *Polym. Engr. and Sci.*, 30, No. 22, 1442–1453 (1990).
16. K. G. Blizard et al., *ANTEC 1992*, pp. 2253–2256.

17. W. Chinsirikul, T. C. Hsu, and I. R. Harrison, Liquid crystalline polymer (LCP) reinforced polyethylene blend blown film: Effects of counter-rotating die on fiber orientation and film properties, *Polym. Engr. and Sci.*, vol. 36, No. 22, 2708–2717, November (1996).
18. Anon. Processing Vectra<sup>®</sup>, *Processing and Troubleshooting Guide (VC-6)*, Ticona (formerly Hoechst Technical Polymers), Summit, NJ.
19. R. Lusignea, J. Piche, and R. Mathisen, in *Polymeric Materials for Electronic Packaging and Interconnection*, ACS Symposium Series 407, pp. 446–455 (1989).
20. L. S. Rubin, K. Jayaraj, and J. M. Burnett, Liquid crystalline polymer multilayer printed circuit boards for controlled coefficient of thermal expansion, *Proceedings IEPS*, September (1991).
21. S. H. Rounsvelle, Liquid crystal polymer—An outstanding dielectric for high performance printed circuit boards, *Proceedings IPC*, October (1993).
22. T. E. Noll, K. Blizard, K. Jayaraj, and L. S. Rubin, Controlled thermal expansion printed wiring boards based on liquid crystal polymer dielectrics, *Proceedings IPC Technical Conference*, Boston, May (1994).
23. K. Jayaraj, T. E. Noll, and K. Blizard, Controlled thermal expansion printed wiring boards based on liquid crystal polymer dielectrics, *Circuit World*, vol. 22, No. 2, 25–30 (1996).
24. D. H. Weinkauff and D. R. Paul, in *Barrier Polymers and Structures*, ACS Symposium Series 423, 60–91 (1990).
25. D. H. Weinkauff and D. R. Paul, Gas transport in liquid crystalline polymers, published in *Liquid Crystalline Polymers*, edited by C. Carfagna, pp. 219–241, Elsevier Science, Inc., New York (1994).
26. R. J. Wright, Simplified absorbance test helps engineers select aroma barriers, *Packaging Technology and Engineering*, March, 16–19 (1999).
27. R. W. Lusignea and K. Bilzard, Processing and applications of liquid crystal polymers and blends, *Proceedings SAMPE*, 1048–1062, April (1994).
28. K. Jayaraj and T. E. Noll, Controlled thermal expansion PCBs, *Printed Circuit Fabrication*, vol. 19, No. 2, 24–41, February (1996).
29. Y. Tanaka, Liquid crystal polymer materials for LSI mounting, *Journal of Japanese Society for Electronics Mounting*, vol. 2, No. 2, March (1999).
30. Y. Tanaka, MCM designs using LCP materials, *IMAPS MCM Application Workshop*, Newport, RI, June 23–25.
31. R. W. Lusignea, Liquid crystal polymers: New Barrier Materials for Packaging, *Packaging Technology and Engineering*, vol. 6, No. 10, October (1997).
32. R. W. Lusignea, Flexible multilayer packaging with oriented LCP barriers, *TAPPI Polymers, Laminations and Coatings Conference*, San Francisco, CA, September (1998).
33. R. W. Lusignea, Coextrusion blow molding with LCP, *SPE ANTEC*, pp. 1034–1038, New York, NY, May (1999).
34. A. Garcia-Rejan, K. Y. Nguyen, W. Michaeli, L. Morich, G. Schmidt, and R. Lusignea, Injection stretch blow moulding of PET/LCP blends for better product performance, *SPE ANTEC*, pp. 1029–1033, New York, NY, May (1999).
35. F. P. LaMantia, *Thermotropic Liquid Crystal Polymer Blends*, Technomic Publishing, Co., Inc., Lancaster, PA (1993).
36. K. G. Blizard and R. R. Haghighat, Processing and properties of polyimide melt blends containing a thermotropic liquid crystalline polymer, *Polym. Engr. and Sci.*, vol. 33, No. 2, 1–9.
37. B. Scharfel and J. H. Wendorff, Molecular composites for molecular reinforcement: A promising concept between success and failure, *Polymer Engineering and Science*, vol. 39, No. 1, 128–151, January (1999).
38. D. G. Baird, S. S. Bafna, J. P. DeSouza, and T. Sun, Mechanical properties of in situ composites based on partially miscible blends of polyetherimide and liquid crystalline polymers, *Polymer Composites*, vol. 14, No. 3, 214–223, June (1993).

39. F. Qiao, K. Migler, and C. C. Han, In-line investigation of shear-induced morphology transition in liquid crystalline polymer/PET blends, *ANTEC '99*, Society of Plastics Engineers, 3911–3915.
40. T. Sun et al., In situ formation of thermoplastic composites Ultem/Vectra<sup>®</sup>, *J. Composite Mat.*, 25, 788–808, July (1991).
41. G. T. Pawlikowski et al., Molecular composites and self reinforced liquid crystalline polymer blends, *Annual Rev. Mat. Sci.*, 21:159–184 (1991).
42. D. M. Malik et al., Characteristics of liquid crystalline polymer polyester polycarbonate blends, *Polym. Engr. Sci.*, 29 (4):600 (1989).
43. A. M. Swkhadia et al., Characterization and processing of blends of polyethylene terephthalate with several liquid crystalline polymers, *ANTEC*, pp. 1847–1851 (1989).
44. R. W. Lusigne, K. Blizard, and R. Haghighat, Extrusion of high temperature thermoplastic liquid crystalline polymer microcomposites, *Ultralloy '90 Symposium*, Shotland Business Research, pp. 151–167 (1990).
45. D. J. Williams, *Technical and Commercial Issues Governing the Development of Thermotropic Liquid Crystal Polyesters (TLCPs) in the 1990s*, PST Group, Harvard, MA (1993).
46. M. S. Reisch, Advanced thermoplastics producers regroup, *Chem. and Engr. News*, 71 (35), 24–39 (1993).